NANOSTRUCTURES: PHYSICS AND TECHNOLOGY

20th International Symposium

Nizhny Novgorod, Russia, June 24–30, 2012

PROCEEDINGS

Academic University Publishing
St Petersburg, 2012

ISBN 978-5-91326-179-3

The International Symposium "Nanostructures: Physics and Technology" is held annually since 1993. The first Symposium was initiated by Prof. Zh. Alferov and Prof. L. Esaki who are its permanent co-chairs. More detailed information on the Symposium is presented on the World Wide Web **http://www.ioffe.ru/NANO2012/**

The Proceedings include extended abstracts of invited talks and contributed papers to be presented at the Symposium. By tradition this book is published before the beginning of the meeting.

The volume was composed at the St Petersburg Academic University from electronic files submitted by the authors. When necessary these files were converted into the Symposium style. Only minor technical corrections were made by the composers.

Design and layout: N. Vsesvetskii
Desk editor: E. Savostyanova

Published by
St Petersburg Academic University
Khlopin str. 8/3, 194021, St Petersburg, Russia
http://www.spbau.ru/

Printed in Russian Federation

The Symposium is held under the auspices of
the Russian Academy of Sciences

Organizers

St Petersburg Academic University — Nanotechnology Research and Education Centre of the RAS

Ioffe Physical-Technical Institute of the RAS

Submicron Heterostructures for Microelectronics Research and Engineering Center of the RAS

Foundation for Support of Education and Science (Alferov's Foundation)

in association with

Official partner — Foundation for Development of the Center of Research and Commercializing of New Technologies —Skolkovo Foundation

Official partner — SITRONICS Microelectronics

Official partner — Fund for Infrastructure and Educational Programs

Branch of Physical Sciences of the RAS

Branch of Nanotechnologies, Information and Computer Sciences of the RAS

Nizhny Novgorod Scientific Centre of the RAS

Ministry of Education and Science of the Republic of Tatarstan

Kazan Scientific Centre of the RAS

Lobachevsky State University of Nizhni Novgorod

Nizhny Novgorod City Administration

Saratov Scientific Centre of the RAS

Samara Scientific Centre of the RAS

St Petersburg Scientific Center of the RAS

Institute for Physics of Microstructures RAS

Acknowledgments

The Organizers gratefully acknowledge the following for their contribution to the success of the Symposium:

Russian Academy of Sciences

Russian Foundation for Basic Research

Optogan Group

Location and Date

Symposium is held in Nizhny Novgorod, Russia, June 24–30, 2012
and arranged as a river tour along the Volga
(Nizhny Novgorod–Kazan–Saratov–Samara)

Co-Chairs

Zh. Alferov
L. Esaki

Advisory Committee

G. Abstreiter (*Germany*)
Zh. Alferov (*Russia*)
Y. Arakawa (*Japan*)
A. Aseev (*Russia*)
G. Bastard (*France*)
D. Bimberg (*Germany*)
L. Eaves (*United Kingdom*)
L. Esaki (*Japan*)
S. Gaponov (*Russia*)
E. Gornik (*Austria*)
Yu. Gulyaev (*Russia*)
N. Holonyak, Jr. (*USA*)
L. Keldysh (*Russia*)
G. Landwehr (*Germany*)
J. Merz (*USA*)
M. Shur (*USA*)
M. Skolnick (*United Kingdom*)
R. Suris (*Russia*)
V.V. Ustinov (*Russia*)

Program Committee

R. Suris, Chair (*St Petersburg, Russia*)
V. Evtikhiev, Secretary (*St Petersburg, Russia*)

A. Andronov (*Nizhny Novgorod, Russia*)
N. Bert (*St Petersburg, Russia*)
C. Chang-Hasnain (*Berkeley, USA*)
A. Chaplik (*Novosibirsk, Russia*)
V. Dneprovskii (*Moscow, Russia*)
M. Dubina (*St Petersburg, Russia*)
V. Dubrovskii (*St Petersburg, Russia*)
A. Egorov (*St Petersburg, Russia*)
A. Gippius (*Moscow, Russia*)
S. Gurevich (*St Petersburg, Russia*)
S. Ivanov (*St Petersburg, Russia*)
P. Kop'ev (*St Petersburg, Russia*)
Z. Krasil'nik (*Nizhny Novgorod, Russia*)
V. Kulakovskii (*Chernogolovka, Russia*)
M. Kupriyanov (*Moscow, Russia*)
X. Marie (*Toulouse, France*)
I. Merkulov (*St Petersburg, Russia*)
V. Panov (*Moscow, Russia*)
O. Pchelyakov (*Novosibirsk, Russia*)
E. Poltoratskii (*Moscow, Russia*)
H. Sakaki (*Tokyo, Japan*)
N. Sibeldin (*Moscow, Russia*)
M. Stutzmann (*Garching, Germany*)
V. Timofeev (*Chernogolovka, Russia*)
V. Volkov (*Moscow, Russia*)
L. Vorobjev (*St Petersburg, Russia*)
V. M. Ustinov (*St Petersburg, Russia*)
A. Zhukov (*St Petersburg, Russia*)

Organizing Committee

M. Mizerov, Chair
(*Submicron Heterostructures for Microelectronics, Research & Engineering Center of the RAS*)
M. Sudenkova, Vice-Chair (*St Petersburg Academic University*)
E. Sibireva, Secretary (*St Petersburg Academic University*)
E. Chuprunov (*Lobachevsky State University of Nizhni Novgorod*)
A. Egorov (*St Petersburg Academic University*)
Y. Filimonov (*Kotelnikov Institute of Radio Engineering and Electronics RAS* (*Saratov Branch*))
A. Gilmutdinov (*Ministry of Education and Science of the Republic of Tatarstan*)
S. Gusev (*Ministry of Education and Science of the Republic of Tatarstan*)
Z. Krasil'nik (*Institute for Physics of Microstructures RAS*)
Yu. Lazarev (*Samara Scientific Centre of the RAS*)
R. Litvinov (*Institute for Physics of Microstructures RAS*)
E. Mozgovoy (*Foundation for Support of Education and Science* (*Alferov's Foundation*))
V. Popov (*Kotelnikov Institute of Radio Engineering and Electronics RAS* (*Saratov Branch*))
A. Rezchikov (*Saratov Scientific Centre of the RAS*)
I. Saunin (*Saratov Scientific Centre of the RAS*)
N. Sibeldin (*Branch of Physical Sciences of the RAS*)
V. Sokolov (*Samara Scientific Centre of the RAS*)

Contents

Plenary Session

Excitons in Nanostructures

Infrared and Microwave Phenomena in Nanostructures

Metal Nanostructures

Nanostructures and Life Sciences

Microcavity and Photonic Crystals

Nanostructure Devices

Nanostructure Characterization

Nanostructure Technology

Wide Band Gap Nanostructures

Spin Related Phenomena in Nanostructures

Quantum Wells and Quantum Dots

Si-Ge Based Nanostructures

Lasers and Optoelectronic Devices

Transport in Nanostructures

2D Electron Gas

Unprinted Papers

The papers listed below are included in the Symposium Program, but not printed in the Proceedings, as the authors had not submitted electronic files.

PS.04i *C. Weisbuch*
High extraction efficiency LEDs: photonic crystals vs. competition

PS.06i *G. Timp*
Using a nanopore for single molecule detection and single cell transfection

PS.08i *V. D. Kulakovskii*
Polarization multistability of the response of optically driven exciton polariton system in planar microcavities

EN.03o *A. Zvezdin*
Inverse transverse magneto-optical Kerr effect

IRMW.04i *V. I. Gavrilenko*
Terahertz response of narrow-gap HgTe/CdTe QWs

MN.03o N. V. Dmitrieva, *V. A. Lukshina*, E. G. Volkova, A. P. Potapov and B. N. Filippov
Nanocrystalline soft magnetic Fe-, Co-based alloys doped by Hf, Mo and Zr with enhanced thermal stability of magnetic properties

MN.05p *M. I. Petrov*, A. A. Lipovskii, O. V. Shustova and Yu. P. Svirko
Glass-metal nanocomposite based gratings

NLS.03o *A. S. Kamzin*
Bioactive calcium-phosphate ceramics with fine-grained magnet component

ND.01i *G. Eisenstein*
Ultrafast dynamics in semiconductor nano structure based optoelectronic devices

ND.05o *I. Shlimak*, A. Butenko, D. I. Golosov, K.-J. Friedland and S. V. Kravchenko
Influence of spin polarization on electron transport in two dimensions

NC.17p *Yu. N. Kulchin*
Photonics of heterogeneous liquid dielectric nanostructures

NC.19p *P. N. Shmakov*, A. P. Dmitriev and V. Yu. Kachorovskii
Current blockade in a disordered single-channel quantum ring

NT.13p *S. A. Gusev*
Complex nanolithography and study of properties metallic nanostructures

WBGN.04p S. V. Ryabtsev, N. M. A. Hadia, *E. P. Domashevskaya*, S. B. Kushev and S. A. Soldatenko
Wirelike SnO_2/In_2O_3 heterostructures and its crystallographic properties

SRPN.05o *K. A. Zvezdin*, A. D. Belanovsky, N. Locatelli, P. N. Skirdkov, F. Abreu Araujo, J. Grollier, V. Cros and A. K. Zvezdin
An efficient dipolar phase-locking of spin-torque vortex nano oscillators

QWQD.01i *Ze Don Kvon*
Topological insulators in HgTe quantum wells and films

20th Int. Symp. "Nanostructures: Physics and Technology"
Nizhny Novgorod, Russia, June 24–30, 2012

III–V and III-nitride nanowires for opto-electronic and energy applications

Lars Samuelson

Solid State Physics/Nanometer Structure Consortium at Lund University, Box 118, S-221 00 Lund, Sweden;
Sol Voltaics AB and Glo AB at Ideon Science Park

Semiconductor nanowires can today be grown with a high degree of perfection and can be turned into realistic devices using various methods for lithographic patterning as well as processing and contacting technologies. With III–V nanowires seen as an add-on technology to silicon, it is easy to see the potential for III–V nanwires enabling active elements for emission as well as detection of photons, in a "more than Moore"-fashion.

I will present the present degree of control of growth and top-down guided bottom-up, or self-assembly, or ideal arrays of designed nanowires. I will describe recently resolved details of how III-nitride nanowires nucleate and their growth is controlled in a one-dimensional nanowire fashion.

Finally, I will present recent progress in the field of state-of-the-art nanowire devices for conversion of sunlight into electricity, i.e. in solar cells, and for the opposite process for conversion of electrical energy into light, i.e. in light emitting diodes. In describing this I will also present a perspective on where these new technologies may lead for real-world applications also in the rather near future.

20th Int. Symp. "Nanostructures: Physics and Technology"
Nizhny Novgorod, Russia, June 24–30, 2012

Carbon nanotubes and nanostructures — multifunctional material for emission electronics

Yu. V. Gulyaev[1], A. N. Saurov[2], N. I. Sinitsyn[3], O. E. Gluhova[4], B. I. Gorfinkel[5], G. V. Torgashov[3] and V. P. Kudyashov[6]

[1] V.A. Kotelnikov Institute of Radioengineering and Electronics, RAS, Moscow, Russia
[2] Institute of Nanotechnology in Microelectronics, RAS, Moscow, Russia
[3] Saratov Division of IRE RAS, Saratov, Russia
[4] N.G. Chernyshevsky Saratov State University, Saratov, Russia
[5] Enterprise "Volga Light", Saratov, Russia
[6] Enterprise "Almaz", Saratov, Russia

Electron field emission from carbon nanotubes was first predicted and experimentally observed in 1993 in Saratov Division of the Institute of Radioengineering and Electronics of the Russian Academy of Sciences and presented at the 7th International conference on vacuum microelectronics (IVMC'94) in Grenoble [1,2]. Since that time many works gave been carried out both on the technologies of synthesizing of carbon nanotubes and nanostructures (plasmochemical and pyrolithic catalysis of carbon nanotubes (CNT), magnetronplasma sputtering of graphite, CVD synthesis of oriented arrays of CNT including separate CNT and matrices of them, creation of magnetofunctional CNT etc.), on investigations of their electronic properties including physics of emission and also on the thechnologies of creation of devices based on electron emission from carbon nanotubes and nanostructures including graphen (see review paper [3]). In this report the authors present the results of their investigations of electron emission from carbon nanotubes and nanostructures and some practical applications of these phenomena.

On the basis of quantum model of carbon nanotubes and nanostructures, including graphen, developed by the authors with the use of universal potential of strong binding it was first established that: 1) graphen ribbons are not destroyed even at compression by 30% with their electronic structures having quite small changes. This makes them a perspective material for flexible transparent electronics. At compression by 10% the work function of nanoribbon goes down by 0.1 eV; 2) the lowest work function 4.3 eV is reached for CNT with internal cross pieces, when the step of cross piece is 1.5 nm; 3) with the growth of electric field up to 8–9 V/nm the work function of CNT goes down by 0.05–0.1 eV. In the case of orientation of the axis of CNT or graphen sheet along the electric field the atomic structure becomes longer by 10–12%. For the first time the prognosis method for appearance of defects in atomic structure of CNT and graphen is developed based on the calculation of the chart of distribution of local stresses in atomic network. This method allows to establish the conditions and spatial regions of destruction of CNT during the process of electron autoemission.

In Saratov division of IRE RAS the autoemission cathodes on CNT are created for microwave devices of short-wave part of centimeter wave range. The technology of doping of CNT films in the process of their growth in plasma is developed. The emission current of such a films in DC operation reaches 2.5 A/cm^2 at the electric field 5–30 V/cm. The processing of CNT films by microwave plasma in oxygen atmosphere leads to the inversion of morphological shape of CNT with the creation of nanotubes of complex shape — bamboo like nanotubes, whose emission abilities are higher than of usual CNT. In the Institute of Nanotechnology in Microelectronics of RAS together with enterprises "Technology" and "Technological Center" the technology of CVD synthesis of oriented arrays and matrices of CNT is developed which allows to produce triode matrices for high power vacuum electronics. The auto electron emission cathode matrices are formed by electron beam lithography and nanoimprint lithography on the basis of CNT bunches grown up by CVD method. These matrices are investigated for stability of emission characteristics, for influence of various factors, for search of maximum emission current density etc. The use of auto emission cathodes on the basis of CNT allows creation of new colour displays. At the enterprise "Technological Center" there are created structurised arrays of CNT for the displays with luminescent screen. The brightness and other parameters of these screens are investigated in joint work with Bergische Universitat (Wuppertal, Germany). At the enterprise "Volga Light" jointly with partners from company "Copy Tele Inc".(USA) the new display type on CNT is developed. The auto emission cathode consists of the mixture of nanoparticles with carbon nanotubes and provides good performance at the voltages 70–80 V with operating voltage not more than 40 V. Here CNT and luminophore are spatially separated due to special technology of their deposition independently one from another.In monochrome mode of operation the brightness of the screen reaches 1000 Cd/m^2, the brightness of colour screen in white colour is about 250–300 Cd/m^2. For to increase brightness and provide uniform luminescence along the display the technology of reinforcement of electron emission from CNT is developed. Experimental specimens of TV displays using CNT electron emission cathode and luminescent screen show quite good performance.

In conclusion it is possible to say that CNT as the source of autoemission current are perspective for creation of a new generation of electron devices: cheap full-colour Field Emission Displays (FED) of high resolution, microwave devices of terahertz frequency range, cheap energy-saving and ecologically safe cathode-luminescent light sources with efficiency 40–80 lm/w and lifetime not less than 10000 hours, various sensors, etc.

References

[1] Yu. V. Gulyaev *et al*., *Revue Le Vide, Les Conches Minces, Supplement au No. 271-Mars-Avril (7-IVMConf., July 4–7, 1994, Grenoble, France)*, 322 (1994).
[2] Yu. V. Gulyaev *et al*., *Vac. Sci. and Technol. B.* **13**, 2, 1995.
[3] A. B. Eletsky, *Russ. Phys. Uspekhi* **49** 172, 402 (2002).

20th Int. Symp. "Nanostructures: Physics and Technology"
Nizhny Novgorod, Russia, June 24–30, 2012

Triplet superconductivity in superconductor/ferromagnet spin valve

I. A. Garifullin

Zavoisky Physical-Technical Institute, Kazan Scientific Center of Russian Academy of Sciences, 420029 Kazan, Russia

Abstract. Recent results of the author concerning the peculiarities of the mutual interaction of ferromagnetism and superconductivity in superconductor/ferromagnet thin film heterostructures are reviewed.

The antagonism of superconductivity (S) and ferromagnetism (F) consists of strong suppression of superconductivity by ferromagnetism because ferromagnetism requires parallel (P) and superconductivity requires antiparallel (AP) orientation of spins. The exchange splitting of the conduction band in strong ferromagnets which tends to align electron spins parallel is larger by orders of magnitude than the coupling energy for the AP alignment of the electron spins in the Cooper pairs in conventional superconductors. Therefore the singlet pairs with AP spins of electrons will be destroyed by the exchange field. For this reason the Cooper pairs can penetrate into an F-layer only over a small distance ξ_{F}. For pure Fe the value of ξ_{F} is less than 1 nm (see, e.g., [1]).

In this talk I will review our recent results concerning the first observation of full spin valve effect and its peculiarities. In the second part of talk I will present the evidence for triplet superconductivity in superconductor/ferromagnet spin valve.

The physical origin of the spin switch effect based on the S/F proximity effect relies on the idea to control the pair-breaking, and hence the superconducting (SC) transition temperature T_c, by manipulating the mutual orientation of the magnetizations of the F-layers in a heterostructure comprising, e.g., two F- and one S-layer in a certain combination. This is because the mean exchange field from two F-layers acting on Cooper pairs in the S-layer is smaller for the AP orientation of the magnetizations of these F-layers compared to the P case.

Recently we have studied the superconducting spin valve effect based on the superconductor/ferromagnet (S/F) proximity effect in the multilayer system CoO/Fe1/Cu/Fe2/In. We succeeded to observe the full effect which means the full transition from the normal into the superconducting state and vise versa by changing the mutual orientation of magnetizations of the iron F layers Fe1 and Fe2 [2]. Moreover we obtained that the value of the spin valve effect $\Delta T_c = T_c^{\mathrm{AP}} - T_c^{\mathrm{P}}$ (where T_c^{AP} and T_c^{P} are the superconducting transition temperatures for antiparallel (AP) and parallel (P) mutual orientations of magnetizations of the Fe1 and Fe2 layers respectively) oscillates with changing its sign when changing the thickness of the F layer Fe2 [3]. Comparison of the obtained experimental data with the recent theory [4] for the same construction shows that the interference of the pairing functions reflected from both surfaces of the Fe2 layer at the Fe2/In interface is responsible for the observed effect. At the same time theory [4] predicts that the existence of the triplet component of the S condensate with non-zero total spin leads to the anomaly in the superconducting transition temperature T_c in an intermediate mutual orientation of the magnetizations of Fe1 and Fe2 layers. As it was mentioned in [4] the T_c suppression in S/F systems takes place due to "leakage" of Cooper pairs into the F part. In this language the generation of the long-range triplet component opens up an additional channel for this "leakage", hence T_c is suppressed stronger.

In the second part of my talk I will present an experimental evidence for the occurrence of the long-range triplet component of the SC condensate in the multilayer spin-valve heterostructure CoO/Fe1/Cu/Fe2/Pb. It is manifested in a nonmonotonic behavior of the SC transition temperature T_c of the Pb layer upon gradual rotation of the magnetization of the ferromagnetic Fe1 layer $\boldsymbol{M}_{\mathrm{Fe1}}$ with respect to the magnetization of the Fe2 layer $\boldsymbol{M}_{\mathrm{Fe2}}$ from the parallel (P) to the antiparallel (AP) orientation. We observe [3] a clear minimum of T_c for the orthogonal configuration of $\boldsymbol{M}_{\mathrm{Fe1}}$ and $\boldsymbol{M}_{\mathrm{Fe2}}$. As follows from our analysis in the framework of the theory of the SC triplet spin valve [4] such minimum of T_c is a fingerprint of the spin triplet component generated by noncollinear magnetizations $\boldsymbol{M}_{\mathrm{Fe1}}$ and $\boldsymbol{M}_{\mathrm{Fe2}}$ [6].

References

[1] L. Lazar, K. Westerholt, H. Zabel, L. R. Tagirov, Yu. V. Goryunov, N. N. Garif'yanov and I.A. Garifullin, *Phys. Rev. B* **61**, 3711 (2000).

[2] P. V. Leksin, N. N. Garif'yanov, I. A. Garifullin, J. Schumann, H. Vinzelberg, V. Kataev, R. Klingeler, O. G. Schmidt, and B. Bc̈hner, *Appl. Phys. Lett.* **97**, 102505 (2010).

[3] P. V. Leksin, N. N. Garif'yanov, I. A. Garifullin, J. Schumann, V. Kataev, O. G. Schmidt, B. Büchner, *Phys. Rev. Lett.* **106**, 067005 (2011).

[4] Ya. V. Fominov, A. A. Golubov, T. Yu. Karminskaya, M. Yu. Kupriyanov, R. G. Deminov, and L. R. Tagirov, *Pis'ma v ZhETF* **91**, 329 (2010) [*JETP Lett.* **91**, 308 (2010)].

[5] P. V. Leksin, N. N. Garif'yanov, I. A. Garifullin, Ya. V. Fominov, J. Schumann, Y. Krupskaya, V. Kataev, O. G. Schmidt, B. Büchner, *Phys. Rev. Lett.* (submitted).

[6] A. F. Volkov, F. S. Bergeret, and K. B. Efetov, *Phys. Rev. Lett.* **90**, 117006 (2003).

20th Int. Symp. "Nanostructures: Physics and Technology"
Nizhny Novgorod, Russia, June 24–30, 2012

Optical control of spins in single and coupled self-assembled quantum dots

Gerhard Abstreiter

Walter Schottky Institut and Physik Department, Institute for Advanced Study,
TU München, 85748 Garching , Germany

I will discuss electro/optical measurements of spin lifetimes of electrons [1] and holes [2] as well as the control and readout of a single spin in self-assembled InGaAs quantum dots embedded in GaAs based diode structures [3,4,5]. In addition the asymmetric optical nuclear spin pumping in similar quantum dots [6] will be presented. Finally I will concentrate on recent results on the ultrafast preparation and manipulation of a single hole spin in coupled quantum dots [7].

References

[1] M. Kroutvar *et al*., *Nature* **432**, 81 (2004).
[2] D. Heiss *et al*., *Phys. Rev.* **B76**, 24136 (2007).
[3] D. Heiss *et al*., *Phys. Rev.* **B77**, 235442 (2008).
[4] D. Heiss *et al*., *Appl. Phys. Letters* **94**, 072108 (2009).
[5] D. Heiss *et al*., *Phys. Rev. B* **82**, 245316 (2010).
[6] F. Klotz *et al*., *Phys. Rev. B* **82**, 121307 (2010).
[7] K. Muller *et al*., *Phys. Rev. B* **84**, 081302 (2011) and *PRL* (2012), in press.

20th Int. Symp. "Nanostructures: Physics and Technology"
Nizhny Novgorod, Russia, June 24–30, 2012

Diffractive nanophotonics

Victor A. Soifer
Image Processing Systems Institute of the RAS, Samara, Russia

Abstract. The paper overviews new results relating to the following topics of diffractive nanophotonics: methods for the numerical solution of Maxwell's equations; optical trapping and micromanipulation; focusing elements and zone plates; photonic crystal structures; diffractive heterostructures in plasmonics; single-resonance diffraction gratings.

Introduction

Nanophotonics studies the interaction of light with particles or substance features whose size is smaller and much smaller than the incoming wavelength, as well as designing devices based on nansocale phenomena.

Among other topics, nanophotonics includes optics of photonic crystals and microstructured waveguides, plasmonics, near field microscopy, metamaterials, and optical micromanipulation.

Diffractive nanophotonics deals with processes and devices in which the wave properties of light come to the forefront. Diffractive nanophotonics is based on the assumption that the light behavior can be described using Maxwell's equations. It is important that characteristic features of the optical elements and diffractive structures should be essentially larger than the atomic size. This enables their optical properties to be described using macroscopic characteristics of permittivity and permeability (in terms of macroscopic electrodynamics). Thus, diffractive nanophotonics studies the diffraction of light by macroobjects with minimal features on the scale of tens of nanometers, down to quantum dots about 10 nm in size. Diffractive nanophotonics is based on solving the direct and inverse problems of the diffraction theory and synthesis of corresponding nanostructures using recording devices and diffractive microrelief fabrication procedures.

This work is based on the results obtained by the team of researchers of IPSI RAS.

1. Methods for numerical solution of Maxwell's equations

When addressing diffractive nanophotonics problems, the most efficient methods for the numerical solution of Maxwell's equations include:

Finite-Difference Time-Domain (FDTD) method for solving Maxwell's equation with regard to the time dependence. This is the most universal approach.

Finite Element Method (FEM) to calculate the diffraction of a monochromatic field, which is based on a piecewise constant approximation of amplitude for triangular grid domains and integral variational relations.

Fourier mode analysis (Rigorous Coupled Wave Analysis-

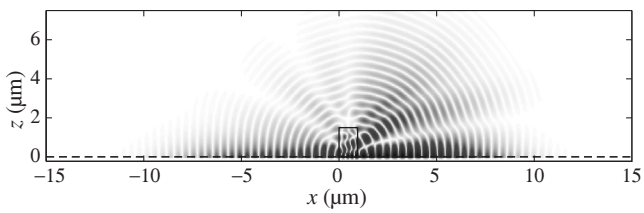

Fig. 1. A plasmon pulse is propagating through a dielectric step (the magnetic field amplitude distribution is shown). The dashed line shows the metal/dielectric interface.

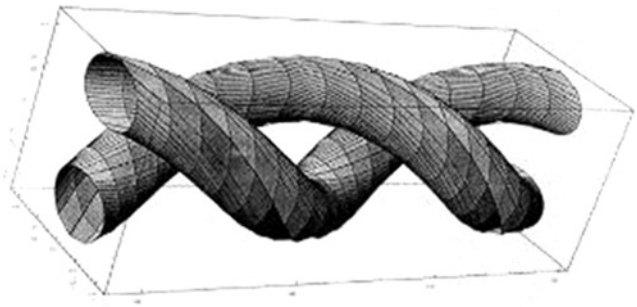

Fig. 2. Light pipes in a singular laser beam with angular orbital momentum, which is used to rotate microparticles.

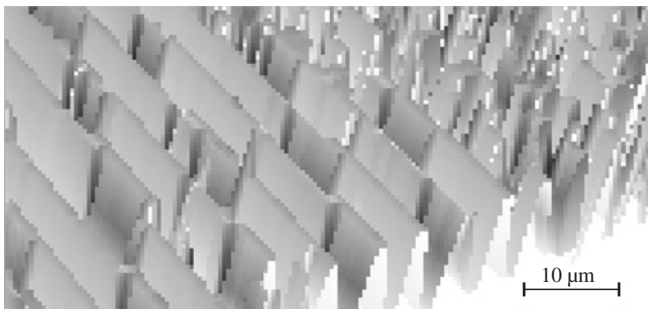

Fig. 3. The central region of a DOE microrelief to form a laser beam for micromanipulation.

RCWA) is best suited for the analysis of the diffraction of a monochromatic radiation by periodic binary structures. The continuous structure is broken down into a set of binary structures.

To illustrate the numerical solution of Maxwell's equations, consider the scattering of a surface plasmon pulse from a rectangular dielectric step found on a metallic surface along which the plasmon is propagating (Fig. 1).

The diffraction of surface plasmon-polaritons (SPP) and plasmon pulses is described in terms of Maxwell's equations. In this paper, the diffraction of the SPPs is simulated using the rigorous coupled wave analysis. In the classical definition, the method is intended to simulate the diffraction of a plane electromagnetic wave by a periodic structure. By artificially introducing periodic boundary conditions and absorbing layers, the method can be adapted to the analysis of diffraction of SPPs and plasmonic pulses. Figure 1 depicts an example of a simulated Gaussian 40-fs plasmon pulse centered at wavelength 800 nm in free space, diffracted by a dielectric step of length 950 nm and height 1.5 μm. The refractive index of the step is 1.7, the ambient dielectric is air, the metal is gold [1].

2. Optical trapping and micromanipulation

To solve the problem of optical trapping and micromanipulation, forces exerted on a dielectric microparticle in a laser beam have been analyzed. It has been proposed that the op-

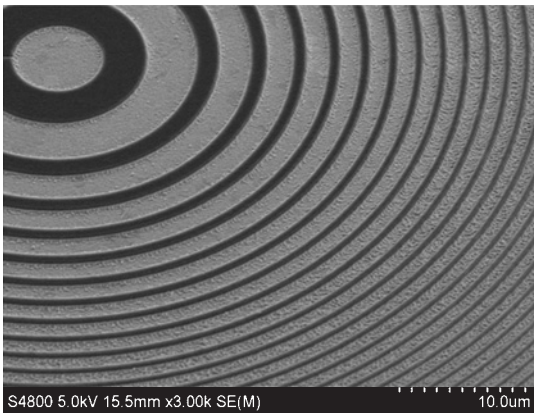

Fig. 4. An SEM image of the ZP obtained at an angle.

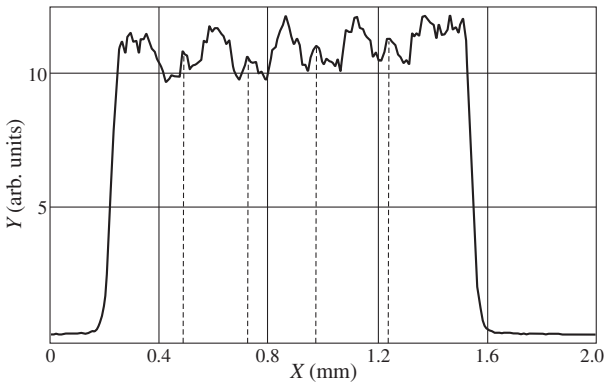

Fig. 5. The X-ray intensity profile at a distance of 60 mm from a four-ZP array.

tical trapping and micromanipulation should be implemented using singular laser beams generated with the aid of diffractive optical elements (DOEs) [2]. An example of light pipes formed as a result of propagation of the singular laser beam energy is shown in Fig. 2. Such laser beams possess an angular orbital momentum that can be partially transferred to a dielectric microparticle trapped in the beam.

Using the photolithographic technique, a binary DOE intended to form the said singular laser beam was fabricated (Fig. 3).

With the aid of DOEs fabricated with a high resolution of 0.5 μm, the problem of trapping and rotating a set of microparticles varying in size from 1 to 5 μm at a speed of 1–5 μm/s has been solved.

3. Focusing elements and zone plates

Focusing of light has been in the focus of our research activities for thirty years, starting with the pioneering work of 1981 [3]. An image of a zone plate (ZP) fragment generated by an electron microscope is shown in Fig. 4. The silver zone plate was fabricated on a membrane, having a diameter of 200 μm, the outermost zone of 287 nm, the microrelief depth of 460 nm, and focal length 250 mm, for hard X-rays of wavelength 2.29 Å (Cr) (quantum energy 5.4 keV). The estimated efficiency is about 3%.

Figure 5 depicts the intensity profile of X-ray radiation having passed through a sequence of four ZPs [4], with their coordinates found at the intersection of dashed lines with the 0X-axis. At the centers of four intensity dips, there are four local intensity peaks, which are produced by focusing of X-rays

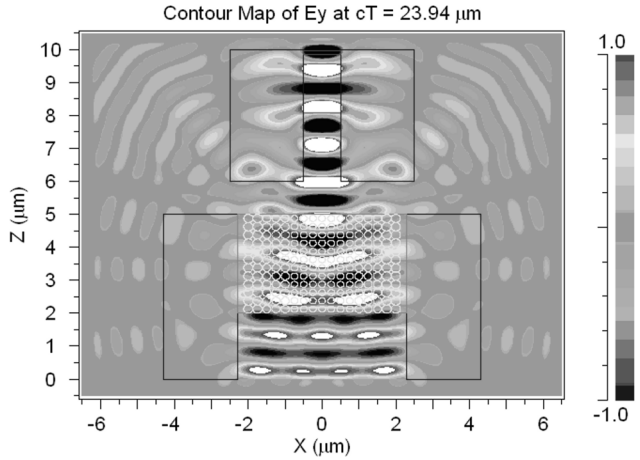

Fig. 6. Propagation of light through a pair of different-thickness waveguides coupled by a PhC lens.

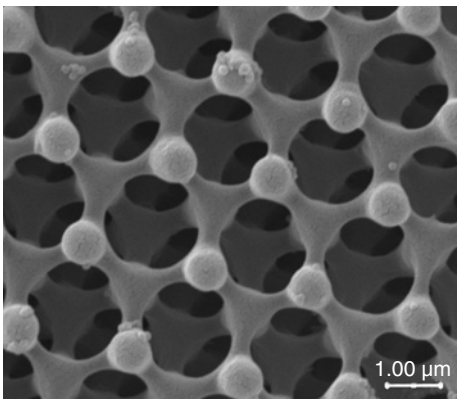

Fig. 7. A 3D PhC fragment of period 2.6 μm.

of wavelength 2.29 Å at a distance of 60 mm from the ZP.

4. Photonic crystal structures

Let us consider two photonic crystal structures. Figure 6 shows the result of light propagation through a photonic crystal (PhC) lens intended to couple two planar waveguides [5]. The simulation of a 2D PhC lens and two waveguides in a silicon film ($n = 2.83$) was conducted for the incident wavelength of 1.55 μm using the FDTD method. The nanohole diameters in the PhC lens were increasing from the axis toward the edges from 160 to 200 nm.

Another type of the structures under analysis is represented by 3D metal-dielectric photonic crystals (PhC) fabricated by the laser-interference lithography. Figure 7 shows an electron image of a 3D PhC containing a 50-nm golden layer coated on a polymer surface.

Figure 8 depicts the reflection spectra of a photonic crystal of period 2.6 μm: 1 — spectrum from the grazing incidence lens $15x$, 2 — spectrum from the IR Schwarzschild lens $15x$, 3 — reflection spectrum of the golden film coated on the photopolymer SU-8, 4 — reflection spectrum of the photonic crystal without golden film coating, 5 — reflection spectrum of the photonic crystal obtained by the finite-difference simulation. The results of spectrometry and the FDTD-aided numerical simulation show that there is a band gap at the wavelength equal to the photonic crystal grating period [6]. Local peaks found on curves 1 and 5 at the wavelength of 2.6 μm show that the PhC has a band gap.

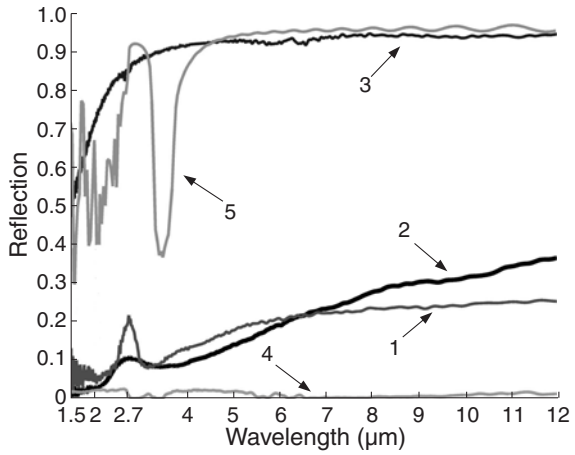

Fig. 8. Reflection spectra of the 3D PhC of period 2.6 μm.

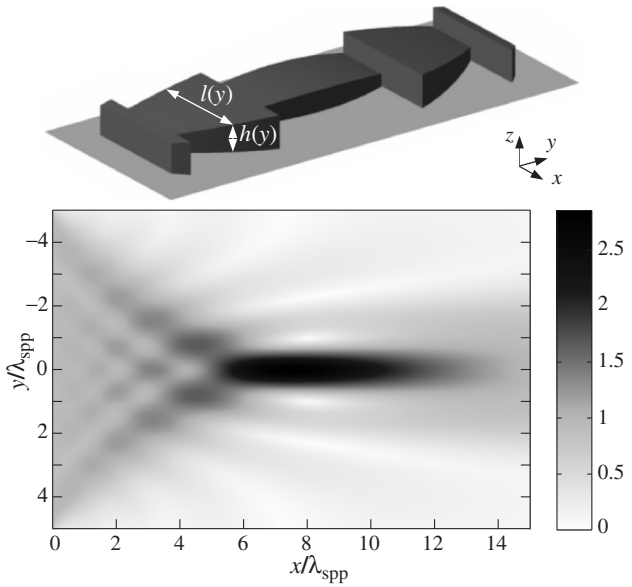

Fig. 9. Geometry of a plasmonic lens and the pattern of focusing surface plasmons.

5. Diffractive heterostructures in plasmonics

Of great significance in nanophotonics are diffractive nanostructures intended to focus surface plasmons. Figure 9 shows an example of a lens for surface electromagnetic waves with varying length and height [7]. The parameters are as follows: lens aperture is 10λ, focal length is 8λ, where $\lambda = 530$ nm is the wavelength of the plasmon. The diffraction efficiency is 79.4%. The lens length l and height h are varying in the range from 816 to 1675 nm and from 169 to 440 nm, respectively.

6. Single-resonance diffraction gratings

Although resonance diffraction gratings have been known for more than 100 years, but technological advances made in recent years in the synthesis of nanoscale structures open new prospects for their use in signal processing.

Based on the Fourier mode analysis, we have designed single-resonance diffraction gratings [8] (Fig. 10) for optical differentiation of picosecond optical pulses (Fig. 11).

The results reported in this work demonstrate that diffractive structures whose parameters have been derived by solving the inverse problem of the diffraction theory enable the creation of novel nanophotonics devices for solving topical applied problems.

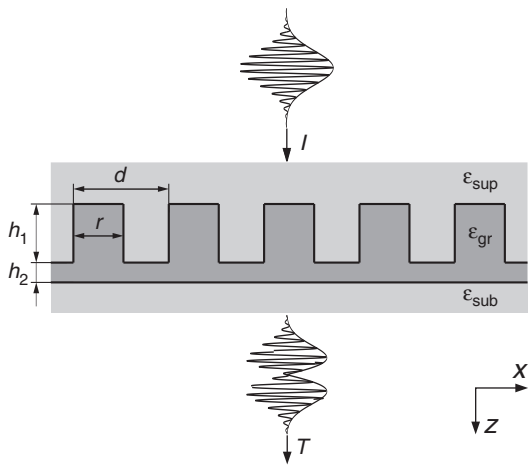

Fig. 10. An example of a diffraction grating for optical differentiation. Grating parameters: $\varepsilon_{gr} = 5.5$, $\varepsilon_{sup} = \varepsilon_{sub} = 2.1$, $d = 1010$ nm; $h_1 = 620$nm; $h_2 = 210$ nm; $r = 530$ nm.

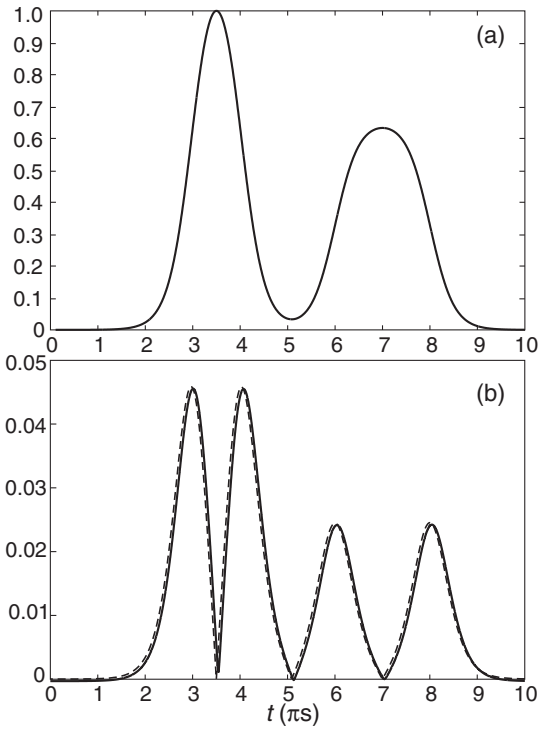

Fig. 11. (a) The envelope of a 10-ps incident pulse ($\lambda_0 = 1550$ nm); (b) the modulus of the transmitted pulse envelope and the modulus of the analytically calculated derivative of the incident pulse envelope (dotted line).

References

[1] *Appl. Phys. Lett.* **98 (22)**, 221108 (2011).
[2] Optical trapping and rotation of microobjects in the vortex laser beams // LAP Lambert Academic Publishing, Saarbrueken, Germany, 200 pp. (2011, in Russian).
[3] Focusing of coherent light into a designed space region using computer-generated holograms, *Letters to JTP* **7 (10)**, 618 (1981, in Russian).
[4] *Computer Optics* **36 (1)**, 65 (2012, in Russian).
[5] *Appl. Opt.* **48 (19)**, 3722 (2009).
[6] *Optics Communications* **284**, 5381 (2011).
[7] *Journal of Optics* **12**, 015001 (2010).
[8] *Optics Letters* **36 (11)**, 3509 (2011).

20th Int. Symp. "Nanostructures: Physics and Technology"
Nizhny Novgorod, Russia, June 24–30, 2012

Delay and distortion of light pulses by exciton resonances in wide-gap semiconductors

T. V. Shubina[1], N. A. Gippius[2], M. M. Glazov[1], A. A. Toropov[1], G. Pozina[3] and B. Monemar[3]

[1] Ioffe Physical-Technical Institute, St Petersburg, Russia
[2] A.M. Prokhorov General Physics Institute, RAS, 119991 Moscow, Russia
[3] Department of Phys., Chem. and Biology, Linköping University, S-581 83 Linköping, Sweden

Abstract. Propagation of light pulses in wide-gap semiconductors, GaN and ZnO, has been studied by time-of-flight spectroscopy. It has been demonstrated that significant light delay exists near an exciton resonance and that this delay is accompanied by pulse distortion and attenuation. Simulation of the pulse shape in the time-energy plane has permitted us to refine excitonic parameters inherent for bulk materials. The time-of-flight studies done over a wide temperature range demonstrate the strong influence of resonant scattering by phonons on the light delay in polar semiconductors.

Optical dispersion at exciton resonances in semiconductors results in a delay of light transfer, which is induced by the variation of the group velocity — a phenomenon studied long ago [1–3]. This delay has been observed by time-of-flight spectroscopy in different semiconductors [4–6]. The current interest in such retardation is enhanced because it is one of the ways to obtain the so-called "slow light", which is needed for optical communication and data processing. Wide-gap semiconductors, like ZnO and GaN, possess strong excitonic resonances that makes them suitable for such application. Light velocities as low as 6000 km/s in ZnO [4] and 2100 km/s in GaN [5] have been recently measured. In view of these findings, the distortion of a pulse shape has attracted special attention [7]. It is worth mentioning that early experiments showed no significant changes in the shape of a light pulse at the excitonic resonances in GaAs [8] and GaP [9], while the optical dispersion near the resonances implies a different group velocity and attenuation for the higher- and lower-energy edges of the pulses [10], that inevitably means their distortion in the time-energy plane. The optical pulse modification is also important for a set of optoelectronic devices — high-frequency ones or those, where the light should propagate a long distance. The frequency and threshold characteristics of such devices depend upon the mechanism of light transfer and on the modification of the light pulse in the vicinity of the excitonic resonances. Here, the results of recent studies of these phenomena in wide-gap semiconductors will be presented. Besides, the advantages of the time-of-fight spectroscopy to determine the excitonic parameters inherent for the bulk materials will be demonstrated.

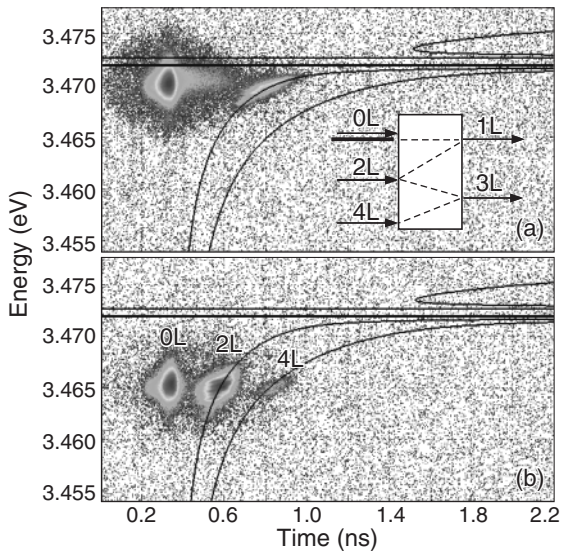

Fig. 1. Time-resolved images of light replicas recorded in a GaN crystal with L=1 mm with variation of the laser wavelength. The inset shows the scheme of the replicas formation. The solid lines are delay dependencies calculated for $2L$ and $4L$ replicas.

The time-of-flight experiments were performed using the pulses of tunable ps and fs lasers propagating through high-quality crystals of different thicknesses ($L = 0.3-2$ mm). The registration has been done using a Hamamatsu streak camera. The delay and distortion of the recorded pulses depict the optical dispersion in the medium. Their bending in the temporal domain evidences the strong variation of group velocity near the exciton resonances at low-temperatures (down to about $\sim$1% of the light velocity in vacuum). It takes place even across the spectral width of the ps pulses, which does not exceed 1–1.5 meV. The experiments have also revealed that the light transmitted through the GaN crystals contains both ballistic and diffusive components [5]. This hampers the analysis of the delay data. However, the time-resolved images recorded with high resolution contain weaker replicas, which appear due to the reflection of light pulses from the sample boundaries (Fig. 1). These reflexes propagate purely as exciton-polaritons without admixture of the diffusive component. Simulation of the delay and attenuation of the light replicas together with reflectivity and transmission spectra, measured in the same samples, have permitted us to determine the exciton oscillator strength and longitudinal-transverse splitting in high-quality GaN [11]. The obtained values (0.0022 ± 0.0002 and 0.85 ± 0.05 meV for A exciton, respectively) turn out to be somewhat less than those currently accepted.

ZnO differs from GaN by the presence of numerous lines of donor bound excitons which influence the complex dielectric function. The maximal delay of the higher-energy pulse edge registered in ZnO approaches 1.6 ns at 3.374 eV for $L = 0.3$ mm [12]. The time-resolved images demonstrate that the general curvature and pulse delay follows the optical dispersion controlled by the exciton-polariton resonances (Fig. 2). The influence of the bound excitons is local, namely, they provide dips cutting the pulses into several parts and induce extra light retardation nearby. To model the distortion of the pulse propagating through ZnO, the initial spectrum of the laser pulse is approximated as a Gaussian. The amplitude and

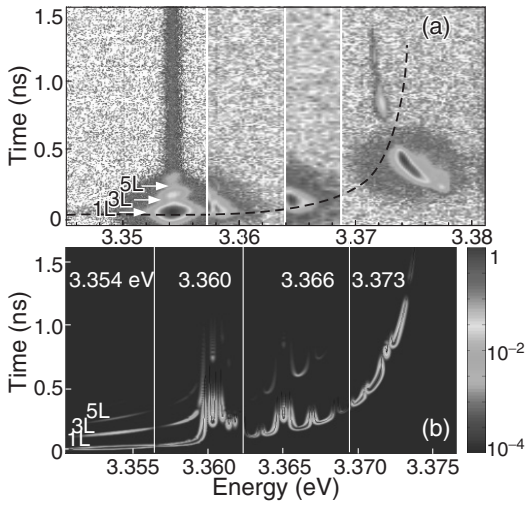

Fig. 2. (a) Combined experimental images of four pulses propagating through the 0.3 mm sample (logarithmic intensity scale). (b) Simulations of Gaussian light pulses of different energies propagating through the same sample using the Gabor transformation.

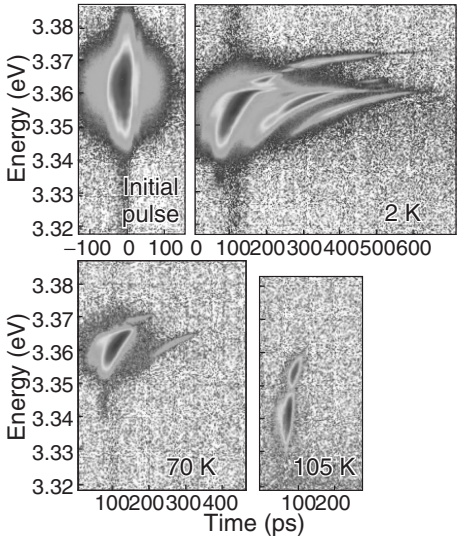

Fig. 3. Time-resolved images of a light pulse with a central energy of 3.364 eV transmitted through a 0.3 mm thick ZnO crystal at different temperatures.

phase of the pulse in the frequency domain are given by the Fourier transform at the boundary of the medium. The pulse shape at the output boundary is modeled assuming the linear regime of the light propagation and taking into account the light reflections from the crystal boundaries. The Gabor transformation has been used to reproduce the broadening induced by the experimental system.

Two severe limitations are discovered in this modeling: (i) The homogeneous width of these resonances must be as small as 3 μeV; (ii) the inhomogeneous width cannot exceed 0.5 meV for the A excitonic series. Otherwise, it would be not possible to observe the transmitted light up to 3.374 eV. It has been found that the oscillator strength of A and B exciton-polaritons is 0.0072 and 0.012, respectively. These parameters are obtained using exclusively the data on the processes taking place inside the crystal, namely, cw transmission and pulse propagation. As a result, they are different from those obtained from the surface-probing techniques, i.e. reflection and PL. This discrepancy suggests that a certain broadening of the excitonic resonances takes place at the crystal surface.

These studies have been performed at low temperatures, that limits the applicability of these results for quantum photonics and optoelectronics. Therefore, the time-of-flight studies of ZnO have been done over a wide temperature range. With a temperature rise, the free exciton resonances are shifted towards lower energies, following the band gap variation. A trivial result of that is the observed attenuation of the pulse, until its complete disappearance. What is more interesting, this shift promotes the resonant interaction of the exciton-polaritons with phonons, whose population increases with the rise of the temperature. Activated first, the acoustic phonons cause the appearance of a tail of scattered light, lower in energy than the initial pulse. At a further temperature increase, several well-separated replicas appear consistently due to scattering by optical phonons. The experiments were carried out up to room temperature by tuning the energy of the laser pulse and monitoring its quenching. Simulation of the pulse shapes has permitted us to derive the homogeneous width of the exciton-polaritons in ZnO, determined by the scattering cross-section dependent on temperature. The width, which equals 3 μeV at 2 K when the scattering by phonons is negligible, approaches 2–3 meV at 300 K. These values, being an order of magnitude smaller than those currently accepted, are well consistent with the theoretical estimation done taking into account the renormalization of the exciton-polariton homogeneous linewidth due to the interaction with optical and acoustical phonons. The output signal with ∼3.3-eV central energy of the impinging pulse, corresponding to the photoluminescence at the room temperature, is an exclusively scattered light for a 0.3-mm propagation length. The delay of this signal is small due to the high group velocity at the energy of the scattered photons.

In conclusion, the optical dispersion near exciton resonances in wide-gap semiconductors has been probed by time-of-flight spectroscopy via local distortion of the pulse shape at different energies. The parameters of exciton-polaritons, inherent for bulk materials, are derived from the simulation of the pulse shape in the time-energy plane. It has been found that the resonant scattering by phonons controls the light delay in polar semiconductors. These findings can be useful to design smart photonic devices.

Acknowledgements

This work has been supported in part by the RFBR grant 10-02-00633, Program of the Presidium of RAS, and EU project "Spinoptronics".

References

[1] L. Brillouin, *Wave Propagation and Group Velocity*(Academic, New York, 1960).
[2] R. Loudon, *J. Phys. A* **3**, 233 (1970).
[3] C. G. B. Garrett and D. E. McCumber, *Phys. Rev. A* **1**, 305 (1970).
[4] G. Xiong *et al*., *J. Phys.: Condens. Matter* **17**, 7287 (2005).
[5] T. V. Shubina *et al*., *Phys. Rev. Lett.* **100**, 087402 (2008).
[6] T. Godde *et al*., *Phys. Rev. B* **82**, 115332 (2010).
[7] D. S. Wiersma, *Nature* (London) **452**, 942 (2008).
[8] R. G. Ulbrich and G. W. Fehrenbach, *Phys. Rev. Lett.* **43**, 963 (1979).
[9] S. Chu and S. Wong, *Phys. Rev. Lett.* **48**, 738 (1982).
[10] L. A. Vainshtein, *Sov. Phys. Usp.* **19**, 189 (1976).
[11] T.V. Shubina *et al*., *Appl. Phys. Lett.* **99**, 101108 (2011).
[12] T.V. Shubina *et al*., *Phys. Rev. B* **84**, 075202 (2011).

20th Int. Symp. "Nanostructures: Physics and Technology"
Nizhny Novgorod, Russia, June 24–30, 2012

Electric generation of vortices in polariton superfluids

M. A. Kaliteevski[1,2], I. A. Shelykh[3], H. Flayac[4] and G. Pavlovic[5]

[1] Ioffe Physical-Technical Institute, St Petersburg, Russia
[2] St Petersburg Academic University, St Petersburg, Russia
[3] Science Institute, University of Iceland, Dunhagi-3, IS-107, Reykjavik, Iceland
[4] Institut Pascal, PHOTON-N2, Blaise Pascal University, CNRS,
24 avenue des Landais, FR-63177 Aubi'ere, France
[5] International Institute of Physics, Av. Odilon Gomes de Lima,
1722, CEP 59078-400 Capim Macio Natal, RN, Brazil

Abstract. We have theoretically demonstrated the on-demand electric generation of vortices in an exciton-polariton superfluid. Electric pulses applied to a horseshoe-shaped metallic mesa, deposited on top of the microcavity, generate a noncylindrically symmetric solitonic wave in the system. Breakdown of its wave front at focal points leads to the formation of vortex-antivortex pairs, which subsequently propagate in the superfluid. The trajectory of these vortex dipoles can be controlled by applying a voltage to additional electrodes. They can be confined within channels formed by metallic stripes and unbound by a wedged mesa giving birth to grey solitons. Finally, single static vortices can be generated using a single metallic plate configuration.

Elementary excitations in superfluid Bose–Einstein condensates (BECs) are quantum vortices, topological defects arising from the Onsager–Feynman quantization rule for the flow

$$m \oint \vec{v}\, d\vec{l} = nh\,.$$

Experimental investigations of the formation of vortices remain one of the topical issues in physics of cold atoms and condensate of exciton polaritons. Recently, optically exited vortices in polariton superfluid were demonstrated [1,2]. However, hybrid states of exciton polariton and Tamm plasmons [3] can be manipulated also by application of external electric field.

In this paper we propose another strategy for the generation of vortices in the polariton superfluid. Contrary to previous proposals, the vortices are not excited optically but electrically. The idea is based on the possibility of creating dynamical confining potentials for the particles, by deposition of metallic contacts on top of the sample [4] and by the application of short voltage impulses to them. For the description of the dynamics of the system, we have used the standard Gross–Pitaevskii equation1 for the macroscopic wave function of the condensate [5].

The temporal distortion of the potential under curved contact lead to a formation of a local nonadiabatic perturbation of the condensate, which generates a noncylindrically symmetric solitonic density wave. The wave converges and in the point of focus wave collapse allowing the nucleation of a vortex-antivortex pair (VAP) propagating along the axis of symmetry of the system, as shown in Fig. 2. The vortices are evidenced by the vanishing density at their core, visible in the color map; the characteristic velocity field tangent to them is seen in panel (b), and the winding of the phase in the anticlockwise (vortex $l = +1$) and clockwise (antivortex $l = -1$) direction around their core is seen in panel (c). The distance separating the vortex and antivortex in the pair related to their speed of propagation depends on the size of the contact, on the applied voltage, and on the concentration of the polariton superfluid. The trajectory of these vortex dipoles can be controlled by applying an electric field in the plane of a microcavity. They can be confined within channels formed by metallic stripes.

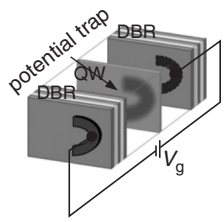

Fig. 1. Vortex gun: microcavity with a metallic contact deposited on top of its DBRs. The metal creates a local potential trap for polaritons. The application of a time-dependent voltage $Vg\kappa$ makes it possible to increase temporally the depth of the trap toward the generation of VAPs.

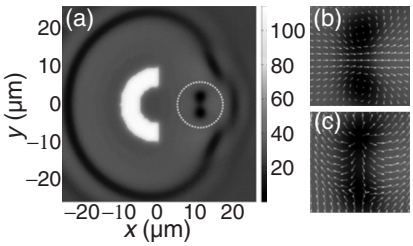

Fig. 2. VAP nucleated by the application of a voltage impulse resulting in a potential well of amplitude 1.5 meV and duration 5 ps to the horseshoe contact. (a) Density $n(x, y)$ (μm-2) of the condensate, 20 ps after the pulse. One clearly sees the solitonic density wave pro-pagating away from the contact (dark regions) and the single VAP (dashed white circle). (b) Velocity field of the condensate. (c) Phase vector field ($\cos\varphi$, $\sin\varphi$).

Propagating VAP can be unbound by a wedged mesa giving birth toso called "grey solitons" [6] (Figure 3). As shown in Figure 3e the phase of the condensate is roughly shifted by $\pi/2$ through the low-density (dark) region, which is characteristic for a gray soliton.

Finally, single static vortices can be generated using a single metallic plate configuration, as shown in Figure 4. After the application of a short electric pulse to the plate, a "lasso" shaped wave is excited. similarly to the one observed in Fig. 2a. Its shape is imposed by the rectangular geometry of the plate and

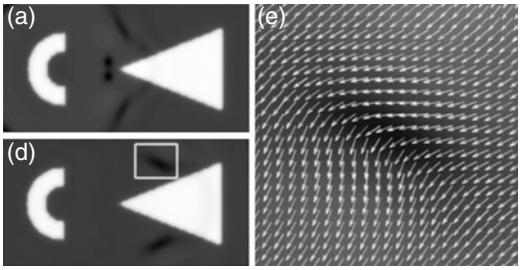

Fig. 3. Splitting of VAP on a metallic wedge. (a,d) Superfluid density at times 10 and 20 ps after VAP creation. The decomposition of a VAP into a pair of pseudotopological excitations propagating along the upper and lower sides of the triangle is evidenced. (e) Phase vector field of the upper topological excitation highlighted by the white square in (d).

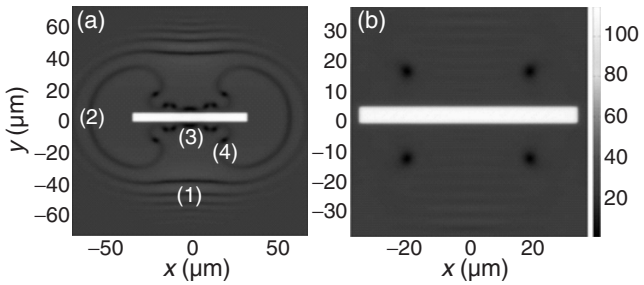

Fig. 4. Generation of single vortices. (a) Superuid density 30 ps after the pulse which exhibit several features: (1) dispersive shock waves, (2) "lasso" soliton broken in (3) VAPs and (4) single vortices. (b) At 80 ps the VAPs have vanished and 4 single vortices remain stable locked there initial position.

is consequently strongly noncylindrical. As a result the wave is unstable and breaks into two types of excitations. VAPs appear and are expelled toward the plate, where they are merged by the high density that reigns, generating phononlike excitations. In addition, stable single noninteracting vortices are generated at each edge of the plate, as shown in Fig. 4b. They remain pinned at their nucleation position.

References

[1] G. Nardin, G. Grosso, Y. Leger *et al*., *Nature Physics* **7**, 635 (2011).
[2] D. Sanvitto Pigeon, S. Pigeon, A. Amo *et al*., *Nature Photonics* **5**, 610 (2011).
[3] M. Kaliteevski, I. Iorsh, S. Brand *et al*., *Phys. Rev. B* **76**, 165415 (2007).
[4] M. Kaliteevski, S. Brand, R. A. Abram *et al*., *Appl. Phys. Lett.* **95(25)** 251108 (2009).
[5] H. Flayac, G. Pavlovic, M. A. Kaliteevski *et al*., *Phys. Rev. B*. **85**, 075312 (2012).
[6] C. A. Jones and P. H. Roberts, *J. Phys. A* **15**, 2599 (1982).

20th Int. Symp. "Nanostructures: Physics and Technology"
Nizhny Novgorod, Russia, June 24–30, 2012

Laterally confined photonic Tamm states and quantum light sources

O. Gazzano[1], S. Michaelis de Vasconcellos[1], A. Lemaître[1], K. Gauthron[1], J. Bloch[1], C. Symonds[2], J. Bellessa[2], *P. Voisin*[1] and P. Senellart[1]

[1] Laboratoire de Photonique et Nanostructures, CNRS, Marcoussis, France
[2] Laboratoire de Physique de la Matière Condensée et Nanostructures, Uni. Lyon 1 and CNRS, Villeurbanne, France

Abstract. Photonic Tamm states are strongly localized optical modes formed due to the specific boundary conditions for the electro-magnetic field at the interface between a periodic stack of dielectric materials (a Bragg mirror) and a metallic layer. They are an electromagnetic analog to the electronic Tamm states formed at the interface between a crystalline solid and vacuum. When the lateral size of the metallic layer is reduced, efficient 3 D confinement of light is obtained. We investigate this new type of "hybrid" metal-semiconductor microcavities and demonstrate their potential by fabricating and characterizing a single photon source.

Introduction

Photonic Tamm states (PTS) are strongly localized optical modes formed due to the specific boundary conditions for the electro-magnetic field at the interface between a periodic stack of dielectric materials (a Bragg mirror) and a metallic layer [1]. They are an electromagnetic analog to the electronic Tamm states [2–4] formed at the interface between a crystalline solid and vacuum. When the lateral size of the metallic layer is reduced, efficient 3D confinement of light is obtained. In spite of absorption in the metal, the quality factor of these original microcavities can be large enough (>1000) for cavity quantum electrodynamics applications. Mode geometry and radiative pattern are similar to those in a Bragg-mirror micropillar cavity of identical size. Compared to alternative solutions such as photonic crystal or micropillar cavities, PTS cavities are considerably easier to fabricate and allow natural coupling to an electrical circuit for current injection or detection, or for electrical fine-tuning. We investigate these new "hybrid" metal-semiconductor microcavities and demonstrate their potential by fabricating a single photon source formed by a single quantum dot deterministically coupled to a PTS cavity [5]. A most intriguing result is the huge inhibition of spontaneous emission for a quantum emitter spatially matched but spectrally detuned from the PTS.

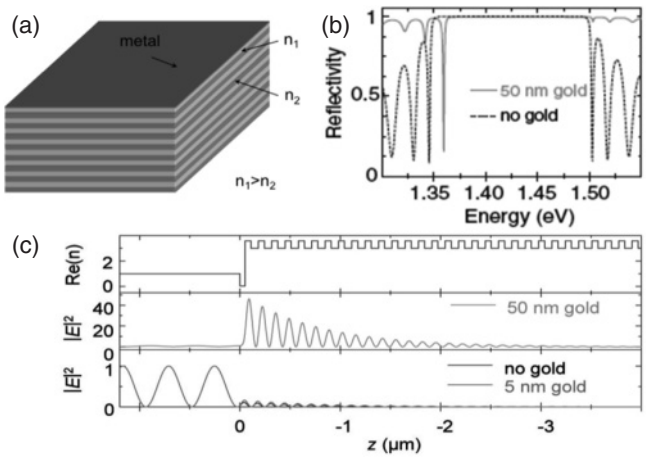

Fig. 1. (a) Structure sustaining a 2D photonic Tamm state; (b) alculated reflectivity spectra without and with a gold layer; (c) real part of the refractive index and electric field intensity at $E = 1.359$ eV, with or without a gold layer.

1. Photonic Tamm state and its lateral confinement

A sketch of the structure supporting a 2D-PTS is shown in Fig. 1a, while Fig. 1b presents the calculated reflectivity of a 40 pair $\lambda/4$ GaAs/AlAs DBR without and with a 50 nm thick gold layer on top, for light propagating along z. Without the gold layer, the mirror stop band is centered at the design energy $E_0 = 1.42$ eV. When the gold layer is added, the PTS appears as a dip in the reflectivity at $E = 1.359$ eV. Figure 1c presents the spatial distribution of the mode intensity along z for $E = 1.359$ eV. The optical field maximum is located 40 nm below the metal interface and decays rapidly in the DBR. The small penetration of the optical field into the metal prevents Joule dissipation to broaden the PTS dispersion, yielding cavity quality factors up to $Q = 1200$. Since PTS does not exist in absence of the gold layer, it can be confined laterally by simply reducing the size of the metallic layer. This leads to the appareance of 0D confined modes whose spectral spacing increases when the gold disc diameter decreases. The investigated structure consists in a 50 nm thick gold microdisk on top of a DBR. Numerical calculations of the modes using FDTD evidence strong lateral confinement under the disk area. To experimentally probe these confined or 0D-PTS, we use a GaAs/AlAs Bragg mirror embedding a dense layer of quantum dots (QD) located 40 nm below the surface. This QD layer acts as an inner source of quasi-white light shining the available photonic modes. Features of measured emission are illustrated in Fig. 2. Quality factor decreases with diameter due to diffraction by disc edges, but still amounts to 490 for $d = 2.5$ μm.

2. Full control of spontaneous emission

Next, we fabricate a source of single photons by deterministically coupling a single QD to a 0D-PTS. QDs are good sources of single photons, but quasi-isotropic emission and high refractive contrast lead to collection efficiency around 1% for QDs in a bulk material. Collection efficiency is improved when QD is coupled to a microcavity: the radiative emission into the confined mode is accelerated by a "Purcell factor" F_p proportional to Q/V where V and Q are the mode effective volume and quality factor. Acceleration of emission leads to a fraction of the QD emission into the mode given by $\eta = F_\mathrm{p}/(F_\mathrm{p} + \gamma)$ where γ is the ratio of the emission rate in all other optical modes to the emission rate in the bulk material. To fabricate the single photon source, we use a sample with a low density QD layer. We use the in-situ lithography technique and

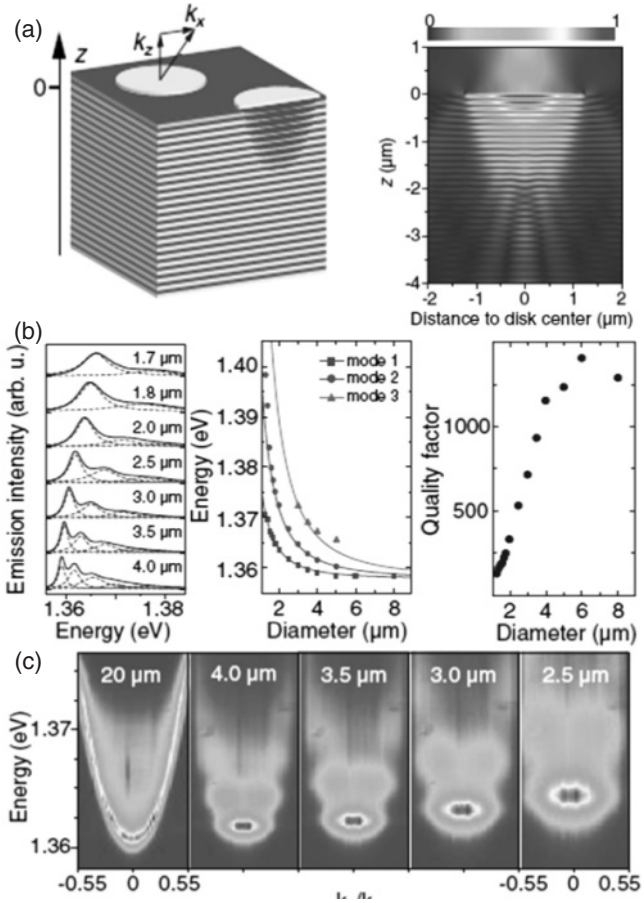

Fig. 2. (a) Structure of investigated structure and FDTD calculation of the 0D-PTS; (b) emission spectra, mode energies and quality factors for various gold microdisc diameters; (c) corresponding radiation patterns.

define a 45 nm thick gold disk with its centre located near a chosen QD. In practice, we chose a couple of slightly detuned QDs, spatially separated by approximately 300 nm, and centered the gold disc at mid-distance between QD1 and QD2, as shown in Fig. 3a. The exciton (X) lines of both QDs were identified during the in-situ lithography step. As shown in Fig. 3b, the QD2 excitonic transition (X_{QD2}) energy is 6 meV below the X_{QD1} line. Other lines emerging from QD1 are observed and identified by power dependence and photon correlation spectroscopy: the biexciton XX_{QD1} and the charged exciton CX_{QD1} lines. The disk diameter of 2.5 μm is such that the 0D-PTS is resonant with the X_{QD1} exciton at 40 K whereas X_{QD2} is strongly detuned. To monitor the modification of spontaneous emission induced by the PTS, we measure the radiative lifetime of the lines X_{QD1} and X_{QD2} as well as the radiative lifetime of several QDs coupled to a 2D-PTS (see Fig. 3c). Lifetimes are measured using laser/signal correlation spectroscopy. Whereas similar QDs in bulk GaAs present radiative decays of 1.3 ns, the lifetimes of the QDs coupled to the 2D-PTS present decays around $t_{Xref} = 2.5$ ns. This moderate inhibition of spontaneous emission corresponds to expectation for QDs 40 nm away from a gold interface, in the band gap of a DBR [6]. Conversely, the lifetime of the X_{QD1} line in resonance to the 0D-PTS is shortened to $t_{XQD1} = 400$ ps. This corresponds to an acceleration of spontaneous emission by a Purcell factor $F_p = 2.8$, close to the expected value $F_p = 2.9$, calculated for $Q = 490$ and considering that the effective volume of the 0D TP mode amounts to 40% of the mode volume of a pillar microcavity with equal diameter. Very strikingly, the radiative decay time measured for X_{QD2} at 10 K is as long as $t_{XQD2} = 52$ ns, evidencing a strong inhibition of spontaneous emission for this QD line. This strong inhibition of spontaneous emission is also observed on other lines like XX_{QD1} (17 ns) and on other devices. It is mostly governed (for QDs spatially matched with the PTS) by the detuning (towards low energies) between QD emission line and fundamental 0D PTS. The theoretical understanding and modeling of this remarkable inhibition is by no way trivial, and is a matter of current research [7]. The single photon emission is characterized using the classical Handburry–Brown and Twiss correlation set-up. Exciton auto-correlation function $g^2(\tau)$ under pulsed excitation shows strong antibunching at zero delay, with measured value $g^2(0) = 0.35 \pm 0.1$. From careful calibration of the set-up, we obtain at saturating power a collection efficiency in a 0.5 numerical aperture equal to 0.2. This value is strongly limited by the diffraction losses causing the low quality factor for small cavity diameters. We anticipate that using a gold disc diameter of 4 μm would allow a collection efficiency of at least 0.6, close to record values. Finally, we point that the strong inhibition of bi-exciton recombination is a drawback for the device performance, since it severely limits the saturation power. This problem would be easily solved by designing a molecular PTS with bonding and anti-bonding modes adjusted to accelerate simultaneously X and XX recombinations.

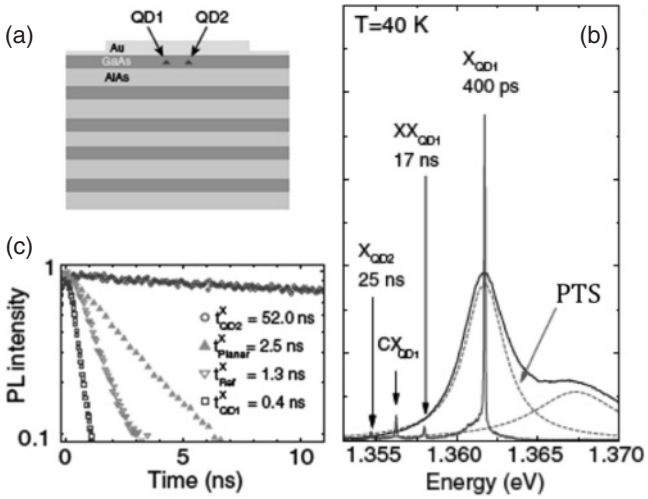

Fig. 3. (a) Scheme of investigated structure; (b) dot emission spectrum together with mode lineshape at 40 K and (c) measured time decay of some QD lines in different devices and conditions.

Acknowledgements
This work was partially supported by French ANR P3N DELIGHT and ERC starting grant 277885 QD-CQED. O.G. is supported by French Délégation Générale de l'Armement.

References

[1] M. Kaliteevski *et al.*, *Phys. Rev.* **B76**, 165415 (2007).
[2] I. E. Tamm, *Zh. Eksp. Teor. Fiz.* **34**, (1933).
[3] J. Bleuse *et al.*, *Appl. Phys. Lett.* **52**, 462 (1988).
[4] H. Ohno *et al.*, *Phys. Rev. Lett.* **64**, 2555 (1990).
[5] O. Gazzano *et al.*, *Phys. Rev. Lett.* **107**, 247402 (2011).
[6] I. Abram *et al.*, *IEEE J. Quantum Electronics* **34**, 71 (1998).
[7] J. P. Hugonin and J. J. Greffet, unpublished results.

20th Int. Symp. "Nanostructures: Physics and Technology"
Nizhny Novgorod, Russia, June 24–30, 2012

Excited states of spatially-indirect Coulomb complexes

M. A. Semina and R. A. Suris
Ioffe Physical-Technical Institute, St Petersburg, Russia

Abstract. The energy-level structure of spatially indirect Coulomb complexes is investigated. Two limiting cases that correspond to the two-dimensional hydrogen atom and planar isotropic harmonic oscillator characterized by high "accidental" degeneracy are considered. Numerical calculations are used to trace the evolution of the energy-level structure between these two limiting cases.

Introduction

An attractive feature of nanoscale semiconductor structures is that they can be used to model a broad range of quantum-mechanical systems. Indeed, almost any potential profile can be built into a semiconductor by means of modern technology and to model experimentally the solution of the corresponding quantum mechanical problem experimentally. A problem of a particle in a potential field $V(\mathbf{r}) \propto -1/r$, where r is the distance to the origin, is well known. In semiconductor structures, problems of this kind include, e.g., finding the energy levels of a donor impurity or an exciton. The specific feature of the Coulomb potential is the accidental degeneracy of energy levels, i.e., the degeneracy irrelated with the spatial symmetry. It is caused by the special symmetry of the Hamiltonian itself which commutes with the Laplace–Runge–Lenz operator [1,2]:

$$\widehat{\mathbf{A}} = (\widehat{\mathbf{p}} \times \widehat{\mathbf{L}} - \widehat{\mathbf{L}} \times \widehat{\mathbf{p}}) - \frac{2me^2}{r}\,\mathbf{r}\,, \qquad (1)$$

Here, $\widehat{\mathbf{p}}$ and $\widehat{\mathbf{L}}$ are the momentum and angular momentum operators, respectively; and e and m are the charge and mass, respectively.

Another special potential is that of an isotropic harmonic oscillator, $V(\mathbf{r}) \propto r^2$. In this case, there is also a non-trivial tensor operator that commutes with the Hamiltonian [3]:

$$\widehat{A}_{ij} = \left(\widehat{p}_i \widehat{p}_j + m^2\omega^2 x_i x_j\right)/2m\,, \qquad i, j = x, y, z\,. \qquad (2)$$

Here, $\widehat{p}_i$ are the components of the momentum operator and ω is the oscillator frequency. The harmonic potential also demonstrate an accidental degeneracy, but the multiplicity is different. It is known from classical mechanics that the Coulomb and harmonic potentials are the only spherically symmetric potentials for which all trajectories corresponding to bound states are closed.

It is interesting to study a real system in which variations in the parameters results in the evolution of the potential from the Coulomb to the isotropic harmonic oscillator potential and analyze how the degeneracies of the levels change between these two limits. While simple system with these properties can hardly be realized in a bulk semiconductor, it can be easily engineered in low-dimensional system. Hereinafter consider an electron in a thin quantum well bound to a donor located in the barrier. This complex naturally appears in δ-doped structures when the dopant atoms are located in the barrier. The interaction potential between the electron and charged center is $V(\rho) \propto (\rho^2 + D^2)^{-1/2}$, where ρ is the electron coordinate in the quantum well plane and D is the spacing between the donor and quantum well. With variations of D, which is the only parameter of the problem, potential changes from the two dimensional (2D) Coulomb potential (donor at the center of the well) to the potential of a planar harmonic oscillator (donor deep inside the barrier). Note, that another suitable system of this kind is a structure with two quantum wells where a spatially indirect exciton, which consists of an electron in one well and a hole in the other, is excited. Here, the parameter that governs the transition between the two limits is the spacing between the quantum wells.

We set the bulk Rydberg $Ry = m_e e^4/2\varepsilon^2\hbar^2$ and Bohr radius $a_B = \hbar^2\varepsilon/m_e e^2$ as the units of energy and length, respectively. In the model of simple bands, the Hamiltonian can be written as follows:

$$\widehat{H} = -\Delta - 2\left(\rho^2 + d^2\right)^{-1/2}\,. \qquad (3)$$

Here, Δ is the 2D Laplace operator acting on the electron coordinates, $\boldsymbol{\rho}$ is the electron radius vector in the plane of the quantum well, d is the dimensionless spacing between the donor and quantum well. In order to obtain the Hamiltonian for the indirect exciton problem, one needs to replace the electron radius vector, $\boldsymbol{\rho}$, by the electron and hole relative coordinate and the electron mass, m_e, by reduced mass.

In the limiting case $d \to 0$ the asymptotic expression for the interaction potential is

$$-2\left(\rho^2 + d^2\right)^{-1/2} \approx -2/\rho\,, \qquad (4)$$

and Hamiltonian (3) corresponds to the 2D hydrogen atom. In the opposite, $d \to \infty$, the asymptotic is

$$-2\left(\rho^2 + d^2\right)^{-1/2} \approx -2/d + \rho^2 d^{-3}\,, \qquad (5)$$

and Hamiltonian (3) corresponds to 2D isotropic harmonic oscillator with the stiffness $\kappa = 2d^{-3/2}$. Thus, a structure of the same type can be used to model both the 2D hydrogen atom and planar harmonic oscillator.

1. Limiting case of two dimensional hydrogen atom

The energy levels of the 2D hydrogen atom are [4]:

$$E_n = -\,(n + 1/2)^{-2}\,, \qquad (6)$$

where $n = 0, 1, 2\ldots$ is the principal quantum number. The nth level is $(2n + 1)$-fold degenerate with respect to the magnetic quantum number, m, which varies from $-n$ to n. The degeneracy is accidental, similarly to the bulk hydrogen atom. The following dimensionless operator, which commutes with Hamiltonian (3) for $d = 0$, is an analogue of the Laplace–Runge–Lenz operator for the 2D problem [4]:

$$\widehat{\mathbf{A}} = (\widehat{\mathbf{p}} \times \widehat{\mathbf{L}}_z - \widehat{\mathbf{L}}_z \times \widehat{\mathbf{p}}) - \frac{2}{\rho}\boldsymbol{\rho}\,, \qquad (7)$$

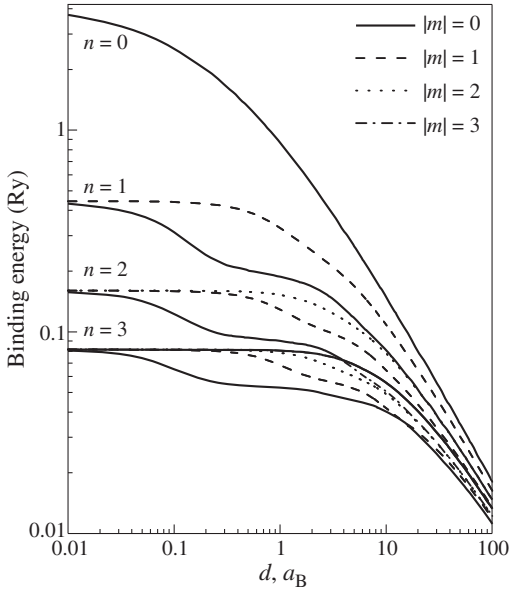

Fig. 1. Exciton binding energy versus the layer spacing d Lines correspond to the four lowest levels in the limiting case $d \to 0$.

where $\widehat{\mathbf{L}}_z$ is the dimensionless operator of the z-component of the angular momentum. For $d \neq 0$, the accidental degeneracy is lifted and there is only degeneracy originating from the axial symmetry of the problem: the energy levels of the states with the same $|m|$ and n coincide.

2. Limiting case of the harmonic oscillator

In the limit of large d the energy eigenvalues are

$$E_p = -2/d + (p+1)d^{-3/2}\,, \tag{8}$$

where $p = 0, 1, 2\ldots$ is the principal quantum number. The pth level is $(p+1)$-fold degenerate. Accidental degeneracy, that appears in this limit, is related to the existence of an operator that commutes with Hamiltonian [5]:

$$S_x = p_x p_y + xyd^{-3}, \quad S_y = \frac{p_y^2 - p_x^2}{2} + \frac{y^2 - x^2}{2d^3}, \tag{9}$$

where x and y are the electron coordinates and p_x and p_y are the corresponding components of the momentum. They are related with the operator (2) as follows:

$$S_x = \left(A_{xy} + A_{yx}\right)/2\,, \qquad S_y = (A_{yy} - A_{xx})/2\,. \tag{10}$$

3. Numerical calculation

Numerical calculations [6] were carried out to illustrate the transformation of the energy levels from one system of accidentally degenerate levels to the other one across the intermediate region where, in addition to the splitting of the energy levels, mixing of states with different principal quantum numbers is important. The binding energies of the states corresponding to the four lowest levels in the limit $d = 0$ are plotted in Fig. 1 as functions of d. For $d \neq 0$ these levels split into four non-degenerate ($m = 0$) and six twofold-degenerate ($|m| = 1, 2$) states. As d increases, the energy level structure is transformed: In addition to splitting, mixing of states corresponding to different energy levels becomes important.

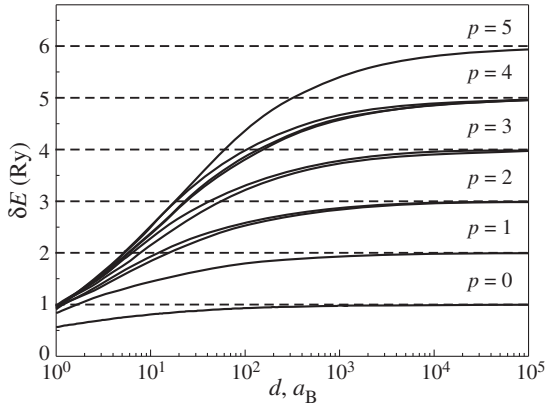

Fig. 2. Variations in δE versus d. Solid lines show the numerical calculation results; dashed lines indicate the limiting values $p + 1$.

Since the energy level degeneracies in two limits are different, in the intermediate region the rearrangement of the levels occurs. Consider, for example, a three-fold degenerate harmonic oscillator level with the quantum number $p = 2$; it is formed when the non-degenerate level originating from the state characterized ($d = 0$) by $n = 1$ and $m = 0$ merges with the twofold-degenerate level originating from the hydrogen states with $n = 2$ and $m = \pm 2$. As d increases, transition to the energy structure of the two dimensional oscillator is observed.

In order to illustrate the transition to the limit of the harmonic oscillator, let us consider the quantity

$$\delta E = (1/2)\,(E_{\rm ex} + 2/d)\,d^{3/2}\,, \tag{11}$$

where $E_{\rm d}$ is the total energy of the donor. As d increases, $\delta E \to p+1$, and the deviation of δE from $p+1$ is a measure of how close is the system to the limiting case of the two dimensional harmonic oscillator. The dependence $\delta E(d)$ is shown in Fig. 2. Evidently, the energy level structure does approach that of the harmonic oscillator, given by (8) and represented by dashed lines in Fig. 2.

4. Conclusions

Thus, considering two systems, an electron in a quantum well bound to a donor in the barrier and a spatially indirect exciton, we have studied the evolution of the energy level structure between two limiting cases characterized by the accidental degeneracy of the energy levels. It has been shown that in both limiting cases, in addition to the level splitting, mixing of states with different principal quantum numbers, that causes the rearrangement of the energy levels, becomes important as the intermediate region is approached.

Acknowledgements

This work was supported by the RFBR, the Presidium of the Russian Academy of Sciences and Federal program on support of leading scientific schools.

References

[1] V. A. Fock, *Z. Phys.* **98**, 145 (1935).
[2] W. Pauli, *Z. Phys.* **36**, 336 (1926).
[3] J. M. Jauch and E. L. Hill, *Phys. Rev.* **57**, 641 (1940).
[4] D. G. W. Parfitt and M. E. Portnoi, *J. Math. Phys.* **43**, 4681 (2002).
[5] R. D.Mota *et al*., *J. Phys. A: Math. Gen.* **35**, 2979 (2002).
[6] M.A. Semina and R.A. Suris, *JETP Letters*, **94 (7)**, 574 (2011).

20th Int. Symp. "Nanostructures: Physics and Technology"
Nizhny Novgorod, Russia, June 24–30, 2012

Photo reflection spectra 150 nm GaAs quantum well embedded between AlAs/GaAs superlattices

B. S. Kulinkin[1], V. G. Davydov[2] and V. A. Gaisin[2]

[1] St Petersburg State Medical University, 6/8 Leo Tolstoy str., 197022 St Petersburg, Russia
[2] Physics Department, St Petersburg State University, Ulyanovskaya 1, Petrodvorets, 198504 St Petersburg, Russia

Abstract. The reectivity spectrum of epitaxial GaAs/AlGaAs heterostructure containing 333 nm and 150 nm GaAs layer was measured. In a spectral range 1.5–1.7 eV the a regular series of narrow lines was observed. The structure of reection spectrum is interpreted by a model involving polariton waves in a wide quantum well.

Introduction

Systems of self-assembled InAs quantum dots (QD's) havebeen intensively studied in recent years due to their importance for fabrication micro- and optoelectronic devices Ref. [1]. The most investigated system with such QD's is system of InAs QD's embedded in GaAs and/or AlAs matrix. In the previous work the reflection spectra of the epitaxial GaAs/AlGaAs heterostructures at $T = 4.2$ K were studied.

1. Reflection [1]

The sample under investigation is epitaxial GaAs/AlGaAs heterostructure containing undoped 333 nm thick GaAs layer enclosed between two GaAs/AlAs superlattices, 30 nm GaAs layer enclosed between two GaAs/AlAs superlattices and GaAs buffer layer of 30 000 nm in thickness.

The reflectivity spectrum was measured using femtosecond Ti:sapphire laser Tsunami produced by Spectra-Physics as wideband light source in Brewster geometry with subsequent normalizing by the spectrum of incident light. In this geometry laser beam is focused at sample surface under angle of about 74° in p-polarization into the spot of approximately 50×150 μm in size. That almost totally suppress nonresonant light scattering off the sample surface. Spectrometer used is based on MDR-23 monochromator combined with Hamamatsu CCD-photodetector and has resolution of 80 μeV.

Utilizing high quality of our heterostructures (and hence narrow reflection lines), we were able to perform independent interpretation of the reflection spectra. Energy positions E of each feature in the reflection spectrum were accurately measured and analysed with respect to their quantum number n. The latter was determined independently assuming quadratic dependence $E(n)$ for high enough n in any of the three models mentioned above (see Fig. 2). It was found that for small quantum numbers $3 \leq n \leq 20$ there are substantial deviations of the $E(n^2)$ dependence slope $\frac{dE}{n\,dn}$ from the value 5 in $3 \leq n \leq 7$ range to almost zero ($\frac{dE}{n\,dn} \approx 0.2$) in $7 \leq n \leq 15$ range and back to 3 for $n \geq 15$. By analysis of this data we made a conclusion that fine structure of the reflection spectra of thick heterostructures should be described using polariton model.

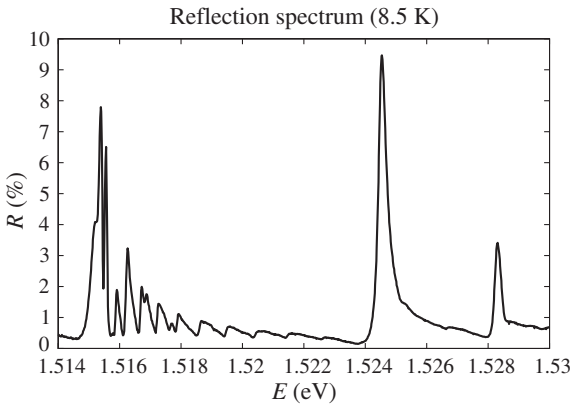

Fig. 1. Reflection spectrum of the sample with thick quantum well.

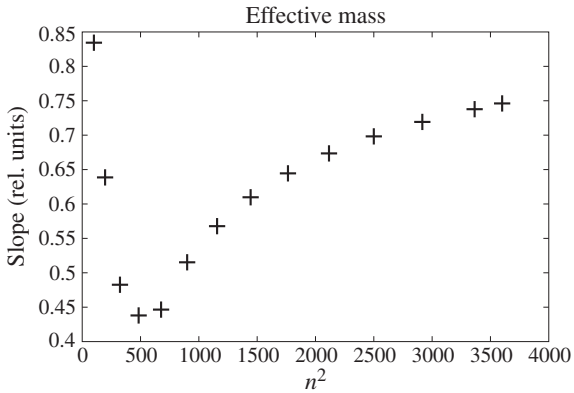

Fig. 2. Effective mass of the confined quasiparticle as finction of the square of quantum nimber n.

2. Electroreflection spectra [2]

The studied heterostructures were grown on GaAs substrates by the gas source molecular beam epitaxy. The 300 nm GaAs buffer layer with a short period AlAs/GaAs superlattice in the middle was grown(at 600 °C) to suppress dislocations. The 2 nm AlAs layer grown on the buffer layer prevents the compositional interfusion between GaAs and the $In_{0.51}Ga_{0.49}P$ barrier layer. One layer of InP QDs with nominal thickness of 4 monolayers (ML) was grown between the $In_{0.51}Ga_{0.49}P$ barrier layers. The growth rate was 0.5 ML/s for InGaP and 0.25 ML/s for InP.

The electroreflectance spectra were measured using a radiation of a continuous wave tunable Ti:sapphire laser or dye lasers as a probe beam. The laser radiation with wavelength 530 or 800 nm was used as a pump beam in the PR experiments. The amplitude modulation of the pump and probe beams at different frequencies (1 MHz and 2 kHz, respectivelly) and a double lock-in detection of the signal modulated at the differ-

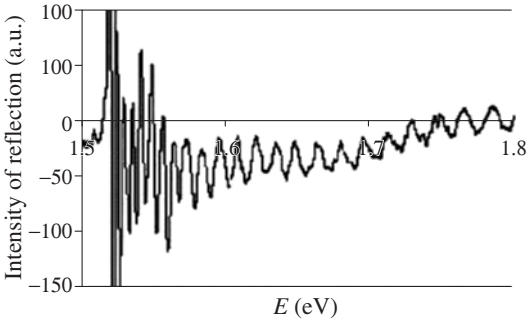

Fig. 3. The electroreflection spectra of the epitaxial GaAs (150 nm)/AlGaAs heterostructures at $T = 4.2$ K.

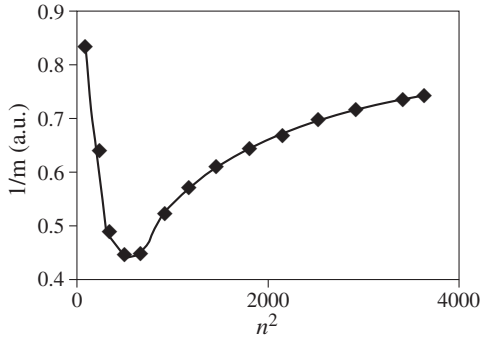

Fig. 4. Effective mass of the confined quasiparticle as finction of the square of quantum number n.

ential frequency allowed us to avoid noises from the scattered light and to detect fractional reflection changes as low as 10^{-7}. In the case of electroreflectance, applied a small ac voltage to the sample at a frequency of about 3 MHz. All experiments were done at the sample temperature 2 or 5 K.

As well as in the previous case quantum numbers n were determined and their energies $E(n)$ and increments dE/dn were plotted against n^2 From the analysis of these plots it follows that an effective mass of the excitonic state depends on the transition energy.

3. Experimental. The potoreflection spectra of the epitaxial GaAs (150 nm)/AlGaAs heterostructures at T = 4.2 K.

Here we present results of the same type of analysis as in the previous case the potoreflection spectra of the epitaxial GaAs (150 nm)/AlGaAs heterostructures at $T = 4.2$ K. The sample containing 150 nm GaAs quantum well between AlAs/GaAs

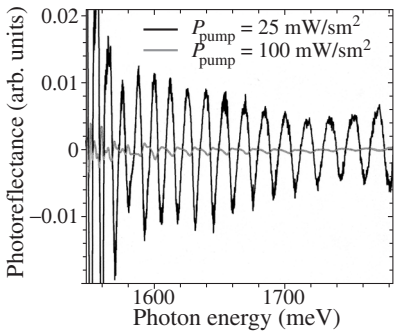

Fig. 5. The photoreflection spectra of the epitaxial GaAs (150 nm)/AlGaAs heterostructures at $T = 4.2$ K.

super lattices Ref. [3]. Obtained spectra demonstrate a series of prominent oscillations in the wider spectral range 1.516–2.1 eV (Fig. 5).

The spectral dependence of the effective mass is quite similar in both samples. Physical mechanisms of the observed anomaly is discussed.

References

[1] D. Bimberg, M. Grundmann, N. N. Ledentsov *et al*., *Quantum Dot Heterostructures* Wiley, NewYork, (2001).

[2] S. V. Poltavtsev, V. A. Gaisin, B. S. Kulinkin *et al*., *in: Proceedings of 18th International Symposium "Nanostructures: Physics and Technology"*, St Petersburg, 108 (2010).

[3] V. A. Maruschyuk, B. S. Kulinkin, V. G. Davydov and V. A. Gaisin, *in: Proceedings of 19th International Symposium "Nanostructures: Physics and Technology"*, Ekaterinburg, Russia, June 20–25, 80 (2011).

[4] I. A. A. Yugova, V. G. Davydov *et al*., *in: Proceedings of 8th International Symposium "Nanostructures: Physics and Technology"*, St Petersburg, 388 (2001).

20th Int. Symp. "Nanostructures: Physics and Technology"
Nizhny Novgorod, Russia, June 24–30, 2012

Near-field mechanism of energy transfer between quantum wells

V. Ya. Aleshkin[1], *L. V. Gavrilenko*[1], D. M. Gaponova[1], Z. F. Krasilnik[1], D. I. Kryzhkov[1], D. I. Kuritsyn[1], S. M. Sergeev[1] and V. G. Lyssenko[2]

[1] Institute for Physics of Microstructures RAS, 603950 Nizhny Novgorod, Russia
[2] Institute for Technology of Microelectronics and High-Purity Materials RAS, 142432 Chernogolovka, Russia

Abstract. We report a study into the process of energy transfer between quantum wells divided by 30 nm thick opaque barriers. It was experimentally observed that the intensity of a photoluminescence signal from a quantum well increased by 15% under resonant excitation of exciton transition in the adjacent quantum well. A radiative mechanism of energy transfer in the near field of emitting exciton is proposed. Within this theoretical model the efficiency of the energy transfer decreases by the power law with a greater distance between the quantum wells. The theory is found to be in a qualitative agreement with the experimental results.

Introduction

The phenomenon of energy transfer between the exciton states in quantum wells (QW) and quantum dots divided by wide tunnel-nontransparent barriers is described in a number of experimental works [1,2]. The mechanisms proposed by different investigators for describing the energy transfer through a wide tunnel-nontransparent barrier vary from work to work. The most common approach involves the Förster–Dexter model [3–5] that implies a nonradiative electrostatic interaction between the dipoles. However, no static dipoles occur in optically excited semiconductors. In this paper we report an experimentally observed increase in the intensity of a photoluminescence signal from a quantum well by resonant excitation of exciton transition in the adjacent quantum well separated from the former one by a 30 nm wide AlGaAs barrier. The observed effect is interpreted within a model of radiative near-field transfer of energy between the tunnel-uncoupled QWs. Such a mechanism implies that the energy is transferred through absorption of light by the quantum well situated in the near field region of the radiating exciton in another QW.

1. Experiment

We studied the photoluminescence (PL) excitation spectra of a GaAs/Al(Ga)As heterostructure with five asymmetric double QWs GaAs/AlAs/GaAs (12.4/12.1, 10.2/9.0, 8.8/8.5, 7.6/7.3 and 6.5/6.2 nm). Each double QW comprised two wells of different thickness, separated by very narrow tunnel-transparent AlAs barriers. Therefore, a QW pair can be regarded as a whole in terms of electron density distribution and charge carrier tunneling. The double quantum wells were separated by 30 nm wide tunnel-nontransparent $Al_{0.3}Ga_{0.7}As$ barriers. The structure was grown on an *n*-type GaAs (001) substrate with the molecular-beam epitaxy method. The spectral resolution was 0.5 nm, the measurement temperature was 8 K.

Fig. 1 illustrates the PL excitation spectra measured at the wavelengths of 802, 793 and 786 nm corresponding to the PL peak positions for three most intensely radiating quantum wells (QW1, QW2 and QW3, respectively). The shaded profile depicts the photoluminescence spectrum for the same QW (the corresponding peaks are shown by sloping arrows). Note that the observed PL is a result of heavy-hole exciton recombination. The dependencies of PL intensity on excitation wave length for the three QWs in question have a number of peaks and are qualitatively alike (Fig. 1).

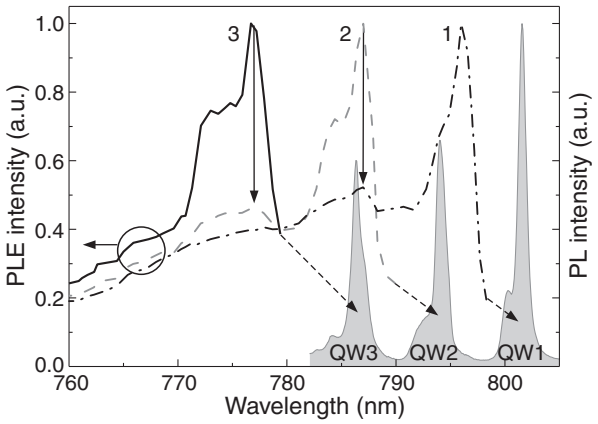

Fig. 1. PL excitation spectra for a GaAs/AlGaAs heterostructure, measured at the wavelengths of 786 (3), 793 (2) and 802 (1) nm, and the PL spectra for three QW (gray profile). The sloping arrows indicate the correspondence between the peaks in the PL spectrum and the PL excitation spectrum. The vertical arrows indicate the correspondence between the specific features in the PL excitation spectra for adjacent double QWs.

2. Model and discussion

Let us take a closer look at the PL excitation spectrum for QW1 (curve 1 in Fig. 1). The first and most intense double peak in the range 796 nm corresponds to the peak of intensive absorption by the light-hole exciton [6] in QW1. The curve shape (double peak) is determined by the asymmetry of double QWs. The next double peak in the spectral region 785 nm does not relate to any possible transitions in QW1. Yet, this peak's shape and position are the same as those of the main, most intense peak (Fig. 1, curve 2) in the PL excitation spectrum of the neighboring QW2, which corresponds to absorption by the light-hole exciton in QW2. The coincidence between the QW1 PL excitation- and the QW2 absorption peaks is indicative of a fairly high efficiency of energy transfer between the QWs. The magnitude of this peak, being defined as a ratio of the peak amplitude to "pedestal", is roughly 0.15. Because of considerable barrier widths between QWs we cannot attribute the effect of energy transfer to tunneling. A similar situation is observed in the study of PL excitation spectra of other QWs, for example, QW2 and QW3.

In the experiments described above and reported in [1,2] the energy transfer between the exciton levels in tunnel-uncoupled

QWs occurred when the quantum energy of laser radiation coincided with the exciton transition energy in a QW. The intensity of PL from the adjacent QW increased appreciably in this case. We attribute this PL intensity growth to the fact that the resonance excitation enhanced radiation of excitons from the former QW is absorbed by the latter QW more effectively than laser radiation. In the first place, radiating excitons are essentially oscillating dipoles, and their radiation contains the near-field components whose contribution largely increases closer to the dipole. Secondly, the electric field of radiation of a dipole lying in the QW plane contains also a z-component (z is the heterostructure growth direction) that can be absorbed in transitions from the light-hole subband in the second QW. Thirdly, an exciton radiates in all directions so part of this radiation propagates at sliding angles to the adjacent QW. The absorptivity of this radiation largely exceeds that for normal incidence radiation. Let us now discuss the influence of these peculiarities on the coefficient of radiation absorption by a quantum well.

A radiating heavy-hole exciton can be represented as a dipole oscillating in the QW plane (xy). We assume the dipole moment vector to have only one component x. If quantum wells are tens of nanometers apart, which is by an order of magnitude shorter than the PL wavelength, it is important to consider the near-field components that rapidly decay with a larger distance from the dipole. The electric field strength in the dipole-radiated wave have the form [7]:

$$\mathbf{E}(\vec{r}) = \left[k'^2[[\mathbf{nd}]\mathbf{n}]\frac{\mathbf{1}}{\varepsilon\mathbf{r}} + \frac{\{\mathbf{3n(nd)} - \mathbf{d}\}}{\varepsilon} \times \left(\frac{1}{r^3} - \frac{ik'}{r^2}\right)\right]\exp\left(ik'r - i\omega t\right), \quad (1)$$

where $k' = \omega/c'$ is the wave vector in the semiconductor, ε and μ — are the dielectric constant and magnetic permeability, respectively; $\vec{n}$ is the unit vector directed from the radiating dipole to the point of observation, $\vec{d}$ is the vector of dipole momentum.

Let us find the near-field part of dipole radiation, that is absorbed by a quantum well lying parallel to plane (xy) at distance R from the dipole. So we need to determine the part of power absorbed in transition from the heavy- and light-hole subbands, respectively.

$$\alpha_{\rm h} = \frac{9\pi}{32}\left(\frac{e^2}{\hbar c}\right)\frac{|\chi_{\rm h}|^2}{\varepsilon^{5/2}\mu^{3/2}k^4R^4}\,\theta\left(\hbar\omega - E_{\rm tr}\right), \quad (2)$$

$$\alpha_{\rm l} = \frac{\pi}{4}\left(\frac{e^2}{\hbar c}\right)\frac{\theta(\hbar\omega - E_{\rm tr})|\chi_{\rm l}|^2}{\varepsilon^{5/2}\mu^{3/2}k^4R^4}\left(\frac{15}{8} + \varepsilon\mu R^2k^2\right), \quad (3)$$

where $k = \omega/c$, $\chi_{h,l}$ are the overlap integrals of the envelope wave functions for heavy and light holes, respectively.

This result was obtained in dipole approximation within the perturbation theory; therefore, it does not fit the case when a QW is too close to the radiating dipole. Distance R should be much larger than the Bohr radius of an exciton, that in a GaAs quantum well does not exceed 10 nm, and the absorption coefficient value should be smaller than unity. The region in which the latter condition is met can be determined in Fig. 2.

As to far-field part of dipole radiation, the magnitude of the estimated coefficient of absorption of this part by QW at transitions from the heavy- and light-hole subbands is 1.6% and 0.7%, respectively. These values are more than twice the estimate for the coefficients of absorption of a normal incidence plane wave by a QW layer. This is due to the fact that the spherically diverging wave of dipole radiation falls onto the QW plane at different, including sliding angles. We now use the proposed model to estimate the increase in the PL signal from one quantum well when its adjacent QW is being laser excited in resonance with a light-hole exciton. The peak magnitude defined as a ratio of the peak amplitude to "pedestal" is 0.16, which is in good agreement with the experimental data.

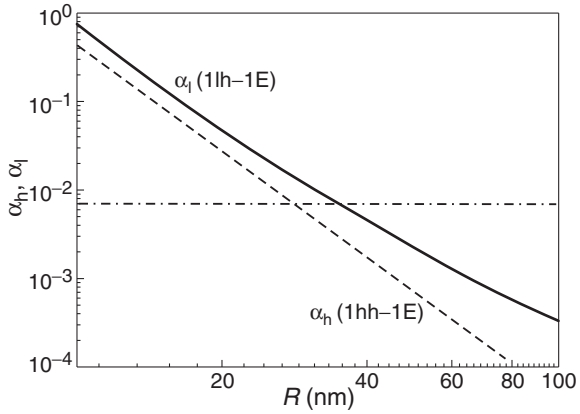

Fig. 2. Dependence of the coefficients of QW absorption of the near-field component of dipole radiation for transitions from the first subband of heavy (hh1) and light (lh1) holes to the first electron subband (e1). For comparison, a horizontal line indicates the absorption coefficient for a plane wave of normal incidence in transitions of carriers from the heavy-hole subband.

Acknowledgements

This work is supported by the RFBR (No. 10-02-01195), Contracts No. 16.518.11.7018 and HIII-4756.2012.2. The authors are thankful to Klaus Sorensen for providing the heterostructures.

References

[1] A. Tomita, J. Shah, R.S. Knox, *Phys. Rev. B* **53**, 10793 (1996).
[2] S.A. Crooker, J.A. Hollingsworth, S. Tretiak, V.I. Klimov, *Phys. Rev. Lett.* **93**, 186802 (2002).
[3] Th.Forster, *Ann. Phys.* **2**, 55 (1948).
[4] D.L. Dexter, *J. Chem. Phys.* **21**, 836 (1953).
[5] S.K. Lyo, *Phys.Rev. B* **81**, 115303-1 (2010).
[6] W.T. Masselink, P.J. Pearah, J. Klem *et al.*, *Phys. Rev. B* **32**, 8027 (1985).
[7] J. Jackson, *The classical electrodynamics*, ed. E.L. Burshtein, Moscow: Mir, 1965, 703 p.

20th Int. Symp. "Nanostructures: Physics and Technology"
Nizhny Novgorod, Russia, June 24–30, 2012

Integral absorption coefficient of a semiconductor inhomogeneous thin film in the exciton resonance spectral range

N. R. Grigorieva

Physics Department, St Petersburg State University,
Ulyanovskaya 1, Petrodvorets, 198504 St Petersburg, Russia

Abstract. By means of a numerical modeling the integral absorption coefficient of a semiconductor inhomogeneous thin film in the exciton resonance spectral range was studied. The dependence of the critical dissipative damping on parameters of inhomogeneous structure was revealed.

Introduction

Optical properties both homogeneous and heterogeneous semiconductor structures in the exciton spectral range are affected spatial dispersion. The influence particularly is manifested in increasing the integral absorption coefficient K with growth of a dissipative damping. The contribution of spatial dispersion in forming optical properties depends on the value of dissipative damping Γ. The Γ values for which spatial dispersion plays considerable role is limited top by the critical value of the damping constant $\Gamma_{\rm cr}$. At exceeding the critical damping, K becomes almost constant (as it's typical for classical oscillator) [1,2]. The variation of the Γ is corresponded to the changing temperature in experiments. The temperature dependence of the integral absorption coefficient was studied experimentally [1–5] for A_2B_6 and A_3B_5 compounds and A_3B_5 heterostructures in order to determine exciton parameters.

1. Results and discussion

In the present work by means of a numerical modeling the integral absorption coefficient of a inhomogeneous thin film is studied in the exciton resonance spectral range as a function of the Γ. The parameters used for modeling the reflection and transmission spectra are as follows: $\varepsilon_0 = 9.4, \omega_0 = 2.5528$ eV, $\omega_{\rm LT} = 0.002$ eV, $M = 0.9m_e$. Two cases were considered. First: a homogeneous thin film with exciton parameters being constant within of a whole volume of the slab. Second: a slab with space-charge region formed by noncompensated ionized defects (with constant concentration of a whole slab volume) and nonzero surface-charge density. That leads to electrical field linearly decreased from surfaces to the center of the slab and as a result to a band bending. So the excitonic parameters such as the resonance frequency and the dissipative damping depends on a spatial coordinate and can be described by the exciton potential given by:

$$\omega_0(z) = \omega_0 + V'(z)\,,$$
$$\Gamma_0(z) = \Gamma_0 + V''(z)\,,$$

were ω_0, Γ_0 — the resonance exciton frequency and the dissipative damping in the homogeneous case; $V'(z)$, $V''(z)$ — spatial coordinate functions describe changing of the resonance exciton frequency and the dissipative damping under the electric field effect. The example of exciton potential depicted in Fig. 1. The inhomogeneous exciton potential gives rise to a specific behavior of an exciton in the structure considered.

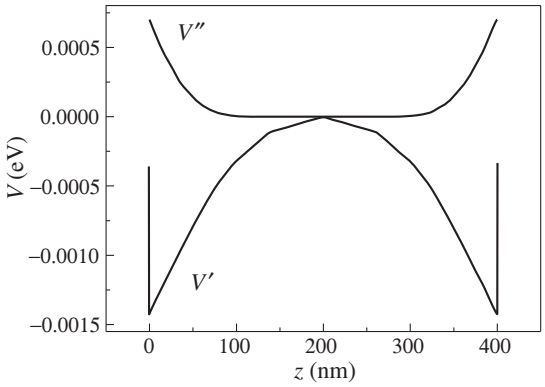

Fig. 1. The changing of the exciton parameters: the resonance frequency (curve V') and the dissipative damping (curve V'') vs. the spatial coordinate z in the inhomogeneous slab.

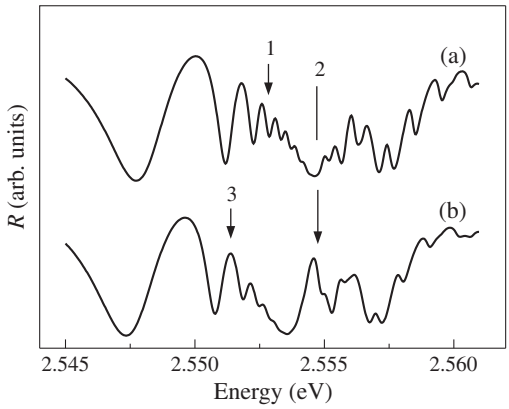

Fig. 2. The reflection spectra for: a) the homogeneous thin film (thickness 400 nm, $\Gamma_0 = 0.0003$ eV); b) the inhomogeneous slab with exciton parameters for the curve a) and exciton potential is shown in Fig. 1). Arrows mark the following spectral positions: 1 — ω_0, 2 — $\omega_{\rm L}$, 3 — the difference ω_0 and $V'_{\rm max}$ ($V'_{\rm max}$ is the maximal $|V'(z)|$ value of the exciton potential on Fig. 1).

The reflection and transmission spectra were calculated in a multilayer approximation of inhomogeneous medium [6,7] by varying such parameters as the film thickness, the defect concentration and the depth of the space-charge region. The integral absorption coefficient was found by numerical integrating the absorption spectrum which in its turn was calculated from transmission and reflection spectra using the expressions widely applied to an experimental data treatment.

The comparison of the reflection spectra for the homogeneous and inhomogeneous films is shown in Fig. 2. The resonance spectral peculiarities of the inhomogeneous slab (Fig. 2b)

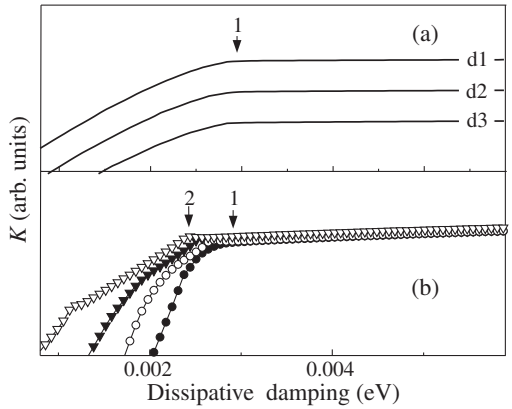

Fig. 3. The integral extinction: a) the homogeneous thin films with different thicknesses: d1 — 600 nm, d2 — 500 nm, d3 — 400 nm; b) the inhomogeneous slab (thickness 400 nm): solid line — homogeneous case for comparison, full circles — 4×10^{16} cm^{-3}, open circles — 5×10^{16} cm^{-3}, full triangles — 6×10^{16} cm^{-3}, open triangles — 8×10^{16} cm^{-3}. Arrows marked following position: (1) Γ_{cr} for the homogeneous thin film; (2) Γ_{cr} for the inhomogeneous slab with 8×10^{16} cm^{-3}.

is shifted to low energy side in respect to that of the homogeneous film (Fig. 2a) in accordance with the exciton potential behavior (Fig. 1). Besides in the region of ω_L the inhomogeneous slab reflection spectrum shows new peculiarity spike structure caused by an attracting effect of the exciton potential.

The $K(\Gamma_0)$ dependence for the homogeneous films possessing different thicknesses are shown in Fig. 3a. Figure shows that the value of Γ_{cr} keeps constant while the of absorption coefficient of a thin film depends on the film thickness. In contrast to the homogeneous film, the Γ_{cr} of inhomogeneous slab depends strongly on the ionized defect concentration (Fig. 3b).

It was revealed that in the case of homogeneous film the Γ_{cr} is independent on the film thickness and can be considered as an effective material parameter. For the case of inhomogeneous slab the Γ_{cr} essentially depends on the defect and impurity concentration and on the depth of the space-charge region. So, in this case Γ_{cr} is a function of the parameters describing sample structure and can be used to characterize band bending near the surfaces and interfaces of heterostructures.

References

[1] F. I. Kreingold *et al*., *JETF Letters* **20**, 201 (1974).
[2] N. N. Akhmediev, *Zh. Eksp. Teor. Fis* **79**, 1534 (1980).
[3] G. N.Aliev *et al*., *Sol. St. Phys.* **36**, 373 (1994).
[4] M. S. Markosov *et al*., *Semicond.* **43**, 656 (2009).
[5] S. A. Vaganov *et al*., em Semicond. **45**, 104 (2011).
[6] A. V. Selkin *et al*., *Vestnik SPbGU* **2** ,87 (1996).
[7] H. Azucena-Coyotecatl *et al*., *Th. Sol. Films* **373**, 227 (2000).

20th Int. Symp. "Nanostructures: Physics and Technology"
Nizhny Novgorod, Russia, June 24–30, 2012

Excitons in graphene

M. V. Entin[1] and *M. M. Mahmoodian*[1,2]

[1] A.V. Rzhanov Institute of Semiconductor Physics, SB RAS, Lavrentieva 13, 630090 Novosibirsk, Russia
[2] Novosibirsk State University, 630090 Novosibirsk, Russia

Abstract. The existance of indirect excitons in monolayer graphene is theoretically evidenced. The excitons are formed from electrons and holes near the opposite conic points. The possibility of moving exciton is conditioned by the trigonal warping of electron spectrum. We calculated the exciton spectrum in the envelope-function approximation. It is stated that the exciton exists in some sectors of the momentum space and has the strong trigonal warping of spectrum.

Exciton is a usual two-particle state of semiconductors. The attraction between electron and hole leads to the lowering of the excitation energy compared to free particles. As a result, the states are formed in the bandgap of a semiconductor. The absence of the gap makes this picture inapplicable to graphene. The immobile exciton is impossible in a material with zero gap. However, a moving electron-hole pair with a finite total momentum has an energy gap that makes the binding of the pair allowable.

We consider the envelope tight-binding Hamiltonian of monolayer graphene:

$$H_{\rm ex} = \epsilon(\mathbf{p}_{\rm e}) + \epsilon(\mathbf{p}_{\rm h}) + V\,(\mathbf{r}_{\rm e} - \mathbf{r}_{\rm h})\ , \qquad (1)$$

where

$$\epsilon(\mathbf{p}) = \gamma_0 \sqrt{1 + 4\cos\frac{ap_x}{2}\cos\frac{\sqrt{3}ap_y}{2} + 4\cos^2\frac{ap_x}{2}}\ , \qquad (2)$$

is single-electron energy, $a = 0.246$ nm is the lattice constant, $\hbar = 1$, $V(\mathbf{r}) = e^2/r$ is the potential energy of electron-hole interaction. The electron spectrum has conic points $\nu\mathbf{K}$, $\nu = \pm 1$, $\mathbf{K} = (4\pi/3a, 0)$, where $\epsilon(\mathbf{p}) \approx s|\mathbf{p} - \nu\mathbf{K}|$, $s = \gamma_0 a\sqrt{3}/2$ is the electron velocity in the conic approximation.

The electron and hole momenta $\mathbf{p}_{\rm e,h}$ can be expressed via pair $\mathbf{q} = \mathbf{p}_{\rm e} + \mathbf{p}_{\rm h}$ and relative $\mathbf{p} = \mathbf{p}_{\rm e} - \mathbf{p}_{\rm h}$ momenta. The momenta $\mathbf{p}_{\rm e,h}$ can be situated near the same ($q \to k \ll 2K$) or near the opposite conic points ($\mathbf{q} = 2\mathbf{K} + \mathbf{k}$, $k \ll 2K$).

We assumed that graphene is embedded into insulator with a large dielectric constant χ, so that the effective dimensionless constant of interaction $g = e^2/(s\chi\hbar) \sim 2/\chi \ll 1$ and the many-body complications are inessential. In the conic approximation, the classical electron and hole with the same direction of momentum have the same velocities s. In a quantum language, the two-particle Hamiltonian contains no terms quadratic in the component of the relative momentum $\mathbf{p}$ along $\mathbf{k}$. That means that the attraction does not result in binding. Thus, the problem of binding demands accounting for the corrections to the conic spectrum. Two kinds of excitons are potentially allowed in graphene: a direct exciton with $k \ll 1/a$ (when the pair belongs to the same extremum) and the indirect exciton with $\mathbf{q} = 2\mathbf{K} + \mathbf{k}$.

Assuming $p \ll k$ (this results from the smallness of g), we get to the quadratic Hamiltonian

$$H_{\rm ex} = sk + \frac{p_1^2}{2m_1} + \frac{p_2^2}{2m_2} + \frac{e^2}{\chi r}\,, \qquad (3)$$

where the coordinate system with the basis vectors $\mathbf{e}_1 \equiv \mathbf{k}/k$ and $\mathbf{e}_2 \perp \mathbf{e}_1$ is chosen, $\mathbf{r} = (x_1, x_2)$. In the conic approximation we have $m_2 = k/s$, $m_1 = \infty$. Thus, this approximation is not sufficient to find m_1. Beyond the conic approximation (but near the conic point) we have for the indirect exciton

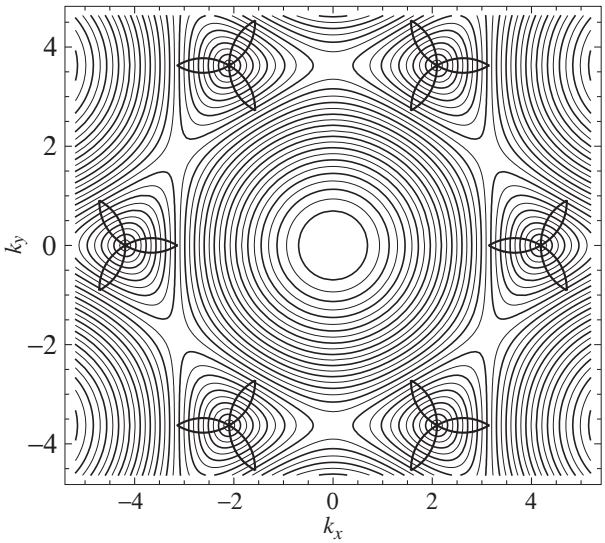

Fig. 1. Relief of the single-electron spectrum. Domains where exciton states exist are bounded by a thick line.

$$\frac{1}{m_1} = \nu\,\frac{sa}{4\sqrt{3}}\,\cos 3\phi_{\mathbf{k}}\,. \qquad (4)$$

where $\phi_{\mathbf{k}}$ is an angle between $\mathbf{k}$ and $\mathbf{K}$.

According to (4), the effective mass m_1 is directly determined by the trigonal contributions to the spectrum and is large in the measure of their smallness: (4), $m_2 \ll m_1$. The sign of m_1 is determined by $\nu\cos 3\phi_{\mathbf{k}}$. If $\nu\cos 3\phi_{\mathbf{k}} > 0$, electrons and holes tend to bind, else to run away from each other. Thus the binding is possible for $\nu\cos 3\phi_{\mathbf{k}} > 0$. Apart from the conic point this condition transforms to

$$(1 + u + v_-)\,(1 + u + v_+)\,(1 + v_- + v_+) > 0\,, \qquad (5)$$

where $u = \cos ak_x$, $v_\pm = \cos((k_x \pm \sqrt{3}k_y)a/2)$.

Fig. 1 shows the domain of exciton existance in the momentum space. This domain covers a small part of the Brillouin zone.

A similar reasoning for the direct exciton gives the negative mass $m_1 = -32/(ksa^2(7 - \cos 6\phi_{\mathbf{k}}))$. As a result, the direct exciton kinetic energy of the electron-hole relative motion is not positively determined and that means impossibility of binding.

To find the indirect exciton states analytically, we solved the Schrödinger equation with the Hamiltonian (3) using the

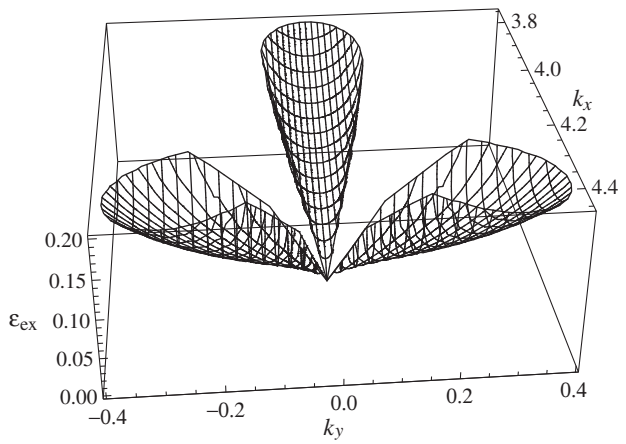

Fig. 2. Binding energy (in eV) of the ground state of indirect exciton in graphene *versus* wave vector in units of reciprocal lattice constant. Exciton exists in the sectors shown in Fig. 1.

large ratio of effective masses. This parameter can be utilized by the adiabatic approximation similar with the problem of molecular levels. Coordinates 1 and 2 play a role of heavy "ion" and "electron" coordinates. At the first stage the ion term in the Hamiltonian is omitted and the Schrödinger equation is solved with respect to the "electron" wave function at a fixed ion position. The resulting "electron" terms then are used to solve the "ion" equation. This gives the approximate ground level of exciton $\varepsilon(\mathbf{k}) = sk - \varepsilon_{\rm ex}(\mathbf{k})$, where the binding energy of exciton is $\varepsilon_{\rm ex}(\mathbf{k}) = \pi^{-1} skg^2 \log^2(m_1/m_2)$. The quantity $\varepsilon_{\rm ex}(\mathbf{k})$ essentially depends on the momentum via the ratio of effective masses m_1/m_2. Within the accepted assumptions, $\varepsilon_{\rm ex}$ is less than the energy of unbound pair sk. However, at a small enough dielectric constant χ, the ratio of both quantities is not too small. Although we have no right to consider the problem with large g in the two-particle approach, it is obvious that the increase of the parameter g can only result in the binding energy growth.

Besides, we have studied the problem of exciton numerically in the same approximation and by means of a variational approach. Fig. 2 represents the dependence of the exciton binding energy on its momentum for $\chi = 10$. Fig. 3 shows the radial sections of the two-dimensional plot. The characteristic exciton binding energies have the order of 0.2 eV.

All results for embedded graphene are applicable to the free-suspended layer if to replace the interaction constant g with a smaller quantity $\tilde{g}$, renormalized by many-body effects. In this case the exciton binding energy becomes essentially larger and comparable to kinetic energy sk.

We discuss the possibility of observation of the indirect excitons in graphene. As we saw, their energies are distributed between zero and some tenth of eV that smears up the exciton resonance. The large exciton momentum blocks both direct optical excitation and recombination. However, a slow recombination and an intervalley relaxation preserve the excitons (when generated someway) from recombination or the decay. On the other hand, the absence of a low-energy threshold results in the contribution of excitons in the specific heat and the thermal conductivity even at low temperature.

It is found that the exciton contribution to the specific heat at low temperatures in the Dirac point is proportional to $(gT/s)^2 \log^2(aT/s)$. It is essentially lower than the electron specific heat $\propto (T/s)^2$ and the acoustic phonon contribution $\propto (T/c)^2$, where c is the phonon velocity. Nevertheless, the exciton contribution to the electron-hole plasma specific heat is essential for experiments with hot electrons.

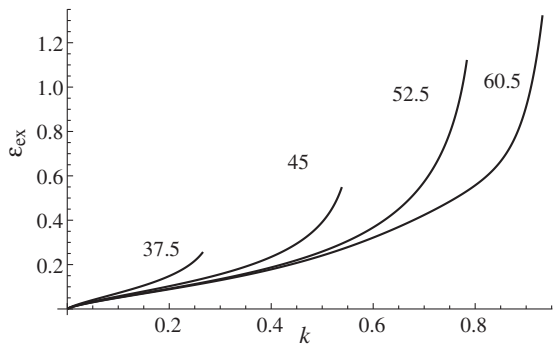

Fig. 3. Radial sections of Fig. 2 at fixed angles in degrees (marked). Curves run up to the ends of exciton spectrum.

In conclusion, the exciton states in graphene are gapless and possess strong angular dependence. This behavior coheres with the angular selectivity of the electron-hole scattering rate [1]. In our opinion, it is reasonable to observe the excitons by means of scattering of external low-energy electrons with energies ∼1 eV on the free-suspended graphene plane in vacuum. Such energy and angle-resolving measurements can reproduce the indirect exciton spectrum.

Acknowledgements

This research has been supported in part by the grants of RFBR No 11-02-00730 and 11-02-12142.

References

[1] L. E. Golub, S. A. Tarasenko, M. V. Entin, L. I. Magarill, *Phys. Rev. B* **84**, 195408 (2011).

20th Int. Symp. "Nanostructures: Physics and Technology"
Nizhny Novgorod, Russia, June 24–30, 2012

Stabilization and active mode-locking of terahertz quantum cascade lasers

Stefano Barbieri

Laboratoire Matériaux et Phénomènes Quantiques, Université Paris 7 and CNRS UMR 7162,
10 rue A. Domont et L. Duquet, 75205 Paris, France

The seminar will focus on the phase-locking and active mode-locking of terahertz (THz) quantum cascade lasers (QCLs). First a technique will be presented that allows to phase-lock THz QCLs to a harmonic of the repetition rate of an erbium-doped fs-fiber laser [1]. This permits the coherent detection of the radiation emitted by these semiconductor lasers with a dynamic range of ∼90 dB in 1 Hz bandwidth (i.e. an NEP of ∼1 pW/Hz). Furthermore the beating between the QCL emission frequency and the harmonic of the repetition rate of the fiber laser is used to measure the free-running intrinsic linewidth of the QCL.

In the second part it will be shown how the phase-locking technique can be exploited for the asynchronous sampling of the waveform emitted by a 2.5 THz QCL when its drive current is modulated with an RF synthesizer [2]. When the modulation frequency is sufficiently close to the laser roundtrip frequency, the QCL enters in a regime of active mode-locking, generating ∼10 ps wide pulses at a repetition rate of ∼13 GHz [3].

References

[1] S. Barbieri *et al*., *Nature Photon.* **4**, 636 (2010).
[2] P. Gellie *et al*., *Opt. Expr.* **18**, 20799 (2010).
[3] S. Barbieri *et al*., *Nature Photon.* **5**, 306 (2011).

20th Int. Symp. "Nanostructures: Physics and Technology"
Nizhny Novgorod, Russia, June 24–30, 2012

Optically tunable metamaterial based on semiconductor superlattice

A. A. Bogdanov[1,2,3] and R. A. Suris[1,2,3]

[1] Ioffe Physical-Technical Institute, St Petersburg, Russia
[2] St Petersburg State Polytechnic University, 195251 St Petersburg, Russia
[3] St Petersburg Academic University, St Petersburg, Russia

Abstract. In this work we theoretically analyzed tunable metamaterial based on the semiconductor superlattice. We show that the signs of the main tensor components of the dielectric function can manipulated by the intensity of the incident light. Therefore, density of photon states is controlled by the incident light intensity.

Introduction

In recent years, there is a great deal of attention devoted to metamaterials. Metamaterials are novel synthetic materials with properties which are usually not appropriate to the natural materials. Due to their unique properties, metamaterials have many potential applications in the optoelectronics, medicine, telecommunications, space industry and other branches of science and industry [1–3].

In the common case, electromagnetic properties of the metamaterials are anisotropic and described by a tensor of the dielectric function. Signs of the main components of the tensor (signature) determine the shape of equal-energy surface in **k**-space. Depending on the signature, the shape can be an ellipsoid, one- or two-sheeted hyperboloid. Manipulation of the tensor components gives the opportunity to manipulate the shape of the equal-energy surface and, therefore, to manipulate the density of the photon states in the metamaterial.

Tunable metamaterial is topical and quite complicated problem. Some models of tunable metamaterials are discussed in [3–5]. Here we suggest new type of the tunable metamaterials based on the semiconductor superlattice.

1. Model

Let us consider undoped periodic type-II semiconductor superlattice of quantum wells (Fig. 1).Within effective medium approximation, dielectric function of the superlattice is a tensor with three non-zero diagonal components:

$$\widehat{\varepsilon}(\omega) = \begin{pmatrix} \varepsilon_\perp(\omega) & 0 & 0 \\ 0 & \varepsilon_\parallel(\omega) & 0 \\ 0 & 0 & \varepsilon_\parallel(\omega) \end{pmatrix} \qquad (1)$$

Frequency dependence of each tensor component we describe within Drude–Lorentz approximation:

$$\varepsilon_s(\omega) = \varepsilon^\infty \left(1 - \frac{\Omega_s^2}{\omega(\omega + i\gamma_s)}\right), \qquad s = \perp, \parallel . \qquad (2)$$

Here ε^∞ is a material permittivity, $\gamma_{\perp,\parallel} = 1/\tau_{\perp,\parallel}$ is an inverse scattering time of transversal and longitudinal electron momentum which is responsible for free carrier absorption. For the sake of simplicity, we put $\gamma_\perp = \gamma_\parallel = \gamma$. $\Omega_{\perp,\parallel}$ is a transversal and longitudinal plasma frequency of electron-hole plasma. In Eq. (2) we do not take into account interband and intersubband transitions. It is justified if operating frequency is less than width of the minigaps in the charge carrier spectrum of the superlattice.

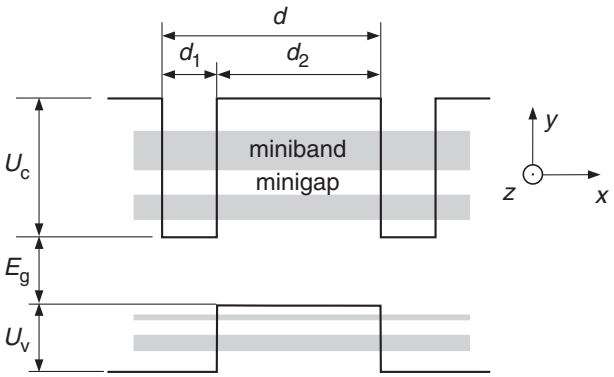

Fig. 1. Superlattice of spatially separated quantum wells.

Usually, holes in semiconductors more heavier than electrons. It is why, in the first approach, we ignore contribution of holes into the plasma frequency of electron-hole gas. Transversal and longitudinal electron plasma frequency are determined as follows:

$$\Omega_{\perp,\parallel}^2 = \frac{e^2}{\pi^2\hbar^3} \sum_i \iiint f_i(\mathbf{p}) \frac{\partial^2 E_i(\mathbf{p})}{\partial p_{\perp,\parallel}^2} d^3p . \qquad (3)$$

Here i is a number of electron miniband, $\mathbf{p}$ is electron momentum, $p_\perp$ and $p_\parallel$ are electron momentum components across and along to the superlattice layers, $E_i(\mathbf{p})$ is the energy of electrons, $f_i(\mathbf{p})$ is the distribution function of electrons in the i-th miniband. This equation is quite common and determines dependence of $\Omega_\perp$ and $\Omega_\parallel$ on the electron spectrum, temperature, and chemical potential of electrons (electron concentration).

Energy spectrum of electrons in superlattice is anisotropic and depends on the i, $p_\perp$ and $p_\parallel$ as follows:

$$E(n, p_\perp, p_\parallel) = E_n(p_\perp) + \frac{p_\parallel^2}{2m_\parallel^*} . \qquad (4)$$

Here $m_\parallel^*$ is in-plane effective electron mass.

The idea of the tunable metamaterial is following. Due to the anisotropic energy spectrum of the carriers in the superlattice, longitudinal and transversal plasma frequencies are different ($\Omega_\perp \neq \Omega_\parallel$). The signs of the components of the dielectric function tensor depend on the relation between $\Omega_{\perp,\parallel}$ and ω. If $\omega < \Omega_{\perp,\parallel}$ then $\varepsilon_{\perp,\parallel} < 0$. If $\omega > \Omega_{\perp,\parallel}$ then $\varepsilon_{\perp,\parallel} > 0$. Manipulation of $\varepsilon_{\perp,\parallel}$ is possible by means of the manipulation of free electrons concentration in the conduction band. For example, free electrons concentration in the conduction band can be manipulated by external light source, temperature or by electron injection. Here we analyze the case of external light source.

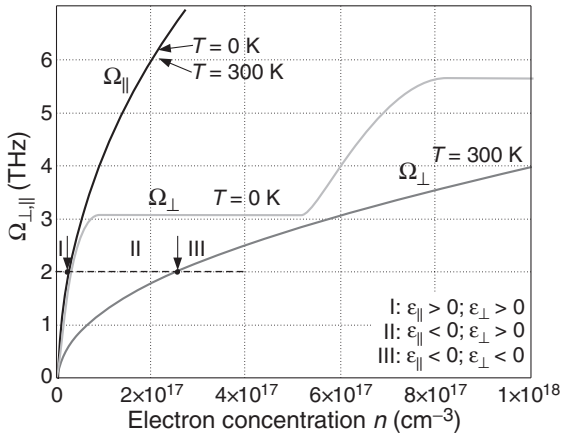

Fig. 2. Dependence of longitudinal and transversal plasma frequency in superlattice on the electron concentration in the conduction band for different temperatures.

2. Results

As an example we consider superlattice with following parameters: $U_c = 0.5$ eV, $U_v = 0.5$ eV, $E_g = 0.4$ eV, $d_1 = 4.5$ nm, $d_2 = 20$ nm, $m_\parallel = 0.05 m_e^*$. Such parameters are close to GaInAs/GaAsSb superlattice. In Fig. 2 we show dependence of $\Omega_{\perp,\parallel}$ on the electron concentration in conduction band for different temperatures. One can see that $\Omega_\perp$ has a staircase behavior. The plateau corresponds to the situation when chemical potential lies in the minigap of the electron spectrum. The plateau smears out as the temperature increases.

Longitudinal plasma frequency does not have implicit dependence on the temperature and depends only on the total electron concentration in the conduction band.

At room temperature, for the frequency 2 THz signature[1] of the tensor changes from (+,+,+) to (+,–,–) at $n = 2.2 \times 10^{16}$ cm $^{-3}$, and changes from (+,–,–) to (–,–,–) at $n = 2.5 \times 10^{17}$ cm^{-3}.

Optical power, P, necessary to provide non-equilibrium electron concentration n can be estimated as follows:

$$P = \frac{l\, n\, \hbar\omega}{\tau}\,. \tag{5}$$

Here $\hbar\omega$ is energy of the incident photon which is about 1 eV, l is film thickness and τ is a lifetime of non-equilibrium electrons which is about tens of nanoseconds. Lifetime of non-equilibrium electrons can be increased up to hundred of microsecond due to the spatial separation of electrons and holes [7, 8]. Hence, for 100 μm film

$$P = \frac{10^{-2} \times 2.5 \times 10^{17} \times 1.6 \times 10^{-19}}{10^{-4}} \approx 4\ \mathrm{W/cm^2}\,. \tag{6}$$

It is quite reasonable value for practical applications.

3. Conclusion

In this work we proposed the idea of optically tunable metamaterial based on the semiconductor superlattice. We show that tensor signature of the dielectric function and, therefore, density of the photon states can be manipulated optically by the incident light with intensity about several W/cm^2.

[1] For short we consider notation $(\pm, \pm, \pm)$ where the first sign corresponds to the sign of $\varepsilon_\perp$ and the second and third signs correspond to the sign of $\varepsilon_\parallel$.

Acknowledgements

This work has been supported by Saint Petersburg Government, by RFBR (project 11-02-00573-a), by the Russian Ministry of Science and Education and by the Program "Fundamental Research in Nanotechnology and Nanomaterials" of the Presidium of the RAS. One of the authors (A. Bogdanov) appreciates the valuable supported of the Dynasty Foundation (Program for Graduate Students and Young Pre-Degree Scientists).

References

[1] H. Chen, C.T. Chan, P. Sheng, *Nature Materials* **9**, 387 (2004).
[2] D.R. Smith, J.B. Pendry, M.C.K. Wiltshire, *Science* **305**, 788 (2004).
[3] A.D. Boardman, V.V. Grimalsky, Y.S. Kivshar, S.V. Koshevaya, M. Lapine, N.M. Litchinitser, V.N. Malnev, M. Noginov, Y.G. Rapoport, V.M. Shalaev, Active and tunable metamaterials, *Laser & Photonics Reviews* **5**, 287 (2011).
[4] S. Ramovic, J. Radovanovic, V. Milanovic, *Journal of Applied Physics* **110**, 123704 (2011).
[5] I. I. Smolyaninov, E. E. Narimanov, *Physical Review Letters* **105**, 067402 (2010).
[6] Yu.S. Kivshar, A.A. Orlov, P.A. Belov, *Proc. of research center of photonics and optical informatics* (Russia, 2010), p. 78 (2010).
[7] V.V. Solov'ev, I.V. Kukushkin, J.H. Smet, K. von Klitzing, and W. Dietsche, *JETP Letters* **84**, 222 (2011).
[8] C. Phelps, J. Prineas, and H. Wang, *Physical Review B* **83**, 153302 (2011).

20th Int. Symp. "Nanostructures: Physics and Technology"
Nizhny Novgorod, Russia, June 24–30, 2012

Terahertz galvanoplasmonic effects in two-dimensional electron system gated by a periodic metal grating with asymmetric unit cell

V. V. Popov[1,2], D. V. Fateev[1,2], T. Otsuji[3], Y. M. Meziani[4], D. Coquillat[5] and W. Knap[5]

[1] Kotelnikov Institute of Radio Engineering and Electronics (Saratov Branch) RAS, 410019 Saratov, Russia
[2] Saratov State University, Saratov, Russia
[3] Research Institute of Electrical Communication, Tohoku University, Sendai, Japan
[4] Dpto. de Fisica Aplicada, Universidad de Salamanca, Salamanca, Spain
[5] Laboratoire Charles Coulomb UMR5221, CNRS&Universite Montpellier 2, Montpellier, France

Abstract. Terahertz galvanoplasmonic effects in a two-dimensional electron system gated by a periodic metal grating with an asymmetric unit cell is studied theoretically. It is shown that the galvanoplasmonic response is several orders of magnitude stronger than conventional photogalvanic response in two-dimensional electron system. Because of that the galvanoplasmonic effects can be used for sensitive detection of terahertz radiation.

Introduction

Direct electric current flowing in a material system with no applied electric force is usually referred to as the galvanic current. Galvanic currents can appear as a result of mechanical stress, chemical reaction, or heat in the system. Photogalvanic response in a two-dimensional electron system (2DES) appears under its illumination by terahertz (THz) radiation [1,2]. Although direct galvanic current appears in this case due to the action of the THz electric (and magnetic) field, the average electric force exerted onto the system is zero. Because of that the photogalvanic response can be interpreted as a result of the ratchet effect [1,2]. The photogalvanic effects usually involve a local nonlinear response of 2DES, while a non-local nonlinear response of 2DES produces only small contribution to the entire photogalvanic effect.

In this paper, the galvanoplasmonic response in 2DES gated by a periodic metal grating with an asymmetric unit cell (Fig. 1) is studied theoretically. A periodic grating gate serves as an efficient antenna element coupling incident THz radiation to the plasmons in 2DES [3]. Also, spatial modulation of the equilibrium electron density in 2DES can be performed via applying the electrical bias in the grating gate. It is shown that, in spite the galvanoplasmonic effect is entirely based on a nonlocal nonlinear response of the 2DES, it can be several orders of magnitude stronger than conventional photogalvanic effects in 2DES.

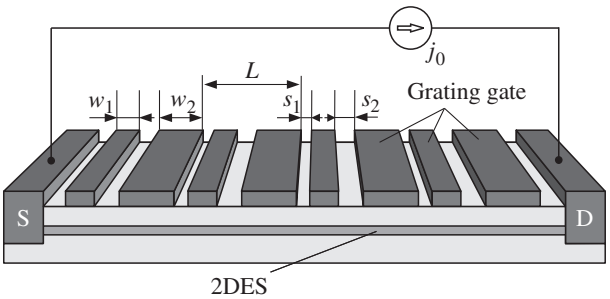

Fig. 1. Schematic view of the 2DES gated by a periodic metal grating with an asymmetric unit cell. External THz wave is incident normally from the top.

1. Basic equations

Plasmon oscillations in 2DES can be described by the hydrodynamic equations

$$\frac{\partial V(x,t)}{\partial t}+V(x,t)\frac{\partial V(x,t)}{\partial x}+\frac{V(x,t)}{\tau}+\frac{e}{m^*}E(x,t)=0, \quad (1)$$

$$e\frac{\partial N(x,t)}{\partial t}-\frac{\partial j(x,t)}{\partial x}=0, \quad (2)$$

where $E(x,t)$ is the oscillating in-plane electric field depending on the time t and coordinate x in the 2EDS plane (x-axis is directed along the periodicity of the structure), τ is the electron momentum relaxation time due to electron scattering in 2DES, $N(x,t)$ and $V(x,t)$ are the electron density and hydrodynamic velocity of electrons in 2DES, respectively, $j(x,t) = -eN(x,t)V(x,t)$ is the electron current density induced in 2DES. There are two nonlinear terms in Eqs. (1) and (2): the second term in the Euler equation, Eq. (1), which describes the nonlinear electron convection in the 2DES, and the product $N(x,t)V(x,t)$, which defines the current density in the continuity equation Eq. (2). The time average of the nonlinear current yields the plasmon-galvanic current. It should be noted that either of the two nonlinear terms vanishes in the case of a uniform oscillating current flowing in 2DES. Therefore, those nonlinearities are related to non-uniform oscillating electric currents inherent in the plasma oscillations. It also means that the galvanoplasmonic current is entirely caused by a nonlocal response of 2DES.

In principle, the both nonlinear terms can contribute to the galvanoplasmonic response. In a periodic structure with a homogeneous 2DES, the electron convection term in the Euler equation [the second term in Eq. (1)] does not contribute to the galvanoplasmonic response of the entire structure incorporating many dozens of periods because the spatial average of this term over the structure period is zero. Therefore, the only source of hydrodynamic nonlinearity in the periodic structure with a homogeneous 2DES is the product $N(x,t)V(x,t)$ defining the current density in 2DES. However, as shown below, the electron convection term in the Euler equation, Eq. (1), can vastly contribute to the galvanoplasmonic current if the equilibrium electron density in the 2DES varies over the structure period.

Due to spatial periodicity of the structure, the Fourier-series

representation of Eqs. (1) and (2) can be performed. Then, the solution of Eqs. (1) and (2) within the lowest order of the perturbation series in respect to the powers of $E(x,t)$ yields the galvanoplasmonic current density $j_0 = j_{\rm dr} + j_{\rm el}$ [4], where

$$j_{\rm dr} = -2e{\rm Re}\sum_{q\neq 0} N_{\omega,q} V^*_{\omega,q} \text{ and } j_{\rm el} = -e\sum_{q\neq 0} N^{(0)}_q V^*_{0,-q} \quad (3)$$

with $N_{\omega,q}$ and $V_{\omega,q}$ being the amplitudes of the spatiotemporal Fourier-harmonics of the oscillating electron density and hydrodynamic electron velocity, respectively, in 2DES at the frequency ω of the incident THz wave, $V_{0,q}$ being the amplitudes of the spatiotemporal Fourier-harmonics of the hydrodynamic electron velocity at zero frequency, $q = 2\pi/L$ being the reciprocal lattice vectors of the periodic grating gate, and $N^{(0)}_q$ being the amplitudes of the spatial Fourier-harmonics of the equilibrium electron density $N^{(0)}(x)$ in 2DES. The values of $N_{\omega,q}$ and $V_{\omega,q}$ are proportional to the first power of the electric-field amplitude $E(x,t)$, whereas $V_{0,q}$ is proportional to the second power of that. The values $N_{\omega,q}$, $V_{\omega,q}$, and $V_{0,q}$ can be calculated by solving Eqs. (1) and (2) in the Fourier representation. The electric-field amplitude $E(x,t)$ induced in the grating-gated 2DES by incident THz wave is calculated in self-consistent linear electromagnetic approach described in [5].

2. Results and discussion

The both galvanoplasmonic currents $j_{\rm dr}$ and $j_{\rm el}$ vanish in the structure with a symmetric unit cell ($s_1 = s_2$) because a net galvanoplasmonic current can appear only in the structure without the center of inversion in the 2DES plane. In the structure under consideration, the center-of-inversion symmetry is broken due to asymmetry of the grating-gate unit cell ($s_1 \neq s_2$). In the structure with a spatially homogeneous 2DES, $j_0 = j_{\rm dr}$, where $j_{\rm dr}$ is the galvanoplasmonic current due to the electron drag by the plasmon wave in 2DES. In the structure with a spatially modulated electron density in 2DES, additional galvanoplasmonic current $j_{\rm el}$ caused by the electrostriction of the electron plasma in 2DES appears. The galvanoplasmonic current $j_{\rm el}$ totally originates from the electron convection term in the Euler equation, Eq. (1). Contribution $j_{\rm el}$ to the total galvanoplasmonic current can be interpreted as the plasmonic ratchet, which appears due to the fact that a spatial profile of the equilibrium electron density distribution in 2DES is laterally shifted from the plasmon-mode waveform in 2DES gated by the grating-gate with an asymmetric unit cell. For strong spatial modulation of the electron equilibrium density in 2DES, the plasmonic ratchet contribution to the net galvanoplasmonic current can be comparable with or even greater than the plasmon-drag contribution.

Although the galvanoplasmonic effect is entirely based on a non-local nonlinear response of the 2DES, it can be several orders of magnitude stronger than conventional photogalvanic effects in 2DES. Considerable enhancement of the galvanoplasmonic current occurs because the plasmon momentum is several orders of magnitude larger compared to the photon momentum at THz frequency.

Assuming the characteristic parameters of 2DES in InGaP/InGaAs/GaAs heterostructure gated by the grating-gate of a micron period with an asymmetric unit cell of sub-micron characteristic dimensions, we demonstrate theoretically (see Fig. 2) that the galvanoplasmonic current density can exceed 70 μA/cm in 2DES with strong spatial modulation of the equilibrium electron density for the fluence of incident THz radiation 1 W/cm^2 at room temperature [6].

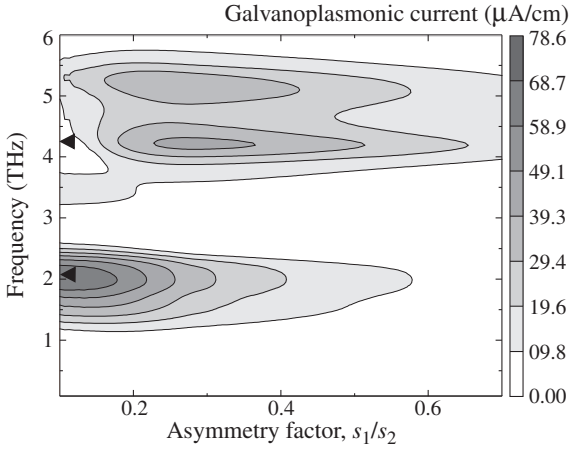

Fig. 2. Galvanoplasmonic current density as a function of THz frequency and the asymmetry factor, s_1/s_2. The 2DES is strongly depleted under the grating-gate fingers of width w_1 while the grating-gate fingers of width w_2 are floating. Characteristic dimensions of the grating gate are $L = 1300$ nm, $w_1 = 600$ nm, $w_2 = 500$ nm. Black triangles at the ordinate axis mark the frequencies of the fundamental and the second-order plasmon modes in the structure.

3. Conclusions

Terahertz galvanoplasmonic effects in 2DES gated by the grating gate with an asymmetric unit cell is studied theoretically. It is shown that the THz galvanoplasmonic response can be several orders of magnitude stronger than conventional THz photogalvanic response in 2DES. Because the plasmon frequencies in 2DES fall within the THz band, the galvanoplasmonic effects can be used for sensitive detection of THz radiation.

Acknowledgements

This work has been supported by RFBR (Grant Nos. 10-02-93120 and 11-02-92101) and by the Russian Academy of Sciences Program "Fundamentals of Nanotechnology and Nanomaterials." Y.M.M. acknowledges the support from the Ministry of Science and Innovation of Spain (Projects PPT-120000-2009-4 and TEC-2008-02281) and the Ramon y Cajal program. The important help of the JST-ANR Japan-France International Strategic Collaborative Research Program "Wireless Communication Using Terahertz Plasmonicnano ICT Devices" (WITH) is also acknowledged. The work was performed under umbrella of the GDR-I project "Semiconductor Sources and Detectors for Terahertz Frequencies."

References

[1] W. Weber *et al*., *Phys. Rev. B* **77**, 245304 (2008).
[2] P. Olbrich *et al*., *Phys. Rev. B* **83**, 165320 (2011).
[3] V. V. Popov, *J. Infrared Milli. Terahz. Waves* **32**, 1178 (2011).
[4] G. R. Aizin *et al*., *Appl. Phys. Lett.* **91**,163507 (2007).
[5] D. V. Fateev *et al*., *Semiconductors* **44**, 1406 (2010).
[6] V. V. Popov *et al*., *Appl. Phys. Lett.* **99**, 243504 (2011).

20th Int. Symp. "Nanostructures: Physics and Technology"
Nizhny Novgorod, Russia, June 24–30, 2012

Tunable whispering gallery mode lasers with controlled absorber

Yu. P. Yakovlev[1], A. M. Monakhov[1], V. V. Sherstnev[1], M. I. Larchenkov[1], A. N. Baranov[2], G. Boissier[2] and R. Teissier[2]

[1] Ioffe Physical-Technical Institute, St Petersburg, Russia
[2] Institut d'Electronique du Sud (IES): Université Montpellier 2, CNRS, IES (UMR CNRS 5214), 34095 Montpellier, France

Abstract. Tunable semiconductor lasers with controlled absorber based on GaInAsSb/GaAlAsSb quantum well heterostructure was fabricated and experimentally studied. The emission wavelength of these lasers shifts from 2.24 to 2.28 lm when the bias on the control contact decreases from the voltage equal to that on the main electrode to 0V when the control contact is grounded. The principle of operation of such a device is given.

Tunable semiconductor lasers attract attention as a promising light source for the laser spectroscopy and fiber optical networks. In this abstract we report about the tunable semiconductor laser with controlled absorber that combines both the construction simplicity and a wide tuning range that is about a half-width of the optical amplification spectra. We have studied the whispering gallery mode (WGM) semiconductor lasers for Mid-IR. The difference of the device under study and the common WGM laser [1] is in the construction of the upper contact. The upper contact in the lasers under investigation consists of two sectors. The parts of the contact were separated by a gap about 10 μm width. The voltage applied to the different parts of the contact was different. One part of the contact (bias) was under the voltage large enough for the lasing and another (control) part was under the lower voltage that changes from 0 (the potential of the substrate) to 0.77 V.

It was found that when the voltage applied to the control contact changes from 0.77 down to zero the spectral position of the laser line shifts from 2.2743 to 2.2352 μm. The lasing spectra for the different control voltages are shown in Fig. 1. The qualitative explanation of the observed effect can be elucidated by Fig. 2. For the sake of simplicity let us consider a single quantum well as an active region at zero temperature. The schematic energy diagram of the emitting part of the laser is shown in Fig. 2a. In the energy interval from E_0, that is the energy distance between the bottoms of the electrons and holes size-quantization subbands to E_1 that is the difference between the Fermi quasi-levels, there is an optical amplification and generation takes place at the energy near the peak of this curve.

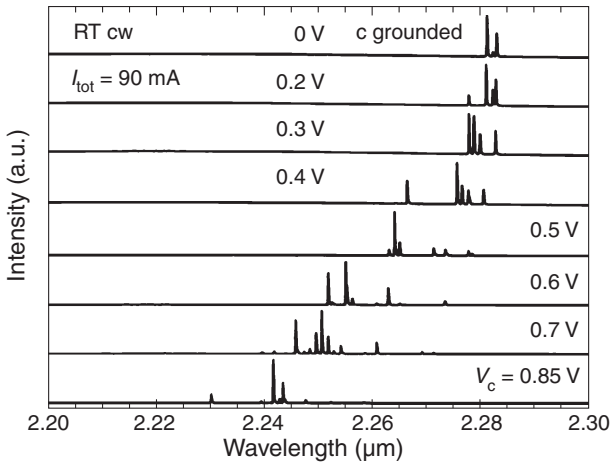

Fig. 1. The spectra of the laser under different biases on the control contact.

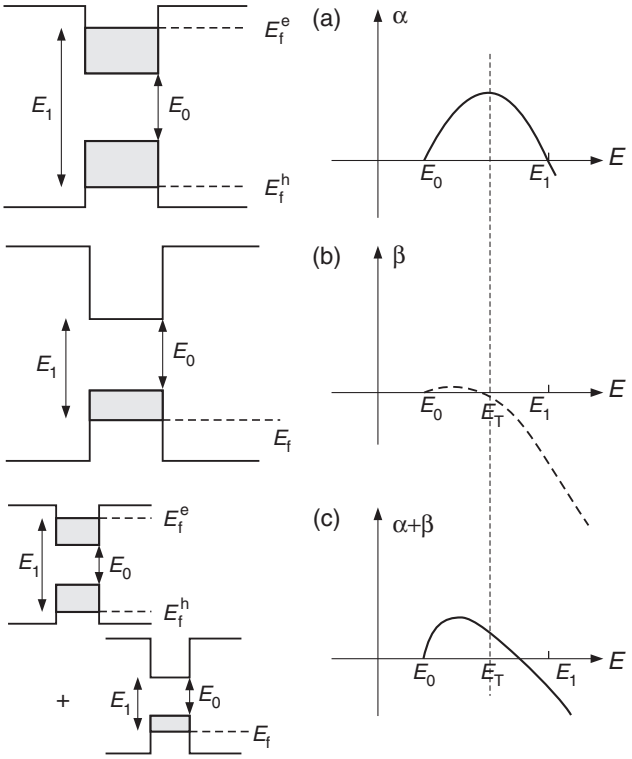

Fig. 2. Sketches of the zone diagram and optical amplification-absorption spectra for a single-well semiconductor laser. (A) — in a lasing regime, (B) — under zero bias and (C) — total amplification spectrum when the control contact is grounded.

When the control contact is grounded (connected to the substrate of the sample) the device effectively consists of two parts. In one part there is the optical amplification with the spectrum shown in Fig. 2a and another part is an absorber with the spectrum β. The gain of the whole device is $G = \exp(\alpha l - \beta l)$ (l is a sector length), so for the same length of these two parts the generation will take place near the peak of the effective gain spectrum that is equal to peak of the $\alpha - \beta$. The optical amplification and absorption spectra for the emitting and control parts of the device are qualitatively looks like that in Fig. 2a,b. One can see that the total amplification-absorption spectrum of the whole device looks like that in Fig. 2c, so there is an energy interval between E_0 and E_T where the optical amplification exists. This amplification is enough for the device to

start lasing due to the high Q-factor of the WGM resonator [2]. When the voltage applied to the control contact changes from that applied to the emitting part down to zero the amplification spectrum smoothly changes from that shown in Fig. 2a to Fig. 2c and results in the smooth shift of the laser emitting spectrum shown in Fig. 1. In summary we would like to say that highly tunable Mid-IR whispering gallery mode semiconductor laser with controlled absorber based on quantum well heterostructure was fabricated. One part of the sector contact is under voltage enough for the lasing and another (control) part was under changed voltage. It was shown that when the voltage applied to the control contact changes from 0 up to 0.77 V the spectral position of the laser lines shifts from 2.235 to 2.274 μm. The mechanism of the tunability for laser with controlled absorber was suggested. Such highly tunable WGM laser can be applied in diode laser spectroscopy

Acknowledgements

This work was partially supported in part by RFBR grant 10-02-93110, 10-02-00548-a and the programm of the Presidium of RAS number 27.

References

[1] A. N. Imenkov, V. V. Sherstnev, M. A. Sipovskaya, A. P. Astakhova, E. A. Grebenshchikova, A. M. Monakhov, K. V. Kalinina, G. Boissier, R. Teissier, A. N. Baranov, and Y. P. Yakovlev, *Tech. Phys. Lett.* **35(9)**, 857 (2009).

[2] A. B. Matsko and V. S. Ilchenko, *IEEE J. Sel. Top. Quantum Electron.* **12(1)**, 3 (2006).

20th Int. Symp. "Nanostructures: Physics and Technology"
Nizhny Novgorod, Russia, June 24–30, 2012

Double bosonic stimulation of radiative THz transitions in polaritonic systems

M. A. Kaliteevski[1,2], I. A. Shelykh[3] and I. G. Savenko[1,3]

[1] St Petersburg Academic University, St Petersburg, Russia
[2] Ioffe Physical-Technical Institute, St Petersburg, Russia
[3] Science Institute, University of Iceland, Dunhagi-3, IS-107, Reykjavik, Iceland

Abstract. We show that planar semiconductor microcavities in the strong coupling regime can be used as sources of stimulated terahertz radiation. Emitted terahertz photons would have a frequency equal to the splitting of the cavity polariton modes. We consider the nonlinear terahertz emission by the system of cavity polaritons in the regime of polariton lasing. To account for the quantum nature of terahertz-polariton coupling, we use the Lindblad master equation approach and demonstrate that quantum microcavities reveal a rich variety of nonlinear phenomena in the terahertz range, including bistability, short terahertz pulse generation, and terahertz switching.

The terahertz (THz) band remains the last region of the electromagnetic spectrum which does not have a wide application in modern technology due to the lack of a solid state source of THz radiation [1]. The fundamental objection preventing realization of such a source is the small value of spontaneous emission rate R of the THz photons. According to the Fermi golden rule, this rate is about tens of inverse milliseconds, while the lifetime of the carrier typically lies in the picosecond range due to efficient interaction with phonons. The spontaneous emission rate can be increased by application of the Purcell effect when the emitter of THz is placed in a cavity for the THz mode, but even in this case cryogenic temperatures are required to provide quantum efficiency of the order of about 1% for a typical quantum cascade structure. Recently, it was proposed that the rate of spontaneous emission for THz photons can be additionally increased by bosonic stimulation if a radiative transition occurs into a condensate state of bosons (see Fig. 1). Radiative transition between polariton states is allowed if upper polariton state is mixed with an exciton state of a different parity. In this case R should be multiplied by occupancy number of the final state, what, in case polariton condensate could add several orders of magnitude to the value of R. Multiplication of R by occupancy number of final state and by number of THz photons in high-Q cavity for THz radiation can make propability of THz emission high enough for the realisation of room temperature solid state THz devces [2].

Due to their excitonic fraction cavity polaritons may efficiently interact with each other. This is why semiconductor microcavities demonstrate pronounced optical nonlinearities even in the regime of the moderate pump powers. This nonlinearities induce coupling of the subsystems of THz and optical photons, and affect the process of formation of polariton condensates. Consequently, the output optical system can be strongly affected by external THz radiation incident on the structure. Basically, the action of an optical polariton laser many be triggered by external THz radiation. We are going to use this peculiar property of polariton lasers for the design of detectors of THz radiation.

Quantum mechanical description of the interacting system of THz photons and microcavity polaritons system can be developed on the basis of on the generalized Lindblad equation for the density matrix [3]. Polaritons exibist pronounced nonlinear properties at excitation level as low as 1 W/sq. cm, and

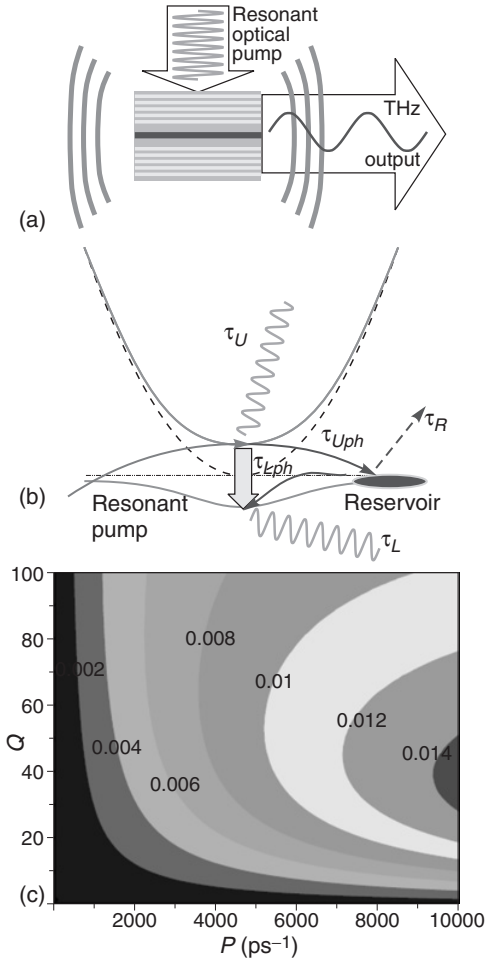

Fig. 1. (a) Schematic diagram of the polariton THz emitter. A planar microcavity is embedded in the lateral THz cavity. (b) Schematic diagram illustrating possible transitions in the system. The vertical axis is energy, the horizontal axis is the in-plane wavevector. (c) Quantum efficiency of the terahertz emitter as a function of the pump intensity P and a quality factor of the terahertz cavity.

therefore system of interacting THz photoon and polaritons demonstrates a variety of intriguing nonlinear effects, including bistability (see Figure 2), THz switching, and generation of short THz wavelets.

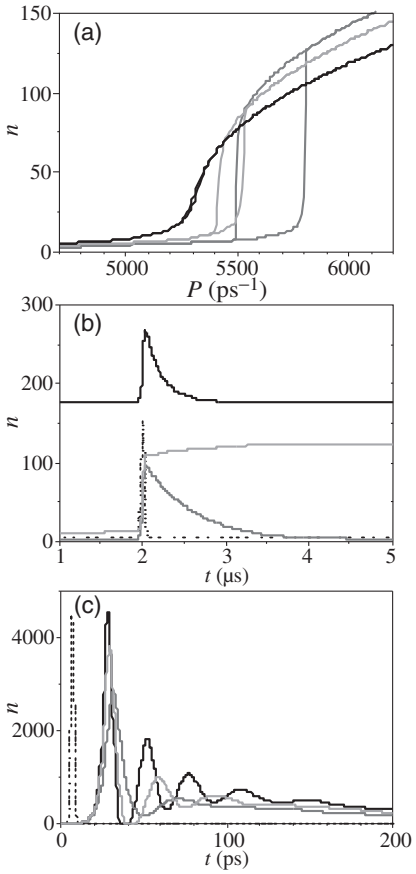

Fig. 2. Occupancy of THz mode in equilibrium state as a function of pumping illustrating bistability 1 K (gray line), 10 K (light gray line), and 20 K (black line) (a). Response of the of the system to short incident THz pulse illustrating switching (b), and temporal dependence of THz occupancy illustrating THz short pulse generation (c) [3].

The equilibrium value of the THz population $n(P)$ demonstrates thresholdlike behavior. For high enough temperatures, below the threshold the dependence of n on P is very weak. When pumping reaches a certain threshold value, the polariton condensate is formed in the lower polariton state, radiative THz transition is amplified by bosonic stimulation, and the occupancy of the THz mode increases superlinearly (Fig. 2a). This behavior is qualitatively the same as in the approach operating with the semiclassical Boltzmann equations. The bistable jump in the dependence n vs. P occurs when the frequency of the pump tunes into the resonance with the cavity mode. The parameters of the hysteresis loop strongly depend on the temperature. It is very pronounced and broad for low temperatures, narrows with the increase of the temperature, and disappears completely at 20 K.

If the system of coupled THz photons and cavity polaritons is in the state corresponding to the lower branch of the S-shaped curve in the bistability region, illumination of the system by a short THz pulse can induce its switching to the upper branch, as demonstrated in Fig. 2c. One sees that the response of the system is qualitatively different for different values of the pump P. If P lies outside the bistability region, the application of a THz pulse leads to a short increase of n, but subsequently the system relaxes to its original state (red and blue curves). However, when the system is in the bistability regime, the switching occurs. Note that this effect is of a quantum nature and cannot be described by using the approach based on the semiclassical Boltzmann equations.

The coherent nature of the interaction between excitons and THz photons makes possible the periodic exchange of energy between polaritonic and photonic modes and oscillatory dependence of the THz signal in time (Fig. 2, centre).The period of the oscillations is sensitive to the number of injected polaritons. If the lifetime of polaritons is less than the period of the oscillations, single pulse behavior can be observed.

References

[1] M. Tonouchi, *Nature Photonics* **1**, 97 (2007).
[2] K. V. Kavokin, M. A. Kaliteevski, R. A. Abram, A. V. Kavokin, S. Sharkova, and I. A. Shelykh, *Appl. Phys. Lett.* **97**, 201111 (2010).
[3] I. G. Savenko, I. A. Shelykh, and M. A. Kaliteevski, *Phys. Rev. Lett.* **107**, 027401 (2011).

20th Int. Symp. "Nanostructures: Physics and Technology"
Nizhny Novgorod, Russia, June 24–30, 2012

Observation of defect mode in spectra of surface magnetostatic waves in ferrite magnonic crystal

Yu. A. Filimonov[1], S. A. Nikitov[2,3], E. S. Pavlov[1] and S. L. Vysotsky[1]

[1] Kotelnikov Institute of Radio Engineering and Electronics (Saratov Branch) RAS, Zelenaya str. 38, 410019 Saratov, Russia
[2] Saratov State University, Saratov, Russia
[3] Kotelnikov IRE RAS, Mochovaya str. 11, 140019 Moscow, Russia

Abstract. Propagation of surface magnetostatic waves in ferrite 1D magnonic crystals with defects of surface periodic structure of etched grooves was investigated. "Groove defect", "strip defect" and "phase jump defect" were made as a grooves or distances between grooves (stripes) differ from parameters of periodic structure. Defect modes were observed inside the first Bragg resonances frequency gap if defect (both "groove" and "strip") size was closed to multiplied period of the surface structure. In case of "phase jump defect" defect mode was found inside the second Bragg resonances frequency gap.

Introduction

Propagation of spin waves (SW) in ferrite films with surface periodic structures is accompanied by arising of band gaps in SW's spectra at wavenumbers corresponding to Bragg condition where is the period of surface structure, n is integer [1,2]. similarly to photonic [3,4] or phononic [5,6] crystals such ferrite structures were called as ferrite magnonic crystals (MC). MCs are intensively investigated as a promising base for miniaturization of signal processing tunable devices [7]. One of important problems in the investigations of real MC is affecting of the magnonic gap by various kinds of imperfection which are inevitably present due technological reasons or specifically introduced to modify the magnonic spectra. Some of possible discrepancies from ideal periodicity like partial randomization [8], modulation of several parameters instead off alone [9], nonuniformity of dissipative parameters distribution [10], quality, profile and finite thickness of boundaries between regions with different magnetic parameters [11,12] were discussed theoretically. Pointed imperfections leads to decrease of the MG bandwidths and some specific effects like SW damping controllable by bias filed [10] and possibility to turn "on" and "off" the MG in SW spectra by turning of magnetic field near some critical value [9]. In last case such systems can be used as switches or filters controlled by magnetic field. As it has been shown by one of us [1], the local modification of the thickness of one of the layers of 1D MC leads to occurrence of discrete levels within the magnonic gap at frequencies corresponding to the halfwavelength standing wave resonances excitation along defect layer length. Note that presence of a single defect of more general form, when both spatial and magnetic parameters are changed, may leads (depending on the defect size and composition) to appearance of either one or several defect modes, or a mini-band of those, within MG or below the bottom frequency allowed in perfect MC [13–15]. Such defect modes can be used for enhancement of nonlinear effects [16,17], designing of MW generators [18] and signal filtering [19].

1. Results of experiments

For experimental investigations 1D MCs with defects of periodic structures were made from YIG film with thickness $h = 14.7$ μm. Non-disturbed part of MC was an array of grooves of $\delta h \approx 1.8$ μm depth, $L_g \approx 80$ μm width etched with lateral period $\Delta \approx 150$ μm — see Figure 1a (alternatively the surface structure can be also represented as an array of stripes of $L_s \approx 70$ μm width distanced at 80 μm from each other) — see Figure 1b. We have investigated several types of 1D MC with structural defect having form of single "groove defect" $L_g^{\text{def}} \neq L_g$ or "strip defect" $L_s^{\text{def}} \neq L_s$ — see the Figure 1a,b. MCs were placed in microstrip delay line in such a way that defects were located in the middle between two microstrip transducers distanced at 3 mm. Value of tangential bias magnetic field corresponding to magnetostatic surface wave exciting was equal to 320 Oe.

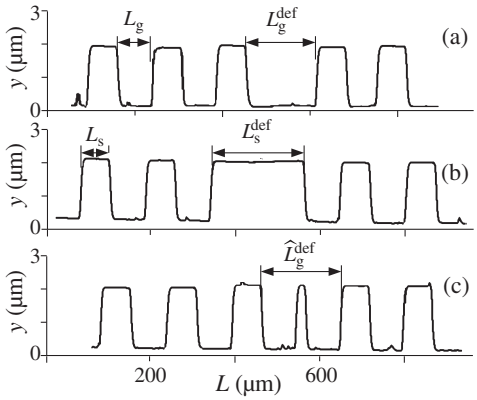

Fig. 1. Profiles of "groove defect" (a), "strip defect" (b) and "phase jump defect" (c) made in 1D YIG MC periodic structure.

The Figure 2 presents a part of amplitude frequency response (AFR) of microstrip delay line for the cases of 1D MC (dotted line) and 1D MC with $L_s^{\text{def}} \approx 150$ μm (clear AFR is shown in insert). One can see the defect mode (marked DM) inside the first Bragg resonance band gap Δf_1. The same results were obtained for MC with both $L_s^{\text{def}} \approx 300$ μm, $L_s^{\text{def}} \approx 600$ μm and $L_g^{\text{def}} \approx 300$ μm, $L_g^{\text{def}} \approx 600$ μm widths. For higher order Bragg resonances stop band (for example, Δf_2) appearance of the defect modes was not so evident like for the first. For defects width L_g^{def} and L_s^{def} closed to 230, 215, 545 μm that are not a multiple of the period defect modes were not detected.

The Figure 3 presents AFR in case of MC with "phase jump defect" in form of narrow $L_s^{\text{def}} \approx 30$ μm strip instead of L_s.

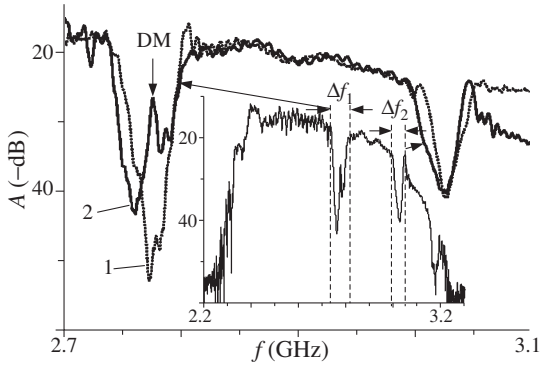

Fig. 2. Amplitide-frequency response of microstrip delay line in cases of 1D MC (dotted line) and 1D MC with "strip defect" $L_s^{\text{def}} \approx 150\ \mu$m (solid line).

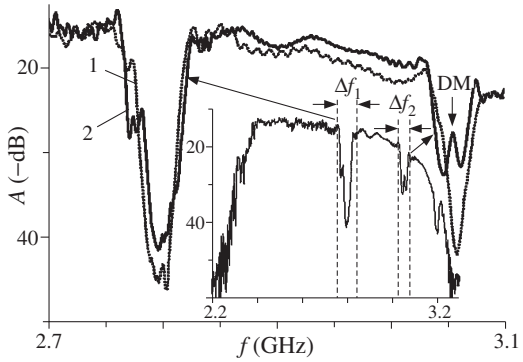

Fig. 3. Amplitide-frequency response of microstrip delay line in cases of 1D MC (dotted line) and 1D MC with "phase jump defect" (solid line).

Such defect can be treated as a phase jump in Bragg lattice and in case when it close to π one can expect appearance of the defect mode just at the Bragg resonance frequency [18]. In our case we have observed appearance of the defect mode in MG corresponds to the second-order Bragg resonance Δf_2, while in first Bragg resonance gap Δf_1 only small perturbations can be found. Note that this narrow stripe defect can be treated as a second order perturbation of "groove defect" with $L_g^{\text{def}} \approx 150\ \mu$m. As this defect is centered in wide groove it can suppress the resonances with maximal amplitude at the center of groove with $L_g^{\text{def}} \approx 150\ \mu$m , on the other hand it would have smaller influence on resonance having nodes at the center. It must be also taken in account, that the geometry size of the defect is not perfectly coincide with profile of the internal magnetic field determining the SW scattering processes.

It should be noted that previously the one- or two-port Bragg resonators were extensively studied [19,20]. The conditions for resonant excitations of Bragg resonators and for defect mode in magnonic crystal are evidently coincide. It is interesting also to understand possibility to exploit groove apodization suggested for suppression the ripples in amplitude Bragg resonator's AFR for controlling parameters of the defect mode

Acknowledgements

This research has received funding from RFBR (grants No. 11-07-12081 and 11-07-00233), Federal Grant-in-Aid Program "Human Capital for Science and Education in Innovative Russia" (governmental contracts No. П485, and 14.740.11.0077), the Grant from Government of Russian Federation for Support of Scientific Research in the Russian Universities Under the Guidance of Leading Scientists (project No. 11.G34.31.0030) and European Community's Seventh Framework Programme under Grant Agreement No. 247556 (NoWaPhen).

References

[1] Nikitov S.A, Tailhades P., Tsai C., J. *Magn. Magn. Mat.* **236**, 320 (2001).
[2] Serga A.A., Chumak A.V. and Hilledrands B. *J. Phys. D.: Appl. Phys.* **43**, 264002 (2010).
[3] Yablonovich E. *Phys. Rev. Lett.* **58**, 2059 (1987).
[4] Joannopulos J.D., Jonhson S.G., Win J.N., Meade R.D. Photonic crystals: Molding the flow of light) (Princeton NJ: Princeton university Press), (2008).
[5] Sigalas M.M., Economou E.N. *J. Sound Vib.* **158**, 377 (1992).
[6] Sigalas M.M., Economou E.N. *Solid State Commun.* **86**, 141 (1993).
[7] Ustinov A.B., Drozdovckii A.V., Kalinikos B.A. *Appl. Phys.Lett.* **96**, 142513 (2010).
[8] Ignatchenko V.A, Mankov V.I., Maradudin A.A. *Phys. Rev. B* **59**, 42 (1999).
[9] Kruglyak V.V., Kuchko A.N., *Physica B* **339**, 130 (2003).
[10] Kruglyak V.V., Kuchko A.N., *Journ. Magn. Magn. Mater.* **272-276**, 302 (2004).
[11] Tkachenko V.S., Kruglyak V.V., Kuchko A.N. *Journ. Mag. Mag. Mater.* **307**, 48 (2006).
[12] Ignatchenko V.A., Mankov Y.I., Maradudin A.A. *Phys. Rev. B* **62**, 2181 (2000).
[13] Kuchko A.A., Sokolovskii M.L., Kruglyak V.V., *Fiz. Met. Metalloved.* **101**, 1 (2006).
[14] Kuchko A.A., Sokolovskii M.L., Kruglyak, *Phys. B* **370**, 73 (2005).
[15] Kruglyak V.V., Sokolovskii M.L., Tkachenko V.S., Kuchko A.N. *Journ. Appl. Phys.* **99**, 08C906 (2006).
[16] Soljacic M., Joannopoulos J.D. *Nature Mater.* **3**, 211 (2004).
[17] Khanikaev A.B., Baryshev A.V., Fedyanin A.A., Granovsky A.B., Inoue M. *Optics Express* **15**, 6612 (2007).
[18] Peskov N.Y., Ginzburg N.S., Kaniskii A.A., Kaminskii A.K., Denisov G.G., Sedykh S.N., Sergeev A.P., Sergeev A.S., *Pis. Zh. Tech. Fiz.* **25**, 19 (1999).
[19] Ishak W.S., *Pros. IEEE* **76**, 171 (1986).
[20] Maeda A., Susaki M., *IEEE Trans. on Magn.* **42**, 3096 (2006).

20th Int. Symp. "Nanostructures: Physics and Technology"
Nizhny Novgorod, Russia, June 24–30, 2012

YIG film based phonon-magnonic crystal

Yu. A. Filimonov[1], Yu. V. Khivintsev[1], S. A. Nikitov[2,3], E. S. Pavlov[1] and S. L. Vysotsky[1]

[1] Kotelnikov Institute of Radio Engineering and Electronics (Saratov Branch) RAS,
Zelenaya str. 38, 410019 Saratov, Russia
[2] Saratov State University, Saratov, Russia
[3] Kotelnikov IRE RAS, Mochovaya str. 11, 140019 Moscow, Russia

Abstract. Magnetoelastic waves propagation in thin film YIG/GGG structure with periodic array of grooves in YIG film was investigated at bias magnetic field directed perpendicular to the surface of the structure. It was shown that in condition of magnetostatic waves' Bragg resonance both magnetic and elastic properties are strongly modified. So the structure can be qualify as phonon-magnonic crystal.

Introduction

During last decade investigation of spin waves (SW) propagating in ferrite magnonic crystals (MC) (usually looks like yttrium-iron garnet (YIG) film with 1D or 2D surface periodic structure) paid a great attention [1,2]. The main reported feature of SW spectra is arising of band gaps at SW's wavenumbers q_n coresponging to Bragg condition $q_n = \pi\, n/\Lambda$ where Λ is the period os surface structure, n is integer, similar to the photonic [3,4] or phononic [5,6] crystals. SW spectra band gaps both give a simple possibility of fundumental investigation of SW propagation in highly dispersive conditions and are perspective for miniaturization of signal processing tunable devices [7]. Note that YIG films are usually epitaxially grown onto gadolinium-gallium garnet (GGG) substrate and YIG/GGG structure is a good medium for propagating of both SW and elastic waves (EW) that particularly can results in forming of hybrid magnetoelastic waves (MEW) that leads to SW spectra reconstructions in the form of anti-crossing (repulsion) of the dispersion curves SW and EW at frequencies where phase matching conditions are fulfilled. MEW were discussed in a lot of publications (for example, [8,9]). However for our knowledge till now the properties of MEW in periodic structures haven't been investigated. The purpose of this work is to discuss the results of experimental investigations of MEW propagation through the YIG/GGG epitaxial structure with microstructured YIG film surface.

1. Magnetoelastic waves in YIG/GGG films

In despite of low enough magnetoelastic coupling constant ($\eta \approx 10^{-3}$) YIG is a very good material for investigation of MEW because both magnetic [10] and [11] losses in this material are extremely low. In experiments with propagating magnetostatic waves (MSW) in YIG/GGG film MEW observed at resonance frequencies which are close to the cut-off frequencies f_N of Lamb-like and shear horizontal (SH) modes [12,13] of the acoustic layered waveguide. Acoustic polarization of the SH-modes doesn't change in the reflection processes, while transverse and longitudinal components of the Lamb-like modes demonstrates mutual transformation under reflection from the waveguide surfaces [14]. Due to pointed peculiarities the surface MSW (SMSW) and forward volume MSW (FVMSW) [10], which can interact with SH-modes with higher efficiency when backward volume MSW (BVMSW) [10], are more preferable for experimental investigation of the resonance interaction of MSW and volume Lamb- and SH-modes of the YIG/GGG structure. Typically YIG film thickness d is much smaller than substrate thickness L_{GGG} and for cut-off frequencies of the SH-modes f_N^{SH} one can write

$$f_N^{SH} \approx \frac{V_t^{GGG}\, N}{2L_{GGG}}\,, \qquad (1)$$

where $V_t^{GGG} \approx 3.57 \times 10^5$ cm/s is velocity of transverse elastic waves in GGG substrate, N is the mode number equal to the number of elastic half wavelength along the thickness of substrate. Note, that efficiency of MSW and EW interaction depends on the overlapping integral I of magnetoelastic field $\mathbf{h_{me}}$ generated by elastic waves due to magnetostriction and SW microwave magnetization $\mathbf{m}$

$$I \sim \int_0^h \mathbf{h_{me}} \times \mathbf{m} dz\,,$$

where the integral had been taken along YIG film thickness in case of uniformity of fields in plane. It is clear that YIG film works like the half wavelength magnetostrictive transducer MSW that can effectively excite travelling shear elastic waves into the substrate [15].

2. Results of experiments

Taking in mind all mentioned circumstances we have prepared the YIG/GGG structure with microstructured YIG surface in the form of periodically etched grooves $\delta d \approx 0.4$ μm in depth and $w \approx 52$ μm in width with period $\Lambda \approx 100$ μm. The thickness of YIG film and GGG substrate were $d \approx 3.8$ μm and $L_{GGG} \approx 596$ μm, respectively. In approximation that microstructuring of the YIG surface conserve ground state in YIG close to the uniform one can use (1) to estimate frequencies where YIG film can be used as a half wavelength EW transducer . Taking in account the velocity of transverse elastic wave in YIG $V_t^{YIG} \approx 3.85 \times 10^5$ cm/s one can find frequencies $f \approx 500$ MHz, where efficiency of MEW exciting will be optimal.

The Figure presents the amplitude-frequency responce (AFR) of the microstrip delay line with microstructured YIG/GGG structure measured under FVMSW excitation at bias field $H_0 \approx$ 1860 Oe (directed parallel to the normall to the YIG surface) and distance between input and output microstrip transducers $S \approx 1.5$ mm. On can see that AFR includes equidistant oscillations distanced by $\Delta f \approx 3.5$ MHz corresponding to the first half-wavelength elastic transverse wave resonance

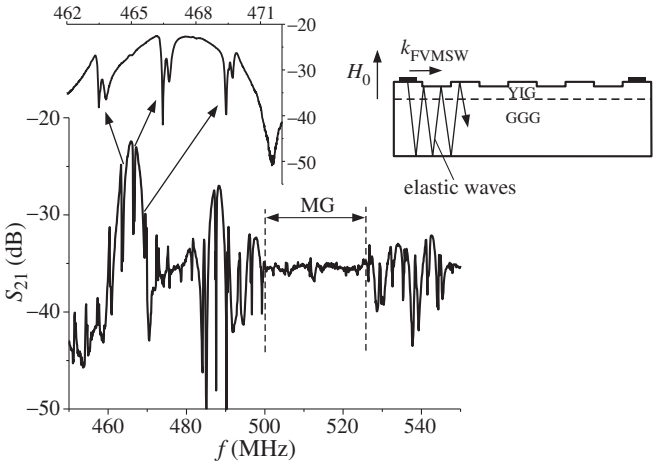

Fig. 1. Amplitude-frequency response of signal transmitted through normally magnetized YIG/GGG epitaxial structure with periodically ($\Lambda \approx 100$ μm) microstructured YIG surface.

through the GGG substrate. Frequencies of this oscillations well defined by (1), where N values are taken from the interval $N \approx 152 \ldots 197$. In general the pointed peculiarities coincide well with previously obtained results [13] and clear correspond to MEW excitations.

However, the amplitude of the transmitted signal in frequency interval $\Delta f \approx 500 \ldots 520$ MHz have dropped up to the level of the direct electromagnetic leakage between transducers. This frequency interval corresponds to FVMSW with wavenumbers $q \approx 300$ cm^{-1} which well corresponds to first Bragg resonance $q_1 = \pi/\Lambda$.

Note that for MEW conditions of Bragg resonance simultaneously must fullfilled both spin and elastic waves, becouse they are in phase mathcing at the magnetoelastic resonance conditions. As a result both magnonic (MG) and phononic gaps must be observed simultaneously. However, one can see that in MG small-amplitude oscillations correspondent to the SH-mode excitations still present. This effect of filtering of the SH-modes at frequencies correspondent to MG formation must be attributed as a partial decoupling of spin and elastic waves, when elastic waves travels to the non-magnetic substrates. As a result, the SH-modes elastic energy is mostly concentrated in the YIG substrate and effectiveness of the Bragg resonance on the small amplitude ($\delta d \ll d \ll L_{GGG}$) surface microstructure must be smaller than for FVMSW energy that is mostly concentrated in YIG film. Nevertheless it is obvious that microstructuring of the YIG surface is accomplished by modulation of both magnetic and elastic properties so we can qualify this structure as hybrid phonon-magnonic crystal (PMC).

Acknowledgements

This research has received funding from RFBR (grants No. 11-07-12081 and 11-07-00233), Federal Grant-in-Aid Program "Human Capital for Science and Education in Innovative Russia" (governmental contracts No. П485, and 14.740.11.0077), the Grant from Government of Russian Federation for Support of Scientific Research in the Russian Universities Under the Guidance of Leading Scientists (project No. 11.G34.31.0030) and European Community's Seventh Framework Programme under Grant Agreement No. 247556 (NoWaPhen).

References

[1] Nikitov S.A, Tailhades P., Tsai C., J. *Magn. Magn. Mat.* **236**, 320 (2001).
[2] Serga A.A., Chumak A.V. and Hilledrands B. *J. Phys. D.: Appl. Phys.* **43**, 264002 (2010).
[3] Yablonovich E. *Phys. Rev. Lett* **58**, 2059 (1987).
[4] Joannopulos J.D., Jonhson S.G., Win J.N., Meade R.D. *Photonic crystals: Molding the flow of light* (Princeton NJ: Princeton university Press), (2008).
[5] Sigalas M.M., Economou E.N. *J. Sound Vib* **158**, 377 (1992).
[6] Sigalas M.M., Economou E.N. *Solid State Commun.* **86**, 141 (1993).
[7] Ustinov A.B., Drozdovckii A.V., Kalinikos B.A. *Appl. Phys. Lett.* **96**, 142513 (2010).
[8] Parekh J.P. *Electr. Lett.* **5**, 322 (1969).
[9] Filimonov Yu.A., Kazakov G.T, Khivintsev Yu.V. *J. Magn. Magn. Mater.* **272–276**, 1009 (2004).
[10] Gurevich A.G. and Melkov G.A. *Magnetization oscillations and Waves)* (CRS Press, Boca Raton), (1996).
[11] Le Craw R.C., Spencer E.G., Gordon E.I. *Phys. Rev. Lett.* **6**, 620 (1961).
[12] H. Van de Vaart, Methews H. *Appl. Phys. Lett* **16**, 153 (1970).
[13] Gulyaev Yu.V., Zilberman P.E., Kazakov G.T., Nam B.P., Sysoev V.G., Tikhonov V.V., Filimonov Y.A., Khe A.S. *JETP Let.* **34**, 500 (1981).
[14] Landau L.D., Lifshitz E.M. *Theory of Elasticity* (Pergamon Press) (1975).
[15] Bommel H.E., Dransfeld K. *Phys. Rev. Lett.* **3** 83, (1959).

20th Int. Symp. "Nanostructures: Physics and Technology"
Nizhny Novgorod, Russia, June 24–30, 2012

Polar phonons and Raman spectra of the long period nitride-based superlattices

M. B. Smirnov and *D. V. Pankin*
Physics Department, St Petersburg State University, Ulyanovskaya 1, Petrodvorets, 198504 St Petersburg, Russia

Abstract. Raman spectra of nitride-based superlattices of various thicknesses of the layers are simulated within dielectric continuum model and the lattice dynamics. Delocalized polar modes of high Raman intensity are revealed. Their frequencies are rather sensitive to the superlattice geometry. This may by useful with the aim of the sample characterization.

Introduction

The interest of group III nitride superlattices (SL) is the fabrication of opto-electronic devices, particularly for the short-wavelength emitters in high-power, high-temperature and high-frequency electronics [1]. An important area of investigations concerns the Raman spectra which provide valuable information on lattice vibrations and the electron-phonon interactions. It was shown that the Raman-active are rather sensitive to the SL's structure [2]. However, informativeness of a Raman spectroscopy study depends on availability of reliable interpretation schemes. Two related theoretical approaches are the quantum mechanical simulations [3] and the dielectric continuum modeling [4]. The former provides a comprehensive description for the short period SLs, the latter is sufficiently accurate for studying the long period SLs. Principal shortcoming of the dielectric continuum model is the lack of information on the Raman scattering intensity. In order to overcome this difficulty, one can use a combined approach: to estimate the Raman scattering tensors of bulk materials by using the quantum-mechanical simulation, and then to employ this information in computer modeling of SLs within the dielectric continuum model. This paper reports results obtained in this direction for the AlN/GaN SLs of the superstructure periods varying from several lattice units up to values comparable with the wavelength of scattered light. Special attention is paid to spectral manifestations of the delocalized propagating modes and the localized interface phonon modes.

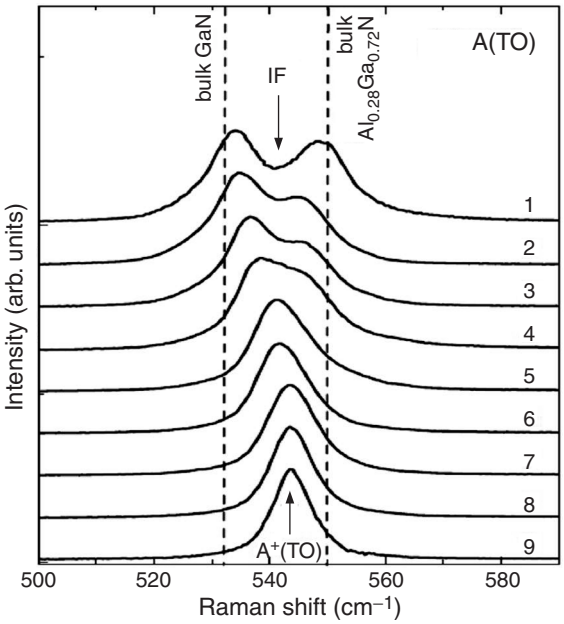

Fig. 2. Experimental A(TO) Raman spectra of the GaN/$Al_{0.28}Ga_{0.72}N$ SLs with $d1 = d2$ and different $d = d1 + d2$. Corresponding s values are as follows: $s = 0.25\,(9)$, $0.5\,(8)$, $1\,(7)$, $2\,(6)$, $4\,(5)$, $8\,(4)$, $16\,(3)$, $32\,(2)$, $150\,(1)$. Positions of the A(TO) lines in bulk constituents are shown by dotted vertical lines. Positions of the A^+(TO) mode in a short period SL and the IF mode in a long period SL are shown by arrows.

1. Calculations

In our lattice dynamics calculations, we deal with SLs built up along hexagonal axis of wurtzite structure. The systems involved $2m$ bilayers of GaN and $2n$ bilayers of AlN. So, one can refer such SLs as $(GaN)_{2m}(AlN)_{2n}$ with $m + n = 12$. The SL's composition is characterized by ratio $f = n/(n + m)$. Raman spectra for A(TO) modes simulated with different f values are shown in Fig. 1.

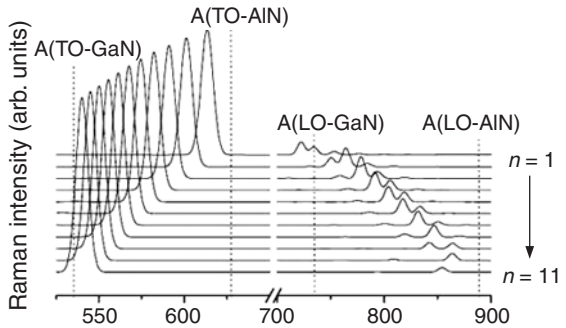

Fig. 1. The x(zz)x Raman spectra of SLs $(GaN)_m(AlN)_n$ calculated for different f values.

One intense spectral line is seen in the A(TO) spectra. Its intensity does not depend on the SL composition, but its frequency varies between values typical of the bulk constituents proportionally to the relative layers thickness. This is a typical one-mode behavior exhibited by some spectral lines of alloys. Experimental Raman spectra of the equi-period GaN/$Ga_xAl_{1-x}N$ SLs with period varying from 2.5 up to 1500 nm are shown in Fig. 2. They clearly manifest that the two mode spectrum transforms into one mode spectrum at decreasing SL period. Characteristic parameter controlling the spectrum transformation is $s = qd$ (here q is the phonon wavelength and d is the SL period).

Dielectric continuum model (DCM) looks for solutions of Maxwell's equations in 1D-layered periodic media in the form

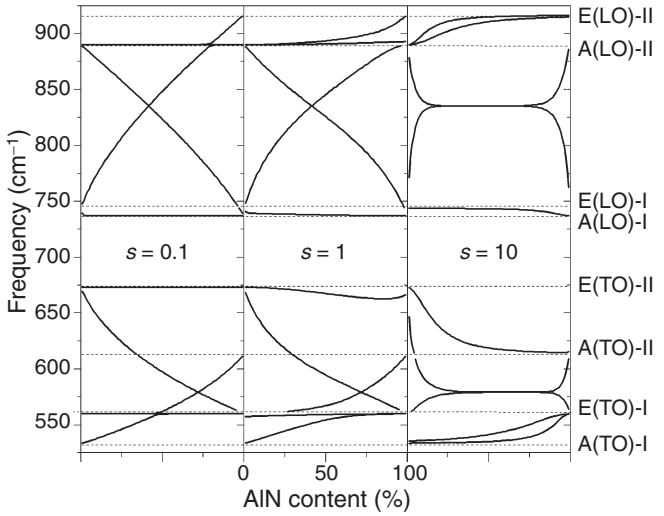

Fig. 3. Frequencies of polar modes of the GaN/AlN SLs in dependence on composition parameter f calculated by DCM at different s values. Experimental data for the A(TO) modes in short period SLs are shown in the left panel by symbols. GaN and AlN components are labeled as I and II.

for the first-type layer and the second-type layer respectively.

$$E_1 \sim \exp(iqx + g_1 z)\,, \qquad -d_1 < z < 0\,, \qquad (1)$$

$$E_2 \sim \exp(iqx + g_2 z)\,, \qquad 0 < z < d_2 \qquad (2)$$

(axes x and z are perpendicular and parallel to the SL axis) within the one-mode approximation for the dielectric constant dispersion

$$\epsilon(\omega) = \epsilon^{\infty}\,\frac{\omega_{\mathrm{LO}}^2 - \omega^2}{\omega_{\mathrm{TO}}^2 - \omega^2}\,. \qquad (3)$$

According to values of g_1 and g_2 parameters, the solutions are classified as propagating (PR), quasi-confined (QC) or interface (IF) modes. Numerical solutions for the GaN/AlN SL of different layer thickness ratios are shown in Fig. 3 in dependence on the composition parameter f.

Modes of the short-period SLs ($s = 0.1$) are shown in the left panel. It is seen that the curves corresponding to the IF and QC modes smoothly merge together forming the continuous $\omega(f)$ dependencies corresponding to the long-wave approximation [2] . That of lowest frequency is very similar to the $\omega(f)$ behavior of the intense A(TO) mode shown in Fig. 1. It is evident that assignment of A(TO) mode as a QC or IF phonon depends on ratio of layer thicknesses: it is a QC mode at $f = 0.46$ and it is an IF mode at $f = 0.48$. The situation is different in the case when SL period is comparable with wavelength of scattered light. Central panel in Fig. 3 (case of $s = 1$) shows the $\omega(f)$ curves for QC or IF modes have no common points: they diverge on approaching to the limit frequency values. Such a behavior indicates considerable coupling of those modes with E(TO)-GaN mode which is no longer confined in the GaN layers. The nature of this coupling is quite evident: for the finite wave vector directed along interface plane, the atomic oscillations in z and x directions are dynamically coupled. The dependencies presented in Fig. 3 show that at $f < 0.47$ curve QC-mode deviates from that of IF-mode not far than 8 cm^{-1}. This provides an estimation of accuracy of the long-wave approximation (see [2]) as 8 cm^{-1} at $s < 1$.

At thicker layers, divergence of the $\omega(f)$ curves for QC and IF modes becomes more pronounced. This is illustrated by curves in the right panel (case of $s = 10$). This evidences a principal distinction between IF and QC modes in a large-period SL. All $\omega(f)$ curves in this panel exhibit large plateaus at $0.2 < f < 0.8$. Physically, this means that frequencies of these modes do not depend on f in case of a long period SL: frequencies of QC modes take the values of the bulk A(TO)-GaN and A(TO)-AlN phonons, and frequency of the IF mode takes the value of 578.5 cm^{-1}. Note, that this value is solution of the equation which describes the IF mode in a isolated GaN/AlN heterojunction.

2. Summary

Numerical microscopic modeling, as well as the dielectric continuum model calculations, show that frequencies of A(TO) and E(LO) polar phonon modes propagating along the interface plane in the binary nitride-based SLs exhibit strong dependence on SL composition. These modes manifest high Raman intensity irrespectively to the layer thickness ratio. This makes them a very sensitive tool for controlling the layer thickness ratio. Increase of the total SL period changes Raman spectra towards the two-mode picture. When rationalized within the dielectric continuum model calculations, these spectral changes provide us an additional valuable information about SL structure.

References

[1] S. Nakamura, *The Blue Laser Diode-GAN Based Light Emitters and Lasers*, Springer, Berlin, 1997.

[2] M. B. Smirnov, S. V. Karpov, V. Yu. Davydov, A. N. Smirnov, E. E. Zavarin and V. V. Lundin, *Phys. Solid State* **79**, 742 (2005).

[3] J. -M. Wagner and F. Bechstedt.l, *Peculiarities of phonons in strained short-period GaN/AlN superlatices: A first principles study*, Springer Proceedings in Physics **87**, 883 (2001).

[4] S. M. Komirenko, K. W. Kim, M. A. Stroscio, M. Dutta, *Phys. Rev. B* **61**, 2034, (2000).

20th Int. Symp. "Nanostructures: Physics and Technology"
Nizhny Novgorod, Russia, June 24–30, 2012

Novel methods of amplification and generation of coherent microwave and terahertz radiation in superlattices

A. V. Shorokhov[1], N. N. Khvastunov[1,2], *O. D. Pozdnyakova*[1], N. S. Prudskikh[1] and K. N. Alekseev[3]

[1] Institute of Physics and Chemistry, Mordovian State University, 430005 Saransk, Russia
[2] Mordovian State Pedagogical Institute, 430007 Saransk, Russia
[3] Loughborough University, Loughborough LE11 3TU, United Kingdom

Abstract. We considered methods of amplification and generation of coherent microwave and terahertz (THz) radiation in superlattice-based devices operating in the single-miniband transport regime based on the using of bichromatic pump field. It is shown that the amplification of the weak probe field in these methods is possible without destructive instabilities

Introduction

The terahertz (THz) spectral range of electromagnetic radiation is located between optical and microwave frequencies. THz radiation has numerous scientific and technological applications ranging from the astronomy to biosecurity. For example, applications in imaging and security are based on non-ionizing property of terahertz radiation which therefore is safer than X-rays. At the same time THz ray can penetrate many visually opaque materials and can be used in visualization of concealed weapons made from metal, ceramics, plastic or other materials. Specific chemicals can be detected as well.

Most advanced generator or amplifier of terahertz waves should be miniature, all-electronic device which radiates or amplifiers an external radiation at temperatures achievable using thermoelectric coolers or, ideally, at room temperature. Development of such devices is a highly challenging task, which requires the use of both advanced materials and novel physical phenomena. Our work is devoted to an exploration of new physical mechanisms of amplification and generation of a coherent THz radiation in semiconductor superlattices [1, 2].

Periodic semiconductor nanostructures, known as semiconductor superlattices, constitute a class of artificial materials allowing a controllable electronic transport with unique quantum properties, such as the existence of energy miniband that is much narrower than the energy band in ordinary bulk semiconductors. The dependence of the electric current trough a superlattice on the applied constant electric field looks a quite different from the familiar Ohm law. It is characterized by the negative differential conductivity (NDC); that is, in some electric field an increase in the field strength results in a decrease of the current. Potential for the use of the superlattice NDC effect in an amplification of THz radiation has been first recognized in the beginning of the 70 s. However, a practical realization of such a device, known as THz Bloch oscillator, was strongly complicated by the development of accompanying space-charge instability, which is typical for all semiconductors with NDC (Ridley–Hilsum–Gunn effect). Since this particular approach has proven unsuccessful at producing radiation sources many times in the past, a significant part of the semiconductor community becomes rather sceptical concerning the use of any superlattices as an amplifying media for the THz waves.

Here we introduce new superlattice-based devices operating in the electron transport regime characterized by usual positive differential conductivity, which therefore can provide a stable amplification of THz waves. To reach the stable net gain at THz frequencies in a superlattice we apply a certain combination of electric fields. A preliminary experiment, which was performed so far only with microwaves, has demonstrated the desirable amplification in a specially designed superlattice device. Importantly, our numerical and analytical calculations show a surprisingly large magnitude of the stable THz amplification, which in particular is much larger than THz gain expected in the Bloch oscillator. We described and analyzed intriguing physical mechanisms resulting in the significant enhancement of amplification in superlattices.

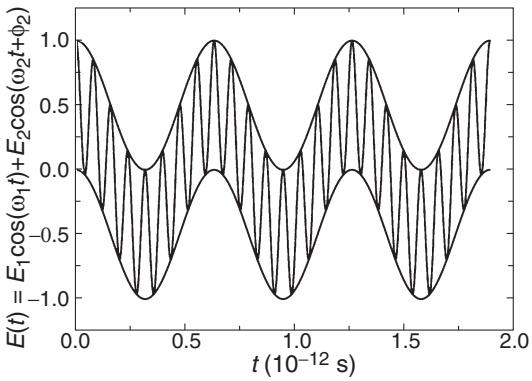

Fig. 1. Bichromatic pump field.

1. Modulated pump filed

We consider a SL under the action of an electric field

$$E_{\text{pump}}(t) = E_0 + E_{\text{mod}}(t) + E_{\text{probe}}\,, \qquad (1)$$

where $E_{\text{mod}}(t) = E_1\cos(\omega_1 t) + E_2\cos(\omega_2 t + \varphi_2)$ is the periodic modulation of the bias, E_0 is the dc-bias, $E_{\text{pr}} = E_3\cos(\omega_3 t)$ is the weak probe field. We suppose that the modulation frequencies are incommensurate with the frequency of the probe field and $\omega_2 = m\omega_1$ ($m = 2, 3, \ldots$).

We define the absorption of the probe ac field E_{pr} in the SL miniband as $A(\omega_3) = \langle \bar{V}(t)\cos(\omega_3 t)\rangle_t$, where $\bar{V}(t)$ is the average velocity of electron in the miniband.

We start with the consideration of small-signal gain in dc-biased superlattice $E_0 \neq 0$. Note that in this case we have the gain only in the case of positive differential conductivity because the necessary condition of electric stability is an operation at a positive slope of time-average current-voltage characteristic. Fig. 2 demonstrates the VI characteristic and gain profile for the modulation with moderate field strengths

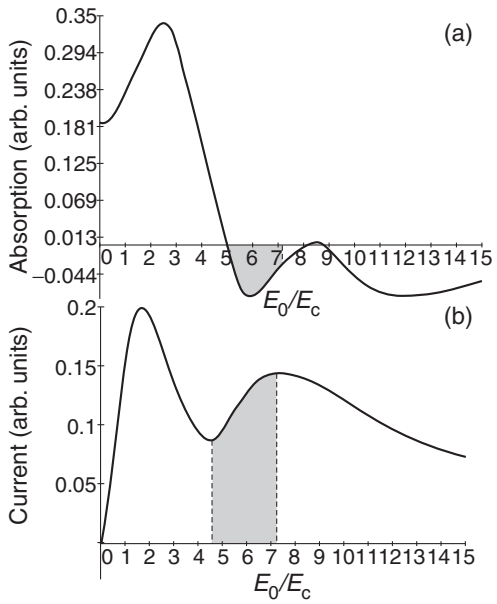

Fig. 2. Dependence of absorption (a) and current density (b) on dc-bias for the case when the second field is the third harmonic of the first field. $\omega_1\tau = 1$, $\omega_2\tau = 3$, $\omega_3\tau = 4.11$. The shade area on Fig. 2a corresponds to the amplification without instabilities; the shade area on Fig. 2b corresponds to the positive differential conductivity.

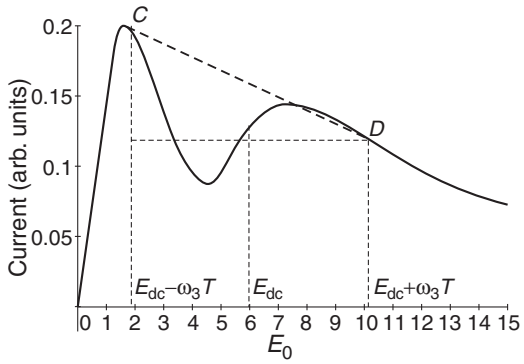

Fig. 3. VI characteristic of SL under the action of a strong bichromatic pump field ($\omega_3\tau = 4.11$). Additionally to the modified Esaki–Tsu peak, one photon-assisted peaks are visible. The operation point is chosen at the part of the second peak with a positive slope ($E_{dc} = 6E_{cr}$). The finite difference at this operation point is negative for a wide range of values demonstrating the possibility of small-signal gain without NDC.

$E_{1,2}$. The field $E_{mod}(t)$ creates an additional peak in the VI characteristic of superlattice (Fig. 2b). This additional peak can be utilized in a similar way as in the earlier theoretical suggestion [3] to achieve THz gain at a stable operation point. Namely, we put the working point at the part of the peak with a positive slope. The result is the gain profile with a negative absorption as shown in Fig. 1a. Note that the shape of the VI characteristic and magnitude of gain can be additionally controlled by a variation of the relative phase φ_2.

Importantly, if $\varphi_2 = 0$ then the absorption of the probe field can be written in the form of finite difference of the Esaki–Tsu current-field dependence

$$A = \frac{j_{dc}\,(E_0/E_{cr} + \omega_3) - j_{dc}\,(E_0/E_{cr} - \omega_3)}{2\hbar\omega_3}\, ed\,, \qquad (2)$$

where d is the superlattice period, $E_{cr} = \hbar/ed\tau$, τ is the relaxation time.

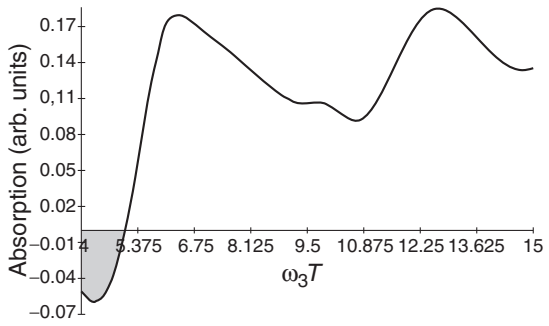

Fig. 4. The dependence of absorption of a weak probe field on the its frequency. The shade area correspond to the amplification without instabilities $\omega_1\tau = 0.8$, $\omega_2\tau = 4$.

Fig. 3 demonstrates the meaning of finite difference. Geometrically, the quantum derivative represents the slope of segment with the length defined by the probe frequency ω_3. The ends of the segment belong to the Esaki–Tsu curve and their locations are determined by the choice of working point. In the quasistatic limit $\omega_3\tau \ll 1$, we immediately get from Eq. (2) the well-known result that the absorption is proportional to the dc differential conductivity at the operation point. On the other hand, as is obvious from the figure, in order to provide small-signal gain in the canonic Bloch oscillator the working point must be in the NDC portion of the Esaki–Tsu characteristic.

In the case of unbiased SL the instabilities will arise due to the absolute negative conductivity (ANC). Fig. 4 illustrates the feasibility of gain in conditions of suppressed electric instability.

2. Conclusions

We theoretically analyzed the feasibility to reach THz gain in dc-biased semiconductor superlattice at room temperature using the bichromatic alternating pump field. We showed that the bichromatic pump field can suppress the formation of high-field electric domains inside the superlattice while still preserve a broadband THz gain at frequencies incommensurate with the pump frequencies. Choice of the operation point at the positive slope of such peak allows to suppress the electric instability. For the search of high-frequency gain in conditions of the positive differential conductivity we employed simple but powerful geometric interpretations of the intraminiband absorption formulas.

Acknowledgements

This work was supported by Russian Ministry of Education and Science within task 'Optical and transport properties of semiconductor nanostructures and superlattices' (project No. 2.26 76.2011) and by Russian Foundation for Basic Research (grant No. 11-02-00699).

References

[1] T. Hyart, N.V. Alexeeva, J. Mattas, and K.N. Alekseev, Terahertz Bloch Oscillator with a Modulated Bias, *Phys. Rev. Lett.* **102**, 140405 (2009).

[2] T. Hyart, A.V. Shorokhov, and K.N. Alekseev, Theory of Parametric Amplification in Superlattices, *Phys. Rev. Lett.* **98**, 220404 (2007).

[3] T. Hyart, K.N. Alekseev, E.V. Thuneberg, *Phys. Rev. B* **77**, 165330 (2008).

20th Int. Symp. "Nanostructures: Physics and Technology"
Nizhny Novgorod, Russia, June 24–30, 2012

Microwave transport phenomena in magnetic metallic nanostructures

V. V. Ustinov and *A. B. Rinkevich*
Institute of Metal Physics, Ural Branch of RAS, 620990 Ekaterinburg, Russia

Microwave properties of magnetic metallic nanostructures with giant magnetoresistive (GMR) effect have been studied. Two main physical reasons causing microwave variations are the microwave analog of the giant magnetoresistive (μWGMR) effect and the ferromagnetic resonance. A comparison is outlined with the DC magnetoresistive effect. Methods of measurement of microwave magnetoresistive effect are presented. The peculiarities of joint observation of ferromagnetic resonance and microwave magnetoresistive effect are specified.

The electron scattering at an interface of a magnetic and non-magnetic metal plays a special role in kinetic properties. This scattering can include inversion of spin direction, the probability of spin inversion being strongly dependent on the magnetization. Therefore, the electrical resistance of nanostructures varies with magnetic field. This effect is known as the giant magnetoresistive effect [1,2]. The GMR of metallic nanostructures is as a rule negative, its magnitude being defined by the magnetization. Magnetoresistance tends to saturation in strong fields corresponding to magnetic saturation. Relative magnetoresistance r is a convenient measure of GMR magnitude, $r = [R(H) - R(0)]/R(0)$, where $R(H)$ is the electrical resistance in magnetic field H. At room temperature r exceeds several dozens percent. The GMR effect has been studied in detail both theoretically and experimentally. It has been shown that the GMR magnitude has an oscillatory dependence on the thickness of non-magnetic layer, which results from the quantum character of electron motion in super-thin metallic layers.

In this paper we intend to discuss in details the μWGMR effect and to elucidate the following problems:

1. Magnetic metallic nanostructures, exchange interaction and giant magnetoresistive effect.
2. Penetration of electromagnetic waves through metallic films and nanostructures.
3. Microwave GMR in Fe/Cr superlattices, Co/PtAg, Co/Cu and FeNi/V nanostructures.
4. Magnetic resonance in microwave penetration through a metallic nanostructure.
5. Microwave properties of cluster-layered nanostructures.
6. Interaction between traveling electromagnetic waves or fields and metallic nanostructures.
7. Sign-alternating microwave magnetoresistive effect.
8. Contactless method of measuring the magnetoresistance.

Variations of the microwave transmission coefficient are induced by two physical reasons: first, the μWGMR and second, variations of impedance and absorption in a nanostructure under magnetic resonance conditions. The first reason leads to a monotonic magnetic field dependence of the transmission coefficient module that is similar to DC magnetoresistive dependence. At the frequencies of centimeter and millimeter wavebands there is one-to-one correspondence between the microwave GMR and DC magnetoresistance [3].

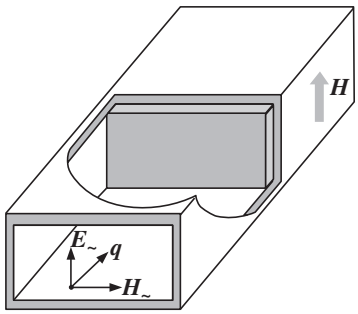

Fig. 1. Scheme of the sample displacement in the waveguide.

The second type of microwave variations is observed only under perpendicular directions of DC and microwave magnetic fields. Resonance variations in Fe/Cr superlattices are present at frequencies exceeding 30–32 GHz. The resonance amplitude is the largest in those nanostructure samples where the resonance falls into the magnetically saturated state. In the cluster-layered Fe/Cr nanostructures the resonance-type microwave variations are absent if the Fe layers are discontinued and magnetic ordering of the layers is absent as well.

The propagation of electromagnetic waves in a rectangular waveguide containing a gyrotropic plate made of a metallic-film nanostructure has been studied. Changes in the propagation constant were calculated for the cases of in-plane and normal magnetizations of the nanostructure. In the region of frequencies and fields that is far away from the condition of ferromagnetic resonance, the changes in the transmission coefficient absolute value are proportional to the changes in resistivity. Besides the damping component a high-frequency electric field contains the penetrating component. Microwave currents flow perpendicularly to layers, and the current-perpendicular-to-plane case is realized.

The microwave measurements are carried out in the frequency diapason from 26 to 38 GHz. The sample was placed into the waveguide as shown in Fig. 1. The experiments performed on Fe/Cr superlattices in the centimeter-wavelength and millimeter-wavelength ranges showed that there is a one-to-one correspondence between their DC magnetoresistance and variation of the microwave penetration.

A change-over into the millimeter-wavelength range allows one to investigate the combined effect of two physical mechanisms on the electromagnetic waves penetration. One of them, a non-resonance mechanism is discussed above, it is directly related to the GMR. The mechanism is essentially determined by the Joule losses of microwave eddy currents in nanostructures and affects the magnitude of the surface impedance. The second mechanism, observed under the FMR conditions, is caused by the magnetic moments precession upon the combined action of two fields: the DC magnetic field and the high-frequency field of an electromagnetic wave. Analyzing the results of penetration of millimeter-wavelength electromagnetic waves through a magnetic metallic nanostructure, one should keep in

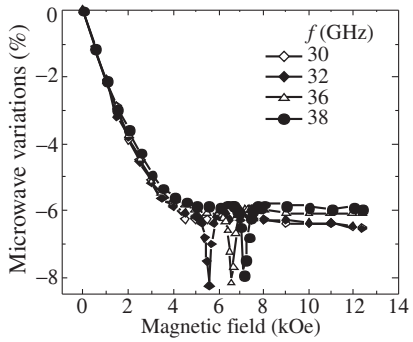

Fig. 2. Changes in the microwave transmission coefficient for the [Cr(19Å)/Fe(23Å)]12/Cr(80Å)/MgO sample versus DC magnetic field at different frequencies.

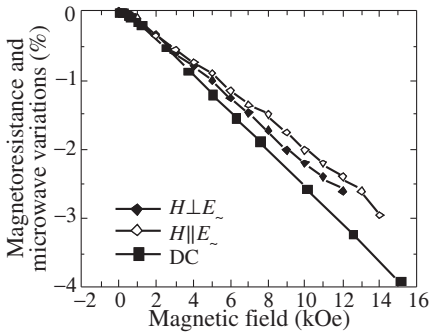

Fig. 3. Field dependences of the static magnetoresistance (r) and the microwave transmission coefficient (r_m) at a frequency of 36 GHz upon two directions of DC magnetic field for cluster-layered nanostructure [Cr(11 Å)/Fe(4 Å)]50/ Cr(85 Å)/MgO.

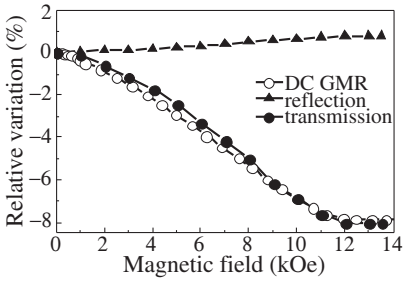

Fig. 4. Plots of microwave reflection and transmission coefficients measured at 32 GHz and the DC magnetoresistance versus magnetic field strength H for a MgO/Cr(80Å)/[Fe(29Å)/Cr(13Å)]$_4$ superlattice: (1) GMR, (2) reflection, (3) transmission.

mind that the overall thickness d of a metal in it is smaller than the depth δ of the skin layer.

Figure 2 displays the results of the measurements carried out on a Fe/Cr superlattice with continuous layers at different frequencies for the case of perpendicular direction of DC and microwave magnetic fields. It is seen that in a certain narrow range of magnetic fields the field dependence of the transmission coefficient r_m exhibits a resonance feature in the form of a minimum. It should be noted that the non-resonant part of the $r_m(H)$ dependence turned out to be much the same in the entire frequency range examined, and is very similar in its behavior to the field dependence of the DC magnetoresistance measured. The resonance contribution was observed at frequencies above 30 GHz, and the field corresponding to the minimum of the transmission coefficient is enhanced with increasing frequency.

The microwave transmission was also investigated on a Fe/Cr superlattice with very thin Fe layers and with cluster-layered nanostructures. The results of Fig. 3 show that there are no resonance changes in the cluster-layered Fe/Cr nanostructure. This agrees well with the results of the measurements of magnetization, in particular, of hysteresis loops.

Analysis of the transmission (D) and reflection (Γ) coefficients, which are defined as the ratios of complex amplitudes of the transmitted and reflected waves to the complex amplitude of an incident wave, gives the following formulas for the coefficients:

$$D=\frac{2Z_m}{2Z_m\mathrm{ch}k_md+Z\mathrm{sh}k_md},\ \Gamma=-1+\frac{2Z_m\mathrm{ch}\,k_md}{2Z_m\mathrm{ch}k_md+Z\mathrm{sh}k_md}, \quad (1)$$

where d is the total metal thickness in the nanostructure and $k_m = (1+i)/\delta$ is the complex wave number in the conducting medium. The impedance of a metal nanostructure Z_m is smaller than the impedance of a waveguide Z, ($|Z_m| \ll Z$). If the system obeys the condition $2Z_m\mathrm{ch}\,k_md \ll Z\mathrm{sh}\,k_md$, which is valid for metal nanostructures with thicknesses above 10 nm in the centimeter and millimeter wavebands, the expressions for the transmission and reflection coefficients simplify to

$$D = \frac{2Z_m}{Z\,\mathrm{sh}\,k_md}, \qquad \Gamma = -1 + \frac{2Z_m}{Z}\,\mathrm{cth}\,k_md\,. \quad (2)$$

If a change in the reflection coefficient is caused only by a change in the resistivity, and $\mu(0) \approx 1$, the relative change in the absolute value of the reflection coefficient can be written as

$$\gamma_m = -D(0)\,[1 - D(0)]\,r\,. \quad (3)$$

Note that the term $\frac{2\rho}{Zd\mu(0)} = D(0)$ is positive, and for metal films with thicknesses above 10 nm it is much smaller than unity: $D(0) \ll 1$. The expression (3) shows that the sign of a change of the reflection coefficient is opposite to the sign of the magnetoresistance r. These changes are much smaller in magnitude than $|r|$, but the character of their dependence on the external magnetic field strength is identical to that of $|r|$.

Figure 4 shows the results of measurements performed at a frequency of $f = 32$ GHz for a superlattice. For the comparison, this figure also shows the field dependence of the relative DC magnetoresistance measured for the same sample. The results demonstrate mutual single-valued correspondence between the $r(H)$ and $r_m(H)$ curves. As can be seen the electromagnetic wave reflection coefficient exhibits much smaller variation than the transmission coefficient and in agreement with the above considerations the change of the former is positive.

Changes in reflection and transmission coefficients may exceed 20%, thus opening prospects for the use of the microwave magnetoresistive effect in controlled microwave devices.

Acknowledgements

The work was done within RAS Program (project No. 01.2.006 13391), with partial support of RAS Program No. 24 and NSh-6172.2012.2 grant.

References

[1] Baibich, M.N., Broto, J.M., Fert, A. *et al.*, *Phys. Rev. Letters* **6**, 2472 (1988).

[2] Binach, G., Grunberg, P., Saurenbach, F., Zinn, W. *Phys. Rev.* **B39**, 4828 (1989).

[3] Rinkevich, A.B., Romashev, L.N., Ustinov, V.V. *Journal of Experimental and Theoretical Physics* **90**, 834 (2000).

[4] Rinkevich, A.B., Romashev, L.N., Ustinov, V.V., Kuznetsov, E.A. *Technical Physics Letters,* **33**, 771 (2007).

20th Int. Symp. "Nanostructures: Physics and Technology"
Nizhny Novgorod, Russia, June 24–30, 2012

Spin-wave excitations and magnetoresistance in one- and two-dimensional bicomponent magnonic crystals

V. K. Sakharov[1], Y. V. Khivintsev[1,2], *Y. A. Filimonov*[1,2] and S. A. Nikitov[2,3]

[1] Kotelnikov Institute of Radio Engineering and Electronics (Saratov Branch) RAS, Zelenaya str. 38, 410019 Saratov, Russia
[2] Saratov State University, Saratov, Russia
[3] Kotelnikov IRE RAS, Mochovaya str. 11, 140019 Moscow, Russia

Abstract. Microstructures in a form of the periodically alternating cobalt and permalloy thin film elements were fabricated and studied using the ferromagnetic resonance and magnetoresistance methods. It was shown that these bicomponent structures can support the standing spin wave modes localized either in the cobalt elements or in the permalloy elements depending on the external field geometry. Also, it is shown that magnetoresistance properties of such structures depend on both magnetic components so that magnetoresistance magnitude is mainly due to permalloy component whereas magnetoresistance field range is mainly due to cobalt component.

Introduction

Magnonic crystals (MC) are artificial materials with periodic spatial modulation of the magnetic properties leading to the formation of the band gap for the spin waves (SW). The MC are a subject of the strong scientific interest due to possible application in microwave signal processing [1,2].

So far, the experimental study of MC was mainly concentrated on the ferrite based structures because of low SW damping in ferrites. However, there is a growing interest to the MC based on ferromagnetic metals which is stimulated by significantly more opportunities for technological manipulations with ferromagnetic metals in the construction of MC. Recently there have been reported on study of the MC which are periodical structures of alternating cobalt (Co) and Permalloy (Py) nanostripes and nanodisks [3–5]. Formation of the band gap in the SW spectrum for these structures was approved by Brillouin light scattering measurements. But, so far, there were no works on study of the SW excitations in such structures using the ferromagnetic resonance (FMR) technique. In this paper we present results of our experimental study of the similar structures with micron sized lateral dimensions using the ferromagnetic resonance (FMR) and magnetoresistance (MR) methods.

1. Samples and experimental technique

The bicomponent structures were fabricated using magnet-ron sputtering, photolithography and ion etching. In contrast to [3] where two lithography steps with required alignment were used to form alternating Co and Py elements we used single lithography process and applied the same photoresist pattern for ion etching of the Co film and lift-off method for the Py film.

We fabricated and tested the samples with various shape of the Co and Py elements: the alternating Co and Py stripes, the rectangular or square Co dots rounded by Py film — see Fig. 1. The lateral dimensions of the elements were in the range from 3.5 to 26 μm. Also, additional test structures of the separate Co and Py elements with the same dimensions as for bicomponent structures were fabricated using ion ething and lift-off for the Co and Py, respectively. In all cases thickness of the ferromagnetic films was 50 nm.

SW excitations in the structures were studied using conventional cavity FMR technique at 9.8 GHz. The FMR spectrum (differential absorbed power as a function of the applied field magnitude) was measured for various orientation of the external in-plane magnetic field. MR was measured by four-probe method at different orientations of the electric current and magnetic field (both applied in the plane of the samples) with respect to the structure symmetry axes.

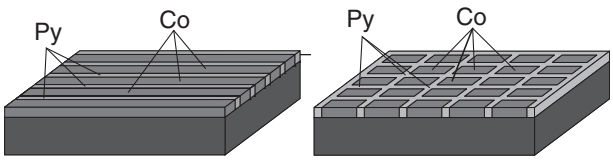

Fig. 1. Bicomponent Co and Py structures.

2. Experiment results and discussion

Fig. 2a illustrates typical features in the FMR spectrum observed for the bicomponent structures with Co and Py elements in a form of the stripes. One can see two strong responses corresponding to the uniform FMR in the Co and Py stripes and the additional weak responses between them — see inset to Fig. 2a. Rotation of the external field shifts the uniform FMR responses due to the shape anisotropy effect which is significantly smaller for the bicomponent structure than for the arrays of the separate stripes — see Fig. 2b and c for comparison. Also, one can see that the presence of the Co around the Py stripes significantly decreases uniform FMR field for Py stripes in the bicomponent structure.

The observed additional responses can be attributed to the formation of the standing SW resonances across the width of the stripes. Earlier such resonances were investigated for the tangentially magnetized separate stripes [6]. The separate stripes can support the resonances of the magnetostatic surface wave (MSSW) and the backward volume magnetostatic wave (BVMSW) with lower and higher resonance fields, respectively, in comparison to the uniform FMR. In Fig. 2b the MSSW and BVMSW resonances can be clearly seen for the Py stripes in the case of the field applied along and perpendicular to the stripes, respectively.

In order to form such resonances in the bicomponent structure there must be conditions for the efficient reflection of the magnetostatic wave (MSW) from the boundaries between the Co and Py elements. Such conditions are realized in the case if MSW can propagate only in one of the material so that the SW modes become localized in the Co or Py elements. This occurs

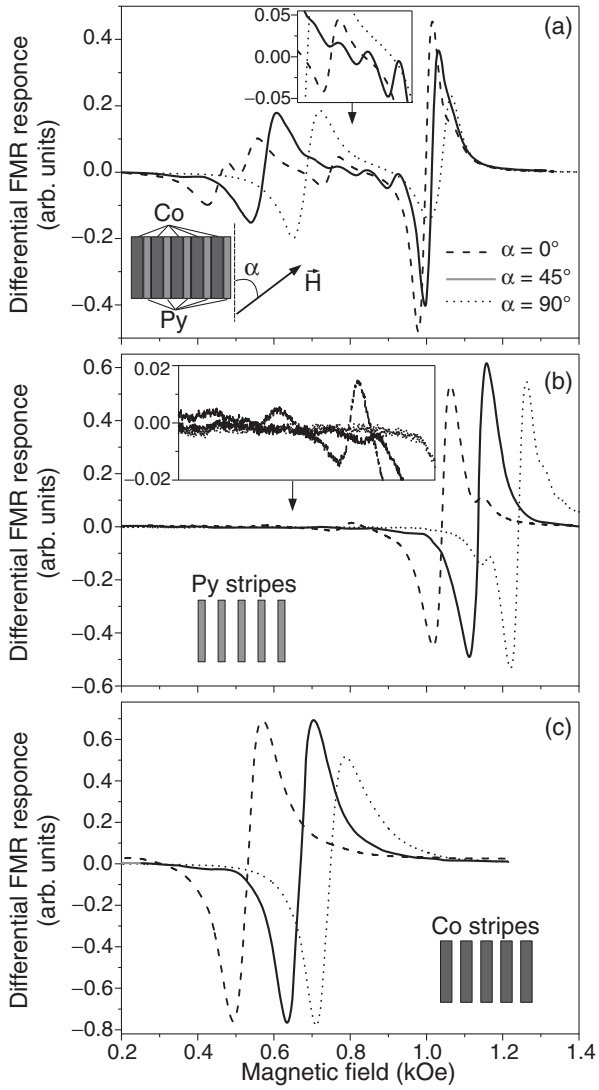

Fig. 2. FMR results for bicomponent striped structure (a) and arrays of the separate Py (b) and Co stripes (c) for the various orientation of the in-plane magnetic field. The stripes width is 6.5 and 3.5 μm for the Co and Py, respectively.

in the frequency range between the uniform FMR frequency for the Co and Py films — see Fig. 3. And this is exactly where the additional responses were observed for the bicomponent structure. Also, we performed calculations of the resonance fields for the spin wave modes neglecting the shape anisotropy effect and the calculations showed good agreement with the experimental results.

The MR measurements showed that the change in the electrical conductivity of the studied bicomponent structures is mainly due to the anisotropic MR effect. The maximum MR was observed for the sample with the alternating Co and Py stripes — see Fig. 4. The magnitude of the MR was found to be close to that as for the test sample of the continuous Py film whereas the fields range corresponding to the MR effect was more close to that as the test sample of the continuous Co film.

3. Conclusion

In this work we experimentally studied the bicomponent periodical structures consisted of alternated Co and Py elements. We have found that the standing spin wave modes which are localized in the Py or Co elements can be observed in such structures. Also, we have shown that in these bicomponent structures the Py component is mainly responsible for the magnitude of the anisotropic MR whereas the Co component defines the MR field range.

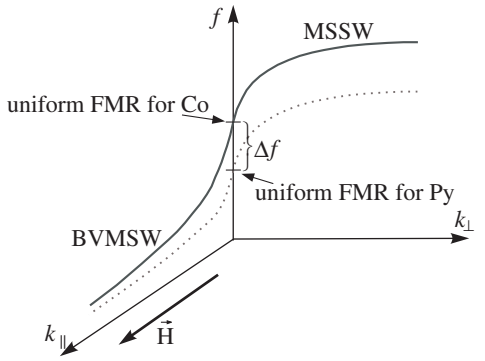

Fig. 3. Dispersion for the BVMSWs and MSSWs propagating along and perpendicular to the bias field in Co (solid) and Py (dotted) films. Δf is the frequency band where the BVMSW and MSSW can propagate only in Co and Py, respectively.

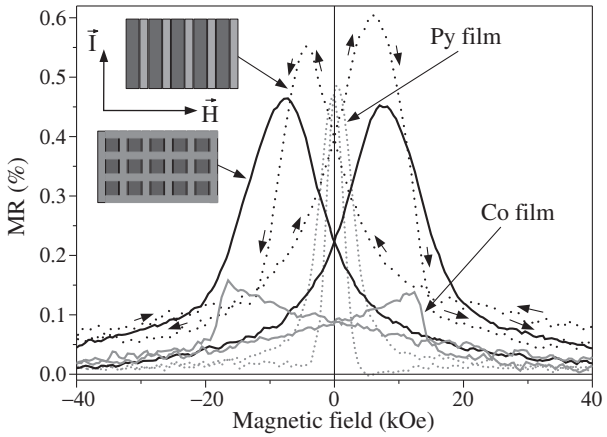

Fig. 4. The MR relatively to the resistance at the field of 300 Oe for the bicomponent structures: Co and Py stripes with the width of 6.5 and 3.5 μm, respectively, and for the 6.5 × 6.5… μm Co dots separated by 3.5 μm wide Py stripes, as well as for the continuous Co and Py films.

Acknowledgements

This work was supported by RFBR (grants No. 11-07-12081 and 11-07-00233), Federal Grant-in-Aid Program "Human Capital for Science and Education in Innovative Russia" (contract No. П485 and 14.740.11.0077), the Grant from Government of Russian Federation for Support of Scientific Research in the Russian Universities Under the Guidance of Leading Scientists (project No. 11.G34.31.0030) and European Community's 7th Framework Programme under Grant Agreement No. 247556 (NoWaPhen).

References

[1] V.V. Kruglyak, S.O. Demokritov and D. Grundler *J. Phys. D: Appl. Phys.* **43**, 264001 (2010).

[2] Z.K. Wang, V.L. Zhang, H.S. Lim, S.C. Ng, M.H. Kuok, S. Jain and A.O. Adeyeye *Appl. Phys. Let.* **94**, 083112 (2009).

[3] A.O. Adeyeye, S. Jain and Y. Ren, *IEEE Trans. on Mag.* **47**, 1639 (2011).

[4] S.L. Vysotskii, S.A. Nikitov, Y.A. Filimonov and Y.V. Khivintsev *JETP Lett.* **88**, 461 (2008).

20th Int. Symp. "Nanostructures: Physics and Technology"
Nizhny Novgorod, Russia, June 24–30, 2012

Surface spin flop transition in $[Fe/Cr]_n$ multilayers observed by the nuclear resonance reflectivity

M. Andreeva[1], A. Gupta[2], G. Sharma[2], S. Kamali[3], K. Okada[4] and Y. Yoda[4]

[1] Faculty of Physics, M.V. Lomonosov Moscow State University, 119991 Moscow, Russia
[2] Indore Center, UGC-DAE Consortium for Scientific Research, 452017 Indore, India
[3] Department of Applied Science, University of California, 95616 Davis, California, USA
[4] Japan Synchrotron Radiation Research Institute, SPring-8, 679-5198 Sayo, Hyogo, Japan

Abstract. Reorientation of the magnetization in separate layers of $[^{57}Fe/Cr]_n$ periodic multilayers characterizing by the antiferromagnetic alignment between ^{57}Fe layers has been investigated by the nuclear resonance reflectivity (NRR) under the applied external field. The experiment has been performed at the BL09 beamline of the Japan SPring-8 synchrotron. At a rather low external field (∼50 Oe) we have detected the variations of the NRR time spectra measured at the critical angle of the total external reflection. We interpret such change by the surface spin flop (SSF) transition. Variations of the intensity of the superstructure magnetic Bragg peaks on the delayed reflectivity curves evidence that at higher applied field the antiferromagnetic structure rotates firstly perpendicular to the external field direction and at a further field increase the layer magnetization ferromagnetically aligns along it. Our experiment demonstrates that NRR is a very sensitive instrument for the depth selective investigations of the magnetic field orientation in multilayers.

Introduction

After the discovery of GMR in antiferromagnet/ferromagnet [F/AF] multilayers [1] a lot of intriguing features have been observed experimentally and predicted theoretically for such structures, in particular a rather peculiar behavior at the applied field [2–6]. Up to now the most detailed picture of the magnetization reorientation in multilayers can be obtained by polarized neutron reflectivity (PNR) [3]. Nuclear resonance reflectivity (NRR) presents an even more informative picture (see e.g. [6–8]) than PNR. In our NRR experiment we we have detected the surface spin flop transition (SSF) at a rather low external field (about 50 Oe).

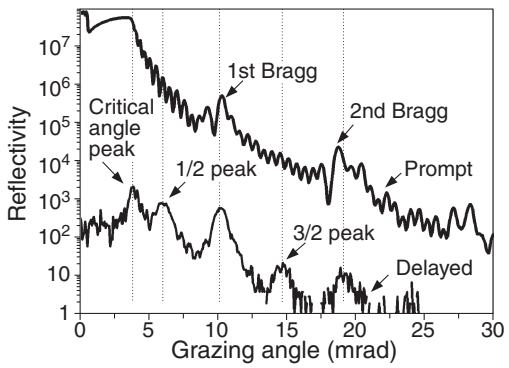

Fig. 1. Prompt and delayed (NRR) reflectivity curves measured from the sample $[^{57}Fe(3.0\ nm)/Cr(1.2\ nm)]_{10}$.

1. Experimental

The measurements have been performed at the Beamline BL09 XU of SPring-8.

NRR presents two types of data: 1. the delayed nuclear resonant reflectivity as a function of the glancing angle which is similar to PNR data; 2. the time spectra of reflectivity measured for the selected grazing angles, which characterize the magnitude and direction of the magnetic hyperfine fields B_{hf} on ^{57}Fe nuclei.

Three samples $[^{57}Fe(2.0\ nm)/Cr(1.2\ nm)]_{10}$, $[^{57}Fe(2.0\ nm/Cr(1.2\ nm)]_{20}$ and $[^{57}Fe(3.0\ nm)/Cr(1.2\ nm)]_{10}$ have been grown in the Indore Center (India) by magnetron sputtering. Moessbauer measurements (CEMS) give the broad line sextet, it indicates on the existence of rather thick interfaces in the multilayer. MOKE measurements confirm the AF interlayer coupling in the samples, but reveal the multi-domain structure of the film.

Without an external magnetic field the pronounced superstructure maxima (1/2 and 3/2) are observed on the delayed reflectivity curves (Fig. 1). That confirms the doubling of the magnetic period due to the antiferromagnetic alignment between ^{57}Fe layers.

The time spectra of reflectivity (Fig. 2) show the quantum beat oscillations which originate from the interference of the waves with different frequencies of hyperfine transitions in the nucleus decay.

The measured time spectra of reflectivity appeared to be quite different at different angles (Fig. 2). The Fourier transform of these spectra allows us to evaluate directly the value of magnetic hyperfine field on ^{57}Fe nuclei and the similarities of the polarization states of resonant spectrum components which originated from different hyperfine field directions in adjacent ^{57}Fe layers. The result (Fig. 2, right part) reveals the decrease of the basic frequency of the quantum beats for the 2nd order Bragg peak comparing with the 1st order Bragg peak. That points out to the smaller value of the hyperfine field in the interfaces between ^{57}Fe and Cr layers.

The interference pattern is different for different magnetization direction. In case when the magnetization in all layers is arranged somehow in the surface plane just 4 hyperfine transitions (1,3,4 and 6) are excited by s-polarized SR (see insert in Fig. 2) [8]. For magnetization directed along the beam the 1 and 4 transitions give the right circular polarization of the emitted waves, 3 and 6 transitions give the left circular polarization. The interference takes place only for waves of the same polarization state and we have just one frequency in the quantum beat pattern. For magnetization directed perpendicular to the beam all 4 transitions have a linear polarization of the emission lines and we have 4 frequencies in the quantum beat pattern.

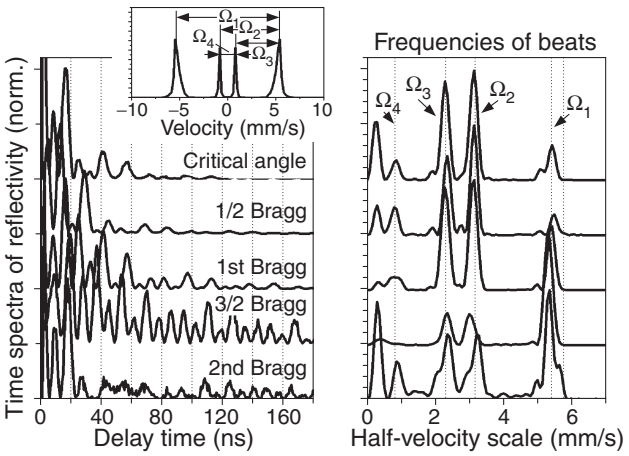

Fig. 2. The time spectra of reflectivity (left side) measured at different Bragg angles and their Fourier transform (right side). The insert presents the resonant spectrum of the ^{57}Fe nucleus excitation at grazing angles when the hyperfine field B_{hf} lies in the surface plane.

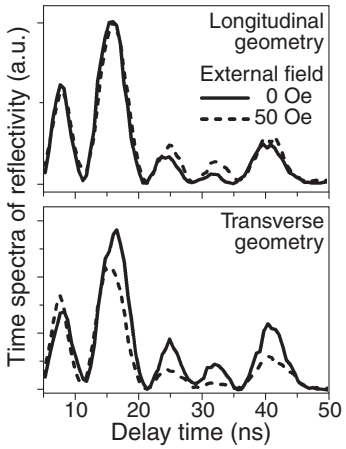

Fig. 3. The time spectra of reflectivity measured for [^{57}Fe(3.0 nm)/Cr(1.2 nm)]$_{10}$ sample at the critical angle (0.218°) without and with a weak external magnetic field (50 Oe).

The interference of waves from adjacent ^{57}Fe layers with different orientation of magnetization is influenced by a space phase shift, which is different for different Bragg maxima, so the quantum beat pattern becomes more complicated.

2. Effect of the external field

The measurements of the delayed angular curves and time spectra of reflectvity were performed at each step of the gradually increasing external field applied in two ways: along the beam (the longitudinal (L-) geometry) and perpendicular to the scattering plane (transverse (T-) geometry).

At the smallest external field 50 Oe we have not seen the change of the intensity of the 1/2 peak. However the time spectra in L- and T-geometry show some change but only at the critical angle (Fig. 3) whereas at the higher angles the time spectra are not changed. This effect is the direct evidence of the surface spin flop (SSF) transition.

The delayed reflectivity curves have started to change noticeably at the external field about 600 Oe: we see the decrease of the 1/2 peak intensity in the L-geometry, but the great increase in the T-geometry (Fig. 4). It is the evidence that at

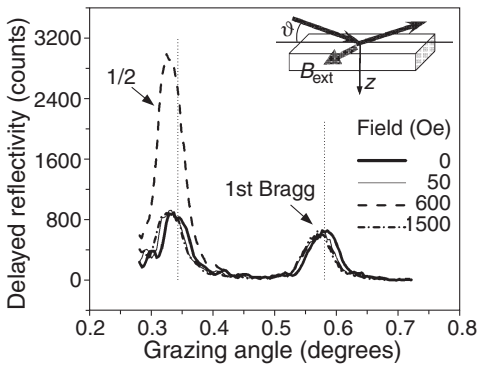

Fig. 4. The angular deoendence of the delyered reflectivity measured for different values of the applied field in T-geometry.

such field the antiferromagnetically coupled magnetizations in the adjacent ^{57}Fe layers rotates perpendicularly to the external filed.

At the highest field 1500 Oe the superstructure 1/2 peak disappears in the L-geometry and is essentially decreased in the T-geometry. Besides in the L-geometry the time spectra of reflectivity show almost single frequency beat pattern, but 4-frequency pattern in the T-geometry. We can conclude that the magnetization in all ^{57}Fe layers aligns almost parallel to the direction of the external field.

The main problem in the data interpretation is the multiple domain structure of the samples. So the observed variations of the delayed reflectivity curve and of the time spectra can not be described only by the rotation of the magnetization in ^{57}Fe layers but the partially coherent mixture with varying parameters of different magnetization states. However our experimental results clearly demonstrate that the time spectra of reflectivity and delayed reflectivity curves are the very sensitive instrument for the depth selective investigations of the magnetic field orientation in multilayers.

Acknowledgements

The work is supported by the RFBR grants No. 12-02-00924-a and No. 10-02-00768-a.

References

[1] M. N. Baibich *et al*., *Phys. Rev. Lett.* **61**, 2472 (1988).
[2] V. V. Ustinov *et al*., *Phys. Rev. B* **54**, 15958 (1996).
[3] V. Lauter-Pasyuk *et al*., *Phys. Rev. Lett.* **89**, 167203 (2002).
[4] V. V. Ustinov *et al*., *JMMM* **300**, e281 (2006).
[5] J. Meersschaut *et al*., *Phys. Rev. B* **73**, 144428 (2006).
[6] T. Diederich *et al*., *Phys. Rev. B* **76**, 054401 (2007).
[7] M. A. Andreeva and B. Lindgren, *Phys. Rev. B* **72**, 125422 (2005).
[8] M. A. Andreeva *et al*., *JETP* **104**, 577 (2007).

20th Int. Symp. "Nanostructures: Physics and Technology"
Nizhny Novgorod, Russia, June 24–30, 2012

Detonation nanodiamonds as a new carbon nanostructure for nanobiotechnology

A. Ya. Vul', M. V. Baidakova, A. T. Dideikin and V. Yu. Osipov
Ioffe Physical-Technical Institute, St Petersburg, Russia

Abstract. The review is devoted to nanodiamond produced by detonation synthesis. The past results related to the main features of detonation technology for producing nanodiamond are highlighted. Effects of technology on the structure of nanodiamond particles as well as functionalization of nanodiamond surface to chemical properties are discussed. The real structure of single nanodiamond particles has been critically reviewed and decision of its aggregation problem emphasized. The review demonstrates that while retaining the merits inherent in diamond, nanodiamonds exhibit a number of essential features, both in structure and in physico-chemical characteristics. These features give one grounds to consider nanodiamonds as a specific nanocarbon material promising for nanobiotechnology.

Introduction

On the turn of the last century, the newly coined word "nanotechnologies" has become one of the most popular and widely used terms. This popularity was apparently rooted in the hope cherished by "nanotechnologists" to develop structures that would approach in complexity those of the protozoa. An analogy between artificial and living organisms was pointed out in the very first monographs on fullerenes, a new allotropic modification of carbon [1].

Today this analogy is universally recognized, and structures of the members of the nanocarbon family more specifically, the fullerenes, nanotubes, and onion form of carbon are imaged as symbols of nanotechnology conferences and nanocarbon structures have won a prominent place among materials planned for use in nanobiotechnology.

This presentation is addressed the technology of production, the structure, properties and applications of a member of the nanocarbon family, namely, detonation nanodiamonds (DND).

1. Detonation nanodiamond technology

It was universally known that it is graphite that represents a thermodynamically stable allotropic form of bulk carbon at room temperature and atmospheric pressure. In industrial synthesis of microcrystalline diamond from graphite, the graphite — diamond phase transition in the presence of metal catalysts is run, as a rule, at temperatures of 1500–1800 °C and pressures above 5 GPa.

The detonation synthesis of nanodiamonds draws essentially from two original ideas [2,3]:

— to use the shock wave produced in detonation of an explosive as a source of high pressure and temperature for synthesis of crystalline diamond from a carbon material;
— to form a diamond crystal by assembling carbon atoms of the explosive itself.

The pressures and the temperature reached at the shock front correspond to the region of thermodynamic stability of diamond in the phase diagram of carbon and are substantially higher than those employed in static synthesis of diamond from graphite, but the time of synthesis is considerably shorter and amounts to a few fractions of a microsecond.

DND were found to have an extremely narrow distribution in size. This remarkable feature is usually attributed to the theoretical prediction that it is diamond rather than graphite that should be thermodynamically stable for carbon particle dimensions less than 5 nm [4].

A substance produced by detonation synthesis is named detonation carbon. Isolation of DND from detonation carbon and their subsequent purification from contaminants is the key step in the synthesis technology [5].

It is well known that a commercial powder of detonation nanodiamonds (DND) and their aqueous suspensions consist of agglomerates of 4–5 nm crystalline diamond grains [6]. We have recently submitted a method for production of stable hydrosol of 4 nm isolated DND particles [7]. The method includes deep purification commercial DND from metal impurities and appropriate control of its residual amount by electronic spin resonance, annealing of purified DND in air and centrifugation. We have also confirmed effect of DND deagglomeration after annealing in hydrogen atmosphere suggested in [8], however positive zeta potential was revealed in that case.

2. Structure and properties of detonation nanodiamonds

The intense studies carried out during the recent years have culminated in formulation of the so-called core-shell model, which is presently universally accepted when describing a single ≈4 nm DND particle. By this model, a DND particle consists of a crystalline core of sp^3 ("diamond") hybridized carbon atoms, which is coated, partially or completely, by a single- or multilayer, fullerene-like sp^2 ("graphitic") hybridized shell. A transition layer of sp^3/sp^2 hybridized carbon may form between the core and the shell with a structure mediated by the DND synthesis and purification techniques employed [6].

Industry produces commercial detonation nanodiamonds in the form of powder and suspensions. DND powder is of a light grey or off-white color, depending on the method and degree of purification employed. SEM studies reveal clearly self-similarity of particles under scaling variation. This is a signature of fractal structure; this structure of DND was reliably corroborated by X-ray small-angle scattering measurements. A typical elemental composition of DND includes about 90% carbon, 5–10% oxygen, 1–3% nitrogen and about 1% hydrogen. The DND IR absorption spectrum derives from surface functional groups and impurities. It reveals absorption bands corresponding to oxygen-containing compounds, more specifically, the hydroxyl, carboxyl and carbonyl groups. One observes

also bands related to the CH bonds in methyl and methylene groups [9].

One of the attractive features of DND is possibility for surface functionalization by metal using ion exchange, this approach gave possibility to produced DND particles with surface modified by Cu, Co, Ni, Fe [10,11]. Detonation nanodiamonds heated in different atmosphere can be transformed to onions and nanographite [12].

3. Applications of detonation nanodiamonds

In view of the unique combination of DND properties, it appeared only reasonable to assume that this material would find broad application in various areas of technology.

Probably the first DND application was associated with development of abrasive compositions for ultrafine mechanical polishing of hard surfaces, including optical elements, semiconductor substrates. Another rapidly expanding area of DND application is the technology of deposition of diamond and diamond-like films on various surfaces [6].

First reports on the use of DND as catalyst carrier have recently appeared. By using a neutral, chemically resistant phase in the form of particles on which a thin film of catalyst, primarily a metal of the platinum group, was deposited, one can enhance substantially the catalysis efficiency, while at the same time cutting noticeably the consumption of noble metals [13].

Progress in the technology of formation of crystallization centers based on the use of suspensions of 4-nm DND particles permits one presently to prepare diamond photonic crystals [14]. An promising application of DND as biomarker is based on using its luminescent properties deriving from nitrogen-vacancy defects in the crystal structure of its particles. High-pressure sintering of DND reveals the presence of nitrogen luminescent centers $N^0(N-V)^-$ in concentrations as high as 10^{-20} cm^{-3} [15].

Production of isolated single-crystal 4 nm particles of DND opens the door for targeted delivery of drugs in living organisms. The rich surface chemistry of ND, the absence of toxic impurities and small size make nanodiamonds a very convenient object for biomedical applications. Creation of specific surface sites on NDs for selective molecular attachment is considered a promising approach for their applications in nanofabrication, self-assembly, nanosensors, bioprobes, drug delivery, pigments, etc. By properly choosing combinations of molecular fragments to be grafted to the surface of DND particles, one will be able to design enterosorbents to ensure programmed slow release of active substances and to maintain their concentration in the organism [16].

Acknowledgement

The research of DND at Ioffe Institute has been supported by Programs of the Presidium of the Russian Academy of Sciences.

References

[1] M. S. Dresselhaus, G. Dresselhaus, P. C. Eklund, *Science of Fullerenes and Carbon nanotubes*, (San Diego California, USA: Academic Press) 357, 1996.
[2] A. I. Lymkin, E. A. Petrov, A.P. Ershov, G. V. Sakovitch, A. M. Staver, V. M. Titov, *Dokl. Akad. Nauk USSR* **302**, 611 (1988).
[3] N. R. Greiner *et al*., *Nature* **333**, 440 (1988).
[4] M.Y. Gamarnik *et al*., *Phys. Rev. B* **54**, 2150 (1996).
[5] V. Yu. Dolmatov, In *Ultra-Nanocrystalline Diamond: Syntheses, Properties and Applications* ed. Olga Shenderova and Dieter Gruen, (New York: William Andrew) 379–404, 2006.
[6] M. Baidakova, A. Vul', *Journal Phys. D: Appl. Phys.* **40**, 6300 (2007).
[7] A.E. Aleksenskiy, E.D. Eydelman, A.Ya. Vul', *NNL* **3**, 68 (2011).
[8] O. A. Williams *et al*., *ACS Nano* **4**, 4224 (2010).
[9] V.Yu. Osipov *et al*., *Diamond and Related Materials* **20**, 1234 (2011).
[10] A.E. Aleksenskii, M. A. Yagovkina, A.Y. Vul', *Phys. Solid State* **46**, 685 (2004)
[11] A. M. Panich *et al*., *J. Phys. D. Appl. Phys.* **44**, 125303 (2011).
[12] T. Enoki *et al*., *Chemistry — An Asian Journal* **4**, 796 (2009).
[13] O.V. Turova *et al*., *Catalysis Communications* **12**, 577 (2011).
[14] D. A. Kurdyukov *et al*., *Nanotechnology* **23**, 015601 (2012).
[15] P.G. Baranov *et al*., *Small* **7**, 1533 (2011).
[16] A. M. Schrand, S. A. C. Hens, O. A. Shenderova, *Critical Rev. Solid State Mater. Sci.* **34**, 18 (2009).

20th Int. Symp. "Nanostructures: Physics and Technology"
Nizhny Novgorod, Russia, June 24–30, 2012

Modular nanotransporters of anti-cancer drugs: the drugs become cell-specific and significantly more effective

A. S. Sobolev

Institute of Gene Biology, Moscow, Russia
M.V. Lomonosov Moscow State University, 119991 Moscow, Russia

Abstract. Modular nanotransporters (MNT) are recombinant multifunctional polypeptides created to exploit a cascade of cellular processes, initiated with membrane receptor recognition to deliver selective short-range and highly cytotoxic therapeutics to the cell nucleus. The multifunctional nanotransporter approach provides a new *in vivo* functional platform for drug development that could, in principle, be applicable to any combination of cell surface receptor and agent (photosensitizers, oligonucleotides, radionuclides) requiring nuclear delivery to achieve maximum effectiveness.

The development of therapeutic options for cancer that are both selective and effective presents a major challenge in contemporary biomedicine. Specific delivery and binding to malignant cell populations can be achieved by targeting cell surface receptors that are either uniquely expressed or overexpressed on cancer cells. After binding to the targeted receptor, the fate of the ligand-drug bioconjugate can be either to remain on the cell membrane or to be transported into the cytoplasm. However, the efficiency of most therapeutics depends on their subcellular localization, and for many of them, the most vulnerable compartment is the nucleus. Furthermore, certain types of therapeutics, such as photosensitizers and Auger electron emitting radionuclides, have ranges of action of less than 100 nm, which is a major advantage for minimizing damage to normal tissues adjacent to tumor tissue, but renders their cytotoxic effectiveness almost exclusively dependent on achieving delivery to the cell nucleus.

Our efforts to achieve these goals have been focused on nanobiotechnological creation of an artificial multifunctional transporting platform, i.e. the recombinant modular nanotransporter (MNT). The MNT is a modular polypeptide that can contain four moieties, i.e. an internalizable ligand to provide target cell recognition and receptor-mediated endocytosis by the cell, an endosomolytic module to facilitate escape from endosomes, a nuclear localization sequence motif to allow active transport into the cell nucleus *via* binding to cytoplasmic importins, and a carrier domain for efficient attachment of the drug [1–4]. In fact, MNT is an artificially generated detail of the cell transport machinery (or a nanodevice, which exploits the cell transport machinery) that was designed for cell-specific transport into a preassigned cellular compartment (the cell nucleus in this case).

Pursuing this strategy, we [1,2,4] designed, produced, and characterized bacterially-expressed MNT comprising either α-melanocyte-stimulating hormone (αMSH) or epidermal growth factor (EGF) for targeting αMSH receptors that are overexpressed on melanoma or the EGF receptor that is overexpressed on several cancers, including head and neck, breast carcinoma, and glioblastoma, the optimized nuclear localization sequence from SV40 large tumor antigen, the *Escherichia coli* hemoglobin-like protein as a carrier module, and a translocation domain of diphtheria toxin as the endosomolytic amphipathic module.

Small-sized (mean hydrodynamic diameter 10.6 ± 0.5 nm) specific multifunctional MNT demonstrated excellent results

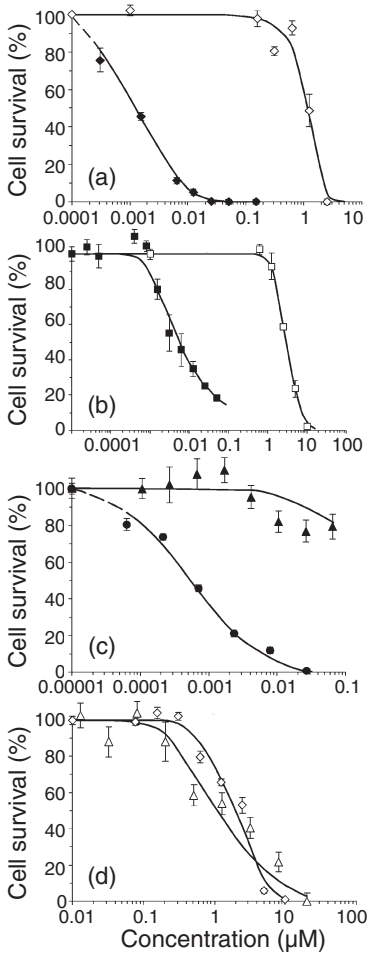

Fig. 1. Photocytotoxicity of photosensitizer-MNT conjugates as compared with free photosensitizers [2]: (a) (chlorin e_6)-MNT (♦) and free chlorin e_6 (◇); (b) (bacteriochlorin p)-MNT (■) and free bacteriochlorin p (□); (c) photocytotoxicity of (chlorin e_6)-MNT estimated on target A431 cells (●) and non-target NIH 3T3 cells (▲); (d) photocytotoxicity of free chlorin e_6 estimated on target A431 cells (◇) and non-target NIH 3T3 cells (△). Mean ± standard error.

in enhancement (up to 3 orders of magnitude) of photodynamic effects of photosensitizers on cancer cell lines *in vitro* and in imparting them cell specificity (Fig. 1a,b). Qualitatively similar effects demonstrated MNT carrying emitters of alpha-particles [5] and Auger electrons (unpublished). MNT can be freeze-dried and kept at room temperature for more than

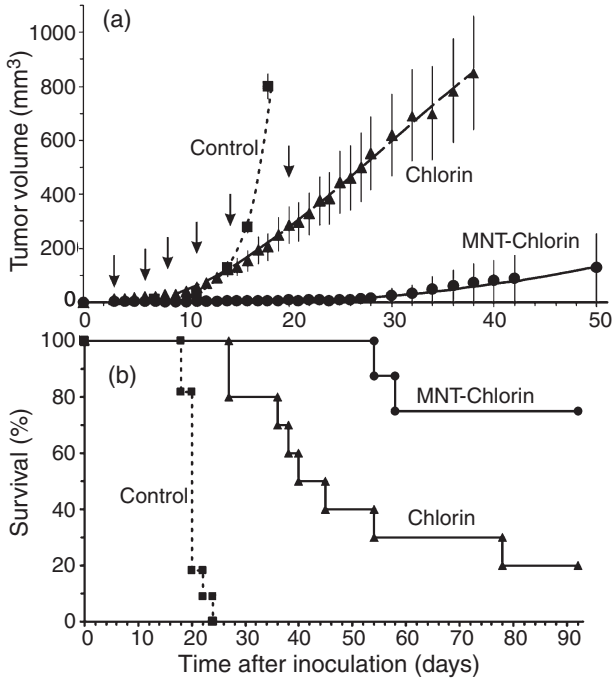

Fig. 2. Photodynamic therapy with chlorin e_6 carried by MNT inhibits A431 human epidermoid carcinoma growth and enhances survival of tumor-bearing Balb/c ByJIco-*nu/nu* mice compared with free chlorin e_6. (a) A431 tumor growth, mean $\pm$ standard error; average tumor volumes are shown up to the last day when all animals were alive. Arrows indicate injection and illumination cycles; bars represent the mean $\pm$ standard error; (b) Kaplan–Meier survival curve. From [4] with kind permission of Dove Medical Press Ltd.

18 months without loss of their activities. They are not toxic and immunogenic for mice. MNT selectively accumulate in tumors, with preferential accumulation in cancer cell nuclei but not in adjacent normal tissue [4].

A 98% inhibition in tumor growth was observed with the MNT carrying photosensitizer chlorin e_6 relative to controls (94% relative to free chlorin e_6, Fig. 2a). Median survival for mice in the control group was 20.0 ± 0.4 days, with all animals succumbing by 24 days (Fig. 2b). In contrast, 75% of animals remained alive in the (chlorin e_6)-MNT group compared with 20% in the free-chlorin e_6 group. Treatment of melanoma by photodynamic therapy is hindered substantially by almost complete absorption of light by melanin. Particularly given the difficulties inherent in photodynamic therapy for melanoma, the two-fold increase in median survival and significant inhibition in tumor growth obtained with the (bacteriochlorin *p*)-MNT in two mouse melanoma models is very encouraging [4].

In summary, these data provide *in vivo* evidence that MNT can selectively deliver drugs to the nuclei of tumor cells expressing a targeted receptor. MNT can improve specificity of drugs that ultimately can result in decreased side effects for patients. Moreover, delivery of drugs requiring nuclear transport to have a meaningful cytotoxic effect can be enhanced significantly through MNT-mediated delivery *in vivo*.

Acknowledgements

This work was supported in part by an RF State contract #16.512.12.2004 and by a National Institutes of Health (USA) grant #NS20023.

References

[1] A. A. Rosenkranz *et al*., *FASEB J.* **17**, 1121 (2003).
[2] D. G. Gilyazova *et al*., *Cancer Res.* **66**, 10534 (2006).
[3] Y. V. Khramtsov *et al*., *J. Control. Release* **128**, 241 (2008).
[4] T. A. Slastnikova *et al*., *Int. J. Nanomed.* **7**, 467 (2012).
[5] A. A. Rosenkranz *et al*., *Int. J. Radiat. Oncol. Biol. Phys.* **72**, 193 (2008).

20th Int. Symp. "Nanostructures: Physics and Technology"
Nizhny Novgorod, Russia, June 24–30, 2012

Resonant state expansion applied to one-, two-, and three-dimensional optical resonators

E. A. Muljarov[1,2], M. B. Doost[1] and W. Langbein[1]

[1] School of Physics and Astronomy, Cardiff University, The Parade, CF24 3AA Cardiff, UK
[2] General Physics Institute, RAS, Vavilova 38, Moscow 119991, Russia

The spectral properties of an optical resonator are characterized by the positions and linewidths of the cavity modes being, respectively, the real and imaginary parts of the eigenfrequencies of the open electromagnetic system. Coupling to an object which is placed inside or in close proximity to the cavity (e.g. light-matter coupling in embedded nanostructures) perturbs the cavity modes changing both their positions and linewidths, mostly affecting high-quality modes of the spectrum.

Recently, a new generation of optical biosensors based on the using of ultra high-quality whispering gallery modes (WGMs) in optical resonators has been proposed [1, 2]. Such sharp resonances cannot be calculated by known methods, or at least need very high computational efforts. To treat such resonances and their perturbations, we have recently developed a rigorous perturbation theory [3] called resonant state expansion (RSE) which was not available in electrodynamics before. The RSE presents a reliable method of calculation of resonant states, and in particular their wave numbers (eigenfrequencies), electric fields, as well as the transmission and scattering properties of an open optical system.

In this work, we apply the RSE to one-, two-, and three-dimensional systems, such as layered dielectric slabs and Bragg-reflector microcavities, dielectric microcylinders and microspheres, with and without perturbations. We test and validate

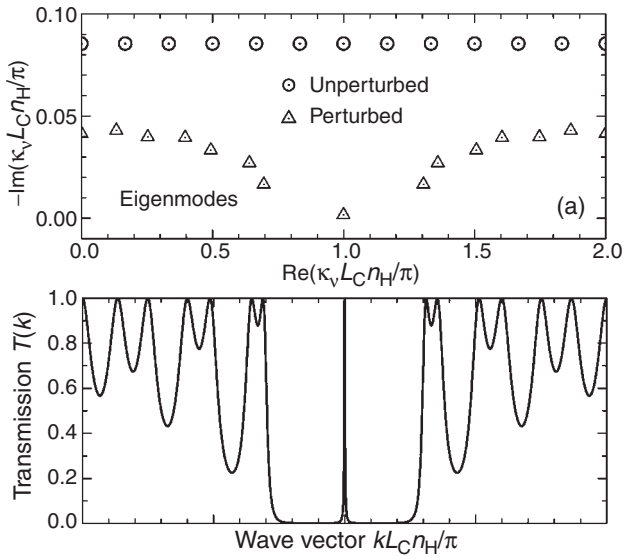

Fig. 1. (a) Wave vectors of resonant states of a microcavity with 3 pairs of Bragg mirrors on each side, calculated via the RSE, using a homogeneous dielectric slab as unperturbed system. (b) Microcavity transmission as a function of the normalized wave vector of the incoming light. L_C and n_C are, respectively, the cavity thickness and refractive index.

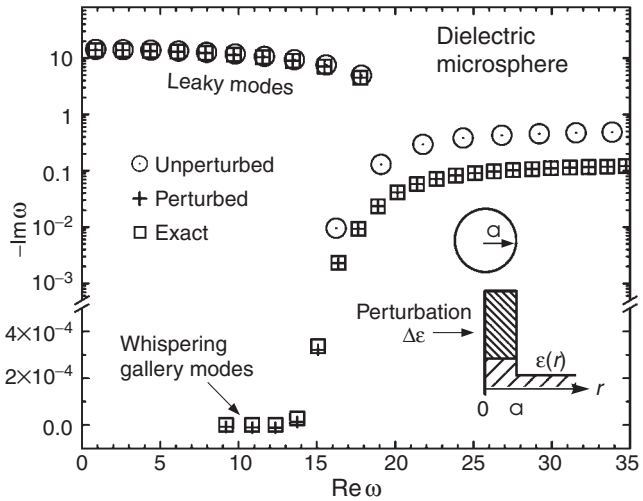

Fig. 2. Eigenmodes of a dielectric microsphere in vacuum, with the angular momentum $l = 20$ (TE modes). The unperturbed states are calculated for $\varepsilon = 2.25$. The perturbed states of the same-radius sphere with dielectric constant $\varepsilon + \Delta\varepsilon$, where $\Delta\varepsilon = 5$, are calculated analytically (open squares) and using the RSE with $N = 200$ basis states (crosses).

the perturbation method on various exactly solvable models and introduce a reliable extrapolation technique which allows us to estimate the accuracy and to improve results by one or two orders of magnitude [4]. The results for a Bragg microcavity (Fig. 1) and for a dielectric microsphere (Fig. 2) clearly demonstrate the quality of our theory: A strong perturbation ($\Delta\varepsilon = 5$ in the case of the sphere) leads to the formation of very sharp resonances, such as WGMs in a microsphere and cavity modes in a microcavity. They are not present in the unperturbed basis but are nevertheless calculated accurately in our method by taking into account a very limited number of basis states.

References

[1] V. S. Ilchenko and L. Maleki, *Proc. SPIE* **4270**, 120 (2001).
[2] J. Lutti, W. Langbein, and P. Borri, *Appl. Phys. Lett.* **93**, 151103 (2008).
[3] E. A. Muljarov, W. Langbein and R. Zimmermann, *Europhys. Lett.* **92**, 50100 (2010).
[4] M. B. Doost, W. Langbein, and E. A. Muljarov, *Phys. Rev. A* **85**, 023835 (2012).

20th Int. Symp. "Nanostructures: Physics and Technology"
Nizhny Novgorod, Russia, June 24–30, 2012

High density polariton phases in semiconductor microcavities

Maurice S. Skolnick
Department of Physics and Astronomy, University of Sheffield, Sheffield S3 7RH, UK

I will begin with a general introduction to the topic of microcavity polaritons emphasizing why the field has excited great interest over recent years, noting key points such as bosonic character, very light polariton mass, advantageous dispersion, and strong interactions. This will be followed by a description of key physics observations including stimulated scattering, Bose–Einstein condensation and long spatial and long temporal coherence.

The application of tunable periodic potentials to the condensed phase will be described showing direct evidence for the suppression of flow under 2D confinement and the transition from extended to fragmented condensates. Finally the creation of polariton soliton wavepackets will be described, where long propagation lengths of the non-dispersing wavepackets is obtained, with very high switching speeds. Key points of polariton physics which lead to soliton creation will be explained. By altering the conditions of pump and holding beams the creation of 'soliton trains' will be presented, a series of non-dispersing wavepackets propagating co-linearly at speeds in excess of 10^6m/s.

20th Int. Symp. "Nanostructures: Physics and Technology"
Nizhny Novgorod, Russia, June 24–30, 2012

Microcavity-controlled coherent coupling of quantum dots

E. A. Muljarov[1,2], K. Sivalertporn[1], F. Albert[3], J. Kasprzak[4], M. Strauß[3], C. Schneider[3], S. Höfling[3], M. Kamp[3], A. Forchel[3], S. Reitzenstein[3,5] and W. Langbein[1]

[1] School of Physics and Astronomy, Cardiff University, The Parade, CF24 3AA Cardiff, UK
[2] General Physics Institute, RAS, Vavilova 38, Moscow 119991, Russia
[3] Technische Physik, Physikalisches Institut, Universität Würzburg and Wilhelm Conrad Röntgen Research Center for Complex Material Systems, Am Hubland, D-97074 Würzburg, Germany
[4] Institut Néel, CNRS et Université Joseph Fourier, BP 166, F-38042 Grenoble Cedex 9, France
[5] Institut für Festkörperphysik, Technische Universität Berlin, Hardenbergstrasse 36, 10623 Berlin, Germany

We demonstrate a coherent coupling of spatially separated quantum dots (QDs). The coupling is achieved and controlled through the photon mode in a micropillar cavity (C) strongly coupled to QD exciton (X) states. The structures consist of self-assembled InGaAs QDs located in the anti-node of the fundamental optical mode of the cavity which stores photons for about 10 ps that has recently enabled pioneering demonstrations of the strong and quantum strong coupling regime [1] in a solid. In such structures a quantum of optical excitation oscillates between the fermionic X and bosonic C photon states. The resulting eigenstates of mixed nature form a polariton Jaynes–Cummings (JC) ladder [2].

By micro-photoluminescence we reveal a triplet of quasi-resonant Xs, which can be tuned into resonance with the cavity as show in Fig. 1. The data show three X-C avoided crossings, each of the three Xs being strongly coupled to the C. The measured tunings are reproduced with the standard coupled oscillator model, using Rabi coupling energies in the 40 meV range. Such multi-polaritonic strong coupling features were previously observed in Refs. [3,4]. To demonstrate the cavity-mediated coherent coupling we employed heterodyne spectral interferometry [5], allowing the measurement of the four-wave mixing (FWM) of the strongly-coupled Xs-C system. The FWM dynamics investigated as a function of temperature is significantly richer than observed in a single exciton case [1].

We have also developed a strict analytic approach to the calculation of the FWM response which is based on a generalization of the JC model [2]. Our theory uses a standard Hamiltonian of a single photonic mode coupled to three two-level systems with dissipation of all components taken into account by a Lindblad super-operator [3,4,6]. To calculate the FWM polarization, we follow our earlier rigorous approach [1,7] to the optical response of a system on a sequence of optical pulses. For the present system excited by two ultrashort pulses it has the following analytic form

$$P_{\mathrm{FWM}}(t,\tau) = \sum_{jk} c_{jk} e^{i\omega_j t} e^{i\lambda_k \tau}\,, \qquad (1)$$

in which λ_k are the complex polariton frequencies of the first (second) rung, for positive (negative) delay times τ, while ω_j are the frequencies of all possible transitions between the ground state and the first rung and between the first and second rung, all contributing to the real-time dynamics. The expansion coefficients c_{jk} are calculated exactly reducing the full master equation for the density matrix to a finite matrix problem. The results of our calculation show a quantitative agreement with the measured FWM dynamics.

We present a direct evidence of the coherent coupling between three QDs using a two-dimensional representation of the FWM in which coherent coupling can be observed unambiguously as off-diagonal signals [8]. The observed coherent coupling demonstrates that the cavity can act as a coupling bus for excitonic qubits.

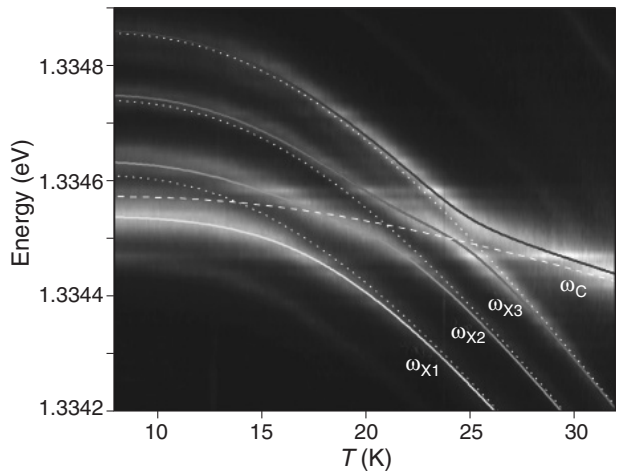

Fig. 1. Measured spectra of micro-photoluminescence and calculated energy positions of quantum dot exciton polaritons in a micropillar cavity at different temperatures.

References

[1] J. Kasprzak, S. Reitzenstein, E. A. Muljarov, C. Kistner, C. Schneider, M. Strauss, S. Höfling, A. Forchel, and W. Langbein, *Nature Mater.* **9**, 304 (2010).
[2] E. Jaynes and F. Cummings, *Proc. IEEE* **51**, 89 (1963).
[3] S. Reitzenstein, A. Löffler, C. Hofmann, A. Kubanek, M. Kamp, J. P. Reithmaier, A. Forchel, V. D. Kulakovskii, L. V. Keldysh, I. V. Ponomarev, and T. L. Reinecke, *Optics Letters* **31**, 1738 (2006).
[4] A. Laucht, J. M. Villas-Boâs, S. Stobbe, N. Hauke, F. Hofbauer, G. Böhm, P. Lodahl, M.-C. Amann, M. Kaniber, and J. J. Finley, *Phys. Rev. B* **82**, 075305 (2010).
[5] W. Langbein and B. Patton, *Optics Letters* **31**, 1151 (2006).
[6] F. P. Laussy, A. Laucht, E. del Valle, J. J. Finley, and J. M. Villas-Boâs, *Phys. Rev. B* **84**, 195313 (2011).
[7] E. A. Muljarov and R. Zimmermann, *Physica Status Solidi* **243**, 2252 (2006).
[8] J. Kasprzak, B. Patton, V. Savona, and W. Langbein, *Nature Photon.* **5**, 57 (2011).

20th Int. Symp. "Nanostructures: Physics and Technology"
Nizhny Novgorod, Russia, June 24–30, 2012

Dynamics of spatial coherence in exciton polariton condensate in semiconductor microcavities

V. V. Belykh[1], D. A. Mylnikov[1], N. N. Sibeldin[1], V. D. Kulakovskii[2], C. Schneider[3], S. Höfling[3], M. Kamp[3] and A. Forchel[3]

[1] P.N. Lebedev Physical Institute, RAS, 53 Leninsky pr., 119991 Moscow, Russia
[2] Institute of Solid State Physics, RAS, 142432 Chernogolovka, Russia
[3] Technische Physik, Physikalisches Institut and Wilhelm Conrad Röntgen Research Center for Complex Material Systems, Universität Würzburg, D-97074 Würzburg, Germany

Abstract. Time evolution of the first order spatial coherence function $g^{(1)}$ of the polariton system in a GaAs microcavity has been investigated under pulsed nonresonant excitation on the basis of Young's double-slit experiment. Above the threshold excitation density, $P_{\rm thr}$, for the polariton Bose–Einstein condensation the long-range spatial coherence in the condensate has been found to set on a picosecond time scale and decay with time highly exceeding the decay time of the condensate density. The coherence initially grows with a nearly constant velocity of 10^8 cm/s at excitation density $P = 2P_{\rm thr}$. The maximum magnitude of $g^{(1)}$ decreases at high P due to the feedback from the condensate on the collisions of condensed polaritons with nonequilibrium reservoir excitons.

Introduction

Studies of semiconductor microcavities (MC) with embedded quantum wells attract considerable attention inspired by the possibility to observe Bose–Einstein condensation (BEC) of mixed exciton-photon states — polaritons in this system. For the last five years, after the first experimental demonstration of nonequilibrium MC polariton BEC [1], a number of related phenomena in the MC polariton system have been discussed: superfluidity [2], quantized vortices [3], spin-Meissner effect [4] and Josephson effect [5].

One of the most important characteristics of condensate states is the first order spatial coherence

$$g^{(1)}\left(\mathbf{r}_1, \mathbf{r}_2, t\right) = \left\langle \psi^*\left(\mathbf{r}_1, t\right) \psi\left(\mathbf{r}_2, t\right)\right\rangle, \qquad (1)$$

i.e. the property of the system to share the same wavefunction at different points $\mathbf{r}_1$, $\mathbf{r}_2$ separated by the distance larger than the thermal de Broglie wavelength at the same time t. The spatial coherence of the MC polariton system can be probed by measuring the coherence of the light emitted from different points on the sample [1, 6]. One of the most interesting questions is how fast coherence is established between different points of the system. This question was addressed by G. Nardin *et al*. [7] who measured the dynamics of the first order spatial coherence of polariton condensate $g^{(1)}$ in a CdTe-based MC using a Michelson interferometer for the given separation x between its regions and evaluated the time of the coherence buildup. They found that the coherence in the condensate in the investigated CdTe MC with a rather disordered potential reaches its maximum value $g^{(1)}(x = 8.5\ \mu\text{m}) \sim 0.3$ after the population and decays very slowly compared to condensate decay. Both the dynamics of spatial coherence and its magnitude in the polariton condensate are highly influenced by potential fluctuations. In addition, they depend strongly on interaction between the polariton condensate and an exciton reservoir whose density exceeds strongly the thermally equilibrium one because of the short polariton lifetime. In the present work we study the spatial coherence (1) dynamics of the polariton system in a high Q GaAs-based MC with a weakly disordered potential in the geometry of Young's double-slit experiment [6] for different slits separation. We have found that in the investigated high Q MC the spatial coherence at small distances x builds up well before reaching the maximum population. The coherence buildup time increases nearly linearly with distance x and its increase exceeds 10 ps at $x > 10\ \mu$m. The maximum $g^{(1)}$ reached in the condensate depends strongly on the exciton reservoir being higher under excitation close to $P_{\rm thr}$ in spite of a smaller condensate density.

1. Experimental details

The sample under study was a half wavelength MC with Bragg reflectors made of 32 (for the top mirror) and 36 (for the bottom mirror) AlAs and $Al_{0.13}Ga_{0.87}As$ pairs providing a Q-factor of about 7000. Four tunnel-isolated GaAs/AlAs QWs were embedded at the positions of the electric-field antinodes of the MC. The Rabi splitting for the sample was about 4.5 meV. All the experiments were performed at 10 K. The sample was excited by the linearly horizontally polarized emission of a mode-locked Ti-sapphire laser generating a periodic train of 2.5-ps-long pulses at a repetition rate of 76 MHz. The angle of incidence of the excitation laser beam was 60° with respect to the sample normal. The excitation photon energy corresponded to the reflection minimum of the mirror at the given angle and was 10–25 meV higher than the energy of the bare exciton. The beam was focused in a 30 μm spot on the sample surface. The photoluminescence (PL) spot was imaged with magnification of 10 on the light-absorbing plate with two opaque vertical slits. The interference pattern of the emission coming from the regions of the sample selected by two slits was focused onto the Hamamatsu streak camera horizontal slit. The similar geometry was used in [6] where $g^{(1)}$ without time resolution was measured. The time and spatial resolution of our system were 3 ps and 2 μm, respectively.

2. Results and discussion

At low excitation density the PL dynamics is relatively slow, the PL spot has a homogeneous Gaussian profile and shows no interference fringes in the double slit experiment for $x > 2\ \mu$m. As the excitation density is increased above the BEC threshold

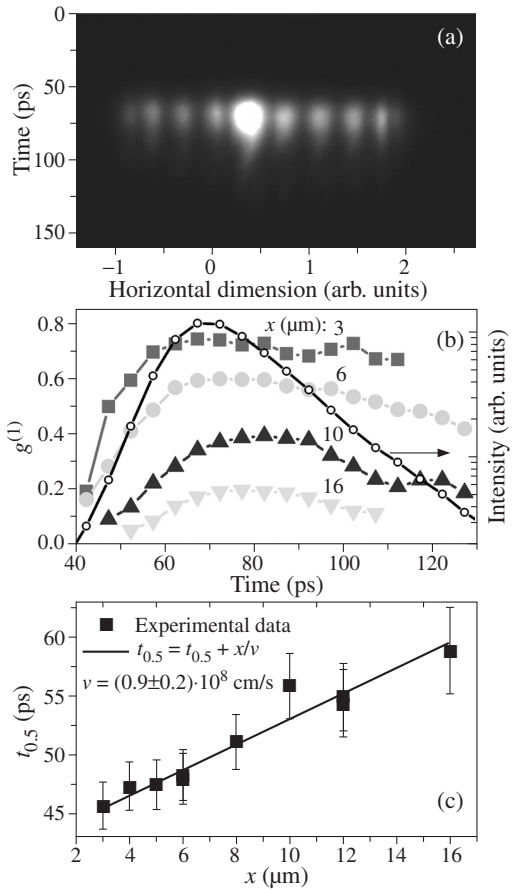

Fig. 1. (a) Streak camera image of the interference pattern from the regions of the sample separated by 10 μm. (b) Spatial coherence dynamics for different separations between condensate regions together with integrated intensity dynamics. (c) Dependence of coherence buildup time $t_{0.5}$ on spatial separation x. Excitation power $P = 2P_{\rm thr}$, photon-exciton detuning is around zero.

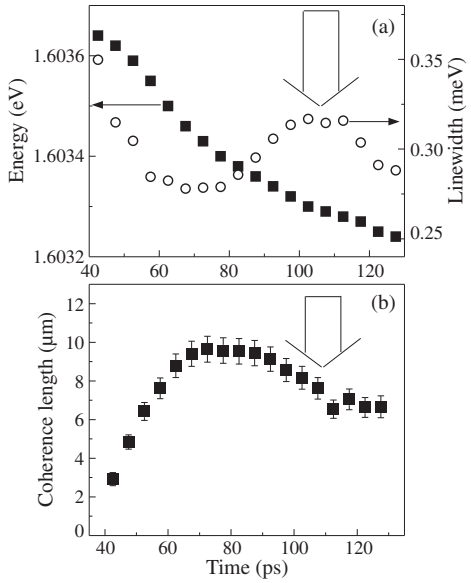

Fig. 2. (a) Dynamics of the energy position (left axis) and width (right axis) of the spectral line. (b) Coherence length dynamics. Arrow indicates the moment of transition from the weak to strong coupling regime. Excitation power $P = 2P_{\rm thr}$, photon-exciton detuning is around zero.

$P_{\rm thr}$, a pronounced increase of the PL intensity occurs followed by the decrease of the spectral line width below the spectral resolution, fast PL dynamics and well resolved interference fringes in the double slit experiment (Fig. 1). The spatial size of the condensed state is about 20 μm.

Figure 1a shows the interference pattern dynamics with a number of well-resolved minima and maxima. The intense central peak is related to the emission transmitted through the absorbing surface of the plate with slits. The visibility of the interference fringes defines the spatial coherence $g^{(1)}(x)$ between two strips on the sample at distance x selected by the slits. The dynamics of the spatial coherence for different separations x is presented in Fig. 1b together with the dynamics of the integrated intensity.

Figure 1 shows that the long-range spatial coherence at small $x \sim 3{-}6$ μm is set in right at the onset of stimulated emission and the value $g^{(1)}$ at $x = 3$ μm reaches its maximum earlier than the condensate density. The formation of the spatial coherence at large distances demands much longer time, over 10 ps. In addition, it is seen that the maximum value of $g^{(1)}$ decreases with increased separation x. Figure 1c displays the time of spatial coherence buildup $t_{0.5}$ defined as the time when $g^{(1)}$ reaches half of its maximum value as a function of x. It is seen that the dependence $t_{0.5}(x)$ is close to linear, which allows defining the velocity of spatial coherence propagation: $v = 10^8$ cm/s. We note that analysis of the time evolution of the energy position and width of the emission line (Fig. 2a) indicates that at $P = 2P_{\rm thr}$ stimulated emission develops in the weak exciton-photon coupling regime with the following transition to the polariton BEC in the strong coupling regime. The transition occurs with the conservation of spatial coherence (Fig. 2b).

Finally, Fig. 1b shows that the decay of the spatial coherence in the whole range of x occurs much slower than that of the condensate density. Note as well that the decrease in the excitation density to the value still higher than $P_{\rm thr}$ results in a pronounced increase in the magnitude of $g^{(1)}$ for $x \approx 10$ μm in spite of a strong decrease in the condensate density. These facts show that the spatial coherence is not defined by the filling factor only. They indicate a dramatic dependence of $g^{(1)}$ on the feedback from the condensate on the collisions of condensed polaritons with thermally nonequilibrium reservoir excitons which makes the exciton polariton system qualitatively different from Bose gas of cold atoms. The effect of the exciton reservoir has been found to diminish with increasing negative detuning of photon and exciton modes. This behavior correlates with the weakening of the interaction of polaritons with exciton reservoir due to the decrease of exciton fraction in the polariton.

References

[1] J. Kasprzak *et al*., *Nature* **443**, 409 (2006).
[2] A. Amo *et al*., *Nature Phys.* **5**, 805 (2009).
[3] K. G. Lagoudakis *et al*., *Nat. Phys.* **4**, 706 (2008).
[4] A. V. Larionov *et al*., *Phys. Rev. Lett.* **105**, 256401 (2010).
[5] K. G. Lagoudakis *et al*., *Phys. Rev. Lett.* **105**, 120403 (2010).
[6] H. Deng *et al*., *Phys. Rev. Lett.* **99**, 126403 (2007).
[7] G. Nardin *et al*., *Phys. Rev. Lett.* **103**, 256402 (2009).

20th Int. Symp. "Nanostructures: Physics and Technology"
Nizhny Novgorod, Russia, June 24–30, 2012

Resonant polarization mixing of electromagnetic modes in opal-like photonic crystals

T. A. Ukleev[1,2], A. V. Sel'kin[1,2], A. Yu. Men'shikova[3] and N. N. Shevchenko[3]

[1] Ioffe Physical-Technical Institute, St Petersburg, Russia
[2] St Petersburg State University, St Petersburg, Russia
[3] Institute of Macromolecular Compounds, RAS, St Petersburg, Russia

Abstract. Bragg reflection spectra are studied for opal-like photonic crystals made of polystyrene spheres. A resonant enhancement of reflectivity is observed in cross-polarization configuration of the analyzer and polarizer when varying the azimuthal orientation of a sample in respect to the incidence plane. The cross-polarization effect takes place at oblique incidence of light on the lateral (111) crystal plane with the plane of incidence being non-perpendicular to the inclined $(11\bar{1})$ crystal plane. The effect is shown to be due to the multiple Bragg diffraction of light when the resonant Bragg conditions are fulfilled at a certain angle of incidence and azimuth simultaneously for the lateral and inclined crystal planes.

Introduction

Opal-like structures considered as a typical example of three dimensional photonic crystals (PhC) have received much attention during last decades both due to their non-trivial optical properties and potential applications in devices [1,2]. A number of interesting and still not adequately explored phenomena occurring in the frequency range of low energy stop-bands are associated with the multiple Bragg diffraction (MBD) effects [3–5]. Most prominently, these phenomena are manifested in reflection spectra at large angles of incidence as a doublet structure of the reflectance contour [5–7]. As a rule, the simplest geometry of reflection is chosen so that the incidence plane of light is perpendicular to both the lateral (111) and inclined $(11\bar{1})$ crystal planes, which corresponds to the incidence plane azimuth $\varphi = 0$ (see Fig. 1). Such geometry allows one, in a rather simple way [5], to analyze separately the contribution to the reflection spectrum from the TE- and TM-electromagnetic modes propagating inside an opal-like PhC: these modes are excited in s- and p-polarization of incident light, respectively. In this work, we discuss novel optical phenomena associated with resonant polarization mixing of electromagnetic modes in opal-like photonic crystals, which is the case, in spite of the high, fcc, symmetry of the sample, when the azimuth φ differs from $m\pi/3$ values ($m = 0, 1, \ldots, 5$).

1. Experimental

The opal-like PhCs under study were prepared from monodispersive polystyrene spheres self-assembled to the films of about 5 μm in thickness. The particles were synthesized by styrene and methacrylic acid emulsifier-free emulsion copolymerization. The Bragg reflection spectra were measured in s-s, p-p and p-s configurations of polarized light when incoming s- or p-polarized radiation was incident on the lateral reflecting surface (111) of the PhC film. The azimuth angle φ of the sample was measured from zero-value which corresponded to the perpendicular orientation of the incidence plane in respect to the inclined crystal planes (002) and $(11\bar{1})$. The sample was precisely oriented using measured Bragg reflection spectra under the MBD conditions [6].

Figure 2 shows the s-s reflection spectra obtained at the azimuthal orientation $\varphi = 15^\circ$ of the plane of incidence. In Fig. 2a, the topogram of all the spectra measured is depicted

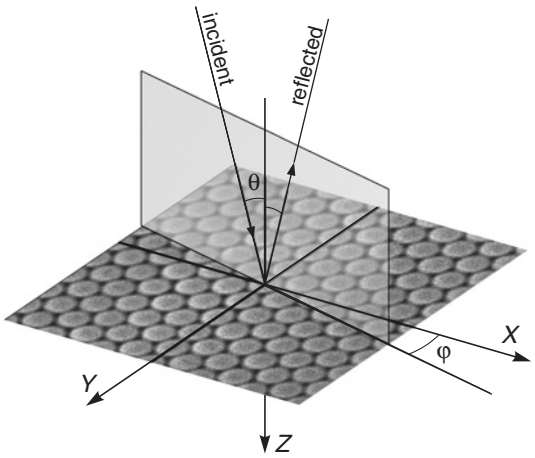

Fig. 1. Geometry of Bragg reflection of light from an opal-like photonic crystal: the XY plane of the reference system coincides with the (111) lateral (reflecting) surface of the sample, the azimuth φ of the plane of incidence is reckoned from the XZ plane which is perpendicular to the inclined crystal planes $(11\bar{1})$ and (002), θ is the angle of incidence.

where, together with the main reflection peak band, the reflectance deep is clearly seen crossing the peak band in the incidence angle range $\sim 50^\circ < \theta < 62^\circ$. Some reflectance contours recorded at three angles of incidence are correlated with the topogram in Fig. 2b. A very surprising effect appears when measuring the same spectra in p-s cross-polarization configuration (see Fig. 3). Instead of expected absence of reflection signal, there exists a rather bright spot on the topogram (Fig. 3a). This spot is observed in the region where the deep in s-s reflection is registered (cf. Fig. 2), the maximum value of the p-s reflectance being about as high as 10%! It should be emphasized here that with decreasing azimuth φ (up to $\varphi = 0$) the p-s reflection intensity tends to zero.

2. Discussion

In accordance with the technique developed in [6] based on comprehensive analysis of Bragg reflection spectra at $\varphi = 0$ we carefully measured the parameter values of the PhC sample under study. The mean distance between neighboring particles placed in the lateral plane is $a_{00} = 279$ nm, the average dielectric constant is $\varepsilon_0 = 2.185$, the coefficient of uniaxial

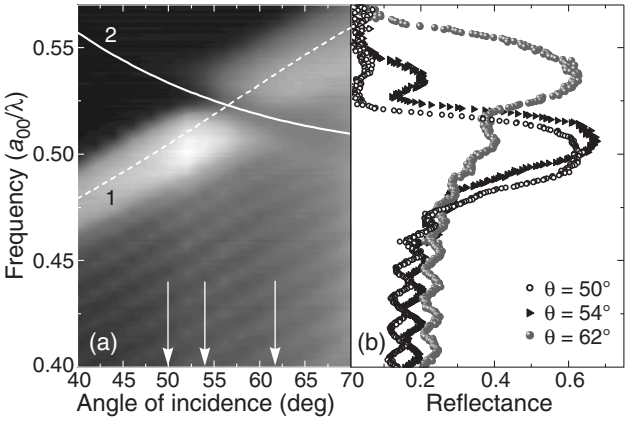

Fig. 2. (a) The topogram of measured reflectance in s-s configuration of polarization at the azimuth $\varphi = 15^\circ$ of the incident plane; superimposed lines are calculated with the formulae (1) and (2) giving Bragg conditions for light reflection from the crystal planes (111) (black dashed line 1) and $(11\bar{1})$ (white solid line 2). (b) s-s reflectance spectra obtained at three different angles of incidence θ, as indicated. a_{00} is the smallest distance between the particle centers in the (111) plane, λ is the wavelength of incident light.

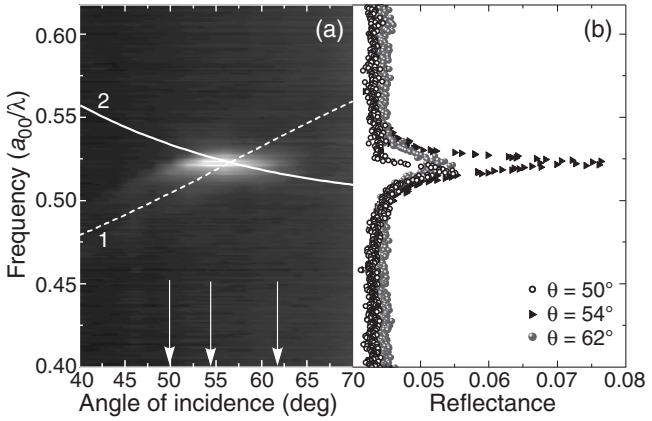

Fig. 3. (a) The topogram of measured reflectance in p-s polarization configuration at the azimuth $\varphi = 15^\circ$ of the incidence plane; superimposed lines are calculated with the formulae (1) and (2) giving Bragg conditions for light reflection from the crystal planes (111) (dashed line 1) and $(11\bar{1})$ (solid line 2). (b) p-s reflectance spectra obtained at three different angles of incidence θ, as indicated. a_{00}/λ is the same as in Fig. 2.

compression along [111] direction is $\eta = 0.94$. These values allow us to describe in a good approximation [7] the spectral positions λ_{111} and $\lambda_{11\bar{1}}$ of the main features appearing in reflection spectra using the following Bragg-type formulae:

$$\lambda_{111} = \sqrt{8/3}a_{00}\eta\sqrt{\varepsilon_0 - \sin^2\theta}, \quad (1)$$

$$\lambda_{11\bar{1}} = \frac{\sqrt{6}a_{00}\eta}{1+2\eta^2}\left(\eta\sqrt{2}\sin\theta\cos\varphi + \sqrt{\varepsilon_0 - \sin^2\theta}\right), \quad (2)$$

where the indices 111 and $11\bar{1}$ differing the wavelengths λ are referred to Bragg diffraction from the corresponding crystal planes. As follows from above formulae, only $\lambda_{11\bar{1}}$ depends on the azimuth φ ($\varphi \in [-\frac{\pi}{6}, \frac{\pi}{6}]$) of the incidence plane. λ_{111} gives the s-s reflection peak band position as a function of the angle of incidence θ, whereas $\lambda_{11\bar{1}}$ describes the behavior of the s-s reflection deep. Figure 2 demonstrates clearly that the spectral positions of the reflectance maxima and deeps are fitted well by Eqs. (1) and (2), respectively. This allows us to consider unambiguously the spectral deep observed at the 15° azimuth in the vicinity of the interception point of the theoretical curves (1) and (2) as being due to the MBD effect. Because the enhancement of reflectivity in cross-polarization configuration (see Fig. 3) takes place also in the vicinity of this interception point, we can ascribe such enhancement to the MBD effect, as well.

3. Conclusion

The results presented in this work demonstrate that in spite of high (nearly cubic) symmetry of opal-like photonic crystals their optical properties exhibit strong anisotropy which becomes very much more pronounced when the multiple Bragg diffraction conditions are fulfilled. In such a case, the resonant polarization mixing of diffraction processes governed by two or more systems of crystal planes takes place. Then for some directions of propagation the TE- or TM-classification of electromagnetic modes fails because the eig enmodes are elliptically polarized. As a result, at p- or s-input polarization, reflected light becomes elliptically polarized, which appears experimentally as a resonant cross-polarization effect. It should be concluded that this effect can be considered as a new direct manifestation of the multiple Bragg diffraction in 3D photonic crystals.

Acknowledgements

The work was supported by the Development Program of St Petersburg State University, Contract No. 11.37.2011 and by the Branch of Physical Sciences of the Russian Academy of Sciences under the Program "Fundamental Problems of Photonics and Physics of New Optical Materials".

References

[1] J. F. Galisteo-López *et al*., *Adv. Matter* **23** 1, 30 (2001).
[2] J. D. Joannopoulos *et al*., *Photonic Crystals: Molding the Flow of Light* (2nd edition), Princeton University Press, Princeton 304 (2008).
[3] H. M. van Driel and W. L. Vos, *Phys. Rev. B* **62**, 9872 (2000).
[4] S. G. Romanov *et al*., *Phys. Rev. E* **63**, 056603 (2001).
[5] A. V. Sel'kin, *Proc. of 12th Symp. "Nanostructures: Physics and Technology"* (St Petersburg, Russia, 2004), Ioffe Istitute, 111 (2004).
[6] A. G. Bazhenova *et al*., *Physics of the Solid State* **49** 11, 2109 (2007).
[7] V. G. Fedotov *et al*., *Phys. Status Solidi B* **248** 9, 2175 (2011).

20th Int. Symp. "Nanostructures: Physics and Technology"
Nizhny Novgorod, Russia, June 24–30, 2012

Bragg diffraction-induced laser pulse splitting in a linear photonic crystal

S. V. Chekalin[2], S. E. Svyahovskiy[1], V. O. Kompanets[2], A. I. Maidykovskiy[1], T. V. Murzina[1], A. A. Skorynin[1], V. A. Bushuev[1] and B. I. Mantsyzov[1]

[1] Department of Physics, M.V. Lomonosov Moscow State University, 119991 Moscow, Russia
[2] Institute of Spectroscopy RAS, Fizicheskaya str. 5, 142190 Troitsk, Moscow Region, Russia

Abstract. Novel optical linear effect of diffraction-induced femtosecond laser pulse splitting in porous silicon-based multilayered linear photonic crystals (PC) has been observed for the first time. We have observed the temporal Bragg diffraction-induced laser pulse splitting (DIPS) into two ones propagating with different group velocities in PC. This phenomenon originates from spatially inhomogeneous light localization within the PC at the Laue scheme of the dynamical Bragg diffraction. Splitting time of the femtosecond pulses passing in each of the diffraction directions depends linearly on the crystal thickness and matches the theoretical estimation. This phenomenon can be used for full optical switching.

Introduction

Linear effect of diffraction-induced pulse splitting (DIPS) in photonic crystal (PC) at the Laue scheme of the Bragg diffraction has been predicted recently [1] for unlimited in transverse direction pulses. In the simplest one-dimensional case, a PC is a multilayered periodic structure. By means of analytical solution of a boundary problem it was shown that an input picosecond laser pulse brakes up within the structure on two pulses propagating with different group velocities. The DIPS effect is explained by spatially inhomogeneous light localization in the PC at the Laue geometry of diffraction. One pulse field is mainly localized within optically low-index layers of the structure, but another pulse field is localized near the high-index layers. Therefore parameters of these pulses can be changed separately by means of changing of low-index or high-index layers optical properties. Such structure of field localization in the PC bulk is caused by wave diffraction. In the PC, each spectral component of a pulse incident at the Bragg angle with respect to the PC layers splits up into a coherent superposition of two transmitted and two diffracted (diffractively reflected) waves. These waves propagate in the PC with two different effective refractive indexes and, as a result, with two different velocities. With an increase in the propagation depth in the PC bulk, these waves are divided into two pulses. Each pulse consists of a pair of coupled waves: one transmitted and one diffracted moving with the same velocity. At the PC output, a pair of transmitted (T) and a pair of diffractively reflected (R) pulses are emitted. Hence, a thin photonic crystal can be used for full optical switching. According to the theoretical description [1], the time interval between the paired pulses propagating in each of the two output diffraction wave directions is proportional to the optical path of light in the PC and to the modulation of the refractive indexes of the neighboring PC layers. The presented results confirm that the laser pulse transmitted through the PC is propagating into two directions corresponding to the transmitted and diffractively reflected waves of nearly equal intensities, each of them, in turn, being splitted into pairs of pulses with the time interval between them of about hundreds of femtoseconds. A linear dependence of the time interval between such pulses on the PC thickness is demonstrated. The experimental results are in a good agreement with the theoretical description based on the DIPS effect.

1. Experimental

The experiments are carried out for one-dimensional porous silicon-based PC consisting of 375 spatial periods of 800 nm thick using a femtosecond Ti-Sapphire laser as a probe pulse. The experimental setup was based on Ti-Sapphire laser (wavelength of 800 nm, pulse duration of 110 fs, pulse repetition rate of 80 MHz, average power of 60 mW). The beam was focused on the sample facet in a spot of 20 μm in diameter. The sample of porous silicon-based photonic crystal (PC) was fabricated by electrochemical etching of p-doped Si(001) (resistivity of 0.002 Ω cm) by the procedure described in [2]. The sample of $0.3 \times 2.0 \times 5.0$ mm in size consisted of 375 pairs of alternating layers with different refraction indices and thickness of 400 nm. After the fabrication the sample was oxidized to form porous quartz structure. In order to make a structure transparent in the visible spectral range the porous silicon PC was annealed in oxygen atmosphere at $T = 900$ °C for two hours thus forming a silicon oxide structure with the refractive indexes of the alternating layers $n_1 = 1.32 \pm 0.03$ and $n_2 = 1.48 \pm 0.03$, respectively. The sides of the structure were mechanically poled to form a plane-parallel slab with an accuracy of 0.1°. The *p*-polarized laser beam was focused on a cleaved edge of the PC into a spot of approximately 20 μm in diameter in the Laue geometry. The sample was maintained on a goniometer, the angle of incidence of the probe beam was varied in the range from 0 to 45°. The signal at the fundamental wavelength passed through the PC and after that was sent to autocorrelometer for measuring its temporal structure. Prior to the temporal measurements, the spatial splitting of the laser pulses in the PC at the Laue diffraction scheme was studied in order to reveal the high structural quality of the periodic multilayered structure as well as of the internal interfaces between the porous layers. It was checked that both transmitted and diffractively reflected beams are registered under the exact fulfillment of the Bragg angular condition at $\Theta = 31°$ for the laser wavelength $\lambda = 800$ nm, in accordance with the theoretical estimations for the structure under study.

2. Results

The observation of the beam propagation inside the PC shows the realisation of a waveguide-like regime. The light diffracted in the sample exhibits the diffraction pattern which consists

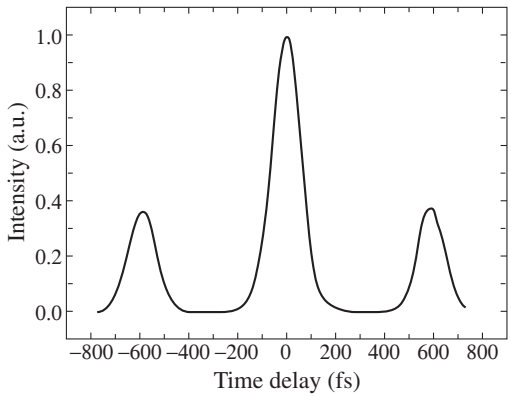

Fig. 1. Autocorrelation function of the light beam transmitted through the annealed porous silicon-based photonic crystal.

of two spatial maxima corresponding to the transmitted and diffracted beams. The angular directions of these maxima satisfy the Bragg law $m\lambda = 2d \sin\alpha$ for $m = \pm 1$. We demonstrated that the direction of the diffracted beam depends on the wavelength of the incident beam in correlation with the Bragg law. Temporal splitting of the *p*-polarized femtosecond laser pulses passed through the structure was observed experimentally by measuring the autocorrelation functions. These functions were measured for the transmitted and diffracted pulses under the fulfillment of the Bragg conditions and normalized to its value at $\tau = 0$. In both cases three maxima were observed, the first one centered at $\tau = 0$ and the two ones shifted for $\tau = \pm 0.57$ ps, that corresponds to the detection of the two pulses shifted in time for approximately $t_{12} = 0.57$ ps. The autocorrelation function of the transmitted beam intensity is shown in Fig. 1. It is worth noting that the temporal shape of all three maxima of autocorrelation function is the same and correlates with the autocorrelation function of a single laser pulse with FWHM of 110 fs. It is clear evidence that the observed dependence corresponds to the true temporal splitting of a laser pulse within the PC. Similar measurements performed for the larger detuning time interval does not reveal the appearance of additional peculiarities. In conclusion, we have observed, for the first time to our knowledge, diffraction-induced pulse splitting effect at the Laue geometrical scheme of the dynamical Bragg diffraction in one-dimensional periodical multilayer porous silicon-based structure with the refractive index modulation in the neighboring layers of 0.16 and the number of periods of 375. We have shown that a temporal delay up to 570 fs is achieved for a 2 mm thick PC for pulse duration 110 fs, and the time delay can be varied by a change of the PC thickness. The observed independence of the temporal delay between the paired pulses on the probe pulse intensity confirms that the DIPS is a linear effect. The DIPS effect leads to double the laser pulse repetition rate and, moreover, is the evidence of a high quality of the PC structure, as the dynamical diffraction effect takes place only in a defectless structure. The DIPS effect can be also arise in 2D and 3D PC where dynamical diffraction at the Laue scheme can be realized, and could be useful, for instance, for time delay in pump-probe spectroscopy and laser physics.

Acknowledgements

This work was supported by Russian Foundation for Basic Research (09-02-00786a).

References

[1] V. A. Bushuev, B. I. Mantsyzov, A. A. Skorynin, *Phys. Rev. A* **79**, 053811-1-5 (2009).

[2] H. Foll, M. Christophersen, J. Carstensen, and G. Hasse, *Materials Science and Engineering* **39(4)**, 93 (2002).

20th Int. Symp. "Nanostructures: Physics and Technology"
Nizhny Novgorod, Russia, June 24–30, 2012

Three- and six-fold axial symmetries in optical spectra of opaline photonic crystals

V. G. Fedotov[1] and A. V. Sel'kin[2,1]

[1] Faculty of Physics, St Petersburg State University, St Petersburg, Russia
[2] Ioffe Physical-Technical Institute, St Petersburg, Russia

Abstract. Optical reflection and transmission spectra of thin three-dimensional opaline photonic crystal films are studied for Γ-L-K and Γ-L-U propagation directions. The spectra are calculated numerically making use of the analytical theory of dynamical diffraction generalized to the case of a high dielectric contrast medium. Diffraction of light from the crystal planes inclined to the film interfaces is found to give rise to the additional extinction bands which do not coincide in spectral positions with the Bragg reflection peaks. Three- and six-fold axial symmetries of optical spectra are discussed in connection with the symmetry of the face-centered cubic lattice.

Introduction

In this paper, we presents results of a theoretical study of the Bragg reflection and transmission of light by thin films of three-dimensional photonic crystals (PhCs). Particular attention is paid to the effects of the multiple Bragg diffraction of light [1] which are discussed in the framework of the dynamical theory of diffraction. By detailed comparison of the reflection and transmission spectra specific effects caused by light diffraction from non-lateral crystal planes are analyzed.

1. Theoretical model

In our calculations we use a previously developed [2] theoretical approach to the analysis of the Bragg reflection and transmission spectra based on the ideas of the dynamical diffraction theory. This approach, in fact, is analytical and therefore allows a detailed study of physical mechanisms of light interaction with PhC media (as opposed to the methods based on the full-wave electrodynamic simulations using intensive and cumbersome computational procedures).

As a model under study, a thin (of 20 monolayers in thickness) opaline PhC film assembled from spherical polystyrene particles was considered [3]. The distance a_{00} between neighboring particles was chosen to be equal to 280 nm, which corresponds to the typical experimental conditions providing observation of effects of interest in the visible spectral range. The possible energy losses associated with absorption and scattering of light were taken into account by adding the imaginary term $i\varepsilon_0''$ ($\varepsilon_0'' = 0.04$) to the permittivity of the PhC. It is assumed that reflecting (lateral) surfaces of the PhC film are parallel to the (111) crystal planes, the crystal direction $[11\bar{1}]$ being in the plane of light incidence. The angle of incidence θ is chosen so that the wave refracted at the interface experiences simultaneous diffraction from the crystal planes (111) and $(11\bar{1})$. In general, this orientation of the incidence plane corresponds to two possible directions of light propagation in the directions Γ-L-K and Γ-L-U within the I Brillouin zone of a reciprocal lattice (see Fig. 1).

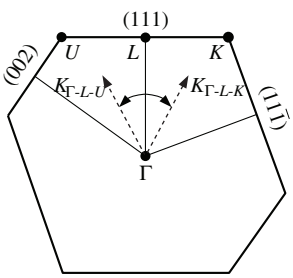

Fig. 1. Cross section of the I Brillouin zone of the face-centered cubic lattice (a truncated octahedron) in the light incidence plane. Two possible light propagation directions, Γ-L-K and Γ-L-U, are shown.

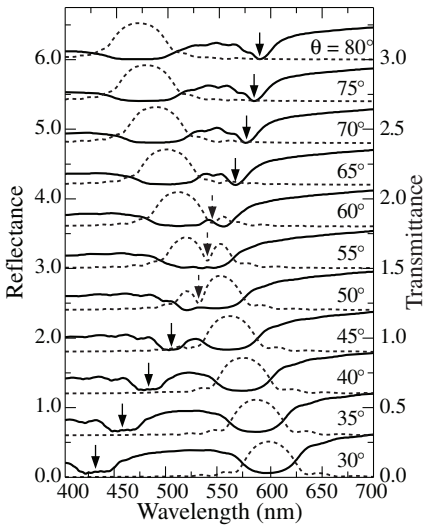

Fig. 2. Calculated transmission (solid curves) and reflection (dashed curves) spectra of an opaline PhC film at different light incidence angles θ for the Γ-L-K propagation direction. Solid arrows mark the position of the extinction bands outside of the (111) Bragg resonance. Dashed arrows show the position of the dips in the Bragg reflection contour.

2. Results and discussion

The results of the numerical calculations performed are shown in Fig. 2 and Fig. 3. As can be seen from these figures, the spectra of the specular reflection and transmission have a complicated structure and are noticeably altered depending on the angle of incidence. The reflection spectra are identical both for Γ-L-K (Fig. 2, dashed curves) and Γ-L-U (Fig. 3, dashed curves) propagation directions, which is consistent with the time reversal symmetry. So, the reflection spectra have to exhibit six-fold axial symmetry. The main feature observed in the reflection spectrum as a relatively broad peak "111" is due to the photonic stop-band (PSB) "111" which is governed by the Bragg diffraction of light from the (111) crystal planes (parallel to the reflecting interfaces of the PhC film). In a narrow range of incidence angles ($\sim 50-60^\circ$) the reflection spectrum takes the shape of a pronounced doublet which is associated with the additional light diffraction from the system of inclined (relative to the reflecting surfaces of the film) planes $(11\bar{1})$.

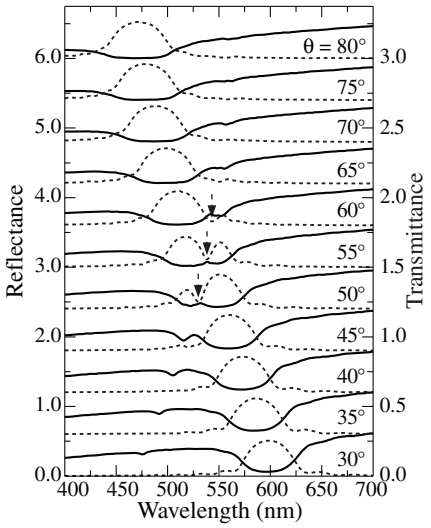

Fig. 3. Calculated transmission (solid curves) and reflection (dashed curves) spectra of an opaline PhC film at different light incidence angles θ for the Γ-L-U propagation direction. Dashed arrows show the position of the dips in the Bragg reflection contour.

This diffraction is accompanied, as discussed in Ref. [2], by the excitation inside the PhC of the additional electromagnetic mode with low group velocity ("slow" light mode), which brings about an additional energy transfer inside the crystal. As a result, the spectrum within the main PSB "111" is shaped by the dip appearing on the "slow" mode frequencies. The spectral position λ_{refl} of the dip in the Bragg reflection band is described with high accuracy by the modified Bragg formula applied to diffraction from the inclined planes $(11\bar{1})$,

$$\lambda_{\text{refl}} = a_{00}\sqrt{2/3}\left(\sqrt{2}\sin\theta + \sqrt{\varepsilon_0 - \sin^2\theta}\right), \qquad (1)$$

which is derived in the approximation of weak spatial modulation of the dielectric function (the "empty" lattice approximation), with an account of refraction of light on the PhC interfaces.

The calculated transmission spectra, as expected, show the band of extinction "111" formed by the main PSB "111". This band shifts to shorter wavelengths with increasing the angle θ and corresponds in its spectral position to the main Bragg reflection peak. However, along with the "111" band in the transmission spectrum for Γ-L-K propagation direction (Fig. 2, solid curves) an additional band of extinction can be seen that shifts to longer wavelengths with increasing θ. This fact is naturally associated with the extinction due to light diffraction from the inclined crystal planes $(11\bar{1})$. On the other hand, as a simple analysis shows, the spectral location of the additional extinction band as a function of θ is not described by Eq. (1). The additional band shifts more rapidly with the incidence angle variation when compared to Eq. (1).

A detailed comparison of the transmission spectrum with the eigenmode dispersion curves for spatially confined PhC shows that the additional extinction band arises in the spectral region where incident light and light diffracted from the only $(11\bar{1})$ planes dominate. In this case, the modified Bragg formula has the form:

$$\lambda_{\text{trans}} = a_{00}2\sqrt{6}\left(2\sqrt{2}\sin\theta + \sqrt{\varepsilon_0 - \sin^2\theta}\right)/9\,. \qquad (2)$$

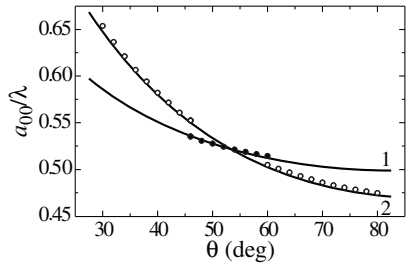

Fig. 4. Spectral positions of peculiarities in the reflection (curve 1) and transmission (curve 2) spectra as a function of the light incidence angle θ. Symbols are taken from the calculated transmission (open circles) and reflection (black circles) spectra. Solid curves is the result of an analysis of the dispersion curves of the eigenmodes in the approximation of the low dielectric contrast. a_{00} is the distance between the neighboring particles forming PhC and λ is the free-space wavelength of light.

In the transmission spectrum for Γ-L-U propagation (Fig. 3, solid curves) the additional broad extinction band is not observed. In this case, Eq. (2) describes the spectral region where light diffracted from the $(11\bar{1})$ planes has low intensity and only incident light dominates. It is important to note here that the light diffraction from the (002) planes is negligible small in either case. So, the transmission spectra have to exhibit three-fold axial symmetry.

In Fig. 4, solid curves show dependences of the dimensionless ratios $a_{00}/\lambda_{\text{refl}}$ and $a_{00}/\lambda_{\text{trans}}$, as a function of θ, calculated using Eq. (1) and Eq. (2). On this figure, symbols correspond to the positions of the dips in the Bragg reflection spectra (black circles) and additional extinction bands in the transmission spectra (open circles), taken from the calculated spectra like that shown in Fig. 2. As can be seen, the curve 1 fits well the black circles and the curve 2 fits well the open ones. Thus, the doublet structure of the Bragg reflection peak in the multiple diffraction spectral range and the additional extinction band in transmission are formed by different mechanisms of diffraction, which can be qualitatively described in the "empty" lattice approximation by two different Bragg-type formulae (1) and (2). This result is highly non-trivial and shows that in spite of the cubic symmetry of opaline PhCs their optical properties exhibit strong anisotropy even though their face-centered cubic crystal lattice is structurally perfect.

Experimental observation of the three-fold axial symmetry in the transmission spectra is difficult due to the presence of crystal lattice twinning and domain structure with a different orientation of domains. Therefore the actual experimental transmission spectrum is registered as an average of two spectra for the Γ-L-K and Γ-L-U incidence directions. To separate these spectra, it is appropriate to use the spectroscopy of single domains [4], which allows one to observe azimuthal anisotropy experimentally.

Acknowledgements

This work was supported in part by the St Petersburg State University Development Program (Research No. 11.37.23.2011).

References

[1] H. M. van Driel and W. L. Vos, *Phys. Rev. B* **62**, 9872 (2000).
[2] V. G. Fedotov *et al*., *Phys. Status Solidi B* **248**, 2175 (2011).
[3] A. G. Bazhenova *et al*., *Phys. Solid State* **49**, 2109 (2007).
[4] L. C. Andreani *et al*., *Phys. Rev. B* **78**, 205304 (2008).

20th Int. Symp. "Nanostructures: Physics and Technology"
Nizhny Novgorod, Russia, June 24–30, 2012

Sintering effects in photonic crystals: simulation of opal-like structure form factors

V. G. Fedotov[1] and A. V. Sel'kin[2,1]

[1] Faculty of Physics, St Petersburg State University, St Petersburg, Russia
[2] Ioffe Physical-Technical Institute, St Petersburg, Russia

Abstract. The sintering effect of structural elements in an opal-like photonic crystal on the spatial Fourier components of the dielectric function is analyzed and a criterion for the use of the analytical Rayleigh–Gans formulae is ascertained.

Introduction

The structure of real self-assembled opal-like photonic crystals (PhCs) is not the ideal close-packed one possessing the face-centered cubic (fcc) crystal lattice. First of all, there exist sintering of spherical particles and deformation of the structure along the direction of sedimentation, which leads to a decrease in the lattice symmetry from O_h to D_{3d}. In this paper, we study how sintering of the structural elements of an opal-like PhC influences their optical reflection spectra. Spatial Fourier components of the dielectric function are computed and a criterion for the use of the analytical Rayleigh–Gans formulae is considered.

1. Theoretical model

The effects of anisotropy of the opal crystal lattice and the sintering effects of spherical particles forming a PhC can be described [1] by two parameters: the coefficient of isotropic sintering $\chi = 1 - a_{00}/D_\perp$ and the coefficient of uniaxial compression $\eta = D_\parallel/D_\perp$, where a_{00} is the distance between the neighboring particles constituting PhC structure in the lateral plane, $D_\perp$ is the diameter of the particles in the lateral plane, and $D_\parallel$ is their size in the [111] direction.

Dielectric function of the two-component PhC media could be written as:

$$\varepsilon(\mathbf{r}) = (\varepsilon_a - \varepsilon_b)\, f(\mathbf{r}) + \varepsilon_b\,, \tag{1}$$

where $f(\mathbf{r})$ is filling function of the PhC structure ($f(\mathbf{r}) = 1$ inside the spheres and $f(\mathbf{r}) = 0$ inside the pores), and ε_a and ε_b are the permittivities of the spheres and pores, respectively. The periodicity of the filling function allows one to decompose it into a Fourier series in the reciprocal lattice vectors,

$$f(\mathbf{r}) = \sum_{\mathbf{G}} f_{\mathbf{G}} e^{i\mathbf{G}\times\mathbf{r}}\,, \tag{2}$$

where $f_{\mathbf{G}}$ are the modulation coefficients of the filling function called also the form factors. These coefficients could be found by inverse Fourier transform of $f(\mathbf{r})$ function,

$$f_{\mathbf{G}} = \frac{1}{V_{\mathrm{WS}}} \int_{\mathrm{WS}} f(\mathbf{r}) e^{-i\mathbf{G}\times\mathbf{r}} \mathbf{dr}\,, \tag{3}$$

where $V_{\mathrm{WS}} = a_{00}^3/\sqrt{2}$ is the volume of the Wigner–Seitz cell (for the fcc lattice it is of the same form as the first Brillouin zone of the body-centered cubic lattice). In this case, the Fourier coefficients $\varepsilon_{\mathbf{G}}$ of permittivity $\varepsilon(\mathbf{r})$ decomposition in the reciprocal lattice vectors are expressed in the terms of form factors as:

$$\varepsilon_{\mathbf{G}} = (\varepsilon_a - \varepsilon_b)\, f_{\mathbf{G}} + \varepsilon_b \delta_{\mathbf{G},0}\,, \tag{4}$$

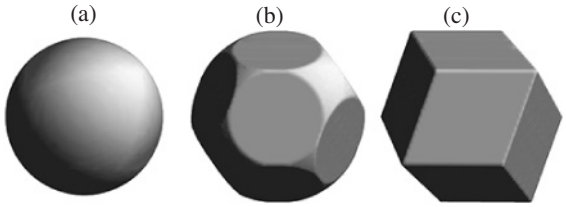

Fig. 1. The volume within which the integration is performed when calculating the form factors of opal-like structure for the case of $\chi = 0$ (a), $\chi = 0.135$ (b), $\chi > 0.24$ (c).

where $\delta_{\mathbf{G},0} = 0$ for $\mathbf{G} \neq 0$ and $\delta_{\mathbf{G},0} = 1$ for $\mathbf{G} = 0$.

In the case of the ideal PhC structure with the fcc lattice (without anisotropic compression, $\eta = 1$) consisting of point-contacted spheres ($\chi = 0$), the Rayleigh–Gans formula can be used [2] to determine the coefficients $f_{\mathbf{G}}$:

$$f_{\mathbf{G}} = \frac{3 f_{00}}{(\mathrm{GR})^3} \left[\sin(\mathrm{GR}) - \mathrm{GR}\cos(\mathrm{GR})\right]\,, \tag{5}$$

where $f_{00} = \pi/3\sqrt{2} \approx 0.74$ is the filling volume fraction of the point-contacted spheres in PhC, G is the length of the reciprocal lattice vector, $R = a_{00}/2$ is the radius of the sphere.

In the case of non-ideal structure there exists no simple analytical expression for the modulation coefficients of the permittivity, therefore one needs to use numerical methods for their calculation. In view of the fact that the filling function is a unity within the spherical particles forming PhC, and is zero outside them, we see that the integration should be carried out over the area occupied by the spheroid S_R in the Wigner–Seitz cell:

$$f_{\mathbf{G}} = \frac{1}{V_{\mathrm{WS}}} \int_{WS \cap S_R} e^{-i\mathbf{G}\times\mathbf{r}} \mathbf{dr}\,. \tag{6}$$

Calculation of the integral was performed numerically using the Monte Carlo method:

$$\int_V e^{-i\mathbf{G}\times\mathbf{r}} \mathbf{dr} = \frac{1}{N} \sum_{i=1}^{N} e^{-i\mathbf{G}\times\mathbf{r}_i}, \mathbf{r}_i \in V\,, \tag{7}$$

where N is the number of trials in the Monte Carlo procedure.

2. Results and discussion

In the absence of sintering ($\chi = 0$) the integration volume is a sphere (Fig. 1a), the integral can be computed analytically, and the result will be the Rayleigh–Gans formula. In the case of non-zero sintering, the integration volume is resulted from cross-section of the sphere by the rhombic dodecahedron and has a complicated shape (Fig. 1b). Finally, for sufficiently large

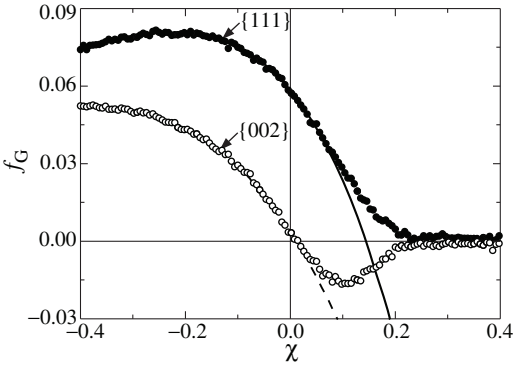

Fig. 2. The filling function modulation coefficients of an opal-like structure depending on the sintering χ for the families of the crystal planes (111) (black circles, solid line) and (002) (open circles, dashed line). Symbols are numerical calculation using the Monte Carlo method. Curves are analytical calculation using the modified Rayleigh–Gans formula.

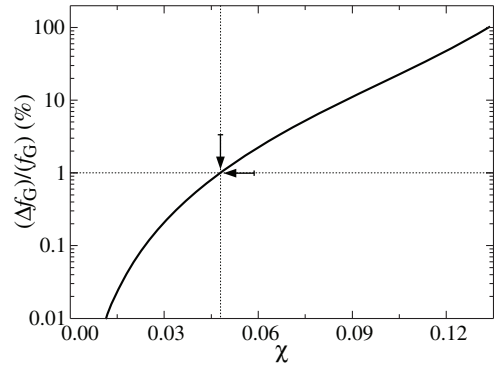

Fig. 3. The relative error as a function of the sintering coefficient χ for the (111) family of crystal planes when calculating the filling function modulation coefficients of an opal-like structure using the modified Rayleigh–Gans formula as compared with exact numerical calculation.

sintering ($\chi > 0.24$), the integration volume is a rhombic dodecahedron (Fig. 1c), that is the Wigner–Seitz cell itself. In this case, the filling factor is a unity and the permittivity modulation coefficients are zeros for all reciprocal lattice vectors.

Choosing the reciprocal lattice vector $\mathbf{G}_{000}$ we obtain the filling factor of the structure under consideration. In the case of negative values of sintering when the distance between the centers of the spheres is greater than their radiuses the value of the filling factor can be calculated analytically. Actually, to ensure the stability of the structure, the particles forming it must be connected by thin bridges.

The results of calculation of form factors for the two systems of crystal planes (111) and (002) are shown in Fig. 2. It is obvious that for the systems of planes from the same family, i.e., $(\pm 1 \pm 1 \pm 1)$ for (111) and (± 200), (0 ± 20), (00 ± 2) for (002), the result must be exactly the same because the corresponding directions are symmetrically equivalent. As can be seen from Fig. 2, at small values of the sintering coefficient, the form factor for the family of planes (002) is much smaller than that for the (111) family, which gives much weaker diffraction of light from the (002) planes compared to the diffraction from the (111) planes.

Taking into consideration that the distance between neighboring particles in the lateral plane and the PhC structure filling

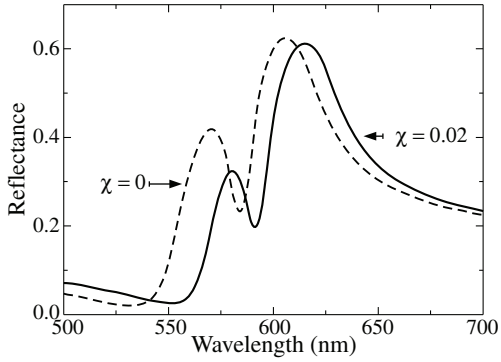

Fig. 4. Calculated Bragg reflection spectra of a semi-infinite opal-like photonic crystal without sintering ($\chi = 0$) (dashed curve) and with sintering ($\chi = 0.02$) (solid curve). The distance between the neighboring spherical particles of the structure in the lateral plane is $a_{00} = 300$ nm, the incidence angle is $\theta = 57^\circ$, the imaginary part of the average permittivity is $\varepsilon_0'' = 0.05$.

factor depend definitely on the sintering, we obtain a modified Rayleigh–Gans formula with the effective R value, $R = a_{00}/(2(1-\chi))$, which can be used to calculate form factors in the presence of sintering. Fig. 2 shows that the corresponding formula accurately describes the dependence of the form factor on the negative values of the sintering coefficient. It can be seen from the comparison of the modulation coefficients computed by the Monte Carlo method and analytically calculated with the modified Rayleigh–Gans formula (Fig. 2) that for small values of the sintering coefficient the modified Rayleigh–Gans formula can also be used practically. It describes accurately the dependence of the modulation coefficient on sintering in the case of positive values of the sintering coefficient.

A detailed comparison (Fig. 3) shows that for the values of the sintering coefficient, not exceeding 0.048, the relative error, when using the modified Rayleigh–Gans formula, does not exceed 1%. Thus, we can infer the applicability of this formula in calculating the modulation coefficients for the case of weak sintering of the spherical particles forming the PhC.

The Bragg reflection spectra for the typical value of the sintering coefficient, $\chi = 0.02$, are calculated with the dynamical multiple diffraction theory generalized to the case of high dielectric contrast in a 3D spatially periodic medium [3]. The spectra calculated show that even a small value of the χ leads to a noticeable change in the reflection spectra (Fig. 4). So, we can conclude that the effect of sintering strongly influences the optical parameters of PhCs and it is necessary to consider it in order to describe correctly the reflection spectra.

Acknowledgements

This work was supported in part by the St Petersburg State University Development Program (Research No. 11.37.23.2011) and by the Russian Academy of Sciences Program "Fundamental Problems of Photonics and Physics of New Optical Materials".

References

[1] A. G. Bazhenova *et al.*, *Phys. Solid State* **49**, 2109 (2007).
[2] D. M. Mittleman *et al.*, *J. Chem. Phys.* **111**, 345 (1999).
[3] V. G. Fedotov *et al.*, *Phys. Status Solidi B* **248**, 2175 (2011).

20th Int. Symp. "Nanostructures: Physics and Technology"
Nizhny Novgorod, Russia, June 24–30, 2012

Luminescence properties of the silicon-iron disilicide nanocomposites and mesa diode structures on their basis

N. G. Galkin[1,3], *E. A. Chusovitin*[1], D. L. Goroshko[1,3], T. S. Shamirzaev[2] and K. S. Zhuravlev[2]

[1] Institute for Automation and Control Processes, FEB RAS, Vladivostok, Russia
[2] A.V. Rzhanov Institute of Semiconductor Physics, SB RAS, Lavrentieva 13, 630090 Novosibirsk, Russia
[3] Far Eastern State University, 690000 Vladivostok, Russia

Abstract. Monocrystalline *p*-type conductivity silicon films with embedded multilayers (up to 10) of iron disilicide nanocrystals are grown on the *n*-type silicon substrates with (111) and (100) orientation by means of reactive deposition, solid phase, and molecular-beam epitaxy. Mesa diodes fabricated from such structures have shown intense electroluminescence in the range of 0.8−1.04 eV under forward and reverse biases.

Introduction

Until recently, light-emitting silicon structures were generally formed by erbium ion implantation [1] or by binary silicide synthesis: in the most cases it was semiconducting iron disilicide (β-$FeSi_2$) [2]. At the same time, ion implantation and molecular-beam epitaxy (MBE) were applied, together with a long-time and high-temperature annealing, to obtain the silicon layer with embedded sphere-shaped β-$FeSi_2$ precipitates with size 100–150 nm [3]. Nowadays there were developed the bases of the technology which provides a silicon layer formation with embedded semiconducting silicide nanocrystals (NC's) [4–6]. Silicon with NC multilayers or uniform distributed NC's inside is brand new composite whose optical and electrical properties largely depend on embedded NC's density, their size, and the distance between NC's in the nanocomposite layer. Introducing different semiconducting silicide NC's with size 5–30 nm in silicon lattice, one may expect the increasing of the radiative recombination efficiency and broadening of the *p-n* junction spectral sensitivity region.

1. Experimental

The growth conditions of β-$FeSi_2$ islands have been discussed in [6]. The iron disilicide NC's in the silicon heterostructures were formed by two methods: (i) solid phase epitaxy (SPE) at 630 °C; (ii) a combination of reactive deposition epitaxy (RDE) at 375 °C with SPE at 475 °C. Multilayer samples with embedded NC's (see Table 1) were formed by exact repeating the first growth step: β-$FeSi_2$ island formation followed by 100 nm-thick silicon layer deposition. Surface morphology of all the samples was investigated by means of scanning probe microscope Solver P47. Photoluminescence (PL) spectra were measured at temperature 5–150 K using a facility incorporating a double monochromator, the Ge-photodiode "Edinburg Instruments", a helium cryostat, and pumping laser YAG:Nd ($\lambda = 532$ nm, $P = 20$ mW). For studying electroluminescence (EL) properties of the silicon heterostructures with embedded β-$FeSi_2$ NC layers, there was fabricated a set of 8 mesa diodes by deposition of Al contacts on the both sides of the heterostructures with subsequent annealing at 470 °C for about 20 minutes. The face contact area was in the range of 1–7 mm^2. To measure EL a direct current supply was used.

2. Results and discussions

By LEED data, silicon capping layer have grown epitaxially over the iron disilicide nanoislands and the surface of the formed nanocomposite layer has a low root-mean square roughness (RMS) (0.2–1.8 nm, samples A, C, D, F, G) for all the samples with initial iron layer thickness no more than 0.4 nm (Table 1) which doesn't depend on the method of β-$FeSi_2$ NC's formation. The increase of the iron layer thickness up to 0.8 nm, as well as the change of the substrate orientation from (100) to (111), leads to the growth of the surface layer roughness (Table 1). In the case of 10 layer sample H the roughness wasn't high (0.2 nm) since the thickness of the 10-th layer was 300 nm which 3 times higher than for other samples. According to high-resolution transmission electron microscopy (HR-TEM) of the grown samples cross-sections, β-$FeSi_2$ NC's [6–8] with size 5–40 nm elastically compressed and their lattice constant reduced by 1.0–2.5% compared to bulk β-$FeSi_2$.

Luminescence properties of all the samples were studded in two modes: photoluminescence (Fig. 1a,b), and electroluminescence (Fig. 2a,b). The PL signal intensity of the samples grown by method (i) decreases according to the following consequence: A, C, D, E, B (Fig. 1a). The maximum PL signal was observed for sample A which has moderate number of layers — 4 and the initial Fe thickness — 0.2 nm. With the increase of the initial Fe coverage PL signal decreases (samples B and E). The shape of the PL spectra in the vicinity of 0.8 eV allows one to assume that a rapid PL signal reducing is observed due to a high density of point defects. There is

Table 1. Parameters of the samples.

Sample	Substrate	β-$FeSi_2$, growth method	Number of layers	Initial Fe coverage (nm)	Capping Si layer roughness (nm)
A	n-Si(100)	(i)	4	0.2	1.78
B	n-Si(100)	(i)	8	0.4	10.84
C	n-Si(100)	(i)	8	0.1	0.73
D	n-Si(111)	(i)	4	0.4	0.32
E	n-Si(111)	(i)	4	0.8	5.72
F	n-Si(100)	(ii)	8	0.2	0.19
G	n-Si(100)	(ii)	8	0.4	0.39
H	n-Si(100)	(ii)	10	0.8	0.2

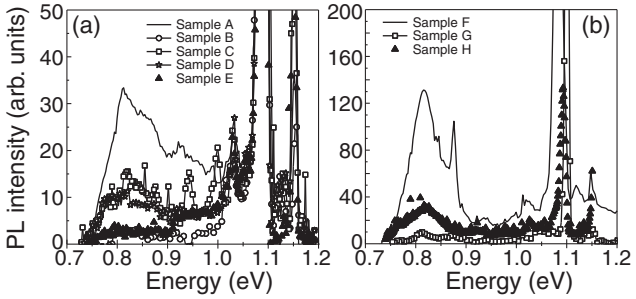

Fig. 1. Photoluminescence spectra registered at 5 K for samples grown using method (i) — a and (ii) — b.

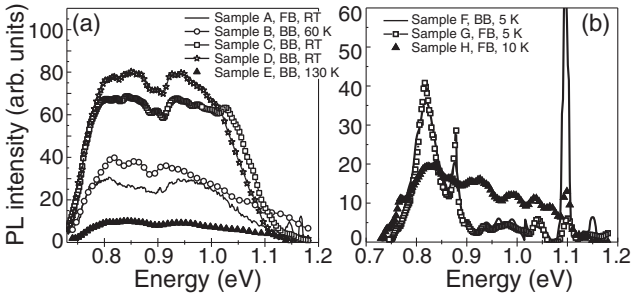

Fig. 2. Electroluminescence spectra for all the grown samples obtained at forward (FB) and reverse (BB) bias. Abbreviation 'RT' in the figures legends denotes — room temperature.

no distinct dislocation PL signal on the spectra of the samples grown by method (i) [3], which supports low density of linear defects in the samples. On the contrary, an intense PL signal form samples F, G, and H, grown by method (ii) [6], contain a significant contribution from the dislocation PL (Fig. 1b) as it was shown in the work [3].

The EL signal from fabricated mesa diodes has been observed up to room temperature (Fig. 2a,b) at significantly low current density — 0.2−17 A/cm^2, for instance in the works [9,10] corresponding current density was up to 85 A/cm^2. The maximum intensity of the EL has been shown by samples C and D with initial Fe coverage 0.4 and 0.1 nm respectively and moderate RMS (Table 1), which corresponds to insignificant point defect concentration. Taking into account the current densities in the mesa diodes which were used to get EL signal, the most efficient EL has sample D (Fig. 2a) with the total amount of Fe 1.6 nm. On the EL spectra of samples A–E fabricated by method (i) (Fig. 2a), a broad band with two peaks of close intensity located in the range of 0.78–0.82 eV and 0.93–0.96 eV has been observed. The main feature of the produced mesa diodes is the EL signal observing both under forward and reverse bias in a wide temperature range (5–300 K). A broad low-energy peak at 0.78–0.82 eV may be a superposition of EL contributions from the embedded β-$FeSi_2$ NC's and dislocations which were found on the TEM images of sample D. An EL signal at 0.83–1.04 eV cannot be assign only to the radiative recombination of an electrons and holes near the dislocations, since the latter characterized by quite narrow peaks [3], so the nature of EL remains undiscovered. Thus, the growth of β-$FeSi_2$ NC's by SPE method results in broadening of the EL region both under forward and reverse bias regardless of the initial Fe coverage. Mesa diodes which have been grown using growth method (ii) with low initial iron thickness (0.2–0.4 nm, see Table 1) have sharp peaks at 0.88, 0.98, and 1.04 eV (Fig. 2b) and broadened peak at 0.82 eV which is in line with EL of dislocations D1–D4 [3] and weak contribution from β-$FeSi_2$ at 0.78–0.80 eV. EL signal in the range of 0.93–0.96 eV for these mesa diodes is not detected. At the forward bias a weak peak at 1.09 eV is detected for each sample which is associated with exciton recombination in silicon [3]. The shape of EL spectrum is changing with increasing of iron coverage in a layer up to 0.8 nm (sample H, Table 1) because of increased contribution from β-$FeSi_2$ and decreased dislocation contribution. Therefore growth method (ii) leads to the increasing of dislocation contribution in the EL for the multilayer samples having low iron coverage (0.2–0.4 nm), while a higher iron coverage results in increasing of the contribution from β-$FeSi_2$; the EL intensity of mesa diodes remains significant compared with exciton radiation.

Let us consider the reasons of 0.78–0.82 eV EL signal appearance at reverse and forward bias. At the reverse bias minority carriers (electrons) move through NC's layer to the *p-n* junction and a part of the electrons radiatively recombine with the holes in the β-$FeSi_2$ nanocrystals located in the *p*-type silicon. At the forward bias electrons flow from the *n*-type electrode through the *p-n* junction to the region with iron disilicide nanocrystals where a part of electrons radiatively recombine with holes in the β-$FeSi_2$ nanocrystals giving rise to the EL.

According to the current-voltage data, the significant EL signal is registered only at the high voltage, when the avalanche breakdown regime takes place, which is a governing condition in EL mechanism. At the reverse bias the center of this breakdown is located in the *p-n* junction region. Broadening of the silicon/β-$FeSi_2$ heterojunction at the reverse bias and formation of an avalanche breakdown is possible. A probable reason of the electroluminescence in the energy range 0.83–1.04 eV could be microplasma radiation which exists in the region of avalanche breakdown near β-$FeSi_2$ nanocrystals both at forward and reverse biases. The same luminescence with a similar spectral composition was registered in the *p-n* junction based on the multi-crystal silicon [11].

Acknowledgements

The work was done under financial support from RFBR (grant No. 11-02-12075-ofi_m) and Russia Federation President (grant No. MK-3007.2011.8).

References

[1] V. P. Kuznetsov *et al*., *Semiconductors* **44**, 385 (2010).
[2] V. E. Borisenko (Eds.), *Semiconducting Silicides*, Berlin: Springer-Verlag, 2000, p.106.
[3] K. Oyoshi *et al*., *Thin Solid Films* **381**, 202 (2001).
[4] N. G. Galkin *et al*., *Thin Solid Films* **515**, 8179 (2007).
[5] N. G. Galkin *et al*., *Rare Metals (Spec. Issue.)* **28**, 585 (2009).
[6] N. G. Galkin *et al*., *Thin Solid Films* **519**, 8480 (2011).
[7] N. G. Galkin *et al*., *Thin Solid Films* **515**, 7805 (2007).
[8] N. G. Galkin *et al*., *J. Nanoscience and Nanotechnology* **8**, 527 (2008).
[9] C. Li *et al*., *Jap. J. Appl. Phys.* **43**, L1492 (2004).
[10] T. Sunohara *et al*., *Thin Solid Films* **508**, 371 (2006).
[11] U. N. Duzhikov *et al*., *Proc. of VII International Conference "Solid State Chemistry and Modern Micro- and nanotechnologies"*, Kislovodsk, Stavropol, SevKavGTU, 2007, 510 p. (printed in Russian).

20th Int. Symp. "Nanostructures: Physics and Technology"
Nizhny Novgorod, Russia, June 24–30, 2012

Optical sensor systems based on nanostructured films of natural polymers for control of gas parameters of environment

S. S. Voznesenskiy[1], A. A. Sergeev[1], Yu. N. Kulchin[1], S. Y. Bratskaya[2], A. Y. Mironenko[2] and M. A. Demchenkov[1]

[1] Institute for Automation and Control Processes FEB RAS, Vladivostok, Russia
[2] Institute of Chemistry FEB RAS, Vladivostok, Russia

Abstract. Optical and waveguide properties of single and multilayer chitosan films of different ionic forms as well as their mutual correlation were investigated. It was shown that single layer waveguide structures are allow to determine the relative humidity value in a wide range. The use of multilayer nanostructured polimer coatings allow one to create sensing layer of optical chemical sensors.

Introduction

The given work is devoted researches of natural polymeric materials, as bases for creation of optical sensor systems for control of gas parameters of environment. Advantages of the optically transparent natural polymers are in their prominent optical and mechanical features as well as in biocompatibility [1]. The natural polysaccharide chitosan has been chosen as object of researches as it possesses good sorption properties and capability to fabrication optically transparent films in a visible wavelenght range [2]. Among different methods to fabricate sensor system, the evanescent wave sensing methods are mostly used to determine the concentrations of chemical agents in environment [3]. Generally, the design of the sensor can be configured as the system where a chemical sensitive layer, comprising chemical reagents in suitable matrices, is deposited onto the optical waveguide.

The relative humidity level or concentration of chemical agent variations leads to a changing of refractive index and/or optical absorption of sensing layer's material and modulating the light propagating through the waveguide [4]. Chitosan is the one of the swelling polymers so it has a refractive index changes in accordance with the humidity. The latter phenomenon has been employed in the design and development of optical absorption sensor for relative humidity monitoring with a waveguide as a sensitive layer.

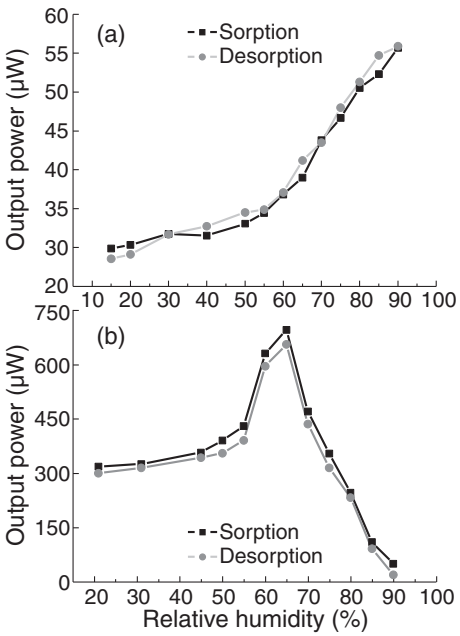

Fig. 1. Variation of output power with relative humidity; a) chitosan acetate, b) chitosan citrate.

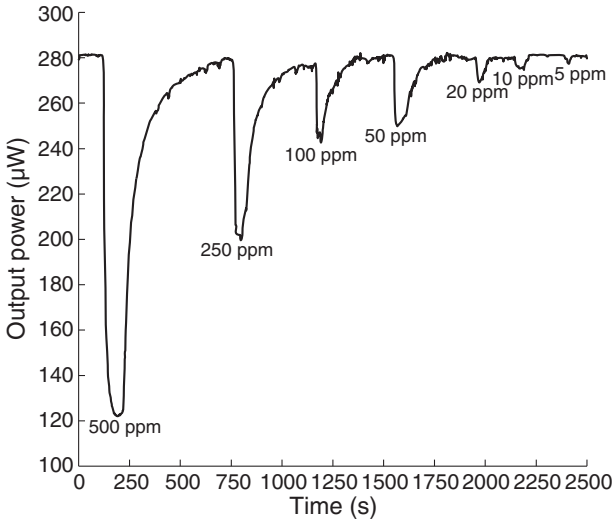

Fig. 2. Response of the ammonia sensor with 12-bilayers to ammonia changing between the 5–500 ppm.

1. Experimental

The chitosan solution was prepared by dissolving 1–5% (w/v) chitosan (molecular weight 500 kDa, deacetylation degree (DD) 80.5%) in aqueous solutions of acetic or citric acid at doubled molar ratio. Polymer solvent was distributed uniformly along the substrate rotating at 500–4000 rpm speed (the speed was changed according to a film thickness required). Waveguide and optical properties of obtained chitosan films were investigated by using a leakproof chamber with the controlled relative humidity level and chemical agents concentration.

2. Results and discussion

The measured refractive index of acetate and citrate films using spectral ellipsometry method is equal $n_A = 1.536$ and $n_C = 1.533$ respectively (humidity level equals to 20%). Once the humidity rises up to 95%, the films refractive index decrease to $n_A = 0.04$ and $n_C = 0.145$ respectively. As consequence acetate and citrate films demonstrates a stable optical response

to changing of relative humidity level (Fig. 1).

For development a chemical sensing system we were used a method based on formation of nanoscaled multilayered polymer coatings containing sensitive reagents on the surface of waveguides. The main advantage of this type of sensors is the possibility to obtain thin polymer films by electrostatic self-assembly at the surfaces of waveguide with precise control of thickness and sensitive reagents content that provides high reproducibility of the sensors. The lambda-carrageenan was used as the anionic component, and as the cationic component was chitosan. This multilayered system also includes a bromothymol blue dye which changes color from yellow to blue in the presence of ammonia. It was discovered that system's sensing features depend upon the thickness of sensing layer. A detection limit of 1–500 ppm of ammonia has been realized.

The obtained results allow one to consider nanostructured optical sensor systems based on ionic forms of chitosan as perspective material with optical properties that can be modified by change of the environment relative humidity. Also described systems offer great promise for the purposes of integrated optical chemical sensors development.

References

[1] K. G. Skryabin *et al*., *Chitin and Chitosan: Preparation, Properties, Applications.*, Moscow: Nauka (2002).
[2] H. Jiang *et al*., *J. Appl. Polym. Sci.* **61**, 7 (1996).
[3] P. V. Lambeck, *Meas. Sci. Technol.* **17**, (2006).
[4] G. Pandraud *et al*., *Sens. & Act.* **85**, (2000).

20th Int. Symp. "Nanostructures: Physics and Technology"
Nizhny Novgorod, Russia, June 24–30, 2012

A new type of superconducting quantum interference device

V. N. Antonov[1], V. L. Gurtovoi[2], *A. V. Nikulov*[2], R. Shaikhaidarov[1] and V. A. Tulin[2]

[1] Physics Department, Royal Holloway University of London, Egham, Surrey TW20 0EX, UK
[2] Institute of Microelectronics Technology, RAS, 142432 Chernogolovka, Moscow region, Russia

Abstract. System with weak phase coherence in two points between two superconducting contours is investigated experimentally. Quantum theory predicts jump between maximum and minimum values of the supercurrent through this superconducting differential double contour interferometer when the quantum number describing angular momentum of superconducting pairs changes in one of the contours. We observed jumps in voltage and in current-voltage characteristics which may corroborate this prediction. The phenomenon observed in our work may be used for construction of a new type of Superconducting Quantum Interference Device (SQUID) which may be superior to the conventional SQUID in measurements of weak magnetic flux and field.

Introduction

The observation on the level of nanostructures some quantum phenomena discovered on the atomic level provide us with ample opportunity of detailed investigations and possible application. One of these phenomena is the Bohr's quantization of the angular momentum $pr = (mv + qA)r = n\hbar$. The energy difference between permitted states of single electron $E_{n+1} - E_n = mv_{n+1}^2/2 - mv_n^2/2 = (2n+1)\hbar^2/2mr^2$ in a ring is much smaller than in atom because its realistic radius $r \approx 500$ nm is much larger than the Bohr radius $r_B \approx 0.05$ nm. But the discreteness of the energy spectrum of real superconducting contour with a section s, pairs density n_s and length l

$$E_n = \oint_l dl s n_s \frac{mv_n^2}{2} = I_{p,A}\Phi_0\left(n - \frac{\Phi}{\Phi_0}\right)^2 \qquad (1)$$

may be strong as well as in atom because of the same quantum number n of all $N_s = sln_s$ pairs [1]. Here $\Phi_0 = 2\pi\hbar/2e \approx 2.07 \times 10^{-15}$ Tm^2 is the flux quantum; $I_{p,A}$ is the amplitude of the persistent current [2]

$$I_p = I_{p,A} 2\left(n - \frac{\Phi}{\Phi_0}\right). \qquad (1a)$$

The energy difference $E_{n+1} - E_n \approx I_{p,A}\Phi_0$ corresponds to temperature $I_{p,A}\Phi_0/k_B \approx 15000$ K at typical value $I_{p,A} = 100$ μA [2]. Thanks to macroscopic area $S \gg \pi r_B^2$ of the real contour it is possible to observe the change of the quantum number n in magnetic field $B = \Phi/S$ [3]. We fabricate asymmetric rings to investigate paradoxical features of quantization phenomena [3–6]. Nanotechnology allows also to make the structure, considered in [7] and shown on Fig. 1, which has weak phase coherence between the wave functions describing superconducting state of two contours. We will present some results of investigation of such structure.

1. Structure and measurements

The structure was fabricated by e-beam lithography to form suspended resist mask and double angle shadow evaporation of aluminum (30 and 35 nm) with intermediate first aluminum layer oxidation. This technology allows to make two independent superconducting square contours weakly connected by two Josephson junctions in the two points J_1 and J_2, Fig. 1. The contours are shifted relative to one another and there are two extra Josephson junctions J_{t1} and J_{t2} because of this technology. Square side is $a \approx 4$ μm while its width is $w \approx 0.4$ μm.

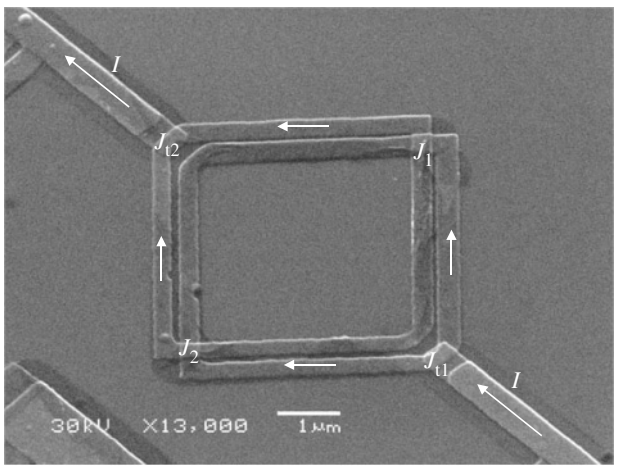

Fig. 1. Investigated aluminum structure consisting of two square contours with the side of $a \approx 4$ μm and line with of $w \approx 0.4$ μm. The external current I passes through the Josephson junctions J_1 and J_2 of the superconducting differential double contour interferometer and the extra Josephson junctions J_{t1} and J_{t2}.

The supercurrent I_s through each Josephson junction is related to the gauge-invariant phase difference $\Delta\varphi$ between the phases of the two superconductors by the current-phase relationship $I_s = I_c \sin\Delta\varphi$. The phase difference on the J_1 and J_2 Josephson junctions should be connected $\Delta\varphi_1 - \Delta\varphi_2 = n_I 2\pi - \pi(1 - a_{sh}/a)(n_u + n_d) + (a_{sh}/a)2\pi\Phi/\Phi_0$ because of the relation

$$\oint_l dl \bigtriangledown \varphi = \oint_l dlp/\hbar = m\oint_l dlv/\hbar + 2\pi\Phi/\Phi_0 = n2\pi \qquad (2)$$

for the phase of the wave function in each contour. Where n_u, n_d and n_I are the quantum numbers describing the phase change along each square contours and along the contour where the external current I can flow, Fig. 1; $a_{sh} \approx 1.1w$ is the technological shift of the contour, Fig. 1. The total supercurrent through the J_1 and J_2 Josephson junctions $I_s = I_{c1}\sin\Delta\varphi_1 + I_{c2}\sin\Delta\varphi_2$ should not depend on the number n_I (because of the relation $\sin(\Delta\varphi + n2\pi) \equiv \sin\Delta\varphi$) and depends on the sum $n_s = n_u + n_d$

$$I_s = I_{c1}\sin\Delta\varphi_1 + I_{c2}\sin\left(\Delta\varphi_1 + \pi(1+s)n_s + s2\pi\frac{\Phi}{\Phi_0}\right). \qquad (3)$$

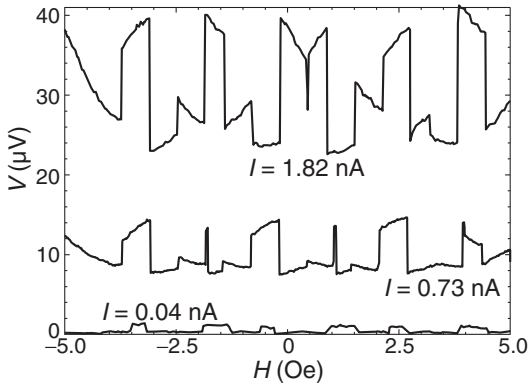

Fig. 2. Voltage jumps due to changes of quantum numbers in magnetic field at different bias currents through the structure $I \approx 0.04, 0.73, 1.82$ nA observed at the temperature $T \approx 0.75 < T_c \approx 1.3$ K.

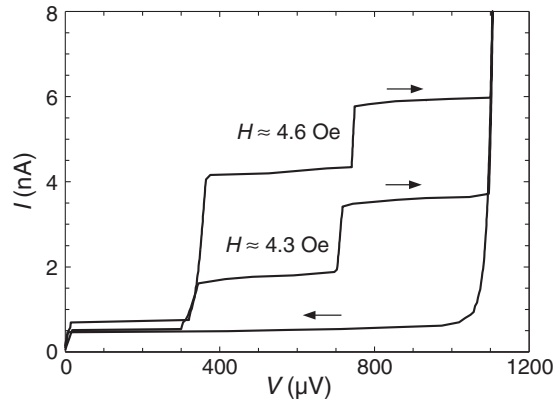

Fig. 3. Current-voltage characteristics of the superconducting differential double contour interferometer measured at the temperature $T \approx 0.44$ K and different magnetic field $H \approx 4.3$ Oe and $H \approx 4.6$ Oe corresponding to the magnetic flux inside each contour $\Phi \approx 3.5\Phi_0$ and $\Phi \approx 3.7\Phi_0$. The arrows indicate the directions of the current sweep. The current difference between positive and negative directions is supercurrent of Cooper pairs through the Josephson junctions.

The maximum value of the supercurrent

$$I_s = I_{c1} \sin \Delta\varphi_1 + I_{c2} \sin (\Delta\varphi_1 + \pi n_s) \qquad (3a)$$

could have only two values $I_{c1} + I_{c2}$ at $n_s = 2k$ and $|I_{c1} - I_{c2}|$ at $n_s = 2k + 1$ if the technological shift $a_{\rm sh}$ was absent $s = a_{\rm sh}/a = 0$. The change of the quantum number in one of the contours from $n_u + n_d = 2k$ to $n_u + n_d = 2k + 1$ should result in the jump of the supercurrent from $I_s = 2I_c$ to $I_s = 0$ (at $I_{c1} = I_{c2} = I_{c1}$) and the jump of the voltage, observed in [8], at an external current I.

Our measurements, Fig. 2, show that the jumps, higher than in [8], are observed even at $s = a_{\rm sh}/a \approx 0.1 \neq 0$. The current-voltage characteristics, Fig. 3, indicate that the supercurrent can change both in the Josephson junctions J_1, J_2 and the extra Josephson junctions J_{t1}, J_{t2}. The voltage, Fig. 2, and the current-voltage characteristics, Fig. 3, change by jump with the change of the quantum number of one of the contours, n_u or n_d. It takes place when the persistent current (1a) approaches to the critical value $I_p \approx I_{p,c}$ at $|n - \Phi/\Phi_0| \approx 2a/\pi\sqrt{3}\xi(T)$ because of the infinitesimality of external current $I \approx 1$ nA $\ll I_{p,c} \approx 1$ mA at our measurements.

2. Possible application

According to (1) the probability $P_n \propto \exp(-E_n/k_{\rm B}T)$ of the quantum number n near $\Phi \approx (n + 0.5)\Phi_0$ of the contour with $I_{p,A} \approx 100\,\mu$A [2] changes from $P_n \approx 0$ to $P_n \approx 1$ in very narrow interval of magnetic flux $\Delta\Phi \approx k_{\rm B}T/I_{p,A} \approx 0.0001\Phi_0$ at $T \approx 1$ K. The supercurrent of the conventional Superconducting Quantum Interference Device (SQUID) [9] change from $I_s \approx 2I_c$ to $I_s \approx 0$ in the interval $\Delta\Phi \approx 0.5\Phi_0$, see for example [10]. The change of the supercurrent of the superconducting differential double contour interferometer (DDCI), Fig. 1, with the quantum number n, corroborated by our measurements, means that DDCI can improve SQUID sensitivity $dV/d\Phi$ thanks to the change of the average value of the supercurrent from $I_s \approx 2I_c$ to $I_s \approx 0$ in much narrower interval of magnetic flux.

Acknowledgements

This work has been supported by a grant "Quantum bits based on micro- and nano-structures with metal conductivity" of the Program "Technology Basis of New Computing Methods", of the Department of Information Technologies and Computing Systems of RAS.

References

[1] A. V. Nikulov, *AIP Conference Proceedings*, Vol. **1101** *"Foundations of Probability and Physics-5"* pp. 134–143 (2009); arXiv: 0812.4118.

[2] V. L. Gurtovoi *et al*., *Zh. Eksp. Teor. Fiz.* **132**, 1320 (2007) (*JETP* **105**, 1157 (2007)).

[3] A.V. Burlakov, V.L. Gurtovoi, A.I. Ilin, A.V. Nikulov, V.A. Tulin, *in Proceedings of 19th International Symposium "Nanostructurec: Physics and Technology"* St Petersburg: Ioffe Institute, 2011 p. 128.

[4] A. A. Burlakov *et al*., *Pisma Zh.Eksp.Teor.Fiz.* **86**, 589 (2007) (*JETP Lett.* **86**, 517 (2007)); arXiv: 0805.1223.

[5] V. L. Gurtovoi *et al*., *Zh. Eksp. Teor. Fiz.* **132**, 297 (2007) (*JETP* **105**, 262 (2007)).

[6] V.L. Gurtovoi, M. Exarchos, R. Shaikhaidarov, V.N. Antonov, A.V. Nikulov, and V.A. Tulin, *in Proceedings of 17th International Symposium "Nanostructurec: Physics and Technology"* St Petersburg: Ioffe Institute, 2009 p. 89.

[7] A.V. Nikulov, *in Proceedings of 18th International Symposium "Nanostructurec: Physics and Technology"* St Petersburg: Ioffe Institute, 2010 p. 367.

[8] I. N. Zhilyaev, S. G.Boronin, A. V. Nikulov and K. Fossheim, *Quantum Computers and Computing* **2**, 49 (2001).

[9] A. Barone and G. Paterno, *Physics and Applications of the Josephson Effect*. Wiley-Interscience, New-York, 1982.

[10] H. Tanaka, Y. Sekine, S. Saito, H. Takayanagi, *Physica C* **368** 300 (2002).

20th Int. Symp. "Nanostructures: Physics and Technology"
Nizhny Novgorod, Russia, June 24–30, 2012

Magnonic logic devices: current status and perspectives

Alexander Khitun
Electrical Engineering Department, University of California Riverside, California, 92521 USA

Abstract. Modern logic circuits consist of a large number of transistors fabricated on a surface of a silicon wafer and interconnected by metallic wires. In the past sixty years, a straightforward approach to functional throughput enhancement was associated with the increase of the number of transistors, which is well known as the Moore's law. Decades of transistor-based circuitry perfection resulted in the Complementary Metal–Oxide–Semiconductor (CMOS) technology, which is the basis for the current semiconductor industry. Unfortunately, CMOS technology is close to the fundamental limits mainly due to the power dissipation problems. The latter stimulates a big deal of interest to the post-CMOS technologies able to overcome the current constrains. Magnonic logic circuits exploiting magnetization as a state variable and spin waves for information transmission and processing is one of the possible solutions. The utilization of waves for data transmission makes it possible to code logic 0 and 1 in the phase of the propagating wave, make use of waveguides as passive logic elements for phase modulation and exploit wave interference for achieving logic functionality. In this work, we review the recent progress in magnonic logic devices development and discuss the perspectives of this approach.

Introduction

Spin wave (magnons) as a physical phenomenon has attracted scientific interest for a long time [1]. Spin wave propagation has been studied in a variety of magnetic materials and nanostructures [2–4]. Relatively slow group velocity (more than two orders of magnitude slower than the speed of light) and high attenuation (more than six orders of magnitude higher attenuation than for photons in a standard optical fiber) are two well-known disadvantages, which explains the lack of interest to spin waves as a potential candidate for information transmission. The situation has changed drastically as the characteristic distance between the devices on chip entered the deep-submicron range. It became more important to have fast signal conversion/modulation, while the short traveling distance compensates slow propagation and high attenuation. From this point of view, spin waves possess certain technological advantages: (i) spin waves can be guided in the magnetic waveguides similar to the optical fibers; (ii) spin wave signal can be converted into a voltage via the inductive coupling; (iii) magnetic field can be used as an external parameter for sin wave signal modulation. The wavelength of the exchange spin waves can be as short as several nanometers, and the coherence length may exceed tens of microns at room temperature. The later translates in the intrigue possibility to build scalable logic devices utilizing spin wave interference.

1. Magnonic logic circuits — principle of operation

The general idea of using spin wave based logic circuit is to exploit wave phenomena such as interference and superposition, which may provide an advantage over the existing CMOS-based circuitry. At the same time, the proposed spin wave devices must be compatible with conventional electron-based devices enabling efficient data exchange. In Fig. 1, it is schematically shown an integrated magneto-electric circuit combining conventional electronic and magnonic parts. The input data are received form the electronic circuit in the form of voltage pulses ad converted into spin waves. Being excited, spin waves propagate through the structure, which consists of magnetic waveguides, interferometers, phase shifters and amplifiers. The data processing in the circuit is accomplished by manipulating the amplitudes or/and the phases of the propagating spin waves. Finally, the result of computation is converted back to a voltage signal and may be provided to the next electronic circuit. The magnetic circuit can be used for general computing (NOT, OR, AND gates) or as a complementary logic block (Magnetic Cellular Nonlinear Network) designed to perform special tasks such as image processing and speech recognition.

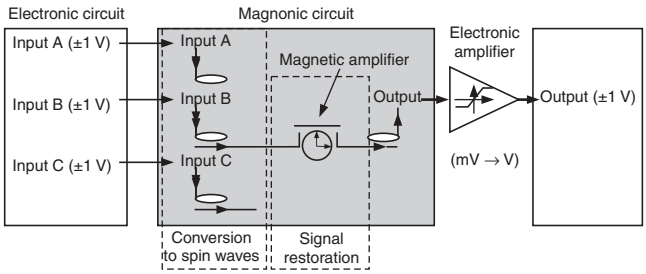

Fig. 1. Schematics of the integrated magneto-electric circuit. The input data are received form the electronic circuit in the form of voltage pulses and converted into spin waves. The data transmission within the magnonic circuit is accomplished via the spin waves only. The magnonic circuit consists of magnetic waveguides, interferometers, phase shifters, memory cells and amplifiers enabling spin wave amplitude/phase modulation. Finally, the result of computation is converted back to a voltage signal provided to the next electronic circuit.

2. Basic elements

There are several basic elements required for spin wave logic circuit construction: converters to translate electric signals into spin wave and vice versa; waveguide structure including combiners and splitters; a spin wave amplifier; a memory cell, which can be switched by a spin wave (e.g. multiferroic cell); and a phase modulator to provide a controllable phase shift to the propagating spin wave. In this section, we review possible approaches to the following devices and define most important parameters for application in logic circuits. Spin waves can be excited by the spin-polarized currents injected into a ferromagnetic film due to the transfer of the spin-angular momentum as was theoretically predicted by Slonczewski [5]. The interaction between spin waves and itinerant electrons is prominent near the interface between non-magnetic and ferromagnetic

layers. The amplitude of the excited spin waves grows exponentially as the current density through the interface exceeds a certain critical value. This phenomenon has been experimentally verified in Co/Cu multilayered structures showing high frequency 40-60GHz current-driven spin wave excitation [6]. Spin wave excitation by the spin-polarized electric current has certain technological advantages and shortcomings. On one hand, spin wave excitation via spin torque requires only point contacts with characteristic size of the order of tens of nanometers, which is in favor of scalable devices. The high-frequency operation is another advantage of the spin torque mechanisms. On the other hand, the overall energetic efficiency may not be high. The threshold current density required for spin wave excitation is higher than 10^6A/cm^2, which implies high operational power. At this moment, it is not clear how much percentage of the consumed power can be transferred into a specific spin wave mode.

Next element to be discussed is a magnonic waveguide. Though there have been an increasing number of experimental studies on spin wave propagation in nanometer-size structures during the past decade [2–4,7], the engineering of magnonic waveguides is mainly an unexplored area. The essential requirements for the waveguide structures in a logic circuit are to provide spin wave propagation with maximum group velocity and with minimum attenuation. The main questions are related to the proper choice of the magnetic material and the optimum waveguide structure. Yttrium-iron-garnet (YIG) and permalloy (NiFe) were used in the demonstrated prototypes [8,9]. Having the same order of magnitude maximum propagation speed, spin waves in non-conducting ferrites possess lower attenuation than in the metallic ferromagnets. On the other hand, the fabrication of a ferrite waveguide such as YIG requires a special Gadolinium Gallium Garnet (GGG) substrate. In contrast, a permalloy film can be deposited onto a silicon platform by using the sputtering technique [9]. The latter is in favor of using permalloy and other metallic ferromagnetic materials (e.g. CoFe, CoTaZr), which fabrication technique is compatible with silicon technology.

3. Discussion

There is a number of problems to be solved before magnonic logic devices will be able to compete with CMOS-based circuits. Some of the described spin wave components have not been experimentally demonstrated. The design of the existing prototypes have to be optimized and improved in order to increase energetic efficiency and scale down the device area. Currently, the most challenging problem is associated with the inductive cross talk between the input and the output ports. The strength of the direct coupling via stray field exceeds the spin wave signal by several times in micrometer scale devices [9]. At this point, it is clear that the use of microwave field for spin wave generation does not fit the scaling requirements. The conducting contours used in the laboratory experiments should be replaced by the point contact devices such as spin torque oscillators or multiferroic elements. Then, all components of the spin wave circuit have to be impedance-matched to provide maximum energetic efficiency and minimize losses. Without any doubt, the realization of the spin wave logic circuits would require a lot of efforts in the area of magnonics. Nevertheless, the advantages offering by the magnonic logic circuitry are significant to justify an extensive research.

References

[1] W. Schilz, *Philips Research Reports* **28**, (1973) 50.

[2] T. J. Silva, C. S. Lee, T. M. Crawford, and C. T. Rogers, *Journal of Applied Physics* **85**, (1999) 7849.

[3] M. Covington, T. M. Crawford, and G. J. Parker, *Physical Review Letters* **89**, (2002) 237202.

[4] M. Bailleul, D. Olligs, C. Fermon, and S. Demokritov, *Europhysics Letters* **56**, (2001) 741.

[5] J. C. Slonczewski, *Journal of Magnetism and Magnetic Materials* **159**, (1996) L1.

[6] M. Tsoi, A. G. M. Jansen, J. Bass, W. C. Chiang, V. Tsoi, and P. Wyder, *Nature* **406**, (2000) 46.

[7] V. E. Demidov, J. Jersch, K. Rott, P. Krzysteczko, G. Reiss, and S. O. Demokritov, *Physical Review Letters* **102**, (2009) 177207.

[8] M. P. Kostylev, A. A. Serga, T. Schneider, B. Leven, and B. Hillebrands, *Applied Physics Letters* **87**, (2005) 153501.

[9] A. Khitun, B. M., Y. Wu, J.-Y. Kim, A. Hong, A. Jacob, K. Galatsis, and K. L. Wang, *Mater. Res. Soc. Symp. Proceedings* **1067** (2008) B01.

20th Int. Symp. "Nanostructures: Physics and Technology"
Nizhny Novgorod, Russia, June 24–30, 2012

Magnetic field controlled LED with S-shaped current-voltage characteristics

A. V. Kudrin[1,2], M. V. Dorokhin[1,2], Yu. A. Danilov[1,2] and B. N. Zvonkov[1]

[1] Research Physical-Technical Institute of the Nizhny Novgorod State University, 603950 Nizhny Novgorod, Russia
[2] Department of Physics of University of Nizhny Novgorod, 603950 Nizhny Novgorod, Russia

Abstract. The light emitting quantum well structure was fabricated by the technique combining vapor-phase epitaxy and laser deposition. S-shaped current-voltage characteristics and magnetodiode effect were observed at 77 K temperature. In pulse bias voltage regime the structure demonstrated large magnetoresistance (∼75 000%) and effective control of an electroluminescence by external magnetic field.

Introduction

It is interest to create light emitting structures whose illumination characteristics (degree of polarization or intensity of luminescence) can be controlled by external magnetic field. Such structures are appropriate for magnetic field sensors (for example read heads for hard drives) interfaced with optical networks. The common approach for designing of similar devices is utilization of some magnetic material or structure (for example spin valve) as magnetic field sensing part of LEDs [1–3]. In this paper we present results on fabrication and characterization of a new type of magnetic field controlled LED on the basis of InGaAs quantum well structure.

1. Experimental

The light emitting structure was grown by the technique combining vapor-phase epitaxy and laser deposition. Firstly a set of undoped layers was grown on n-GaAs (001) substrate by vapor-phase epitaxy at 620 °C: 0.8 μm buffer GaAs layer, three $In_xGa_{1-x}As$ quantum wells (10, 9 and 8 nm thick with In content x = 0.1, 0.15 and 0.2, consequently) separated by 26 nm GaAs spacer layers. Top quantum well was covered by 13 nm GaAs spacer layer. The vapor-phase epitaxy layers had p-type background doping with hole concentration about 5×10^{15} cm^{-3}. On the top GaAs spacer at 410 °C were deposited doping Mn layer (∼1 monolayer thick) and 50 nm GaAs cap layer. Deposition of these layers was performed by laser ablation of solid Mn and GaAs targets at reduced pressure in hydrogen flow.

Au ohmic contact to the top of the structure was performed by thermal evaporation in vacuum. Sn ohmic contact to the substrate was formed by spark firing. In the fabricated structure, substrate and Mn layer with GaAs top layer acted as n and p regions, consequently. Circular mesa-structures of 500 μm diameter have been defined by conventional photolithographic and wet etching techniques. Current-voltage characteristics had been taken at 77 K. The magnetic field was varied in 0–4000 Oe range.

2. Results and discussion

Fig. 1 shows the forward biased current-voltage (I-V) characteristics of the structure at 77 K. The most remarkable aspect about the I-V characteristics is an S-shaped peculiarity (negative differential resistance) that appears in current sweep measurements (curve 1 on Fig. 1). As consequence of presence of

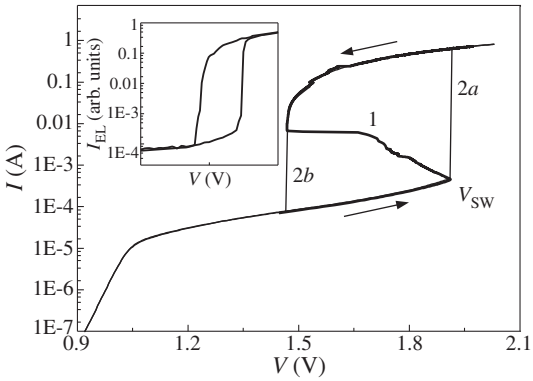

Fig. 1. Current-voltage characteristics at 77 K of the structure for the current (curve 1) and the voltage (curves 2) sweep measurements. The arrows indicate the direction of the voltage sweep. The inset shows the electroluminescence intensity as a function of bias voltage.

the S-shaped I-V characteristics, the hysteresis region occurs at voltage up-sweep from 0 to 2.1 V and down-sweep from 2.1 V to 0 (curves 2a and 2b on Fig. 1, consequently).

Above voltage V_{SW} the current passed through structure drastically increases (about three orders of magnitude), i.e. the switching from the high-resistance to the low-resistance state occurs. The switching voltage V_{SW} is about 1.8–1.9 V depending on mesa-structure location on the surface that probably relates to some lateral nonuniformity of the structure. The switching to the low-resistance state is accompanied by the appearance of electroluminescence related to radiative recombination of carriers in quantum wells. The inset to Fig. 1 shows a plot of integral electroluminescence intensity as a function of bias voltage.

Applying an external magnetic field in plane of the structure (i.e. perpendicular to the current pass direction in the mesa-structures) causes the shifting of the I-V characteristics to higher voltage values (Fig. 2). It leads to increasing the switching voltage to the low-resistance state ($V_{SW\,Field}$) in magnetic field from the V_{SW} value. The influence of external magnetic field on I-V characteristics can be due to the magnetodiode effect caused by the Lorentz force acting on the moving charge carriers in a diode [4].

It was observed that applying pulse forward voltage in range from V_{SW} to $V_{SW\,Field}$ allows switching the structure to the high-resistance state by external magnetic field. Fig. 3 depicts the resistance and the electroluminescence intensity dependences on magnetic field at 77 K for pulse bias voltage of 1.88 V.

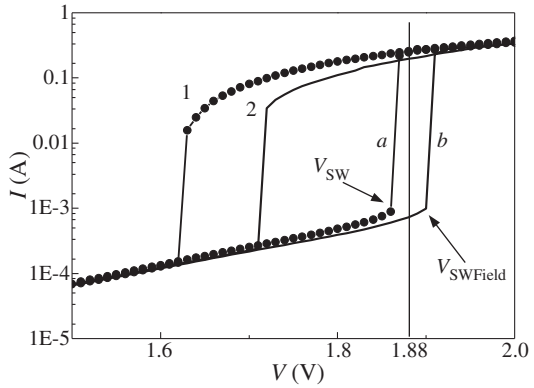

Fig. 2. Current-voltage characteristics at 77 K of the structure for the voltage sweep measurements without magnetic field (curves 1) and in magnetic field of 4000 Oe (curves 2).

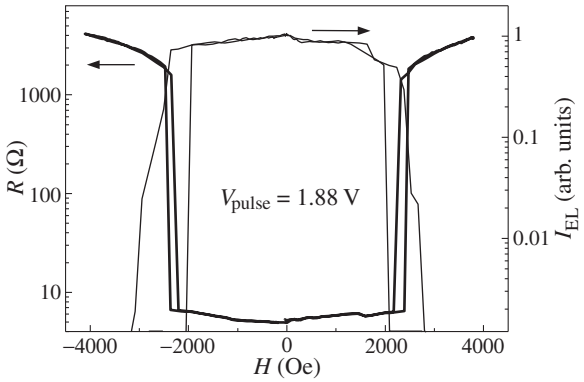

Fig. 3. The resistance and electroluminescence intensity dependences on magnetic field at 77 K for pulse bias voltage of 1.88 V.

The switching of the structure to the high-resistance state is accompanied by total luminescence quenching (Fig. 3). It should be note that the magnetoresistnce value is about ∼75 000% (the resistance changes from 5 to 3750 Ohm).

We suppose that this observed resistance transition induced by magnetic field is related to simultaneous presence of magnetodiode and negative differential resistance effects.

Consider I-V characteristics shown in Fig. 2. At zero magnetic field the structure after applying bias of 1.88 V is in the low-resistance state (according to I-V characteristics (branch a)) inasmuch as applied voltage is higher that the V_{SW} value. After removing applied voltage and repeated applying, the structure will remain in the low-resistance state.

In magnetic field (for example, of 4000 Oe) I-V characteristics describes by branch b (Fig. 2). In this case after applying forward bias of 1.88 V, the structure will be in the high-resistance since the switching voltage to the low-resistance state ($V_{SW\,Field}$) in given magnetic field is higher that 1.88 V. After removing applied voltage and repeated applying, the structure will remain in the high-resistance state.

Now consider the increasing of the magnetic field from 0 to 4000 Oe when the pulse voltage of 1.88 V is applied to the structure (Fig. 4). As it was considered before, in zero magnetic field the structure will remain in the low-resistance state. With increasing of the magnetic field strength, the I-V characteristic shifts to higher voltage values (magnetodiode effect). In particular, in the magnetic field of ≈2300 Oe applied voltage of 1.88 V will be lower that the switching voltage $V_{SW\,Field}$, and therefore after next voltage pulse (i.e. after voltage removing

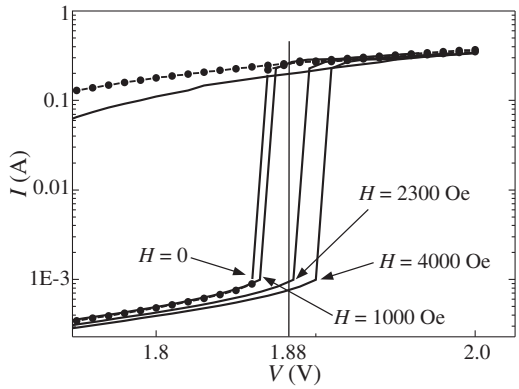

Fig. 4. Current-voltage characteristics at 77 K of the structure for the voltage sweep measurements at different values of magnetic field.

and applying) structure will be switched to the high-resistance state. For pulse voltage in range from V_{SW} to $V_{SW\,Field}$ the switching to the high-resistance state will occur in different values of magnetic field (Fig. 4). It is allow to choose the magnetic field strength that trigger the transition from the low-resistance state to the high-resistance state and consequently electroluminescence quenching. Thus the fabricated structure is a new device that can be used as effective magnetoresistive element and as magnetic field controlled light emitting diode.

Acknowledgements

The work was supported by the Grant of President of Russian Federation (MK-5198.2012.2) and RFBR 10-02-00739.

References

[1] D. Saha *et al.*, *Appl. Phys. Lett.* **93**, 194104 (2008).
[2] I. Appelbaum *et al.*, *Appl. Phys. Lett.* **83**, 4571 (2003).
[3] A. V. Kudrin *et al.*, *Tech. Phys. Lett.* **37**, 1168 (2011).
[4] A. A. Abramov *et al.*, *Semiconductors* **37**, 1078 (2003).

20th Int. Symp. "Nanostructures: Physics and Technology"
Nizhny Novgorod, Russia, June 24–30, 2012

Effective magnetic anisotropy of ferrimagnetic-ferroelectric composite

V. A. Orlov and I. N. Orlova
Krasnoyarsk State Pedagogical University, Lebedevoy 89, 660049 Krasnoyarsk, Russia

Abstract. The problem of reduction of energy of magnetic reversal of the composite material consisting from ferrimagnetic nanocylinders, placed in ferroelectric matrix is investigated. The effective constant of anisotropy is calculated.

Introduction

Now the problem of decrease in power expenses for magnetic reversal of composite materials which are used in devices of non-volatile memory is actual. Here we offer quantitative estimations of the mechanism of reduction of a magnetic field of switching of magnetization ferrimegnetic inserts in ferroelectric a matrix at the electric field appendix.

1. Model. An effective constant of an uniaxial anisotropy without electric field

Let's consider a model of the composite film represented by a matrix from a ferroelectric with the ferromagnetic cylinders implanted in it (see Fig. 1).

Ferroelectrics (ferroelectric material) possess strong electrostriction properties (piezoeffect and inverse piezoeffect). The nature of these phenomena consist in (i) origin of the superficial charge when one applyes a mechanical stress (piezoeffect) or (ii) a deformation of a material at a location of an electric field (boomerang effect). Magnitudes of deformation or elastic stress are so great that there was an idea to use these matrixes for providing a deformation of a ferromagnetic with strongly expressed magnetostrictive properties to control the parameters of local anisotropy with a hope to ensure magnetization switching in weak magnetic fields [1–5].

Linear dimensions of the cylinders in a diameter are less than those required for a 1D criterion for used ferromagnetic [2], so the magnetization of cylinders can be considered approximately homogeneous. It is supposed that a bit-by-bit data recording is provided perpendicularly to the recording surface. Then, one of the main problems is a stability of magnetization

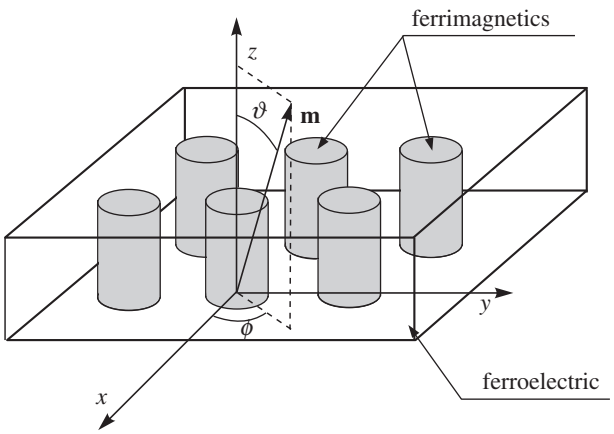

Fig. 1. A model of a ferrimagnetic-ferroelectric film for magnetic recording.

along the long axis of cylinders, and the influence of elastic stresses between cylinders and the matrix on this stability.

To deal with these problems it is reasonable to consider the energy of the individual ferromagnetic cylinder which we represent in the form $W = W_\mathrm{a} + W_\mathrm{s} + W_\mathrm{D}$. Here W_a is the energy of the crystallographic anisotropy of the cylinder:

$$W_\mathrm{a} = -K\,(\mathbf{ml})^2 V\,, \tag{1}$$

the characteristic energy of a demagnetized field is:

$$W_\mathrm{s} = \frac{1}{2}\,\mu_0 M_\mathrm{s}^2 V \mathbf{m}\widehat{\mathbf{N}}\mathbf{m}\,, \tag{2}$$

the energy of magnetistatic interaction with remaining crystal grains wel present in a dipole approximation:

$$W_\mathrm{D} = \frac{\mu_0 M_\mathrm{s}^2 V^2}{4\pi} \sum_n \left(\frac{\mathbf{mm}_n}{r_n^3} - 3\,\frac{(\mathbf{mr})(\mathbf{m}_n\mathbf{r}_n)}{r_n^5} \right), \tag{3}$$

where $\mathbf{m}$ and $\mathbf{l}$ are the unit vectors of magnetization and an axis of local anisotropies, accordingly, K is an anisotropy constant, V is the cylinder volume, M_s is a saturation magnetisation, r_n is a radius vector which connects a selected cylinder with the cylinder with the number n, $\mathbf{m}$ is a magnetization vector of the n-th cylinder, $\widehat{\mathbf{N}}$ is a tensor of demagnetization factors of a cylinder.

From (1)–(3) energy W for our model can be written as:

$$K_\mathrm{ef} = K - \frac{1}{2}\,\mu_0 M_\mathrm{s}^2 \Delta N - 1.056\,\frac{\mu_0 M_\mathrm{s}^2 V}{4\pi a^3}. \tag{4}$$

The stability of the magnetization of the selected cylinder is lost if the sign of the effective constant, K_ef, changes. For reversal of the magnetization of such a cylinder it is necessary to apply an external field, which is possible to estimate from the equation: $HM_\mathrm{s} = K_\mathrm{ef}$, where the field is measured in induction units.

2. Anisotropy of a composite within electric field

As the next step we consider the influence of the elastic stresses from a matrix on the values of constant of crystallographic anisotropy. A reason of the origin of a mechanical stress is a difference of the relative deformations of a ferromagnetic and a ferroelectric when the electric field is applied.

In that case the magnitude of the shift of the ferrimagnetic-ferroelectric interface Δx is:

$$\Delta x \approx \frac{\kappa_\mathrm{f} d_\mathrm{f} + \kappa_\mathrm{m} d_\mathrm{m}}{\kappa_\mathrm{f} l_{0\mathrm{m}} + \kappa_\mathrm{m} l_{0\mathrm{f}}}\, l_{0\mathrm{f}} l_{0\mathrm{m}} E\,. \tag{5}$$

Here E — electric field, $d_{\rm f}$ and $d_{\rm m}$ are the piezoelectric modulus of a ferromagnetic and a ferroelectric matrix materials, correspondingly, $l_{0\rm f}$, $l_{0\rm m}$ are the linear dimensions of the regions participating in a deformation, $\kappa_{\rm f}$ and $\kappa_{\rm m}$ are the Young modules of materials.

Stresses are defined from the expression:

$$\sigma_{\rm f} = \frac{d_{\rm f} l_{0\rm f} - d_{\rm m} l_{0\rm m}}{\kappa_{\rm f} l_{0\rm m} + \kappa_{\rm m} l_{0\rm f}} \kappa_{\rm m} \kappa_{\rm f} E \,. \qquad (6)$$

A presence of a mechanical stress leads to a modification of a constant of a crystallographic anisotropy. The correction has the form:

$$\Delta K_{\rm E} = \frac{3}{2} \lambda_{\rm f} \sigma_{\rm f} = \frac{3}{2} \frac{d_{\rm f} l_{0\rm f} - d_{\rm m} l_{0\rm m}}{\kappa_{\rm f} l_{0\rm m} + \kappa_{\rm m} l_{0\rm f}} \kappa_{\rm m} \kappa_{\rm f} \lambda_{\rm f} E \,. \qquad (7)$$

Here $\lambda_{\rm f}$ is a constant of magnetostriction of a ferromagnetic.

Taking into account the correction for the effective constant of anisotropy we have (For a case $l_{0\rm f} \approx l_{0\rm m}$):

$$\begin{aligned} K_{\rm ef} &= K + \frac{3}{2} \frac{(d_{\rm f} - d_{\rm m})}{\kappa_{\rm f} + \kappa_{\rm m}} \kappa_{\rm f} \kappa_{\rm m} \lambda_{\rm f} E - \frac{1}{2} \mu_0 M_{\rm s}^2 \Delta N \\ &- 1.056 \frac{\mu_0 M_{\rm s}^2 V}{4\pi a^3} \,. \qquad (8) \end{aligned}$$

Let's estimate intensity of the electric field, providing the amendment $\Delta K_{\rm E}$, comparable with other composed in $K_{\rm eff}$. Stability Magnetizations of the allocated cylinder it is lost at change of a sign on the effective constants. For a composite $BiFeO_3$-$CoFe_2O_4$ within the thickness $h = 200$ nanometer the numerical estimation gives value electric pressure of switching of magnetization $U = Eh \approx 14$ In that It will be coordinated with results of direct measurements [2].

Acknowledgement

Authors thank G. P. Berman (USA) for useful discussions.

References

[1] Li Yan *et al*., *Appl. Phys. Lett.* **94**, 192902 (2009).
[2] F. Zavaliche *et al*., *NANO Lett.* **7**, 1586 (2007)
[3] Ying-Hao Chu *et al*., *Nature materials* **7**, 478 (2008).
[4] F. Zavaliche *et al*., *Appl. Phys. Lett.* **87**, 252902 (2005).
[5] Weida Wu *et al*., *Phys. Rev. Lett.* **104**, 217601 (2010).

20th Int. Symp. "Nanostructures: Physics and Technology"
Nizhny Novgorod, Russia, June 24–30, 2012

Photonics of self-organizing biomineral nanostructures

Yu. N. Kulchin
Institute for Automation and Control Processes, FEB RAS,
690041 Vladivostok, Russia

Abstract. This paper presents the results of studies on the structure, chemical composition, optical, and nonlinear optical characteristics of DSGS spicules and their artificial biomimetic analogues as new materials for photonics.

Introduction

The possibilities of using optical radiation for the transmission and processing of more and more increasing volumes of information are stimulating the search for principally new technologies aimed at developing the requisite components for communication systems and devices for generating and detecting radiation, and designing optoelectronic computers. Nanophotonic objects such as photonic crystals have been attracting increasing attention recently as promising systems for solving such problems [1]. It is known that Nature has already created various materials with photonic crystal properties, the diversity of these materials including noble opal, the pollen of the butterfly's wing, the beetle's chitin shell, and the mother-of pearl of a shell which grow due to self-organization — one of the most promising technologies. The basic structural components of living systems almost entirely consist of ordered arrays of protein and hydrocarbon molecules. This specific feature of living systems is due to the ability of biological macromolecules to self-organize in solutions [2]. The latter property allows the manufacturing of uniquely intricate nanostructures, providing high efficiency per unit mass without putting in extreme requirements for primary materials and energy. Unfortunately, most natural protein complexes are unstable to temperature variations and chemical actions and can also be easily damaged by bacteria. As a result, direct analogues of biological systems have not found wide applications for manufacturing ordered nanostructures.

At the same time, a rather broad group of biological organisms exists which can concentrate in themselves mineral substances, which are contained in extracellular structures formed by complex composite substances-biominerals. Because they contain two components, organic (proteins or polysaccharides) and mineral (salts or oxides of elements), these self-organizing structures are stable against the action of many environmental factors [2].

A spectacular example of organisms with metabolism based on the self-organizing biomineralization is deep-sea glass sponges (DSGSs), which possess a cellular mechanism of selective accumulation of silicon from water and a complex protein-functioning mechanism, jointly providing the construction of a skeleton system from ordered silicon dioxide nanostructures [2,3]. In this connection, the study of the morphology and physical and chemical properties of elements of the biomineral skeleton in these objects, in which a mineral component is represented by silicon dioxide, and of the biosilicification process itself in living nature, is of great interest for the development of nanotechnologies.

Along with investigations of biomineralization processes in living nature, researchers in many laboratories are attempting to synthesize biomineral materials with the help of available biopolymers: proteins and polysaccharides. In doing so, biomimetic nanostructured materials are synthe-sized by sol-gel chemistry methods, which are mainly used in the synthesis of inorganic oxides of silicon, titanium, aluminium, and other chemical elements and are complementary to chemical processes proceeding in living systems.

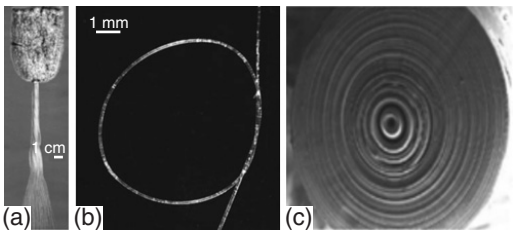

Fig. 1. Photographs of *Hyalonema sieboldi* DSGS (a), a fragment of its basal spicule (b), and an SEM photograph of a processed end of a spicule (1157 magnification) (c).

Further in this paper the results of studies on the structure, chemical composition, optical, and nonlinear optical characteristics of DSGS spicules and their artificial biomimetic analogues as new materials for photonics are presented.

1. Morphology and physicochemical characteristics of glass sea sponges

There are about 3000 species of sea sponges, of which about 500 belong to hexacorallia DSGSs [4]. In this paper, we introduce the results of studies of the three types of DSGSs: Hyalonema sieboldi, Pheronema sponge, and Sericolophus hawaiicus, which mainly inhabit the southern seas of the Pacific Ocean. A photograph of a typical sample of sponges of this type is displayed in Fig. 1a. Basal (anchor) spicules of these sponges, which can reach up to 1m in length, possess an extraordinary elasticity, allowing one to literally knot them (Fig. 1b), whereas skeletal spicules are rather rigid. We selected for studies samples of basal spicules homogeneous over the thickness with lengths from 20 mm to 50 cm and diameters from 40 μm to 1 mm.

A detailed scanning electron microscopic (SEM) study of the transverse sections of basal spicules shows that each of them consists of many axial concentric layers, their number varying from a few dozen to a few hundred, depending on the sponge type and age (Fig. 1c). Each of the concentric layers of a spicule consists of silicon dioxide nanoparticles 20 to 120 nm in size closely packed in a matrix formed by collagen-like nanofibrils and separated between themselves by nanometer protein layers (Fig. 1c) [3,5,6]. All the spicules have a central nucleus representing an axial protein filament 1–2 mm in diameter, localized as shown in Fig. 1, and a set of surrounding silicon dioxide and protein component layers [7].

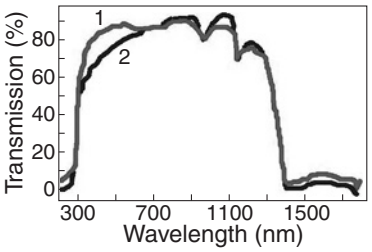

Fig. 2. Transmission spectra of *Pheronema raphanus* DSGS spicule materials: curve 1, basal spicule; curve 2, skeletal spicule.

The thickness of layers containing silicon dioxide particles is more than 100 times larger than the thickness of separating protein layers.

Studies performed by the method of energy-dispersive X-ray spectrometry have given evidences that spicules consist mainly of silicon (max 33%), oxygen (max 66%), and carbon (max 9%), with trace amounts of Na and K [8,9]. It was also established that the chemical composition of the layers is not constant and depends on their location, the sponge shape, and the spicule type.

The study of mechanical characteristics of basal spicules by the method of dynamic ultramicrohardnessmetry [7,10] have shown that the Young modulus for basal spicules of sea sponges is close to its value for natural opal. It was found that the distribution of the Young modulus over the transverse section of a basal spicule is inhomogeneous and changes from its periphery to center from 33,000 to 40.000 GPa. The mechanical properties of basal spicules observed in experiments are determined by their layered structure and the presence of an organic matrix [3,9], providing their enhanced mechanical strength and flexibility.

The distribution of the refractive index of a basal spicule over its section measured by the interferometric method [11] demonstrated that the refractive index of layers surrounding the central axial filament is about 1.45–1.48 and decreases to 1.39–1.41 at spicule edges [5,7], in good agreement with the results reported in paper [11].

The transmission spectrum of the spicule material was recorded in the range from 200 to 1700 nm [9]. Figure 2 demonstrates the transmission spectrum of a Pheronema raphanus basal spicule, which is typical for spicules of all types studied here. One can see that the spicule material transmits radiation rather well in the visible and near-infrared spectral ranges. The absorption lines observed at 770, 960, and 1150 nm belong to hydrated silicates contained in spicules, which is consistent with the results obtained in Ref. [11] for basal spicules of a Hyalonema sieboldi sponge and other types of sea sponges [3]. The average power loss of the 633-nm laser radiation in the waveguide propagation mode was about 0.1 dB m^{-1} for almost all the spicules studied in our work. The experimental studies of the transverse intensity distribution of radiation propagating in spicules showed that the radiation was concentrated in the axial region — 20 μm in size and its spatial distribution was nearly Gaussian [12,13].

The layered structure of basal spicules also gives rise to the periodic variation of the refractive index over the transverse section on the nano- and micrometer scales. In such a layered structure, the guided radiation modes can propagate with an effective refractive index lower than the refractive index of silicon dioxide. These modes are strongly coupled with light guiding axial layers. Because of the great difference between the refractive indices of alternating axial layers, the radiation power flux is strongly reflected in the radial direction. In this case, due to a great number of layers in a spicule, for certain values of the effective refractive index of propagating modes the phasing condition can be fulfilled for light fluxes propagating in layers, thereby reducing radiation losses [14].

As shown in papers [12,15], light can propagate in DSGS spicules only at certain angles to the spicule axis. The resonance wavelength of such a radiation will directly depend on the thickness of layers with a high refractive index. As a result, basal spicules should have forbidden bands, similar to those in photonic crystals. Because the thickness of axial layers with a high refractive index is small, resonance conditions will be fulfilled for the waves propagating at angles close to $\pi/2$ with respect to the normal to the spicule axis. This means that the single-mode propagation regime with the increased size of the mode spot is preferable for radiation guided in basal DSGS spicules. The results of numerical simulations show that this size can reach 20 [12]. As the layer thickness is varied from 200 nm to 1 μm, the wavelength resonances of guided radiation will lie in the spectral range from 300 to 1200 nm, in good agreement with experimental findings.

To confirm the presence of photonic crystal properties of basal spicules in glass sea sponges, the propagation of extremely low-energy 0.01-nJ pulses through them was additionally investigated. Forty-fs, 800-nm pulses were generated by a Ti:sapphire laser at a repetition rate of 1 kHz. The emission spectrum of the laser is presented in Fig. 3a. As expected, the spectra of transmitted radiation for all basal spicules exhibited oscillations. This is illustrated in Fig. 3b by the transmission spectrum of a basal spicule 190 μm in diameter and 40 mm in length, with the central channel 2 μm in diameter and 280-nm-thick axial layers with a high refractive index. Experimental studies have given evidences that due to biological growth the thickness of axial layers of basal spicules deviates somewhat from measured average values. Because of this, according to Ref. [14], the maxima of the experimental transmission spectrum are found to be somewhat smoothed and superimposed on a pedestal, resulting in the comparatively smooth spectrum as a whole.

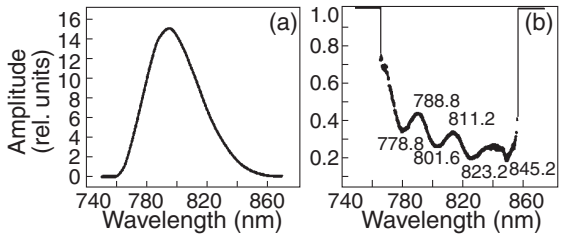

Fig. 3. Radiation spectra of ultrashort pulses before (a) and after (b) transmission through a *Hyalonema sieboldi* DSGS spicule (40 nm in length and 190 μm in diameter).

Thus, the studies have shown that the presence of periodic axial cylindrical silicon dioxide layers in basal DSGS spicules leads to the formation of forbidden photonic bands in them and, therefore, spicules of deep-see glass sponges represent a new type of natural photonic crystals.

2. Nonlinear optical properties of DSGS spicules

Upon excitation of basal spicules by 12-ns, 30-mJ, 532-nm second harmonic pulses from an Nd:YAG laser at a pulse rep-

etition rate of 10 Hz, a considerable increase in the fluorescence intensity in the long-wavelength region was observed [7]. Figure 4 demonstrates the normalized fluorescence spectra of basal spicules 140 μm in diameter and 5 cm in length obtained at different pumping radiation intensities. One can see that the spectra have a maximum in the long-wavelength region at 770 nm, whose position is independent of the laser excitation intensity at the spicule entrance. The spectra differ greatly from the relevant fluorescence spectrum of a usual multimode silica fiber [13]. This is probably explained by the presence of large organic complexes in spicules of glass sea sponges. The measurements of the dependence of the maximum fluorescence intensity at 770 nm on the excitation power showed that this dependence saturated when the excitation power was increased more than 10-fold. This demonstrates the nonlinearity of the light energy transformation in spicules related to a high concentration of organic complexes inhomogeneously distributed in them [16]. A specific feature of glass sea sponges is their fluorescence lifetime. The fluorescence lifetime of basal spicules measured at different excitation powers reaches a few dozen microseconds, considerably exceeding these lifetimes, for example, for sea zooplankton or quartz optical fibers ($\sim 10^{-10}-10^{-9}$ s) [17].

A unique property of glass sea spicules as optical fibers with a periodically changing transverse distribution of the refractive index is the complicated frequency profile of the dispersion for light pulses propagating in them, which substantially differs from analogous profile for conventional optical fibers. As a result, new nonlinear-optical phenomena and new regimes of spectral-temporal transformation of ultrashort light pulses can be observed in such "optical fibers".

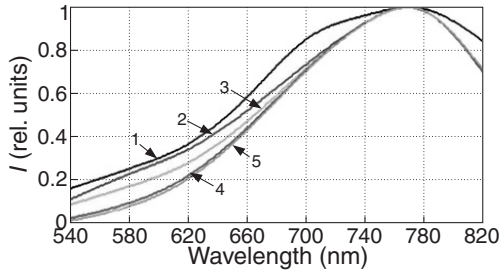

Fig. 4. Normalized fluorescence spectra of a *Hyalonema sieboldi* basal spicule at different relative excitation energies of 532 nm, 12 ns input pulses (pulse repetition rate is 10 Hz, the maximum pulse energy is 30 mJ). Attenuation coefficients of the pulse energy are 1 (curve 1), 0.3 (2), 0.2 (3), 0.13 (4), and 0.1 (5).

In this connection, a model was constructed to describe the propagation of ultrashort pulses in spicules taking into account the combined action of dispersion effects, non- linear polarization, and ionization nonlinearity leading to the self-phase modulation of the light field and efficient transformation of the pulse spectrum to a supercontinuum; in addition, the propagation of ultrashort pulses in DSGS spicules was numerically simulated and studied experimentally [18]. Experiments were performed using a Spitfire ProTi:sapphire laser complex (Spectra Physics, USA) emitting 0.9-mJ, 40-fs, 800-nm single pulses at a pulse repetition rate of 100 Hz with a spectral FWHM of 35 nm.

On coupling 5-nJ ultrashort pulses into different DSGS spicules 5–15 mm in length, the self-focusing of radiation was observed with the formation of "hot regions" in the transverse intensity distribution of transmitted light beams. The shape of emission spectra in these regions noticeably changed [19]. The nonlinear-optical coefficient of the spicule material measured in the self-focusing of ultrashort pulses in spicules was $n_2 \approx 8.8\times10^{-16}$ cm^2 W^{-1}, which exceeds this coefficient for silica by more than three times, and by approximately 10^3 times for air.

As the laser pulse energy was increased above 20 nJ, the stable formation of a supercontinuum was observed in the spectrum of radiation transmitted through spicules, while prolonged repeated irradiation by 0.1–0.9-mJ pulses caused the optical breakdown of the spicule material. Figure 5a displays a photograph illustrating the transformation of the spectrum of a 100 nJ femtosecond pulse transmitted through a Hyalonema sieboldi sponge spicule 200 μm in diameter and 1.5 cm in length to a supercontinuum covering the visible spectrum down to 400 nm. Figure 5b shows that the observed spectrum of ultrashort pulses transmitted through a spicule considerably broadens upon increasing the spicule length.

Because the peak intensity of unfocused ultrashort pulses could achieve $\sim 7\times10^{10}$ W cm^{-2} in experiments, this resulted in the considerable enhancement of nonstationary processes such as transient spatial self-focusing and multiphoton ionization of the spicule material, and the short-wavelength edge of the supercontinuum shifted to 300 nm as the spicule length increased.

The simulation of the intensity spectral distribution of ultrashort light pulses in the 750 $\pm$850 nm region transmitted through a spicule and its comparison with experimental data showed that the group velocity dispersion $\beta_2 \approx 2.8\times10^3$ ps^{2}m^{-1} for spicules is an order of magnitude lower than this dispersion in similar silica fibers, which is explained by the significant contribution from the waveguide part of dispersion due to the multilayer quasiperiodic structure of the cladding [15] compared to the c ontribution from the component caused by the spicule material.

3. Biosilicate nanocomposite materials and their nonlinear-optical properties

As mentioned in the Introduction, inorganic oxides are mainly synthesized by sol-gel chemistry methods [20]. Their synthesis is performed, as a rule, by using the two-stage introduction of biopolymers into a silicate matrix at the sol-gel transition stage; this process does not cause the mineralization of biomacromolecules. In Refs [19,21], a new, one-stage method was proposed for the synthesis of biomimetic hybrid nanocomposite materials based on a silicon-containing tetraxis (2-hydroxyethyl) orthosilicate precursor (THEOS) (50%) and Na alginate (0.5–1%), Na hyaluronate (0.1–2%), and xanthane (0.5–2%) polysaccharides. This method does not involve the stage of sol solution formation that takes place in the conventional two-stage process.

In this case, the structure of the inorganic component of the nanocomposite material being produced is determined by a polysaccharide organic matrix, similarly to the formation of inorganic compounds in living organisms occurring due to their precipitation (biomineralization) on biomacromolecules serving as templates. In this connection, the mechanism of formation of such biosilicates resembles one of the mechanisms used by Nature for the synthesis of spicules.

By proceeding this process at a low temperature, we fabricated the samples of transparent biosilicate materials with

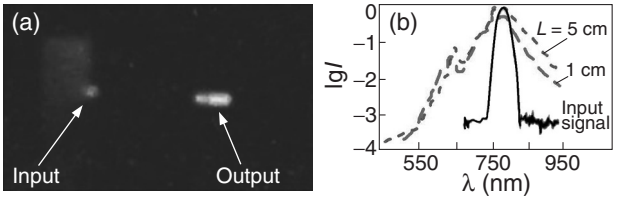

Fig. 5. (a) Photograph of supercontinuum generation by 40 fs, 800 nm, 100 nJ ultrashort pulses in a *Hyalonema sieboldi* sponge spicule 200 μm in diameter and 1.5 cm in length. (b) Supercontinuum spectrum after the transmission of pulses through a *Sericolophus hawaiicus* sponge spicule 250 μm in diameter.

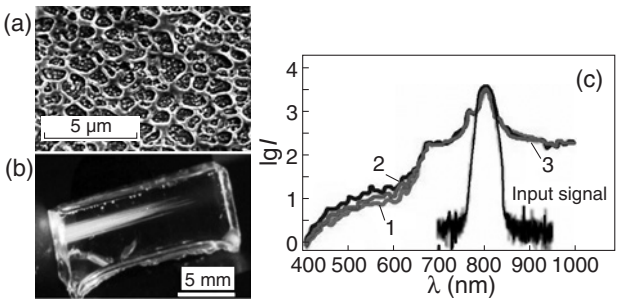

Fig. 6. (a) SEM photograph of a section of an Na hyaluronate nanocomposite sample. (b) Photograph of an Na hyaluronate nanocomposite sample and a filament produced in it. (c) Supercontinuum spectra generated in nanocomposite materials based on the following complexes: THEOS (50%)+xanthane (0.5%) (curve 1); THEOS (50%)+Na hyaluronate (0.25%) (curve 2), and THEOS (50%)+Na alginate (0.25%) (curve 3).

transmission in the spectral range from 350 to 1400 nm virtually the same as that of the DSGS spicule material [19]. The refractive index of the synthesized materials was $n \approx 1.517$. The organic macromolecules contained in small concentrations in these materials play the role of a morphological matrix in the form of intricately intersected fibrils penetrating the entire material (Fig. 6a). The rest of the material volume is filled with spherical silicate particles (with an average diameter of 60 nm) deposited onto the organic matrix. Figure 6b gives a photograph of a transparent nanocomposite synthesized in an aqueous solution containing 50% of the THEOS precursor and 1% of sodium hyaluronate. The sample length is 15 mm [19].

The study of the interaction of unfocused 1 mJ femtosecond laser pulses (the laser beam diameter was 7 mm, and pulse repetition rate 100 Hz) with synthesized nanocomposite biomimetic media revealed that the nonlinear-optical parameters of these media were considerably higher than those for DSGS spicules [19]. The spectra of ultrashort pulses transmitted through xanthane, Na-alginate, and Na hyaluronate composite samples 10 mm in length demonstrate that the nonlinearity of the interaction of intense ultrashort pulses with these materials manifests itself much stronger (Fig. 6c). Here, the self-phase modulation of pulses caused by the Kerr nonlinearity of a medium and the self-focusing of pulses play the main role, which, together with other nonlinear-optical processes, leads to the formation of filaments in samples (Fig. 6b) and a supercontinuum. The best conversion efficiency of the pulse energy to a supercontinuum was achieved in sodium hyaluronate samples, for which higher energy levels were observed in supercontinuum spectrum (Fig. 6c). Sodium alginate samples proved to be optically unstable, while xanthane samples strongly absorbed ultra-short laser pulses.

A comparison of total supercontinuum energies PSC generated in the spectral range from 400 to 650 nm in samples with the same geometry and different bioorganic additions (up to 1% in weight) revealed that PSC for sodium hyaluronate samples was more than twice the PSC for xanthane samples. The stable generation of a supercontinuum was observed in sodium hyaluronate samples even with a thickness as small as 1 mm. The approximate estimate of the nonlinear-optical coefficient of the sodium hyaluronate material based on the experimental study of the filamentation process in samples and data in paper [19] gives the value of $n_2 \sim 29 \times 10^{-14}$ cm^2 W^{-1}, which exceeds this coefficient for the DSGS spicule material by more than two orders of magnitude.

Another important feature of the supercontinuum generation in this material relates to the dependence of the total supercontinuum power PSC on the concentration of sodium hyaluronate polysaccharide and sample length [19], which allows one to control the nonlinear-optical parameters of the material itself and functional elements based on it.

4. Conclusion

The studies considered above have shown that the combination of proteins and polysaccharides created by Nature and self-organized with silicon dioxide extracted from sea water under natural conditions produced a unique nonlinear-optical biomineral nanocomposite material combining the flexibility and strength of a protein with the elasticity and strength of silicon dioxide, which is promising for applications in photonics. This process can be reproduced under artificial conditions using the adaptable sol-gel technology, which opens up a broad perspective for manufacturing new passive and active optoelectronic devices.

References

[1] G. I. Churyumov *et al*., *Usp. Sovrem. Radioelektron.* **11**, 35 (2005).
[2] M. A. Meyers *et al*., *Prog. Mater. Sci.* **53**, 1 (2008).
[3] W. E. G. Muller *et al*., *Biosensors Bioelectron.* **21**, 1149 (2006).
[4] S. P. Leys *et al*., *Adv. Marine Biol.* **52**, 1 (2007).
[5] Yu. N. Kulchin *et al*., *Vestn. Dal'nevost. Otd. Ross. Akad. Nauk* **1**, 27 (2007).
[6] Yu. N. Kulchin *et al*., *Opt. Memory Neural Networks* **16**, 189 (2007).
[7] Yu. N. Kulchin *et al*., *Kvantovaya Elektron*. **38**, 51 (2008).
[8] A. N. Galkina *et al*., *Khim. Fiz. Mezoskop.* **11**, 310 (2009).
[9] S. S. Voznesenskii *et al*., *Ross. Nanotekhnol.* **5**, 126 (2010).
[10] Yu N Kulchin, *Rare Met.* **28** (Special issue), 66 (2009).
[11] J. Aizenberg *et al*., *Proc. Natl. Acad. Sci. USA* **101**, 3358 (2004).
[12] Yu. N. Kul'chin *et al*., *Pis'ma Zh. Tekh. Fiz.* **34**, 633 (2008).
[13] Yu. N. Kulchin *et al*., *Photonics of Biomineral and Biomimetic Structures and Materials*, Moscow: Fizmatlit 2011.
[14] S. O. Konorov *et al*., *Zh. Eksp. Teor. Fiz.* **96**, 85 (2003).
[15] Yu. N. Kul'chin *et al*., *Opt. Spektrosk.* **107**, 468 (2009).
[16] D. V. Maslov *et al*., *Kvantovaya Elektron.* **36**, 163 (2006).
[17] G. P. Agrawal, *Nonlinear Fiber Optics* San Diego Academic Press (1995).
[18] Yu. N. Kulchin *et al*., *In Biosilica in Evolution, Morphogenesis, and Nanobiotechnology*, Berlin: Springer (2009).
[19] Yu. N. Kulchin *et al*., *Laser Phys.* **21**, 630 (2011).
[20] B. Dunn *et al*., *Acta Mater.* **46**, 737 (1998).
[21] Yu. A. Shchipunov, *Promising Directions in the Development of Nanotechnologies at the Far Eastern Branch* **2**, Vladivostok: Dal'nauka (2009).

20th Int. Symp. "Nanostructures: Physics and Technology"
Nizhny Novgorod, Russia, June 24–30, 2012

Auger recombination and dynamics of the photoluminescence in InGaAsSb/AlGaAsSb and GaAs/AlGaAs quantum wells

M. Ya. Vinnichenko[1], L. E. Vorobjev[1], D. A. Firsov[1], M. O. Mashko[1], G. A. Melentyev[1], L. V. Gavrilenko[2], D. I. Kuritsyn[2], L. Shterengas[3] and G. Belenky[3]

[1] St Petersburg State Polytechnic University, 195251 St Petersburg, Russia
[2] Institute for Physics of Microstructures, 603950 Nizhny Novgorod, Russia
[3] Department of Electrical and Computer Engineering, State University of New York at Stony Brook, New York 11794, USA

Abstract. Time resolved photoluminescence was studied in InGaAsSb/AlGaAsSb quantum wells with different compositions of barrier solid solution and with different width of the quantum wells. The optical phonon emission time was estimated from the analysis of photoluminescence rise time. Electron lifetime related to resonant Auger recombination was estimated. Dynamics of photoluminescence in differently doped GaAs/AlGaAs quantum wells was investigated under different excitation levels.

Introduction

The study of photoluminescence (PL) dynamics in nanostructures with quantum wells (QWs) gives information about the processes of charge carrier capture in QWs, about the energy relaxation processes and carrier lifetime.

We investigated heterostructures based on InGaAsSb/AlGaAsSb QWs promising for the development of CW mid infrared lasers ($\lambda = 2 \ldots 4\,\mu$m) operating at room temperature. The dynamics of PL was investigated at the wavelength corresponding to the maximum intensity using the "up-conversion" method in nanostructures with ten $In_{0.53}Ga_{0.47}As_{0.24}Sb_{0.76}/Al_{0.7}Ga_{0.3}As_{0.056}Sb_{0.944}$ quantum wells. The structures differed by their quantum well widths: 4, 5, 6, 7 and 9 nm.

The PL dynamics was also investigated in nanostructures with undoped and n-doped GaAs/AlGaAs quantum wells.

1. Experimental part

Band diagrams in Sb-contained structures were calculated using the Kane model taking into account the nonparabolicity of energy bands. This should be considered in the investigated structures because the Auger electrons have energies comparable to the band gap. It was estimated that in the sample with 5 nm QW width at $T = 77$ K, the distance between the split-off valence band and the ground state of the holes is approximately equal to the effective band gap (Fig. 1):

$$E(hh1) - E(so1) \cong E(e1) - E(hh1)\,. \qquad (1)$$

Equation (1) corresponds to the condition of resonant Auger recombination of two holes and an electron. The resonant Auger recombination reduces the nonradiative lifetime for two–three orders of magnitude [1] and consequently affects the characteristics of lasers based on these nanostructures.

The time dependence of PL intensity $J^{\nu}_{\mathrm{PL}}(t)$ was investigated at different intensities of optical pumping J_{ex} for temperatures $T = 77$ and 300 K. The structures were pumped by 150 fs pulses of radiation at 100 MHz frequency and quantum energy $h\nu_{\mathrm{ex}} = 1.17$ eV. At such energy of photons the excitation of electron-hole ($e - h$) pairs occurs only in QW due to transitions $hh1 \rightarrow e1$ and $hh2 \rightarrow e2$. Note that in these conditions, the concentration of excited $e - h$ pairs is smaller in comparing with the case of excitation of charge carriers in the barrier [2].

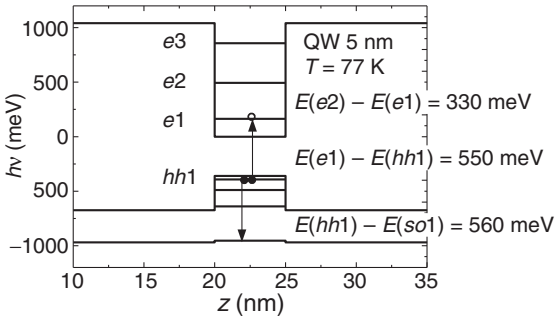

Fig. 1. The scheme of energy levels in structure with 5 nm InGaAsSb/AlGaAsSb QW width at $T = 77$ K. The arrows show the process closed to the resonant Auger recombination.

For reference, the PL dynamics was also investigated in similar nanostructures with InGaAsSb/InAlGaAsSb QWs. In these structures the pumping energy exceeds the energy gap of barrier material. Here the carriers were excited in the barrier, but not only in QW as in the first structures.

Analysis of PL intensity rise allowed us to estimate the optical phonon emission time τ_{PO}. For example, for the structure with QW width of 5 nm (see Fig. 2, curve 1) and pumping in the QW τ_{PO} is approximately equal to 0.25 ps. Dynamics of PL rise in nanostructures with pumping in the barrier reveals "fast" and "slow" parts (Fig. 2, curve 2).

We associate the "fast" growth with the energy relaxation processes of charge carriers excited in the quantum well. Emission time of polar optical phonon was estimated from the "fast" exponential growth as 0.28 ps. The times τ_{PO} in similar structures with InGaAsSb/InAlGaAsSb and InGaAsSb/AlGaAsSb QWs are approximately equal. Intensity of optical excitation does not affect the time of "fast" PL rise.

The "slow" growth of PL intensity can be explained with the processes of carrier diffusion and ballistic transit from the barrier into the QW. The time of "slow" PL growth (50–90 ps) increases with the pumping level. It can be associated with slowing down the electron diffusion at high pumping levels when high electron density in the barrier region leads to the rise of electron-electron scattering and to the decrease of electron mobility and diffusion coefficient.

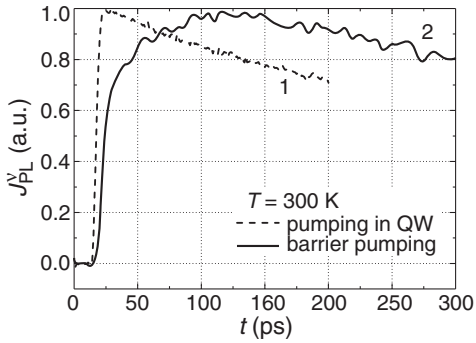

Fig. 2. The time dependences of normalized PL intensity at room temperature under optical pumping in QW (1) and in barrier region (2).

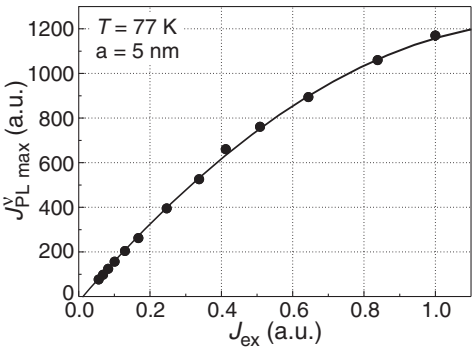

Fig. 3. Dependence of the PL intensity on the pumping level at the maximum for sample with 5 nm wide QW at $T = 77$ K. The maximum of J_{ex} corresponds to pumping laser power of 30 mW.

The recombination rate R for structures with QW excitation was determined from the rate equation under the assumption that at the initial stage of relaxation the electron density is proportional to the intensity of pumping:

$$n|_{t\approx 0} \equiv n_0 \propto J_{ex}\,, \tag{2}$$

$$\frac{dn}{dt} = -n\,R(n)\,, \tag{3}$$

$$-R(n) = \frac{1}{n}\frac{dn}{dt} = \frac{1}{J_{ex}}\frac{dJ^{\nu}_{PL}(t)}{dJ_{ex}(t)}\frac{dJ^{\nu}_{PL}(t)}{dt} = \frac{1}{J_{ex}}\left(\frac{dJ^{\nu}_{PL}(t)}{dJ_{ex}}\right)^{-1}\frac{dJ^{\nu}_{PL}(t)}{dt}\,. \tag{4}$$

It should be noted that the time dependence of PL intensity $J^{\nu}_{PL}(t)$ does not correspond to time dependence of carrier concentration.

To determine $R(n)$ a derivative $dJ^{\nu}_{PL}(t)/dJ_{ex}$ was calculated from the dependence of the PL intensity in the maximum on the pumping level (see Fig. 3).

Recombination rate R as a function of J_{ex} for the two samples is shown in Fig. 4. The value of R in the quantum well structure with a width of 5 nm quadratically increases with increasing the excitation level, corresponding to the contribution of Auger processes. In similar structure with a QW width of 7 nm and other structures the recombination rate does not increase with pumping level because the contribution of non-resonant Auger processes to the probability of recombination is small for all the structures due to the relatively low concentration of the excited carriers in QW [1]. Thus, the resonant Auger recombination is observed in structure with quantum

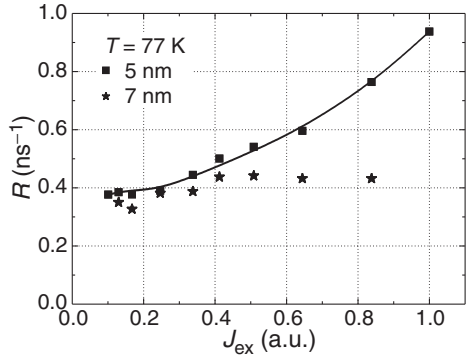

Fig. 4. Dependence of recombination rate on excitation level for two structures with different well width.

well width of 5 nm only, which confirms the correctness of our calculations.

From the recombination rate at low pumping levels (Fig. 4), the lifetime of charge carriers τ_{SHR} related to the Shockley–Read–Hall recombination was determined. We found a tendency to a weak reduction of this time with decreasing the QW width (roughly from 3.5 to 2 ns at $T = 77$ K), which can be explained with increasing the imperfections of heterojunctions.

The PL dynamics was also investigated in nanostructures with undoped and n-doped GaAs/AlGaAs quantum wells. These studies were conducted to determine the mechanisms of electrons energy relaxation and the lifetime of charge carriers in GaAs/AlGaAs QWs. In experiments we used resonant pumping into the second QW subband. The dynamics of the PL was studied at two wavelengths corresponding to the electron transition to heavy-hole level $hh1$ from the bottom of the ground level $e1$ (780 nm) and from the states in the subband $e1$ with energies exceeding the bottom of the subband on the optical phonon energy (765 nm). In undoped quantum wells at low pumping levels the raise of the PL intensity at a wavelength of 780 nm consists of a "fast" section ~1 ps and "slow" section ~100 ps. At a wavelength of 765 nm, the PL dynamics also shows "fast" part of raising ~0.7 ps. These results can be explained by considering the contribution of excitons and phonons in the recombination and energy relaxation.

Acknowledgements

This work was supported by grants of Russian Federal Target Program 'Kadry' for 2009–2013, the Russian Foundation for Basic Research, St Petersburg Government and NSF (Grant No. DMR0710154).

References

[1] L. V. Danilov and G. G. Zegrya, *Semiconductors* **42**, 550 (2008).
[2] D. A. Firsov *et al.*, *Semiconductors* **44**, 50 (2010).

20th Int. Symp. "Nanostructures: Physics and Technology"
Nizhny Novgorod, Russia, June 24–30, 2012

Visualization of lasing modes on mirror of WGM-laser by the AFM method

M. S. Dunaevskiy[1], P. A. Alekseev[1,3], A. M. Monahov[1], A. N. Baranov[2], P. Girard[2], R. Teissier[2] and A. N. Titkov[1]

[1] Ioffe Physical-Technical Institute, St Petersburg, Russia
[2] Institut d'Electronique du Sud, UMR 5214 UM2-CNRS, CC082, Universite Montpellier 2, Montpellier, France
[3] St Petersburg Electrotechnical University "LETI", 197376 St Petersburg, Russia

Abstract. The spatial distribution of lasing modes on the cleavage mirror of disk-shaped whispering-gallery mode (WGM) laser was found using a new method of atomic-force microscopy (AFM). That AFM method developed in this work allows visualization of radiation distribution at the mirror of WGM-laser with a resolution better than 1 micron. The method is based on the detection of a small shift of the resonance frequency of AFM-probe under heating with laser radiation.

There were studied cleaved WGM-laser structures n-GaSb/ n-$GaAl_{0.9}AsSb$/$GaAl_{0.35}AsSb$/p-$GaAl_{0.9}AsSb$/p-GaSb with two GaInAsSb quantum wells in the active region. The diameter of obtained semi-disk was $D = 280$ μm. The lasing wavelength of this structure was $\lambda = 2.1$ microns and the power of emission was about 3 mW. The scheme of the laser is shown at Fig. 1a.

The two-pass AFM technique was used in order to visualize IR-radiation at the laser mirror. In the first pass the surface topography was measured in tapping mode regime. In the second pass the AFM-probe was moved along the surface at a given height $h = 50$ nm, while it was oscillating at a mechanical resonance frequency and the phase shifts of oscillations were detected $\Delta\phi(x, y)$. A key feature of this experiment was to work in vacuum conditions, since it allowed: (i) to reduce the heat transfer from the AFM-probe and (ii) to increase the quality factor of the AFM-probe oscillations up to the values of $Q = 2 \times 10^4$. The measured phase shift $\Delta\phi$ is linearly related to the shift $\Delta\omega$ of the resonance frequency of the cantilever $\Delta\phi \sim Q \times \Delta\omega/\omega$. When heated by laser radiation sizes of the cantilever (L — length, t — thickness, w — width) should increase linearly with the heating. $\Delta\omega/\omega = (dt/t–2dL/L) = -\alpha_L \Delta T \sim I_{light}$.

Here α_L is the coefficient of thermal expansion of silicon cantilever ($\alpha_L(Si) = 3 \times 10^{-6}$ K^{-1}) and ΔT is the change of AFM-probe temperature. The minimum detectable value of the phase shift is $\Delta\phi_{min} = 0.1^\circ$ limited by the noise of the system. Then, under vacuum conditions using a cantilever with high quality factor $Q \sim 2 \times 10^4$ it should become possible to detect small heating of the AFM-probe $\Delta T_{min} \sim 0.1$ K. If we assume, that at least the one tenth of the IR laser radiation is absorbed by the electrons in highly doped silicon probe ($\alpha \sim 100$ cm^{-1}) and taking into account the known size of the probe, its mass ($m \sim 4 \times 10^{-8}$ g) and specific heat ($c = 0.7$ J/gK) it can be roughly estimated the heating of the probe $\Delta T \sim 1$ K which is already a detectable value.

Figure 1 show the results of measurements on the mirror of the WGM-laser. The scanning area (shown in Fig. 1 b–d) is located at a distance of 10 microns from the peripherals edge of semi-disk (Fig. 1a). The lasing modes of WGM-laser should be spatially localized in the periphery of the disc resonator. Indeed, the laser generation modes have been found only there. At the AFM image of mirror surface topography (Fig. 1b) there can be distinguished AlGaAsSb cladding layers with high Al content. It has been shown earlier [1] that layers with high Al content are strongly oxidized and thus appear on the surface as elevations, which makes it easy to identify the AlGaAsSb cladding layers. The IR-radiation in the lasing regime ($I > I_{th} = 45$ mA) should be localized in the waveguide located between the cladding layers. In the phase image (Fig. 1c) one can see three bright spots at $x = 5$, 9.5 μm and $x = 13.5$ μm in the waveguide that corresponds to the lateral intensity distribution of radiation emerging from the surface. Fig. 1d shows the phase profiles taken along the waveguide for different values of current passing through the structure. It can be seen that at currents that are smaller than the lasing threshold ($I < 45$ mA) the phase profile is weak and does not demonstrate any features. From optical measurements it is known that at small currents weak spontaneous incoherent radiation is emitted from the surface. When the current exceeds the lasing threshold ($I > 45$ mA) the phase profile significantly changes giving rise to the appearance of three bright spots. The spots intensity is modulated by a series of equidistant lines separated by 1 μm what is approximately the half of the laser generation wavelength. The nature of this interference like effect is not clear. One possible explanation could be the near-surface standing wave that may appear at the boundary between two media with different refractive indices.

In the explanation of the observation of three lasing spots it should be considered that the radial distribution of radiation intensity in the WGM-laser is described by the square of the Bessel functions of high order $J_m(\rho)$ (where m is approximately equal to the number of wavelengths that fit the circle length of the disk) [2]. The different modes correspond to the coincidence of different roots of this function $J_m(\rho)$ with the position of edge of the disk. Thus, the observed three lasing spots in the phase image may correspond to three extrema of $J_m(\rho)$ function in our case. Therefore, in this work it was developed the new method to visualize the spatial modes of the radiation on the surface of cleaved WGM-lasers with submicron resolution.

Acknowledgements

Authors (M.S.D., P.A.A. and A.N.T.) are grateful to Yu.P.Yakovlev for an attracting of our interest to the studied phenomena.

This work has been supported by Russian Foundation for Basic Research grant (10-02-93110 ILNACS), grant of President of Russia for leading scientific schools NSh-3008.2012.2,

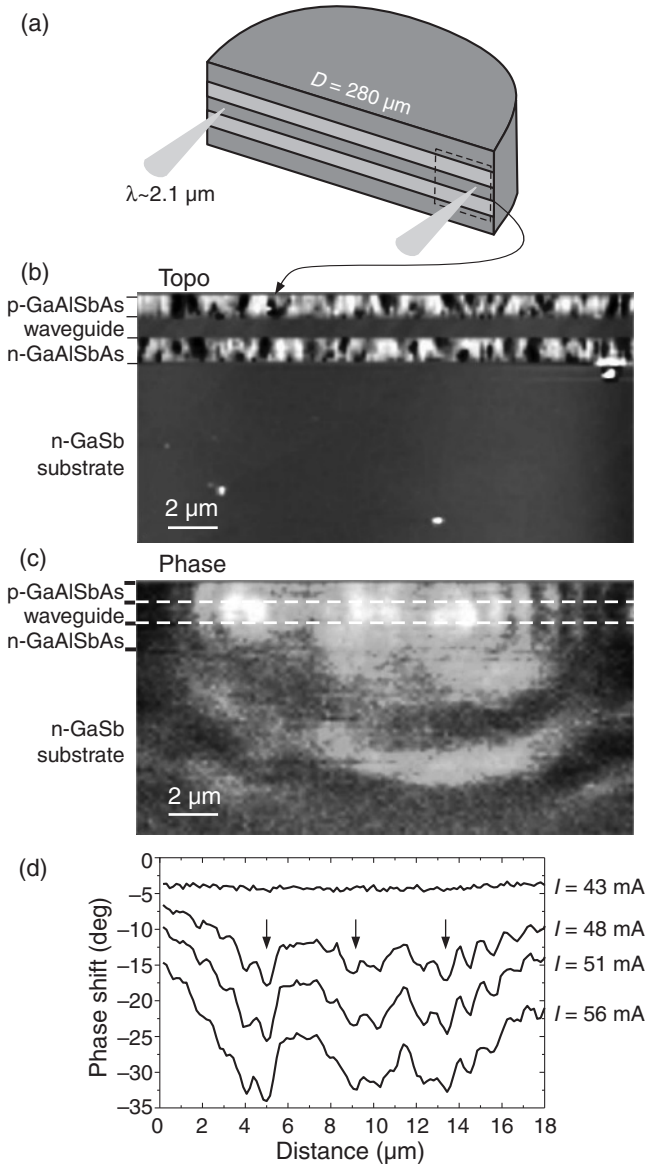

Fig. 1. (a) The geometric scheme of the cleaved WGM-laser structure; (b) AFM topography of laser mirror; (c) phase image contrast related with the absorption of light at the mirror surface of WGM-laser; (d) phase profiles taken along the waveguide for different values of current passing through the WGM-laser structure.

Basic Research Program No. 24 of the Presidium of the Russian Academy of Sciences.

References

[1] P. A. Dementyev, M. S. Dunaevskii, A. V. Ankudinov, I. V. Makarenko, V. N. Petrov, A. N. Titkov, A. N. Baranov, D. A. Yarekha, R. Laiho, *Appl. Phys. Lett.* **89**, 081103 (2006).

[2] A. M. Monakhov, V. V. Sherstnev, A. P. Astakhova, Y. P. Yakovlev, G. Boissier, R. Teissier, A. N. Baranov, *Appl. Phys. Lett.* **94**, 051102 (2009).

20th Int. Symp. "Nanostructures: Physics and Technology"
Nizhny Novgorod, Russia, June 24–30, 2012

Structure analysis of carbon-based substances using X-ray spectroscopy techniques

M. D. Sharkov[1], M. E. Boiko[1], A. V. Bobyl[1], S. N. Ivashevskaya[2], Y. V. Zubaichus[3] and S. G. Konnikov[1]

[1] Ioffe Physical-Technical Institute, St Petersburg, Russia
[2] Geology Institute of the Karelian Center of the RAS, Petrozavodsk, Russia
[3] National Research Center "Kurchatov Institute", Moscow, Russia

Abstract. A sample of human protein ceruloplasmin, an organic Langmuir–Blodgett (LB) film, and two ultra-disperse diamond (UDD) samples have been analyzed via EXAFS (Extended X-Ray Absorption Fine Structure) and SAXS (Small-Angle X-Ray Scattering) methods. Vicinities of Cu atoms in the protein matrix have been suggested to be substantially ionized at radii about 0.2 nm. Sizes of the largest UDD grains and UDD superstructure periods have been appreciated. The hypothesis that UDD grains consist of onion-like shells around the diamond core has appeared to be consistent with the obtained SAXS data. The thickness and number of the LB film sample layers have been estimated.

Introduction

Different carbon-based structures involved in modern technologies require much information about the structure of materials. It is often important to obtain these data without destroying the samples. A solution of this task is provided, e.g., by x-ray analysis methods: EXAFS (Extended X-Ray Absorption Fine Structure) spectroscopy, SAXS — Small-Angle X-Ray Scattering, etc.

The SAXS technique is usually applied to detect clusters, small crystal and powder grains, and superlattice periodicity with sizes from several nanometers up to dozens of nm. The developed technique is sensitive even to far larger grains and scarcer superlattices, with sizes about 500 nm, as well as to nm sizes. Besides, the new technique provides a better precision in comparison with earlier practice.

Analysis of EXAFS spectra is known to consist of several steps. Some of them, like oscillations separation, are usually performed by methods which might lead to incorrect results. Other steps, like Fourier window definition, had not been studied until our recent works. The considered method is successful in solving these problems.

1. SAXS measurement and analysis

The SAXS technique is known to allow one to solve a triple task, namely: to determine the biggest grain sizes; to evaluate the so-called sample fractal dimension which is concerned to the sample geometry; to define superstructure features within the sample [1].

The SAXS spectra of two UDD samples and an organic LB film have been measured and analyzed. Figure 1 represents the SAXS data for an UDD specimen.

Analysis of the obtained SAXS data has shown grains of sizes up to 40–50 nm to be observed in the both specimens. Also, SAXS data intervals corresponding to fractal dimension values between 1 and 2 have been found for the both samples, that being a characteristic of linear and planar atomic structures. Particularly, onion grain coatings may influence SAXS data in this way. Finally, the SAXS spectrum shown at Fig. 1 has a wide peak which has been decomposed into several Bragg peaks corresponding to superlattice interplanar distances approximately equal to 5, 6.5, 9, and 14.5 nm. Another SAXS data set has yielded a periodic structure with interplanar distances about 130–170 nm.

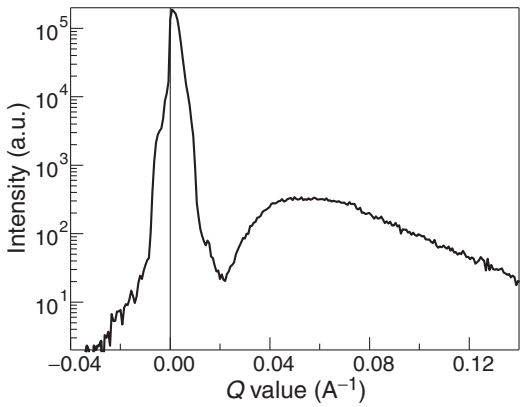

Fig. 1. SAXS measurement data for an UDD sample.

The LB film SAXS spectrum has been proven to contain several separate Bragg peaks surrounded by less intensive peaks called satellite ones. Hence the number of film layers as well as their thickness may be estimated. The considered sample has happened to include 10 layers each of intrinsic width about 6 nm.

2. EXAFS analysis

The new EXAFS spectrum analysis technique is developed [2,3].

It is assumed that EXAFS oscillations are extracted by the method based on the variation principle. The idea to extract the spectrum oscillations is to suggest a functional which is minimized by the sought smooth EXAFS component [3]. The view of the appropriate Euler–Lagrange equation is

$$\left(\frac{d^2}{dE^2} - C^2\right)\mu_0 = C^2(A - \mu)$$

with two parameters A and C. The boundary conditions of the first type are input for the task to be unambiguous.

In our earlier works, a crude estimation for the both EXAFS Fourier window limits was assumed [2,4] basing on the dependence of EXAFS treatment results on these limits for some metal spectra (V, Cr, Co, Cu). Now, a procedure to define immediately the Fourier window limits has been suggested.

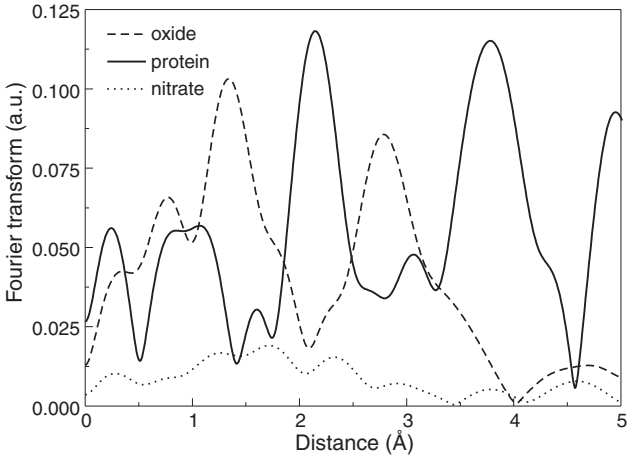

Fig. 2. FT of Cu K edge EXAFS for ceruloplasmin sample. Also the FT of Cu_2O and $Cu(NO_3)_2$ [6] are shown.

Particularly, the human protein ceruloplasmin EXAFS spectrum has been treated by the described method. The protein molecule is known [5] to contain several thousands of atoms, and only 6 Cu within them. Nevertheless, the spectrum was obtained at the STAR lab device (Samsung Inc., Suwon, South Korea). Fig. 2 represents the results of EXAFS analysis for this spectrum.

The comparison of the Fourier transformed EXAFS for the protein, oxide, and nitrate allows one to formulate a hypothesis that the closest neighbors of Cu atoms in the protein matrix are possible to be anions with the filled external electron shell (i.e. O^{2-}, S^{2-}). The hypothesis [6] about the triangle of three Cu atoms with edges about 0.4 nm also seems to be valid.

Acknowledgements

This work is dedicated to the memory of Dr. Konstantin Pogrebitsky.

We are grateful to Dr. Yu. N. Yuriev and Dr. Y. K. Cho (KRISS Institute, Taejon, South Korea) for measuring the human protein ceruloplasmin Cu K edge EXAFS spectrum for this work.

References

[1] M.E. Boiko, K.Ju. Pogrebitsky, M.D. Sharkov, A.P. Morovov, M.G. Vasin. *Proc. of the 8th PPXRD*, Glasgow, UK, 2009; M.E. Boiko, *Proc. of the XI International Conference on Small-Angle Scattering*, Upton, NY, USA, 1999.

[2] K.Ju. Pogrebitsky, M.D. Sharkov. *Semicond.* **44**, No. 7, 723 (2010).

[3] M.D. Sharkov, K.Ju. Pogrebitsky, S.G. Konnikov. *Tech. Phys.* **52**, No. 8, 1089 (2007).

[4] M.D. Sharkov, K.Ju. Pogrebitsky, M.E. Boiko. *Proc. of the Advanced Research Workshop "NanoPiter-2010"*, SPb, Russia, 2010.

[5] P. Bielli, L. Calabrese. *Cell. Mol. Life Sci.* **59**, 1413 (2002).

[6] G. Martens, P. Rabe, N. Schwentner, A. Werner. *Phys. Rev. B* **17**, 1481 (1978).

20th Int. Symp. "Nanostructures: Physics and Technology"
Nizhny Novgorod, Russia, June 24–30, 2012

Scanning tunnelling spectroscopy of silicene on highly oriented pyrolitic graphite

A. I. Mashin[1], A. V. Nezhdanov[1], *D. O. Filatov*[2] and D. A. Antonov[1]

[1] N.I. Lobachevskii University of Nizhny Novgorod, 603095 Nizhny Novgorod, Russia
[2] Research Physical-Technical Institute of the Nizhny Novgorod State University, 603950 Nizhny Novgorod, Russia

Abstract. Scanning tunnelling spectroscopy (STS) has been applied to the investigation of the local density of states (LDOS) in the epitaxial silicene on highly oriented pyrolitic graphite (HOPG) for the first time. The filled-states and the free-states STS images with the atomic spatial resolution as well as the tunnel spectra reflecting the electronic structure of silicene nave been obtained. The Si atoms in the epitaxial silicene/HOPG have been found to be in the sp^2-hybridization states.

Introduction

Recently, an increasing interest to silicene, which is the silicon ananlogue of graphene arised [1]. However, unlike carbon, silicon is not available in the graphite-like form. Therefore, in order to obtain the signle sheet graphene like Si layers, an approach based on using various substrates as the templates for the epitaxial growth to make Si atoms to arrange in the two-dimensional honeycomb lattice, has been being developed in recent years. For instance, scanning tunnelling microscopy (STM) studies of the epitaxial silicene on Ag(111) [2] and on on Ag(110) [3] have been reported. However, no Scanning Tunnelling Spectroscopy (STS) studies of silicene have been reported yet. So far, the electronic structure of silicene still remains unrevealed experimentally.

In Ref. [4] we have reported on the growth of the Si monolayers on highly oriented pyrolitic graphite (HOPG) by Molecular Beam Epitaxy (MBE) for the first time. The STM studies have demonstrated the Si atoms in the single-layered films to be arranged in the same lattice as the carbon atoms on the HOPG surface.

Here we report on the first-time investigation of the Local Density of States (LDOS) in the silicene on HOPG by STS. The filled-states and the free-states STS images with the atomic spatial resolution as well as the tunnel spectra reflecting the electronic structure of silicene nave been obtained. The Si atoms in the epitaxial silicene/HOPG have been demonstrated to be in the sp^2-hybridization states.

1. Experimental

The samples for investigation have been grown using Omicron Multi Probe RM ultrahigh vacuum (UHV) setup. Si was deposited at room temperature onto the freshly cleaved HOPG substrates from Omicron EFM-3 E-beam evaporator. More details on the growth and characterization of the Si/HOPG samples can be found in Ref. [4].

The STM/STS investigations have been carried out *in situ* using Omicron UHV AFM/STM LF1 scanning tunneling/atomic force microscope at room temperature. The STM probes from Pt-Ir wire were sharpened by cutting. The STS images were acquired by measuring the I-V curves of the tip-to-sample contact in every point of the scan.

2. Results and discussion

The STS images of HOPG used as a reference [Figs. 1a and b, respectively] demonstrated well known rhombic lattice pattern originating from the AB-stacking in graphite. Due to the AB-stacking, only three atoms of the six ones in the honeycomb cell are seen in the STS images. In contrary, in the STS images of silicene [Figs. 1c and d] all Si atoms are seen, like in the STM images of graphene [5] that can be explained by the absence of the AB-stacking in the case of silicene.

The filled-states images of the Si atoms [Fig. 1d] have nearly triangular shape. The same pattern has been observed in the

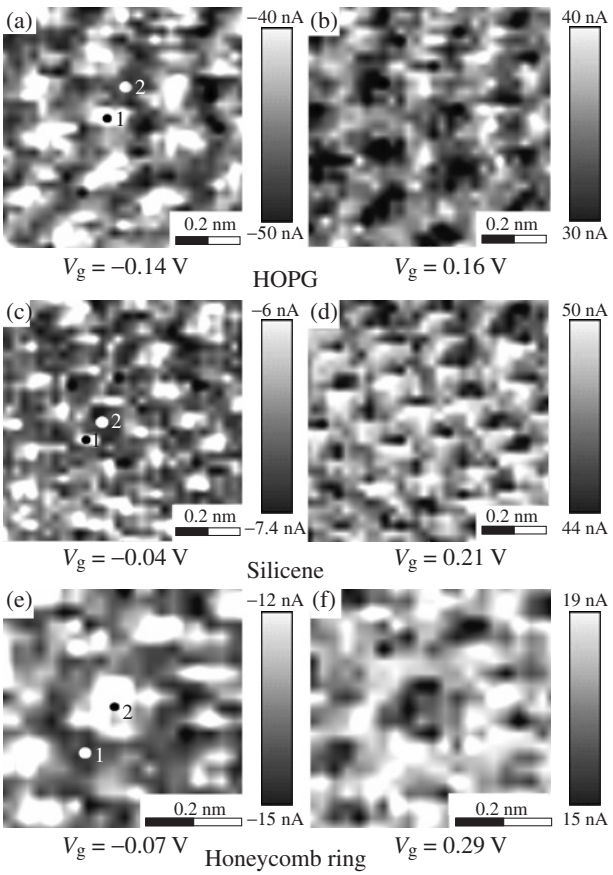

Fig. 1. Free states (a,c,e) and filled states (b,d,f) STS images of The HOPG surface (a,b), of the silicene layer (c,d), and of the honeycomb Si structure (e,f). The figures (1) and (2) denote the points of measurement of the tunnel spectra shown in Fig. 2.

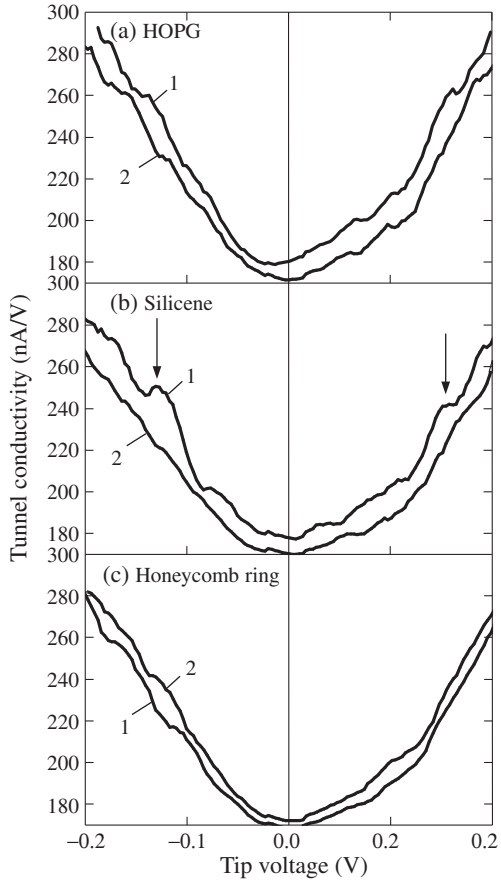

Fig. 2. The differential tunnel conductivity spectra of the tip contact to the HOPG surface (a), to the silicene layer (b), and to the honeycomb Si structure (c). The curve numbers correspond to the points of measurement of the tunnel spectra in Fig. 1.

filled-states STM images of the carbon atoms in graphene [5]. At present, two principal models of the structure of the single layer Si sheets are considered in the theoretical simulations: i) silicene that is full analogue of graphene, and ii) Si(111) layer as in bulk Si [1,6]. Both structures produce the honeycomb patterns. However, in silicene the Si atoms are in the sp^2-hybridization state while in Si(111) structures they are in the sp^3-hybridization one. The triangular pattern of LDOS is a characteristic one for the sp^2 hybridization state while in the Si(111) structure this pattern is valid for the "downbound" Si atoms only. In the latter case, we come back to the rhombic pattern of the STM image again. So far, one can conclude that the Si atoms in silicene/HOPG are likely in the sp^2-hybridization state.

On the other hand, the theoretical calculations have predicted the sp^3-hybridization state of Si atoms in the single layer Si sheets [i.e. Si(111) structure] rather than the sp^2-hybridization one due to the stability reasons [1,6]. However, these calculations were concerned on the free-standing Si films while in the structures studied in the present work the silicene islands were lattice-matched to the HOPG substrate [4]. Probably, the interaction with the HOPG substrate makes the Si atoms to take the sp^2 hybridization state.

In Figs. 2a and b, the differential conductivity spectra of HOPG and silecene, respectively are presented. The spectra have been obtained by the numerical differentiation of the measured I-V curves with the nonlinear smoothing. The tunnel spectra demonstrated the electronic properties of the Si atoms in silicene/HOPG to differ from the ones of the carbon atoms on the HOPG surface [notice, for example, the peaks on curve 1 in Fig. 2b marked by the arrows].

Besides the silicene islands, some areas covered by Si atoms arranged into an unusual honeycomb lattice have been observed on the HOPG substrate [4]. In this lattice, the Si atoms are arranged in the honeycomb rings surrounding the missed Si atom in the center of the ring so that the carbon atoms in the underlying surface HOPG layer are seen in these places [Figs. 1e and f]. The formation of such structure has been attributed to the extremely high compressive strain in the complete epitaxial silicene/HOPG layer so that the formation of the lattice with missed Si atoms would favor the strain relaxation. Although the LDoS pattern of the Si atoms in the honeycomb rings were similar to those of the Si ones in silicene their tunnel spectra were different [cf. Figs. 2b and c] that could be explained by less stain in the former case. Note that Si surrounding affect the electronic properties of the carbon atoms in the centers of the rings [cf. curve 2 in Fig. 2c and curve 1 in Fig. 2a].

3. Conclusions

The results of the present study demonstrate the electronic structure of epitaxial silicene/HOPG to be generally similar to the ones of graphene. The triangular pattern of the filled-states STS images of the Si atoms points to the sp^2-hybridization state of the Si atoms in the epitaxial silicene/HOPG that has been attributed to the effect of the substrate.

Acknowledgements

The authors gratefully acknowledge the financial support by Russian Foundation for Basic Research (09-02-01365-a).

References

[1] G. G. Guzmán-Verri and L. C. Lew Yan Voon, *Phys. Rev. B* **76**, 075131 (2007).
[2] B. Lalmi, H. Oughaddou, H. Enriquez, A. Kara, S. Vizzini, B. Ealet and B. Aufray, *Appl. Phys. Lett.* **97**, 223109 (2010).
[3] P. D. Padova, C. Quaresima, C. Ottaviani, P. M. Sheverdyaeva, P. Moras, C. Carbone, D. Topwal, B. Olivieri, A. Kara, H. Oughaddou, B. Aufray and G. L. Lay, *Appl. Phys. Lett* **96**, 261905 (2010).
[4] A. V. Nezhdanov, D. O. Filatov, D. A. Antonov, S. Yu. Zubkov, A. I. Mashin and A. V. Ershov, *Semicond.* **45**, 56 (2011).
[5] S. H. Rhim, Y. Qi, G. F. Sun, Y. Liu, M. Weinert and L. Li, *Phys. Rev. B* **84**, 125425 (2011).
[6] S. Cahangirov, M. Topsakal, E. Aktürk, H. Sahin and S. Ciraci, *Phys. Rev. Lett.* **102**, 236804 (2009).

20th Int. Symp. "Nanostructures: Physics and Technology"
Nizhny Novgorod, Russia, June 24–30, 2012

Surface conductivity of (Au,Ag)/Si(111) submonolayer films

D. A. Tsukanov[1,2], M. V. Ryzhkova[1], D. V. Gruznev[1,2], A. V. Matetsky[1], L. V. Bondarenko[1], E. A. Borisenko[1], A. V. Zotov[1,2] and A. A. Saranin[1,2]

[1] Institute for Automation and Control Processes FEB RAS, 690041 Vladivostok, Russia
[2] Far Eastern Federal University, 690000 Vladivostok, Russia

Abstract. The surface structure and the electrical conductance of the (Au,Ag)/Si(111) two-dimensional system have been studied with low-energy electron diffraction (LEED), scanning tunneling microscopy (STM) and four-point probe method *in situ*. It has been found that the early unpublished Si(111)$\sqrt{93} \times \sqrt{93}$-(Au,Ag) structure forms at 350 °C. The electrical conductance of the Si(111)$\sqrt{93} \times \sqrt{93}$-(Au,Ag) is higher then that for the Si(111)$\alpha - \sqrt{3} \times \sqrt{3}$-Au surface phase. The changes in electrical conductance of the substrate surface during its structural transformations from $\alpha - \sqrt{3} \times \sqrt{3}$-Au to $\sqrt{93} \times \sqrt{93}$-(Au,Ag) and finally to $\sqrt{21} \times \sqrt{21}$-(Au,Ag) and after silver deposition on the corresponding surfaces have been measured at room temperature. The possible factors influencing the surface conductivity are discussed.

Introduction

Recently the phase transitions have attracted both experimental and theoretical interest in surface physics. Many studies focus on phase transitions on two- and one-dimensional systems and possible occurrence of a metal-to-semiconductor transition that can be promising for the future application in nanoelectronics. Usually there are two ways to cause such transition, one is the temperature lowering of studied system and second — adding a small amount of adsorbate atoms. We note however that former is not suitable for the practical use and interesting only from fundamental point of view while last case is quite suitable for technologies on the base of molecular beam epitaxy. Reports in the literature [1–3] indicate that one of the outstanding candidates for this purpose is Ag and Au adsorbed two-dimensional system on the Si(111) surface.

A phase transition phenomenon is a good stimulus for the study of charge carrier transport due to the possibility to control the electrical properties in ultra-thin layers. A small amount of adsorbate atoms is enough to significantly change the nature of the layer, for example, from semiconductor to metallic. The transition from Si(111)$\sqrt{3} \times \sqrt{3}$-Ag, semiconducting surface to Si(111)$\sqrt{21} \times \sqrt{21}$-(Au,Ag), surface with metallic bands, is a very good illustration of such behavior [4].

In the present study, using low-energy electron diffraction, scanning tunneling microscopy and four-point probe measurements the changes in surface structure and conductivity were studied after silver adsorption onto the Au-induced Si(111) surface reconstructions.

1. Experimental

The experiments were performed in ultra-high-vacuum chamber with the base pressure in the $\sim 10^{-10}$ Torr range. The rectangular substrates were cut from standard $n-$type Si(111) wafers with resistivity 10 Ω cm (for STM study, size $12 \times 2 \times 0.45$ mm^2) and 45 Ω cm (for surface conductivity study, size $15 \times 5 \times 0.45$ mm^2). Atomically clean Si(111)7×7 surfaces were prepared *in situ* by flashing to 1280 °C after first outgassing the samples at 600 °C for several hours. Gold and silver were deposited from the Au- and Ag-wrapped tungsten filaments at a rate of 0.4 and 1.0 monolayer/minute, respectively (1 monolayer (ML) = 7.8×10^{14} atoms/cm^2). All STM images were acquired in a constant-current mode at room temperature. To characterize electrical properties of the grown (Au,Ag)/Si(111) structures, the sample conductivity $\sigma = I/V$ (where I is the applied current through a pair of adjacent probes and V is the voltage drop measured by another pair of probes) was measured in siemens (Sm) using square four-point probe method. The tungsten probes were situated in square cones of 0.6×0.6 mm^2 in size.

2. Results and discussions

Deposition of the atomic silver onto the sample with the $\alpha\sqrt{3}$-Au structure holding at 350 °C leads to the series of changes in the surface structure as observed by LEED. Formation of the surface structure that looks similar to a $\sqrt{93} \times \sqrt{93}$ one takes place after 0.1 ML of the silver dose evaporation onto heated substrate. But closer inspection of this surface by STM observations (Fig. 1) showed that $\alpha\sqrt{3}$-Au surface after 0.1 silver evaporation on it results in elimination the network of domain walls and formation of periodicity which was identified using Fourier transformation as two-domain $\sqrt{93} \times \sqrt{93}$. The possible unit cell expands at 21° with respect to 1×1 periodicity of initial surface and can be written as Si(111)$\sqrt{93} \times \sqrt{93}$-(Au,Ag)-R21°. Indeed, if comparing the LEED scheme of $\sqrt{39}$ and $\sqrt{93}$ structures it is seen that LEED pattern of the surface structure formed after Ag deposition onto $\alpha\sqrt{3}$-Au surface at 350 °C is in good agreement with $\sqrt{93} \times \sqrt{93}$ scheme, while $\sqrt{39} \times \sqrt{39}$ scheme in turn agrees better with ringlike diffraction of the $\beta - \sqrt{3} \times \sqrt{3}$-Au phase [5]. The further deposition leads to formation of the Si(111)$2\sqrt{3} \times 2\sqrt{3}$-(Au,Ag) (hereafter $2\sqrt{3}$-(Au,Ag)) surface phase and disappearance of regions with the $\sqrt{93}$-(Au,Ag) structure. At adsorbed of atomic silver over 0.3 ML only the $\sqrt{21}$-(Au,Ag) forms. According to [6] the $\sqrt{21}$-(Au,Ag) structure forms at total coverage of gold and silver about 1.1–1.2 ML that coincides with our estimation.

Fig. 2 shows the results of surface conductivity measurements of the (Au,Ag)/Si(111) system after silver deposition onto $\alpha - \sqrt{3}$-Au holding at 350°‘ and cooling down to RT in comparison with those after the silver deposition onto $\alpha - \sqrt{3}$-Au at RT. Initial conductivity of the sample with the $\alpha - \sqrt{3}$-Au reconstruction was 1.9 ± 0.2 mS. After formation of the Si(111)$\sqrt{39} \times \sqrt{39}$-(Au,Ag) reconstruction the sample conductivity increases up to 2.4 ± 0.1 mS. This is in a general consistency with LEED observations that show clear regular spots of $\sqrt{39} \times \sqrt{39}$ periodicity meaning the presence of the

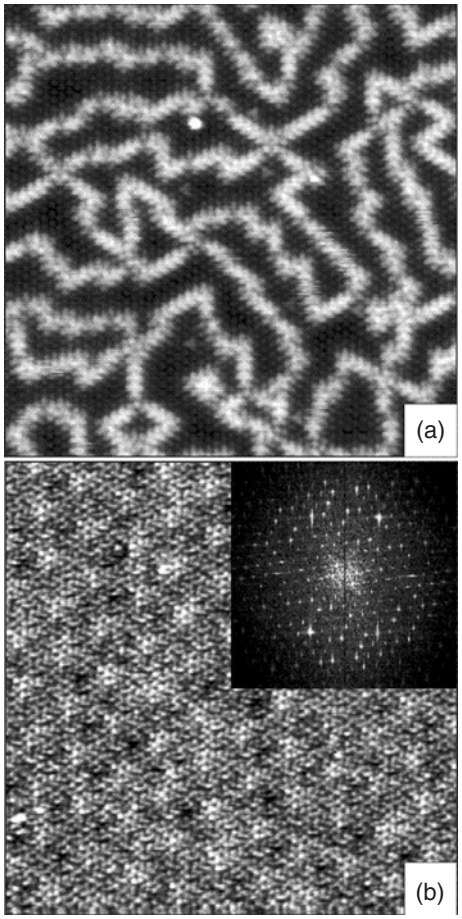

Fig. 1. 34×34 nm STM images of (a) Si(111)$\alpha-\sqrt{3}\times\sqrt{3}$-Au (1.4 V sample bias, 1 nA tunneling current) and (b) Si(111)$\sqrt{93}\times\sqrt{93}$-(Au,Ag)-R21° (0.5 V sample bias, 0.2 nA tunneling current) reconstructions. Insert shows Fourier-transformed image from $\sqrt{93}\times\sqrt{93}$-(Au,Ag) surface.

more regular structure in comparison with $\alpha-\sqrt{3}$-Au picture that contains streaks due to the domains walls inherent in this phase and confirmed by STM data (see Fig. 1). Effect of Ag adsorption onto the $\alpha-\sqrt{3}$-Au surface was argued to be twofold; directly doping electrons that change the space-charge layer or surface states properties and ordering the domain walls. Similar behavior was detected after the deposition of In atoms on the $\alpha-\sqrt{3}$-Au reconstruction accompanied by the elimination of the domain walls network and resulting in the increasing of surface conductance at about 0.7 ± 0.3 mS [7]. It is seen from Fig. 2 that the deposition of the silver at RT onto $\alpha-\sqrt{3}$-Au surface leads to minimum of surface conductance at silver coverage of about 0.2 ML due to depleted layer condition.

Ag-induced reconstruction from $\sqrt{93}\times\sqrt{93}$-(Au,Ag) to $2\sqrt{3}$-(Au,Ag) is accompanied with further increasing of conductance until only $2\sqrt{3}$-(Au,Ag) surface phase is formed. It results in surface conductance decreasing but after appearance of the $\sqrt{21}$ LEED spots the conductance increases again. The $\sqrt{21}$-(Au,Ag) surface phase has relatively high surface conductance because of the large contribution of the surface states in carrier transport [8]. It is well known that space-charge layer in subsurface region of $\sqrt{21}$-(Au,Ag) reconstruction is depleted. But in our case the deposition of silver at RT onto this reconstruction results in decreasing in conductance which shows the hole-accumulated conditions under $\sqrt{21}$-(Au,Ag) phase.

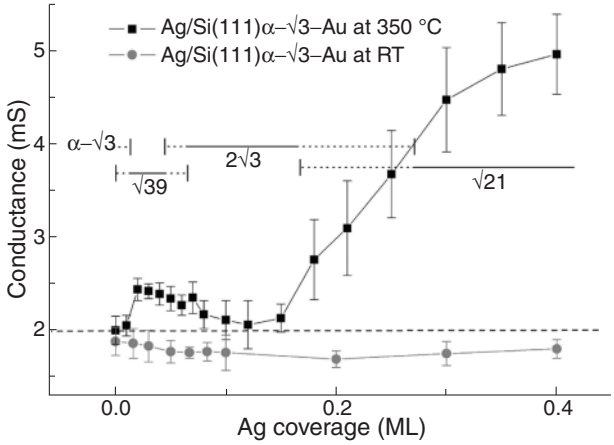

Fig. 2. The electrical conductance during the structural transitions after the deposition of atomic silver onto Si(111)$\alpha-\sqrt{3}\times\sqrt{3}$-Au surface holding at 350 °C and Si(111)$\alpha-\sqrt{3}\times\sqrt{3}$-Au surface at RT.

3. Conclusions

Using LEED, STM and four-point-probe method, we have studied surface structure and electrical conductance changes of binary noble metal adsorbed (Au,Ag)/Si(111) surface. The early unpublished Si(111)$\sqrt{93}\times\sqrt{93}$-(Au,Ag) surface phase has been obtained. It forms as a result of the deposition of 0.01–0.02 ML of silver onto the Si(111)$\alpha-\sqrt{3}\times\sqrt{3}$-Au surface phase at 350 °C. The changes in electrical conductance of Si(111) substrate during structural transformations from Si(111)$\sqrt{93}\times\sqrt{93}$-(Au,Ag) to Si(111)$2\sqrt{3}\times2\sqrt{3}$-(Au,Ag) and finally to Si(111)$\sqrt{21}\times\sqrt{21}$-(Au,Ag) have been studied.

Acknowledgements

This work was supported by the Russian Foundation for Basic Research (Grants Nos. 11-02-98516 and 12-02-00621) and the Ministry of Education and Science of the Russian Federation (Contracts Nos. P1284, 14.740.11.1230 and NSh-774.2012.2).

References

[1] Y. L. Gavrilyuk *et al.*, *Surf. Sci.* **297**, 345 (1993).
[2] A. Ichimiya *et al.*, *Surf. Rev. Lett.* **1**, 1 (1994).
[3] J. Nogami *et al.*, *Surf. Sci.* **306**, 81 (1994).
[4] S. Hasegawa *et al.*, *Prog. Surf. Sci.* **60**, 89 (1999).
[5] H. M. Zhang *et al.*, *Phys. Rev. B* **63**, 195402 (2001).
[6] I. Matsuda *et al.*, *Phys. Rev. B* **82**, 165330 (2010).
[7] D. V. Gruznev *et al.*, *Surf. Sci.* **605**, 1420 (2011).
[8] T. Hirahara *et al.*, *Phys. Rev. B* **73**, 235332 (2006).

20th Int. Symp. "Nanostructures: Physics and Technology"
Nizhny Novgorod, Russia, June 24–30, 2012

Growth of topological insulator Bi_2Te_3 thin films on Si (111) substrates by MBE

S. Borisova[1], J. Krumrain[1], G. Mussler[1], M. Luysberg[2] and D. Grützmacher[1]

[1] Peter Grünberg Institut - 9 & JARA - Fundamentals of Future Information Technology, Forschungszentrum Jülich, 52425, Germany
[2] Peter Grünberg Institut - 5 & Ernst Ruska-Centrum für Mikroskopie und Spektroskopie mit Elektronen, Forschungszentrum Jülich, 52425, Germany

Abstract. Topological insulator Bi_2Te_3 films have been grown by molecular beam epitaxy on Si (111) substrates. The evolution of the surface morphology during the growth has been investigated by in-situ scanning tunneling microscopy (STM). The growth starts by a nucleation of separate islands and subsequently turns into a layer-by-layer growth mode. Despite this, the grown film is found to be single crystalline and fully relaxed from the first atomic layer.

Introduction

Growth of thin films of complex layered materials attracts considerable attention for understanding of fundamental phenomena as well as due to a variety of their potential applications in electronics and spintronics. Although a number of hexagonal layered materials has been investigated in the last years, the new wave of the interest to thin films started few years ago motivated by a discovery and first measurements in graphene [1] and topological insulators (TI) [2]. Until now, preparation of ultra thin films of different layered materials from bulk crystals by exfoliation plays the most important role for investigation of their properties, in order to create effective devices based on the novel properties of the films. However, the development of a sustainable technology suitable for a technologically reproducible device production and offering the possibility to adjust their electronic properties will rely on a more advanced thin film technology. Molecular beam epitaxy (MBE) provides a high reproducibility in the film thickness at the atomic level, a high purity and a precise control of the doping. In this sense, growth of thin films of topological insulators on non-native Si substrates is quite promising.

Successful growth of high quality ultrathin films on non-native substrates with a large lattice mismatch via van der Waals epitaxy has been already demonstrated for different systems of layered materials [3,4]. Recently it has been shown that Bi_2Te_3 films can be successfully grown on Si (111) substrates by MBE via one-step approach [5], i.e. the film is deposited directly on Si, without a buffer layer growth. However, detailed understanding of nucleation and growth dynamics of Bi_2Te_3 films is completely missing thus far. Moreover, a direct access to the Si/Bi_2Te_3 interface may provide us with diverse information concerning the presence of strain in the films and the formation of the defects.

1. Experimental

TI Bi_2Te_3 films have been grown on n-type doped (3−6 Ω cm) Si (111) substrates by solid source MBE. The substrates were chemically cleaned in a H_2SO_4 **2:1** H_2O_2 solution for 10 min in an ultrasonic bath, and dipped in 5% hydrofluoric acid, which causes a H-passivation of the Si surface. Next, the substrates have been placed into the UHV MBE chamber and annealed at 700 °C for 10 minutes to desorb the H atoms from the surface.

The substrates have been overgrown at a constant substrate temperature of $T_S = 550$ °C in the Te overpressure regime [5]. The effusion cell temperatures are kept at $T_{Bi} = 500$ °C and $T_{Te} = 340$ °C, which corresponds to a Te/Bi partial pressure ratio in the MBE chamber of approximately 20. The thickness of deposited films is controlled by a variation of the growth time, whereas all other parameters are kept constant. The growth rate of Bi_2Te_3 is 0.14 nm/min. The base pressure in the chamber is 3×10^{-8} mbar and never exceeded 8×10^{-8} mbar during the film deposition.

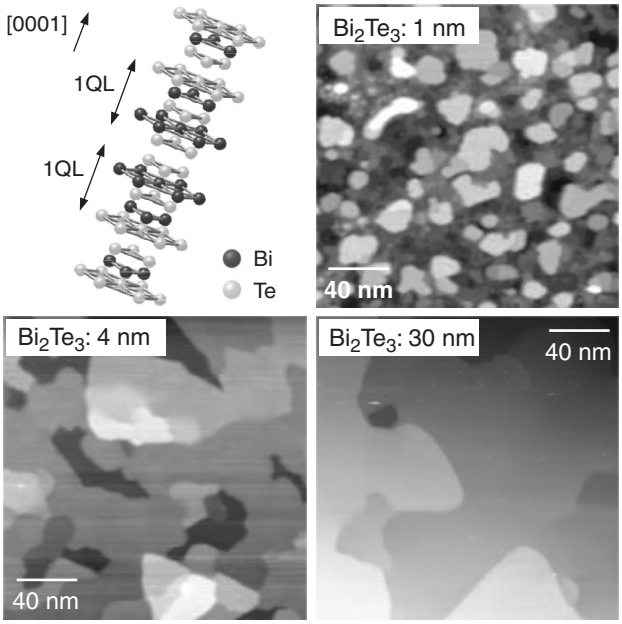

Fig. 1. A unit cell of Bi_2Te_3 consists of alternating hexagonal Bi and Te atom sheets. The unit cell consists of 3 QL, which are weakly bounded by van der Waals bonds. The lines connecting the atoms are depicted for convenience and have no physical sense. The atom bonds are not shown. The in-situ STM images represent the evolution of the surface morphology during the Bi_2Te_3 deposition for the film thickness of 1, 4 and 30 nm. Increasing the film thickness increases the width of the atomic terraces.

Directly after deposition, the samples have been transferred under UHV to the in-situ STM chamber (base pressure better than 1×10^{-10} mbar), and the measurements have been performed in the topography mode. The high resolution scanning transmission electron microscopy (STEM) measurements have

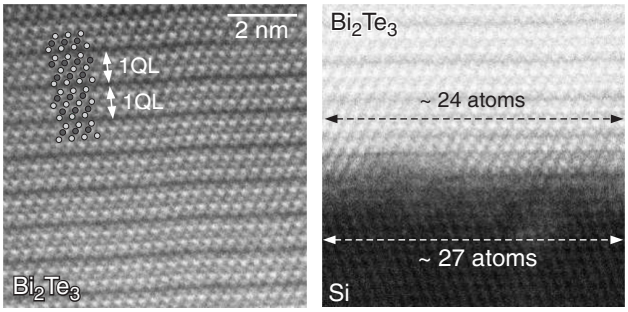

Fig. 2. High resolution STEM images of the MBE grown film in {110} projection of the Si substrate. In the left panel, the correspondent atomic model is represented. The right panel demonstrates the Si/Bi_2Te_3 interface. The slight amorphisation of the interface is due to the sample preparation by FIB.

been carried out at the FEI Titan 80-300 facility ex-situ, using specimen prepared by focused ion beam (FIB) processing.

2. Surface morphology during the growth

The unit cell of Bi_2Te_3 is represented in Fig. 1. The in-plane and out-of-plane lattice constants are $a = 4.38$ Å and $c = 30.51$ Å, respectively [6]. The unit cell consists of 3 quintuple layers (QL). The QLs possess no unoccupied atomic bonds at the surface and are bounded to each other by weak van der Waals interaction. The height of a QL is approximately 1 nm.

The growth of Bi_2Te_3 on Si (111) starts by a nucleation of separate islands, which turns into layer-by-layer growth mode with an increase of the film thickness (see Fig. 1). The STM images show that the film is single crystalline from the very beginning, and the growth takes place without the formation of an amorphous or polycrystalline layer. The surface defects (missing atoms, small holes, steps) at the Si surface probably serve as nuclei for the Bi_2Te_3 islands.

The average size of the atomic terraces is significantly different for the films with thicknesses of 4 and 30 nm. Moreover, the typical step height is 1 nm (i.e. 1 QL) for the 30 nm thick film, whereas the steps at the 4 nm thick film are mostly sub-QL steps. The sub-QL steps are related to the layers, which are thinner than 1 QL, and, hence, possess dangling bonds at the surface. A significant difference in the terrace width is observed, it is contributed to a higher adatom mobility at the QL surfaces, compared to the sub-QL surfaces. Indeed, the adatom mobility is strongly affected by the dangling bonds, which are present at the surface of a not completed QL. Besides the layer-by-layer growth in the sub-QL growth mode (4 nm), formation of the islands has also been observed. However, the density of the islands is two orders of magnitude lower than for the 1 nm film. In contrast, no islands are observed for the 30 nm thick film. Thus, the sticking of the adatoms at the step edges is preferable, and the QL growth is regarded as an equilibrium growth mode.

3. Atomic structure of the Bi_2Te_3 film

High resolution STEM measurements confirm a high crystal perfection of the Bi_2Te_3 film (see the left panel in Fig. 2). A model of the Bi_2Te_3 crystal structure in projection on the {110} plane of the substrate is shown as an overlay and matches to the imaged structure.

In [5] it was shown by X-rays diffraction (XRD) that the 30 nm thick Bi_2Te_3 film is fully relaxed in bulk. However, it remained unclear, whether there is any stress in the thin interface layer, due to its small contribution to the total signal. The Si/Bi_2Te_3 interface is imaged by STEM with atomic resolution (see the right panel in Fig. 2). The difference in the lattice constants of Si and Bi_2Te_3 measured directly at the interface is in accordance with the calculated lattice mismatch of them of 14%. Therefore, the Bi_2Te_3 is fully relaxed even from the first QL.

In Fig. 2 it is observed that the Si/Bi_2Te_3 interface has been slightly destroyed due to its amorphisation during the sample preparation. This evidences that the substrate and the film are only weakly bound. Indeed for STEM specimen of a fairly large thickness the observation of the amorphous interface is absent. The orientation of the Bi_2Te_3 film matches to the orientation of the Si substrate [5], which is typical for van der Waals epitaxy. The influence of dangling bonds of the Si substrate is eliminated by surface passivation with Te. Thus, we have found that the growth of Bi_2Te_3 films takes place via van der Waals epitaxy. In [4] only the layer-by-layer growth of hexagonal materials via van der Waals epitaxy is investigated on the substrates with the similar structure. These substrates possess wide atomically flat terraces and no dangling bonds at the surface. In contrast, the surface defects of the Si substrates and the strong bonds within an individual QL have a significant impact on the growth dynamics of the films.

In addition, the formation and the morphology of crystal defects such as twins, stacking faults and dislocations will be discussed.

References

[1] K.S. Novoselov, A.K. Geim, S.V. Morozov *et al*., *Nature* **438**, 197 (2005).
[2] D. Hsieh, D. Qian, L. Wray *et al*., *Nature* **452**, 970 (2008).
[3] A. Koma, K. Sunouchi, and T. Miyajima, *Microelectronic Engineering* **2**, 129 (1984).
[4] A. Koma, *J. Crystal Growth* **201/202**, 236 (1999).
[5] J. Krumrain, G. Mussler, S. Borisova *et al*., *J. Crystal Growth* **324**, 115 (2011).
[6] B. Y.-Y. Li, G. Wang, X.-G. Zhu *et al*., *Advanced Materials* **22**, 4002 (2010).

20th Int. Symp. "Nanostructures: Physics and Technology"
Nizhny Novgorod, Russia, June 24–30, 2012

Influence of shadow effect on the growth and shape of InAs nanowires

M. A. Timofeeva[1], N. V. Sibirev[1], M. Tchernycheva[2,3], J. Harmand[3] and V. G. Dubrovskii[1,4]

[1] St Petersburg Academic University, St Petersburg, Russia
[2] Institut d'Electronique Fondamentale, Universite Paris-Sud XI, F91405 Orsay, France
[3] CNRS-LPN, Route de Nozay, 91460 Marcoussis, France
[4] Ioffe Physical-Technical Institute, St Petersburg, Russia

Abstract. We report the influence of shadow effect originating from neighbor nanowires on the nanowire growth. The nanowire axial and radial growth rates and the nanowire shape are shown to be strongly dependent on the nanowire surface density and the direction of incident fluxes. Theoretical predictions are compared with the experimental shapes of InAs nanowires grown by the Au-catalyzed molecular beam epitaxy. In particular, the barrel-like shape observed in dense arrays of InAs nanowires is well described by the model. Very importantly, we show that the shadow effect helps to avoid radial growth and to preserve the cylindrical nanowire shape.

Introduction

One-dimensional nanostructures such as nanowires (NWs) have been extensively investigated for the unique electrical and optical size effects [1] and for possible use in nanoelectronics [2]. The shape of semiconductor NWs has a strong impact on their physical properties [3]. Numerous works have been devoted to theoretical and experimental studies of NW shape for different semiconductor materials, namely Ge [3], GaAs [1]. Most theoretical models for NW growth were developed either for isolated NWs completely neglecting the influence of neighbors [3,4], or assuming that neighbor NWs compete for the diffusion flux from the substrate surface [5]. However, these models fail to describe the growth of dense NW arrays. This is due to the shadowing of NW sidewalls, an effect which plays an important role when the incident angle of the deposition flux is not perpendicular to the surface. This effect may influence the NW radial growth rate as well as the rate of their elongation. A detailed analysis the influence of shadowing on the axial and radial growth rates is presented in this work.

1. Theoretical model

Our model takes into account the processes of NWs growth: direct impingment into the droplet and on the sidewalls with flux J, desorption and adsorption processes, diffusion of adsorbed atoms along the NW sidewalls to the droplet, and also the nucleation at the liquid-solid interface (axial growth of NWs), on the NW sidewalls (radial growth) and on the substrate surface (substrate growth). The NW shape can be then characterized by the radius $R(x, L(t))$ and the length $L(t)$, where x is the distance from the surface and t is the growth time. The points $x = 0$ and $x = L(t)$ correspond to the NW base and top, respectively. Radial growth rate can be described by a local function of the adatom concentration on the sidewalls nf following the expression [6]:

$$\frac{dR}{dt}(x, L) = I\left(n_f(x, L)\right)\Omega_s\,, \qquad (1)$$

where $I(n_f(x, L))$ is the nucleation rate and Ω_s is the elementary volume in the solid phase. The nucleation rate is a steep exponential function of adatom concentration:

$$I(n_f) = I_0 \exp\left(\Gamma \frac{n_f - n_m}{n_m}\right), \qquad (2)$$

where n_m is the maximum adatom concentration on the sidewalls, I_0 is the nucleation rate at this concentration, and Γ is the nucleation parameter which is approximately equal to the number of atoms in the critical nuclei and therefore is much larger than one. In order to find the axial growth rate, we use the material balance equation in the droplet in the form:

$$\frac{dL}{dt} = J\Omega_s \frac{1+\cos\alpha}{2} - 2\Omega_s D_f \frac{1}{R_d}\left.\frac{\partial n_f}{\partial x}\right|_{x=L}, \qquad (3)$$

where L — NW length, R_d — the droplet radius. To calculate the shadowing coefficient $s(y)$, we assume that the NWs are randomly distributed on the substrate. To calculate the coordinate-dependent concentration of sidewall adatoms, we use the standard system of equations and also we include the term describing the shadow effect.

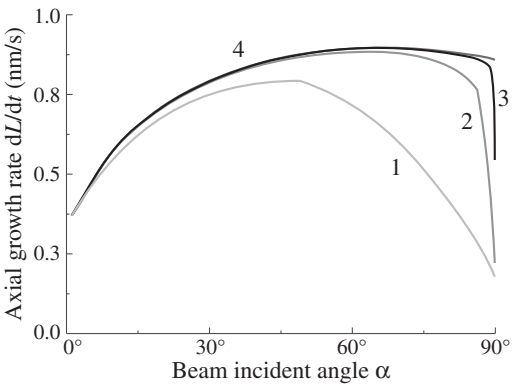

Fig. 1. Dependence of the axial growth rate on the incident angle at different NW densities: (1) $N = 10^{10}$ cm^{-2}, (2) $N = 10^9$ cm^{-2}, (3) $N = 10^8$ cm^{-2}, (4) $N = 10^6$ cm^{-2}.

2. Nanowires growth rate and shape

We describe the influence of NWs density and deposition flux angle on the NW growth rate and shape. Fig. 1 shows theoretical dependences of the axial growth rate on the incident angle for different NW densities. The obtained dependences of the axial growth rate on the NW density are presented in Fig. 2 for different incident angles of the impinging flux. Theoretical predictions have been compared with the experimentally observed NW shape in the case of dense arrays of InAs NWs obtained by MBE. A typical shape of NWs is shown in Fig. 3, along with the SEM image of the selected NW.

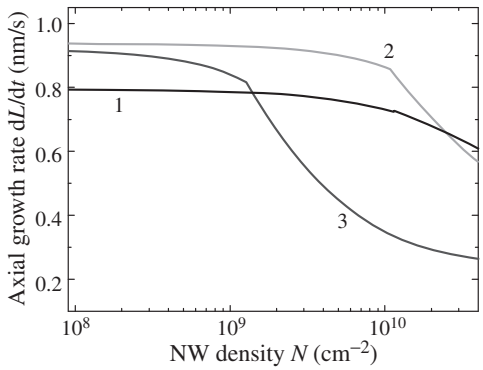

Fig. 2. Dependence of the axial growth rate on the NW density at different incident angles: (1) $\alpha = 16.7^\circ$, (2) $\alpha = 45^\circ$, (3) $\alpha = 85^\circ$ — to avoid break within formula.

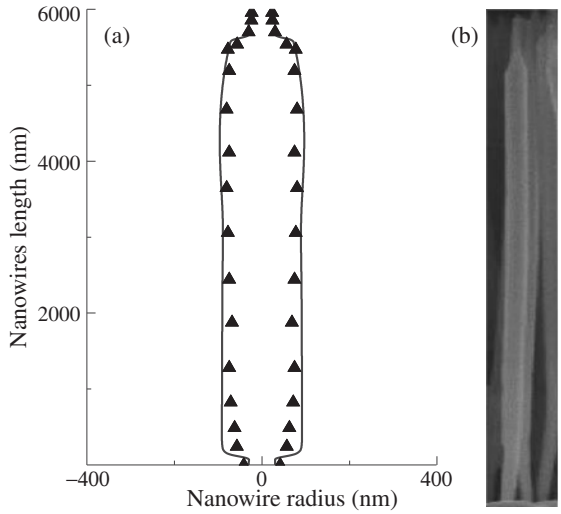

Fig. 3. (a) theoretical (solid line) and experimental (triangles) shape of the selected InAs NW. (b) SEM image of selected NW.

3. Conclusions

We have developed a theoretical model for the NW growth taking into account the shadowing effect. It is shown that for dense NW arrays and at large enough incident angles of the beam during molecular beam epitaxy, the NW axial growth rate is limited not only by the effective diffusion length of adatoms but also by the fact that a large part of a given NW is shadowed by its neighbors. This leads to the decrease of NW length compared to the case of widely spaced NWs. More importantly the shadow effect is very important in reducing the radial growth and thus helps to preserve the cylindrical NW shape by suppressing the material influx onto the shadowed areas of NW sidewalls.

Acknowledgements

This work was partially supported by the European FP7 Marie Curie PEOPLE projects FUNPROB and SOBONA, different grants of the Russian Foundation for Basic Research and different contracts with the Russian Ministry of Education and Science.

References

[1] K. Hiruma, M. Yazawa, K. Haraguchi, K. Ogawa, T. Katsuyama, M. Koguchi, H. Kakibayashi, *J. Appl. Phys.* **74**(5), 3163 (1993).

[2] S. A. Dayeh, D. P. R. Aplin, X. T. Zhou, P. K. L. Yu, E. T. Yu, D. L. Wang, *SMALL* **3**(2), 326 (2007).

[3] C. B. Jin, J. E. Yang, M. H. Jo, *Appl. Phys. Lett.* **88**, 193105 (2006).

[4] J. C. Harmand, G. Patriarche, N. Péré-Laperne, M.-N. Mérat-Combes, L. Travers, F. Glas, *Appl. Phys. Lett.* **87**, 203101 (2005).

[5] Y. Kim, H.J. Joyce, Q. Gao, P.P. Tan, C. Jagadish, M. Paladugu, J. Zou, A.A. Suvorova, *NanoLett.* **6(4)**, 599 (2006).

[6] D.L. Dheeraj, G. Patriarche, H. Zhou, J.C. Harmand, H. Weman, B.O. Fimland, *J. Cryst. Growth* **311**, 1847 (2009).

20th Int. Symp. "Nanostructures: Physics and Technology"
Nizhny Novgorod, Russia, June 24–30, 2012

Vacuum scanning microscopy and nanopatterning based on a hollow tip

A. P. Cherkun, B. N. Mironov, *S. A. Aseyev* and S. V. Chekalin
Institute of Spectroscopy, 142190 Troitsk, Russia

Abstract. For the study and possible nanomodification of a surface in vacuum we prepared a novel scanning microscope, which uses a dielectric microcapillary instead of traditional tip. A diameter of an aperture at the apex of such tip can be as low as 100 nm and even less than this value. A hollow tip allows us to create micro-beams of the ions or the electrons by passing the charged particles through the capillary. Also it can act as the probe of the scanning microscope.

Introduction

The study of the large organic molecules on a surface with spatial nano-resolution in combination with high element (chemical) selectivity represents fairly interesting problem. In order to resolve it we are developing the approach, in which the molecular ions after femtosecond laser desorption can be extracted through a microcapillary and then can be directed into a time-of-flight mass-spectrometer (Fig. 1). There are two advantages of the ultrafast desorption. At first, ultrashort laser irradiation makes it possible to carry out multiphoton processes without significant heating of a sample. It means, that spurious, or thermal desorption can be minimized. Secondly, femtosecond laser can allow study of the process with high temporal resolution. Below is the place for the first figure (30 mm in height).

1. Experimental

Below is the place for the second figure (30 mm in height).

In order to move a hollow nanotip along a surface with possible nanometer accuracy we designed and assembled a novel vacuum scanning microscope. It uses a home-made piezo-translator. Two photos of the microscope are given in Figs. 3,4. Here are: 1) a carriage of Z-module, 2) a rail of Z-module, 3) a base of Z-module, 4) XY — microscopic stage, 5) a module of XY — piezo-tube, 6) a tray, 7) a suspended load, 8) a ring

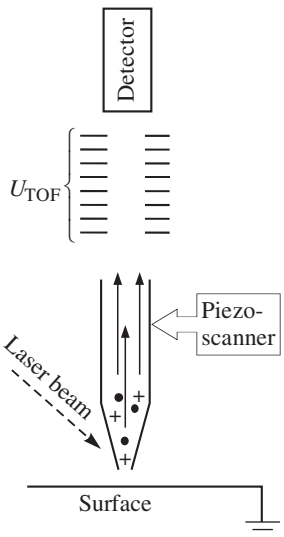

Fig. 1. The sketch of a 'nanoplane'. This approach is intended for a study of a surface with high spatio-elemental resolution. (Note, that the term 'nanoplane' has been introduced by Prof. V. S. Letokhov.)

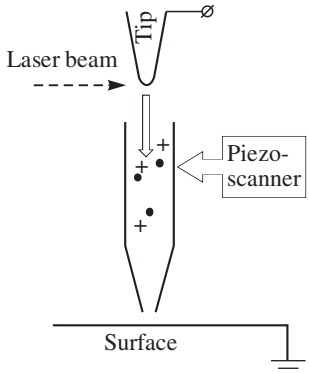

Fig. 2. The schematic of a 'nanopencil' for possible nanopatterning on a surface.

of the base of vibro-pendant, 9) sockets, 10) a head of XY — piezo-tube, 11) a body of tuning fork, 12) an assembly plate, 13) cables of tuning fork with sockets, 14) a capillary, 15) a sample, 16) a rotary-transmission cantilever mechanism, 17) a horn of tuning fork. In the experiments the microscope was located in vacuum. Below is the place for the third figure (30 mm in height).

Below is the place for the next figure (30 mm in height).

A vacuum chamber was pumped by a turbomolecular pump to a pressure of the order of 10^{-9} Pa. The femtosecond laser pulses were produced by the Spectra-Physics/Newport laser system with an amplifier Spitfire Pro, running at a repetition rate up to 1 kHz. Here we used linearly polarized light with a wavelength $\lambda \approx 0.8$ μm, pulse duration $\tau \approx 40$ fs and energy

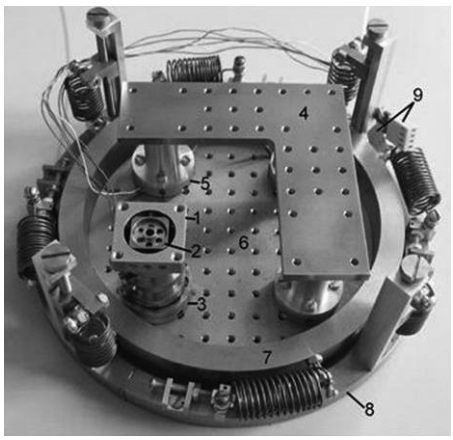

Fig. 3. The vacuum scanning microscope, designed and assembled at the Institute of Spectroscopy.

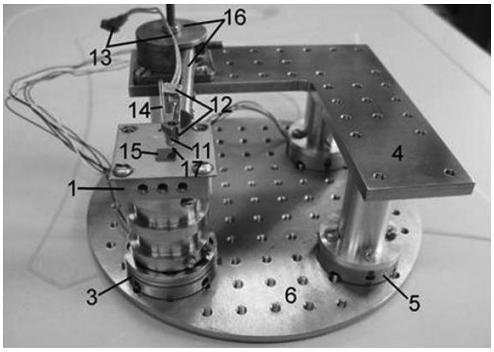

Fig. 4. The vacuum scanning microscope with hollow tip.

up to 0.5 mJ/pulse. The laser radiation was focused in the vacuum chamber by a lens.

2. Results

Using our scheme (Fig. 2) we created a micro-beam of Au-photoions and managed to produce a gold microstructure on a silicon surface. This was first successful demonstration of our approach. Also as by-product result it allowed us to determine a lifetime of hollow dielectric tip in the scanning mode.

Acknowledgements

This work has been supported in part by the Russian Fund for Basic Research, grants 11-02-00796 and 10-02-00469.

References

[1] M. P. Grams, A. M. Cook *et al*., *J. Phys. D: Appl. Phys.* **39**, 930 (2006).
[2] S. A. Aseyev, B. N. Mironov *et al*., *JETP Letters.* **87**, 361 (2008).

20th Int. Symp. "Nanostructures: Physics and Technology"
Nizhny Novgorod, Russia, June 24–30, 2012

Magnetic ordering in Co nanoparticle arrays on CaF_2(110) and MnF_2(110)

D. A. Baranov[1], S. V. Gastev[1], C. Rodrigo[2,3], J. L. F. Cuñado[2,3,4], P. Perna[3,4], F. Teran[2,3], A. Bollero[2,3], J. Camarero[2,3,4], L. Pasquali[5], V. V. Fedorov[1], S. M. Suturin[1], A. V. Nashchekin[1] and N. S. Sokolov[1]

[1] Ioffe Physical-Technical Institute, St Petersburg, Russia
[2] Instituto "Nicolas Cabrera", Universidad Autònoma de Madrid, 28049, Madrid, Spain
[3] Instituto Madrileño de Estudios Avanzados en Nanociencia (IMDEA-Nanociencia), Campus Universidad Autònoma de Madrid. 28049 Madrid, Spain
[4] Departamento de Fisica de la Materia Condensada, Universidad Autònoma de Madrid, 28049, Madrid, Spain
[5] University of Modena, Italy Department of Materials Engineering

Introduction

Further progress in magnetic data storage devices requires a deeper understanding of the physical nature of phenomena occurring in ordered systems of magnetic nanoparticles. An interesting possibility of fabrication of ordered cobalt nanoparticle arrays has been demonstrated in [1,2], where grooved and ridged CaF_2(110) surface has been used as an anisotropic template. It was later shown that dense Co arrays grown on this surface can demonstrate considerable magnetic anisotropy [3,4]. Magnetic nanoparticle arrays on antiferromagnetic substrates are very attractive because of possibility of overcoming superparamagnetic limit [5] as well as important application of ferromagnet-antiferromagnet he-terostructures in spin valves [6]. In this paper, comparative study of magnetic anisotropy in Co/MnF_2(110) and Co/CaF_2(110) heterostructures has been carried out using magnetooptical Kerr effect (MOKE) measurements at room temperature.

1. Experimental

As it was shown earlier [7], the interaction of CaF_2 molecules with Si(001) surface at the temperatures higher than 650 °C results in formation of the wetting layer, which initiates subsequent growth of CaF_2(110) layer with running along [1$\bar{1}$0] direction grooves and ridges. Their characteristic width depends on the growth temperature. In present work, after the wetting layer formation, growth of main CaF_2(110) layer was performed at relatively low temperature (450 °C). As the result, the characteristic size of the ridges was about 5 nm, which is significantly smaller than their average size in samples studied previously [4]. After that, MnF_2 epitaxial layer in metastable orthorhombic phase [8] was grown on the half of the structure with use of a shutter. During the growth, the MnF_2 layer inherited the main crystallographic directions of CaF_2 and also showed similar corrugated surface. Then, the whole area of structure was covered at room temperature by 2–5 nm thick metallic cobalt layer. Finally, to prevent Co oxidation, the structure was covered by 3 nm thick protective CaF_2 layer. AFM and SEM-images do not show any significant difference in size and arrangement of Co particles on MnF_2 and CaF_2 grown during one epitaxial procedure. In present work, magnetic properties measurements of CaF_2/Co/MnF_2/CaF_2/Si(001) and CaF_2/Co/CaF_2/Si(001) heterostructures were performed by vectorial MOKE. The main feature of the experimental method used in this study is the possibility of simultaneous measurements of both (longitudinal and transversal) magnetization components. It provides valuable information on magnetization vector rotation in plane of the sample. Special attention was paid to the shapes of the initial magnetization curves and hysteresis loops. These measurements enabled investigation of microscopic mechanisms of magnetization reversal in studied structures.

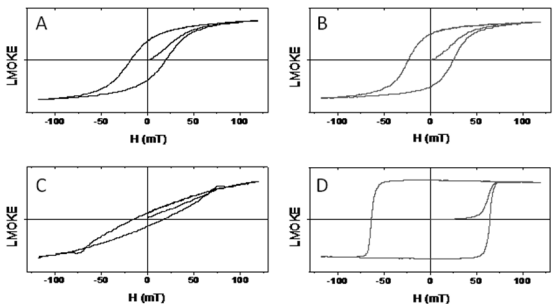

Fig. 1. Hysteresis loops and IM curves for Co/CaF_2 (a,b) and Co/MnF_2 (c,d) for magnetic field parallel to the fluoride ridges — (b,d) and almost perpendicular to the ridges ($\phi = 82^\circ$) — (a,c).

2. Results and discussion

The hysteresis loops and the initial magnetization (IM) curves of Co nanoparticle arrays on CaF_2 and MnF_2 for magnetic field orientations along and across the ridges are shown in Fig. 1. One can notice that the magnetic anisotropy of Co/CaF_2 structures is not so large. The shapes of hysteresis loops at the field directions along and across the ridges are almost identical, and only the coercivities vary. In case of H parallel to the ridges, H_c is approximately twice larger than that for the orthogonal direction. The IM curves for this structure (see Fig. 1a,b) begin from almost linear dependence on the magnetic field applied, then saturate at higher fields. Thus the shape of this curve is almost independent on the magnetic field orientation. There are significant differences observed in the Co/MnF_2 structures. First of all, the shapes of the hysteresis loops are different for H along and across the MnF_2(110) ridges. In the former case it has a rectangular shape, but for the latter case the loop is closed. The IM curves are shown at the same graphs of Fig. 1. While in case of Co/MnF_2 (Fig. 1c) when H orthogonal to the corrugation this dependence is in principle the same as observed on Co/CaF_2 (Fig. 1a), the parallel orientation of the corrugation and magnetic field gives an

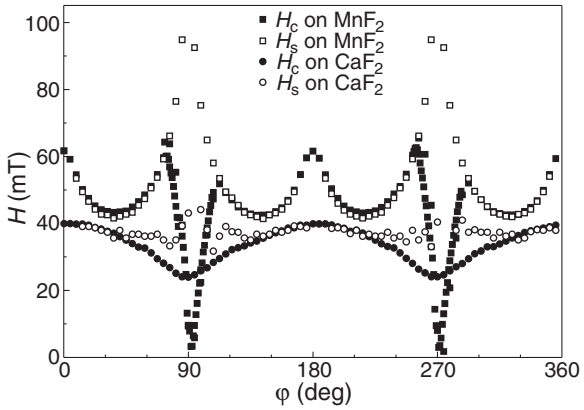

Fig. 2. Dependencies of coercivity H_c and switching field H_s on angle ϕ between direction of ridges and magnetic field H for Co/CaF_2 (circles) and Co/MnF_2 (squares).

entirely different IM curve. On the contrary when H is parallel to the corrugation (Fig. 1d) full magnetization of the Co/MnF_2 remains close to zero until the field reaches about 2/3 of H_c and then during the further increase of the magnetic field it saturates quickly. This behaviour is usually observed when the system has strong uniaxial anisotropy. Thus one can see that the magnetic anisotropy of cobalt arrays on MnF_2 is much stronger than on CaF_2. The orientational dependences of H_c and H_s for Co/CaF_2 and Co/MnF_2 shown in Fig. 2 also confirm this difference. One can see that Co/CaF_2 minima of H_c at the angles are close to the 90 and 270°, have smooth shape and relatively shallow. However, one can see, that the minima at H_c curves for MnF_2 are much sharper and deeper. Moreover additional minima can be observed at about 40, 140, 210 and 320°. The anisotropy value can be naturally determined as: $A = (H_{c\parallel} - H_{c\perp})/(H_{c\parallel} + H_{c\perp})$. For Co arrays on CaF_2 and MnF_2 with effective 4 nm coverage it gives A=0.29 and 0.89 correspondingly. Presented in Fig. 2 angular dependences of switching field H_s show quite small Co anisotropy on CaF_2 but on the contrary, for Co/MnF_2 structure H_s shows strong peaks near to 90 and 270° as well as weaker maxima near 0 and 180°. This indicates that the magnetization process corresponds to the domain wall propagation. It should be noted that such a distinction in magnetic properties between Co arrays on CaF_2 and MnF_2 remains also for the samples with different Co coverage. The values of the magnetic anisotropy for all the samples in this series are listed in the table. The table shows that the decrease of Co effective coverage from 5 to 3 nm results in decrease of magnetic anisotropies values (excepting A_{MnF_2} in 5615). However for 2 nm of Co on MnF_2 the anisotropy remains high, so far for all the samples in the series the ratio A_{MnF_2}/A_{CaF_2} is increasing with the decrease of Co coverage. This indicates the significant role of MnF_2 in the magnetic anisotropy enhancement even at the temperatures much higher than the Neel temperature of MnF_2 (67 K). Particular features of the hysteresis loop shapes and IM curves described above could be explained by following magnetic structure features: Co nanoparticles on MnF_2 form elongated along the corrugation direction single domain magnetic clusters. Magnetization reversal in each cluster occurs by the nucleation of one small domain oriented along the external magnetic field with subsequent enlargement of this domain. However it does not occur with the field orientation across the corrugation. Also in this case the IM curve indicates gradual reversal of the magnetization vector. On the contrary, Co nanoparticle arrays on CaF_2, can be described in the framework of the Stoner–Wohlfarth model i.e. the coherent rotation of the magnetisation for the single domain particles with the uniaxial anisotropy and presence of easy axes direction dispersion [4].

Table 1. Magnetic anisotropy values.

Sample	Co (nm)	A_{CaF_2}	A_{MnF_2}	A_{MnF_2}/A_{CaF_2}
5615	5	0.34	0.48	1.4
5677	4	0.29	0.89	3.1
5655	3	0.10	0.60	6
5676	2	—	0.50	—

3. Conclusion

Magnetic properties of cobalt nanoparticle arrays on MnF_2 (110) and CaF_2(110) with different (2–5 nm) coverage were studied by vectorial MOKE method. All samples showed much stronger interaction between Co nanoparticles in case when they are formed on manganese fluoride surface. As a result of this interaction, formation of the elongated Co magnetic domains on the MnF_2(110) surface takes place. At the same time, such domains are not present on the neighbouring part of the same structure in which Co particles are formed on CaF_2(110) layer.

Acknowledgements

This work was supported by ONDA project FP7-PEOPLE-2009-IRSES-247518, as well as by the Ministry of the Education and Science of the Russian Federation under contract No. 16.513.11.3095. The authors appreciate stimulating discussions with J. Nogues and B. B. Krichevtsov.

References

[1] N. Yakovlev *et al.*, *Current Applied Physics* **6**, 575 (2006).
[2] L. Pasquali *et al.*, *Surf. Sci.* **600**, 4170 (2006).
[3] B. B. Krichevtsov *et al.*, *Physics of the Solid State* **49**, 1481 (2007).
[4] B. B. Krichevtsov *et al.*, *Physics of the Solid State* **51**, 118 (2009).
[5] Skumryev *et al.*, *Nature* **423**, 850 (2003).
[6] Bae Seongtae *et al.*, Spin Valves in Spintronics Applications: Materials, Device Applications, and Electrical, VDM Verlag Dr. Müller, ISBN: 978-3639234794.
[7] N. S. Sokolov *et al.*, *Applied Surface Science* **234**, 480 (2004).
[8] A. K. Kaveev *et al.*, *Journ. Appl. Phys.* **98**, 013519 (1–8) (2007).

20th Int. Symp. "Nanostructures: Physics and Technology"
Nizhny Novgorod, Russia, June 24–30, 2012

Ballistic electron emission microscopy of $Ni_xSi_{1-x}/HfO_2/Si$ metal-oxide-semiconductor stacks

D. O. Filatov[1], M. A. Isakov[1], S. V. Tikhov[2], A. V. Zenkevich[3] and Yu. Yu. Lebedinskii[3]

[1] Research Physical-Technical Institute of the Nizhny Novgorod State University, 603950 Nizhny Novgorod, Russia
[2] Physics Department, N.I. Lobachevsky University of Nizhny Novgorod, 603950 Nizhny Novgorod, Russia
[3] NRNU Moscow Engineering Physics Institute, 115409 Moscow, Russia

Abstract. Ballistic electron emission microscopy/spectroscopy (BEEM/BEEs) has been applied for the first time to the investigation of the HfO_2/n-Si(001) based metal-oxide-semiconductor (MOS) stacks with the gates from the non-stoichiometric compounds Ni_xSi_{1-x} ($x = 0.33-1$) deposited by Pulsed Laser Deposition (PLD). The energy barrier height at the Ni_xSi_{1-x}/HfO_2 interface has been measured as a function of x.

Introduction

For decades, the improvement of the metal-oxide-semiconductor field eeffect transistors (MOSFETs) has been based on the scaling of their sizes, in particular, of the gate dielectric thickness [1]. At some point, further scaling of the MOSFETs based on the traditional SiO_2/Si stacks had approached the fundamental limits [2]. The replacement of SiO_2 by *high-*κ dielectrics as well as of the *poly*-Si gates by the metal ones had become inevtiable and has been implemented several years ago [3]. HfO_2 based dielectrics has been incorporated into CMOS technology, and nickel silicide is used as a gate material, while the band alignment in the n- and p-type Si based MOS stacks is controlled by the marker layers of ternary oxides placed at dielectric/Si interface [4]. Nevertheless, the development of the methodology to analyze the band alignment at the metal/dielectric interface is still of interest, to control the band diagram of the MOS stacks and ultimately to functionalize the metal/dielectric interfaces for both logic and memory applications.

The use of the non-stoichiometric Ni_xSi_{1-x} compounds for the metal gates is expected to allow controlling the electron workfunction of the gate material and, therefore, the band diagram of the MOS stacks [5]. In the present work we have applied Ballistic electron emission microscopy/ spectroscopy (BEEM/BEES) to measure the potential barrier height at the Ni_xSi_{1-x}/HfO_2 interface ΔE (Fig. 1) in the $Ni_xSi_{1-x}/HfO_2/n$-Si MOS stacks as a function of x. BEEM has been used to measure the energy barriers in the MOS stacks widely [6]. In the present work we have applied for the first time the BEEM/BEES techniques to study the electronic structure of the HfO_2/Si based MOS stacks with the nickel silicide gates.

1. Experimental

HfO_2 films of $\approx$ 3 nm in thickness were deposited onto the n-Si(001) substrates by atomic layer deposition (ALD). The electron concentration in Si was $\approx 2 \times 10^{15}$ cm^{-3}. A thin ($\approx$ 0.5 nm) SiO_2 layer was introduced between HfO_2 and the Si substrate in order to provide better quality of HfO_2/Si interface. Ni_xSi_{1-x} gate electrodes 30−40 nm in thickness were deposited on HfO_2 by Pulsed Laser Deposition (PLD) through a mask at 300 K by co-deposition of Ni and Si from the elementary targets. The composition of Ni_xSi_{1-x} was defined by the number of pulses per each target and was checked by Rutherford Backscattering Spectroscopy (RBS). The value of x in the investigated structures was varied within 0.33−0.75. Also a structure with the Ni gates of $\approx$ 9 nm in thickness was investigated.

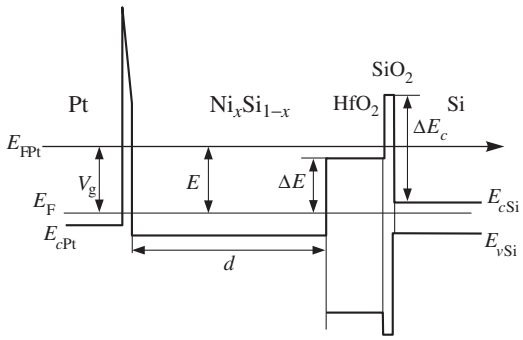

Fig. 1. A schematic band diagram of a Pt STM tip contact to the $Ni_xSi_{1-x}/HfO_2/SiO_2/n$-Si MOS stack in the regime of BEEM measurement.

The BEEM investigations were carried out in ambient air at 300 K using a home made setup based on NT MDT Solver Pro Scanning Probe Microscope. The STM probes were made from a Pt wire sharpened by cutting. More details on the apparatus design and on the measurement technique can be found in Ref. [7].

2. Results and discussion

In Fig. 2a and b the typical STM and BEEM images, respectively of a $Ni_xSi_{1-x}/HfO_2/SiO_2/n$-Si(001) stack ($x = 0.75$) are presented. The possibility of the STM investigations of the Ni_xSi_{1-x} films in ambient air was not obvious *a priori* because of the native oxide covering the surface. Nevertheless, the specific resistivity of the Ni_xSi_{1-x} films was low enough [$(2-5) \times 10^{-4}$ Ωcm [7]] to acquire the reproducible STM images. Then, we succeeded to acquire the BEEM images of the $Ni_xSi_{1-x}/HfO_2/SiO_2/n$-Si stacks in spite of rather high thickness of the Ni_xSi_{1-x} gates (typical base thicknesses d in the BEEM measurements do not exceed $\approx$10 nm [6]), the most probably, due to lower electron concentration ($n \approx 5 \times 10^{20}$ cm^{-3} [8]) and, therefor, longer electron free path length in Ni_xSi_{1-x} as compared to the typical metals. Note that the electron-electron scattering is known to be the primary

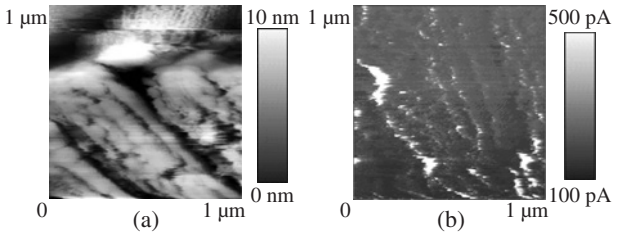

Fig. 2. STM (a) and BEEM (b) images of the $Ni_{0.75}Si_{0.25}$/HfO_2/SiO_2/n-Si(001) stack. $I_t = 10$ nA, $V_g = -2$V.

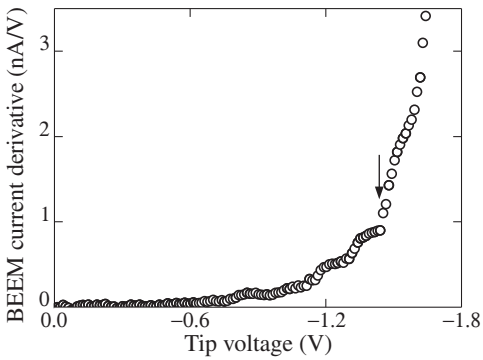

Fig. 3. The differential BEES spectrum of the $Ni_{0.75}Si_{0.25}$/HfO_2/SiO_2/n-Si(001) stack.

mechanism limiting the electron free path length near the Fermi level in metals [6].

The STM image of the Ni_xSi_{1-x} surface [Fig. 2a] demonstrated the herring-bone parquet pattern, which most likely reflects the polycrystalline structure of the film. Similar pattern has been observed in the BEEM images [Fig. 2b], which could be explained assuming that the BEEM image pattern was determined by the local reduction of the Ni_xSi_{1-x} film thickness at the grain boundaries.

Fig. 3 presents a typical differential BEES spectrum of a Ni_xSi_{1-x}/HfO_2/SiO_2/n-Si(001) stack ($x = 0.75$) dI_c/dV_g *vs* V_g where I_c is the collector current and V_g is the gap voltage (Fig. 1). The dI_c/dV_g spectra were obtained by numerical differentiation of the measured $I_c(V_g)$ curves. The threshold at $V_g \approx -1.4$ V has been ascribed to the conduction band edge (or, more exactly, to the mobility gap egde) of HfO_2. Several steps at $V_g > -1.4$ V were ascribed to the electron transport through the defect states in the HfO_2 mobility gap [7]. The background current increasing slowly with V_g was attributed to the spreading resistance of the Ni_xSi_{1-x} films.

The dependence of the potential barrier height ΔE at the Ni_xSi_{1-x}/HfO_2 interface presented in Fig. 4 was a non-monotonic one. The lowest values of ΔE were obtained for $x \approx 0.5$ corresponding to the NiSi phase, the highest — for Ni. Therefore, by varying x from 0.5 to 1 one can adjust ΔE within $\approx$ 1 eV. Also the values of ΔE extracted from the data on the electron workunction in Ni_xSi_{1-x} by Scanning Kelvin Microscopy (SKM) and C-V measurements [8] are plotted in Fig. 4. The SKM and BEES data agree qualitatively. The quantitative disagreement can be ascribed to the effect of the surface states at the Ni_xSi_{1-x} interface [8]. On the contrary, the agreement between the BEES and C-V data was worse that can be explained by too high leakage current through the ultrathin dielectric layer [8]. Indeed, the workfunction of the gate material derived from C-V measurements on MOS stacks with

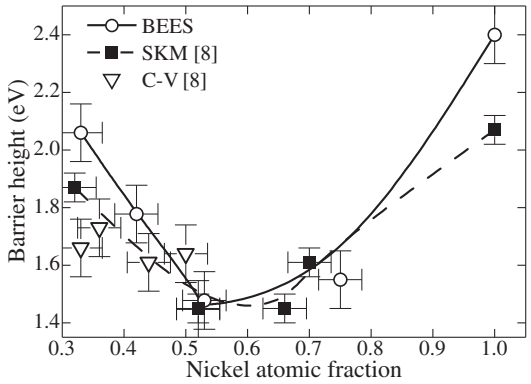

Fig. 4. The dependence of the potential barrier height at the Ni_xSi_{1-x}/HfO_2 interface ΔE on x.

nm-thick gate dielectric is not reliable. On the other hand, BEES provides direct measurement of the barrier heights in MOS stacks [6].

3. Conclusions

The results of the present study demonstrate the possibility to investigate the MOS stacks with the Ni_xSi_{1-x} gates by BEEM/BEES in ambient air. The values of the barrier height at the Ni_xSi_{1-x}/HfO_2 interface determined by BEES for $x = 0.33-1$ agree with the ones calculated from the values of the electron workfunction in Ni_xSi_{1-x} measured by SKM but disagree with the ones calculated from the C-V data that was associated with too high leakage current through a tunnel transparent HfO_2 layer.

Acknowledgements

The authors gratefully acknowledge the financial support by Russian Ministry of Education and Science (1.22.07).

References

[1] S. Luryi, J. Xu and A. Zaslavsky, *Future Trends in Microelectronics: Up the Nano Creek*, Hoboken: Wiley-IEEE, 2007.

[2] T. Wilhite, *Moore's Law: Still Great After 2008?* Amazon Digital Services B00158IXSW, 2009.

[3] D. M. Harris and N. H. E. Weste, *CMOS VLSI Design: A Circuits and Systems Perspective*, Boston: Addison Wesley, 2010.

[4] K. Anshumali, T. Chappel, W. Gomes, J. Miller, N. Kurd and R. Kumar, *Intel Technol. J.* **14**, Issue 4 (2011).

[5] M. Terai, T. Hase, K. Shibahara and H. Watanabe, *Jpn. J. Appl. Phys.* **49**, 036504 (2010).

[6] W. Yi, A. J. Stollenwerk and V. Narayanamurti, *Surf. Sci. Rep.* **64**, 169 (2009).

[7] M. A. Lapshina, M. A. Isakov, D. O. Filatov, S. V. Tikhov, Yu. A. Matveev and A. V. Zenkevich, *J. Surf. Investgations: X-ray, Synchrotron, and Newtron Techniques* **4**, 411 (2010).

[8] D. A. Saveliev, D. O. Filatov, E. S. Demidov, D. M. Druzhnov and S. M. Plankina, *Bull. N. I. Lobachevskii University of Nizhny Novgorod: Solid State Physics Series*, 2005, Issue 5, p. 35.

20th Int. Symp. "Nanostructures: Physics and Technology"
Nizhny Novgorod, Russia, June 24–30, 2012

Electrophysical and structural properties of novel metamorphic GaAs/InGaAs/InAlAs HEMTs containing strained superlattices and inverse steps in the metamorphic buffer

G. B. Galiev[1], I. S. Vasil'evskii[2], S. S. Pushkaryov[1,2], E. A. Klimov[1], A. L. Kvanin[2], R. M. Imamov[3], P. A. Buffat[4] and E. I. Suvorova[3,4]

[1] Institute of Ultrahigh Frequency Semiconductor Electronics RAS, 117105 Moscow, Russia
[2] National Nuclear Research University "MEPHI", 115409 Moscow, Russia
[3] A.V. Shubnikov Institute of Crystallography RAS, 119333 Moscow, Russia
[4] Ecole Polytechnique Federale de Lausanne, CH-1015 Lausanne, Switzerland

Abstract. A new design of high In content HEMT with short-period strained $In_xGa_{1-x}As/In_yAl_{1-y}As$ superlattices in the metamorphic buffer grown on (100) GaAs substrates have been developed. Specimens were characterized by SEM, TEM/HRTEM/STEM/EDS and AFM methods. The quality of surface and structure as well the transport characteristics of this heterostructure were compared with the properties of linear graded metamorphic buffer HEMT (MHEMT) with three $In_xAl_{1-x}As$ inverse steps terminated by $In_xAl_{1-x}As$ healing layers. A better quality of surface smoothness and interlayer structure as well a higher Hall mobility was found for HEMT with inserted superlattices in the metamorphic buffer.

Introduction

$In_xAl_{1-x}As/In_yGa_{1-y}As/GaAs$ based high-electron mobility transistors (HEMTs) with indium content $x \geq 0.7$ are expected to possess a high carrier mobility and thus the improved high-frequency response. All this can be achieved due to the proper design scaling and structural characteristics of HEMTs as the presence and density of dislocations, stacking faults, stresses and layer roughness.

Eventually it was shown that metamorphic linear graded [1,2] and step graded [3] buffers can accommodate the lattice mismatch between GaAs and the active InAlAs/InGaA layers. Thus, the low dislocation density in the active layers led to the high electron mobility of MHEMTs. In this work, molecular beam epitaxy was used to grow new types of high indium content MHEMT structures on (100) GaAs substrates. Surface characterization of the MHEMTs was performed by scanning electron microscopy (SEM) and atomic force microscopy (AFM). Transmission electron microscopy (TEM) and scanning transmission electron microscopy (STEM) was used for structure investigation and actual indium content distribution along the MHEMTs. The transport properties of both MHEMTs were measured by Hall effect and proved them to be suitable for the devices.

1. Materials

Two types of heterostructures were grown: sample No. 1 containing InAlAs linear graded metamorphic buffer (MB) divided by two strained short-period superlattices InGaAs/InAlAs (SL1 and SL2) and sample No. 2 containing InAlAs linear graded MB divided by two pairs of inverse steps (IS) and healing layers (HL).

For both samples, the first GaAs buffer layer and a 5-period $Al_{0.52}Ga_{0.48}As/GaAs$ superlattice (SL0) were grown at $T = 590$ °C to improve the substrate morphology. Then the MB and HL were grown at $T = 400$ °C to suppress the penetration of threading dislocations. Finally, the active layers (channel, spacer, barrier and the cap layer) were grown at $T = 470$ °C to obtain better morphology.

Tables 1 and 2 summarize the MB layer arrangement in the samples. Active regions were the same for both samples and consist of channel layer $In_{0.76}Ga_{0.24}As$ (thickness 165 Å), spacer layer $In_{0.70}Al_{0.30}As$ (64 Å), δ-Si doped layer ($N_S = 2.2 \times 10^{12}$ cm^{-2}), barrier layer $In_{0.70}Al_{0.30}As$ (220 Å) and cap layer $In_{0.76}Ga_{0.24}As$ (73 Å).

Table 1. The structure of the MB for sample No. 1.

$In_{0.70}Al_{0.30}As$ (HL) 1600 Å
$In_{0.75}Al_{0.25}As \rightarrow In_{0.70}Al_{0.30}As$ (IS) 460 Å
$In_{0.70}Al_{0.30}As \rightarrow In_{0.75}Al_{0.25}As$ (MB) 800 Å
SL2{$In_{0.60}Ga_{0.40}As/In_{0.75}Al_{0.25}As$}×5 {34 Å/56 Å}
$In_{0.45}Al_{0.55}As \rightarrow In_{0.70}Al_{0.30}As$ (MB) 0.43 μm
SL1{$In_{0.35}Ga_{0.65}As/In_{0.50}Al_{0.50}As$}×5 {32 Å/36 Å}
$In_{0.05}Al_{0.95}As \rightarrow In_{0.45}Al_{0.55}As$ (MB) 0.68 μm

2. Experimental details and discussion

The Hall mobility μ_e and sheet carrier density n_S were measured to be around 10500 cm^2/(V s)$^{-1}$ and 1.45×10^{12} cm^{-2} at 300 K, and 33300 cm^2(V s)$^{-1}$ and 1.38×10^{12} cm^{-2} at 77 K for sample No. 1. Sample No. 2 showed $n_S = 8700$ cm^2(V s)$^{-1}$ and $\mu_e = 1.84 \times 10^{12}$ cm^{-2} at 300 K; $n_S = 22800$ cm^2 (Vs)$^{-1}$ and $\mu_e = 1.76 \times 10^{12}$ cm^{-2} at 77 K.

Table 2. The structure of the MB for sample No. 2.

$In_{0.70}A_{l0.30}As$ (HL) 1100 Å
$In_{0.72}Al_{0.28}As \rightarrow In_{0.70}Al_{0.30}As$ (IS) 300 Å
$In_{0.49}Al_{0.51}As \rightarrow In_{0.72}Al_{0.28}As$ (MB) 0.34 μm
$In_{0.49}Al_{0.51}As$ (HL) 1100 Å
$In_{0.52}Al_{0.48}As \rightarrow In_{0.49}Al_{0.51}As$ (IS) 200 Å
$In_{0.25}Al_{0.75}As \rightarrow In_{0.52}Al_{0.48}As$ (MB) 0.38 μm
$In_{0.25}Al_{0.75}As$ (HL) 1200 Å
$In_{0.28}Al_{0.72}As \rightarrow In_{0.25}Al_{0.75}As$ (IS) 200 Å
$In_{0.05}Al_{0.95}As \rightarrow In_{0.28}Al_{0.72}As$ (MB) 0.34 μm

Fig. 1. AFM images (13 × 13 μm) of the surface of researched samples.

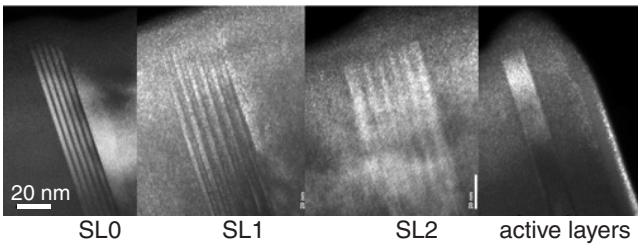

Fig. 2. Dark field TEM images ($g = 200$) of the superlattices and active layers in sample No. 1.

The roughness of the MHEMT surfaces reflects the quality of their structure due to the presence (or the absence) of dislocations and stacking faults accumulating through the layers. AFM images (Fig. 1) reveal a significant difference in morphology between surfaces of samples No. 1 and No. 2. The surface of sample No. 1 exhibits a characteristic 'cross-hatched' relief indicating a two-dimensional growth mode and the existence of misfit dislocations while the surface of sample No. 2 shows the presence of numerous emerging threading dislocations and stacking faults. Root mean square roughness is 7 and 14 nm for samples No. 1 and No. 2, respectively.

Obviously that the quality of the surface of sample No. 1 with superlattices in the metamorphic buffer is better than the surface of sample No. 2. TEM images of the structure of each superlattice and the channel in sample No. 1 were shown in Fig. 2. The measured thickness for the channel, spacer, barrier and cap layer are respectively 18, 6.5, 22 and 7.3 nm that are very close to the expected 16.4, 6.4, 21.9, 7.3 nm.

The STEM images (sample No. 1) obtained along the [110] direction showed that superlattices SL1 and SL2 inserted into the metamorphic buffer interfaces are efficient enough to prevent the penetration of threading dislocations into the upper layers (Fig. 3). However, interfaces themselves can serve as a source to new dislocations. For instance, arrows in Fig. 4 point out dislocations that go trapped into the active layers. We also observed (center of Fig. 3) a band of dislocations in the graded buffer between the SL1 and the SL2 superlattices, which abruptly stops in the middle of the image.

3. Conclusion

Two new layer designs for high In content HEMTs were developed. The HEMT contained the metamorphic buffer with embedded strained superlattices showed better quality of surface and structure, as well a higher Hall mobility than HEMT with inverse steps and healing layers obtained at the same growth

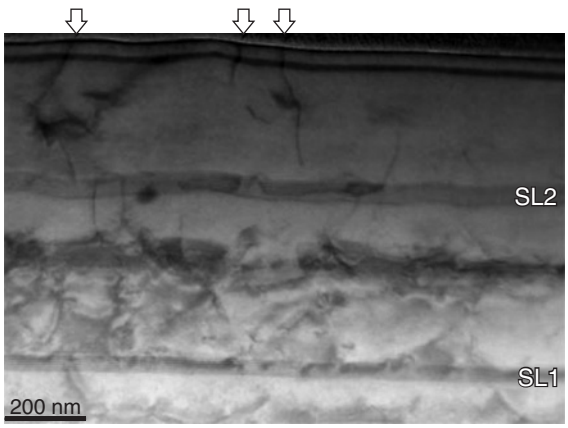

Fig. 3. STEM image ($g = 004$) along the [110] direction taken from sample No. 1.

conditions. The density of threading dislocations in the active area of sample No. 1 was much lower in comparison with sample No. 2 as well stacking faults were not observed in sample No. 1. We believe that the future optimization of growth parameters, as well as the architecture of the metamorphic buffers and superlattices, will still allow us to improve further the transport properties of these structures.

Acknowledgements

This work is supported by the Ministry of Education and Science of the Russian Federation under contracts Nos. 14.740.11.0869 and 16.513.11.3113, FCP "Kadry" NK-616P(39), by the Russian Academy of Sciences under program No. 24, by the RFBR grant No. 11-07-00050 and by the Mokerov Foundation for the Support of Education and Science.

References

[1] K. K. Ryu, S. C. Kim, An D. *et al*., *Journ. of the Korean Phys. Society.* **56 (5)**, 1509 (2010).

[2] W. E. Hoke, T. D. Kennedy, A. Toraby *et al*., *J. Cryst. Growth.* **251**, 827 (2003).

[3] S. Mendach, C. M. Hu, Ch. Heyn *et al*., *Physica E.* **13**, 1204 (2002).

20th Int. Symp. "Nanostructures: Physics and Technology"
Nizhny Novgorod, Russia, June 24–30, 2012

Study of copper phtalocyanine nanofilms by reflectance anisotropy spectroscopy

V. L. Berkovits, *A. B. Gordeeva*, V. A. Kosobukin and E. I. Terukov
Ioffe Physical-Technical Institute, St Petersburg, Russia

Abstract. Thin copper phtalocyanine (CuPc) films grown on crystal GaAs and glass substrates were studied by reflectance anisotropy spectroscopy. It is demonstrated that this technique is effective in characterizing the optical anisotropy of CuPc nanofilms associated with orientation of CuPc molecules. The orientation effect is found for GaAs(001) surface, but not for glass one. Optical model is proposed describing the observed features in reflectance anisotropy spectra of CuPc nanofilms depending on their thickness.

Introduction

Metalphtalocyanines (MPc) are known to be organic molecular semiconductors with high carrier mobility, strong optical absorption, chemical and thermal stability. Owing to these properties MPc nanofilms are very prospective for application in electronic, light and photovoltaic devices, etc. [1]. Efficiency of the devices can considerably depend on the structure of MPc films especially at small thicknesses. Therefore, it is an urgent task to search for the new *in-situ* optical techniques for effective characterizing the structure-determined anisotropy of MPc nanofilms.

In this work, reflectance anisotropy (RA) spectroscopy is applied to examine inherent in-plane anisotropy of copper phtalocyanine (CuPc) nanofilms. Influence of both crystal GaAs (001) and glass substrates on molecular stacking in CuPc nanofilms is investigated with the technique, used earlier to study surfaces (interfaces) of metals and cubic semiconductors.

1. Model and basic consideratrion

Thin films of CuPc were formed of material, obtained by template synthesis. At source temperature 550–600 °C and residual pressure of 10^{-5} Pa CuPc was deposited for 20 minutes on substrates made of glass or doped GaAs(001) with impurity concentration $n \sim 2 \times 10^{18}$ cm^{-3} at room temperature. The substrates were prepared as strips, and then smaller in size GaAs strip was put on glass and fixed with a holder to provide similar condition for films formation on both substrates. The film thickness was then varied from minimum 20 nm at one side of sample up to maximum 150 nm at another side depending on the molecular beam incidence relative to the strip plane. In this way, dependence of RA spectra on the film thickness was measured for the same sample by moving the light spot along the strip. The thickness at different points of a strip was measured with atomic-force microscope.

The RA spectroscopy technique measures the spectral dependence of the anisotropy signal

$$\frac{\Delta R}{R} = 2\,\frac{R_\alpha - R_\beta}{R_\alpha + R_\beta}\,. \qquad (1)$$

Here, R_α and R_β are the reflectivities of normally incident light waves with orthogonal linear polarization directions α and β, the common axis of CuPc permittivity and molecular polarizability coinciding with β in our experiment. In this work, RA spectra are studied in the wavelength range 250–800 nm.

Flat molecules of CuPc have in-plane $\chi_\parallel$ and normal $\chi_\perp$ polarizability components. Thin films (thickness <100 nm) are known to be composed by crystalline α-form, whose molecules are aggregated in columns along the substrate normal. The plane of CuPc molecules in α-form makes a tilt angle θ ($\approx 26.5^\circ$) to a substrate surface. Since $|\chi_\perp| \ll |\chi_\parallel|$, the molecular polarizability has tensor components $\chi_{\alpha\alpha} \approx \chi_\parallel \cos^2\theta$ and $\chi_{\beta\beta} \approx \chi_\parallel$ in the polarization directions α and β. Then, nearly diagonal tensor of permittivity is defined by the components $\varepsilon_{\alpha\alpha} \approx \varepsilon_\parallel \cos^2\theta$ and $\varepsilon_{\beta\beta} \approx \varepsilon_\parallel$. For the model "vacuum / anisotropic CuPc film / substrate" the RA signal (1) reads

$$\frac{\Delta R}{R} = \frac{1}{2}\mathrm{Re}\left(\frac{\Delta\varepsilon}{\sqrt{\varepsilon_2}}\,t_1^2\,\frac{(F-1)\left(1+r_2^2F^{-1}\right)+2ir_2\phi}{(r_1+r_2F)\,(1+r_1r_2F)}\right). \qquad (2)$$

Here, $\varepsilon_2 \approx \varepsilon_\parallel$ is the isotropic unperturbed permittivity in CuPc film plane, $\Delta\varepsilon = \varepsilon_{\beta\beta} - \varepsilon_{\alpha\alpha} = \varepsilon_\parallel \sin^2\theta$ is the anisotropy perturbation, $F = \exp(i\phi)$, $\phi = 2\sqrt{\varepsilon_2}\omega d/c$, and d is the film thickness. In Eq. (2), r_n and t_n define reflection and transmission of light at n-th interface ($n = 1, 2$) enumerated in the direction of normal incidence. If the sample is rotated around the normal at an angle φ relative the direction β, one finds $\Delta\varepsilon \sim \sin^2\theta\cos 2\varphi$ and

$$\frac{\Delta R}{R} \sim \sin^2\theta\cos 2\varphi \qquad (3)$$

in Eq. (2). It is seen from Eq. (3), that non-zero RA signal appears from a film, if its molecules make a tilt angle $\theta \neq 0$ with a substrate. Dependence of the phase-sensitive RA signal (2) on the rotation angle φ is maximum at $\varphi = 0$, when the principal dielectric axis in the film plane coincides with the direction β. The tilt θ and rotation φ angles are below used to characterize the orientation of flat CuPc molecules ordered in a film.

2. Results and discussion

The RA spectra $\Delta R/R$ were measured for CuPc films depending on their thickness d and the angle φ [2]. For CuPc film, initial orientation of the principal dielectric axes ($\varphi = 0$) was experimentally fixed in the apparatus on rotating the substrate around its normal until the maximum of the anisotropy signal $\Delta R/R$ is achieved. The spectra $\Delta R/R$ measured at $\varphi = 0$ for CuPc nanofilms on a glass substrate [2] reveal broad features. Those correspond to molecular absorption Q-band (550–700 nm) and a broad near-violet band (260–400 nm) including B-band (about 360 nm). Both bands are mainly due to $\pi - \pi^*$ transitions polarized in the planes of molecules. It is of importance that existence of RA spectra $\Delta R/R$ does evidence that molecules in the related CuPc nanofilm are actually tilted relative the plane of optically isotropic substrate. In varying φ from $\varphi = 0$ to $\varphi = 45^\circ$ the scale of $\Delta R/R$ spectrum was observed to decrease down to zero in accordance with Eq. (3) and

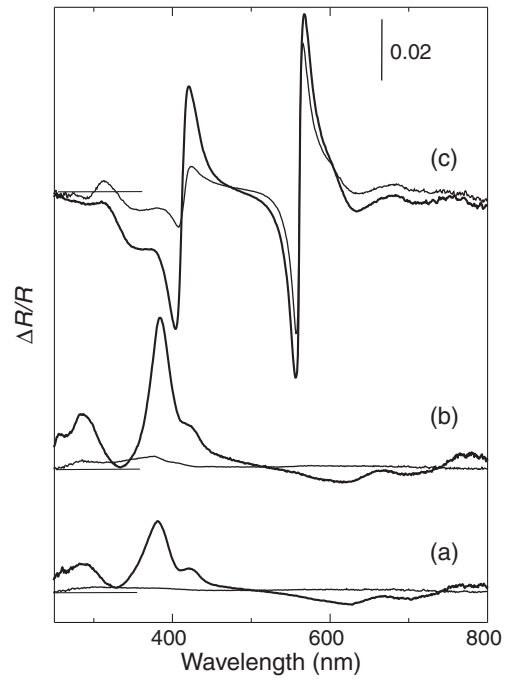

Fig. 1. Spectra $\Delta R/R$ measured for CuPc films of thicknesses 20 (a), 33 (b) and 140 (c) nm grown on GaAs(001) substrate. Thick lines show $\Delta R/R$ spectra at $\varphi = 0^\circ$, when linear polarization of incident wave coincides with the directions β and [110] on GaAs(001). Thin lines show the related $\Delta R/R$ spectra measured after rotation of the sample at angle of $\varphi = 45^\circ$ around its normal.

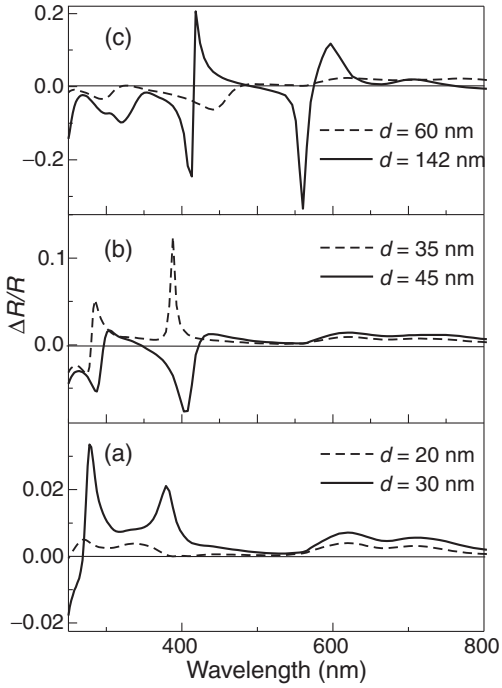

Fig. 2. Spectra $\Delta R/R$ at $\varphi = 0^\circ$ calculated for CuPc films with various thicknesses d on GaAs(001) substrate.

then to change its sign, the shape of spectral features remaining unchanged.

Measured spectra of CuPc the films with a few thicknesses from 20 up to 140 nm grown on GaAs(001) substrate are presented in Fig. 1. Figs. 1a and b show that for thinner films a feature near the wavelength 370 nm dominates, its scale is maximum at $\varphi = 0$ (thick curves) and becomes very small at $\varphi = 45^\circ$ (thin curves). At $\varphi = 0$, the principal dielectric axis of a CuPc film coincides with [110] direction in GaAs crystal substrate. Consequently, the observed φ-dependences of $\Delta R/R$ reveal an aligning effect of GaAs crystal substrate on CuPc molecules despite chemical bonding between the substrate and film is absent. Characteristic of thinner absorption films is a dihedral tilt angle θ between the plane of CuPc molecules and the surface of GaAs substrate with the intersection line being along [110] direction in GaAs.

In increasing the film thicknesses up to 50 nm, $\Delta R/R$ spectra increase their scale, too, without a change of their shape. Since $\Delta R/R$ remains maximum at $\varphi = 0$, the orientation of film molecules relative the crystal substrate being conserved. For CuPc film grown on GaAs(001), further increase of thickness results in the following. First, the shape of $\Delta R/R$ spectra changes considerably. Actually, for 140 nm thick CuPc film the shape of 370 nm in $\Delta R/R$ spectrum looks like a negative derivative of a bell-shape curve (Fig. 1c), and a larger feature of similar shape rises in a range near 580 nm. Second, the orientation of molecular polarizability axes of CuPc relative the high-symmetry crystal surface directions appears to change. This follows from Fig. 1c which shows that in the scales of $\Delta R/R$ signals measured at the angles $\varphi = 0$ and $\varphi = 45^\circ$ are comparable. It implies for thick films ($d > 70$ nm) the planes of CuPc molecules rotate around the sample normal in the outer part of a film where $\Delta R/R$ signal is induced. It can be related to thickness-dependent relaxation of molecule-substrate interaction.

Spectra $\Delta R/R$ calculated from Eq. (2) are shown in Fig. 2 in the resonant ranges of Q- and B-bands. For CuPc films on GaAs(001) substrate, used were the spectra of dielectric function from [3] measured for CuPc film on Si(110) for linear light polarizations along and perpendicular to the film plane. It is found that the former dielectric function provides better agreement with experiment for thin films ($d \lesssim 40$ nm), while the latter one does that for thick films ($d \gtrsim 100$ nm). To conclude, in thin CuPc films molecular columns are perpendicular to the substrate plane and molecular polarization is the largest in this plane.In thick films, molecular columns of the upper layers tend to line up in parallel with the substrate plane, and molecular polarization is perpendicular to the substrate plane. As a whole, calculated RA spectra shown in Fig. 2 for CuPc films with various thicknesses are in qualitative agreement with the observed RA spectra (Fig. 1). In addition, Fig. 2b shows that near the wavelength 400 nm the sign of spectrum $\Delta R/R$ evaluated for intermediate thicknesses changes. Similar behavior was also observed in our experiments.

Acknowledgements

This work was partly supported by the Russian Foundation for Basic Research, grant No. 11-02-00162, and the Russian State Contract 16.526.12.6017.

References

[1] X. Simon, J.-J. Andre. *Molecular Semiconductors. Photoelectrical Properties and Solar Cells*. Eds: J.M. Lehn, Ch.-W.-Rees. Springer-Verlag, Berlin 1985.

[2] V. L. Berkovits, A. B. Gordeeva, V. A. Kosobukin, E. I. Terukov, *Tech. Phys. Lett.* **38**, 286 (2012).

[3] O. D. Gordan, M. Friedrich, D. R. T. Zahn, *Organic Electronics* **5**, 291 (2004).

20th Int. Symp. "Nanostructures: Physics and Technology"
Nizhny Novgorod, Russia, June 24–30, 2012

Plasmon diagnostics of the nitride nanolayer formed on GaAs by N_2^+ low-energy implantation

V. M. Mikoushkin, E. V. Likhachev and V. V. Bryzgalov
Ioffe Physical-Technical Institute, St Petersburg, Russia

Abstract. Nitride nanolayer of about 4 nm thickness formed on GaAs (100) by N_2^+ ions with energy $E_i = 2500$ eV has been studied by electron energy loss spectroscopy (EELS). Plasmon diagnostics for quantitative chemical analysis of the nitrated layer has been essentially advanced using the values of plasmon energies for contributing chemical phases GaAs, GaN and GaAsN measured in one experiment with relatively high accuracy. The estimated chemical composition of the nitride layer has confirmed a domination of GaAsN alloy previously revealed by photoelectron and Auger spectroscopy, which demonstrates a reliability of the diagnostics under development.

Introduction

Some of the most promising A_3B_5 nitrides, such as narrow bandgap GaAsN and InN, are not stable enough to high growth or annealing temperatures, as well as to plasma particle impact and to degradation induced by oxygen [1,2]. Therefore these materials very often contain contri-butions of undesirable chemical phases being a result of material decay or uncontrolled growth of additional phases. To control these processes and to obtain more perfect materials, diagnostics of A_3B_5 nitride chemical composition are needed. Such diagnostics based on the methods of x-ray photoelectron spectroscopy with using synchrotron radiation [3] and Auger spectroscopy [4,5] were developed for GaAs nitrides in solving the problem of nitride nanolayer fabrication on GaAs. Unfortunately these diagnostics are difficult to use for on-line and in situ control in growth technologies because of the problems with combining diagnostic and technological equipment. In addition, the methods used in developed diagnostics are based on the registration of secondary process — photo or Auger emission which signals are characterized by relatively low intensity. Essentially higher sensitivity provides the method of electron energy loss spectroscopy (EELS) due to utilizing intensive signal of reflected electrons. Diagnostics for quantitative chemical analysis of GaAs-nitrides has been essentially advanced in this work on the basis of EELS in studying the nitride nanolayer formed on GaAs by N_2^+ low-energy implantation. Compatibility of EELS with technological equipment makes this diagnostic perspective for in situ on-line control of A_3B_5 nitride fabrication.

1. Experimental details

The experiment was carried out at high vacuum conditions ($P < 2 \times 10^{-10}$ Torr) in an electron LHS-11 (Leybold AG) spectrometer equipped with a hemispherical energy analyzer. A film of GaAs(100) with a thickness of about 100 nm grown by molecular beam epitaxy on a GaAs(100) substrate [6] was taken as a sample. The surface nitridation was effected by a beam of N_2^+ ions with energy $E_i = 2500$ eV after etching the surface with an Ar^+ ion beam. All stages of sample treatment were accompanied by measuring the Auger electron spectra in the mode allowed the known elemental sensitivity coefficients to be used for evaluating the elemental composition of samples [7]. The concentration of nitrogen in the implanted layer was $[N] \sim 2.5$ at%. The thickness of the implanted layer was estimated as the average projected range of nitrogen ions, $\langle x \rangle = 3.9$ nm, which was calculated for the given ion energy using the well known SRIM 2006 code [8].

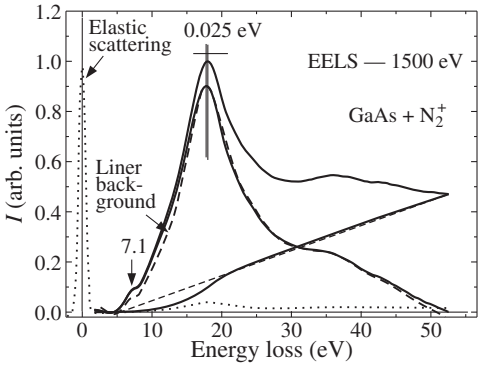

Fig. 1. EELS spectrum of nitride nanolayer shown with and without contribution of multiply scatted electrons.

Energy spectra of diagnostic electrons with energy $E_e = 1500$ eV recoiled from the sample surface at normal direction were measured. Fig. 1 shows EELS spectrum of nitride nanolayer in the scale of energy losses ΔE. Zero point in this scale ($\Delta E = 0$) corresponds to the center of the peak of elastically scatted electrons. Taking into account the experiment geometry and the mean free path $\lambda \sim 1.5$ nm of electrons underwent one inelastic scattering, one should conclude that the information contained in the EELS spectrum refers to the near surface region of the probed layer without the contribution of GaAs substrate. The prominent peak ($\Delta E = 17.8$ eV) is connected with bulk plasmon excitation, and less intensive one ($\Delta E \sim 35$ eV) — to excitation of two plasmons. Small peaks at $\Delta E < 7$ eV may be related to surface plasmon in Ga clusters formed under ion bombardment. The Plasmon peaks are superimposed on the continuous background related to multiple inelastic scattering of electron in solid. Fig. 1 illustrates two different procedures of background subtraction: liner (dushed line) and "Shirly" (solid line). One can see negligible difference of these procedures in the area of the main maxima.

2. Results and discussion

A critical point in quantitative characterization of the chemical composition of the nitrided layer performed earlier by Auger- and photoelectron spectroscopy (AES, PES) [3–5] is the reliability of the conclusion about the minor contribution of GaAs chemical phase. In contrast to study [3–5], an inten-

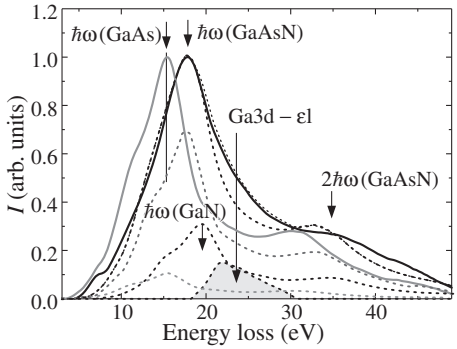

Fig. 2. EELS-spectra of GaAs (left curve) and GaAs implanted by nitrogen ions with energy $E_i = 2500$ eV (right curve). The last one is decomposed into different contributions (dotted lines).

sive signal of GaAs in photoelectron spectra was detected in many former works [9–13], though it was explained by the contribution of GaAs substrate due to comparability of the mean free path of the photoelectrons with the thickness of nitrided layer. Experimental conditions of this work exclude the contribution of the substrate. But the phase of GaAs can be formed due to low stability of alloy with high nitrogen concentration against external impacts such as ion bom-bardment: $GaAs_{1-x}N_x - (1-x)GaAs + xGaN$ [2,4]. Decay of alloy also enhances the content of the more stable chemical phase of GaN characterized by lower Gibbs energy. On the other hand, the fact of low GaAs concentration may be the evidence of the reverse process of alloy creation. This process can be induced by secondary ion cascades generated by implanted ions. Ion cascades induce mixing the atoms of the material, input of energy into the system and formation of the GaAsN phase. This experiment confirms the possible role of ion cascades in GaAsN phase creation.

Fig. 2 shows EELS spectra of GaAs before and after implantation (left and right solid curves, respectively). The bulk plasmon energy of the implanted layer $\hbar\omega = 17.8$ eV proved to be between the plasmon energies $\hbar\omega = 15.5$ eV and $\hbar\omega = 19.5$ eV [14] in GaAs and GaN, respectively. This position corresponds to plasmon of dilute alloy GaAsN because the valence electron density and, consequently, the plasmon energy must be in between the values in GaAs and GaN. Decomposition of the implanted layer spectrum was done using GaAs spectrum as the elementary one for all constituents. Relative intensity of elementary spectrum in the decomposition is proportional to the corresponding fraction of the chemical phase. Fig. 2 shows contributions of GaAsN (main contribution), GaN (minor contribution) and GaAs (marginal contribution). Thus the conclusion about the domination of the narrow bandgap alloy GaAsN in the implanted layer previously made on the basis of PES and AES study has been confirmed by the data of EELS experiment. The importance of this result is that PES and AES supply the information about chemical bondings on the atomic level. These methods do not strictly proof creation of chemical phases which fill extended areas with chemical properties of certain materials. Since plasmons are located in the extended area, plasmon spectroscopy definitely identifies chemical phases.

Agreement between experimental and calculated spectra proved to be impossible without adding the contribution of asymmetric structure at $\Delta E = 24$ eV tinted in Fig. 2. This loss energy is close to Ga3d absorption edge ($E_B \sim 20$ eV). Analogous contribution was revealed in [16] in GaN film and assigned to electron transitions Ga3d $\rightarrow \epsilon f$ from Ga3d core level to unoccupied states. Analysis of this contribution revealed a fine structure of unoccupied states Ga3d $\rightarrow \epsilon f$: 21.5, 24.0, 26.5 eV. Measuring the observed electron transitions Ga3d $\rightarrow \epsilon f$ enables a EELS diagnos-tics of unoccupied states in Ga-containing compounds, which seems to be competitive with the method of near-edge x-ray absorbtion fine structure spectroscopy (NEXAFS) with using synchrotron radiation.

3. Conclusions

Nitride nanolayer formed on GaAs (100) by N_2^+ ions with energy $E_i = 2500$ eV has been studied by EELS at the experimental conditions when electrons ejected by only nitrated layer without contribution of GaAs substrate were collected. Subtraction of the multiply scatted electron background and decomposition of remaining plasmon spectra enabled obtaining the bulk plasmon energies in different chemical phases and, finally, the quantitative evaluation of the nitrated layer chemical composition which showed the domination of the narrow bandgap alloy GaAsN in the layer. Thus, the diagnostics for quantitative chemical analysis of GaAs-nitrides has been essentially advanced. Compatibility of this diagnostics with technological equipment makes it perspective for in situ on-line control of A_3B_5 nitride fabrication. The observed electron transitions Ga3d $\rightarrow \epsilon f$ are suggested to be used for EELS diagnostics of unoccupied states in Ga-containing compounds, which seems to be competitive with NEXAFS method.

Acknowledgements

This study was performed in the frame of the Ioffe Institute annual plan.

References

[1] M. Henini, Editor, Dilute Nitride Semiconductors, Elsevier Ltd., Amsterdam (2005).
[2] V. M. Mikoushkin *et al*., *Bull. Russ. Acd. Sci.: Phys.* **72**, 609 (2008).
[3] V. M. Mikoushkin, V. V. Bryzgalov *et al*., *Phys. Status Solidi (C)* **6**, 2655 (2009).
[4] V. M. Mikoushkin, *Tech. Phys. Lett.* **36**,1136 (2010).
[5] V. M. Mikoushkin, *Appl. Surf. Sci.* **257**, 4941 (2011).
[6] Yu. S. Gordeev *et al*., *Tech. Phys.* **48**, 885 (2003).
[7] L. E. Davis *et al*., Handbook of Auger Electron Spectroscopy, 2nd ed., Perkin-Elmer Corp., Minnesota, 1976.
[8] J. F. Ziegler, J. P. Biersack, U Littmark., The Stopping and Range of Ions in Solids, Pergamon Press, New York, 1985.
[9] L. A. DeLouise, *J. Vac. Sci. Technol. A* **10**, 1637 (1992).
[10] J. S. Pan *et al*., *J. Mater. Res.* **13**, 1799 (1998).
[11] Y. G. Li *et al*., *Appl. Surf. Sci.* **174**, 175 (2001).
[12] S. Meskinis, K. Slapikas *et al*., *Vacuum* **77**, 79 (2004).
[13] P. Kumar, M. Kumar *et al*., *Appl. Surf. Sci.* **256**, 517 (2009).
[14] A.M. Sanchez *et al*., *Phys. Rev. B.* **70**, 035325 (2004).

20th Int. Symp. "Nanostructures: Physics and Technology"
Nizhny Novgorod, Russia, June 24–30, 2012

Structure and surface morphology of $Al_xGa_yIn_{1-x-y}As_zP_{1-z}$/GaAs(100) heterostructures

P. V. Seredin[1], E. P. Domashevskaya[1], A. V. Glotov[1], V. E. Ternovaya[1], I. N. Arsentyev[2], D. A. Vinokurov[2], A. L. Stankevish[2] and I. S. Tarasov[2]

[1] Voronezh State University, Universitetskaya pl. 1, 394006 Voronezh, Russia
[2] Ioffe Physical-Technical Institute, St Petersburg, Russia

Abstract. Epitaxial MOCVD heterostructures on the basis of the five-component $Al_xGa_yIn_{1-x-y}As_zP_{1-z}$ solid solutions were grown in the range of compositions isoperiodic to GaAs. By methods of X-ray diffraction and atomic force microscopy it is shown that on the surface of heterostructures are present nanosized objects having the shape of islets which can be built on a surface of solid solution in the linear direction. On the basis of calculations of crystalline lattice parameters taking into account internal stresses it is possible to assume that new compound is a phase on the basis of $Al_xGa_yIn_{1-x-y}As_zP_{1-z}$ solid solution.

Introduction

Development of epitaxial methods of growth, and in particular MOCVD method, allows to create unique semiconductor heterostructure on the basis of A_3B_5 solid solutions. Combinations of binary semiconductor anionic compounds, such as GaAs, AlAs, InAs, GaP, InP, AlP allow to gain heterojunctions which electrophysical properties are manageable at the expense of changes in composition. Today it is known that on the basis of $Al_xGa_yIn_{1-x-y}As_zP_{1-z}$ laser diodes excluding necessity of control of their working temperature can be gained up to 150 °C. All it makes optoelectronic systems on the basis of $Al_xGa_yIn_{1-x-y}As_zP_{1-z}$ extremely claimed [1–2]. It is clear that the semiconductor epitaxial heterostructures containing quantum-dimensional inhomogeneities represent very difficult objects for investigations. Their structure and properties are in a strong dependence from technology of growth. Therefore definition of lattice parameters, frequencies of optical and interface phonons in systems with inhomogeneities, including quantum-dimensional are of high practical value and are perspective from the point of view of making optoelectronics devices, and nanosized objects structure studying depending on requirements of formation and guidance of their properties. Therefore examination of structure and surface morphology, and also optical properties in IR-range of MOCVD heterostructures on the basis of $Al_xGa_yIn_{1-x-y}As_zP_{1-z}$ solid solutions isoperiodic to GaAs became the purpose of our scientific research.

1. Sample preparation

Five-component $Al_xGa_yIn_{1-x-y}As_zP_{1-z}$ solid solutions were grown using EMCORE GS 3/100 installation by MOCVD epitaxial method in the vertical reactor with high velocity of GaAs (100) substrate holder. The epitaxy temperature was 750 °C, the reactor pressure was 77 Torr and the substrate holder's rotation rate was 1000 rpm. The epitaxial layer thickness of solid solution is 1 micron.

2. Experimental

On the basis of the data, given by the complex of structural and spectral methods, we can draw a series of important conclusions concerning the structure and substructure of five-component solid solutions $Al_xGa_yIn_{1-x-y}As_zP_{1-z}$. The analysis conducted by methods of high resolution X-ray diffraction showed that the solid solutions given have good structural quality of growth and small internal tensions, caused by the mismatch of lattices, which can be clearly seen in the shape of diffractional reflections. However, more detailed research of the X ray structural analysis shown that part of solid solutions are not single-phase. Along with the main phase $Al_xGa_yIn_{1-x-y}As_zP_{1-z}$ in the solid solution appears an additional phase with a lattice parameter larger than the primary solid solution. The appearance of a five-component solid solution matrix of the new phase is reflected in surface morphology of five-component solid solutions. Atomic Force Microscopy revealed that the surface of heterostructures with the new phase present nanoscale objects shaped nanoislands, which can be arranged on the surface of the solid solution not statistically, but strictly linearly. Typical dimensions of such nanoislands are: diameter — 30–50 nm, height 1–2 nm. The distance between the lines of the ordered nanoinhomogeneities arrangement ∼500 nm. Analyzing all the experimental data and theoretical calculations based on lattice parameters taking into account the internal stresses [3–4], we can assume that nanoscale heterogeneity on the surface of the epitaxial film is based on the phase of $Al_xGa_{1-x}As$ solid solution.

Acknowledgements

We acknowledge the Karlsruhe Nano Micro Facility (KNMF, www.kit.edu/knmf) of the Forschungszentrum Karlsruhe for provision of access to instruments at their laboratories and we would like to thank Dr. H. Leiste for assistance in using laboratory Thin film characterisation methods. For financial support we acknowledge: Grant of the President of the Russian Federation MK-736.2011.2.

References

[1] High performance materials and processing technology for uncooled 1.3 μm laser diodes. Roberta Campi Doctoral Thesis. Royal Institute of Technology, (KTH), Stockholm.
[2] 3-D Projection full color multimedia display WIPO Patent Application WO/2007/127269.
[3] E. P. Domashevskaya *et al*., *Surface and Interface Analysis* **8/4**, 828 (2006).
[4] P. Seredin *et al*., *Semiconductors* **45/11**, 1433 (2011).

20th Int. Symp. "Nanostructures: Physics and Technology"
Nizhny Novgorod, Russia, June 24–30, 2012

Resistive switching in graphene/ZnO nanorods structures

O. V. Kononenko[1], O. O. Kapitanova[2], G. N. Panin[1,4] and A. N. Baranov[3]

[1] Institute of Microelectronics Technology and High Purity Materials, RAS,
142432 Chernogolovka, Moscow Region, Russia
[2] Moscow State University, Department of Materials Science, 119992 Moscow, Russia
[3] Moscow State University, Chemistry Department, 119992 Moscow, Russia
[4] Quantum-functional Semiconductor Research Center, Department of Physics,
Dongguk University 26, Seoul 100-715, Korea

Abstract. Vertically aligned ZnO nanorods were synthesized by hydrothermal solution phase synthesis on few-layer-graphene grown by chemical vapor deposition on Cu foil and transferred to a Si/SiO_2 substrate. ZnO nanorods were deposited on the graphene film by hydrothermal method. Nanorods demonstrated high structural performance and good optical characteristics. Niobium electrodes were fabricated on nanorod tips and Ti/Pt electrodes were deposited on the graphene film. I-V characteristics measured on this structure demonstrated unipolar resistive switching. The difference between two resistive states was about 10^4. Such structures can be used for working out of the future devices of non-volatile memory.

Introduction

Among various carbon nanostructures, graphene as a single atom two-dimensional (2D) sp^2 hybrid carbon sheet shows unique properties for both fundamental research [1–4] and promising applications in condensed-matter physics, electronics, and material science [5–11]. The interest to the graphene-based structures has been extremely increased after empirical discovery of graphene sheets in 2004 [12].

The growth of semiconductor nanocrystals on graphene layers is particularly interesting because nanostructures, such as nanocrystals and nanorods, can offer additional functionality to graphene in advanced electronics and optoelectronics. Graphene has a great potential for novel electronic devices due to its remarkable electrical and thermal properties including a carrier mobility exceeding 10^4 $cm^2/V\,s$ and a thermal conductivity of 10^3 W/mK [13–14]. Accordingly, with the excellent electrical and thermal characteristics of graphene layers, growing semiconductor nanostructures on graphene layers would enable their novel physical properties to be exploited in diverse sophisticated device applications.

Zinc oxide is a unique functional semiconductor material with a wide forbidden band (3.37 eV), high bonding energy of the exciton (60 meV) at room temperature, and an effective ultraviolet luminescence. Materials based on ZnO can be used as components of gas sensor controls, LCD-matrices, solar batteries, photocatalysts, luminescent materials, lightemitting diodes, powder lasers, and composite materials. Zinc oxide is a biocompatible material with antiseptic properties. ZnO nanorods can be potentially use for electronics and optoelectronics [15,16]. For such devices, vertically aligned ZnO nanorods have been produced either by catalytic gas phase syntheses [17,18] or by solution phase syntheses [19]. In particular, hydrothermal solution phase synthesis ensure process scalability and cost efficiency. Using this catalyst-free method, vertically aligned ZnO nanorods can be grown under atmospheric pressure and low temperature.

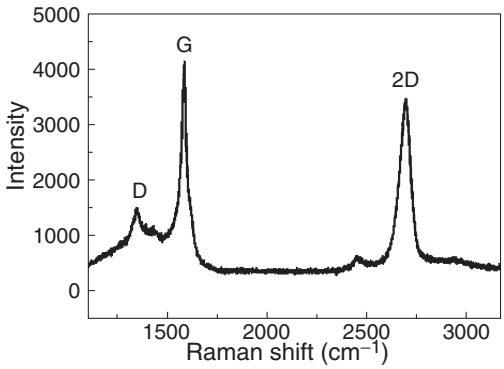

Fig. 1. Raman spectra of graphene film.

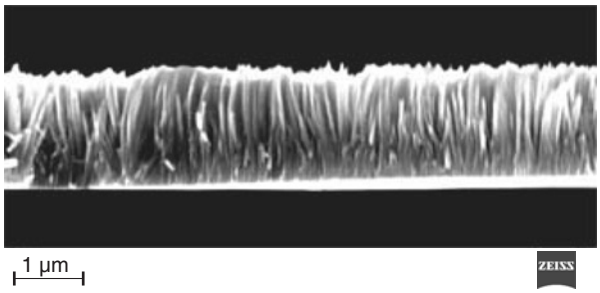

Fig. 2. SEM image of vertically oriented zinc oxide nanorods grown on on the few-layer-graphene film on Si/SiO_2 substrate by hydrothermal solution phase synthesis.

In this work we have studied electrical properties of structures consisted of ZnO nanorods vertically grown on a few-layer-graphene film.

1. Experimental

Graphene was synthesized by chemical vapor deposition (CVD) on Cu foil and transferred to a Si/SiO_2 substrate. Micro-Raman spectroscopy confirmed the successful preparation of the graphene layers and was used to determine the number of graphene layers.

ZnO nanorods array was fabricated on the graphene film on oxidized silicon substrate by a commonly reported hydrothermal method [20,21]. The optical qualities of the as-grown ZnO nanostructures on the graphene layers were examined in XL 30S field emission gun high-resolution scanning electron microscope (HRSEM) with a Mono CL system for cathodo-

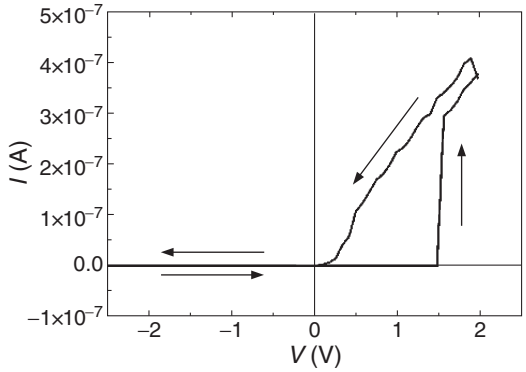

Fig. 3. I-V curves of the Nb/ZnO nanorods/graphene/TiPt structure.

luminescence (CL) spectroscopy. The light emitted from the sample can be directed into the slits of the monochromator, which is mounted on the SEM. In order to insulate graphene layer and to fill the space between ZnO nanorods, we used solution deposition of PMMA (Fig. 2). After the deposition of PMMA nanorod tips were opened by etching in oxygen plasma. Then niobium electrodes were deposited onto ZnO tips. Ti/Pt electrodes were deposited onto the graphene film. I-V characteristics of the devices were measured using Keithley 2635 source-meter.

2. Results and discussions

A typical Raman spectrum of a graphene film transferred to a Si/SiO_2 substrate is shown in Fig. 1. The sharp peaks are indicative of the crystallinity of the films and the plot shows several distinct peaks, one at about 1580 cm^{-1} (G peak) and the other at about 2690 cm^{-1} (2D peak). The peak at around 1580 cm^{-1} is attributed to sp^2 phonon vibrations. The 2D peak is used to confirm the presence of graphene and it originates from a double resonance process that links phonons to the electronic band structure. A peak occurring at about 1350 cm^{-1} (D band) indicates phonon scattering at defect sites and impurities. Also, defective films will result in signals at around 1610 cm^{-1} which arise from phonon scattering at crystal lattice defects. The width of G and 2D Raman peaks was larger for thicker layers.

To estimate the crystal perfection of nanorods grown on the graphene film, we studied their cathode-luminescence (CL) spectra. CL spectra were measured in two modes: direct and panchromatic, which allowed a comparison of the emission areas and the electron microscopy image of the nanorods on the substrate. The CL spectra showed that the grown nanorods were of high quality. The spectra contain only one strong UV band of the edge emission peaking at 382 nm due to free exciton recombination and no green and blue lines which are usually attributed to point defects in ZnO, such oxygen and zinc vacancies.

Current-voltage (I-V) characteristics of the fabricated structures are shown in Fig. 3. Bias to the structure swept at a constant rate from 0 to 2 V and back from 2 to -2 through 0 and back to zero initial state. The structure showed a sharp unipolar resistive switching. Ratio of the currents on and off was about 10^3, and the threshold voltage transition to a low resistive state was about 1.5 V. Such structures can be used for working out of the future devices of non-volatile memory.

References

[1] K. S. Novoselov *et al.*, *Nature* **438**, 197 (2005).
[2] M. I. Katsnelson *et al.*, *Solid State Commun.* **143**, 3 (2007).
[3] J. C. Meyer *et al.*, *Nature* **446**, 60 (2007).
[4] F. Schedin *et al.*, *Nat. Mater.* **6**, 652 (2007).
[5] X. Wang *et al.*, *Angew. Chem.* Int. Ed. **47**, 2990 (2008).
[6] S. Gilje *et al.*, *Nano Lett.* **7**, 3394 (2007).
[7] W. Bao *et al.*, *Nano Lett.* **8**, 3345 (2008).
[8] J. T. Robinson *et al.*, *Nano Lett.* **8**, 3137 (2008).
[9] R. Arsat *et al.*, *Chem. Phys. Lett.* **467**, 344 (2009).
[10] C. Stampfer *et al.*, *Nano Lett.* **8**, 2378 (2008).
[11] X. Liang *et al.*, *Nano Lett.* **7**, 3840 (2007).
[12] K. S. Novoselov *et al.*, *Science* **306**, 666 (2004).
[13] Y. B. Zhang *et al.*, *Nature* **438**, 201 (2005).
[14] A. A. Balandin *et al.*, *Nano Lett.* **8**, 902 (2008).
[15] Z. L. Wang and J. Song, *Science* **312**, 242 (2006).
[16] M. Law *et al.*, *Nat. Mater.* **4**, 455 (2005).
[17] M. H. Huang *et al.*, *Science* **292**, 1897 (2001).
[18] T.-J. Kuo *et al.*, *Chem. Mater.* **19**, 5143 (2007).
[19] G. Xia *et al.*, *Nanotechnology* **20**, 225301 (2009).
[20] L. Greene *et al.*, *Nano Lett.* **5**, 1231 (2005).
[21] K. H. Tam *et al.*, *J. Phys. Chem. B* **110**, 20865 (2006).

20th Int. Symp. "Nanostructures: Physics and Technology"
Nizhny Novgorod, Russia, June 24–30, 2012

STM investigation of structural properties of Si layers deposited on Si(001) vicinal surfaces

L. V. Arapkina[1], V. A. Chapnin[1], K. V. Chizh[1], L. A. Krylova[1] and V. A. Yuryev[1,2]

[1] A.M. Prokhorov General Physics Institute, RAS, Vavilov str. 38, 119991 Moscow, Russia
[2] Technopark of GPI RAS, Vavilov str. 38, 119991 Moscow, Russia

Abstract. This report covers investigation of the structural properties of surfaces of Si epitaxial layers deposited on Si(001) vicinal substrates with different miscuts. We have shown processes of generation and growth of surface defects to depend on tilt direction of a Si(001) wafer and epilayer growth mode. We suppose these effects to be connected with interaction of monoatomic steps.

Introduction

A structure of a Si(001) epitaxial layer surface, especially its defects, could affect the formation of nanostructures. Perfect, defectless Si epilayers grown on Si(001) vicinal substrates are of special importance for such industrially significant problem as controllable formation of Ge/Si(001) nanostructures for optoelectronic device applications. This report covers experimental investigation of structural properties of surfaces of Si epitaxial layers deposited on Si(001) vicinal surfaces of substrates with different miscuts.

1. Experimental

Experiments were carried out in UHV using GPI-300 STM coupled with Riber EVA 32 MBE chamber [1]. Epitaxial layers were deposited by MBE on substrates cut from Si(001) vicinal wafers tilted ∼0.2° towards the [110] or [100] direction. Initial surfaces were treated by the RCA etchant. Before Si deposition, we cleaned the surfaces by the standard methods of preliminary annealing at 600 °C and decomposition of the SiO_2 film under a weak flux of the Si atoms at 800 °C [2]. The substrate temperature during Si deposition was chosen in the range from 360 to 700 °C.

2. STM data

We have explored structural properties of Si epitaxial films deposited on Si(001) vicinal substrates depending on the growth temperature and the rate of Si deposition. Two modes of Si epitaxial growth have been observed. We have found that the step-flow growth goes on at the temperatures above 600 °C whereas the island growth takes place at the temperatures below 600 °C. Samples grown at the step-flow growth mode have smooth surfaces composed of terraces bounded by monoatomic steps. STM data shown in Figs. 1 and 2 are related to the Si epilayers deposited on the wafers tilted towards the [110] and [100] direction respectively.

2.1. Surfaces tilted towards [110]

At first, we consider STM data for Si/Si(001) surfaces tilted towards the [110] direction. The surface is composed by S_A and S_B monoatomic steps [3]; S_B steps are wider than S_A ones. We have observed formation of such defects as faceted pits on these surfaces. In Fig. 1, an initial stage of the defect formation is shown. There observed the local stoppage of growth of an S_B step and appearance of two S_A steps instead. In other words, we have observed a gap of the S_B step. The S_A steps repulse each other and the defect cannot be overgrown quickly. The bottom of the deep pit has a rectangular shape and a long side of it formed by the S_A step.

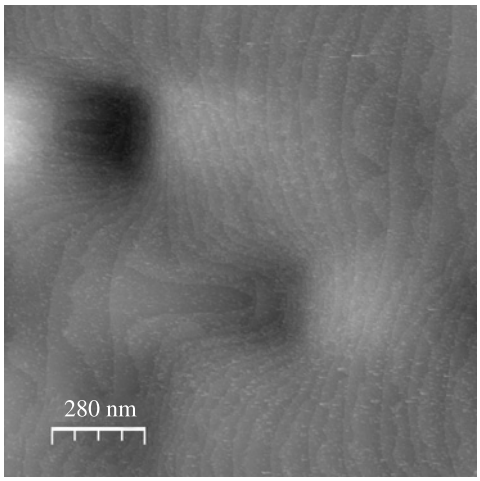

Fig. 1. STM image of the surface of the 50-nm Si epilayer deposited at 650 °C on the Si(001) vicinal wafer tilted ∼0.2° towards [110], the deposition rate was ∼0.3 Å/c.

2.2. Surfaces tilted towards [100]

STM data for the Si/Si(001) surface tilted towards the [100] direction are presented in Fig. 2. The surface is composed by bent monoatomic steps. In this case every monoatomic step consists of short parts of S_A and S_B steps and runs along the [100] direction. There are local disarrangements of the structure. We suppose this kind of defects to be connected with a process of transition from the mixed $S_A + S_B$ monoatomic step to two single S_A and S_B steps instead of formation of the D_B step.

We have investigated the structural properties of the Si film surface depending on the rate of Si deposition. We have found that reduction of the Si deposition rate from 0.3 Å/c (Fig. 2) to 0.1 Å/c (Fig. 3) results in appearance of the structure formed by monoatomic steps running along the [110] direction and formation of shapeless pits on the surface instead of the structure formed by the bent monoatomic steps which run along the [100] direction.

2.3. Effect of temperature reduction

In Figs. 4 and 5, we present STM data for surfaces of the epilayers deposited at the temperatures of 550 and 470 °C.

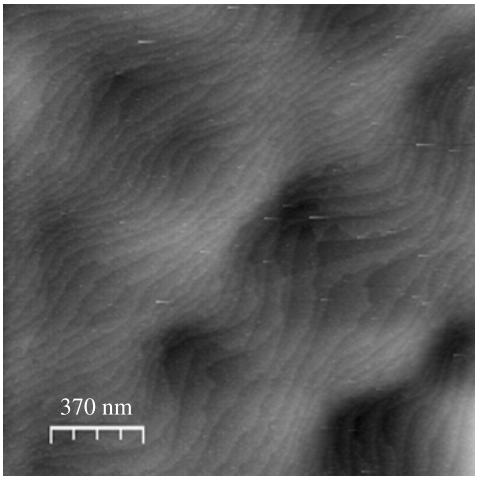

Fig. 2. STM image of the surface of the 50-nm Si epilayer deposited at 650 °C on the Si(001) vicinal wafer tilted ∼0.2° towards [100], the deposition rate was ∼0.3 Å/c.

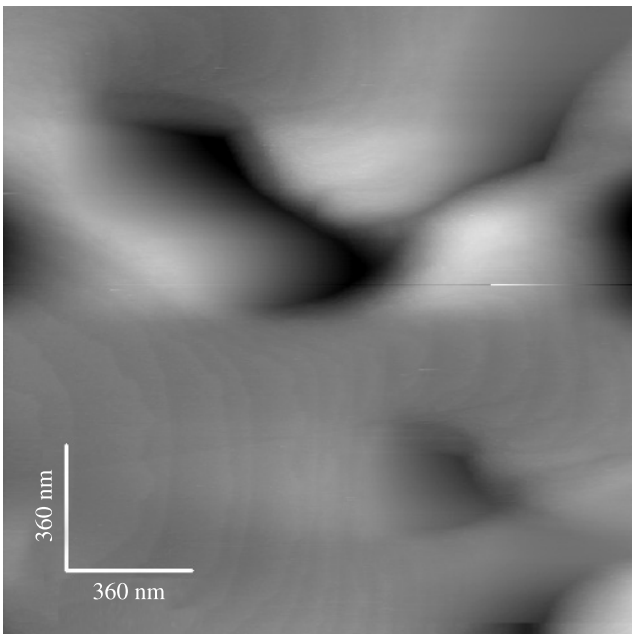

Fig. 3. STM image of the surface of the 50-nm Si epilayer deposited at 650 °C on the Si(001) vicinal wafer tilted ∼0.2° towards [100], the deposition rate was ∼0.1 Å/c.

Surfaces of the samples grown at 550 °C consist of S_A and S_B monoatomic steps (Fig. 4). The mixed $S_A + S_B$ monoatomic steps which are typical for the Si(001) surfaces tilted towards [100] and obtained at higher temperatures are not observed. At this temperature, the transitional mode of the epilayer growth, intermediate between the island growth and the step-flow one, is observed for both tilt directions.

Further reduction of the temperature down to 470 °C results in the island growth mode (Fig. 5). The Si/Si(001) surface is composed by small islands. In both causes such defects as pits are present on the surface. The structural properties of the surfaces of Si epilayers grown at the island growth mode do not depend on the direction of the surface tilt.

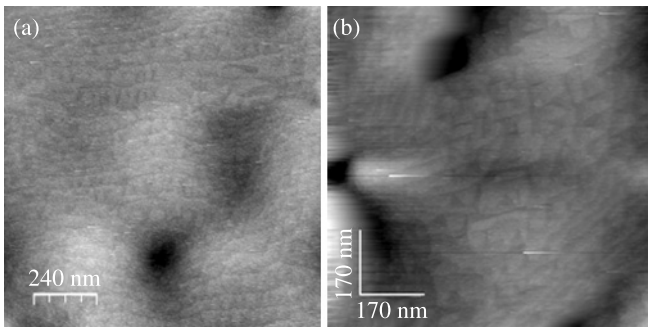

Fig. 4. STM image of the surface of the 50 nm thick Si epilayer deposited at 550 °C on the Si(001) vicinal wafer (deposition rate is ∼0.3 Å/c); tilt is ∼0.2° towards (a) [110] and (b) [100].

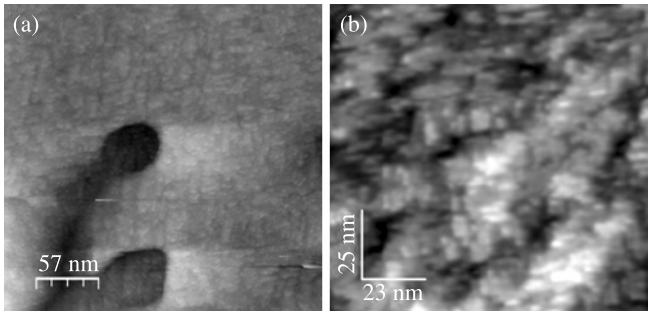

Fig. 5. STM image of the surface of the 50 nm thick Si epilayer deposited at 470 °C on the Si(001) vicinal wafer (deposition rate is ∼0.3 Å/c); tilt is ∼, 0.2° towards (a) [110] and (b) [100].

3. Conclusion

Summarizing the above we can conclude that processes of generation and growth of surface defects arising during epitaxial growth of Si films on Si(001) vicinal substrates depend on tilt direction of a Si(001) wafer and the epilayer growth conditions. We suppose the observed effects to be a consequence of mutual interactions of monoatomic steps.

Acknowledgements

This research has been supported by the Ministry of Education and Science of Russian Federation through the contracts No. 14.740.11.0069 and 16.513.11.3046. Facilities of Center of Collective Use of Scientific Equipment of GPI RAS were utilized in this research. We appreciate the financial and technological support.

References

[1] V. A. Yuryev *et al*., *Nanoscale Res. Lett.* **6**, 522 (2011).
[2] L. V. Arapkina *et al*., *JETP Lett.* **92**, 310 (2010).
[3] D. J. Chadi, *Phys. Rev. Lett.* **59**, 1691 (1987).

20th Int. Symp. "Nanostructures: Physics and Technology"
Nizhny Novgorod, Russia, June 24–30, 2012

Diamond nanostructures

V. I. Konov, I. I. Vlasov, T. V. Kononenko, V. V. Kononenko, M. S. Komlenok, S. M. Pimenov, V. G. Ralchenko and D. N. Sovyk

A.M. Prokhorov General Physics Institute of RAS, Moscow, Russia

Abstract. Two approaches to fabrication of diamond nanostructures are described. The first is based on selected regimes of CVD diamond growth. It is also shown that high intensity laser radiation allows to produce graphitic and hollow nanostructures both on the surface and in the bulk of diamond samples.

Diamond is a unique material showing a number of extreme properties such as record values of thermal conductivity ($\leq$2000 W/m K) at room temperature, broadband (in the range from UV to MW) transmittance, sound velocity (18.4 km/s), carrier mobility ($\geq$4000 cm^2/V s). It is an excellent insulator and can be a high quality p-type semiconductor (B-doped). Besides, it has a unique radiation stability, chemical inertness, high hardness, biocompatibility and a number of other important features, which determine numerous existing and potential applications. Some of them can be based on specific features of nanostructured diamond.

Several approaches to fabrication of diamond nanostructures can be considered. The first [1] is based on growth of thin CVD diamond films. For the case when standard gas mixtures CH_4:H_2 are essentially enreached with methane and argon is added, so called ultra-nanocrystalline (UNCD) diamond films can be deposited on a number of substrates. The thickness of such coatings is varied between $\approx$50 nm and 10 μm. They consist mostly of nanograines of diamond (4–20 nm) in a matrix of nanographite and polyacetilene. The UNCD coatings are very hard ($\leq$80$-$90 GPa) and smooth (surface roughness $\approx$20$-$50 nm). If during CVD process N_2 is also used, the films are based on diamond nanorods rather than on nanocrystals of diamond and contain more graphitic material than regular UNCD [2]. The diameter of nanorode diamond core is about 5–6 nm, length — 100–150 nm.

Under typical CVD growth conditions (CH_4/H_2 ratio $\leq$5%, deposition temperature 700$-$1000 °C) polycrystalline diamond films (PCD) are produced. Their thickness can be as large as few mm and they can be detached from a substrate by chemical etching, thus forming a membrane or plate. If Si substrate is highly polished and nanostructured, then in the cause of CVD deposition and high nucleation density ($\leq 10^{11}-10^{12}$ cm^{-2}) this structure can be filled with diamond deposit. Then by means of post growth chemical etching of the substrate the diamond replica (negative) of the initial silicon surface structure is formed. This approach is called a "replica technique" and allows, for example, to produce arrays of vertical diamond nanorods, sharp needles or photonic crystals [3].

Laser is a perfect tool for post-growth micro and nanostructuring of diamond materials: single crystal, poly and nanocrystalline diamond, diamond-like (amorphous) coatings [4]. The key element in laser processing of diamond is its thermal phase transformation (graphitization) which takes place at $T \geq T_g \approx$ 700 °C. Diamond is transparent and chemically inert. In contrast graphitic phases are opaque and highly reactive. There are two ways to produce nanostructures on a diamond surface. The first is local laser heating and graphitization. Thus conducting nanofeatures with lateral resolution of about $\lambda/2$ (λ — laser wavelength) and thickness ranging from 10 up to 100 nm can be made. After additional chemical etching (e.g. thermal oxidation) the graphitic material can be removed and corresponding hollow nanostructures produced.

If laser intensity is high enough to reach graphite vaporization temperature $T_b \approx$ 4000 °C, diamond ablation takes place with rates up to 5 μm per pulse for laser pulses with duration below microsecond. Diamond surface ablative nanostructuring is usually carried out with ultra-short (fs or ps) or UV laser pulses. If the surface temperature during the laser pulse action $T_g < T < T_b$, laser assisted reactive etching (e.g. oxidation) of the graphitized layer is realized. Short pulsed laser etching rates in air are as low as $10^{-1}-10^{-3}$ nm/pulse — this regime was called reactive nanoablation. Moreover, for clear diamond nanoablation can be performed below surface graphitization threshold with even smaller rates $10^{-3}-10^{-4}$ nm/pulse.

It was also shown that diamond-graphite phase transformation under intense laser radiation can occur in the bulk of a diamond sample. To achieve this, visible or near IR laser radiation should be used to guarantee its negligible absorbtion for low intensity. Sharp focusing of the beam inside the sample provides huge rise of laser intensity within a small focal volume that initiates efficient non-linear absorbtion of the radiation, diamond heating and graphitization. To localize the graphitized volume, laser pulse energy should be minimized that can be achieved by means of ultra-short pulses. Moving the position of the focal volume inside the sample, complex one, two and three dimensional graphitic structures could be fabricated inside single crystal diamond with rates up to about 100 nm/pulse. The width of produced lines could be of submicron value for 3 μm diameter focal spots of Ti:Al_2O_3 (λ = 800 nm) femtosecond laser. It is expected that tighter focusing and use of shorter wavelength lasers will result in smaller size graphitic structures. It should be also noted that if part of the laser produced graphitic structure touches the diamond surface, complimentary chemical etching leads to formation of hollow structures in diamond bulk.

References

[1] V.I. Konov, A.A. Smolin, V.G. Ralchenko, S.M. Pimenov, E.D. Obraztsova, E.N. Loubnin, S.M. Metev and G. Sepold, *Diamond and Related Materials* **4**, 1073 (1995).

[2] I. Vlasov, O. Lebedev, V. Ralchenko, E. Goovaerts, G. Bertoni, G. Van Tendeloo and V. Konov, *Advanced Materials* **19**, 4058 (2007).

[3] A.A. Zakhidov, R.H. Baughman, Z. Iqbal, C. Cui, I. Khayrullin, S. Dantas, J Marti, V.G. Ralchenko, *Science* **282**, 897 (1998).

[4] V.I. Konov, *Laser Photonics Reviews*, 1–28, (2012).

20th Int. Symp. "Nanostructures: Physics and Technology"
Nizhny Novgorod, Russia, June 24–30, 2012

Step-terraced morphology of GaAs(001) surface with straight monatomic steps induced by misfit dislocations

I. O. Akhundov[1], N. S. Rudaya[1], *V. L. Alperovich*[1,2], S. N. Kosolobov[1], A. V. Latyshev[1,2] and A. S. Terekhov[1]

[1] Institute of Semiconductor Physics, 630090 Novosibirsk, Russia
[2] Novosibirsk State University, 630090 Novosibirsk, Russia

Abstract. The evolution of the surface morphology of GaAs/AlGaAs heterostructures bonded to glass is experimentally studied under anneals in the conditions close to equilibrium between the GaAs(001) surface and Ga and As vapors. Along with atomically flat terraces separated by monatomic steps, which are characteristic of a vicinal surface, we observed the formation of a rectangular grid of dislocation-induced monatomic steps due to partial relaxation of thermo-mechanical strains. As compared to the "vicinal" steps, which have a curved shape determined by the long-period variations of the surface relief, the dislocation-induced steps are straight, oriented along the [110] and [1$\bar{1}$0] crystal axes, and more stable to thermal fluctuations.

Introduction

Atomically flat semiconductor surfaces are needed for fundamental surface science, device applications, and reproducible fabrication of nanoscale structures. Crystal surfaces prepared by standard chemo-mechanical polishing are disordered on a microscopic scale and inevitably have some residual long-wavelength variations of the surface relief. By allowing surface migration at elevated temperatures, the microscopic disorder can be effectively reduced, and the surface can be brought to an ordered step-terraced morphology, with a set of atomically flat terraces separated by monatomic steps. Regular step-terraced silicon surfaces are obtained by annealing in vacuum [1,2]. The application of this method to III-V semiconductors is hindered by high and different evaporation rates of the III and V components. To circumvent this difficulty, one can use annealing in the conditions close to equilibrium between the semiconductor surface and the vapors of the III and V components. This approach yields step-terraced surfaces of GaAs(001) epi-ready substrates [3].

A problem of preparing semiconductor surfaces with morphology close to the ideal step-terraced surface is that on real surfaces the steps are not perfectly straight, because their shape and the local width of terraces are determined by long-period variations of the surface relief, which can not be reduced at reasonable temperatures and durations of annealing. In the present study we proved experimentally the opportunity to form a grid of ultimately straight monatomic steps induced by dislocations, which are generated due to relaxation of thermo-mechanical strains in GaAs/AlGaAs heterostructures bonded to glass substrates.

1. Experimental

AlGaAs/*p*-GaAs/AlGaAs double heterostructures with the GaAs and AlGaAs layer thicknesses in the range of 0.5–2 μm were grown on GaAs(001) substrates. The heterostructures were bonded to glass plates by diffusion bonding. The GaAs substrate and AlGaAs stop-layer were removed by selective wet etching. The absence of dislocations in the heterostructures after bonding and chemical etching was confirmed by the photoluminescence intensity topography. The anneals of these bonded-to-glass structures were performed in the conditions of equilibrium between the GaAs surface and Ga and As vapors. The equilibrium conditions were provided by the presence of the saturated Ga-As melt. The morphology of the surface was studied *ex situ* by atomic force microscopy (AFM). The details of annealing and AFM measurements are described earlier [3].

2. Results and discussion

To study the evolution of the morphology of the GaAs surface under strain relaxation, isochronous one-hour anneals at successively increased temperatures were performed. The strain in the semiconductor structure builds up under heating due to the difference in the thermal expansion coefficients of the structure and the glass. Plastic relaxation of the strain takes place above the dislocation generation threshold, which depends on the strain and temperature.

The AFM images of the GaAs surface after the anneals are shown in Fig. 1(a–d). Due to annealing at 575 °C distinct islands and pits bounded by steps of one or two-monolayer (ML) height are formed (Fig. 1a) on the initially rough surface (not shown). It is seen that the increase of the annealing temperature leads to the increase of the mean size of island (Fig. 1b) and, eventually, to the formation of the step-terraced morphology, which consists of atomically flat terraces separated by curved monatomic steps (Fig. 1c,d). The widths of the terraces and the curvature of these steps are determined by the angle of misorientation from the singular (001) crystal face and by smooth variations of the surface relief. It is seen from Fig. 1 that along with these curved steps, which are characteristic of vicinal surfaces, a rectangular grid of straight steps is formed on the surface. Like the cross-hatch patterns on the surfaces of epitaxial films grown on lattice mismatched Si(001) and GaAs(001) substrates [4,5], these steps are directed along the [110] and [1$\bar{1}$0] crystal axes and apparently have the same origin arising from plastic relaxation of mechanical strain by generation of misfit dislocations. However, unlike typical cross-hatch patterns, which are usually rough and can be seen by an optical microscope or even by a naked eye, here we observe dislocation-induced steps of monatomic height. This is confirmed by the height distribution function (Fig. 1e) determined for the surface area, which is denoted in Fig. 1c by the dashed line and contains flat terraces on both sides of a straight dislocation-induced step. Also, the cross-section shown in

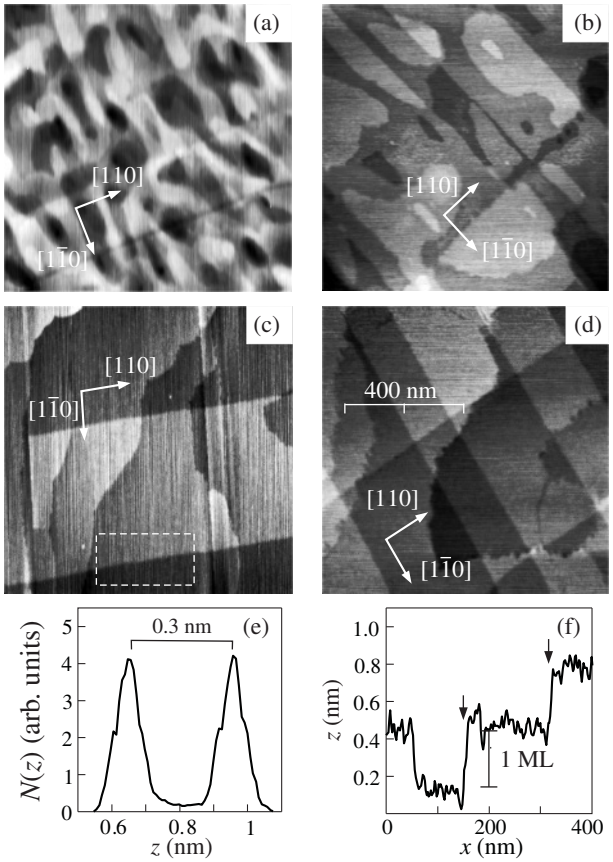

Fig. 1. 1×1 μm^2 AFM images of the GaAs(001) surface of the GaAs/AlGaAs structure bonded to glass after annealing at various temperatures T: (a) $T = 575$ °C, (b) 600 °C, (c) 650 °C, (d) 675 °C. (e) height distribution function calculated over the rectangular region shown by the dashed line in Fig. 1c. (f) z-x cross-section of the 400-nm segment shown in Fig. 1d.

Fig. 1f proves that within the experimental accuracy both the "dislocation" and "vicinal" steps have the same height of approximately 0.3 nm corresponding to the period of the GaAs lattice in the [001] direction. Along with this similarity, the dislocation and vicinal steps are qualitatively different in a few respects. The first apparent difference is that the dislocation steps are straight and have definite crystallographic directions, while the vicinal steps are curved, and their shape and direction are determined by uncontrollable smooth variations of the surface relief. Second, there are no intersections within the set of vicinal steps, while the dislocation steps intersect with each other and with the vicinal steps. Third, at a surface fragment with a certain sign of the miscut angle, all vicinal steps have the same sign. Thus, vicinal steps form a monotonically descending (or ascending) staircase. On the contrary, as it is seen from Fig. 1, the sign of dislocation steps may change from one step to another. Therefore, dislocation steps form a set of mutually orthogonal stripes with non-monotonic interchange of lower and higher lying terraces. Finally, the dislocation steps have higher stability to thermal fluctuations as compared to the vicinal steps. The higher thermal stability is proved by the AFM image obtained after anneal at high temperature $T = 675$ °C (Fig. 1d). The small-scale ($\sim$10 nm) undulations of the vicinal steps are clearly seen in Fig. 1d, while the dislocation steps remain relatively straight. The higher stability of dislocation steps can be tentatively explained by the anisotropy of step linear tension, i.e. by smaller linear tension of the steps oriented along the $\langle 110 \rangle$ axes. The strains induced by the dislocations may also contribute to the stability of the dislocation steps.

A tentative microscopic explanation for the formation of the dislocation-induced steps is as follows. In strained (001) films of cubic semiconductors (Ge, Si, GaAs) plastic relaxation occurs primarily via the formation of 60° misfit dislocations [4–6]. Dislocation half-loops are generated in the $\{111\}$ glide planes. Each of the half-loops consists of a 60° misfit dislocation, which lies in the (001) plane, and two threading segments, crossing the film and outgoing the surface. A dislocation half-loop produce a step of monatomic height along the straight line connecting the intersections of the threading segments with the surface. The misfit dislocation develops due to the half-loop extension by the glide of threading segments in opposite directions towards the sample edges. For the films with thicknesses exceeding the mean distance between the dislocations, the profile of the dislocation-induced surface displacement has the shape of a rectangular monatomic step [5], in accordance with the results presented here in Fig. 1. To our knowledge, this is the first reliable observation of the step-terraced morphology with dislocation-induced monatomic steps produced due to plastic relaxation in a strained semiconductor film. It should be noted, that Lutz *et al*. [4] identified faint lines in AFM images of partially strain relaxed 80-nm thick GeSi film grown on Si substrate as dislocation-induced steps of monatomic height. However, the surface of the film was not smooth enough to measure the profile of the dislocation lines with sufficient accuracy.

In summary, we demonstrated an opportunity to form a step-terraced surface morphology, which consists of a rectangular grid of straight dislocation-induced monatomic steps, by means of plastic relaxation of GaAs(001) layers. This morphology is qualitatively different from that of a vicinal surface, in which the direction and shape of the steps and the terrace width depend on variations of the surface relief. The straightness and definite direction of the dislocation-induced steps are potential advantages for fabrication of regularly organized nanoscale structures on step-terraced semiconductor surfaces.

Acknowledgements

This work was supported by the Russian Foundation for Basic Research (Grant No. 11-02-00991) and by the Russian Academy of Sciences.

References

[1] H.-C. Jeong and E. D. Williams, *Surface Sci. Reports* **34**, 171 (1999).
[2] A. V. Latyshev, A. L. Aseev, A. B. Krasilnikov and S. I. Stenin, *Surf. Sci.* **213**, 157 (1989).
[3] V. L. Alperovich *et al*., *Appl. Phys. Lett.* **94**, 101908 (2009).
[4] M. A. Lutz *et al*., *Appl. Phys. Lett.* **66**, 724 (1995).
[5] A. M. Andrews *et al*., *J. Appl. Phys.* **95**, 6032 (2004).
[6] Yu. B. Bolkhovityanov *et al*., *J. of Crystal Growth* **293**, 247 (2006).

20th Int. Symp. "Nanostructures: Physics and Technology"
Nizhny Novgorod, Russia, June 24–30, 2012

Formation of graphane by annealing of a few layer graphene intercalated with organic molecules

I. V. Antonova[1], I. A. Kotin[2], V. A. Volodin[1] and V. Ya. Prinz[1]

[1] A.V. Rzhanov Institute of Semiconductor Physics, SB RAS, Lavrentieva 13, 630090 Novosibirsk, Russia
[2] Novosibirsk State Technical University, 630092 Novosibirsk, Russia

Abstract. Possibility to create a few layer graphane by means of intercalation of the organic molecules into few layer graphene films with subsequent annealing at temperature of molecule polymerization was demonstrated. Polymerization leads to releasing of hydrogen atoms. Increase in annealing temperature leads to increase in graphane/graphene relation.

Introduction

Atoms or molecules being attached to the atoms of graphene in a strictly periodic manner result in an essentially different electronic and crystalline structures of material. An example for this is graphane, the stoichiometric derivative of graphene, a wide-gap semiconductor (3–3.5 eV), in which hydrogen atom is bonded to each carbon atom [1]. Graphane retains the hexagonal lattice and its period is markedly shorter than that of graphene. It was shown [1, 2] that by exposing graphene to atomic hydrogen (for instant in hydrogen plasma [3]), it is possible to transform this highly-conductive semimetal into an insulator. Graphane attracts a high interest of researchers because the reaction with hydrogen is found to be reversible so that the original metallic state and lattice spacing are restored by annealing. So, the chemical modification of graphene becomes promising for creation a whole range of new two-dimensional crystals with designed electronic and other properties.

In the present study we had demonstrated possibility to create a few layer graphane by means of intercalation of the organic molecules (N-methylpyrrolidone, NMP) into few layer graphene (FLG) films with subsequent annealing at temperature of NMP polymerization. Polymerization leads to releasing of hydrogen atoms and formation of graphane areas on every graphene planes in the film. Polar solvents, such as NMP has well-known capability to penetrate in between graphene layers and ability to create chemically non-modified graphene-NMP solutions. NMP are widely used for preparation graphene suspensions for various applications. NMP, which matches the surface energy of graphene, are very effective for stabilization of few-layer graphene sheet in solution, preventing their re-aggregating and providing a unique basis for further processing. As a result, we have created the few-layer graphene-based films with reproducible and tunable electronic properties dependently on the graphene/graphane relation.

1. Results and discussion

Electrostatic exfoliation of graphene or FLG from highly oriented pyrolytic graphite and transfer of exfoliated FLG layers onto a 300-nm SiO_2/Si substrate were used for production of FLG flakes. For studies we had chosen a flake with width of 5–10 μm and thickness up to 4 nm. Then, intercalation of N-methylpyrrolidone (C_5H_9NO) into the exfoliated FLG flakes was performed during 7–14 days. Annealing of NMP-intercalated structures were made at a set of temperatures in the range of 80–300 °C during 5 min in air ambient.

AFM images are revealed that starting with the 190 °C annealing temperature the bright islands are formed on the surface of NMP-FLG structures (Fig. 1a). Increase in annealing temperature leads to increase in bright island areas and density. For annealing temperatures 270–300 °C intercalated structures are found to form the scrolls with diameters 1–10 μm dependently on film thickness.

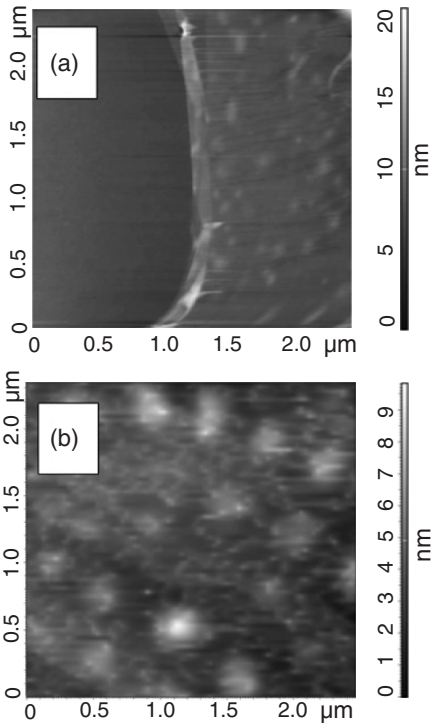

Fig. 1. AFM image of surface structure annealed at 190 °C (a) and 250 °C (b). The height of bright islands is about $\approx$ 2 nm for (a) and 3–4 nm for (b).

Raman spectra for these temperatures (190–250 °C) demonstrate the substantial transformations in comparison with spectra for non-annealed samples. The intensity of the D line becomes strongly increased. Moreover, a 1500 cm^{-1} line was additionally revealed in the Raman spectra; this band is known to be a disorder-induced first-order scattering band similar to the D line [2]. Also, peaks at 1625 and 2980 cm^{-1} appeared in the spectra. According to [1], the growth of the sharp D peak and the appearance of an additional peak at 1620 cm^{-1}, called D', and also the emergence of a peak around 2950 cm^{-1}, being the combination mode of D and D'-vibrations, are attributed to interruptions of π-electron delocalization subsequent to the formation of C–H sp^3-bonds. These changes in Raman spectra

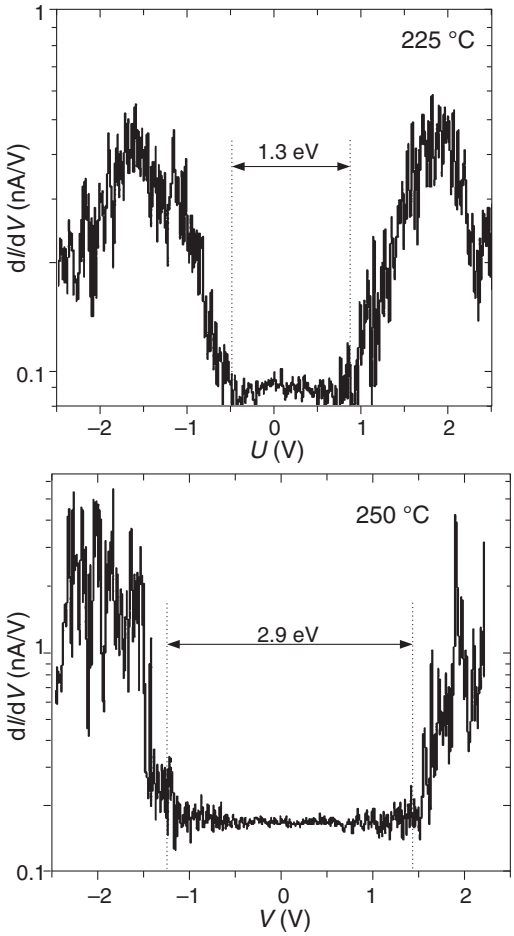

Fig. 2. STS measurements of dI/dV characteristics for structures annealed at temperatures 225 and 250 °C.

for structures annealed at $T > 190$ °C clearly demonstrate hybridization of carbon atoms from sp^2 to a distorted sp^3-state [1–3]. Broadening of the G and D lines, normally observed during graphene oxidation, was not observed in the Raman spectra of our samples.

Results of STS measurements in the form of dI/dV characteristics measured at structures annealed at different temperatures in the range 190–250 °C are shown in Figure 1b. The dI/dV characteristics clearly demonstrate that a band gap was open in our structures. According to data measured at different points, band-gap values ΔE_G in our structures varied in the range from 0 to 2.9 eV. Change in annealing temperature tunes the bandgap value. Resistivity of our annealed structures was found to be of 3–7 orders higher then resistivity of initial FLG flakes.

The calculations made in [4] show that it is energetically favorable for adsorbed hydrogen to arrange in graphane islands, where every C atom binds to a hydrogen atom resulting in a local re-hybridization from sp^2 to sp^3 bonding. Such graphane islands are appeared bright ones in the STM images of [4]. Formation of graphane islands could be realized in graphene systems by, for example, patterned hydrogen adsorption templated by a self-assembled molecular layer. We had suggested that our bright islands in the AFM images are also attributed to graphane islands. The appearance of sp^3 hybridization of carbon atoms is clearly observed in Raman spectra. Strong increase in resistivity of layers in combination with increase in bandgap observed by STS with increase in annealing temperature are supported this suggestion. Moreover, dependence of measured bandgap value EG versus of the area covered with bright islands at the surface of samples annealed at different temperatures was found to be correlated with dependence of E_G versus hydrogen coverage calculated in [4]. Increase in resistivity of our structures with annealing temperature is also in a good agreement with formation and increase in area of insulating graphane islands. We have to mention here, that in intercalated structures annealed at $T > 190$ °C such processes as polymerization or polycondensation, proceeding with the release of hydrogen atoms, are well-known for NMP.

2. Conclusion

We have demonstrated that annealing of the few-layered graphene structures intercalated with organic molecules NMP leads to formation of the graphane islands due to polymerization of NMP and releasing of hydrogen atoms.

Acknowledgements

This study was supported by the Russian Foundation for Basic Research under Grants 11-02-00722, 12-02-01275 and interdisciplinary integration project of SB RAS.

References

[1] D. C. Elias, R. R. Nair, T. M. G. Mohiuddin, S. V. Morozov, P. Blake, M. P. Halsall, A. C. Ferrari, D. W. Boukhvalov, M. I. Katsnelson, A. K. Geim, K. S. Novoselov, *Science* **323**, 610 (2009).

[2] A. Gupta, G. Chen, P. Joshi, S. Tadigadapa, P. C. Eklund *et al.*, *Nano Letters* **6**, 2667 (2006).

[3] Z. Luo,T. Yu, K. Kim, Z. Ni, Y. You, S. Lim *et al.*, *ACS Nano* **3**, 1781 (2009).

[4] R. Balog, B. Jorgensen, L. Nilsson, M. Andersen, E. Rienks, M. Bianchi, M. Fanetti, E. Lægsgaard, A. Baraldi, S. Lizzit, Z. Sljivancanin, F. Besenbacher, B. Hammer, T. G. Pedersen, P. Hofmann, L. Hornekær, *Nature Materials* **9**, 315 (2010).

20th Int. Symp. "Nanostructures: Physics and Technology"
Nizhny Novgorod, Russia, June 24–30, 2012

New approach to create a few-layer fluorographene with nanoswell surface relief

N. A. Nebogatikova[1,2], I. V. Antonova[2], V. A. Volodin[2] and V. Ya. Prinz[2]

[1] Novosibirsk State University, Pirogov str. 2, 630090 Novosibirsk, Russia
[2] A.V. Rzhanov Institute of Semiconductor Physics, SB RAS, Lavrentieva 13, 630090 Novosibirsk, Russia

Abstract. In the present study we have demonstrate that fluorination of graphene or few-layer graphene (FLG, thickness less than 10 nm) was achieved using an HF treatment of pristine graphene flakes. A network of fluorographene was revealed on the surface of graphene films already after treatment of samples in a 5% solution of HF in water lasting for 4–5 min. A periodic nanoswell relief and a step-like increase in film resistance (up to 100 GΩ) were found on the surface of graphene films treated in the solution during times longer than 5 min. was observed. We have also reveald that the fluorination process can be suppressed by a preliminary treatment of graphene in isopropyl alcohol.

Introduction

Fluorographene (FG) is one of the main derivatives of graphene attracting huge interest for last few years. It is a stoichiometric derivative of graphene with fluorine atom attached to each carbon atom [1]. FG is stable material (up to temperature 400 °C) and a high-quality insulator (resistivity $>10^{12}$ Ω) with optical bandgap 3 eV [1, 2]. In the present report, we demonstrate a new, very simple approach for creation of FG. This process uses treatment of graphene or few-layer graphene in aqueous solution of hydrofluoric acid yielding fluorogrphene or few-layer FG with nanoswell relief on the surface.

Synthesis of FG is generally performed using two main methods. In the first method, mechanical exfoliation of graphene flakes from fluorinated graphite is used. Fluorinated graphite is normally created by exposing graphite to a fluorinating agent (F_2 or XeF_2) at enhanced temperature (120–400 °C) for a long time (ten or more hours) [3–5]. Graphite fluoride can also be obtained at room temperature using a reaction of graphite with a gaseous mixture of F_2, HF, and MF_n (the volatile fluorides MFn used were IF_5, BF_3, and ClF_3) followed by subsequent treatment of the resulting material in a fluorine-containing ambient at temperatures 100–600 °C (see [4] and references within). However, one cannot obtain fully fluorinated graphite. Mechanical cleaving of individual atomic planes of FG from commercially available fluorinated graphite was found to be a surprisingly difficult task [4], and only multilayered samples of non-stoichiometric FG were reported. Moreover, FG sheets were found to be extremely fragile and prone to rupture due to many structural defects resulting from the harsh fluorination conditions used to obtain bulk fluorinated graphite [4]. In the second method, FG is created by mechanical exfoliation of graphene flakes from graphite with subsequent fluorination of the flakes by a procedures described above. Due to the small sizes of graphene flakes, it is possible to obtain fully fluorinated graphene flakes with the use of the XeF_2 agent using treatments lasting for about 2 weeks [3]. Since XeF_2 rapidly etches Si substrate and readily diffuses even through of amorphous SiO_2, it appears impossible to use SiO_2/Si substrates in the fluorination procedure; using a chemically inert support is therefore normally required. The need for an inert support makes the whole process rather a complicated procedure [4].

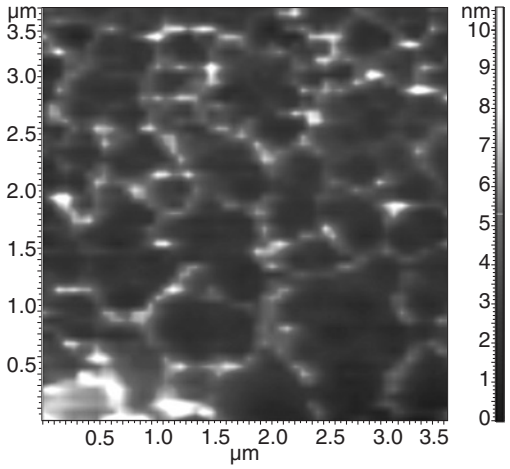

Fig. 1. AFM images of the surface of samples treated in 5% solution of HF in water during 9 min.

1. Results and discussion

Fluorination of graphene or few-layer graphene (with thickness below 10 nm) by means of HF treatment during few minutes is suggested in the present study. Such treatment resulted in dramatic changes of structural and electrical properties of the material. The interaction of graphene with HF observed as a function of HF treatment duration exhibited a two-stage behavior.

At the first stage, Raman spectra of samples treated in HF:H2O solution demonstrated an increase in D-peak intensity (1350 cm^{-1}) and a decrease in the intensity of G and 2D peaks (respectively 1580 cm^{-1} and 2700 cm^{-1}). A network relief with height 3–4 nm was revealed on the surface of such samples by atomic force microscopy (AFM). Grain boundary mapping is assumed to be responsible for the formation of this network. The resistivity of the graphene structures remained roughly unchanged at this stage of HF treatment. A surprising finding was that in HF-treated structures the current value in the $I_{ds}(V_g)$ characteristics measured in transistor configuration using the substrate as the gate electrode varied over 4–5 orders of magnitude with variation of gate voltage V_g. On the contrary, reference (not treated in HF:H_2O) few-layer graphene samples demonstrated variation of drain-source current Ids within 30%. This effect was found to be due to an increase of carrier mobility. Thus, our films shortly treated in HF:H_2O demonstrated a

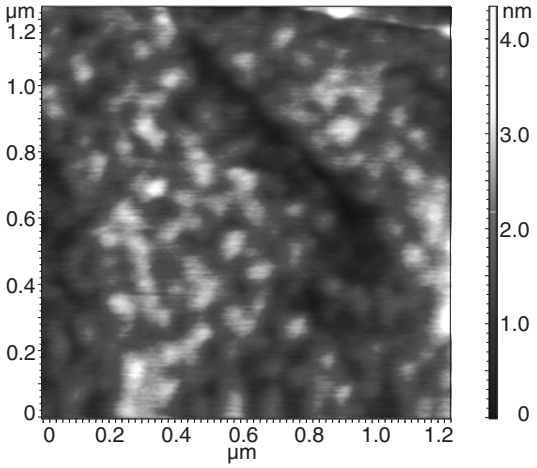

Fig. 2. AFM images of the surface of samples treated in 5% solution of HF in water during 9 min.

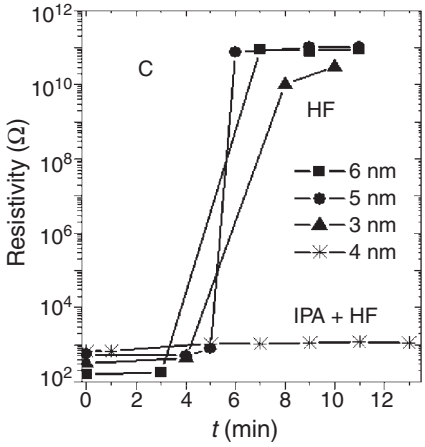

Fig. 3. Resistivity of various few-layer graphene flakes versus the HF-treatment duration t. The few-layer graphene thickness is given in the figure sheet as a parameter. The curve labeled IPA + HF in (2) refers to the sample that was preliminarily (before HF-treatment) treated for 20 min in isopropyl alcohol (IPA).

high potential in management with their conductivity.

The second stage of the graphene-HF interaction proceeded over HF treatment times of 30 s for graphene proper and over times of 5 min for structures with thickness 3–5 nm. At this stage, graphene-related peaks disappeared from Raman spectra. A step-like increase in resistivity (up to 100 GΩ) was observed in such structures. This modification of few-layer graphene properties suggests the formation of FG during treatment of graphene in HF:H_2O solution. A periodic nanoswell relief (step $\approx$ 50−100 nm and height $\approx$ 2−6 nm depending on treatment duration and sample thickness) was observed by AFM on the surface of the samples. Thermal stability of our FG samples was tested by giving them an additional anneal. It is known that hydrogen desorption from graphene occurs at temperatures $\approx$ 200−290 °C [3]. On the other hand, C-F bonds are stable up to $\approx$ 400 °C [1,2]. We have performed an annealing of one of the FG samples at temperature 300 °C for 1 h. The properties of the annealed structure showed no changes after annealing. Repeated measurements performed over a one-year period proved time stability of created material.

Fluorine ions present in HF/water solution were found to be necessary for the fluorination reactions. For comparison, several graphene samples were given treatment in HF vapor. The duration of the latter treatment was varied from 1 min to 17 hours. It was found that the resistivity value remained unchanged over 17 h of HF vapor treatment. We would like to mention here that such samples showed no changes in Raman spectra as well.

The fluorination process could be made controllable using a preliminary treatment of graphene in isopropyl alcohol. The latter treatment was found to suppress fluorination of graphene in HF/water solution. Combination of the two treatments gives one a key for nanodesign of graphene-based devices.

2. Conclusion

The new approach to create fully fluorinated graphene by treatment of graphene samples in a solution of hydrofluoric acid in water is suggested. It was found that a few minute treatment (>5 min for the 5% HF:H_2O solution) of the samples with thickness lower than 10 nm was sufficient for observing a transition to insulator due to graphene fluorination. The obtained FG presents a high-quality insulator with resistance $>10^{11}$ Ω and a periodic nanoswell relief (step about 100 nm).

Acknowledgements

This study was supported by the Russian Foundation for Basic Research under Grants 11-02-00722, 12-02-01275a and interdisciplinary integration project of SB RAS.

References

[1] S.-H. Cheng, K. Zou, F. Okino, H. R. Gutierrez, A. Gupta, N. Shen, P. C. Eklund, J. O. Sofo, J. Zhu, *J. Phys. Rev. B.* **81**, 205435 (2010).

[2] R. R. Nair, W. Ren, R. Jalil, I. Riaz, V. G. Kravets, L. Britnell, P. Blake, F. Schedin, A. S. Mayorov, S. Yuan, M. I. Katsnelson, H.-M. Cheng, W. Strupinski, L. G. Bulusheva, A. V. Okotrub, I. V. Grigorieva, A. N. Grigorenko, K. S. Novoselov, A. K. Geim. *Small.* **6**, 2877 (2010).

[3] S. Ryu, M.Y. Han, J. Maultzsch, T.F. Heinz, P. Kim, M.L. Steigerwald, L.E. Brus. *Nano Letters* **8**, 4597 (2008).

[4] Cheng S.-H., Zou K., Okino F., Gutierrez H. R., Gupta A., Shen N., Eklund P.C., Sofo J. O. Zhu J. J., *Phys. Rev. B.* **81**, 205 (2010).

[5] R. R. Nair, W. Ren, R. Jalil, I. Riaz, V. G. Kravets, L. Britnell, P. Blake, F. Schedin, A. S. Mayorov, S. Yuan, M. I. Katsnelson, H. M. Cheng, W. Strupinski, L. G. Bulusheva, A. V. Okotrub, I. V. Grigorieva, A. N. Grigorenko, K. S. Novoselov, A. K. Geim, *Small.* **6**, 2877 (2010).

[6] Withersy F., Duboisz M., Savchenko A.K. *Phys. Rev. B.* **82**, 1 (2010).

20th Int. Symp. "Nanostructures: Physics and Technology"
Nizhny Novgorod, Russia, June 24–30, 2012

First principle simulations of the Me adatom diffusion on the 1/3 ML Si(111)$\sqrt{3}\times\sqrt{3}$ metal induced surfaces

Yu. V. Luniakov

Surface Physics Department, Institute for Automation and Control Processes, 690041 Vladivostok, Russia

Abstract. Using Nudged Elastic Band (NEB) optimization the minimal energy paths and diffusion parameters for an additive Me adatom moving on the corresponding Me induced Si(111)$\sqrt{3}\times\sqrt{3}$ surface have been obtained. The height of the activation energy barrier is shown to be determined by the metallic atomic radius of the diffusing metal: 0.44 eV for Pb, 0.36 for Sn, 0.22 eV for In, 0.13 eV for Ga and 0.08 eV for Al. The Arrhenius pre-exponential factors obtained in harmonic approximation are so high as $\sim 10^{13}$, supporting the considered single adatom diffusion model.

Introduction

Si(111)$\sqrt{3}\times\sqrt{3}$ surface obtained for 1/3 ML of Me adsorbate coverage is a very popular model system and a perspective subject from the experimental and theoretical viewpoint. The room temperature structure $\sqrt{3}\times\sqrt{3}$ with 1/3 of a monolayer (ML) of adatoms is well known today and might be expected to be one of the best-understood reconstructions in surface science. In this structure there is one Me adatom among three neighboring T_4 sites of the bulk-terminated Si(111)1×1 layer, occupying the threefold symmetric T_4 site above the second-layer Si atoms as shown in Fig. 1*a*. This type of the structure is formed on the Si(111) surface by group III metal atoms Al, In, Ga, Pb, a group IV metal atom Sn and a group V metal atom Bi [1].

The Ge(111) and Si(111) surface with Sn and Pb adsorbates has been the subject of intensive experimental and theoretical investigations due to their structural transitions at temperatures 210 and 250 K for Sn and Pb on the Ge(111) surface, respectively [2–7], and at temperature 86 K for Pb on the Si(111) surface [8]. In this context, the Pb/Si(111) system is a very attractive playground for a study of diffusion. For example, the study of the different paths and activation energies for the diffusion of single Pb adatoms adsorbed on the $\sqrt{3}\times\sqrt{3}$ surface can be performed experimentally at the atomic resolution. As was shown by Brihuega *et al*. [9], a Pb induced surface can be prepared atomically clean defect free and an investigation of a single adatom diffusion is feasible. In their following work Brihuega *et al*. [10] have identified the nature and adsorption sites of the additional Pb adatoms and accurately determined the diffusion parameters of a single Pb adatom on the perfect defect free Pb induced Si(111)$\sqrt{3}\times\sqrt{3}$ surface. A measurement of the hopping rate in a temperature range from 145 to 165 K gives the activation energy value $E_d = 0.45 \pm 0.01$ eV and the pre-exponential factor (prefactor) $A = 10^{13.0\pm0.4}$ Hz. The purpose of the present work is to investigate the possibility of a single extra Me adatom diffusion on all known Me induced Si(111)$\sqrt{3}\times\sqrt{3}$ surfaces, formed at Me coverages 1/3 ML, namely, for Sn, Pb, Al, Ga, In and Bi, using a reliable DFT simulation tools.

1. Methods of calculations

For the first principle simulations we employed the local density approximation (LDA) after Ceperley–Alder [11] in the Perdew–Zunger parametrization [12] for the exchange and correlation functional with projector-augmented wave pseudopotentials (PAW) [13, 14], implemented in VASP ab-initio program [15]– [18]. The surface has been simulated by a periodic slab geometry with Si(111)$4\sqrt{3}\times 4\sqrt{3}$ Me induced unit cells, containing six silicon atomic layers and one Me adsorbate layer. The dangling bonds of the bottom slab layer have been saturated by hydrogen atoms. The hydrogen atoms and bottom layer silicon atoms have been fixed and the rest atoms have been set free to move. A vacuum region of more than 10 Å has been incorporated within each periodic unit cell to prevent interaction between adjacent surfaces. Wave functions were represented using a plane-wave basis set with a kinetic energy cutoff of 250 eV. The Brillouin zone integration was performed with one Γ-point for so large as $4\sqrt{3}$ supercell. The dependency of formation energy on the kinetic energy cutoff, k-points number as well as the number of Si layers has been checked out and found to have a negligible effect on the total energy differences. A special care was taken for a choose of the number of $\sqrt{3}$ unit cells in the supercell to minimize the interaction of the extra Me adatoms in the neighboring cells. An investigation of the dependency of the activation energy barrier height on the number of $\sqrt{3}$ cells in the supercell shows that four $\sqrt{3}$ cells will be sufficient enough.

The migration barriers for Me adatom were calculated using the NEB method [19, 20], that is a method for calculating of a diffusion barrier between two known minimum energy sites by optimization of a number of intermediate images of the adatom along the diffusing path. For finding the true saddle point, corresponding to the transition state, a special dimer method [21,22], has been applied. The pre-exponential factors of the Arrhenius function $\nu = A\, e^{-E_d/kT}$ have been calculated using harmonic transition state theory approach [23]:

$$A = \frac{kT}{h}\frac{\prod_{i=1}^{3N-1}\left(1-e^{\frac{-h\nu_i^*}{kT}}\right)}{\prod_{i=1}^{3N}\left(1-e^{\frac{-h\nu_i}{kT}}\right)}, \qquad (1)$$

where ν is the observed oscillation frequency, E_d is the activation energy, T is the temperature, N is the number of the moving atoms, k and h are the Boltzmann and the Planck constant, respectively. The product over all vibrational frequencies ν_i is calculated for the equilibrium state with the minimal energy and the product over $N-1$ vibrational frequencies ν_i^* is calculated for the transition state with one imaginary frequency, obtained using transition state NEB approach (dimer method) [21, 22].

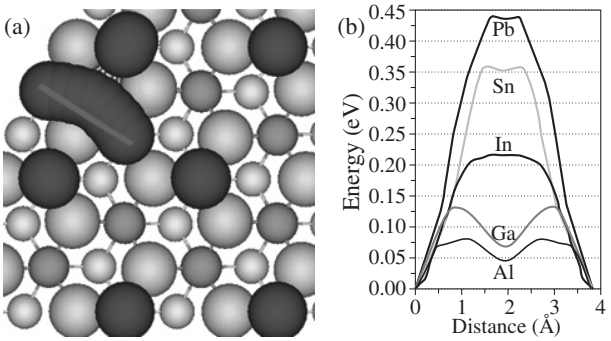

Fig. 1. (a) The minimum energy path of Me adatom diffusion obtained by NEB optimization of the intermediate images between two equilibrium configuration with the additive Me adatom, located in a vacant T_4 site, and (b) the corresponding energy profiles. Me atoms are shown by the large black circles, the topmost Si atoms of the 1st layer are shown by the largest gray circles, the 2nd layer Si atoms are shown by the smaller gray circles, the 4th layer Si atoms are shown by the smallest gray circles.The adsorption sites T_1, T_4 and H_3 are marked by text labels.

2. Results and discussions

The simulation of a movement of the additive Me adatom on the corresponding Me induced Si(111)$\sqrt{3} \times \sqrt{3}$-Me surface with Me = Al, Ga, In, Pb and Sn demonstrates that the minimum energy path is passing around the first layer Si atom T_1 through the hollow H_3 site (Fig. 1*a*). The dependence of the height of the energy barrier on the distance, passed by the extra Me adatom, is shown in Fig. 1*b*. For simplicity the distances passed by the Me adatom have been projected to the line connecting the neighboring T_4 sites, so that the whole distance will be equal to the 2D-lattice period 3.81 Å. The calculations show that the diffusion barrier is the highest for the Pb adatom and the lowest for the Al adatom, let alone the Bi adatom, where the Bi trimer formation is taking place. The activation barriers height are summarized in Table 1. We can see that the height of the activation barrier is in correlation with the Me atomic radius: the "smaller" metals such as Ga and Al moves easier than the "larger" metals such as Pb and Sn. The "largest" metal Bi for some reasons prefers to form trimers [24]. For better understanding of the dependency of the activation barrier on the Me adatom nature additive investigations are required.

The comparison of the calculated activation energy barrier height for the Pb adatom diffusion on the corresponding Si(111)$\sqrt{3} \times \sqrt{3}$-Pb surface with the experimental data obtained by Brihuega *et al*. [10] gives very good agreement, supporting the considered mechanism of the single metal adatom diffusion. The calculation of the Arrhenius prefactor A (Eq. 1) have been performed for an average temperature, used by Brihuega *et al*. for the experimental determination of the prefactor $T = \frac{165+145}{2} = 155$ K. The calculated prefactor $A = 3.13 \times 10^{12}$ Hz, obtained for the atomic displacement of 0.01 Å, is in agreement with the experimental one $A = 10^{13.0 \pm 0.4}$ Hz, thus supporting the considered single adatom diffusing mechanism. For other Me adatoms the Arrhenius activation prefactors have not been calculated due to their high CPU time requirement. Unfortunately there are no experimental data for metals other that Pb to compare with. But the good agreement of the calculated data with the experiment in the Pb case gives a hope that the results obtained are quite correct.

Table 1. The activation energy barrier heights (in eV) for different metals moving on the corresponding Me-induced surfaces in comparison with the atomic radii (in Å).

Metal	Experimental	Calculated	Atomic radius
Pb	0.45 [10]	0.44	1.70
Sn		0.36	1.63
In		0.22	1.58
Ga		0.13	1.40
Al		0.08	1.43
Bi		−1.55	1.78

References

[1] V. G. Lifshits, K. Oura, A. A. Saranin and A. V. Zotov, Metals on semiconductors in Handbook Physics of covered solid surfaces. Landolt-Börnstein New Series, Group III: Condensed Matter, Vol. 42. Berlin, Heidelberg: Springer, 2001. P. 259.

[2] M. Carpinelli, H. A. Weitering, E. W. Plummer and R. S. Stumpf *Nature* **381**, (1996)398.

[3] A. Goldoni, C. Cepek and S. Modesti, *Phys. Rev. B.* **55**, (1997) 4109.

[4] A. Goldoni and S. Modesti, *Phys. Rev. Lett.* **79**, (1997) 3266.

[5] J. Avila, A. Mascaraque, E. G. Michel, M. C. Asensio, G. LeLay, J. Ortega, R. Pérez and F. Flores, *Phys. Rev. Lett.* **82**, (1999) 442.

[6] J. M. Carpinelli, H. H. Weitering, M. Barkowiak, R. Stumpf and E. W. Plummer, *Phys. Rev. Lett.* **79**, (1997) 2859.

[7] R. S. Stumpf, J. M. Carpinelli and H. H. Weitering, *Phys. Rev. B* **59**, (1999) 15779.

[8] I. Brihuega, O. Custance, R. Pérez and J. M. Gómez-Rodríguez, *Phys. Rev. Lett.* **95**, (2005) 046101.

[9] I. Brihuega, O. Custance, M. M. Ugeda and J. M. Gómez-Rodríguez, *Phys. Rev. B* **75**, (2007) 155411.

[10] I. Brihuega, M. M. Ugeda and J. M. Gómez-Rodríguez, *Phys. Rev. B* **76**, (2007) 035422.

[11] D. M. Ceperley and B. J. Alder, *Phys. Rev. Lett.* **45**, (1980) 566.

[12] J. P. Perdew and A. Zunger, *Phys. Rev. B* **23**, (1981) 5048.

[13] P. E. Blöchl, *Phys. Rev. B* **50**, (1994) 17953.

[14] G. Kresse, and D. Joubert, *Phys. Rev. B* **59**, (1999) 1758.

[15] G. Kresse and J. Hafner, *Phys. Rev. B.* **47**, (1993) 558.

[16] G. Kresse and J. Hafner, *Phys. Rev. B* **49**, (1994) 14251.

[17] G. Kresse and J. Furthmuller, *Phys. Rev. B* **54**, (1996) 11169.

[18] G. Kresse and J. Furthmuller, *Comput. Mater. Sci.* **6**, (1996) 15.

[19] G. Henkelman, B. P. Uberuaga, and H. Jonsson, *J. Chem. Phys.* **113**, (2000) 9901.

[20] G. Henkelman and H. Jonsson, *J. Chem. Phys.* **113**, (2000) 9978.

[21] J. Kästner and P. Sherwood, *J. Chem. Phys.* **128**, (2008) 014106.

[22] A. Heyden, A. T. Bell and F. J. Keil, *J. Chem. Phys.* **123**, (2005) 224101.

[23] G. H. Vineyard, *J. Phys. Chem. Solids* **3**, (1957) 121.

[24] M. Saitoa, T. Ohno, T. Miyazaki, *Applied Surface Science* **237**, (2004) 80.

20th Int. Symp. "Nanostructures: Physics and Technology"
Nizhny Novgorod, Russia, June 24–30, 2012

SPM bipolar pulsed nanostructuring of graphitic layers

S. V. Kosheleva[1], *V. D. Frolov*[2] and V. I. Konov[2]

[1] Moscow State Institute of Radiotechnics, Electronics and Automation, Moscow, Russia
[2] A.M. Prokhorov General Physics Institute of RAS, Moscow, Russia

Abstract. Local ablation of highly oriented pyrolytic graphite by SPM probe was investigated. The gap between the tip and sample surface was varied. Mono and bipolar electric impulses were applied. Influence of various processing parameters on graphite ablation rates was investigated. Shallow craters and structures with halfwidth as low as 15 nm were produced. Electro-mechanical mechanism of graphite nanoablation is discussed.

Introduction

Graphene has many fascinating physical properties and potential applications. Until now, in most of the experiments relatively uniform and extended ($\geq$5$-$10 μm) lists of graphene where used, while nanostructured graphene can demonstrate extraordinary features that open new frontiers in photonics and electronics. For example, when graphene element size is less than 5 nm it becomes comparable with the De Broil wavelength in this material and thus one can expect quantum-size effects in such graphene nanostructures. Etching and ablation of materials by Scanning Probe Microscope (SPM) looks like a serious alternative to electron and ion beam lithography for nanostructuring. It is a direct processing technology (no need of protecting mask) and potentially comparable or even better spatial resolution can be obtained for very sharp tips. Local anodic oxidation (LAO) in air has been considered as a mechanism of graphite SPM nanostructuring [1–3]. In our previous experiments [4] it was shown that SPM chemical etching of highly oriented pyrolytic graphite (HOPG) is accompanied by mechanical action of SPM probe and depends on the polarity of the applied electrical pulse. (HOPG is traditionally used for modeling of graphene because its surface shows the same chemical behavior as single layer graphene). The aim of this work is to investigate dynamics of HOPG nanoablation by SPM (ablation rates) and test the possibility to improve spatial resolution of the produced nanostructures by means of bipolar electrical pulses.

1. Experimental

The experiments were carried out with SPM Solver P47, using conducting (n-type) Si cantilevers in both contact and noncontact modes at ambient conditions. The force constant was $Fc \sim 20\ N/m$, tip radius was $r \sim 10$ nm. Nanoobjects on the HOPG surface were formed by applying a series $N = 30-1000$ of voltage pulses between the sample and the grounded probe. Uni- or bipolar pulses had total duration $\tau = 2-60$ ms. The value τ was determined as $\tau = \tau_p + \tau_n$ (τ_p, $U_p = +10$ V and τ_n, $U_n = -10$ V are duration and amplitude of positive and negative pulses, respectively). The sample surface morphology was tested before and after the actions...

2. Experimental results and discussions

In the case of unipolar negative pulses no surface modification was observed. It was found that positive pulse action strongly depended on the gap ΔZ between the tip and the sample surface. For $\Delta Z \geq 0$, protrusions were detected as a result of multiple-pulsed SPM action. HOPG removal (ablation) could be realized only for $\Delta Z = -5$ nm (that corresponds to the probe pressure on the sample surface $P \approx 0.1$ μN). It should be noted that the crater depth was smaller than the protrusion height. Another requirement for the crater formation was the air humidity (60–80% in our experiments). The ablation rates $R = D/N$ (D — depth of the crater produced by N pulses) for bipolar pulses as dependences on τ_p (lower scale, leading negative pulse with $\tau_n = 30$ ms) and τ_n (upper curve, leading positive pulse $p = 30$ ms) are presented in Fig. 1. As a reference the dashed line $R(\tau_p)$ for unipolar positive pulse is also given. One can see that unipolar positive pulse ablation rate grows linear with τ_p. Application of bipolar pulses leads to lower ablation rates and for long enough subsequent pulses in both cases the R value saturates at the level $R \geq 3 \times 10^{-3}$ nm/pulse. This rate is much smaller than can be achieved for unipolar positive pulse ($R \geq 3 \times 10^{-3}$ nm/pulse). Both curves $R(\tau_p)$ and $R(\tau_n)$ for bipolar pulses are well approximated by the exponents with equal constants $\tau_{no} = \tau_{po} = 5$ ms. We believe that in spite of lower R for bipolar pulses their application to graphite surface nanostructuring can be beneficial, because these regimes should be more stable to pulse parameters fluctuations.

The crater profiles, obtained for bipolar (curves 1a and 1b in Fig. 2) and unipolar (curve 2 in Fig. 2) pulses give an obvious evidence of the advantage of bipolar HOPG nanostructur-

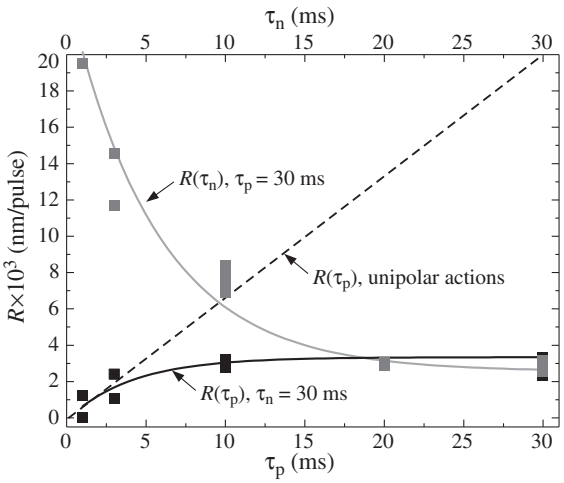

Fig. 1. The dynamics of removal process. The dashed line shows the averaged dependence of rate R on the positive pulse duration τ_p in the case of unipolar actions. Exponential fits of dependences $R(\tau_n)$ at ($\tau_p = 30$ ms and $R(\tau_p)$ at $\tau_p = 30$ ms are shown by solid lines. The positive and negative pulse amplitudes are $U_p = 10$ V and $U_n = -10$ V, respectively.

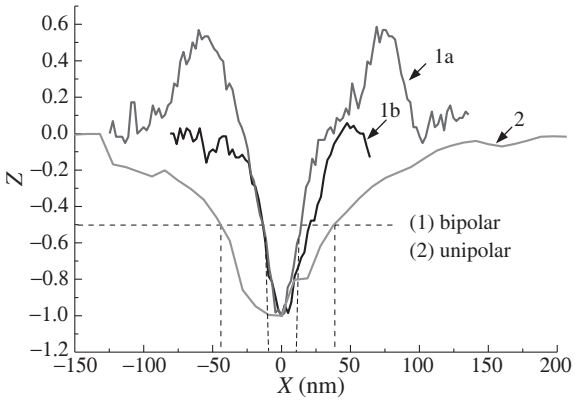

Fig. 2. The crater profiles: (1a) after bipolar pulse actions; (1b) the same region after cleaning; (2) after unipolar pulse actions. On the plot, the ordinate Z is normalized to the crater depth D. The dashed lines show halfwidths of the formed craters.

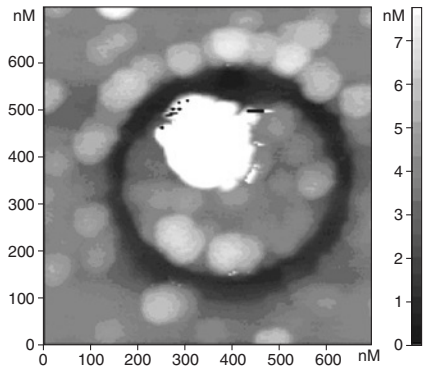

Fig. 3. Circle groove produced by SPM ablation. The structure depth is ∼4 nm, the width is ∼50 nm.

ing. This approach allowed to produce craters with diameter at halfwidth of only $d = 15$ nm, that is much smaller than it was possible with unipolar STM action ($d \approx 80$ nm). It is also important to note that lateral size of the crater bottom is close to the tip radii. This can be the evidence that further sharpening of the tip will lead to better spatial resolution of the developed technique. An important feature of the crater, produced by bipolar pulses, is its vulkano shape, that is a part of the sample material is ejected to the areas close to the crater boarders. It was found that this carbon material can be removed by contact mechanical probe scanning of the surface area around the crater (compare curves 1a and 1b in Fig. 2).

Not only craters but various fine surface nanostructures could be fabricated by STM probe on HOPG samples. One of the examples is demonstrated in Fig. 3.

The following interpretation of the obtained experimental data on graphite ablation by electrically pulsed and mechanically contacted STM probe can be proposed. Application of positive pulses between the probe and substrate via a thin adsorbed water layer leads to delivery of hydroxyl and oxygen ions to the sample surface (see, e.g., [5]) and formation of thin layer (clusters) of graphite oxide and soot [3,4]. The latter is removed (ejected) from the gap between the cantilever tip and the crater walls mechanically (by pressure applied to the SPM tip). Besides, an influence on material removal can cause electrical energy deposition and explosion in the adsorbed layer [6]. While application of negative pulses should result in hydrogenation of the graphite sample surface which blocks its oxidation.

3. Conclusions

It is shown that bipolar electrically pulsed STM cantilever can be an effective tool for nanoablation of HOPG. Further improvements in tip geometry and application of the developed technique to graphene processing are expected to allow production of nanostructures with record spacial resolution in the range 1–5 nm, thus opening the possibility to fabricate new quantum-sized graphene arrays.

References

[1] D-H. Kim, J-Y. Koo and J-J. Kim *Phis. Rev.* **B 68**, (2003) 113406.
[2] J-G. Park, C. Zhang and B. Wang, *Nanotechnology* **18**, 405306 (2007).
[3] S. Neubeck, F. Freitag, R. Yang and K. S. Novoselov, *Phys. Status Solidi B* **247, 11–12**, 2904 (2010).
[4] V. D. Frolov, V. I. Konov, S. M. Pimenov and S. V. Kosheleva, *J. Phys.: Conf. Ser.* **291**, 012035 (2011).
[5] F.S.-S. Chien, W.-F. Hsieh, S. Gwo, J. Jun, R.M. Silver, A.E. Vlada'r, J.A. Dagata, *J. Vac. Sci. Technol.* **B 23**, 66 (2005).
[6] X.N. Xie, H.J. Chung, C.H.Sow, K. Adamiak, A.T.S. Wee, *J. Am. Chem. Soc* **127**, 15562 (2005).

20th Int. Symp. "Nanostructures: Physics and Technology"
Nizhny Novgorod, Russia, June 24–30, 2012

Why GaN nanowires grow without assistance of catalyst or lattice mismatch: a scaling approach

V. G. Dubrovskii[1,2], V. Consonni[3,4], L. Geelhaar[4], A. Trampert[4] and H. Riechert[4]

[1] St Petersburg Academic University, St Petersburg, Russia
[2] Ioffe Physical-Technical Institute, St Petersburg, Russia
[3] Laboratoire des Materiaux et du Genie Physique, CNRS -– Grenoble INP, 38016 Grenoble, France
[4] Paul-Drude-Institut für Festkörperelektronik, 10117 Berlin, Germany

Abstract. Self-induced growth of nanowires (NWs) is a fundamental phenomenon which is qualitatively different from the known growth mechanisms, such as the stress-driven formation of quantum dots or metal-catalyzed vapor-liquid-solid growth of NWs. We present the experimental data demonstrating the most important features of self-induced formation of GaN NWs synthesized by molecular beam epitaxy (MBE) on Si substrates, either covered with a crystalline AlN lattice mismatched layer or a SixNy amorphous interlayer. In particular, we show that GaN never nucleates in the NW form. Rather, the nanostructures emerge as 3D nanoislands, and the island-to-wire transformation occurs only after the base dimension exceeds a certain critical value. We then develop a scaling model that explains the self-induced formation of GaN NWs by the anisotropy of surface energies coupled with the scaling growth anisotropy. The model elucidates the physical origin of the shape transformation at the critical radius. We also present some kinetic considerations showing why the scaling growth laws occur. The scaling length-time, radius-time and length-radius dependences are in a good agreement with the experimental data. The scaling properties of self-induced GaN NWs should be considered fundamental; however, the scaling indices can be tuned by the deposition conditions. This provides a powerful tool to control the NW morphology during growth.

Semiconductor NWs are promising building blocks of future nanoelectronic, nanophotonic and nanosensing devices. The self-induced NW formation is an attractive approach to ease their synthesis and improve functionality. In particular, the self-induced growth of GaN NWs on Si substrates has drawn much attention, since it provides a new way for monolithic integration of high quality GaN nanostructures with Si platform. The self-induced approach is advantageous in many respects. First, it does not require advanced lithography or other sophisticated methods of substrate preparation. Second, self-induced NWs do not suffer from several drawbacks of the vapor-liquid-solid NWs, such as the crystallographic polytypism or Au contamination. As NWs in general, self-induced GaN NWs enable a radical decrease of dislocation density induced by the lattice mismatch. The NW geometry is excellent for the formation of optical Ga(In)N/Al(Ga)N heterostructures. The controlled synthesis of self-induced NWs requires, however, a deeper understanding of their growth mechanisms, and the initial nucleation step in particular. In this talk, we discuss the growth mechanisms of self-induced GaN NWs on Si substrates, and relevant theoretical models of self-induced NW formation. We first describe the experimental data regarding the GaN NWs obtained by MBE on Si(111) substrates, either covered with a crystalline AlN lattice mismatched layer (LML) [1] or with a SixNy amorphous interlayer (AL) [2]. The most important points can be summarized as follows. First, no Ga droplet is detected at the NW top by electron microscopy imaging, so the self-catalytic effect cannot explain the NW formation. Second, the self-induced approach commonly employs specific MBE growth conditions: a highly nitrogen-rich vapor phase is required and often combined with high substrate temperature. Third, GaN never nucleates in the NW morphology. Rather, the nanostructures emerge as 3D nanoislands having a fixed shape. In a LML case, 3D nanoislands undergo the series of shape transformations, whereby the misfit dislocations are

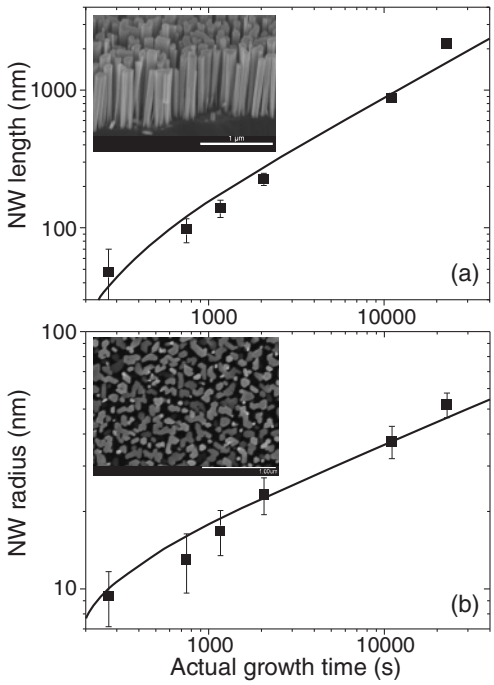

Fig. 1. Experimental (symbols) and theoretical (lines) length-time (a) and radius-time dependences of self-induced GaN NWs, the inserts showing SEM images of samples grown for and 3 hours.

developed at the interface prior to the NW formation [1]. During growth on an AL (where the epitaxial constraint should be very weak) the spherical cap (SC) islands transform directly to NWs [2]. This growth transformation occurs at a critical radius of about 5 nm [2]. Fourth, GaN NWs are hexahedral, restricted by six equivalent m-plane vertical sidewalls that are by definition the low energy planes. Fifth, self-induced GaN NWs usually grow in both vertical and radial directions, which

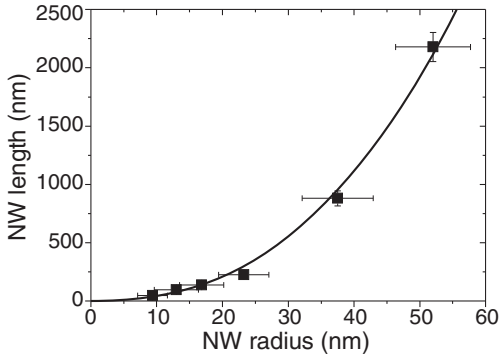

Fig. 2. Scaling length-radius dependence of self-induced GaN NWs, the line corresponds to the scaling law.

is well supported by the results of our ex-situ scanning electron microscopy (SEM) and transmission electron microscopy (TEM) analyses.

In particular, Figs. 1 and 2 show the length-time, radius-time and length-radius dependences of MBE grown GaN NWs on an AL. The lines are theoretical fits discussed in detail later on. The curve in Fig. 2 corresponds to the power law fit $L = 0.138R^{2.44}$ giving the scaling super-linear behavior. This feature should be considered fundamental in the self-induced approach and requires a new theoretical insight into the fundamentals of GaN NW growth.

In the second part of the talk, we present a quasi-equilibrium scaling model of NW nucleation, which is schematized in Fig. 3 [3]. The model is based on the comparison of the formation enthalpies of an isotropic 3D island and an anisotropic NW of the same volume, whose length L increases with the radius R as R^{α} (the scaling index α equals 2.44 in our MBE conditions). Our model predicts two distinct stages of system evolution: (i) Nucleation and isotropic growth of islands at small enough radii. At a certain time, the base dimension hits the first critical radius at which the surface energy difference becomes zero. This eventually leads to the development of straight NW sidewalls and onsets the growth anisotropy. (ii) Anisotropic NW growth is preferred between the two critical radii, because the growth anisotropy decreases the surface energy at a given volume. The NW height increases faster than the radius. Anisotropic elongation again becomes more energetically costly than isotropic growth at the second critical radius, since, at this time, the increase of sidewall surface area outweighs their low energy in the overall energy balance. However, kinetic limitations might prevent this second transformation. We also discuss a kinetic growth model that explains the scaling growth behavior from kinetic considerations of the step flow radial growth and the shadow effect. The scaling growth laws are given by the following equations:

$$L = L_0\left[1 + \frac{(\alpha+1)}{\alpha}\frac{aV(t-t_0)}{L_0R_0}\right]^{\alpha/(\alpha+1)}$$

$$R = R_0\left[1 + \frac{(\alpha+1)}{\alpha}\frac{aV(t-t_0)}{L_0R_0}\right]^{1/(\alpha+1)}; \quad L = L_0\left(\frac{R}{R_0}\right)^{\alpha}$$

Here, α is the growth index, a is the quantity of the order of diffusion length of Ga on the NW sidewalls, t is the actual NW growth time, t_0 is the duration of exponential growth stage, V is the Ga flux, L_0 and R_0 are the initial length and radius at t_0, respectively. Lines in Figs. 1 and 2 are theoretical fits obtained

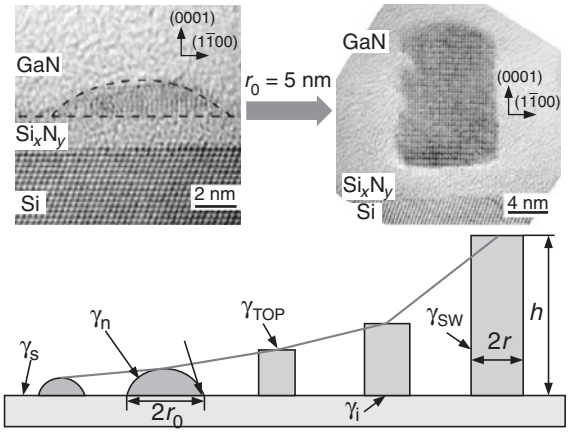

Fig. 3. Cross-sectional view TEM images of GaN SC islands and NWs on a SixNy AL demonstrating the shape transformation at the SC radius of 5 nm (top); model schematics illustrating the parameters used and the NW growth anisotropy (bottom).

with $\alpha = 2.44$, $\alpha = 51$ nm, $L_0 = 38$ nm and $R_0 = 10$ nm, at $V = 0.045$ nm/s, showing a fairly good quantitative correlation with the experimental data. Finally, we show how the growth models developed earlier for III–V vapor-liquid-solid NWs [4] can be applied to the case of self-induced GaN NWs. In conclusion, we have demonstrated the scaling length-time, radius-time and length-radius growth laws of self-induced GaN NWs obtained by MBE. The scaling properties of GaN NWs should be considered fundamental; however, the scaling indices can be tuned by the deposition conditions. This provides a powerful tool to control the NW morphology during growth.

References

[1] V. Consonni *et al.*, *Phys. Rev. B* **81**, 085310 (2010).
[2] V. Consonni *et al.*, *Phys. Rev. B* **83**, 035310 (2011).
[3] V.G. Dubrovskii *et al.*, submitted to *Phys. Rev. B*
[4] V.G. Dubrovskii *et al.*, *Phys. Rev. Lett.* (2012), accepted for publication.

20th Int. Symp. "Nanostructures: Physics and Technology"
Nizhny Novgorod, Russia, June 24–30, 2012

SA-MOVPE in nitrogen ambient for InAs nanowire integration on silicon

K. Sladek, F. Haas, D. Grützmacher and H. Hardtdegen
Peter Grünberg Institute (PGI-9), Forschungszentrum Jülich and JARA, 52425 Jülich, Germany

Abstract. The integration of III-V nanowire device structures into silicon technology calls for concepts which allow their highly dense but well controlled production without employing temperatures detrimental to Si devices. We will demonstrate that selective area metal organic vapor phase epitaxy (SA-MOVPE) with nitrogen as the carrier gas is the way to go to fabricate InAs nanowires on patterned Si (111) substrates. It was found that much lower pre-epitaxial annealing temperatures and source partial pressures are needed to fabricate nanowires in comparison to the usual carrier gas H_2. The results of the ongoing optimization of their fabrication process will be presented.

Introduction

For future nanoscale electronics as well as optoelectronic applications, InAs nanowires are desirable for integration into existing silicon technology due to their intrinsic conductivity. The MOVPE process is the method of choice for their formation due to its high volume production capability. For the application envisaged highly pure InAs nanowires which align vertically to the silicon substrate surface are needed. The most common growth approach is the catalyst assisted vapor liquid solid (VLS) MOVPE, which has the disadvantage of possible catalyst contamination in the wire and which is carried out at such low growth temperatures, that carbon incorporation cannot be avoided. Therefore the alternative selective area (SA) MOVPE [1] fabrication of nanowires has been under vivid investigation. In the past we have shown, that the growth parameter window of the SA-MOVPE of InAs nanowires can be enhanced and displaced towards temperatures [2] at which the decomposition of the source materials is more complete if N_2 is used as the carrier gas resulting in higher purity nanowires [3]. The need for growth and vertical alignment of the nanowires on Si (111) has been a challenge in the past because of silicon's non-polarity and its stable oxide. Therefore a more complicated pre-epitaxial substrate treatment — consisting of chemical cleaning and thermal annealing at temperatures above 900 °C [4] — is usually needed compared to SA-MOVPE growth on III-V substrates. Such high temperatures are detrimental to Si device technology. In this paper we investigate the influence of nitrogen carrier gas on pre-epitaxial substrate treatment as well as on the subsequent InAs nanowire growth on Si (111) and compare our results to those obtained if H_2 is the MOVPE carrier gas.

1. Experimental

Two inch Si (111) wafers were thermally oxidized with a resulting SiO_2 thickness of 30 nm and structured by electron beam lithography and CHF_3 reactive ion etching. Prior to growth the samples were cleaned in a solution of H_2SO_4 and H_2O_2 and dipped into 1% diluted hydrofluoric acid to remove the native oxide and to form a hydrogen passivated silicon surface in the SiO_2 mask openings. Subsequently the samples were immediately transferred into the low pressure MOVPE reactor chamber. The samples were annealed at 750 °C in nitrogen and arsine (AsH_3) ambient for 5 min. to further clean the SiO_2 surface and remove H_2 and O_2 from the Si surface.

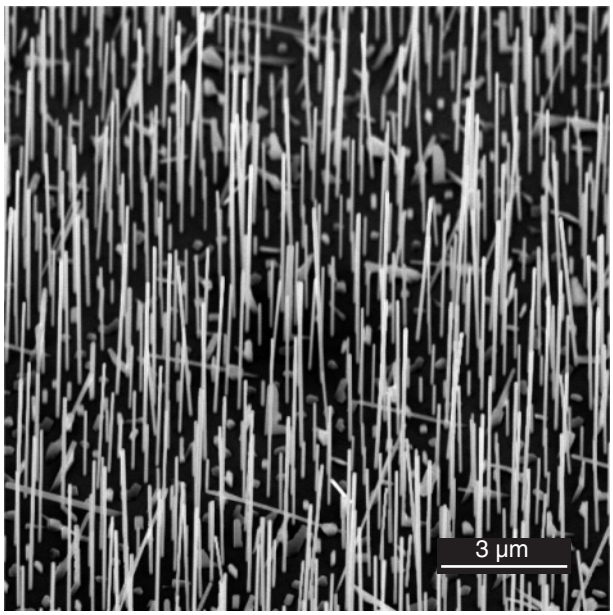

Fig. 1. Nanowires deposited with similar parameters as used for their growth on GaAs (111)B. Beside many vertical nanowires lots of differently oriented structures are visible.

Next, growth was initiated using AsH_3 and trimethyl indium (TMIn) as precursors in an N_2 carrier gas. The working pressure was kept at 20 hPa and a total gas flow rate of 3100 sccm was adjusted. Starting point for the study were conditions as previously employed for growth of InAs nanowires on GaAs (111)B substrates [2] at a temperature of 650 °C. In comparison the additional influence of an alternating precursor supply (as reported by Tomioka *et al*. [4]) using different temperatures and precursor partial pressures at the nucleation stage of nanowire growth was investigated to increase the amount of vertically standing nanowires. All samples were characterized by scanning electron microscopy (SEM).

2. Results

Fig. 1 shows an SEM image in tilted geometry of nanowires on Si (111) grown under a condition similar to our established growth on GaAs substrates [2].

The wires randomly exhibit at least four different growth directions corresponding to the four possible ⟨111⟩ directions in contrast to the purely vertical growth on GaAs (111)B where only one B-polar ⟨111⟩ direction is pointing out of the sub-

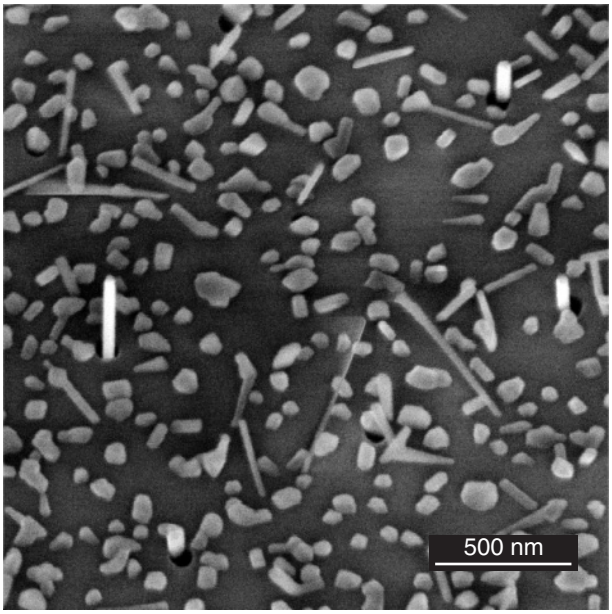

Fig. 2. Growth result after the introduction of an alternating precursor supply as in [4]. Bright and vertical low aspect ratio nanowires in the SiO2 mask openings can be observed as well as pronounced nucleation on the mask.

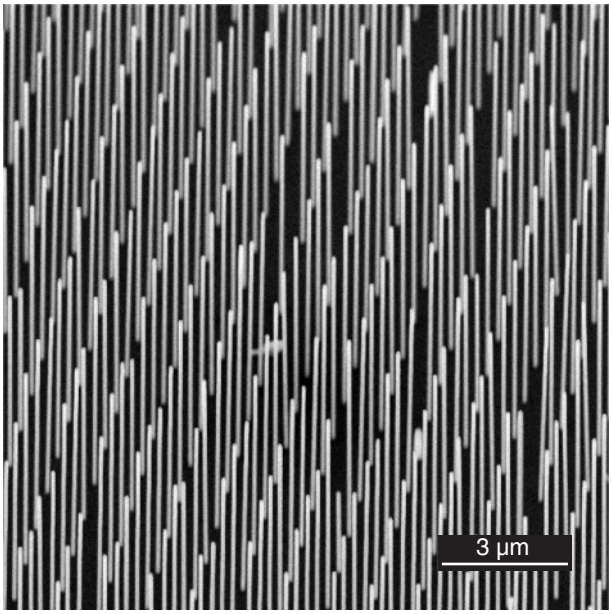

Fig. 3. Increased yield of vertical nanowires and very good selectivity after a similar growth procedure as in Fig. 2 but with adapted temperature and lower precursor partial pressures.

strate's surface. More importantly the amount of wire-shaped structures is relatively high despite the much lower pre-epitaxial annealing temperature and short annealing time compared to the established growth procedures in hydrogen based MOVPE [4]. Obviously it is found that in nitrogen ambient a thermal treatment of the Si (111) surface is already very effective at much lower temperatures than in hydrogen ambient. Next, the influence of the alternating precursor supply was investigated with the aim to increase the amount of vertical wires. The sample grown under equivalent conditions as described in [4] exhibits a strongly reduced selectivity with a significant amount of nucleation on the SiO_2 layer as shown in Fig. 2.

Nevertheless small InAs columns are visible in the mask openings indicating a crystalline base. Obviously this growth condition didn't produce nanowires in the desired way. Given that the ideal growth temperature is generally around 100 °C higher with N_2 carrier gas compared to H_2 carrier gas [2] and the growth rate was also found to be significantly higher due to the less reactive nature of nitrogen we finally increased the temperature during the alternating precursor supply step by 100 °C. In addition we also reduced the overall precursor supply and the nanowire growth rate to 1/4 compared to the previous two growth conditions. As can be seen in Fig. 3 the resulting growth exhibited a very good selectivity while at the same time the amount of vertical InAs nanowires is highly increased.

In future experiments we will investigate even lower annealing temperatures and optimize the alternating precursor supply with respect to further increase the amount of vertical wires.

3. Summary

We have successfully confirmed the ability to produce InAs nanowires on Si (111) substrates by SA-MOVPE with nitrogen as the carrier gas. It was found that compared to SA-MOVPE with hydrogen carrier gas a much lower pre-epitaxial annealing temperature of at most 750 °C as well as a very short annealing time in the order of a few minutes is sufficient to achieve nanowire growth. We adopted the already by Tomioka et al. established step flow sequence for SA-MOVPE with H_2 carrier gas and adapted the temperature as well as the partial pressures to comply with the differing demands of SA-MOVPE with N_2 carrier gas. As a result we were able to increase the yield of vertically standing InAs nanowires on Si (111). Finally we conclude that especially for the integration of InAs nanowires on silicon SA-MOVPE in nitrogen ambient is a very promising and advantageous fabrication method.

References

[1] J. Motohisa, J. Noborisaka, J. Takeda, M. Inari and T. Fukui, *Journal of Crystal Growth* **272**, 180 (2004).
[2] M. Akabori, K. Sladek, H. Hardtdegen, Th. Schäpers and D. Grützmacher, *Journal of Crystal Growth* **311**, 3813 (2009).
[3] K.Sladek, A. Winden, S. Wirths, K. Weis, C. Blömers, Ö. Gül, T. Grap, S. Lenk, M. v. d. Ahe, T. E. Weirich, H. Hardtdegen, M. I. Lepsa, A. Lysov, Zi-An Li, W. Prost, F. -J. Tegude, H. Lüth, Th. Schäpers, D. Grützmacher, *physica status solidi (c)* **9**, 230 (2012).
[4] K. Tomioka, J. Motohisa, S. Hara and T.Fukui, *Nano Letters* **8**, 3475 (2008).

20th Int. Symp. "Nanostructures: Physics and Technology"
Nizhny Novgorod, Russia, June 24–30, 2012

Catalyzed growth of nanowires: surface energies and growth modes

A. D. Bolshakov[1] and V. G. Dubrovskii[1,2]

[1] St Petersburg Academic University, St Petersburg, Russia
[2] Ioffe Physical-Technical Institute, St Petersburg, Russia

Abstract. A thermodynamical model of vapor-liquid-solid nanowire growth was developed. Surface energy of the system was studied as a function of nanowire radius and contact angle between the catalyst droplet surface and nanowire top facet. It was found that minimum of the energy relates to two different growth modes. When the Nebol'sin–Shchetinin (NS) condition is satisfied the droplet doesn't wet the nanowire sidewalls. If the NS condition is broken wetting mode occurs. In this mode the droplet entirely surrounds the sidewalls. Investigation shows that even in case of fulfilled NS condition local minima of the surface energy in both modes exist.

Introduction

Nanowires (NWs) are free standing structures with a high value of aspect ratio. NWs of different semiconductor materials have recently attracted a lot of attention because of their importance for nanoscale electronics, photonics, and sensing [1]. Such structures are usually fabricated via the vapor-liquid-solid (VLS) mechanism [2]. For practical applications it is necessary to control the morphology and crystal structure of NWs . The latter depend on growth mechanism [3,4]. Nebol'sin and Shchetinin [5] presented an inequality for the surface energies: while the inequality is satisfied the triple phase line (TPL, the line separating the vapor, liquid, and solid phases) position at the NW top is stable and standard VLS growth occurs. Lately Glas *et al*. have shown that the NS condition is equivalent to the TPL nucleation condition [3]. According to modern concepts [6] nucleation at the TPL leads to formation of wurtzite (WZ) structure during growth process of III-V semiconductor materials that exhibit zinc blende (ZB) structure in bulk. In Au-assisted growth processes III-V NWs often demonstrate spontaneous ZB-WZ polytypism [7], and desired phase purity is unfortunately still hard to achieve.

1. Theory

VLS growth of NW is shown schematically in Figure 1. The system consists of cylindrical nanowire of a radius r with a catalyst droplet having the shape of a spherical segment. The droplet with a contact angle β wets a segment of length y of the NW sidewall — Figure 1a; the nonwetting case, corresponding to $y = 0$ is shown in Figure 1b; Figure 1c shows the wetting case with a maximum length of wetted segment, which value from geometrical considerations in spherical geometry is given by $y_{\max} = -2r\cot\beta$. In our investigation we consider five surface energies shown in Figure 1: those of the horizontal solid-liquid interface $\gamma_{\rm SL}$, the liquid-vapor interface $\gamma_{\rm LV}$, the NW top facet in contact with the vapor $\gamma_{\rm SV}$, the NW sidewalls in contact with the vapor $\gamma_{\rm WV}$, and the vertical solid-liquid interface $\gamma^l_{\rm SL}$. The significant for our research part of the total surface energy of the system (the droplet, the NW of length L = constant and the substrate) is the surface energy that depends on position of the droplet

$$F = \frac{2\pi r^2}{1+\cos\beta}\,\gamma_{\rm LV} + \pi r^2\gamma_{\rm SL} - 2\pi r y\left(\gamma_{\rm WV} - \gamma^l_{\rm SL}\right). \quad (1)$$

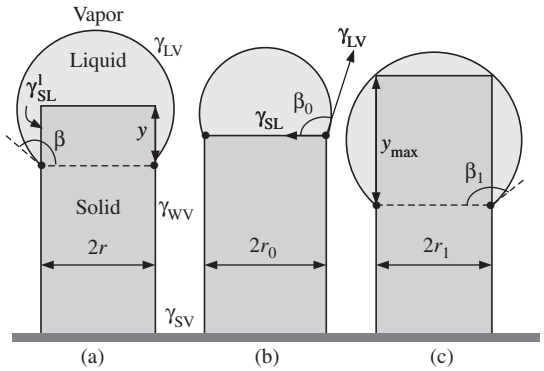

Fig. 1. VLS growth in different geometries: unstable configuration with intermediate y (a); system geometry in nonwetting case $y = 0$ (b); wetting case $y = y_{\max}$ (c).

We assume volume of the droplet to be constant

$$V = \frac{\pi r^3}{3}\,f(\beta) - \pi r^2 y = \text{const}\,, \quad (2)$$

where $f(\beta) = \frac{(1-\cos\beta)^2(2+cos\beta)}{\sin^3\beta}$. As long as V = const we may express F as function of r and β using (2). To find the stable configurations of the drop lets find the minima of the surface energy (1)

$$\frac{\partial F(r,\beta)}{\partial\beta} = \frac{2\pi r^2}{(1+\cos\beta)^2}\left(\gamma_{\rm LV}\sin\beta + \gamma^l_{\rm SL} - \gamma_{\rm WV}\right). \quad (3)$$

This derivative equals zero at $\beta = \beta_* : \gamma_{\rm WV} = \gamma_{\rm LV}\sin\beta_* + \gamma^l_{\rm SL}$. Now we define second order partial derivative at this particular point

$$\left(\frac{\partial^2 F(r,\beta)}{\partial\beta^2}\right)_{\beta=\beta_*} = \frac{2\pi r^2}{(1+\cos\beta_*)^2}\,\gamma_{\rm LV}\cos\beta_*\,. \quad (4)$$

We can conclude from last two expressions, that if the contact angle exceeds $\pi/2$, then β_* can not be a point of minimum surface energy as $\frac{\partial^2 F(r,\beta)}{\partial\beta^2} \propto \cos\beta_* < 0$. Which means that when $\beta > \pi/2$ no stable configuration exists [8], except configurations occurring at the F domain boundaries which are $y = 0$ and $y = -2r\cot\beta$. On the other hand when $\beta < \pi/2$ only nonwetting configuration occurs. We will discuss this case later.

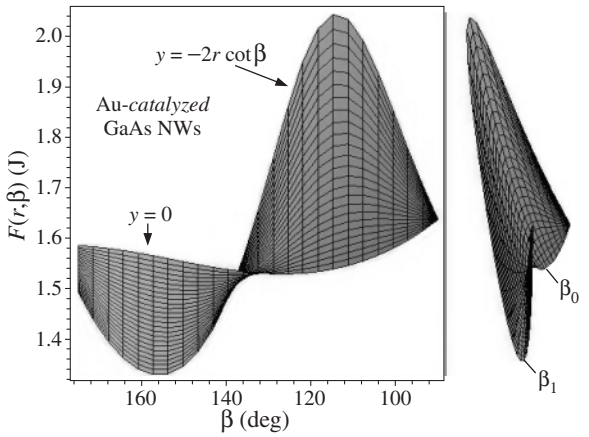

Fig. 2. Surface energy in case of Au-catalyzed GaAs NW growth.

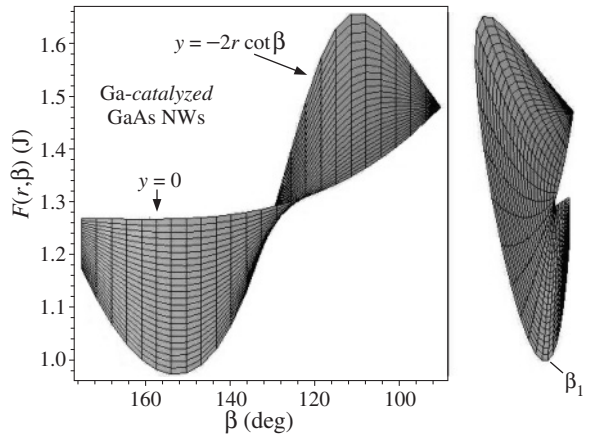

Fig. 3. Surface energy in case of Ga-catalyzed GaAs NW growth.

Using equation (2) we express the surface energy (1) on the boundaries divided by a constant πr_c^2 as function of β

$$\phi_-(\beta) = \rho_-^2(\beta)\left(\frac{2\gamma_{\rm LV}}{1+\cos\beta} + \gamma_{\rm SL}\right), \quad (5)$$

$$\phi_+(\beta) = \rho_+^2(\beta)\left(\frac{2\gamma_{\rm LV}}{1+\cos\beta} + \gamma_{\rm SL} + 4\left(\gamma_{\rm WV} - \gamma_{\rm SL}^l\right)\cot\beta\right), \quad (6)$$

where we used indexes "-" and "+" to denote functions values at nonwetting and wetting boundaries respectively, $r(\beta)_\pm$ are equations of the boundary curves in (r, β) coordinate system.

$$\rho_-(\beta) = \frac{r_-(\beta)}{r_c} = \left[\frac{(1+\cos\beta)\sin\beta}{2-\cos\beta-\cos^2\beta}\right]^{1/3},$$

$$\rho_+(\beta) = \frac{r_+(\beta)}{r_c} = \left[\frac{(1+\cos\beta)\sin\beta}{2+5\cos\beta+5\cos^2\beta}\right]^{1/3},$$

$$r_c = (3V/\pi)^{1/3}. \quad (7)$$

The boundary functions have the following properties:

1. Functions $\rho_-(\beta)$ and $\rho_+(\beta)$ do have only two cross points $\beta = \pi/2$ and $\beta = \pi$. Note that $\phi_-(\pi/2) = \phi_+(\pi/2) = (2\gamma_{\rm LV} + \gamma_{\rm SL})/2^{2/3}$ and $\phi_-(\pi) = \phi_+(\pi) = 2^{2/3}\gamma_{\rm LV}$

2. Minimum of the surface energy (5) in nonwetting case occurs at a point β_0 :

$$\gamma_{\rm SL} + \gamma_{\rm LV}\cos\beta_0 = 0, \quad (8)$$

$\beta_0 > \pi/2$ due to $\gamma_{\rm SL}, \gamma_{\rm LV} > 0$. From that statement we can deduce that no stable configuration occurs when $\beta < \pi/2$. Minimum of the surface energy F exists at point β_0 only if derivative (3) is positive. The latter equals NS condition [5]. We conclude that nonwetting configuration is stable only if β_0 exists and

$$\gamma_{\rm WV} < \gamma_{\rm LV}\sin\beta_0 + \gamma_{\rm SL}^l. \quad (9)$$

3. Value β_1 relating to a minimum of the surface energy in wetting case might be found from the equation

$$(\gamma_{\rm SL} - \gamma_{\rm LV}\cos\beta_1)(1+3\cos\beta_1)\sin\beta_1 + \left(4+6\cos\beta_1-2\cos^2\beta_1\right)\left(\gamma_{\rm LV}\sin\beta_1 + \gamma_{\rm SL}^l - \gamma_{\rm WV}\right) = 0.$$

For most VLS growth systems this equation has two roots, corresponding to minimum and maximum of F.

2. Catalyst droplet surface energy in GaAs NW growth process

We plotted 3d graphs, based on the developed model, of the surface energy of catalyst droplet on top facet of GaAs NW as a function of r and β for two material systems with Au and Ga catalyst. Parameters used in calculations are presented in the Table 1. As you can see from Figure 2 surface energy of Au droplet has a local minimum in nonwetting case, but the lowest energy relates to wetting mode, while Ga droplet has only one minimum in wetting mode (Fig. 3).

Table 1.

	$\gamma_{\rm WV}$ (J/m^2)	$\gamma_{\rm LV}$ (J/m^2)	$\gamma_{\rm SL}^l$ (J/m^2)	$\gamma_{\rm SL}$ (J/m^2)
Au	1.5	1	0.75	0.6
Ga	1.5	0.8	0.75	0.75
	β_* (deg)	β_0 (deg)	β_1 (deg)	
Au	131	127	156	
Ga	110	–	153	

3. Conclusions

We have developed a theoretical model of VLS nanowire growth. It was found that if droplet position of the minimum surface energy in nonwetting configuration satisfy the NS condition then minima of the surface energy exist in both growth modes, otherwise only wetting configuration occurs. Calculated surface energy of the Au catalyst droplet on GaAs NW in wetting mode turned out to be lower than energy in nonwetting case. Only wetting mode is found to be stable in system with Ga catalyst on GaAs NW.

References

[1] T. Bryllert *et al*., *Nanotechnology* **17**, S227 (2006).
[2] W. Lu, C. M. Lieber, *Nat. Mater.* **6**, 841 (2007).
[3] F. Glas *et al*., *Phys. Rev. Lett.* **99**, 146101 (2007).
[4] V. G. Dubrovskii *et al*., *Phys. Rev. B* **80**, 205305 (2009).
[5] V. A. Nebol'sin, A. A. Shchetinin, *Nonorganic materials* **39/9**, 1050 (2003).
[6] J. Johansson *et al*., *Cryst. Growt Des.* **9**, 766 (2009).
[7] M. Moewe *et al*., *J. Appl. Phys* **104**, 044313 (2008).
[8] V. G. Dubrovskii *et al*., *Nano Lett.* **11**, 1247 (2011).

20th Int. Symp. "Nanostructures: Physics and Technology"
Nizhny Novgorod, Russia, June 24–30, 2012

Epitaxial stabilization of orthorhombic phase in NiF_2 layers on CaF_2/Si(111)

A. G. Banshchikov[1,2], K. V. Koshmak[1,3], A. V. Krupin[1], T. Kawase[2], M. Tabuchi[2,4] and N. S. Sokolov[1]

[1] Ioffe Physical-Technical Institute, St Petersburg, Russia
[2] Venture Business Laboratory, Nagoya University, Nagoya 464-8601, Japan
[3] Dipartimento di Ingegneria dei Materiali e dell' Ambiente, Universita di Modena e Reggio Emilia, Via Vignolese 905-41100-Modena, Italy
[4] Synchrotron Radiation Research Center, Nagoya University, Furo-cho, Chikusa-ku, Nagoya 464-8603, Japan

Abstract. Using electron and high resolution X-ray diffractometry, it was found that NiF_2 layers on a $CaF_2(111)$/Si(111) template grow epitaxially in metastable orthorhombic phase. It was established that the epitaxial relations between NiF_2 and CaF_2 layers are the following: $(100)NiF_2 \| (111)CaF_2$, $[001]NiF_2 \| [1\bar{1}0]CaF_2$.

Introduction

It has been recently suggested to overcome the superparamagnetic limit for maximal density of magnetic memory storage by using exchange bias effect in ferromagnet-antiferro-magnet heterostructures [1]. Though this effect is widely used in the reading heads of hard drives of modern computers, its microscopic mechanisms still remain unclear. In this respect, studies of ferromagnet — iron group difluoride heterostructures are attractive because of relatively simple magnetic structure of these fluorides. Among them, nickel fluoride (NiF_2) is of particular interest due to its magnetic structure different from the other fluorides [2]. It is known that at high pressures and temperatures transformation of its rutile type tetragonal crystal structure to the orthorhombic $CaCl_2$ type structure takes place [3]. In this work, epitaxial growth at different conditions and crystal structure of NiF_2 films on Si(111) substrates have been studied.

1. Experimental

The heterostructures were grown by molecular beam epitaxy at Ioffe Physical-Technical Institute. To avoid chemical reaction between silicon substrate and nickel fluoride molecules, 100 nm thick CaF_2 buffer layer was grown at 700 °C on atomically clean Si(111). The growth temperature of NiF_2 layers was 350−450 °C; their thickness was from 100 to 900 nm. Characterized by atomic force microscopy, surface morphology of NiF_2 layers demonstrated very smooth surface for 350 °C growth temperature and appearance of tetrahedral protrusions with low surface density at 450 °C.

Reflection high-energy electron diffraction (RHEED) with 15 keV electron energy was used to monitor crystalline quality of epitaxial layers and Si substrate. X-ray diffraction characterization of NiF_2 films was performed at Nagoya University using ATX-G (Rigaku, Co) diffractometer in double crystal setting and CuK_α-radiation. The $\theta - 2\theta$ curves were measured in symmetrical Bragg geometry in the $(10-60^\circ)\theta$ range.

2. Results and discussion

Fig. 1a shows RHEED pattern of 100 nm thick CaF_2 (111) buffer layer grown at 700 °C. Well-pronounced streaks indicate single crystallinity of the film and smooth surface at atomic level. The electron beam was directed in parallel with $[1\bar{1}0]$ CaF_2 azimuth for all structures. RHEED pattern observed after

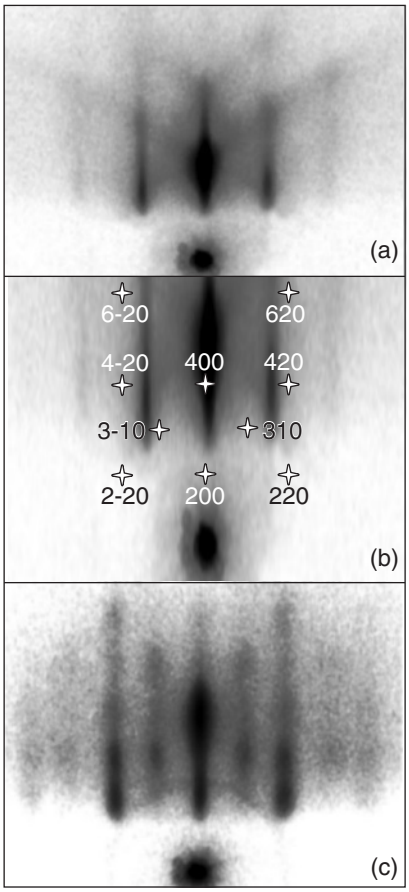

Fig. 1. RHEED patterns of 100 nm thick CaF_2 buffer layer on Si(111) (a); 6 nm thick NiF_2 grown at 350 °C (b); 100 nm thick NiF_2 at 350 °C (c). Electron beam is parallel to $[1\bar{1}0]CaF_2$.

the growth of NiF_2 6 nm thick layer at 350 °C is shown in Fig. 1b. Index marks shown in this figure correspond to the expected positions of diffraction spots for NiF_2 orthorhombic structure, in which [001] direction is parallel to the electron beam. One can see that there is a good coincidence of observed and expected positions of the diffraction spots. Reasonably good correspondence between experiments and calculations was also observed for $[11\bar{2}]$ CaF_2 azimuth. In this case, [010] direction of NiF_2 orthorhombic structure was parallel to the direction of the electron beam. Fig. 1c shows RHEED pattern taken from NiF_2 100 nm thick layer. Well pronounced streaks,

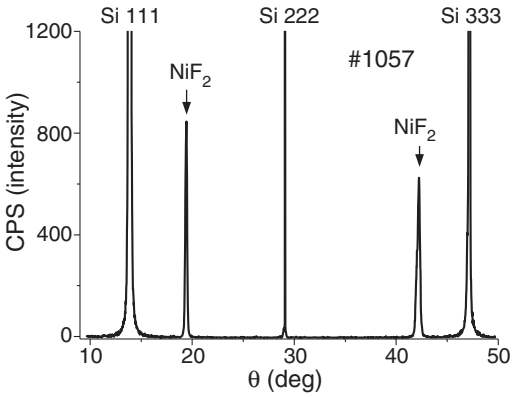

Fig. 2. X-ray diffraction $\theta-2\theta$ curve of heterostructure with 100 nm thick NiF_2 epitaxial layer (# 1057), measured in symmetrical Bragg geometry.

indicating rather smooth surface of the layer are clearly seen.

Thus, RHEED data analysis suggests formation of NiF_2 metastable orthorhombic phase in studied epitaxial films; however accuracy of this technique is not sufficient for precise measurements of the lattice parameters, which could prove existence of this metastable phase in the layers. For this reason, X-ray diffraction studies have been carried out.

Fig. 2 shows $\theta - 2\theta$ XRD curve of # 1057 structure. In addition to the intense 111 and 333 peaks from silicon substrate and forbidden Si 222 reflection one can see two well pronounced diffraction peaks from NiF_2 layer at $\theta = 19.72^\circ$ and $\theta = 42.46^\circ$.

In the bottom of Table 1, angular positions of the most close to NiF_2 reflections shown in Fig. 2 for the ortho-rhombic [3] and tetragonal [4] phases are presented. Very good coincidence of observed positions of the peaks with expected positions of 200 and 400 reflections for the orthorhombic phase proves that in these structures NiF_2 met-astable orthorhombic phase is stabilized during epitaxial growth. Such effect of heteroepitaxial stabilization was earlier observed for MnF_2 layers grown on Si substrate [5,6].

Comparing presented in the Table 1 angular positions of these reflections for other structures grown at different temperatures (350–450 °C) and having thickness of NiF_2 layer from 100 to 900 nm, one can conclude that formation of this metastable phase is well reproducible. No traces of stable tetragonal phase were observed in the structures grown at 350 and 400 °C. However weak reflections belonging to the stable tetragonal phase were observed in the $\theta - 2\theta$ curves of the structures grown at 450 °C. This can be naturally explained by competition between processes of heteroepitaxial stabilization and formation of stable tetragonal phase.

From presented above RHEED and XRD data epitaxial relations between NiF_2 layer and CaF_2 layer can be derived. First, according to X-ray diffraction data $NiF_2(100)$ plane is parallel $CaF_2(111)$ plane. The second epitaxial relation is obtain from RHEED data: $[001]NiF_2||[1\bar{1}0]CaF_2$. It is worth mentioning that established epitaxial relations are valid only for one structural domain in the NiF_2 layer. Because of three fold symmetry of $CaF_2(111)$ surface, at least three rotational domains in the NiF_2 layer are expected. To clarify the domain structure of this layer diffraction measurements in other geometries are needed.

Table 1. Comparison of angular positions of 200 and 400 reflections observed in this work with those obtained for the orthorhombic phase from Ref. [3] and tetragonal phase from Ref. [4].

Sample	NiF_2 layer thicknes, nm	Growth temperature, °C	θ_{200}, deg	θ_{400}, deg
1057	100	350	19.72	42.46
1059	300	350	19.74	42.45
1061	300	400	19.72	42.43
1062	100	450	19.74	42.48
1067	900	350	19.72	42.43
Orthorhombic $CaCl_2$ type phase			19.74	42.50
Tetragonal rutile type phase			19.35	41.50

3. Conclusion

Well-reproducible epitaxial growth of NiF_2 layers on CaF_2 (111)/Si(111) heteroepitaxial substrates has been achieved. Grown structures were characterized by RHEED and high resolution X-ray diffraction in symmetrical Bragg geometry. It was shown that at 350–450 °C NiF_2 crystallizes in metastable orthorhombic phase with the following epitaxial relations: (100) $NiF_2\|$ (111) CaF_2, $[001]NiF_2\|$ $[1\bar{1}0]CaF_2$. It was found that the effect of epitaxial stabilization is strong enough to stabilize metastable phase in the layer as thick as 0.9 μm. This enables further studies of this phase magnetic structure by neutron diffraction.

Acknowledgements

The authors are thankful to I. V. Golosovsky and S. M. Suturin for fruitful discussions. Support of Venture Business Laboratory of Nagoya University during visit of A. G. Banshchikov November–December 2009 is greatly appreciated. This work was supported by ONDA project FP7-PEOPLE-2009-IRSES-247518, as well as by the Ministry of the Education and Science of the Russian Federation under contract No. 16.513.11.3095.

References

[1] V. Skumryev *et al*., *Nature* **423**, 850 (2003).
[2] M. T. Hutchings *et al*., *Phys. Rev. B*, **2**, 1362 (1970).
[3] A. E. Austin *et al*., *J. Phys. Chem. Solids*, **30**, 1282 (1969).
[4] J. C. Taylor *et al*., *Acta Crystallogr. B*, **30**, 554 (1974).
[5] A. K. Kaveev *et al*., *J. Appl. Phys.* **98**, 013519 (2005).
[6] R. N. Kyutt *et al*., *J. Phys. D: Appl. Phys.* **40**, 4896 (2007).

20th Int. Symp. "Nanostructures: Physics and Technology"
Nizhny Novgorod, Russia, June 24–30, 2012

Simulation of silicon nanocluster formation in Si suboxide layers

E. A. Mikhantiev[1], I. G. Neizvestny[2], S. V. Usenkov[2] and *N. L. Shwartz*[2]

[1] Novosibirsk State Technical University, 630092 Novosibirsk, Russia
[2] A.V. Rzhanov Institute of Semiconductor Physics, SB RAS, Lavrentieva 13, 630090 Novosibirsk, Russia

Abstract. Silicon nanocluster formation during high temperature annealing of Si suboxide layers was analyzed using Monte Carlo simulation. The main process in phase separation of SiO_x layer into Si and SiO_2 was Si and O atom diffusion. Simulation demonstrated important role of silicon monoxide in the process of silicon nanoclusters (nc-Si) formation. SiO generated at high temperatures accelerated excess silicon aggregation into Si nanoclusters. Silicon monoxide dissociation nearby nc-Si assisted silicon dioxide shell formation around silicon cluster. Dependence of cluster size distribution on temperature, annealing time and composition of suboxide silicon layer was analyzed.

Introduction

Silicon nanocrystals (nc-Si) embedded in silicon oxide matrix have potential applications in optical devices in Si-compatible technology [1,2] due to efficient room temperature luminescence [3]. Si nanocrystals are produced with different techniques. The common technique is high temperature annealing of substoichiometric SiO_x thin films [4]. During high temperature annealing of substoichiometric layers silicon monoxide creation takes place [5,6]. Since luminescence properties of nc-Si are determined by shape and size distribution of nanocrystals, by crystal-oxide interface and composition of oxide matrix, it is desirable to examine atomic mechanism of silicon nanocrystal formation. In this work atomic-scaled analysis of silicon nanocluster aggregation during high temperature annealing of SiO_x layers were fulfilled using lattice Monte Carlo model. In the model along with silicon and oxygen diffusion silicon monoxide creation, dissociation and diffusion were considered.

1. Monte Carlo model and simulation results

Simulation was carried out using software developed for investigation processes in Si-SiO_2 system on the base of diamond-like lattice model [7]. Partially filled diamond-like crystal lattice enables to arrange SiO_4 tetrahedrons with silicon atom in the centre. To simulate SiO_x layer annealing 3-component system was considered: 1 — Si, 2 — O, 3 — SiO. Simulation was fulfilled using following energies of single covalent bonds: $E_{\mathrm{Si-Si}} = 1.1$ eV, $E_{\mathrm{Si-O}} = 2.5$ eV, $E_{\mathrm{O-O}} = 0.6$ eV. Bivalence of oxygen atoms was provided by weakening of oxygen bond energies in improper configurations ($E_{\mathrm{Si-O;\,eff}} = 1.5$ eV). Chemical reactions of silicon monoxide creation and dissociation were included in the model. Activation energies of chemical reactions were dependent on the sort and number of the nearest neighbors of reactants: $E_{\mathrm{R1}} = 3.7{-}8.2$ eV (SiO creation), $E_{\mathrm{R2}} = 2.0{-}3.2$ eV (SiO dissociation). Considering silicon monoxide molecule mobile and volatile the binding energy for SiO for all configurations was chosen 1.4 eV and SiO desorption energy was equal 1.6 eV. The starting state of the model layer was a random distribution of silicon and oxygen atoms with Si:O ratio $1 : x$ ($1 \le x \le 2$) over lattice sites (30% of lattice sites were vacant). The main process in phase separation of SiO_x layer during annealing into Si and SiO_2 was random walk of Si and O atoms and tendency of the system to minimum of free energy. With covalent energy values given above SiO_4 tetrahedrons were easily formed and excess silicon atoms gathered into nc-Si. It was necessary to introduce some additional driving force to achieve silicon agglomeration into compact 3D clusters. In the model such driving force imitating strain at Si/SiO_2 interface was introduced with additional energy parameter dE_{cov} [8]. Using this model simulation of SiO_x layers annealing was carried out at temperature diapason $1173 \le T \le 1573$ K.

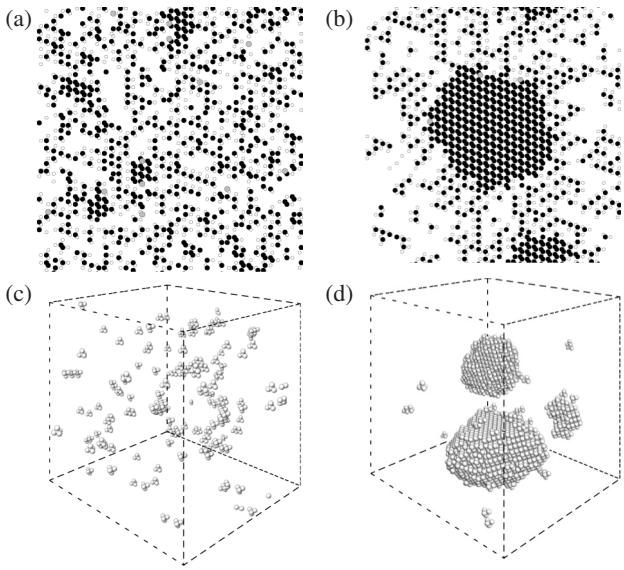

Fig. 1. Fragment of SiO_x layer after annealing at $T = 1373$ K: cross-sections for $x = 1.1$, annealing time $t_{\mathrm{a}} = 0.01$ s (a), $t_{\mathrm{a}} = 3$ s (b); 3D views ($t_{\mathrm{a}} = 1$ s) for $x = 1.7$ (c), $x = 1.5$ (d). Silicon atoms are marked in black color and oxygen in grey color (a,b); in 3D views oxygen atoms are not shown.

Fig. 1 shows a series of snapshots from the simulations. In cross-section images one can see that silicon clusters are embedded in SiO_2 matrix. For the same annealing time diameter of nc-Si increased with degree of Si supersaturation in initial layer (Fig. 1c,d). Dependence of average nc-Si size on annealing time for different x and temperature was obtained. Cluster size increased with annealing time and Si supersaturation. Maximal cluster size corresponds to SiO composition. Silicon starts to gather into clusters only when excess silicon value in SiO_x layer exceeds some definite value ($x < 1.75$). In Fig. 2 size distribution of nc-Si at different moments of annealing time is shown. From simulation we have found that the process of silicon cluster formation consists of several stages. At the initial stage SiO_4 tetrahedrons and small nc-Si of different

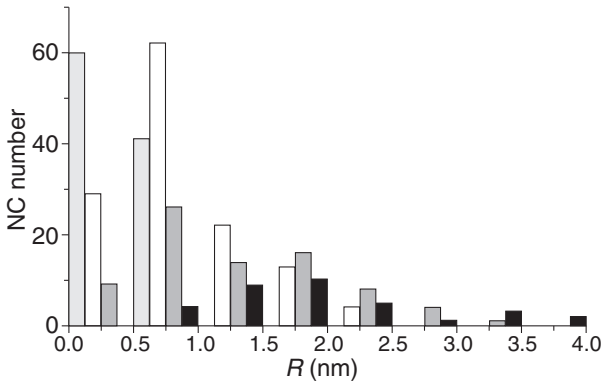

Fig. 2. nc-Si size distribution at different moment of annealing time at $T = 1373$ K for $x = 1.4$: dashed bars — $t = 0.01$ s, white bars — 0.1 s, gray bars — 0.2 s, black bars — 1 s.

shape were formed. At the following stage clusters were enlarged due coalescence and silicon adatom diffusion. Increase of nc-Si size due to coalescence is predominant mechanism at the stage where the cluster density is large. At the last stage when distances between separate clusters became large slower enlargement was observed (similar to Ostwald ripening during growth process). Duration of each stage was depended on annealing temperature and composition of initial SiO_x layer. Presence of mobile silicon monoxide substantially accelerates nc-Si formation at high temperatures. At high temperatures silicon monoxide continuously generates and decays at nc-Si/SiO_2 interface. SiO particles are more mobile than silicon atoms so silicon monoxide moves faster than silicon through silicon dioxide matrix from one cluster to another being additional silicon carrier. Fig. 3 demonstrates annealing of SiO_2 film with layer of nonstoichiometric composition ($x = 1.5$). Generated SiO molecules in SiO_x area either dissociated and took part in nc-Si formation or were removed from the system due to diffusion through vacancy sites in silicon dioxide matrix with following desorption. Depending on annealing temperature either aggregation of excess silicon in nanoclusters occurred or cavities formed (Fig. 3). This result is in agreement with experimental data on annealing of SiO_2 layers after Si ion implantation [9].

2. Monte Carlo model and simulation results

In this work atomic-scaled analysis of Si-nanocluster formation in Si suboxide matrix was carried out using lattice Monte Carlo model. It was found that phase separation of SiO_x layer into Si and SiO_2 is driven by suboxide penalty arising from incomplete Si and O coordination. At high temperatures along with silicon and oxygen atom diffusion of silicon monoxide plays the significant role in silicon cluster formation. Mobile silicon monoxide accelerated the process of excess Si aggregation into clusters and allowed oxide shell formation around silicon cluster. Three stages in the process of silicon aggregation into clusters were detected: 1) silicon cluster nucleation and SiO_4 tetrahedrons formation, 2) coalescence of neighbor nc-Si, 3) slow enlargement of separately located clusters. Time of each stage was depended on annealing temperature and composition of initial SiO_x layer.

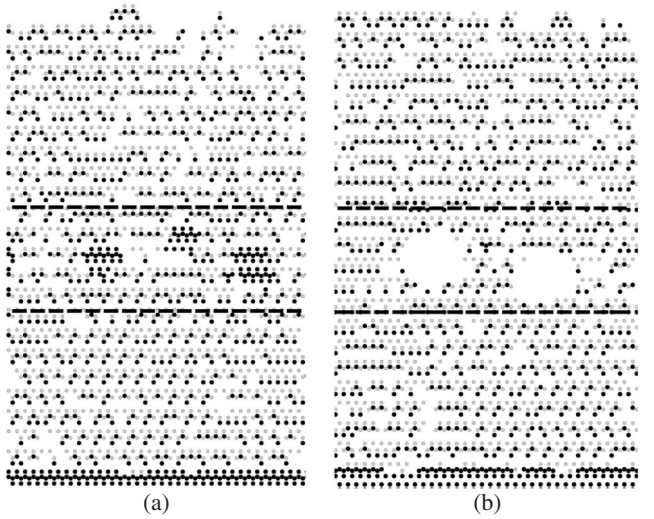

Fig. 3. Cross-section fragments of SiO_2 film on silicon substrate containing layer with excess Si after annealing at $T = 1323$ K (a) and $T = 1423$ K (b). Si is marked in black, O in grey color, doted lines indicate layer of nonstoichiometric composition.

Acknowledgements

This work was supported by RFBR (grant 11-02-00045) and the projects according to basic research RAS Program.

References

[1] L. Pavesi, L. Dal Negro, C. Mazzoleni, G. Franzo, F. Priolo, *Nature* **408**, 440 (2000).
[2] P. Pellegrino, B. Garrido, C. Garcia, J. Arbiol, J. R. Morante, M. Melchiorri, N. Daldosso, L. Pavesi, E. Scheid, G. Sarrabayrouse, *J. Appl. Phys.* **97**, 074312 (2005).
[3] F. Iacona, G. Franzo, C. Spinella, *J. Appl. Phys.* **87**, 1295 (2000).
[4] D. Comedi, O. H. Y. Zalloum, E. A. Irving, J. Wojcik, T. Roschuk, M. J. Flynn, P. Mascher, *J. Appl. Phys.* **99**, 023518 (2006).
[5] D. Tsoukalas, C. Tsamis, P. Normand, *J. Appl. Phys.* **89**, 7809 (2001).
[6] K. Furukawa, Y. Liu, H. Nakashima, D. Gao, K. Uchino, K. Muraoka, H. Tsuzuki, *Appl. Phys. Lett.* **72**, 725 (1998).
[7] A. V. Zverev, I. G. Neizvestnyi, N. L. Shwartz, Z. Sh. Yanovitskaya, *Nanotechnologies in Russia* **3**, 367 (2008).
[8] E. A. Mikhantiev, I. G. Neizvestny, S. V. Usenkov, N. L. Shwartz, *Avtometriya* **47** 5, 88 (2011).
[9] V. Beyer, J. von Borany, K.-H. Heinig, *J. Appl. Phys.* **101**, 053516 (2007).

20th Int. Symp. "Nanostructures: Physics and Technology"
Nizhny Novgorod, Russia, June 24–30, 2012

Microtubes and corrugations formed from ZnTe/CdTe/CdHgTe

S. V. Mutilin, R. A. Soots, A. B. Vorob'ev, D. G. Ikusov, N. N. Mikhailov and V. Ya. Prinz
Institute of Semiconductor Physics, SB RAS, Lavrentieva 13, 630090 Novosibirsk, Russia

Abstract. Variously shaped shells were formed from ZnTe/CdTe/CdHgTe/HgTe/CdHgTe heterostructures containing a HgTe quantum well. The curvature radius of the tubular shells was 12 μm, while that of corrugations, 13 μm.

Introduction

Currently, high-mobility mercury cadmium telluride (MCT) structures attract much attention due to their extraordinary band properties. In a HgTe quantum well of sufficiently large width (>6.3 nm) sandwiched in between wide-band $Cd_xHg_{1-x}Te$ ($x \approx 0.7$), the band structure of HgTe becomes inverted, making the HgTe semimetal. In such structures, a strong spin splitting due to Rashba effect with energies of order 30 meV is observed [1]. The gapless structure of HgTe QWs makes it possible to prepare unique 2D systems involving several types of charge carriers (2D electrons and/or holes) [2]. A specific feature here is that such electrons and holes are contained in one and the same layer, i.e. they a not spatially separated.

So far, only planar MCT structures have been fabricated and studied. The formation of semiconductor shells with small radius of curvature from semiconductor heterofilms [3] for MCT structures opens up new potentialities in this field. Bent films offer a much broader range of possibilities in controlling their physical properties in comparison with traditional planar heterostructures due to the capability of bent films to change their curvature in a broad range. The curvature of semiconductor shells affects the 2D electron and hole transport in the films due to the following factors: (1) strain generation or redistribution causing a local modification of band-gap energy (up to 1 eV) [4], (2) change of gradient of the normal component of an external magnetic field, which governs transport of 2D electron or hole gas in shell walls [5], (3) change of geometric potential [6]. It was shown experimentally that the gradient of the normal component of an external magnetic field due to surface curvature can exceed 10^6 T/m, and it drastically modifies the magnetotransport properties of 2D electron gas [7]. The possibility to realize in one and the same layer several types of charge carriers permits obtaining new interesting results related with surface curvature.

As applied to CdHgTe/HgTe/CdHgTe shells, of interest is investigation of spin-dependent phenomena. In shells, spin phenomena are susceptible both to the effect due to the curvature itself [5] and to the effect due to gradient of the normal component of an external magnetic field [8] and strain [9]. Recent experiments showed that already small deformations (10^{-4}) in the plane of 2D hole gas alter the spin splitting due to the spin-orbital interaction by 20% [10]. The high sensitivity of the spin-orbital coupling to deformations is a property important, in the first place, to spintronics. Corrugations allow creation of intricate strain profiles (periodic or sign-alternating) with relative lattice strains amounting to a few percents; such profiles cannot be obtained using any other known method. In particular, in a shell one can obtain a nontrivial dependence of strain on coordinates for which manifestation of the spin quantum Hall effect can be expected [11]. Thus, a first step in the way towards an efficient control of spin-orbital interaction using deformations is creation of shells from a material with strong spin-orbital coupling, for instance, from MCT. Moreover, MCT structures are widely used in fabrication of IR photodetectors. A combination of MCT structures with different band-gap energies on one chip enables fabrication of third-generation IR photodetectors in which the double-band principle is inplemented (detectors operating in two wavelength regions, 3 to 5 μm and 8 to 12 μm, have a number of advantageous features in comparison with single-frequency IR sensors [12]. Successful realization of MCT-based shells with 2D electron gas makes it possible to employ such shells as IR photodetectors with tunable absorption band (multispectral detectors) due to strain redistribution and, hence, band-gap energy variation over the shell.

Today, an unresolved problem in the path towards realization of the above-described possibilities is the lack of processes permitting formation of shells and taking the material properties of MCT into account. The present study was undertaken to develop of a process for forming MCT-based shells.

1. Experimental

MCT samples were grown by molecular-beam epitaxy on a semi-insulating GaAs (013) substrate in an MBE process described in [13, 14]. The active part of the structure was grown on a relaxed CdTe buffer layer. The sequence of layers in the structure is shown in Fig. 1. On top of the heterostructure, a 250-nm thick CVD SiO_2 layer was provided, deposited at temperature 250°. Following deposition of this layer, the exposed areal parts of the film were etched through to the substrate using standard optical lithography and nonselective liquid etching in a weak solution of bromine in isopropyl alcohol. We used a

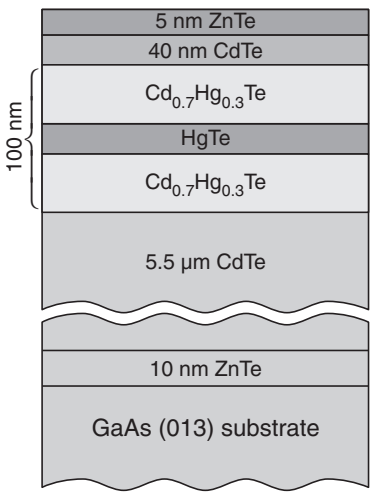

Fig. 1. Sequence of layers in the MCT-based heterostructure.

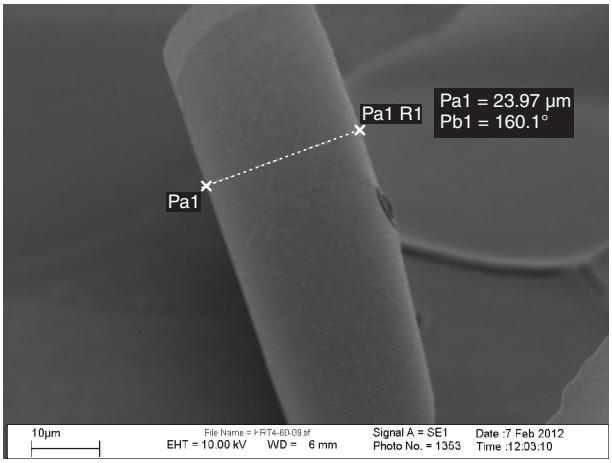

Fig. 2. A tubular MCT shell. The tube wall thickness is approximately 400 nm, including 250 nm occupied by the SiO_2 layer, and 150 nm, by the heterostructure comprising the ZnTe stressor and the MCT-based heterostructure with QW. The tube radius is 12 μm.

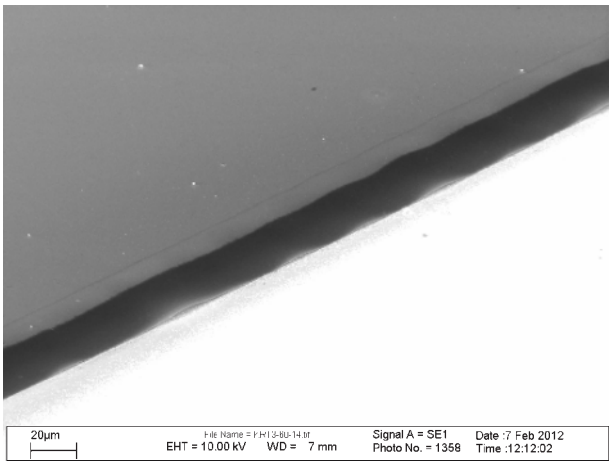

Fig. 3. A periodically corrugated MCT shell. The corrugation period is approximately 50 μm, and the corrugation amplitude is 10 μm. The curvature radius at the corrugation chest is 13 μm.

few bromine-based etchants, including solutions of bromine in HBr, ethylene glycol, and methanol [15, 16]. The best etching uniformity was reached in a solution of Br_2 in isopropyl alcohol. The etching rate was approximately 2 μm/min. The essence of the reaction is as follows. Bromine anions dissolve Cd and Hg on the surface, forming bromides of Cd and Hg soluble in isopropyl alcohol. The probability of tellurium bromide formation is low; most likely, tellurium dissolves in isopropyl alcohol in pure form. After the etching of a mesastructure, the strained film was separated from the substrate using selective etching of a sacrificial layer. The sacrificial layer was a 5.5-μm thick CdTe buffer layer. Under partial relaxation of the internal stress [17], the ZnTe/CdTe/CdHgTe/HgTe/CdHgTe film bent to form a scroll (Fig. 2) or a periodical corrugation (Fig. 3) formed at film edges. The stressor was a top 5-nm thick ZnTe layer. For selective etching of CdTe with respect to CdHgTe, we used solutions of iodine in dimethyl formamide of various concentrations ranging from 1% to 15% [18]. The etching selectivity of CdTe sacrificial layer is due to the fact that the solubility of the products of the reaction of CdI_2 with pure Te is much higher than the solubility of HgI_2 in dimethyl formamide (by more than 50 times). The etching rate was approximately 1 to 5 μm/min. Since the ZnTe stressor was etched in the above etchant as readily as CdTe, the top SiO_2 layer served not only a mask in etching the film to the substrate, but also as a protective layer for the ZnTe stressor.

Figures 2, 3 show SEM images of several formed shells. The measured diameter of the tube was 24 μm, this value being in agreement with the one calculated on the assumption of a bilayered strained film [19] ($\Delta a/a \approx 0.057$, $d_1 = 5$ nm, $d_2 = 140$ nm, $\nu \approx 0.3$):

$$D = \frac{1}{3}\,\frac{(d_1+d_2)^3}{d_1 d_2(1+\nu)(\Delta a/a)}\,. \qquad (1)$$

The lateral size of a single corrugation was about 50 μm; hence, the radius of curvature calculated by formula $k = 2\pi^2 A/L^2$ (where A and L are the corrugation amplitude and period) is of order 13 μm.

2. Conclusions

To summarize, for the first time variously shaped shells involving a ZnTe stressor and an active CdTe/CdHgTe/HgTe/CdHgTe layer containing a HgTe QW were fabricated. The diameter of formed tubes was 24 μm, the curvature radius of corrugations, approximately 13 μm.

Acknowledgements

The authors are grateful to M. M. Kachanova, L. A. Nenasheva and T. A. Gavrilova for technical assistance. SEM images were taken at the CUC "Nanostructures". This work was partially supported by the Russian Foundation for Basic Research (Grant No. 12-02-00918-a).

References

[1] Y. S. Gui *et al.*, *Phys. Rev. B* **70**, 115328 (2004).
[2] Z. D. Kvon *et al.*, *Low Temp. Phys.* **37**, 202 (2009).
[3] V. Ya. Prinz *et al.*, *Physica E* **6**, 828 (2000).
[4] V. M. Osadchii *et al.*, *Phys. Rev. B* **72**, 033313 (2005).
[5] L. I. Magarill *et al.*, *JETP* **86**, 771 (1998).
[6] R. C. T. da Costa *et al.*, *Phys. Rev. A* **23**, 1982 (1981).
[7] A. B. Vorob'ev *et al.*, *Phys. Rev. B* **75**, 205309 (2007).
[8] A. Kleiner *et al.*, *Phys. Rev. B* **67**, 155311 (2003).
[9] B. Habib *et al.*, *Phys. Rev. B* **75**, 153304 (2007).
[10] B. Habib *et al.*, *Semicond. Sci Technol.* **23**, 064002 (2009).
[11] B. A. Bernevig *et al.*, *Phys. Rev. Lett.* **96**, 106802 (2006).
[12] A. Rogalski *et al.*, *Rep. Prog. Phys.* **68**, 2267 (2005).
[13] S. A. Dvoretsky *et al.*, *J. electron. mater.* **39**, 918 (2010).
[14] S. A. Dvoretsky *et al.*, *Avtometriya (in Russian)* **43**, 104 (2007).
[15] V. Srivastav *et al.*, *J. Electron. Materials* **34**, 11 (2005).
[16] V. Srivastav *et al.*, *Opto-Electronics Review* **13**, 197 (2005).
[17] V. Ya. Prinz *et al.*, *Physica E* **24**, 54 (2004).
[18] Z. F. Tomashik *et al.*, *Russian J. Inorg. Chem.* **50**, 1765 (2005).
[19] M. Grundmann *et al.*, *Appl. Phys. Lett.* **83**, 2444 (2003).

20th Int. Symp. "Nanostructures: Physics and Technology"
Nizhny Novgorod, Russia, June 24–30, 2012

Elastic energy relaxation in core-shell nanostructures

M. V. Nazarenko[1], N. V. Sibirev[1] and V. G. Dubrovskii[1,2]

[1] St Petersburg Academic University, St Petersburg, Russia
[2] Ioffe Physical-Technical Institute, St Petersburg, Russia

Abstract. Low-temperature growth of InGaAs/GaAs nanopillars onto silicon is essential to enable scalable monolithic integration of optoelectronic devices with silicon integrated circuits. This study deals with a theoretical investigation of elastic stress arising due to lattice mismatch in such heterostructures . The elastic energy is shown to concentrate only near the core-shell interface and the relaxation due to free outer interface is shown to be very effective, so that dislocation formation may be avoidable in such heterostructures. This opens a way for high material quality essential for device applications.

Introduction

The heterogeneous integration of optoelectronic and electronic integrated circuits is poised to transform personal electronics because it will not only enable a vast range of otherwise unattainable capabilities, but will also reduce power consumption, weight and size. To facilitate scalable manufacturing, monolithic integration of lattice-mismatched single-crystalline materials is of paramount importance. Direct growth of III-V thin film on silicon substrates has been very challenging because of high epitaxy temperatures that are incompatible with CMOS circuits, and large mismatches of lattice constants and thermal expansion coefficients between III-V compounds and silicon compromise reliability and performance [1]. As such, there has been a focus on growing three-dimensional nanostructures, which show great promise to overcome these difficulties [2,3].

Recently a completely new growth mechanism that yields catalyst-free, self-assembled, single-crystalline nanoneedles and nanopillars, which consist of InGaAs core-shell heterostructures, was reported on [3]. Here we perform an theoretical investigation of elastic stress occurring in core-shell nanopillars when lattice mismatch ε_0 occurs between the core and the shell.

1. Elastic energy calculation

To model a nanopillar we consider a model of two long coaxial cylinders (see Fig. 1). Our consideration is based on the solution for a single long hollow cylinder subjected to internal and external pressure, as presented in [4]. We assume generalized plane strain condition. Using cylindrical coordinates (r, φ, z) with z along the cylinder length the governing equation in axially symmetric case reduces to

$$\frac{\partial^2 u_r}{\partial r^2} + \frac{1}{r}\frac{\partial u_r}{\partial r} - \frac{u_r}{r^2} = \frac{\partial}{\partial r}\left[\frac{1}{r}\frac{\partial}{\partial r}(r u_r)\right] = 0 \qquad (1)$$

with u as radial displacement. We assume that both core and shell have the same Young's modulus E and Poisson's ratio ν. We also assume that both the base and the top of the structure are flat facets and no gap exist between the core and the shell, so our boundary conditions are

$$u_r^s\big|_{r=C} - u_r^c\big|_{r=C} = \varepsilon_0 C \qquad (2)$$

$$u_z^s\big|_{z=L} - u_z^c\big|_{z=L} = \varepsilon_0 L \qquad (3)$$

$$u_z^s\big|_{z=0} - u_z^c\big|_{z=0} = 0, \qquad (4)$$

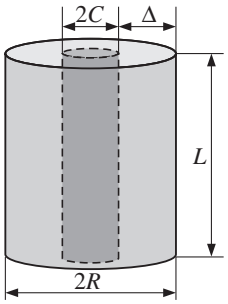

Fig. 1. Coaxial cylinder model. C — nanopillar core radius, Δ — nanopillar shell thickness, L — nanopillar length, R —nanopillar shell outer radius.

here indexes 's' and 'c' denote shell and core respectively, ε_0 is lattice misfit and C, R, and L are core radius, outer shell radius and cylinder length respectively. Equation (2) means that there is no gap at the side interface, the other two account for no gap at the top and bottom facets (equations (3) and (4) respectively). It follows that a vertical force exists between the core and the shell to keep the end facets flat. Using [4] we readily arrive at a generalized solution for shell strain tensor ε and stress tensor σ in terms of pressure p at the core-shell interface.

Note that both ε and σ are diagonal matrices in the chosen coordinates due to axial symmetry of the problem. We can also find core stress and strain in a similar fashion.

All that is left before getting complete solution is determining p using (2)–(4). The result is

$$p = \varepsilon_0 E \frac{R^2 - C^2}{2(1-\nu)R^2}. \qquad (5)$$

Now we can calculate total elastic energy W as

$$W = \int_0^L \mathrm{d}z \int_0^{2\pi} \mathrm{d}\varphi \int_C^R \frac{\varepsilon_{rr}\sigma_{rr} + \varepsilon_{\varphi\varphi}\sigma_{\varphi\varphi} + \varepsilon_{zz}\sigma_{zz}}{2} r\,\mathrm{d}r. \qquad (6)$$

2. Results and discussion

To compare core-shell growth with the traditional thin film growth and to study elastic energy relaxation, we consider the elastic energy W_{2D} of a uniformly strained 2D layer of the same volume on a semi-infinite substrate with the same lattice misfit, Young's modulus and Poisson's ratio and relative elastic energy Z:

$$Z \equiv \frac{W}{W_{2D}}. \qquad (7)$$

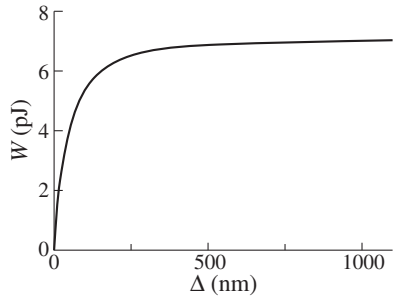

Fig. 2. Total elastic energy W against shell thickness Δ. The material parameters correspond to GaAs/$In_{0.2}Ga_{0.8}$As pair (2% mismatch).

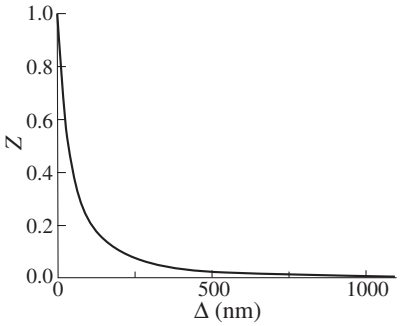

Fig. 3. Relative elastic energy Z against shell thickness Δ. The material parameters correspond to GaAs/$In_{0.2}Ga_{0.8}$As pair (2% mismatch).

Now we consider Z as a function of shell thickness $\Delta \equiv R - C$. To analyze an extreme case we use big O notation: $|O(x)| \leq Mx$ if $x < x_0$ for some positive M and x_0.

We arrive at

$$Z = \frac{\left(1-\nu^2\right) C^2}{\Delta^2} + O\left(\frac{C^3}{\Delta^3}\right), \qquad \Delta \to \infty. \qquad (8)$$

The result (8) for a very thick shell means that Z tends to zero as Δ tends to infinity, i.e. the elastic stress is almost fully relaxed due to core-shell geometry. To clarify, we write the total elastic energy as

$$W = \pi E \varepsilon_0^2 \left(1+\nu\right) C^2 L + O\left(\frac{C}{\Delta}\right), \qquad \Delta \to \infty, \qquad (9)$$

to show that total elastic energy approaches a constant value as shell thickness increases. This means that the elastic stress in the shell is contained near the core-shell interface: the internal part on the shell is stressed as much as it would be in the thin film case, while the outer regions are effectively relaxed.

This behavior is illustrated by Fig. 2 and Fig. 3, which show total and relative energy correspondingly against shell thickness. Material parameters used relate to the experimental data on GaAs/$In_{0.2}Ga_{0.8}$As nanopillars presented in Ref. [5]: $E = 86$ GPa, $\nu = 0.31$, $\varepsilon_0 = 2\%$. Nanopillar length L is 5 μm, core radius C is 100 nm. These results shows that core-shell geometry is even better in elastic energy relaxation than laterally confined axial heterostructures, such as free vertical standing nanowires. While laterally confined axial heterostructures do allow for infinite coherent growth below certain critical diameter due to elastic energy relaxation [6], the relative elastic energy is inversely proportional to the layer *thickness* [7], whereas in the core-shell geometry the relative stress energy is inversely proportional to the layer *thickness squared* (see (equation (8)).

3. Conclusions

Effective elastic energy relaxation means that dislocation formation might be effectively suppressed due to core-shell geometry. Normally, dislocation formation decrease effective lattice misfit and serve as the only way to decrease elastic energy. Indeed, thin film growth in a lattice mismatched system always results in dislocation formation, otherwise the elastic energy would have increased infinitely with layer thickness. However, since the core-shell geometry allows for a very effective energy relaxation by itself, dislocation formation becomes avoidable. This allows for high material quality essential for device applications.

Acknowledgements

This work was partially supported by different grants of RFBR, Presidium RAS and the Ministry of Education and Science of Russia.

References

[1] A. W. Fang *et al*., *Opt. Express* **14**, 9203 (2006).
[2] F. Olsson, M. Xie, S. Lourdudoss, I. Prieto and P. A. Postigo, *J. Appl. Phys.* **104**, 093112 (2008).
[3] M. Moewe, L. C. Chuang, S. Crankshaw, K. W. Ng and C. Chang-Hasnain, *Optics Express* **17**, 7831 (2009).
[4] A. F. Bower, *Applied Mechanics of Solids* , (New York: CRC Press) 820 pages, 2009.
[5] K. W. Ng *et al*., submitted to *Nano Lett.*.
[6] F. Glas, *Phys. Rev. B*, **74**, 121302(R) (2006).
[7] X. Zhang, V. G. Dubrovskii, N. V. Sibirev and X. Ren, *Cryst. Growth Des.* **11**, 5441 (2011).

20th Int. Symp. "Nanostructures: Physics and Technology"
Nizhny Novgorod, Russia, June 24–30, 2012

Application of optical methods for the study of symmetry of local centers (system GR1 in diamond)

V. A. Gaisin[1], V. G. Davydov[1], E. L. Chirkov[1], S. L. Berdnikov[1], B. S. Kulinkin[2], A. P. Skvortsov[3], V. L. Masaytis[4], V. A. Nevolin[5] and T. K. Gureeva[6]

[1] Physical Faculty, St Petersburg State University, Ulyanovskaya 1, Petrodvorets, 198504 St Petersburg, Russia
[2] St Petersburg State Medical University, 6/8 Leo Tolstoy str., 197022 St Petersbug, Russia
[3] Ioffe Physical-Technical Institute, St Petersburg, Russia
[4] Ministry of Natural Resources and Ecology of the Russian Federation Federal Agency of Mineral Resources Federal State Unitary Enterprise A. P. Karpinsky Russian Geological Research Institute (FGUP VSEGEI), Sredny pr. 74, 199106 St Petersburg, Russia
[5] TSENTRSIBGEO Research and Production Center Limited Liability Company Region Krasnoyarsk Krai, Karl Marks str. 62, 309, 660049 Krasnoyarsk, Russia
[6] Krasnoyarsk City Administration, Karl Marks str. 93, Krasnoyarsk, Russia

Abstract. In our work the absorption and luminescence spectra of the primary radiation induced centres in the GR-1 band are investigated. These centers are produced in all types of diamond as a result of irradiation by electrons or neutrons. The zero phonon line at 741 nm characterize this type of radiation damage. The treated diamonds have a green coloration Interaction with two quasilocal lattice vibration (340 and 780 cm^{-1}) is revealed. Decomposition of the spectra into components is performed, the magnitude of the Stokes is determined. On the basis of the analysis of the obtained results the conclusion is drawn on possible presence in structure of the center of vacancy and substitutional nitrogen atom.

Introduction

Presently the interest to the study of structures with lowered regularity steadily grows. The modern techniqus of MBE growth allow to growth the structures with quantum dots (QD's), quantum wells (QW's), the quantum whisker which are possessing improved properties as compared with the bulk materials — a high quantum yield of luminescence in narrow lines at positions well corresponding to positions of lines in the spectra of absorption, reflectivity and excitation of luminescence.It should be noted that the quantum size objects such as QW's and QD's can be formed due to the processes of self-organization in a number of materials at their synthesis. (See for a rewiev Ledentsov [1]). In this respect the different modifications of carbon derivatives are of interest.

1. Graphite. Its vibrational spectrum in which the low-frequency bending modes were detected indicates that it can be considered as almost two-dimensional compound.

2. Grafen which is a two-dimensional connections

3. Fulleren C60 and C70. (Analog of QD's)

4. Natural diamonds.

Diamond is of special interest. In comparison with other crystals the diamond possesses a number of unique properties-the large width of the forbidden gap (indirect transition at 5.5 eV). Diamond contains considerable number of various impurities, in particular the nitrogen which stabilize the mechanical properties of diamond. Impurity atoms of nitrogen enter the natural diamonds in the form of single substitution atoms, pairs, triads and etc., producing the defect clusters, involving hundreds of atoms — the analogy of QD's of various sizes. Nitrogen, besides, forms in diamond the planes containing the thousands of atoms — the analogy of two-dimensional QW's. The irradiation of natural diamond by neutrons, protons, electrons and so on leads to formation of primary radiative defects — vacancies and interstitial atoms of carbon. At annealing of irradiated diamonds the redistribution of single radiative defects takes place leading to formation of carbon complexes — clusters and complexes including primary defects and impurity atoms. From this point of view the diamond is analogues to a glass or polymeric matrix in which the QD's are formed.In the case of point defects formed by isolated substitutional heavy atoms the quasilocal lattice vibrations (QLV) appear in diamond. Absorption and luminescence spectra of such defects are governed by interaction of electronic states with quasilocal lattice vibrations and vibrations of diamond lattice. Strength of interaction is defined by stokes shift and is directly connected with the change of equilibrium positions of both the substitutional atom and the diamond atoms in the nearest environment. Depending on the magnitude of the Stokes shift the changes can extend on several coordination spheres. From this point of view the point defects in diamond demonstrate the analogy to the self-organized QD's in heterostructures. It seems that the diamond is a perspective material for the study of the influence of external perturbations (magnetic, electric fields, change of degree of polarization, etc) on the QD's states.

1. Exprimental

In our work the absorption and luminescence spectra of the primary radiation induced centres in the GR-1 band are investigated. These centers are produced in all types of diamond as a result of irradiation by electrons or neutrons. The zero phonon line at 741 nm characterize this type of radiation damage. The treated diamonds have a green coloration. When irradiated diamonds are heated at $T \geq 500^{\circ}$C the GR-1 band will decrease up to disappearance while the new radiation/annealing centers appear and increase in strength: 503, 515, 525, 575, 594.4, 805.5 nm.

2. Results and discussion

Presently there is no completely established model of the defects responsible for the GR-1 band. In the literature two models are discussed.

1 — The primary radiation induced defect centres — vacancies.

2 — Vacancies trapped by other defects, mainly nitrogen centres.

Interaction with two quasilocal lattice vibration (340 and 780 cm^{-1}) is revealed. Decomposition of the spectra into components is performed, the magnitude of the Stokes is determined. On the basis of the analysis of the obtained results the conclusion is drawn on possible presence in structure of the center of vacancy and substitutional nitrogen atom. The obtained results are in consent with the data of work [2], where the linear Stark effect has been observed for the investigated line (741 nm) which indicates the absence of the inversion symmetry for the centre studied. As was mentioned earlier, the system 741 nm (GR1) appears in natural diamonds of all types as a result of radiation exposure to neutrons, protons, alpha particles, electrons and gamma rays. According to the work [3] the fluence of fast neutrons necessary for the creation of this centre amounted to the value of 1.5×10^{17} cm^2 and 1.3×10^{18} cm^2 for the energy $E > 3$ MeV and $E > 100$ keV respectively. The fluence of thermal neutrons amounted to the value of 1.9×10^{18} cm^2. The dose of gamma rays-radiation equals 3 Grad. The activation energy $E = 2.43$ eV . According to the literary data, the system 741 nm (GR1) is interpreted as the result of electron-vibration transitions in the centre which consists of isolated single vacancy, i.e. in the primary radiation defect [4] Perhaps, this conclusion was based on:

i) — in the paper [2] a linear Stark effect was observed for the investigated line 741 nm,

ii) — the system 741 nm (GR1) occurs in diamonds in the early stages of the radiation exposure that creates radiation defects, these being vacancies and interstitial carbon atoms,

iii) — it was assumed that no temperature transformation or annealing of the primary radiation defects occurs.

According to the data of the work [3], this migration of vacancies takes place in the temperature range of 400–500 K, with the energy of activation being about 500 MeV. In this paper, in contrast to the common views [4], we associate the system 741 nm (GR1) with the manifestation of one of the secondary radiation defects — a complex of the vacancy and the nitrogen atom that is located in the next to the vacancy atomic site in the crystal structure. We proceeded from the reliability of the first two theses:

i) — in the work [2] a linear Stark effect was observed for the investigated line 741 nm,

ii) — the system 741 nm (GR1) occurs in diamonds in the early stages of the radiation exposure that creates radiation defects, these being vacancies and interstitial carbon atoms.

We assumed that the annealing of the primary radiation defects of the vacancies and the interstitial carbon atoms, in contrast to the thesis iii), occurs in the early stages of the creation of defective centers:

i) — directly during the process of irradiation and

ii) — during the time necessary for the collapse of the induced radiation In the framework of this model, an observation of two quasilocal lattice vibrations located in the acoustic range (0–800 cm^{-1}) with the frequencies of 340 and 780 cm^{-1} in the electronic-vibration spectra of absorption and luminescence of the system 741 nm (GR1), held in this work, becomes clear. According to modern notions in the theory of electron-vibration spectra of impurity centers, in the crystals of cubic syngony only one quasilocal lattice vibration can be associated with the vacancy and the heavy impurity substitution of a regular atomic site. Impact diamonds have a similar colour [5]. We assume that the black colour of the irradiated and impact diamonds is caused by the micro-phase of the graphite. This assumption is confirmed by the data of the x-ray analysis of impact diamonds [5, 6].

References

[1] D. Bimberg, M. Grundmann, and N. N. Ledentsov *et al*., *Quantum Dot Heterostructures* (Wiley, NewYork), 1999.
[2] A. A. Kaplyanskii *et al*., *FTT* **12**, 3530 (1970).
[3] A. G. Alekseev *et al*., *Technical Physics Letters* **26**, 304 (2000).
[4] V. B. Kvaskova *et al*., *Natural Diamonds of Russia* (1994).
[5] V. L. Masaytis *et al*., *Huge adtrobleme Russia* (1994).
[6] S. A Vishnevsky *et al*., *Impaktnye diamonds*. Novosibirsk (1997).

20th Int. Symp. "Nanostructures: Physics and Technology"
Nizhny Novgorod, Russia, June 24–30, 2012

"Surface" magnetic anisotropy and low-temperature effects in the system of ferrite nanocrystals of $CoFe_2O_4$

A. N. Bludov[1], K. A. Mozul'[2], L. P. Ol'khovik[2], V. O. Pashchenko[1], Z. I. Sizova[2], E. V. Shurinova[2] and V. V. Vashchenko[3]

[1] B. Verkin Institute for Low Temperature Physics and Engineering, 61103 Kharkov, Ukraine
[2] Karazin Kharkov National University, 61077 Kharkov, Ukraine
[3] State Scientific Institution "Institute for Single Crystals", 61001 Kharkov, Ukraine

Introduction

One of the factors responsible for the specificity of the magnetic properties of small particles is the effect of the surface. Violation of the elemental composition and the local symmetry of the crystal structure of the surface layer of particle forms an additional contribution to the energy of the effective magnetic anisotropy. It was interesting to estimate the importance of the contribution of the "surface" anisotropy for a high dispersive system of nanocrystals of spinel type ferrite of $CoFe_2O_4$.

1. Experimental

The investigations were performed on a system of particles with an average size of 9.2 nm synthesized using the sol-gel technology [1]. Have been measured magnetization curves and the main limiting hysteresis loops in fields up to 50 kOe in the temperature range 4.2–500 K.

Abnormally high values of the coercive force H_c for small ferrite particles at low temperatures and character of its temperature dependence in general, reflect the value and nature of changes in the magnetocrystalline anisotropy field H_{ak} (figure).

However, there are noticeable quantitative differences: if the macroscopic analogue in the range of 4.2–250 K H_{ak} changed to 68%, the change in H_c for the investigated system of nanocrystals is 98%.

From the experimental values of H_c, using the formula Neel [2] for a system of the crystallites of a cubic syngony (in the case $K_1 > 0$) $H_c = 0.32H_a$, was determined the effective magnetic anisotropy field Haef. Considering the specificity of small particles — the presence of three contributions to the effective magnetic anisotropy

$$H_a^{ef} = H_{ak}\left(1 - \frac{V^{surf}}{V}\right) - H_a^{dem} \pm H_a^{surf}\,\frac{V^{surf}}{V}, \quad (1)$$

where V — volume of the particle, V^{surf} — the volume of its surface layer, H_a^{surf} — field of "surface" magnetic anisotropy, H_a^{dem} — anisotropy field of particle shape. Volume V^{surf} of the surface layer with thickness 1 nm [3] was 37 % of the particle volume for the average particle size, assuming an octahedral shape. The temperature dependence of magnetocrystalline and surface anisotropy, and their contribution to the effective anisotropy is shown in the figure (the contribution of the anisotropy of particle shape is negligible). Discovered at 60 K changing the sign of contribution of "surface" anisotropy and temperature dependence of the anomalies of the specific magnetization and high-field susceptibility suggest the change in magnetic manner in the structure of the surface layer [4].

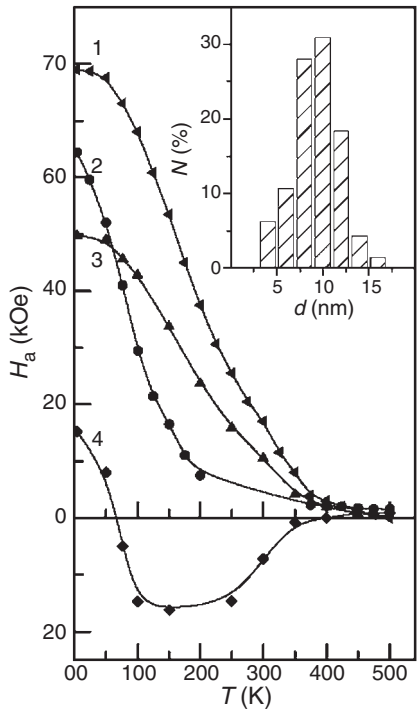

Fig. 1. Temperature dependence of the effective magnetic anisotropy field and contributions forming it of system of the nanocrystals of CoFe2O4 in comparison with the magnetocrystalline anisotropy of macroscopic analogue: 1 — H_{ak}, 2 — H_a^{ef}, 3 — $H_{ak}(1 - V^{surf}/V)$, 4 — $H_{as}V^{surf}/V$.

References

[1] Sh. Sun *et al.*, *Am. Chem. Soc.* **126**, 273 (2004).
[2] L. Neel *et al.*, *Compt. rend* **224**, 1488 (1947).
[3] A. H. Morrish *et al.*, *J. Appl. Phys.* **63**, 4258 (1988).
[4] S. N. Zinenko *et al.*, *JETF* **123**, 1073 (2003).

20th Int. Symp. "Nanostructures: Physics and Technology"
Nizhny Novgorod, Russia, June 24–30, 2012

Nanocomposites $A^{III}B^{V}$-metals as wire metamaterial media

A. V. Atrashchenko[1,2], V. P. Ulin[1], V. P. Evtikhiev[1]

[1] Ioffe Physical-Technical Institute, St Petersburg, Russia
[2] National Research University of Information Technologies, Mechanics and Optics, St Petersburg, Russia

Abstract. Nanocomposites GaP-Cu and AlGaP-Cu which is a medium consisting of wires with hexagonal arrangement and the parameters of rods diameter 20 nm and length 2 μm have been fabricated by electrochemical etching and electrochemical deposition. SEM (Scanting Electron Microscopy) and Auger electron spectroscopy measurements have been made. Optical measurements of transmission and absorption spectra at different angles have been made.

The idea to use the wire (or nanorod) medium to create metamaterials was proposed in 2003 [1]; these materials are called wire metamaterials. For operation in radio and microwave range the wire metamaterials can be formed by mechanical assembling of metallic wires into arrays. However, for operation in THz, IR and visible wavelength range the fabrication of such materials is of extreme difficulty. After all, in 2008 [2] the wire metamaterial for near-IR range based on porous Al_2O_3 fabricated by anodization and filled with a metal (Ag) by the electrochemical deposition was demonstrated.

In this work we demonstrate nanocomposites based on nanoporous $A^{III}B^{V}$ semiconductors (by electrochemical method [3]) and investigate the optical, structural and electrical properties. In comparison with Al_2O_3, the use of $A^{III}B^{V}$ semiconductors allows using other properties such as non-linearity near the absorption edge or high refractive indexes. It is worth noting that among $A^{III}B^{V}$ semiconductors there exist transparent ones in the visible spectrum (GaP and AlGaP). We have reached good results in the creation of such matrixes (InP, GaP, GaAs) in a wide range of options while preserving the structural perfection [4]. We can fabricate the matrix with the following parameters: pores size from 20 to 300 nm, the depth up to 100 μm (i.e., the aspect ratio larger than 10000) and we can control the propagation direction (along the crystallographic axis), shape, wall thickness and porosity (Fig. 1). All this will allow us to use unfilled matrixes for different types of sensors.

The pores in these matrixes can be filled by using the method of electrochemical deposition (Ni, Cu, Au, Ag) or the method of capillary filling (In, Ga and In/Ga-Au/Ag eutectic). Figure 2 shows the nanoporous matrix (the pores diameter is 20 nm, wall thickness is 40 nm and depth is about 6 μm) based on GaP (111)B n-type semiconductor filled with metal

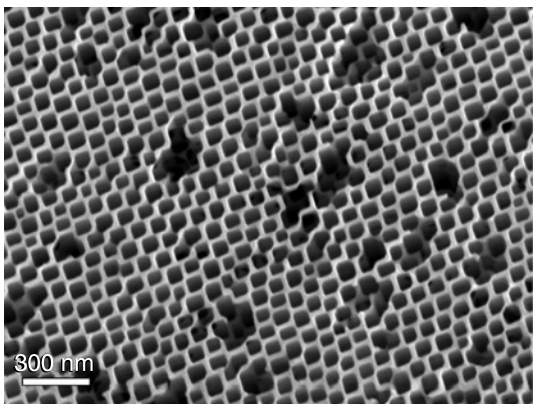

Fig. 1. SEM image of the surface of InP matrix

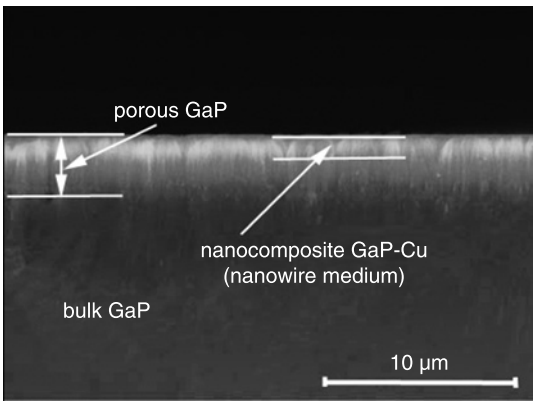

Fig. 2. SEM image of the surface cross-section of GaP matrix.

(copper) to the depth of 2 μm. SEM and Auger electron spectroscopy measurements have demonstra-ted that we fabricated wire nanocomposite GaP-Cu which is a medium consisting of wires with hexagonal arrangement and the parameters of rods diameter 20 nm and length 2 μm.

Peculiarities of the optical properties of nanocomposites (GaP-Ag/Au and AlGaP-Ag/Au) created with various parameters are under investigation. However, the first optical measurements of wire nanocomposites based on GaP-metal and AlGaP-metal show that they are perfect candidates for wire metamaterial in the visible range. The fitting of parameters of nanoporous matrix will help us to understand and tune nonlinear properties of the nanorod metamaterial [5]. Using these properties will be centered on constructing superlenses for high-resolution imaging or hiding structures through optical cloaking.

Acknowledgements

Work was supported by Ministry of Education and Science of the Russian Federation (contracts Nos. 14.740.11.0270 and 14.740.11.1232), grant of Presidium RAS. The authors are indebted to P. A. Belov for valuable discussions.

References

[1] P. A. Belov, *Microw. Optical Technology Lett.* **37**, 259 (2003).
[2] J. Yao, Zh. Liu, Y. Liu, *et al*, *Science* **321**, 930 (2008).
[3] V. P. Ulin, S. G. Konnikov, *Semiconductors* **41**, 832 (2007).
[4] A. V. Atrashchenko, V. N. Katz, V. P. Ulin, V. P. Evtikhiev, V. P. Kochereshko, *Physica E*, in press (2012), http://dx.doi.org/10.1016/j.physe.2012.02.012.
[5] G. A. Wurtz, R. Pollard, W. Hendren, *et al*, *Nature Nanotechnology* **6**, 107 (2007).

20th Int. Symp. "Nanostructures: Physics and Technology"
Nizhny Novgorod, Russia, June 24–30, 2012

Photoluminescent centers in CVD and detonation nanodiamonds

I. I. Vlasov[1], V. G. Ralchenko[1], O. Shenderova[2], S. B. Orlinskii[3], S. Turner[4], A. A. Shiryaev[5], I. Sildos[6] and V. I. Konov[1]

[1] General Physics Institute, 38 Vavilov str., 119991 Moscow, Russia
[2] International Technology Centre, 8100-120 Brownleigh Drive, Raleigh, NC, 27617, USA
[3] Federal Center of Shared Facilities of the Kazan State University, 420008 Kazan, Russia
[4] EMAT, University of Antwerp, Groenenborgerlaan 171, 2020 Antwerp, Belgium
[5] Institute of Physical Chemistry RAS, Leninsky pr. 31, 119991 Moscow, Russia
[6] Institute of Physics, University of Tartu, Riia str. 142, 51014 Tartu, Estonia

Nanodiamond (ND) with stable and efficient photoluminescent centers formed on a base of impurity atoms is an advanced material for production of both one-photon emitting sources [1] and brightly luminescent labels [2] depending on the impurity content in one diamond particle. Photoluminescent properties of CVD nanodiamonds containing Si impurity and detonation nanodiamonds containing N imputity were studied in this work. We have demonstrated that the luminescent "silicon-vacancy" (SiV) defects can be formed and are stable within 5-nm diamond crystallites produced by CVD technique [3]. A spatial distribution of the luminescent SiV centers within continuous diamond films and two-dimensional arrays of isolated diamond nanoparticles grown at different deposition and doping conditions was studied. As an example, a SiV luminescence image of CVD film grown at high seeding density and doped with Si from silicon substrate is shown in Fig. 1.

A systematic study of microstructure, concentration, and spatial distribution of nitrogen-related defects in different classes of dynamically synthesized nanodiamonds with primary particle sizes ranging from 5 to 50 nm using high-resolution transmission electron microscopy, spatially resolved electron energy loss spectroscopy, confocal Raman and photoluminescence spectroscopy, and pulsed electron paramagnetic resonance spectroscopy has been carried out. The highest concentration of atomic nitrogen in a diamond core (3–5 at %) was found in NDs produced from explosive. The highest concentration of nitrogen paramagnetic centers (1.2 ppm) was detected in NDs synthesized from a mixture of graphite and explosive. Well-pronounced narrow-band photoluminescence at 575 and 637 nm wavelengths related to "nitrogen-vacancy" (NV) centers was observed in primary ND particles of different origin with sizes larger than 30 nm [4] (Fig. 2). Prospects of controllable formation of SiV and NV centers in the nanodiamonds are discussed.

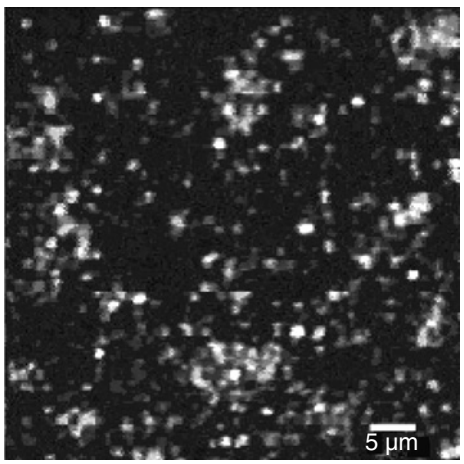

Fig. 1. Confocal SiV luminescence mapping within CVD nanodiamond film at 658 nm laser excitation. Blue-red-white is a colour sequence corresponding to emission intensity increase.

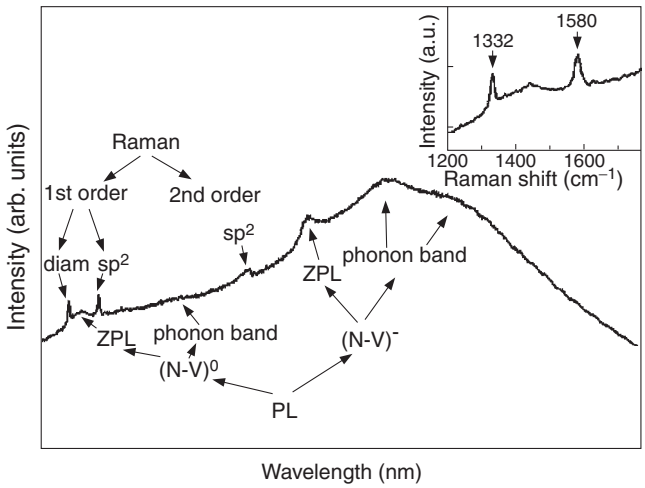

Fig. 2. Typical photoluminescence (PL) spectrum recorded at RT for luminescent detonation ND particles with size larger than 30 nm. The excitation wavelength is 532 nm.

Acknowledgements

This study was supported by the Ministry of Education and Science of the Russian Federation, State contract No. P925, the RFBR grant No. 11-02-01432, the grant of RAN program No. 24, the grant of President of the Russian Federation NSH-3076.2012.2.

References

[1] J. Tisler *et al*., *ACS Nano* **3**, 1959 (2009).
[2] A. M. Schrand, S. C. Hens, and O. A. Shenderova, *Critical Reviews in Solid State and Materials Sciences* **34**, 18 (2009).
[3] I. I. Vlasov *et al*., *Adv. Mater* **21**, 808 (2009).
[4] I. I. Vlasov *et al*., *Small* **6**, 687 (2010).

20th Int. Symp. "Nanostructures: Physics and Technology"
Nizhny Novgorod, Russia, June 24–30, 2012

From UV to IR by graphite oxide reduction

V. M. Mikoushkin[1], V. V. Shnitov[1], S. Yu. Nikonov[1], A. T. Dideykin[1], P. Vul'[1], A. Ya. Vul'[1], D. A. Sakseev[1], D. V. Vyalikh[2] and O. Yu. Vilkov[3]

[1] Ioffe Physical-Technical Institute, St Petersburg, Russia
[2] Institut für Festköperphysik, Technische Universität Dresden, D-01062 Dresden, Germany
[3] Fock Institute of Physics, St Petersburg State University, 198904 St Petersburg, Russia

Abstract. Transformation of the chemical composition and electron structure of graphite oxide (GO) nanolayers as a result of their annealing in hydrogen has been studied by X-ray photoelectron spectroscopy using synchrotron radiation. It has been established that both the chemical composition and bandgap width of GO can be controlled by varying the temperature and duration of heat treatment. By this means, the GO nanolayers can be smoothly modified from dielectric to conductor through semiconductors with the bandgap width varied in the range $E_g = 2.9{-}0$ eV.

Introduction

Graphite oxide (GO) is widely used in many applications due to unique properties [1,2]. One of the most important properties of GO is the ability to readily form a colloidal suspension in water that consists of GO flakes. Using this suspension, it is possible to prepare GO films of unlimited area and any thickness beginning with subnanometer values. In the past decades, much effort has been devoted to developing transparent conducting GO-films and flexible displays. In recent years, the interest in GO has sharply increased in connection with the discovery of graphene [3] and the possibility of using GO nanolayers as initial materials for obtaining graphene-like layers and even graphene by GO reduction [1,2]. GO is commonly accepted to be a dielectric. However reduction of GO in hydrogen makes it possible to obtain graphite- and graphene-like layers characterized by high conductivity and nearly zero bandgap widths. A possibility of smooth variation of GO bandgap width was shown in research [4]. This paper being a continuation of the research [4] presents the results of an extended investigation of the chemical composition and electron structure of GO nanolayers transformed by the reduction in hydrogen. Reduced GO nanofilms with bandgap width ranged from $E_g = 2.9$ eV to $E_g = 0$ eV were fabricated using the hydrogen restoration technology.

1. Experimental details

The initial GO was synthesized via oxidation of the natural crystalline graphite by potassium permanganate in sulfuric acid in the presence of sodium nitrate, using a procedure that was close to that described in [5]. Then, sample films were prepared on the surface of silicon substrates by evaporating a drop of GO suspension. Finally, the films were annealed in a quartz reactor at various temperatures.

The chemical composition and electron structure of GO were studied by XPS at the Russian-German synchrotron radiation beamline of the BESSY (Berlin) electron storage ring [6]. The photoelectron spectra were measured using a VG SPEC hemispherical analyzer of the experimental station at the Russian-German Laboratory, which provided a spectral resolution of $\Delta E = 0.15$ eV. In order to ensure the uniformity of hydrogenation and exclude photoinduced charging of the samples, investigation was performed on thin GO films. The film thickness was evaluated by comparing the line intensities in the C1s spectra of a GO film and a massive pyrolytic graphite (HOPG) sample [4]. GO films with an average thickness of 2–3 monolayer were studied.

2. Results and discussion

Figure 1 presents the typical photoelectron spectra of C1s core levels excited by X-ray photons with an energy of $h\nu = 450$ eV in a sample of HOPG, initial GO film, and the films annealed at $T = 410$ and 800 °C. The spectrum of the initial film displays peaks that correspond to carbon in three functional groups present in GO: O=C–OH ($E_b = 290.2$ eV), C–O–C ($E_b = 288.1$ eV), and C–OH ($E_b = 285.8$ eV). These C1s binding energies are close to the corresponding values observed previously [1,7–9], although the differences reach 0.2–0.5 eV. In the spectrum of initial (unheated) GO, the C1s line virtually does not contain a contribution due to the sp^2 state of carbon in graphene sheet ($E_b = 284.3$ eV), which is evidence of a high efficiency of the oxidation method employed. Another important feature is that the contributions from carboxyl (CO-OH) and, especially, epoxide (C-O-C) groups are several times smaller as compared to those in the spectra reported previously [1,7–9]. Since these groups are localized predominantly at the edges of GO flakes [1], it may be concluded that the flakes studied here are rather large. This conclusion is confirmed by the scanning electron microscopy (SEM) image of a thin GO film shown in Fig. 2. Analysis of the SEM image al-

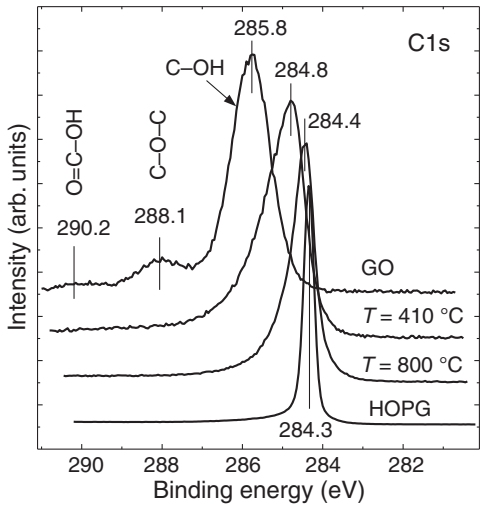

Fig. 1. C1s photoelectron spectra of HOPG, initial GO film and the films annealed in hydrogen at different temperatures.

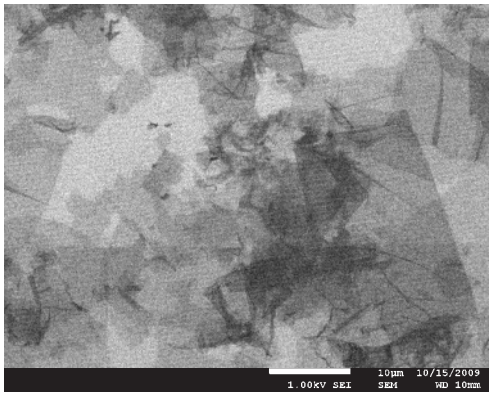

Fig. 2. SEM image of GO film on silicon substrate.

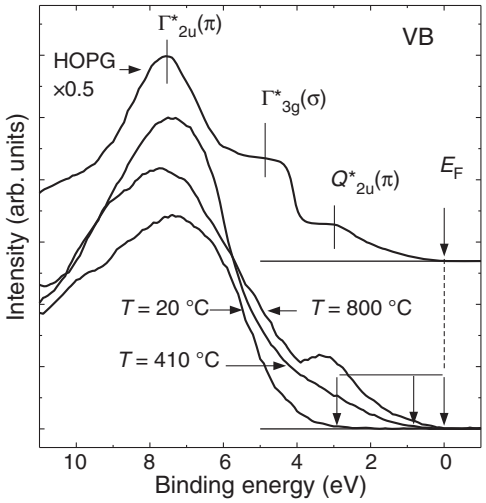

Fig. 3. Valence-band photoelectron spectra of HOPG, initial GO film and the films annealed in hydrogen at different temperatures.

lows the average GO flake size to be estimated at about 30 μm, which exceeds the dimensions of analogous objects previously reported in the literature [10].

The spectra presented in Fig. 1 show that oxide groups gradually disappear and the sp^2 state contribution grows with increasing temperature of heat treatment, which is evidence for the effective reduction of carbon sheets over the entire volume of thin GO films. In the sample annealed at T = 800 °C, the contribution of the sp^2 state ($E_b = 284.3$ eV) predominates.

Physical properties of GO films were characterized by the photoelectron spectra of the valence band shown in Fig. 3. For comparison, Fig. 3 presents the spectrum of HOPG, which shows that the top of the valence band almost coincides with the Fermi level. At the same time, the spectrum of the unheated GO film reveals a large gap between the valence band edge and the Fermi level ($V_B - E_F = 2.9$ eV), which is a part of the wide band ($E_g > 2.9$ eV) that is typical of dielectrics and wide-bandgap semiconductors.

It should be noted that GO studied is characterized by a much wider bandgap than that reported in [11], which is probably related to the concentration of oxide groups on the surface rather than at the edge of GO flakes. According to the photoelectron and optical absorption spectroscopy data, the samples studied in [11] had $V_B - E_F = 1.7$ eV and $E_g = 1.78 \pm 0.04$ eV. The proximity of these values indicates that (i) GO is a wide-bandgap n-type semiconductor in which a donor level is close to the bottom of the conduction band and (ii) the gap between

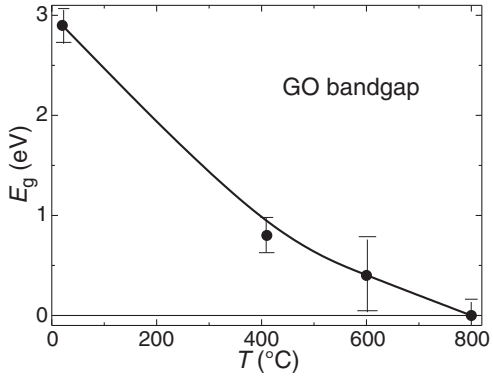

Fig. 4. Dependence of GO bandgap width on the annealing temperature.

the valence band edge and the Fermi level as measured by the photoelectron spectroscopy equals to within 0.1 eV to the bandgap width: $V_B - E_F \sim E_g$. Fig. 3 and 4 show that an increase in the annealing temperature leads to narrowing of the bandgap. After treatment at T = 800 °C, the edge of the valence band attains the Fermi level, which is indicative of the appearance of metallic conductivity in the reduced GO film.

3. Conclusions

It was found that the GO films synthesized in this study are characterized by a relatively large average flake size and oxide groups localized predominantly on the surface of carbon layers. Apparently, this chemical structure accounts for the fact that the bandgap width in the initial GO films reaches the level of $E_g \sim$ 2.9 eV, which significantly exceeds the previously reported values. It was demonstrated that an increase in the temperature of annealing allows the bandgap width to be decreased so as to smoothly pass over the entire optical spectrum, including the violet and visible ranges, and eventually obtain a material with high conductivity.

Acknowledgements

This study was supported in part by the Russian–German Laboratory at synchrotron BESSY II.

References

[1] S. Stankovich, D. A. Dikin *et al.*, *Carbon* **45**, 1558 (2007).
[2] Y. H. Wu *et al.*, *J. Appl. Phys.* **108**, 071 301 (2010).
[3] K. S. Novoselov, A. K. Geim *et al.*, *Science* **306**, 666 (2004).
[4] V.M. Mikoushkin *et al.*, *Tech. Phys. Lett.* **37**, 942 (2011).
[5] A. Dideykin *et al.*, *Diamond Relat. Mater.* **20**, 105 (2011).
[6] S. I. Fedoseenko, D. V. Vyalikh, I. E. Iossifov *et al.*, *Nucl. Instr. Meth. Phys. Res. A* **505**, 718 (2003).
[7] H.-K. Jeong *et al.*, *Chem. Phys. Lett.* **460**, 499 (2008).
[8] D. Yang, A. Velamakanni *et al.*, *Carbon* **47**, 145 (2009).
[9] D. W. Lee *et al.*, *J. Phys. Chem. B* **114**, 5723 (2010).
[10] S. Park, R. S. Ruoff, *Nature Nanotechnol.* **4**, 217 (2009).
[11] H.-K. Jeong *et al.*, *Europhys. Lett.* **92**, 37 005 (2010).

20th Int. Symp. "Nanostructures: Physics and Technology"
Nizhny Novgorod, Russia, June 24–30, 2012

Synchrotron radiation photoemission study of 2DEG creation at the n-GaN surfaces under Ba adsorption

S. N. Timoshnev[1], G. V. Benemanskaya[1], M. N. Lapushkin[1] and G. E. Frank-Kamenetskaya[2]

[1] Ioffe Physical-Technical Institute, St Petersburg, Russia
[2] St Petersburg State Institute of Technology, 190013 St Petersburg, Russia

Abstract. Electronic structure of the ultrathin Ba/*n*-GaN(0001) interfaces has been studied *in situ* in an ultrahigh vacuum using ultraviolet photoelectron spectroscopy. Photoemission spectra from valence band and Ga 3*d*, Ba 5*p*, Ba 4*d* core-level spectra were studied for the clean *n*-GaN surface and Ba/*n*-GaN interface in the Ba submonolayer coverage region. Cardinal change in the electronic band structure and in surface states was found. The formation of a 2D degenerate electron gas in accumulated layer was revealed on the *n*-GaN surfaces during adsorption of Ba atoms.

Introduction

Surface and interface properties of III-nitride semiconductors, their hetero- and nanostructures have been the subject of modern research. They are widely used in implementation of optoelectronic devices over a wide spectral range from the visible to the ultraviolet light and in development of new electronic devices, e.g. HFET and HEMT where accumulation layer plays a cardinal role. The accumulation layer is a new nanoobject, which can appear on the surface of a *n*-type semiconductor when the bands are considerably curved so that the conduction band edge is situated below the Fermi level E_F on the surface. In this case, a narrow nanopotential well is formed. Here, the electron motion in the accumulation layer potential along the normal z to the surface is restricted, and the size quantization effect is observed. The electron motion over the surface (xy) is free, and corresponding energy components are not quantized. These electron states constitute a 2D degenerate electron gas (2DEG). The studies of the accumulation layer and the size-quantization effects are important for fundamentally research and for their urgent applications in microelectronics. Accumulation layer is infrequently inherent for semiconductor surfaces. As regards III-nitrides, our studies using threshold photoemission spectroscopy were revealed formation of the accumulation layer at the *n*-GaN surfaces under Cs adsorption with the transition from depletion to electron accumulation [1–3]. Earlier, an AL was revealed for the clean surfaces of In-containing semiconductors InAs, InSb, and InN [4–6].

1. Experimental

Experiments were carried out at BESSY II, Helmholtz Zentrum, Berlin (Germany) with the use of synchrotron radiation with photon energies in the range of 60–400 eV. Photoemission studies were performed *in situ* in an ultrahigh vacuum of 5×10^{-10} Torr at room temperature. The spectra of normal photoemission from the valence band, spectra of surface states and Ga 3*d*, Ba 5*p*, Ba 4*d* core-level spectra were measured. The samples *n*-GaN(0001) were grown on a (0001) sapphire substrate by metal-organic chemical-vapor deposition (MOCVD) and doped with silicon (4×10^{17} cm^{-3}). The band-gap width corresponds to $E_g = 3.4$ eV. AFM probing has shown the atomically smooth surfaces [1]. The samples of *n*-GaN(0001) were annealed *in situ* directly in a vacuum at a temperature of about 900 K. Atomically pure barium was deposited on the sample surface from a standard calibrated source. Step-by-step submonolayer coverage from 0.1 monolayer (0.1 ML) to 1.5 ML of Ba were adsorbed on the clean GaN surface.

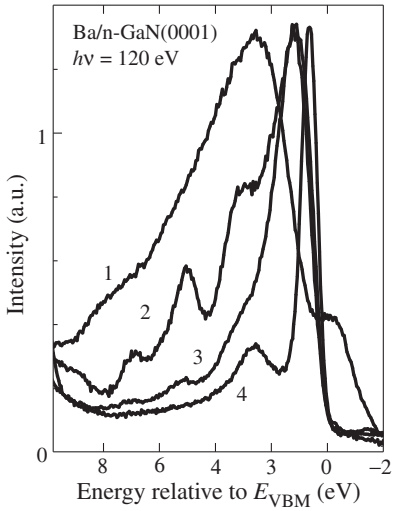

Fig. 1. Spectra of the normal photoemission from the valence band for three different Ba coverages on the *n*-GaN(0001) surface: 1 — clean surface, 2 — 0.25 ML, 3 — 0.5 ML, 4 — 1.5 ML. Excitation energy $h\nu = 120$ eV.

2. Results and discussion

In Fig. 1 drastic change in valence band spectra of the *n*-GaN(0001) sample under Ba adsorption is shown. Ba coverages were varied from 0.25 to 1.5 ML. The most substantial changes are observed in full valence band spectra up to 8 eV. The photoemission intensity in this range sharply decreases with an increase in the barium coverage. The shoulder near E_{VBM} immediately disappears during first deposition of small Ba coverage. Origin of this shoulder can be explained with Ga-dangling bond surface state. At the coverage of 0.25 ML Ba an appearance of three peaks at energy of 2.7, 5.0, and 6.6 eV are observed in the spectra below the valence band maximum E_{VBM}. These peaks could be also associated with the surface states of GaN. At the coverage of 1.5 ML Ba only one of them peaks at energy of 2.7 eV has remained.

It has been found that a decrease in the intensity in spectral region of the valence band can been attributed to the interaction between the surface states of GaN substrate and adsorbed Ba atoms. Energy width of valence band is found to drastic decrease from 10 eV for the clean GaN up to 1.5 eV under Ba

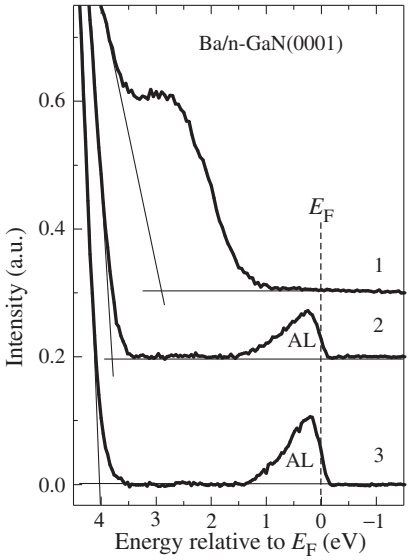

Fig. 2. Spectra of the normal photoemission from the accumulation layer for different Ba coverages on the n-GaN(0001) sample: 1 — clean surface, 2 — 0.9 ML, 3 — 1.5 ML. Excitation energy $h\nu$ = 120 eV.

monolayer adsorption. This value of width is a good agreement with theoretical consideration [7].

New photoemission peak with the quasi-metallic character is found to appearance at the Fermi level in the band gap of GaN under Ba adsorption. Fig. 2 shows this effect in photoemission spectra at Ba coverage of 0.9 ML (curve 2) and increasing peak intensity in the spectrum for Ba coverage of 1.5 ML (curve 3). The surface-Fermi level position is found to be changed from significantly below the conduction band minimum (CBM) at the clean n-GaN surface to high above the CBM by Ba adsorption, with the transition from depletion to electron accumulation occurring at low coverages. As can been seen in Fig. 2 the energy difference $E_{\mathrm{VBM}} - E_{\mathrm{F}}$ is increased from 2.8 eV for clean n-GaN surface up to 4.0 eV for Ba coverage of 1.5 ML on n-GaN surface. This effect is evidence that the depth of the potential well of the accumulation layer increases. It is established that the peak AL is due to formation of a two-dimensional electron gas 2DEG in the accumulation nanolayer in the close vicinity of the surface.

Acknowledgements

This work was supported by the grant # 11-02-00114-a of RFBR, by the grant of the program "Quantum mesoscopic and disordered systems" of Presidium of RAS and by young scientists support program of Presidium of RAS.

References

[1] G. V. Benemanskaya *et al*., *JETP* **103**, 441 (2006).
[2] G. V. Benemanskaya *et al*., *Surf. Sci.* **603**, 2474 (2009).
[3] G. V. Benemanskaya *et al*., *JETP Lett.* **91**, 971 (2010).
[4] V. Aristov *et al*., *Phys. Rev. B* **60**, 7752 (1999).
[5] M. G. Betti *et al*., *Phys. Rev. B* **63**, 155315 (2001).
[6] I. Mahboob *et al*., *Phys. Rev. B* **69**, 201307 (2004).
[7] T. Strasser *et al*., *Phys. Rev. B* **60**, 11577 (1999).

20th Int. Symp. "Nanostructures: Physics and Technology"
Nizhny Novgorod, Russia, June 24–30, 2012

Electron spin dynamics in quantum wells and quantum dots

M. M. Glazov
Ioffe Physical-Technical Institute, St Petersburg, Russia

Abstract. We report on theoretical and experimental progress in electron spin dynamics studies by means of the pump-probe technique. The mechanisms of the spin coherence generation by means of short optical pulses are discussed and the microscopic origin of the spin Faraday and Kerr rotation signals is analyzed. We consider particular examples of coherent spin dynamics phenomena, including resonant spin amplification, spin mode-locking, nuclei-induced electron spin precession frequency focusing, and cyclotron effect on spin beats.

Introduction

A lot of experimental and theoretical efforts are concentrated on spin dynamics studies in semiconductors and semiconductor nanostructures, see Refs. [1–4] for review. Among various methods, the pump-probe technique is the most versatile tool for non-destructive studies of electron spin coherence. This two-beam technique is based on the following: first, circularly polarized pump pulse excites electron spin polarization. Afterwards, a second linearly polarized probe pulse arrives at a sample and its polarization plane is rotated due to the spin Faraday effect (in the transmission geometry) or the spin Kerr effect (in the reflection geometry). The probe pulse may acquire some ellipticity. The Faraday or Kerr rotation angle as well as induced ellipticity are proportional to the magnetization of the sample, hence one can monitor electron spin dynamics by varying the delay between the pump and probe pulses. In some experiments additional linearly or circularly polarized control pulse is used in order to manipulate electron and hole spins, see Ref. [4] and references therein for details.

1. Resonant spin amplification and spin precession mode-locking

Systems with localized electrons, in particular, singly charged quantum dots and n-type quantum wells with the low-density electron gas where charge carriers are localized on potential fluctuations offer very long spin relaxation times and efficient coupling of electron and nuclear spins [1]. In these systems one usually deals with the ensembles of electrons having different localization energies, g-factors and experiencing different nuclear fields [1,4].

The interaction of a localized electron with the circularly or linearly polarized optical pulse whose carrier frequency is close to the singlet trion resonance frequency can be efficiently described in the framework of the two-level model where the ground state corresponds to an electron and excited one corresponds to the trion. For given circular polarization of the incident pulse, only those electrons whose spins are antiparallel to that of photocreated ones participate in the trion formation. For instance, under σ^+ pumping the trions are formed only in the dots where the electron spin z component equals to $+1/2$ due to optical selection rules. The long-living electron spin coherence is formed either as a result of the hole-in-trion spin relaxation or due to applied magnetic field in the Voigt geometry (i.e. perpendicular to the light propagation axis). In the former case, hole looses its spin orientation rapidly and electrons returning from trions after their recombination are depolarized, while those carriers which did not take part in the trion formation keep their spin orientation. In the latter case, the spins of the electrons which did not participated in tron formation precess around the external field, while electron spins in trions do not. It results in an imbalance of the resident electron spins and those returned after the trion recombination. Similarly, the efficiencies of interaction for the circular components of the linearly polarized probe pulse tuned in the vicinity of the trion resonance are different in magnetized systems, because only one circular component can cause the formation of trions for the resident electron with a given spin orientation [4]. Hence, the spin Faraday, Kerr and ellipticity signals can be observed after all recombination processes took place, as seen in Fig. 1. The detailed theory of the spin signals for singly charged quantum dot arrays and quantum wells with the low-density electron gas is presented in Refs. [4,5], here we briefly describe basic features of the spin signals.

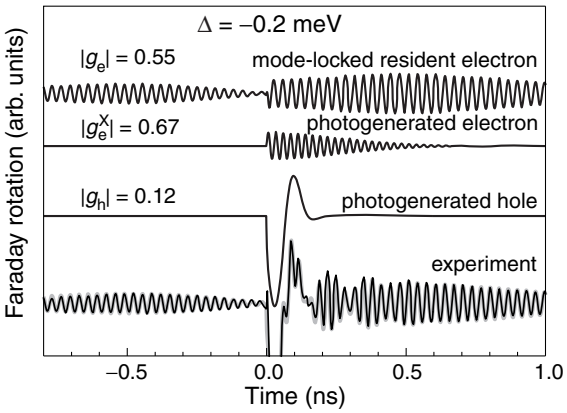

Fig. 1. Faraday rotation signal (bottom curve) at almost spectrally degenerate pump and probe pulses. The fitting is superimposed over the experimental curve. The curves presented above (from top to bottom): signal related with the long living spin polarization in charged quantum dots, signal related with electron-in-exciton spin precession in neutral quantum dots, and signal related with hole spin precession (both in neutral quantum dots and in trions). Measurements are carried out on the structure consisting of 20 layers of InGaAs/GaAs quantum dot layers with the dot density in each layer 10^{10} cm^{-2}, the structure is doped in such a way, that there is one electron per dot on average. Temperature $T = 6$ K, magnetic field $B = 4$ T. Data are reproduced from Ref. [4].

First, strong spin signals are observed at negative pump-probe delays, i.e. then the probe pulse arrives before the next pump pulse. In fact, spin coherence studies are carried out by the trains of pump and probe pulses and the signals at negative delays are due to the accumulation of spins from the previous

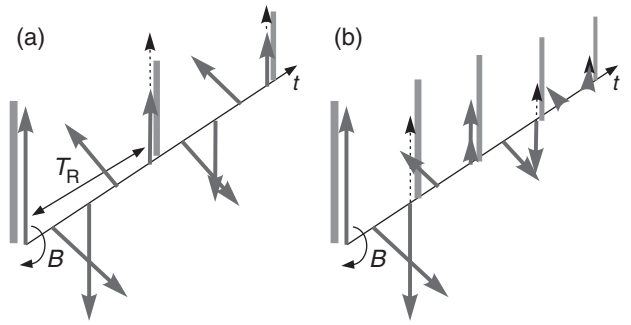

Fig. 2. Schematic illustration of the resonant spin amplification. Pump pulse arrival time moments are marked. Solid arrows show the electron spin orientation at different time moments. Dotted arrows shown the spin polarization generated by the pump pulses. Top panel shows the case of equal spin precession and repetition periods, $T_R = T_L$, in the bottom panel pulses arrive twice more often: $T_R = T_L/2$. Data are reproduced from Ref. [4].

pulses. For localized electrons, the spin relaxation time exceeds by far the pump pulse repetition period ($T_R \approx 13$ ns as a rule). The efficiency of spin accumulation depends dramatically on the relation between the spin precession period T_L and repetition period, as illustrated in Fig. 2. If $T_R = NT_L$, where N is an integer, the spins are added in phase and the spin polarization in enhanced, otherwise it is suppressed. This phenomenon is knows as *resonant spin amplification* (RSA).

In inhomogeneous arrays of quantum dots the spins are resonantly amplified only in those dots where $T_L = T_R/N$ leading to the *spin mode-locking*: the spin signal rapidly decays (on the time scale of several nanoseconds) and reappears again before the next pump pulse [6]. Additionally, hyperfine interaction of electron and nuclear spins can result in the spin precession frequency focusing and enhancement of signals at negative delays [7,8].

Another specific feature of inhomogeneous ensembles is the different temporal behavior of spin Faraday and ellipticity signals, e.g. amplitude of Faraday signal can be non-monotonic function of time delay, see Fig. 1. This is a result of different spectral sensitivity of spin Faraday and ellipticity effects which probe different subensembles of spins [4,5].

2. Cyclotron effect on coherent spin precession

Now we turn to the high-mobility two-dimensional electron systems with relatively high charge carrier density where excitons and trions are screened. The principles of electron spin coherence generation in this case are as follows [4]: the circularly polarized pump pulse generates spin polarized electrons and holes, holes loose their spin rapidly and recombine with unpolarized resident carriers. As a result, the spin polarization remains in the electron ensemble. The mechanisms of the spin coherence probing are related with the Pauli blocking of optical transitions for a given circular component of the linearly polarized probe and with the Hartree–Fock renormalizations of transition energies [4].

The spin dynamics in high-mobility quantum well systems is governed by the spin-orbit coupling. In non-centrosymmetric systems like most semiconductor quantum wells the electron spin degeneracy is lifted and the spin experiences an effective field $\mathbf{\Omega_k}$ which depends on the magnitude and direction of electron wave vector $\mathbf{k}$. If the temperature is low

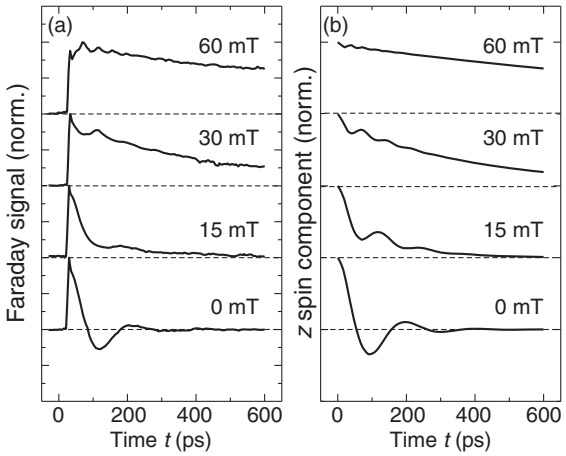

Fig. 3. (a) TRFR measurements in various small perpendicular magnetic fields measured on high-mobility GaAs (001) sample at 400 mK. (b) Calculated time evolution of the z component of the spin polarization for magnetic fields corresponding to measurements in (a). Data reproduced from Ref. [12].

enough and mobility of the carriers is high enough, the condition $\Omega_k \tau > 1$ holds, where τ is the single electron momentum scattering time. Hence, the electron spin precesses around $\mathbf{\Omega_k}$ [9–11]. In (001)-oriented quantum wells this field lies in the structure plane, hence optically excited z-spin component oscillates with time even in the absence of an external field, see bottom curve in Fig. 3a.

Unexpectedly, the application of external magnetic field along z axis strongly modifies electron spin dynamics, see Fig. 3a: the spin beats frequency increases, and the long-living spin polarization tail appears. The analysis shown that it is a combined effect of the cyclotron motion of electrons and spin-orbit interaction [12]: the magnetic field induces rotation of electron wave vector $\mathbf{k}$ with the cyclotron frequency ω_c, as a result the effective field $\mathbf{\Omega_k}$ rotates as well, and the electron spin experiences time-dependent field. Thus, cyclotron effect manifests itself in the spin beats: the spin precession frequency (provided that the spin splitting is isotropic in the structure plane) equals to $\sqrt{\Omega_k^2 + \omega_c^2}$. The spin relaxation is also slowed down due to "motional narrowing" effect caused by the rotation of $\mathbf{\Omega_k}$-field, it results in the long living tail formation [12]. This theoretical model quantitatively describes experiment, see Fig. 3b.

3. Resonant spin amplification and anisotropic spin relaxation

In symmetric semiconductor quantum wells grown along $z \parallel [110]$ axis the effective spin precession frequency is parallel to the growth axis, $\mathbf{\Omega_k} \parallel z$. In this case electron spin, initially aligned along z-axis, does not experience the effective field and its relaxation/decoherence can be very slow while relaxation of the in-plane spin components is relatively fast, see [13] for review.

This specific form of the spin-orbit coupling results in a very special magnetic field dependence of electron spin polarization accumulated as a result of resonant spin amplification. Figure 4 shows a typical RSA trace measured on the high mobility (110)-oriented GaAs quantum well sample. The signal contains a series of peaks corresponding to the commensura-

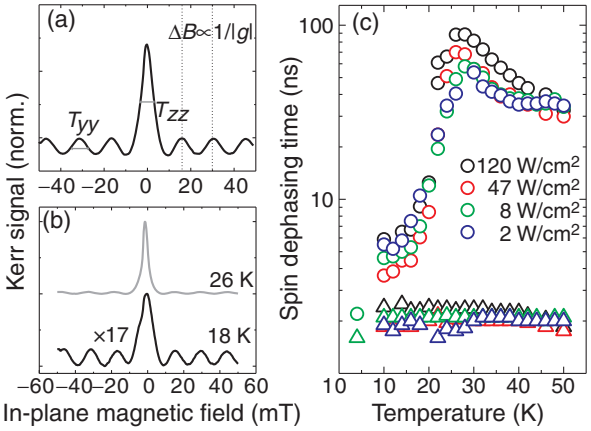

Fig. 4. (a) Typical RSA trace measured on a high-mobility 2DES grown in the [110] direction. The influence of the trace features on sample parameters is indicated. (b) RSA traces measured at 18 and 26 K. The data has been normalized and shifted. (c) Out-of plane (T_{zz}, open circles) and in-plane (T_{yy}, open triangles) spin dephasing times for different excitation densities as a function of temperature. Data reproduced from Ref. [14].

bility of the spin precession period in the external field and the pump pulse repetition period $T_R = 12$ ns. The peak width and height are related with the spin relaxation rates. We clearly see that the resonant spin amplification peak centered around zero magnetic field is more pronounced than the RSA peaks for finite fields, whose heights and widths are equal in the magnetic-field range investigated. This trace shape is a direct evidence of the specific spin-orbit field symmetry in almost symmetric (110)-oriented systems which is predominantly oriented along the sample growth axis $z \parallel [110]$. Indeed, for long spin relaxation time T_{zz} the z spin component is efficiently accumulated at zero magnetic field, resulting in constructive interference of spins created by the train of pump pulses and giving rise to a large Kerr signal at negative time delays. For applied in-plane magnetic fields, the optically oriented electron spins precess into the sample plane, and therefore, more rapid dephasing occurs. However, some spin polarization remains within the sample during the time between subsequent pump pulses, and if the Larmor precession frequency is commensurate with the repetition rate, constructive interference occurs, resulting in weaker and broader maxima.

The results of experimental data fitting by the model developed in Refs. [4, 14] are presented in Fig. 4c. One can see that while the in-plane spin relaxation time T_{yy} remains almost constant as a function of temperature, the z-component spin relaxation time T_{zz} dramatically increases and reaches about 100 ns at about 30 K. Such a high value of T_{zz} may be limited by random fluctuations of the Rashba field arising from the dopant ions [13]. At low temperatures, the system under study demonstrates some frozen asymmetry which manifests itself in short spin relaxation times T_{zz} related with regular Rashba field caused by this asymmetry. At high temperatures the asymmetry disappears and only fluctuations remain, resulting in ultra-long spin relaxation times for free electrons.

To conclude, the pump-probe technique can be used to identify the electron spin dynamics in semiconductor nanostructures.

Acknowledgements

I am grateful to M. Bayer, Al. L. Efros, E. L. Ivchenko, T. Korn, D. R. Yakovlev, and I. A. Yugova for fruitful discussions. This work was partially supported by RFBR, programs of RAS and RF President Grant NSh-5442.2012.2.

References

[1] M. I. Dyakonov, ed. *Spin Physics in Semiconductors*. Springer-Verlag: Berlin, Heidelberg (2008).
[2] T. Korn, *Phys. Reports* **494**, 415 (2010).
[3] M.W. Wu, J.H. Jiang, and M.Q. Weng, *Phys. Reports* **493**, 61 (2010).
[4] M.M. Glazov, *Physics of the Solid State* **54**, 1 (2012).
[5] I.A. Yugova, M.M. Glazov, E.L. Ivchenko and Al.L. Efros, *Phys. Rev. B* **80**, 104436 (2009).
[6] A. Greilich, D. R. Yakovlev, A. Shabaev, Al. L. Efros, I. A. Yugova, R. Oulton, V. Stavarache, D. Reuter, A. Wieck, and M. Bayer, *Science* **313**, 341 (2006).
[7] A. Greilich, A. Shabaev, D. R. Yakovlev, Al. L. Efros, I. A. Yugova, D. Reuter, A. D. Wieck, and M. Bayer, *Science* **317**, 1896 (2007).
[8] M. M. Glazov, I. A. Yugova, and Al. L. Efros, *Phys. Rev. B* **85**, 041303(R) (2012).
[9] V. N. Gridnev, *JETP Letters* **74**, 380 (2001).
[10] M.M. Glazov and E.L. Ivchenko, *JETP* **99**, 1279 (2004).
[11] M. A. Brand, A. Malinowski, O. Z. Karimov, P. A. Marsden, R. T. Harley, A. J. Shields, D. Sanvitto, D. A. Ritchie, and M. Y. Simmons, *Phys. Rev. Lett.* **89**, 236601 (2002).
[12] M. Griesbeck, M. M. Glazov, T. Korn, E. Ya. Sherman, D. Waller, C. Reichl, D. Schuh, W. Wegscheider, and C. Schueller, *Phys. Rev. B* **80**, 241314(R) (2009).
[13] M. M. Glazov, E. Ya. Sherman, V. K. Dugaev, *Physica E* **42**, 2157 (2010).
[14] M. Griesbeck, M. M. Glazov, E. Ya. Sherman, D. Schuh, W. Wegscheider, C. Schueller, T. Korn, *Anisotropic spin relaxation revealed by resonant spin amplification in (110) GaAs quantum wells*, arXiv:1111.5438 (2011); *Phys. Rev. B*, in press.

20th Int. Symp. "Nanostructures: Physics and Technology"
Nizhny Novgorod, Russia, June 24–30, 2012

Nuclear spin dynamics of InGaAs QDs ensemble in transverse magnetic field

S. Yu. Verbin[1,2], I. Ya. Gerlovin[1], I. V. Ignatiev[1,2], M. S. Kuznetsova[1,2], R. V. Cherbunin[1,2], K. Flisinski[2], D. Reuter[4], A. D. Wieck[4], D. R. Yakovlev[2,3] and M. Bayer[2]

[1] Spin Optics Laboratory, St Petersburg State University, 198504 Petrodvorets, St Petersburg, Russia
[2] Experimentelle Physik 2, Technische Universität Dortmund, 44221 Dortmund, Germany
[3] Ioffe Physical-Technical Institute, St Petersburg, Russia
[4] Angewandte Festkörperphysik, Ruhr-Universität Bochum, Bochum, D-44780 Germany

Abstract. Time-resolved Hanle effect for the negatively charged InGaAs/GaAs quantum dots has been studied using various protocols of the excitation intensity modulation. The data obtained have been analyzed in the frame of original model of different behavior of longitudinal and transverse components of nuclear spin polarization. Such analysis of experimental results has allowed to determine the times of rise and decay of these components. Their dependences on magnetic field strength have been found quite different. The observed behavior of nuclear polarization could not be explained in the frame of existing phenomenological models.

Introduction

The polarization and relaxation of electron and nuclear spins in semiconductor quantum dots (QDs) is highly influenced by the hyperfine interaction [1,2]. Dynamical nuclear polarization (DNP) can be efficiently generated by optical orientation of electron spins. On the other hand, the electron spin dynamics sensitively depends on the state of the nuclear spin system. Most experimental data about the DNP in QDs have been obtained in magnetic fields applied along the axis of optical excitation and signal detection (Faraday geometry), see e.g., Ref. [2] and references therein.

In magnetic fields applied perpendicular to the optical axis (Voigt geometry), the polarization of the electron spin is measured *via* the photoluminescence (PL) polarization dependence on the magnetic field (Hanle curve). The optically created nuclear spin is directed along the total field acting on the nuclei, which is the sum of external field and effective electron field (Knight field). Under strong enough optical pumping, the nuclear spin polarization is efficiently developed and its effective magnetic field affecting the electron (Overhauser field) may be considerably larger than the external magnetic field. The Overhauser field becomes tilted with the total field when the external magnetic field increases, which gives rise to depolarization of electron spin and causes the dips in Hanle curve near the central peak. Further increase of the external field gives rise to decrease of the nuclear field followed by partial recovery of electron spin polarization. This simplified picture of physical processes qualitatively explains the appearance of W-shaped Hanle contour [1,3].

The time evolution of the Hanle contour has been used for the analysis of the DNP dynamics in this paper.

1. Experimental

The sample with 20 layers of self-assembled InGaAs/GaAs QDs annealed at temperature 980 °C was studied. Each QD contained one resident electron on average, which is supplied by the delta-doped barrier layers. All the experiments were done at a temperature of 2 K. A split-coil superconducting magnet was used for applying the magnetic fields up to 1.5 T perpendicular to the direction of the sample optical pumping.

The PL of the sample was excited by a circularly polarized light of continuous waves (cw) Ti-Sapphire laser, whose wavelength was tuned to the wetting layer optical transition at energy of 1.465 eV. The intensity of exciting light was modulated by acousto-optical modulator forming square-wave light pulses separated by dark time intervals with necessary durations, t_{exc} and t_d, correspondingly. The electron spin polarization was determined *via* measuring the negative circular polarization (NCP) degree of PL [4].

The relaxation of DNP was studied by the measurement of NCP degree of PL during the short time interval, $t_{det} = 1$ ms, at the beginning of light pulse after dark time intervals with various t_d. It was supposed that during short t_{det} the excitation does not almost change the nuclear polarization. The whole Hanle curves and its central parts measured after various t_d are shown in Figs. 1a and b, correspondingly. The Hanle curve after small t_d (<20 μs) has nearly the same shape as at cw excitation. The increasing of t_d results in smoothing of W-shape and in narrowing of the Hanle curve.

The opposite behaviour of Hanle contour has been observed when the DNP rise dynamics has been studied. It has been done *via* the dependence of NCP on the time delay after switching on of the exciting light. At the first moment the Hanle curve has smooth shape and the minimal width. Then the curve width increases and the dips appear around the central peak forming the W-shape of the Hanle contour. The maximal curve width and dip depth analogous to observed ones at cw excitation are reached after the excitation during tens of ms.

2. Calculation and discussion

It may be concluded from the experimental data that the developing of DNP leads to the decrease of electron spin orientation at the small values of transverse magnetic field (near the dips of W-contour) and to the degree increase at larger field values (at the Hanle curve wings). We propose that large width of Hanle curve at cw excitation is a result of appearing of $B_{DNP\perp}$ stabilized by quadropole splitting of nuclear spin states along the optical axis [5,6]. From other hand, $B_{DNP\parallel}$ almost should not play the role at high magnetic fields [1,2].

As it follows from the above explanation of W-shaped Hanle

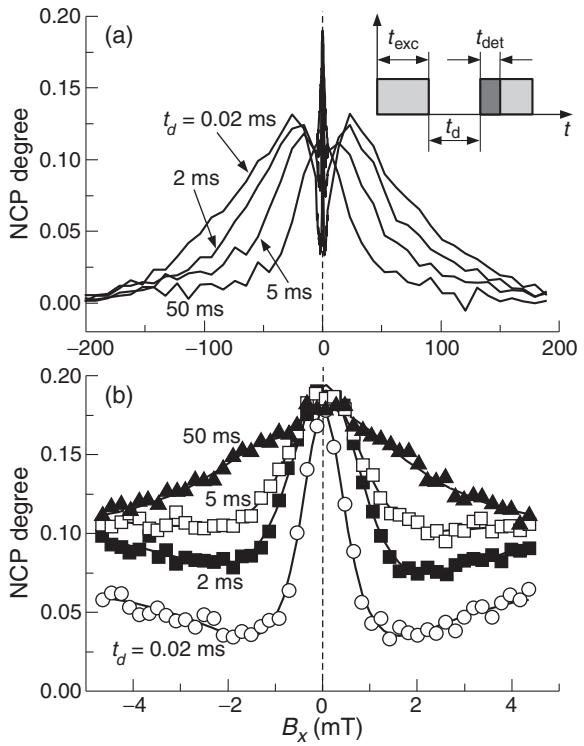

Fig. 1. Dependence of Hahle contour on t_d at fixed $t_{exc} = 100$ ms and at excitation density $I_{exc} = 40$ W/cm^2. (a) — the whole curves; (b) — central part of curves at various t_d shown near every curve, solid lines are for the glide of eye.

contour, the dynamics of DNP components $B_{DNP\|}$ and $B_{DNP\perp}$, which are parallel and perpendicular to external magnetic field, may be estimated from the temporal behaviour of the contour dips around its central peak and of Hanle curve width, correspondingly. Such analysis has been done in [7] in the model firstly concerning the role of nuclear spin fluctuations [8] for Hanle contours. The dependences of observed electron spin polarization on $B_{DNP\|}$ and $B_{DNP\perp}$ have been deduced in the frame of this model.

It has been found that $B_{DNP\|}$ is present only at relatively small fields up to 10 mT. $B_{DNP\|}$ increases up to the maximal value $B^0_{DNP\|} \approx 40$ mT after switching on of the excitation. The rise and decay times for $B_{DNP\|}$ have nearly equal values of about 5 ms. The effective field of nuclear spin fluctuations component parallel to external magnetic field has been determined too. It has been found to be ≈ 25 mT. Both the time and effective field values mentioned above are independent of the external field strength.

On the contrary, $B_{DNP\perp}$ arises only when the field strength exceeds 10 mT. The rise and decay times for this component are found to be remarkably different and to have an opposite dependence in the magnetic field range 0.02–0.1 T (see Fig. 2). The maximal value $B^0_{DNP\perp}$ increases up to $\approx$60 mT with the field rise.

We believe that the presence of this component of nuclear polarization is due to large quadrupole splitting of nuclear spin states in the quantum dots under study. The external field dependence of $B_{DNP\perp}$ is proposed as a result of nuclear spin relaxation at photogenerated carriers.

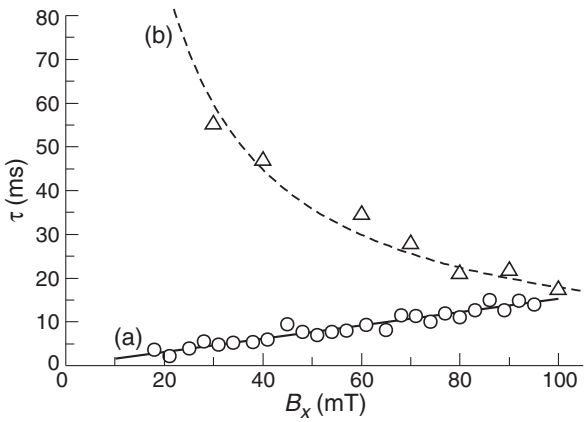

Fig. 2. Field dependence of $B_{DNP\perp}$ characterictic times. (a) — the rise time, (b) — the decay time. Lines are for the glide of eye.

3. Conclusion

The obtained experimental data on time-resolved Hanle effect have been firstly analyzed in the model concerning the role of nuclear spin fluctuations. The times of rise and decay of longitudinal and transverse components of nuclear spin polarization have been detrmined. Their dependences on magnetic field strength have been found quite different. The observed behavior of nuclear polarization could not be explained in the frame of existing phenomenological models and for its explanation it is need to develop adequate theory of nuclear spin system dynamics in QD at high quadropole splitting.

Acknowledgements

This work has been supported in part by the grants of the Russian Federation Government (# 11.G34.31.0067) and the Ministry of Education and Science (# 02.740.11.0214) and of Deutsche Forschungsgemeinschaft.

References

[1] *Optical Orientation*, ed. F. Meier and B. P. Zakharchenya (North Holland, Amsterdam) (1984).
[2] V. K. Kalevich *et al.*, in *Spin Physics in Semiconductors*, ed. M. I. Dyakonov (Berlin: Springer) ch. 11, p. 309 (2008).
[3] D. Paget *et al.*, *Phys. Rev. B* **15**, 5780 (1977).
[4] I. V. Ignatiev *et al.*, *Optics and Spectroscopy* **106**, 375 (2009).
[5] R. I. Dzhioev *et al.*, *Phys. Rev. Lett.* **99**, 037401 (2007).
[6] R. V. Cherbunin *et al.*, *J. Phys.: Conf. Ser.* **245**, 012055 (2010).
[7] S. Yu. Verbin *et al.*, *JETP* **114**, 778 (2012).
[8] I. A. Merkulov *et al.*, *Phys. Rev. B* **65**, 205309 (2002).

20th Int. Symp. "Nanostructures: Physics and Technology"
Nizhny Novgorod, Russia, June 24–30, 2012

Suppression of electron spin relaxation in a wide GaAs/AlGaAs quantum well with a lateral confining potential

A. V. Larionov[1], A. V. Sekretenko[1] and A. I. Il'in[2]

[1] Institute of Solid State Physics, RAS, 142432 Chernogolovka, Russia
[2] Institute of Microelectronic Technology and Ultra-High-Purity Materials, RAS, 142432 Chernogolovka, Russia

Abstract. The coherent spin dynamics of electrons laterally confined in a wide GaAs quantum well with the use of a special mosaic electrode deposited onto the sample plane has been investigated. Electron spin lifetime measurements have been carried out in structures with a different size of orifices in the mosaic electrode by means of the time-resolved Kerr rotation technique. The electron spin lifetime in the lateral traps has been found to increase strongly with the decreasing of orifices in the mosaic electrode. The observed electron spin lifetime dependence can be interpret in terms of D'yakonov–Perel' spin relaxation mechanism.

Introduction

Semiconductor spintronics has a particular interest to manipulate and to control carrier spin dynamics in non-magnetic materials by utilizing the spin-orbit interaction (see, e.g., [1–3]). In three- and two-dimensional carrier systems, spin-orbit coupling creates a randomizing momentum-dependent effective magnetic field; the corresponding relaxation process is known as the D'yakonov–Perel' (DP) mechanism [4]. In an ideal 1D system, a complete suppression of the DP spin relaxation has been predicted, if the lateral width of a 2D channel is reduced to be on the order of the electron mean free path (see, e.g., [5]). We believe that an artificial 3D-confinement in plane of 2D-system may suppress of the electron spin relaxation, as it was predicted in [6].

This work continues our previous studies ([7, 8]) of the spin dynamics of electrons placed in a regular array of specific potential wells in the plane of a GaAs quantum well. The ensemble of such potentials, in limit — quantum-sized, can be a new class of induced quantum dots. Perfection of the manufacturing technology will provide a minimum scatter in the parameters of the induced quantum dots, i.e., in their lateral size and, consequently, in the value of the confining potential. Along with the use of high-quality GaAs quantum wells, this provides good prospects for the use of an induced quantum dot as a basic element for making spin memory units.

1. Sample and experimental setup

Experiments were carried out on a GaAs/AlGaAs heterostructure with a single 25 nm GaAs quantum well. The structure is a Schottky photodiode, in which a silicon-doped 30 nm GaAs quantum well serves as an internal electrode, whereas a special electrode with a regular ensemble of micron-sized orifices (mosaic electrode) serves as an external Schottky gate. The electric bias was applied between the internal electrode and the external Schottky gate. The structure was fabricated by electron lithography with the use of the lift-off technology and a SEM EVO-50 electron microscope equipped with a Nanomaker hardware/software complex. The diameter of the orifices in the mosaic electrode was approximately 1.7, 1.2 and 0.8 μm, and center-to-center and edge-to-edge distance between the orifices were 2.1−2.2 and 0.35−0.45 μm, respectively (see Fig. 1).

The sample was placed in the magnetic field in the Voigt geometry at 2 K in an optical cryostat with a solenoid up to 6 T. Electron spin dynamics in the heterostructure with the mosaic electrode was studied by means of the time-resolved Kerr rotation technique (TRKR). A pulsed-shaped 100-femtosecond Ti:sapphire laser with a repeating frequency of 80 MHz was used. The circularly polarized pump pulse produced spin orientation of electrons in the sample, which was detected via the polarization rotation angle of the linearly polarized probe beam reflected from the sample. The measurements were carried out in the spectrally degenerate regime, in which the wavelengths of the pump and probe laser beams coincide. The signal was measured with the use of double lock-in detection, which effectively suppressed an unwanted signal produced by the pump light scattered by the mosaic electrode. A mechanical delay line allowed us to perform measurements with a time interval between the pump and probe pulses of up to 6 ns with a step of 10 ps.

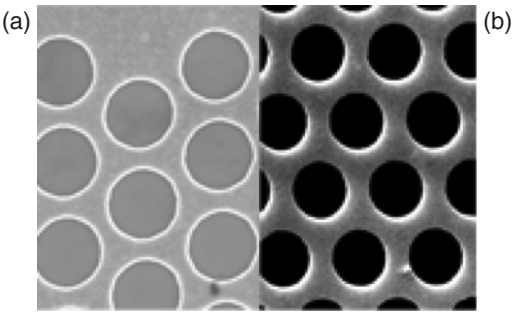

Fig. 1. Scanning electron microscopy images of the mosaic electrode with two diameters of the orifices — 1.7 (a) and 1.2 μm (b), respectively.

2. Experimental results and discussions

An external magnetic field in Voigt geometry allows one to observe spin quantum beats in TRKR signal due to Larmor precession of coherently excited electron spins in CQWs around the field direction. Experimental data can be fitted by exponentially damped oscillations containing the beating frequency Ω and a single decay time: $I = I_0 \exp(-t/T) \cos \Omega t$, where $\Omega = \mu_B g_e B/\hbar$, g_e is the in-plane electron g-factor. The measurements with the mosaic electrode were performed at a fixed laser excitation energy spectrally coinciding with the position of a 1sHH exciton (E $\simeq 1520 \pm 0.1$ meV).

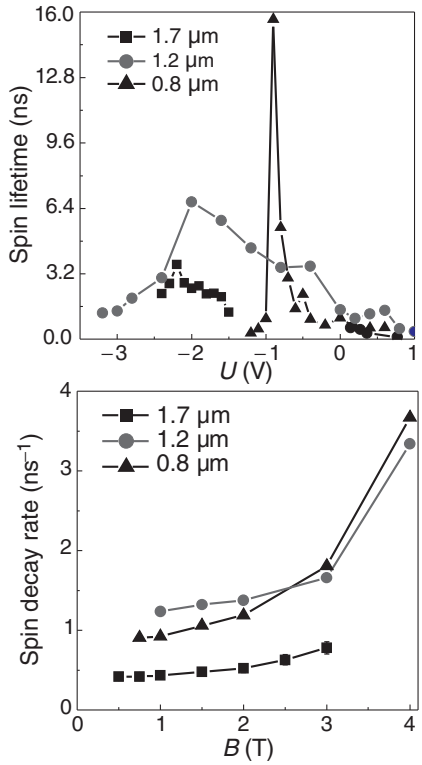

Fig. 2. (a) The electron spin lifetime as a function of applied bias for three sizes of orifices: 1.7 (quadratic symbols), 1.2 (circular symbols) and 0.8 μm (triangular symbols). (b) The electron spin decay rate as a function of external magnetic fields for three sizes of orifices: 1.7 (quadratic symbols), 1.2 (circular symbols) and 0.8 μm (triangular symbols).

Figure 2a shows the fitting results of the electron spin lifetime for the for three sizes of orifices: 1.7 (quadratic symbols), 1.2 (circular symbols) and 0.8 μm (triangular symbols) as a function of applied bias. The spin dynamics of electrons confined inside the orifices of three different sizes is qualitatively similar. One can see that 30% decreasing of electron confinement yields more than 2 times increasing of the electron spin lifetime. It can indicate to an attenuation of the electron spin relaxation that is caused by the D'yakonov–Perel' mechanism in structures under investigations. The Kerr signal emerges at a larger ($>$2.5 V) negative bias corresponding to strong band bending. As was indicated in [7], a possible reason could be a strong increase in the radiative recombination time of an indirect exciton due to the quenching of the electron-hole exchange interaction. Thus, the lifetime of the electron spin at a small negative bias ($U<$0.5 V) is determined by the electron-hole exchange interaction; the interaction weakens and the spin relaxation time becomes shorter with an increase in the bias. The disappearance of the Kerr signal at large negative biases ($U > -2.5$ V) is seemingly due to electrons going beneath the electrode or(and) appearance of a dense 2D-electron gas.

An indication of strong three-dimensional confinement of electrons in the orifice of the mosaic electrode is the magnetic-field dependence of the electron spin lifetime presented in Fig. 2b. Figure 2b shows the electron spin decay rate as a function of external magnetic fields for three sizes of orifices: 1.7 (quadratic symbols), 1.2 (circular symbols) and 0.8 μm (triangular symbols). This behavior of the inverse lifetime of the electron spin is quite typical for self-organized quantum

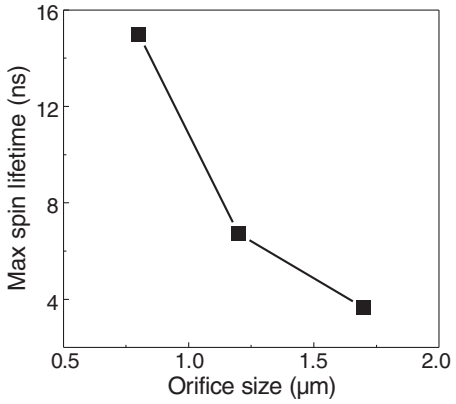

Fig. 3. (The maximum value of electron spin lifetime as a function of orifices sizes.

dots and can be qualitatively described by an electron g-factor spreading that is appeared due to electron localisation.

Finally, we have plotted the maximum spin lifetime as a function of orifices sizes (see Fig. 3). One can see strong non-linearity of the electron spin lifetime vs the orifices size. We believe that further increasing of electron spin lifetime can be achieved by decreasing of orifices size. The optical measurements can be limited by diffraction limit (fundamental problem) and radiative electron lifetime (maximum 40 nsec for 25 nm GaAs quantum well). Last problem can be solved by using of more wide quantum wells (40 nm, for example), or structures of II types.

To summarize, electron spin dynamics in a wide GaAs/AlGaAs quantum well with a special mosaic electrode fabricated on the surface has been investigated for three sizes of orifices. The lifetime of the electron spin in the structure with the mosaic electrode has been found to increase more than twice at 30% decreasing of electron confinement. It can indicate to an attenuation of the electron spin relaxation that is caused by the D'yakonov–Perel' mechanism.

References

[1] Lommer G., Malcher F. and Roessler U., *Phys. Rev. Lett.* **60**, 728 (1988).
[2] Datta S. and Das B., *Appl. Phys. Lett.* **56**, 665 (1990).
[3] Kato Y., Myers R.C., Gossard A.C. and Awschalom D.D., *Nature* **427**, 50 (2004).
[4] D'yakonov M.I. and Perel' V.I., *Zh. Eksp. Teor Fiz.* **60**, 1954 (1971).
[5] Kiselev A. and Kim K.W., *Phys. Rev. B* **61**, 13115 (2000).
[6] I.S. Lyublinskii, *Pis'ma Zh. Eksp. Teor Fiz.* **83**, 395 (2006).
[7] R. V. Cherbunin, M. S. Kuznetsova, I. Ya. Gerlovin *et al.*, *Fiz. Tverd. Tela* **51**, 791 (2009).
[8] A. V. Larionov, A. V. Sekretenko, and A. I. Il'in, *JETP Letters* **93**, 269 (2011).

20th Int. Symp. "Nanostructures: Physics and Technology"
Nizhny Novgorod, Russia, June 24–30, 2012

Pseudospin polarization phenomena and quantum hall ferromagnetism in the HgTe quantum well

M. V. Yakunin[1], A. V. Suslov[2], S. M. Podgornykh[1], A. P. Savelyev[1], S. A. Dvoretsky[3] and N. N. Mikhailov[3]

[1] Institute of Metal Physics, Ural Branch of RAS, 620990 Ekaterinburg, Russia
[2] National High Magnetic Field Laboratory, Tallahassee, Florida 32310, USA
[3] Institute of Semiconductor Physics, 630090 Novosibirsk, Russia

Abstract. Magnetoresistivity features connected with the pseudospin level coincidences under tilted fields in a Γ_8 conduction band of the HgTe quantum well were found to align along two sets of trajectories in a $(B_\perp, B_\parallel)$ plane between the perpendicular and parallel field components: a traditional one ascending from zero and a new series descending from a single point $B_\parallel^0$ on the $B_\parallel$ axis. Shown is that the $B_\parallel^0$ point yields a field of the full pseudospin polarization of the electronic system, which agrees with the data on the electron redistribution between two subbands obtained from FFT of oscillations along circle trajectories in the $(B_\perp, B_\parallel)$ plane and with the point on the magnetoresistivity under pure $B_\parallel$ separating a complicated weak field dependence from the monotonous one. Trajectories in both series are almost straight meaning a linear pseudospin polarization dependence on magnetic field. In the quantum Hall range of $B_\perp$ the pseudospin polarization manifests in anticrossings of magnetic levels, which were found to strongly nonmonotonously depend on $B_\perp$.

Introduction

Spin polarization underlies the basic principles of spintronics devices. On the other hand, in the samples of quantum Hall quality, it opens up a rich and varied phenomenology, giving opportunity to investigate the role of inter-particle interactions, and can lead to formation of ordered many-particle ground states, including ferromagnetic ones [1]. The conduction band in the inverted band structure of the HgTe quantum well (QW) wider than 6.3 nm [2] is characterized by a rather large value of g^*m^*/m_0, the effective Lande g-factor multiplied by the effective to free mass ratio, that suggests easy conditions for spin polarization when applied to a traditional Γ_6 band. It is not quite correct to characterize the states of a Γ_8 band by spin due to a complicated nature of this band thus it is better to change it for pseudospin. One of goals in our investigation is to show the degree of analogy between behavior of the Γ_8 conduction band states under tilted and parallel magnetic fields and the spin states of a traditional Γ_6 band (the term 'spin' is conditionally used for Γ_8 states in the further text).

We present a study of quantum magnetotransport in a 20.3 nm wide HgTe symmetric QW with the electron gas density $n_S = 1.5 \times 10^{15}$ m^{-2} and mobility of 22 m^2/Vs. The structure reacts to the IR illumination with some persistent increase in n_S but mainly in an improvement of its quality.

1. Coincidences

Rich patterns of the spin level coincidences were observed in HgTe QW under tilted magnetic fields that extend into the range of high field component $B_\perp$ perpendicular to the layer where the quantum Hall effect (QHE) is well realized [3]. The coincidences manifest as sharp transformations of $\rho_{xx}(B_\perp, B_\parallel)$ minima into local peaks and concomitant local smoothings of the QH plateaux at the integer filling factors ν. They were found to reside on trajectories of different kinds in the $(B_\perp, B_\parallel)$-plane [3]. First, they align on a set of straight beams going up from zero with tilt angles θ_r satisfying a traditional relation for the coincidences:

$$g^*m^*/m_0 = 2r\cos\theta_r \qquad (1)$$

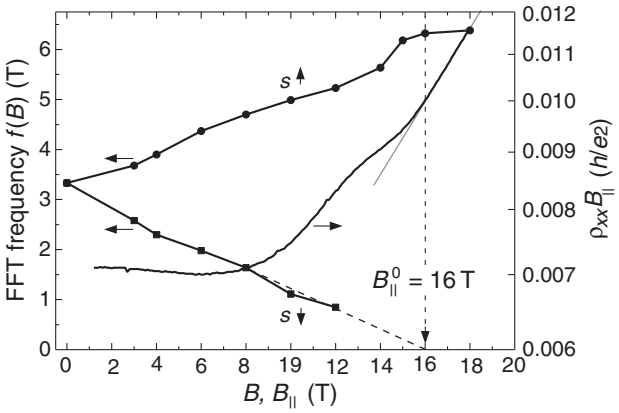

Fig. 1. FFT frequencies along circle trajectories as compared to the convergence point $B_\parallel^0$ position (dashed vertical) and to MR under pure parallel field.

with $r = 1, 2, 3\ldots$ being the ratios of the spin to cyclotron gaps [4]. This fact indicates a good analogy with a Γ_6 band. Observed linear trajectories in the HgTe QW mean an almost field independent g^*m^*/m_0 and a linear field dependence of the spin polarization [5,6].

Second, another system of traces along the coincidences, descending from a single point $B_\parallel^0$ on the $B_\parallel$ axis, is well seen in the experimental pictures as a set of ridges going through the MR peaks [3]. This trajectories are formed by the sets of coincidences along any of the fixed upper spin sublevel. Each group of such coincidences on the second-type trajectory is characterized by a fixed value of $M \equiv \nu - r = 1, 3, 5\ldots$, and a corresponding trajectory on the $(B_\perp, B_\parallel)$-plane is described in terms of the Γ_6-like band as:

$$B_\parallel = \frac{2\sin\theta_r}{g^*(m^*/m_0)}(B_1 - MB_\perp), \qquad M = 1, 3, 5\ldots, \quad (2)$$

which yields straight lines for high enough tilts. Here $B_1 = hn_S/e$ is the $\rho_{xx}(B_\perp)$ minimum position for $\nu = 1$.

The expression for the convergence point $B_\parallel^0$ may be read from Eq. (2) as: $g^*\mu_B B_\parallel^0 = 2E_F$ (E_F — the Fermi level for a spin unresolved case, μ_B — the Bohr magneton), thus yielding

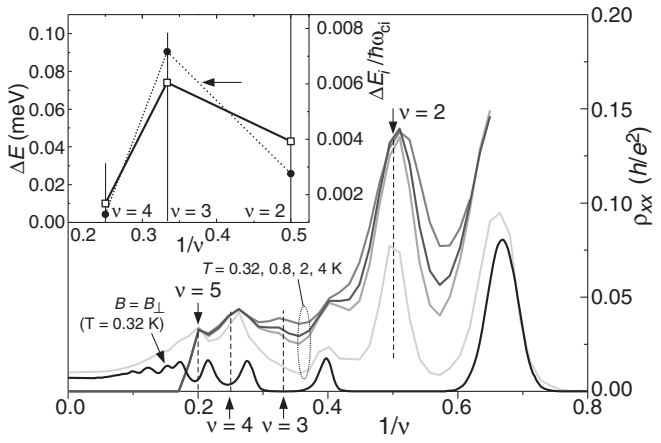

Fig. 2. Cross-sections of $\rho_{xx}(B_\perp, B_\parallel)$ along the $M = 1$ trajectory at $T = 0.32, 0.8, 2, 4$ K as compared to oscillations under pure perpendicular fields. Inset: The deduced activation energies at $\nu = 2, 3, 4$ and their ratios to corresponding cyclotron energies.

the sense of this point — it is the field of a full spin polarization of the electronic system.

Another way to estimate the redistribution of electrons between two spin subbands is to perform a Fourier analysis of oscillations in $\rho_{xx}(1/B_\perp)$ taken along the circle trajectories in the $(B_\perp, B_\parallel)$-plane for fixed values of the total field B [7,8]. In this case, only $B_\perp$ is a variable in the description of magnetic levels $E_{\mathrm{N},s} = (N + 1/2)\hbar eB_\perp/m^* \pm g^*\mu_\mathrm{B}B/2$ while B is constant. This yields two spin series periodic in $1/B_\perp$ for $E_{\mathrm{N},s} = 2E_\mathrm{F} > g^*\mu_\mathrm{B}B$ resulting in two lines of FFT frequencies f *vs.* B (Fig. 1), which describe electron densities in the subbands: $n_{\mathrm{S}i} = f_i e/h$. The lines diverge from a single point with the lower line going to zero (exhausting of the upper subband) and the upper line simultaneously saturating for $n_{s\uparrow} = n_\mathrm{S}$ thus indicating the moment of the full spin polarization.

The above results are compared in Fig. 1 with MR in a pure $B_\parallel$ and seen is that just the field of full spin polarization separates two kinds of dependences in $\rho_{xx}(B = B_\parallel)$: a somewhat complicated function at lower fields from a monotonously increasing one at higher fields as has been observed in a number of studies [5,6,9,10].

2. Anticrossings

At higher $B_\perp$, where the QHE is well developed, the MR features for coincidences acquire a complicated structure with local ρ_{xx} peaks splitted in couples of peaks [3]. This indicates the formation of anticrossings at the points of expected level coincidences. The anticrossings depend nonmonotonously on $B_\perp$: it manifests pronouncedly stronger at $\nu = 3$ than the neighboring ones at $\nu = 2$ and 4, positioned along the same descending trajectory for $M = 1$ (Figure 2). The $\nu = 3$ anticrossing is dramatically enhanced after illumination that indicates a high sensitivity of the anticrossings to the changes in the sample quality, which is typical for electronic phase transitions [1,11]. The activation gaps deduced from the temperature dependences of MR at anticrossings (Fig. 2) confirm the nonmonotonicity with the $\nu = 3$ gap being more than half an order larger than those for its neighbors. This result looks counterintuitive since the overlapping of magnetic levels with decreased $B_\perp$ seems to monotonously destroy the causes for appearing of anticrossings as it has been observed so far on other materials [11,12].

A conventional explanation of anticrossings is in terms of the magnetic anisotropy in the electronic system [1,12]: as the approaching spin levels swop their order in energy relatively the Fermi level, the Hartree–Fock energy of the system may decrease due to changes in the many-body interaction concomitant to changes in the spin polarization. The decrease starts before the level crossing, due to a hybridization of the levels, and the crossing in fact does not occur, the stronger is the energy gain the larger is the anticrossing gap. The systems reacting to transitions into spin ordered states under QHE conditions are the QH Ferromagnets (QHF). Estimations for an easy-axis QHF in a 2D layer [1] does not yield a sensible difference for anticrossings at $\nu = 2$, 3 and 4. That's why we tentatively attribute the observed difference to the coupling of $B_\parallel$ with the orbital degree of freedom in a QW of a finite width resulted in a different charge density profiles across the QW for the two spin levels [12]. This coupling enhances a magnetic anisotropy energy for the $\nu = 3$ coincidence as compared to that for $\nu = 2$ since its $B_\parallel$ is about a factor of 1.5 higher resulting in a shrinkage of the wave functions and thus the increased difference between them. On the other hand, the coincidences at $\nu \geq 4$ are restored because they go outside of the QH range of $B_\perp$ [11,12].

Acknowledgements

Supported by RFBR, project 11-02-00427. A portion of this work was performed at the National High Magnetic Field Laboratory, which is supported by National Science Foundation Cooperative Agreement No. DMR-0654118, the State of Florida, and the U.S. Department of Energy. Authors are grateful to E. Palm, T. Murphy, J. H. Park, and G. Jones for help with the experiment.

References

[1] T. Jungwirth and A. H. MacDonald, *Phys. Rev. B* **63**, 035305 (2000).
[2] M. König *et al.*, *J. Phys. Soc. Jpn.* **77**, 031007 (2008).
[3] M. V. Yakunin *et al.*, *Physica E* **42**, 948 (2010); *J. Phys.: Conf. Ser.* **334**, 012030 (2011); *AIP Conf. Proc.* **1399**, 599 (2011); *ibid.* **1416**, 19 (2011); *Proc. 19h Int. Symp. "Nanostructures: Physics and Technology"*, 42 (2011).
[4] R. J. Nicholas *et al.*, *Solid State Comm.* **45**, 911 (1983); *Phys. Rev. B* **37**, 1294 (1988).
[5] B. Nedniyom *et al.*, *Phys. Rev. B* **80**, 125328 (2009).
[6] K. F. Yang *et al.*, *New Journal of Physics* **13**, 083010 (2011).
[7] F. F. Fang, P. J. Stiles, *Phys. Rev.* **174**, 823 (1968).
[8] E. Tutuc *et al.*, *Phys. Rev. Lett.* **88**, 036805 (2002).
[9] J. Yoon *et al.*, *Phys. Rev. Lett.* **84**, 4421 (2000).
[10] I. L. Drichko *et al.*, *Phys. Rev. B* **79**, 205310 (2009).
[11] S. Koch *et al.*, *Phys. Rev. B* **47**, 4048 (1993); W. Desrat *et al.*, *Phys. Rev. B* **71**, 153314 (2005).
[12] T. Jungwirth *et al.*, *Phys. Rev. Lett.* **81**, 2328 (1998).

20th Int. Symp. "Nanostructures: Physics and Technology"
Nizhny Novgorod, Russia, June 24–30, 2012

Graphene nanoring as a tunable source of polarized electrons

J. Munárriz[1], F. Domínguez-Adame[1] and *A. V. Malyshev*[1,2]

[1] GISC, Departamento de Física de Materiales, Universidad Complutense, E-28040 Madrid, Spain
[2] Ioffe Physical-Technical Institute, St Petersburg, Russia

Abstract. We propose a novel spin filter based on a graphene nanoring fabricated above a ferromagnetic strip. The exchange interaction between the magnetic moments of the ions in the ferromagnet and the electron spin splits the electronic states, and gives rise to spin polarization of the conductance and the total electric current. We demonstrate that both the current and its polarization can be controlled by a side-gate voltage. This opens the possibility to use the proposed device as a tunable source of polarized electrons.

Introduction

Graphene is a material with a combination of many remarkable properties, such as, large electron mobility and spin-coherence lengths up to several microns [1–3]. These features have spurred the interest in graphene as a material of choice for spintronic devices which exploit both the charge and the spin degrees of freedom of the electron as the basis of their operation. Already in 2006, Geim and coworkers used soft magnetic NiFe electrodes to inject polarized electrons into graphene and found spin valve effects [4]. Since then, various spin-related effects in different nanostructures based on graphene have been investigated [5–8], which suggested the possibility of designing spintronic devices based on graphene nanostructures for memory storage, spin diodes, etc.

1. Results and discussion

Recently we have proposed a novel design of quantum interference device based on a graphene nanoring, in which all edges are of the same type to reduce scattering at the bends [9]. Electron transport in the device can be controlled by a gate voltage applied across the nanoring between two side electrodes. The relative phase of the electron wave function in the two arms of the ring can be varied by the side-gate voltage, leading to constructive or destructive interference at the drain, which results in conductance oscillations and electric current modulation. In this paper we show that such controlled interference can also be used to design an efficient spin filter device. The latter can be achieved by fabricating a nanoring above a ferromagnetic insulator (see Fig. 1 for the schematics of the device), in which case the combination of the exchange splitting and the effect of the side-gate voltage can result in controllable spin-polarized electric current.

The sample that we consider is a nanoring made of nanoribbons of width $w = 15.5$ nm with armchair edges. The full length of the ring is $L = 179$ nm while the full width is $W = 108$ nm.

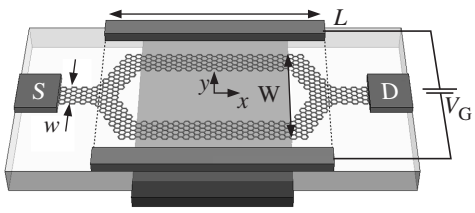

Fig. 1. Schematic view of the graphene nanoring fabricated above a ferromagnetic layer (shown as the blue bar in the figure).

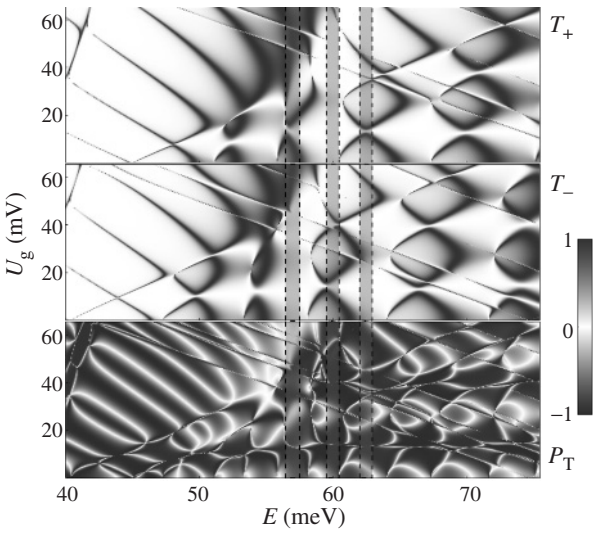

Fig. 2. Transmission coefficients $T_\pm$ of spin up (down) states and the degree of the transmission polarization P_T as functions of the carrier energy E and the side-gate voltage U_G.

We calculated the transmission coefficients for spin up and spin down electrons and the transmission polarization degree P_T. These results are shown in Fig. 2. As can be seen, the sign of the transmission polarization is almost independent of the side-gate voltage for some energies (see the leftmost and the middle shadowed strips), while for others both the polarization degree and its sign can be changed by the side-gate (see, e.g., the rightmost shadowed strip). The latter opens a possibility to control the polarization of the current by the electrostatic gate.

To demonstrate the possibility of the current polarization control, we calculated the total current together with its polarization degree P. We assume that Fermi energies of both the source and the drain are set to some value by a back-gate voltage and then one of these levels is shifted with respect to the other by the source-drain voltage. Upper and lower limits of the three shadowed strips in Fig. 2 give the source and drain Fermi energies, respectively, which were used to calculate electric currents. Results of such calculations are presented in Fig. 3, showing total currents (dotted lines) and their polarization degrees P (solid lines) for three cases. Upper, middle and lower panels correspond to the leftmost, middle and rightmost shadowed strips in Fig. 2, respectively.

As expected, the electric current can be highly polarized. For some combinations of the source and drain Fermi energies (voltages), the sign of the current polarization remains the same

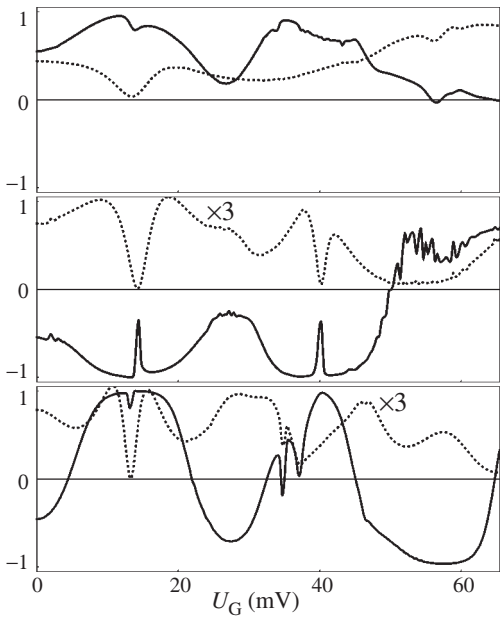

Fig. 3. Total electric current through the device (dotted lines) and its polarization degree (solid lines) as functions of the side-gate voltage U_G. Upper, middle and lower panels correspond to the leftmost, middle and rightmost shadowed strips in Fig. 2.

within wide ranges of the side-gate voltage (see the upper and the middle panels of Fig. 3). Nevertheless, as can be seen from the lower panel, the source and drain Fermi energies can be adjusted in such a way that the current polarization can be changed in almost its entire possible range $[-1, 1]$ by the side-gate voltage, suggesting that the proposed device can operate as a controllable source of spin-polarized electrons.

Acknowledgements

Work at Madrid was supported by MICINN (Projects Mosaico and MAT2010-17180).

References

[1] C. L. Kane and E. J. Mele, *Phys. Rev. Lett.* **95**, 226801 (2005).
[2] N. Tombros, C. Jozsa, M. Popinciuc, H. T. Jonkman and B. J. van Wees, *Nature* **448**, 571 (2007).
[3] O. V. Yazyev, *Nano Lett.* **8**, 1011 (2008).
[4] E. W. Hill, A. K. Geim, K. Novoselov, F. Schedin and P. Blake, *IEEE Trans. Magn.* **42**, 2694 (2006).
[5] Z. P. Niu and D. Y. Xing, *Eur. Phys. J. B* **73**, 139 (2010).
[6] M. Ezawa, *Eur. Phys. J. B* **67**, 543 (2009).
[7] F. S. M. Guimarães, A. T. Costa, R. B. Muniz and M. S. Ferreira, *Phys. Rev. B* **81**, 233402 (2010).
[8] F. Zhai and L. Yang, *Appl. Phys. Lett.* **98**, 062101 (2011).
[9] J. Munárriz, F. Domínguez-Adame and A. V. Malyshev, *Nanotech.* **22**, 365201 (2011).

20th Int. Symp. "Nanostructures: Physics and Technology"
Nizhny Novgorod, Russia, June 24–30, 2012

Metastable and spin-polarized electronic states in mesoscopic structures with localized electron-electron interaction

Vladimir A. Sablikov
Kotelnikov Institute of Radio Engineering and Electronics, 141190 Fryazino, Moscow District, Russia

Abstract. The formation of spin-polarized electronic states is studied in the practically important case where the electron-electron interaction is spatially localized, as it takes place in many mesoscopic structures coupled to non-interacting electron reservoirs. We found that a metastable state can exist in addition to the ground state. Depending on parameters, the system can be spontaneously polarized in the ground or metastable state. The presence of metastable state leads to unusual transport properties. In particular, this state could explain the 0.7 feature of the conductance of quantum point contacts.

Introduction

Recent experiments revealed many features of quantum transport in quantum point contacts (QPC) and quantum wires, such as the well-known 0.7 feature of the conductance, new plateaus of the conductance in the presence of applied voltage, unusual temperature dependence of the conductance, the zero-bias anomaly. It is commonly believed that they are associated with the formation of a spin-polarized state, however existing theories of such states fail to explain these experiments. It is obvious that their understanding requires new approaches.

Here, we pay attention to the fact that in many cases the electron-electron interaction is spatially nonuniform. It is concentrated in a relatively small region, closely coupled to reservoirs where electrons interact weakly. This motivated us to consider electronic states in such nonuniform system and to clarify whether the spontaneous breaking of the spin symmetry occurs due to exchange interaction in this case. We have arrived at unexpected result that a metastable state can appear in some range of parameters (interaction strength, chemical potential, temperature, external potential). This fact substantially changes understanding of the electronic structure of QPCs and transport features.

The spin-polarized state of free electrons is usually associated with the exchange interaction, which is known to lead to the ferromagnetism [1]. The formation of this state is well studied for homogeneous systems. If the interaction parameter exceeds a critical value, a sudden phase transition occurs from the paramagnetic state to the fully spin polarized state.

However, one can expect that in heterogeneous systems the situation substantially changes since the energy gain due to the polarization in the interaction region is accompanied by the increase in the kinetic energy in surrounding regions of the reservoirs where electrons do not interact. In this work we analyze the thermodynamic potential of such a system and show that spin-polarized state can appear as the metastable or the ground state. In the first case, the thermodynamic potential has a local minimum, though the global minimum corresponds to the unpolarized state. In any case the spin polarization is not full.

1. Main results

Consider a model one-dimensional or two-dimensional system in which the repulsing electron-electron interaction acts in a finite region. Our study is based on thermal Hartree–Fock approximation [2], according to which the thermodynamic potential $\Omega = \langle \hat{H} - \mu\hat{N} - T\hat{S} \rangle$ is minimized within the approach of self-consistent field.

The requirement that the first variation of the thermodynamic potential $\delta\Omega$ is zero, leads to an equation for one-particle wave functions. The stability of these states is investigated by analyzing the second variation $\delta^2\Omega$. The problem is simplified by supposing that the interaction is short-range one: $V_{\rm ee}(\mathbf{r}-\mathbf{r}') \approx v(\mathbf{r})\delta(\mathbf{r}-\mathbf{r}')$, and does not depend on the spin. Finally, we arrive at the following equation for one-particle wave functions:

$$\left[\frac{\mathbf{p}^2}{2m_{\rm e}} + U(\mathbf{r}) + v(\mathbf{r})n_{\bar{s}}(r)\right]\Psi_{\mathbf{k}s} = \varepsilon_{\mathbf{k}s}\Psi_{\mathbf{k}s}\,, \qquad (1)$$

where $\mathbf{k}$ is wave vector, s spin index, $\bar{s} = -s$, $U(\mathbf{r})$ one-particle potential, $n_{\bar{s}}$ is the electron density with the spin opposite to s,

$$n_{\bar{s}} = \sum_{\mathbf{k}'} |\Psi_{\mathbf{k}'\bar{s}}|^2 \rho_{\rm F}\left(\varepsilon_{\mathbf{k}'\bar{s}}\right)\,,$$

$\rho_{\rm F}$ being the Fermi distribution function.

Equation (1) is a nonlinear problem for the eigenfunctions which has generally several solutions. We solve this problem in some specific cases of interest.

1.1. One-dimensional model

The interaction is located in a region of length L, where $v = v(x)$ and there is an external one-particle potential $U(x)$. This region simulates a QPC in 1D model. Outer regions correspond to electron reservoirs where the chemical potential is μ.

First, let us consider the case where the interaction region is short, $kL \ll 1$. The results are illustrated in Fig. 1 where the average densities of electrons n_s and $n_{\bar{s}}$ in the interaction region are shown as functions of the interaction parameter, $b = m_{\rm e}\bar{v}a/\hbar^2$, for $U = 0$ and zero temperature. Generally, there are three solutions: i) unpolarized state existing in the whole range of the interaction strength and ii) spontaneously polarized state with $n_s \neq n_{\bar{s}}$, which exists when $b > b_{\rm c}$, with $b_{\rm c}$ being a critical value estimated numerically as $\sim$1.9. Near the critical point, $|n_s - n_{\rm c}| \sim (b - b_{\rm c})^{1/2}$. With increasing the temperature the critical value $b_{\rm c}$ shifts up and the polarized branches of the graph draw together.

The thermodynamic potential contains three components:

$$\Omega \approx \Omega_{\rm res} + \Omega_{\rm cloud}(n_\uparrow, n_\downarrow) - \bar{v}Ln_\uparrow n_\downarrow\,, \qquad (2)$$

where $\Omega_{\rm res}$ is the thermodynamic potential of the reservoirs, $\Omega_{\rm cloud}$ originates from electron clouds that appear in the reservoirs due to disturbance produced by the interaction region,

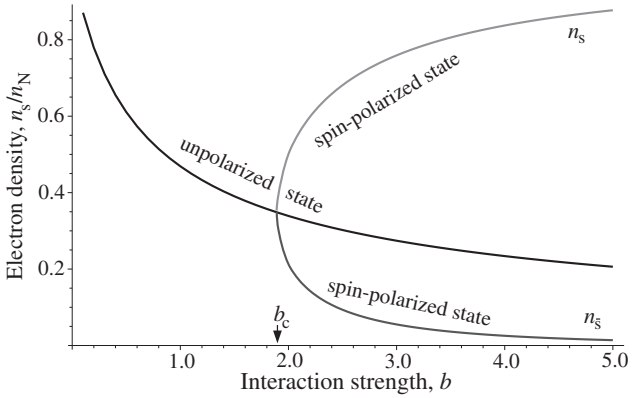

Fig. 1. Electron densities in the interaction region as functions of the interaction parameter for $T = 0$ and $U = 0$, with n_s being normalized by $n_N = \sqrt{2m_e\mu}/(\pi\hbar)$.

and the third term is the interaction energy, with $\bar{v}$ being the average of $v(x)$ within the interaction region.

It is evident that the interaction term diminishes the thermodynamic potential of the unpolarized state as compared with that of polarized state. The cloud term acts contrary. The competition of this effects determines what state is energetically more advantageous. In the case of purely 1D system (including the reservoirs) the thermodynamic potential of the polarized state turns out to be lower than that of the unpolarized state.

The analysis of the second variation of Ω shows that $\delta^2\Omega \geq 0$ in both states.

Other limiting case where the interaction region is long ($kL \gg 1$) was studied with using quasiclassical approximation, which is justified for slow varying $U(x)$ and $v(x)$. In this case, the electron density $n_s(x)$ is determined locally by the interaction parameter $b(x) = v(x)/\pi\hbar\sqrt{2m_e/[\mu - U(x)]}$. There are several solutions. First, the unpolarized solution exists in the whole range of the b variation. At $b > 2/\sqrt{3}$ there are two solutions corresponding to spontaneous spin polarization. In the range $1 < b < 2/\sqrt{3}$, there are four polarized solutions at zero temperature. Two of them are unstable. With increasing the temperature, these solutions rapidly disappear.

1.2. Two-dimensional model

The metastable states exist also in systems of higher dimensionality, but the critical conditions and the ratio of the thermodynamic potentials of the polarized and unpolarized states essentially changes since the configuration of the electron cloud around the interaction region is changed. We consider the 2D case where the electron-electron interaction is located within a small region of radius R. Strightforward solution of Eq. (1) with simplifying assumption that $kR \ll 1$ shows that the metastable state appears when the interaction parameter, $b = m_e\bar{v}\bar{n}R^2[\pi/2 - \gamma - \ln(k_F R/2)]/\hbar^2$, exceeds a critical value b_c (γ is Euler constant, k_F is Fermi momentum). The dependence of the electron densities n_s in the interaction region on b is qualitatively similar to that shown in Fig. 1. The critical parameter b_c depends on the build-in potential U, the Fermi level μ and temperature T. Numerically $b_c \approx 4$ for $U = T = 0$.

The thermodynamic potential is described by Eq. (2) but the specific expression of Ω_{cloud} is changed. Analyzing $\Omega(n_\uparrow, n_\downarrow)$ we have found that the thermodynamic potential of the polarized state can be higher than that of the unpolarized state.

2. Concluding remarks

We have shown that metastable electronic state can appear in the mesoscopic structures in addition to the ground state. This effect arises when the electron-electron interaction is localized in a relatively small region of space. One of the metastable and ground states can be spontaneously spin-polarized while the other state is unpolarized. This is an unexpected result since it is commonly known that the spin-polarized state of free electrons arising due to the exchange interaction is an unique state. The mechanism of the polarized state formation differs from the known Bloch transition [1]. Spin density arises as a result of spin-dependent scattering of electrons incident from reservoirs on the interaction region, rather than spin-splitting of the conduction band bottom. One of the important factors, due to which the metastable state exists, is that the filling factor of the electronic states penetrating into the interaction region is determined by the spectrum formed in the non-interacting reservoirs. The energy difference between the polarized and unpolarized states is of the order or the interaction energy of electrons.

The presence of metastable state leads to specific features of the transport properties such as additional plateaus of conductance and shot noise. Particularly, the metastable state could explain the 0.7 feature of the conductance of QPCs [3] if one suppose that the electron-electron interaction is localized within the constriction and the electron clouds are distributed in the reservoirs of higher dimensionality. At the temperature of the order of the interaction energy of electrons in the constriction, the metastable and ground states are occupied practically equally, so that the conductance is roughly estimated as $\sim 0.5(1 + 0.5)\, 2e^2/h$. In addition, if the metastable state is spin-polarized, the temperature dependence of the conductance expected from our model is qualitatively close to that observed in the experiments.

Acknowledgements

This work was supported by Russian Foundation for Basic Research (project No. 11-02-00337) and programs of Russian Academy of Sciences.

References

[1] G. Giuliani, G. Vignale, *Quantum theory of the electron liquid*, Cambridge University Press, New York, 2005.
[2] N.D. Mermin, *Annals Phys* **21**, 99 (1963).
[3] See special issue of *J. Phys.: Condens. Matter*, **20**, No. 16 (2008) devoted to the 0.7 feature and interactions in one-dimensional systems.

20th Int. Symp. "Nanostructures: Physics and Technology"
Nizhny Novgorod, Russia, June 24–30, 2012

Exciton magnetic polarons localization in type-II ZnSSe/ZnMnSe multiple quantum wells

A. V. Chernenko[1], A. S. Brichkin[1], S. V. Sorokin[2] and S. V. Ivanov[2]

[1] Institute of Solid State Physics, RAS, 142432 Chernogolovka, Russia
[2] Ioffe Physical-Technical Institute, St Petersburg, Russia

Abstract. Time-resolved and CW photoluminescence spectra of ZnSSe/ZnMnSe multiple quantum wells obtained under above band gap excitation at temperatures $T = 2-20$ K in magnetic field of up to 10 T in Faraday and Voigt geometries show two dominant lines. An analysis of their behavior under various excitation power, magnetic fields and temperatures shows that they correspond to recombination of free or localized excitons and bound exciton magnetic polarons. Photoluminescence studies reveal 1LO and 2LO phonon replicas of the polaron line and absence of the replicas of the exciton line. It gives one an additional evidence of strong polaron localization and demonstrates its reduction with magnetic field and temperature. The Huang–Rhys factor of the magnetic polaron is up to three times smaller at $B = 10$ T than its value at zero magnetic field $S \simeq 0.3 \pm 0.1$. Possible mechanisms of polaron non-magnetic localization are proposed.

Introduction

Studies of exciton magnetic polarons in type-I diluted magnetic semiconductor (DMS) structures showed that the spin-relaxation time often exceeds the exciton life-time, which prevents formation of exciton magnetic polarons (EMP) [1]. Type-II quantum wells are promising structures for study of the EMPs under equilibrium conditions since the life-time of excitons and exciton complexes is expected to be long because of indirect optical transition.

Results of our studies reveal presence of two broad lines in photoluminescence (PL) spectra of type-II structures, which differently depend on variations of pumping power, temperature and magnetic field. Experimental results allow us to attribute the upper energy line to the recombination of weakly localized indirect excitons and the lower energy line to recombination of impurity bound EMPs. Our results show that the polaron effect in the structures under study is relatively small and polaron formation energy is even smaller than that in type-I DMS structures.

Studies of LO-phonon replicas of the polaron line indicate substantial reduction of the exciton-phonon coupling with increasing magnetic field , which may be a result of delocalization of bound excitons by magnetic field and suppression of magnetic polarons (magnetic localization).

1. LO-phonon replicas and their relation to exciton localization

The spectra of two MBE grown samples containing 10 periods of $Zn_{0.9}Mn_{0.1}Se$[8nm]/$ZnS_{0.16}Se_{0.84}$[18nm] (sample # 1) and $Zn_{0.84}$ $Mn_{0.16}Se$ [8nm] /$ZnS_{0.16}$ $Se_{0.84}$[18nm](sample # 2) quantum wells(QWs') are studied.

The results of CW magnetic field measurements in Faraday geometry presented in Fig. 1 show evolution of nophonon (NP), 1LO- and 2LO-phonon replicas of EMP line in magnetic field in Faraday geometry for sample # 2. The results of analysis of the ratios I_{1LO}/I_{NP} and $2I_{2LO}/I_{1LO}$ reveal their decrease for both samples. The ratios are obtained by means of the gaussian multipeak analysis with substraction of the background. The analysis shows certain decrease of the ratios although small intensities of the replicas, their large spectral width and uncertainty in the background determination lead to a large error.

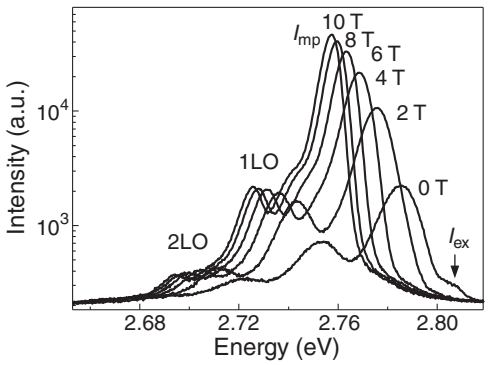

Fig. 1. PL spectra of sample # 2 ($x = 16\%$) in Faraday geometry, subject to various magnetic field strength.

Within the Frank–Condon approximation the intensity of j-th phonon-assisted replica is $I_j = S^j e^{-S}/j!$, where j=0,1 . . . n. The ratio $S = I_{LO}/I_{NP}$ is the Huang–Rhys factor that determines the strength of polar exciton-LO-phonon coupling. It was argued in Ref. [2, 3] that the ratio I_{1LO}/I_{NP} reflects the dependence of exciton-phonon interaction on exciton kinetic energy and may strongly overestimate the real value of Huang–Rhys factor whereas the ratio $S = 2I_{2LO}/I_{LO}$ is more appropriate for these purposes.Although bound rather than free exciton lines are of our interest both ratios $S = I_{LO}/I_{NP}$ and $S = 2I_{2LO}/I_{LO}$ are used in analysis.

The Huang–Rhys factor is given by the expression

$$S = \sum_{\mathbf{q}} \frac{|V_{\mathbf{q}}|^2}{\hbar\omega_{LO}} |\rho_{\mathbf{q}}|^2 , \qquad (1)$$

where $\rho_{\mathbf{q}}$ is the Fourier transform of the charge distribution and

$$|V_{\mathbf{q}}|^2 = \frac{2\pi e^2}{V} \left(\frac{1}{\epsilon_\infty} - \frac{1}{\epsilon_0}\right) \left(\frac{1}{\mathbf{q}}\right)^2 \qquad (2)$$

is the square of amplitude $V_{\mathbf{q}}$ of exciton-LO-phonon polar interaction [4].

Since electron and hole envelopes are slowly varying functions of coordinates, the charge distribution of the exciton ground state is [4]

$$\rho_{\mathbf{q}} = \langle F\,(\mathbf{r}_e = \mathbf{r}, \mathbf{r}_h = \mathbf{r}) \left| e^{i\mathbf{q}\mathbf{r}_e} - e^{i\mathbf{q}\mathbf{r}_h} \right| F\,(\mathbf{r}_e = \mathbf{r}, \mathbf{r}_h = \mathbf{r}) \rangle, \quad (3)$$

where $F(\mathbf{r}_e, \mathbf{r}_h)$ is the exciton envelope function and $\mathbf{r}_e$ and $\mathbf{r}_h$ are electron and hole coordinates, respectively.

The binding energy of indirect excitons in the structures is expected to be relatively small <5 meV that is comparable with the charge carrier localization energy. The model of phonon-assisted donor-acceptor pairs recombination is appropriate in this case. Within the effective mass approximation the wave-function of an electron-hole pair localized on a donor and an acceptor is merely a product of electron $f_e(\mathbf{r})$ and hole $f_h(\mathbf{r})$ envelopes $F(\mathbf{r}_e, \mathbf{r}_h, \mathbf{R}) = f_e(\mathbf{r}_e) f_h(\mathbf{r}_h - \mathbf{R})$. Here $\mathbf{r}_e$ and $\mathbf{r}_h$ are electron and hole coordinates with respect to acceptor and donor centers, respectively, and $\mathbf{R}$ is the distance between the centers.The measured value of S is the sum of S of individual donor-acceptor pairs over their distribution in the excitation spot. The exact analytical expression for S that accounts for anisotropy of hole masses is very complicated and can be found elsewhere in literature. By neglecting the hole mass anisotropy the Huang–Rhys factor can be expressed as follows [4]

$$S = \left(\frac{1}{\epsilon_\infty} - \frac{1}{\epsilon_0}\right) \frac{e^2}{a_e \beta} \frac{1}{\hbar\omega_{LO}} \left(\frac{5}{16}(1+\beta) - \Delta\right),$$

where

$$\Delta = \frac{1}{\alpha}\left(1 - \frac{\Delta_e + \Delta_h}{(1-\beta^2)^3}\right),$$

$\Delta_e = (1-3\beta^2+(1-\beta^2)\beta\alpha)\exp(-2\beta\alpha)$, $\Delta_h = (3-\beta^2+(1-\beta^2)\alpha)\exp(-2\alpha)$ and coefficients $\alpha = R/a_h$, $\beta = a_h/a_e$. Here a_e and a_h are electron and hole localization radii,respectively.

These expressions explain why LO-phonon replicas of the exciton line are not observed in PL spectra whereas the replicas are well visible for EMP line; it is because of much stronger localization of the electrons and holes in the case of EMP.

The measured value of $S \simeq 0.3 \pm 0.1$ is the result of summation of Huang–Rhys factors of individual pairs over the distribution of R, a_h, a_e. However, one can roughly estimate possible range of parameters α and β by using the above expression. For instance, taking $R = 80$ Å and $a_h \simeq 40$ Å (direct exciton radius) the value $\beta \simeq 0.93-0.94$, which matches our experimental data at $B = 0$ T can be obtained. Assuming that the exciton localization is related to formation of type-II A^0X centers the reduction of S is than caused by their destabilization in magnetic field often observed in past [1]. In this case the decrease of S is caused by the increase in a_h.

2. Mechanisms of polaron localization

The upper energy line (I_{ex}) in Fig. 1 was attributed by Toropov *et al*. [5] to recombination of EMP formed by weakly localized excitons, whereas the lower energy line was related to EMP consisted from the strongly localized *e-h* pair. In order to explain coexistence of two types of quasiparticles two types of localization potentials with different in-plane localization sizes ∼20−30 nm and ∼4 nm and two mechanisms of spin relaxation are proposed.

However, experimental results are well explained if one assumes the dominant role of non-magnetic localization.The fast relaxation of excitons(*e-h* pairs) can be caused by capture of free excitons, or even holes(electrons) by a localization potential of non-magnetic origin.

The lines related to recombination of acceptor and donor bound excitons often dominate in spectra of undoped bulk DMS materials [6, 7] and QWs [1], while the intensity of free exciton line is often much weaker. The bound exciton complexes (A^0X and D^0X) demonstrate saturation behavior with increase of excitation power, strong reduction of intensity with increase of temperature, and destabilization in magnetic field. This is very similar to that of lower energy line observed in our spectra presented in Fig. 1. Time-resolved measurements on exciton complexes in bulk ZnSe show that the life-time of bound excitons is much longer that life-time of free excitons [7], that resembles behavior of our lines, i.e. the lines demonstrate properties very similar to free and impurity bound excitons in type-I II-VI materials.

The dominant mechanism of hole (exciton) localization can be related not only to residual impurities (donors and acceptors) but also to charged vacancies interstitial atoms and structural defects. Such defects are responsible for the well-known effect of self-compensation in II-VI materials [6].

Pictures similar to those in Fig. 1 were observed in other structures [8]. It was proposed their that the effects were sample specific ones and were depend on MBE growth conditions. The formation of sample specific defects appeared during MBE growth can explain the difference between the spectra of the samples with $x = 10\%$ and $x = 16\%$. The larger Mn content favors formation of potential traps for the charge carriers such as vacancies and interstitial atoms in the vicinity of the interface.

Acknowledgements

This work has been supported by RFBR grants.

References

[1] D.R.Yakovlev and W.Ossau in "Introduction to the Physics of Diluted Magnetic Semiconductors" (eds. J. Kossut and J.A. Gaj) Springer Series in Material Science 144, (Springer-Verlag, Verlin Heidelberg) 2010.

[2] S.Permogorov, in Excitons, edited by E.I.Rashba and M.D. Sturge(Noth-Holland, Netherlands, 1982), Chap. 5.

[3] H.Zhao and H.Kalt, *Phys. Rev. B* **68**, 125309 (2003).

[4] M.Soltani, M.Certier, R.Evrard, and E.Kartheuse, *J. Appl. Phys.* **78**, 5626 (1995).

[5] A. A. Toropov, Ya. V. Terent'ev, S. V. Sorokin, S. V. Ivanov, T. Koyama, K. Nishibayashi, A. Murayama, Y. Oka, J. P. Bergman, I. A. Buyanova, W. M. Chen, and B. Monemar, *Phys. Rev. B* **73**, 245335 (2006).

[6] J.Gutowski, N.Presser and G.Kudlek, *Phys. Stat. Sol. A*, **120**, 11 (1990).

[7] F.Bogani, S.Grifoni, M.Gurioli, and L.Morolli, *Phys. Rev. B* **52**, 2543 (1995).

[8] T. Stirner, J. Miao, W.E. Hagston, S. Takeyama, G. Kerczewski,T. Wojtowich, and J. Kossut, *Phys. Rev. B* **60**, 11545 (1999).

20th Int. Symp. "Nanostructures: Physics and Technology"
Nizhny Novgorod, Russia, June 24–30, 2012

Ferromagnetic effect of $\delta\langle$Mn$\rangle$ doping in GaAs/InGaAs heterostructures: galvanomagnetic and luminescence studies

M. V. Dorokhin, Yu. A. Danilov, A. V. Kudrin, I. L. Kalent'eva, M. M. Prokof'eva, O. V. Vikhrova and B. N. Zvonkov

Research Physical-Technical Institute of the Nizhny Novgorod State University, 603950 Nizhny Novgorod, Russia

Abstract. The ferromagnetic effect of $\delta\langle$Mn$\rangle$ doping of a GaAs barrier on the properties of InGaAs/GaAs quantum well heterostructures has been investigated. It has been shown that the galvanomagnetic properties and circular polarization of electroluminescence of samples are strongly correlated. The possible mechanisms of the effects observed are discussed with the use of the technology parameters variation affecting the ferromagnetic properties.

Introduction

The diluted magnetic semiconductors (DMS) like GaAs:Mn or InAs:Mn are the key element of the spintronic devices [1,2]. The main feature of the DMS is the combination of semiconductor and ferromagnetic properties originating from the interaction of holes with Mn ions [1]. Although the exact microscopic mechanisms of ferromagnetism are still under discussion [1,2] it has been proven that DMS act as a source of spin polarized carriers and thus may be used in a set of devices operating with the spin [1]. It should be noted that in the broader meaning DMS implies not only uniformly doped A3B5:Mn layers but delta-doped layers as well. For example ferromagnetic $\delta\langle$Mn$\rangle$-doped GaAs layer has been used in [3] for the spin polarization of holes in the *p*-AlGaAs/GaAs heterostructures. In our earlier work it has been supposed that ferromagnetic interaction of $\delta\langle$Mn$\rangle$-doped layer with holes in closely located GaAs/InGaAs quantum well (QW) leads to a hole spin polarization and circular polarization of QW emission [4].

In the present paper we have carried out the detailed investigation of effect of in the $\delta\langle$Mn$\rangle$ doping on the properties of GaAs/InGaAs QW system. Ferromagnetic properties are revealed via a set of interrelated phenomena such as anomalous Hall effect and circularly polarized electroluminescence (EL) of light-emitting diode based on the latter structure. The investigation has been carried out in a wide range of magnetic fields and temperatures. Possible mechanisms for ferromagnetic interaction and EL circular polarization are discussed.

1. Experimental

The InGaAs/GaAs QW structures were fabricated by two-stage epitaxial growth method. A 0.5 μm-thick buffer GaAs layer (doped with Si up to 10^{17}cm^{-3}), a 3 nm thick undoped GaAs layer, the $In_xGa_{1-x}As$/GaAs QW ($x = 0.1-0.2$; width $d_{QW} =$ 10 nm) and thin ($d_s = 2-12$ nm) undoped spacer GaAs layer were grown sequentially at 650 °C on GaAs (001) substrates by metal-organic vapor phase epitaxy (MOVPE) at atmospheric pressure. At the next stage the $\delta\langle$Mn$\rangle$-doped layer and the GaAs cap layer were grown at 400 °C in the same reactor by the laser sputtering of Mn and GaAs targets, respectively. The nominal densities of Mn in layer were $\sim 0.6-2 \times 10^{14}$. In the present work the investigation of the samples has been carried out by means of two independent techniques: A) circularly polarized electroluminescence of the diodes based on the latter samples and B) anomalous Hall effect (AHE) measurements within the same samples. For the fabrication of the diode structures (A) an Au Schottky contact was formed at the top of the sample by vacuum thermal evaporation of metal. Back ohmic contact was formed by sparkling of Sn foil.

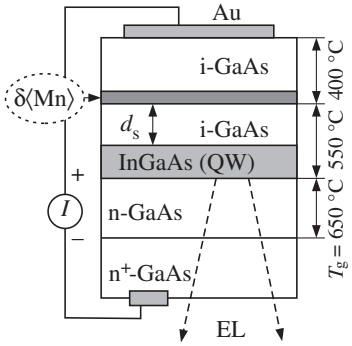

Fig. 1. The schematic diagram of investigated samples.

For the AHE measurements instead of Au deposition standard contacts for Van-der Paw geometry have been used. In this case low-diffusion Ohmic contacts were fabricated on sample surface. Unlike the EL the Hall measurement geometry implies current flowing along the sample surface. We suppose that the Hall effect current flew only within $\delta\langle$Mn$\rangle$ and the QW without shunting via the buffer layer. The schematic sketch of investigated structures is shown in Fig. 1, and the technological details were described elsewhere [4]. The polarized electroluminescence spectra have been measured at temperature range $T = 2-80$ K. Electroluminescence was measured under the forward bias of Schottky diode (positive potential relatively to base). For the measurements of luminescence in the magnetic field the samples were placed into a closed-cycle cryostat. The magnetic field $B = 0-0.4$ T was normal to the QW plane (Faraday geometry). The degree of circular polarization (CP) was evaluated by formula: $P_C = (I^+ - I^-)/(I^+ + I^-)$, where $I^{+(-)}$ are the intensities of the left(right)-hand polarized QW emission spectrum. The anomalous Hall effect has been measured within the same range of magnetic fields and temperatures.

2. Results and discussion

As it was shown previously in the magnetic field the EL becomes circularly polarized, i.e. the intensity of left circular polarization component becomes higher than one with right polarization (Fig. 2) [4]. Independently a series of experiments studying anomalous Hall effect carried out in [5] has revealed

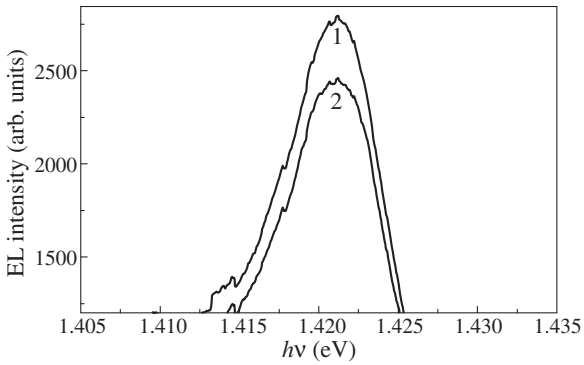

Fig. 2. EL spectra of $\sigma+$ (1) and $\sigma-$ (2) polarized emission.

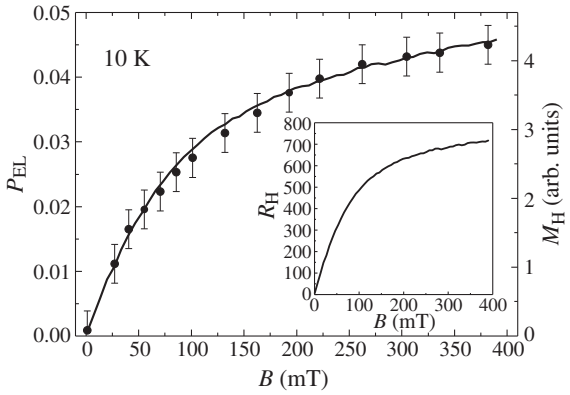

Fig. 3. The magnetic field dependencies of circular polarization degree (dots) and relative magnetization (line) of sample with InGaAs/GaAs QW and $\delta\langle$Mn$\rangle$-layer. Insert shows the dependence of Hall resistance on B.

the ferromagnetism in $\delta\langle$Mn$\rangle$-layers fabricated in the similar growth mode. In the present paper we have demonstrated a strong correlation between AHE a circular polarization. At the Fig. 3 one can see the magnetic field dependencies of a circular polarization degree of investigated diode (Fig. 3, curve 1) and of Hall resistance of same diode structure (insert to Fig. 3). The dependence of P_C on the magnetic field (B) is closely similar to the field dependence of relative magnetization (MH) (Fig. 3, curve 2). The latter has been derived from the AHE by dividing Hall resistance by the square of layer resistance according to the techniques described in [6].

One other manifestation of a ferromagnetic effect on the properties of the samples may be revealed through temperature dependencies investigation of both AHE and CP (not shown). With the increase of the measurement temperature from 10 to 40 K the magnetic field dependencies for both AHE and CP linearize becoming linear at the temperature of 30–40 K (depending on the sample parameters). This is accompanied by strong decrease of a circular polarization degree from the value of 0.05–0.1 to $<$0.01. According to the latter data one could suppose that the Curie temperature of the ferromagnetic $\delta\langle$Mn$\rangle$ layer lies within range of 30 to 40 K.

It should be noted that the ferromagnetic properties of a $\delta\langle$Mn$\rangle$ layer are independent on the presence or absence of InGaAs/GaAs quantum well, that is evidenced by an anomalous Hall effect obtained for single $\delta\langle$Mn$\rangle$-layer in GaAs in [7]. It means that all properties of investigated structures are driven by ferromagnetism in $\delta\langle$Mn$\rangle$. In case of luminescence the main mechanism driving circular polarization is believed to be an interaction between Mn ions and holes in the quantum well [4]. Anomalous Hall effect is in turn driven by spin dependent scattering of carriers in the magnetic field [5,7]. In both cases the efficiency of interaction depends on the sample parameters. It has been found that the most crucial parameters of investigated samples are the spacer layer thickness between a quantum well and a δ-layer and the In content in the quantum well (determining the energy position of a heavy hole level in the quantum well). In addition, the AHE strongly depends of a current distribution between 2 conducting channels: $\delta\langle$Mn$\rangle$ and quantum well. The latter parameter is hard to evaluate moreover it depends on any parameter of fabrication technology. The investigation has shown that the increase of the spacer layer thickness leads to decrease of circular polarization degree. The supposed reason for this is a decrease of interaction efficiency decreasing the spin polarization of holes in the QW. In turn unpolarized holes in the QW don't give contribution to the AHE. The increase of a spacer layer thickness may thereby lead to the AHE becoming linear even at low temperatures — if the sample parameters provide most of the current to flow through a QW.

Thus we have investigated the ferromagnetic effect of $\delta\langle$Mn$\rangle$ doping of a GaAs barrier on the properties of InGaAs/GaAs quantum well heterostructures. It has been shown that anomalous Hall effect and circularly polarized luminescence are strongly related and determined by an interaction of holes in the QW with Mn ions in the ferromagnetic $\delta\langle$Mn$\rangle$-layer.

Acknowledgements

The work was supported by RFBR 10-02-00739, Federal target program "Scientfic and pedagogical staff of innovational Russia", Grant of President of Russian Federation (MK-5359. 16.120.11).

References

[1] I. Zutic *et al*., *Rev. Mod. Phys.* **76**, 323 (2004).
[2] V. F. Sapega *et al*., *Phys. Rev. Lett.* , **94**, 137401 (2005).
[3] A. M. Nazmul *et al*., *Phys. Rev. Lett.* , **95**, 017201 (2005).
[4] M. V. Dorokhin *et al*., *J. Phys.D, Appl.Phys.* **41**, 245110 (2008).
[5] O. V. Vikhrova *et al*., *Tech. Phys. Lett.* **35**, 643 (2009).
[6] H. Ohno *et al*., *Phys. Rev Lett.* **68**, 26645 (1992).
[7] A. V. Kudrin *et al*., *Tech. Phys. Lett.* **36**, 511 (2010).

20th Int. Symp. "Nanostructures: Physics and Technology"
Nizhny Novgorod, Russia, June 24–30, 2012

Spin polarization of transport current passing through Co_2CrAl ferromagnetic films

E. M. Rudenko, I. V. Korotash, A. A. Krakovny and *D. S. Dubyna*
G.V. Kurdyumov Institute for Metal Physics, 03680 Kyiv, Ukraine

Abstract. Multilayer multicontact MoRe/Co_2CrAl-I-Pb structures with different thickness of the Co_2CrAl ferromagnetic layer were produced and studied. The impact of the ferromagnetic layer on non-spin-polarized charge carriers injected into it was studied. Estimate of the spin diffusion length in Co_2CrAl ferromagnetic film was made.

Introduction

The study of peculiarities of charge and spin transport in planar multilayer structures formed by ferromagnetic (F) and superconductors (S) is of substantial interest for spintronics [1]. Well-known works [1,2] studied the impact of the degree of current spin polarization on the differential conductivity of tunnel junctions or that of spin-polarized injection on the superconducting state [3–5]. Yet, many problems of spintronics require experimental data about superconducting current passing through ferromagnetic layers. The study of these phenomena, when ferromagnetic has a high degree of spin polarization and is used as a spin injector in multilayer structures of spintronic devices is of particular importance.

Co_2CrAl film can serve as one of such ferromagnetics. Heusler Co_2CrAl alloy is a ferromagnetic semimetal, which is in the metallic state for one spin polarization and in the dielectric state for the other [6].

In the ferromagnetic layer, depending on the degree of spin polarization, there is some excess concentration of electrons with parallel spins. When one passes a non-spin-polarized current in the direction perpendicular to the surface of the ferromagnetic film the spin polarization should occur if the thickness of the ferromagnetic film is larger than the spin-diffusion length l.

In the present paper we studied the impact of the Co_2CrAl ferromagnetic layer on charge carriers injected into it from the MoRe superconductor and estimated Co_2CrAl spin-diffusion length l_{Co_2CrAl}, which is an important parameter for spintronics. Studies of the multilayer multi-junction S_1/F-I-S_2 (MoRe/Co_2CrAl-I-Pb) structures that had different thicknesses of ferromagnetic layers — 100 nm and 200 nm — were carried out.

1. Experimental

The MoRe/Co_2CrAl-I-Pb structure is a cruciform junction (Fig. 1) which was produced as follows. At first, from the target on the heated sapphire substrate, MoRe superconductor film was deposited by DC-magnetron sputtering through a mask. The residual vacuum in the chamber was 4×10^{-6} torr. MoRe film was deposited in an argon atmosphere with the deposition rate 100 nm/min. The thickness of the MoRe film was $d_{MoRe} \approx 100$ nm and the critical superconducting transition temperature $T_c = 9.5$ K. After deposition of the MoRe film, Co_2CrAl ferromagnetic film was deposited on it by the flash evaporation method through another mask when the substrate was heated. Vacuum in the chamber was 1×10^{-6} torr, the thickness of the Co_2CrAl film $d_1 \approx 100$ nm. The natural oxide on the Co_2CrAl film surface, which was used as a tunnel barrier (I), was formed by controlled oxidation of the film in the laboratory. After that, Pb film of $d_{Pb} \approx 100$ nm thickness was deposited on ferromagnetic film surface by thermal evaporation method. Vacuum in the chamber was 2×10^{-6} torr. The area of the tunnel junction was $\approx 2 \times 10^{-4}$ cm^2. In the same way, MoRe/Co_2CrAl-I-Pb structure was formed, with Co_2CrAl film thickness $d_2 \approx 200$ nm.

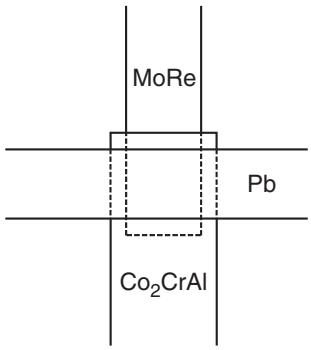

Fig. 1. Scheme of MoRe/Co_2CrAl-I-Pb structure (top view).

Current-voltage characteristics (CVC) of the MoRe/Co_2 CrAl-I-Pb junctions obtained were measured in the transport Dewar flask at liquid helium temperature 4.2 K by four-terminal sensing.

2. Results and discussion

As was shown in [4], for establishing spin polarization of tunnel current in the low-resistance junctions its impact on the stability of nonequilibrium superconducting state (NSS) can be used. It was found that for the NSS instability to occur we need spin-polarized tunnel currents of injection by an order of magnitude lower than in the case of ordinary non-spin-polarized currents. We used this effect for recognizing signs of spin polarization in our experiments.

Fig. 2a shows two CVC of the MoRe/Co_2CrAl-I-Pb structure in which the thickness of the Co_2CrAl ferromagnetic film $d_1 \approx 100$ nm. These CVC correspond to different current application to the tunnel barrier. In the first case (curve 1) the current was applied to the Co_2CrAl ferromagnetic film, in the other (curve 2) it was applied to the MoRe superconducting film and then it passed through the ferromagnetic film. It is seen that the instability of NSS (voltage jumps in the CVC shown by the arrows in the figure) in the Pb film in the first case occurs when the critical injection current $I_{ci1}(100) = 43$ mA. This value gives the critical specific injection level $q_{ci1}(100) = I_{ci1}(100)/\upsilon_1 = 2.15 \times 10^7$ A cm^{-3}. Here υ_1 is the volume of the Pb film which is under injection and equal

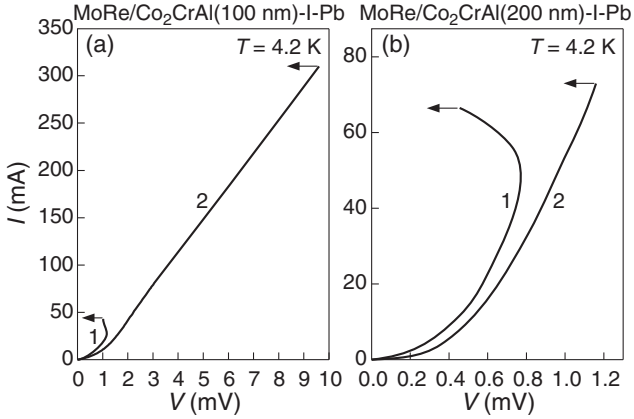

Fig. 2. CVC of MoRe/Co_2CrAl-I-Pb structures at $T = 4.2$ K; a) thickness of the Co_2CrAl film $d_1 \approx 100$ nm; b) thickness of the Co_2CrAl film $d_2 \approx 200$ nm.

to the product of $S\,d_1$ (S is the area of the tunnel junction). Such a value $q_{ci1}(100)$ corresponds to the spin-polarized injection [4]. CVC of the junction (curve 2) differs significantly from the first case in its shape and the value of the critical injection current $I_{ci2}(100) = 310$ mA when current is applied to the MoRe film and passes through the Co_2CrAl ferromagnetic film with thickness $d_1 \approx 100$ nm. In this case we have $q_{ci2}(100) = 1.55 \times 10^8$ A cm^{-3}, which is almost seven times higher than $q_{ci1}(100)$. We obtained $q_{ci2}(100) \gg q_{ci1}(100)$ despite the fact that injection of quasiparticles occurs in the "wide"-source regime $eV \gg 2\Delta_{Pb}$ (Δ_{Pb} is energy gap of the lead). In this case a large number of nonequilibrium quasiparticles are generated as a result of re-absorption of high-energy phonons relaxation. The presence of re-absorption in the Pb film can increase the concentration of nonequilibrium quasiparticles by more than an order and leads to a decrease of the critical injection current. The large value of $q_{ci2}(100)$ is a sign of the lack of spin polarization of the current which passes through the Co_2CrAl ferromagnetic film. It means that the spin diffusion length of Co_2CrAl film l_{Co_2CrAl} is larger than 100 nm.

Fig. 2b shows two CVC of MoRe/Co_2CrAl-I-Pb structure in which the thickness of the Co_2CrAl ferromagnetic film $d_2 \approx 200$ nm. As in the case for a $d_1 \approx 100$ nm film, the current to the tunnel barrier was applied to the Co_2CrAl ferromagnetic film (curve 1) as well as to the MoRe superconducting film and then it passed through the Co_2CrAl ferromagnetic film (curve 2). It is seen that the shapes of the CVC are almost identical. They are similar to curve 1 in Fig. 2a and differ significantly from curve 2 in the same figure. Critical currents of instability had values of $I_{ci1}(200) = 67$ mA and $I_{ci2}(200) = 73$ mA. They give close values of $q_{ci1}(200) = 3.35 \times 10^7$ A cm^{-3} and $q_{ci2}(200) = 3.65 \times 10^7$ A cm^{-3}. These $q_{ci1}(200)$ and $q_{ci2}(200)$ values indicate the presence of spin-polarized tunnel injection current [4]. The difference between $q_{ci2}(200)$ and $q_{ci1}(200)$ can be due to the fact that spin diffusion length l_{Co_2CrAl} is probably somewhat larger than the thickness of the Co_2CrAl ferromagnetic film.

Conclusion

It has been shown that spin polarization of transport current does not occur when it passes from the superconducting film through the Co_2CrAl film of the ferromagnetic semimetal 100 nm thick. Spin polarization of transport current at the film with thickness 200 nm is observed. The degree of spin polarization of current is close to the degree of polarization of the ferromagnetic film itself.

The experimental data and the method of estimating of the spin diffusion length could be used for developing spintronic devices.

References

[1] S. A. Wolf *et al*., *Science* **294**, 1488 (2001); I. Malajovich *et al*., *Nature* **411**, 770 (2001); M. L. Roukes, *Nature* **411**, 747 (2001); S. Das Sarma, *American Scientiest* **89**, 516 (2001); I. Žutič *et al*., *Rev. Mod. Phys.* **76**, 323 (2004).

[2] P. M. Tedrow *et al*., *Phys. Rev.* **B7**, 318 (1973); A. I. Dyachenko *et al*., *Low. Temp. Phys.* **32**, 1085 (2006).

[3] E. M. Rudenko *et al*., *Low. Temp. Phys.* **36**, 186 (2010); E. M. Rudenko *et al*., *Low. Temp. Phys.* **37**, 614 (2011).

[4] E. M. Rudenko *et al*., *Metal Physics & Advanced Technologies* **31**, 429 (2009); E. M. Rudenko *et al*., *Physica C* **470**, 378 (2010).

[5] V. A. Vas'ko *et al*., *Phys. Rev. Lett.* **78**, 1134 (1997); *Appl. Phys. Lett.* **73**, 844 (1998); Z. W. Dong *et al*., *Appl. Phys. Lett.* **71**, 1718 (1997).

[6] I. Galanakis *et al*., *Phys. Rev.* **B66**, 174429 (2002).

20th Int. Symp. "Nanostructures: Physics and Technology"
Nizhny Novgorod, Russia, June 24–30, 2012

Peculiarities of two-state lasing in quantum-dot lasers

A. E. Zhukov[1,2], Yu. M. Shernyakov[2,1], D. A. Livshits[3], M. V. Maximov[2,1], A. V. Savelyev[1], F. I. Zubov[1] and V. V. Korenev[1]

[1] St Petersburg Academic University, St Petersburg, Russia
[2] Ioffe Physical-Technical Institute, St Petersburg, Russia
[3] Innolume GmbH, Konrad-Adenauer-Allee 11, 44263 Dortmund, Germany

Abstract. Spectral and power characteristics of quantum-dot lasers operating in regime of simultaneous lasing via ground-state and excited-state optical transitions (two-state lasing) are studied in a wide range of operation conditions. It is demonstrated that neither self-heating nor increase of the homogeneous broadening are responsible for quenching of the ground-state lasing beyond the two-state lasing threshold. It is found that difference in electron and hole capture rates into quantum dots strongly affects light-current curve and, therefore, should be taken into consideration. Modulation p-type doping of quantum dots is shown to enhance the peak power of GS lasing transition. It is demonstrated for the first time that different groups of QDs are responsible for GS- and ES-lasing in the two-state lasing regime.

Introduction

For various applications, e.g. optical data transmission and pumping of Raman amplifiers, efficient lasers operating around 1.3 μm are requested. Lasers based on self-organized InAs / InGaAs quantum dots (QDs) offer attractive combination of extremely low threshold current density and high characteristic temperature. The required wavelengths can be achieved if the laser operates on the ground-state (GS) optical transition. However, as current increases an additional line ($\lambda < 1.2$ μm), associated with the first excited-state (ES1) transition, appears in lasing spectra [1]. Suppression of this two-state lasing as well as maximization of the GS spectral component are desired for a majority of applications.

1. Quenching of GS spectral component

Analysis of QD laser behavior based on rate [2] and master [3] equations predicts that optical power of the GS spectral component reaches its maximal value at threshold of the two-state lasing and then persists. However a number of experimental facts revealed that the GS power declines down to its complete quenching [4,5]. Among possible reasons laser self-heating in CW regime [4] and/or increase of homogeneous broadening [5] were mentioned.

To clarify this question we studied broad-area 4-mm-long laser (single plane of InAs/InGaAs QDs) mounted onto temperature-stabilized heatsink in pulse regime (300 ns at 2 kHz). The GS-lasing survives up to 68 °C. Typical lasing spectrum taken at 17 °C in the two-state lasing regime is depicted in insert of Fig. 1. L-I curve and its spectral components are presented in Fig. 1. It is seen that the GS-component reaches its maximum at 5 A beyond the onset of two-state lasing (3 A). A complete quenching of the GS lasing is observed at 12 A. As current increases in this interval, the GS peak position shifts by only 0.4 nm (from 1262.9 to 1263.3 nm) which corresponds to a negligible temperature increment of about 1 °C. Therefore one can conclude that self-heating of the active region can not be a primary reason of the GS lasing quenching.

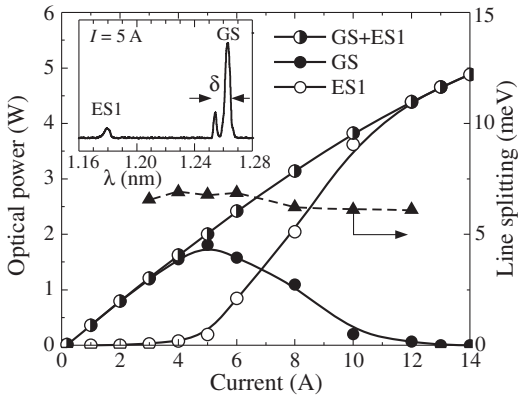

Fig. 1. Laser power — total (GS+ES1), ground-state component (GS), first excited-state component (ES1). Triangles — splitting of GS line. Insert: Lasing spectrum.

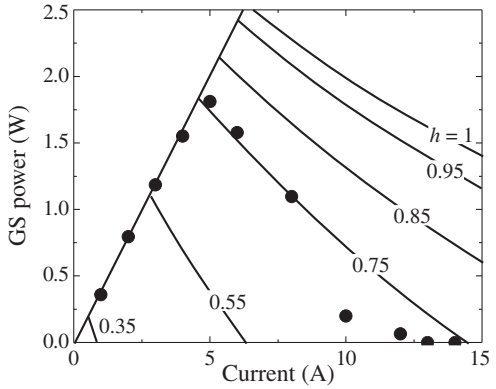

Fig. 2. L-I curves for ground-state component. Lines — calculation for different ratio of hole-to-electron relaxation rates. Circles — experimental data.

It was suggested [5] that the GS lasing quenching could be explained by increase of the homogenous broadening. According to [5] the homogenous broadening can be estimated from spectral splitting of the GS line in lasing spectrum (marked as "δ" in inset of Fig. 1). However, we found that the splitting remains very stable (or even decreases from 6.9 to 6.1 meV) as current increase (see Fig. 1). Therefore, the quenching can not be associated with the aforementioned reason as well.

2. Effect of difference in electron and hole relaxation rates

Energy separation of ground- and excited-state energy levels of holes in QDs is much smaller than kT. As a result the hole levels are occupied with nearly equal probability and, therefore, electrons of the ground-state level compete with electrons of

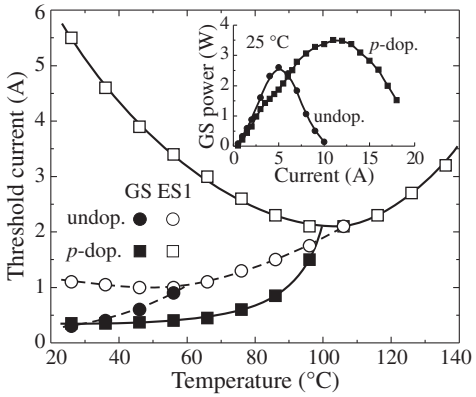

Fig. 3. Threshold vs temperature for ground-state lasing (GS) and first excited-state lasing (ES1) in lasers with undoped and *p*-type doped QDs. Insert: power of GS-line vs current.

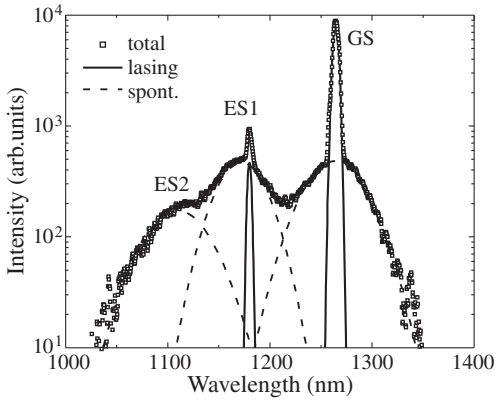

Fig. 4. Emission spectrum: squares — total, solid curves — lasing emission, dashed curves — spontaneous emission.

the excited-state level for the same holes. Such asymmetric distribution of holes and electrons, as it was proposed in [6], could explain the GS lasing quenching. As soon as the two-state lasing starts, recombination of ES1 electrons with holes prevails over recombination of GS electrons because of higher degeneracy of the ES1 electron level. We found that reasonable agreement between modeling results and experiment those can only be achieved under assumption that electron and hole relaxation rates into QDs are different.

Fig. 2 shows the calculated evolution of the GS power with pump current for various ratio of the hole-to-electron relaxation rates h. It is clearly seen that slower hole capture leads to earlier GS power dumping as well as to lower value of the GS peak power. The best agreement with our experimental data is found for h of about 0.75. Higher rate of electron relaxation (i.e. $h < 1$) is probably associated with higher electron velocity in the matrix/wetting layer.

3. Effect of *p*-type doping

It has been demonstrated that modulation doping of QD region with *p*-type impurities leads to improvement of temperature stability of the threshold current [7]. Therefore, one can expect certain effect of p-doping on the two-state lasing behavior as well.

We studied two 0.6-mm-long lasers (10 planes of InAs / InGaAs QDs) of identical design: one with undoped active region and another with modulation doping (10 acceptors per QD). Temperature dependences of threshold currents of the GS- and ES1-lasing are shown in Fig. 3. It is seen that at room temperature the GS-lasing thresholds nearly equals for both structures (0.35 A). At the same time, the ES1-lasing in the *p*-type doped laser starts at much higher current (5.5 A) as compared to the undoped counterpart (1.1 A). Moreover, maximum temperature of the GS-lasing also increases (from 55 to 100 °C). Insert of Fig. 3, where current dependence of the GS-power is shown, demonstrates that the GS spectral component in the *p*-type doped QD laser reaches noticeably higher peak power (3.6 W) as against the undoped laser (2.4 W).

4. Conclusion

Thus, it is demonstrated that the most probable reason for the GS lasing quenching is asymmetry of electron and hole carrier distributions. Additionally, difference in capture rates of electrons and holes has to be taken into consideration. We also found that the GS-component reaches its maximum beyond the threshold of the two-state lasing and that different groups of QDs are responsible for GS- and ES1-lasing in the two-state lasing regime. Finally, we demonstrated that *p*-type modulation doping of QDs leads to noticeable suppression of the ES1-lasing thereby resulting in enhancement of peak power of the GS spectral component.

Acknowledgements

The work is supported in different parts by Russian Ministry of Science and Education, Russian Foundation for Basic Research, Programs of Fundamental Studies of the Russian Academy of Sciences.

References

[1] A. E. Zhukov *et al*., *Semicond. Sci.Technol.* **18**, 774 (2003).
[2] A. Markus *et al*., *IEEE J.S.T.Q.E.* **9**, 1308 (2003).
[3] A. Markus, A. Fiore, *phys. stat. sol. (a)* **201**, 338 (2004).
[4] H.-M. Ji *et al*., *Jpn. J. Appl. Phys.* **49**, 072103 (2010).
[5] M. Sugawara *et al*., *J. Appl. Phys.* **97**, 043523 (2005).
[6] E. A. Viktorov *et al*., *Appl. Phys.Lett.* **87**, 053113 (2005).
[7] S. Fathpour *et al*., *Appl. Phys. Lett.* **84**, 5164 (2004).

20th Int. Symp. "Nanostructures: Physics and Technology"
Nizhny Novgorod, Russia, June 24–30, 2012

Electronic and optical properties of colloidal CdSe nanoplatelets

R. Benchamekh[1,2], J. Even[2], J.-M. Jancu[2], M. Nestoklon[3], S. Ithurria[4], B. Dubertret[4] and *P. Voisin*[1]

[1] Laboratoire de Photonique et Nanostructures, CNRS, 91460 Marcoussis, France
[2] FOTON, Université Européenne de Bretagne, INSA-Rennes and CNRS, Rennes, France
[3] Ioffe Physical-Technical Institute, St Petersburg, Russia
[4] Laboratoire de Physique et d'Etude des Matériaux, CNRS and ESPCI, 75231 Paris, France

Abstract. CdSe nanoplatelets show perfectly quantized thicknesses of few monolayers. They present a situation of extreme, yet well defined quantum confinement. We discuss their single particle properties in an advanced tight-binding model, and calculate Coulomb interactions in a suitable effective mass approach, including large self-energy corrections due to image-charge effects and exciton binding energies.

Introduction

CdSe nanoplatelets (NP) are new nano-objects that have been recently grown using colloidal methods [1]. They grow in the cubic zinc-blende (ZB) phase, are atomically flat over large lateral size up to hundred nanometers, and they display perfectly quantized thicknesses of a few monolayers. While the detailed mechanism of their growth is still a matter of investigations, early structural observations suggest that saturation of (001) surfaces with organic ligands prevents growth in this direction, while allowing lateral extension in other crystallographic directions. Remarkably, both (001) surfaces are terminated with Cd, hence nanoplatelets are not exactly stoechiometric: a n-monolayer platelet has n Se atomic planes and $n+1$ Cd planes. For this reason, nanoplatelets have the same D2d point group symmetry as ordinary common anion quantum wells. It seems that carboxylic ligands terminated with $C=O$ saturate the dangling bonds on Cd surface atoms, leading to an atomic layer of CdO on both sides. Importantly, this situation prevents (001) surface reconstruction and pinning of the Fermi level into mid-gap surface states. As a matter of fact, these nanoplatelets show very promising optical properties with strong and narrow emission lines at both room and cryogenic temperatures. From a point of view of electronic property modeling, they offer a unique opportunity to test theories in an extreme, yet perfectly quantized, quantum confinement regime. Besides, enhancement of exciton binding energy due to combination of 2D character, large in-plane electron effective mass and relatively small dielectric constant results in rather novel situation. Here, we discuss tight-binding (TB) calculations of the nanoplatelets electronic properties, and consider self-energy corrections due to image-charge effects as well as exciton binding energies in a simple effective mass model fitted to reproduce TB single particle states.

1. Single particle states

The extended-basis $spds^*$ tight binding model [2] is known as an efficient empirical-parameter full-band representation of semiconductor electronic properties. Parameter transferability from bulk to quantum heterostructures is very good. However the model has inherent parameter richness and its major difficulty is the solution of the inverse problem of finding TB parameters out of known features of the bulk band structure. This was done systematically for III-V and IV-IV semiconductors, but not yet for II-VI materials. We start with a parameterization of bulk CdSe obtained from an interpolation of ab-initio electronic structure and experimental band gaps in both wurtzite and cubic phases. Next, using this TB parameterization and a rough approximation of large conduction and valence band offsets for the Cd-O bonds, we model the NP electronic properties. Note that an atomistic method is definitely required to account for nanoplatelet stoechiometry defect. Main results are summarized in Table 1. Quantum confinement is comparable to bandgap, which is rather remarkable for a large gap quantum well-like structure. Yet it is much smaller than the naive evaluation $\hbar^2\pi^2/2mL^2$, due to strong non-parabolicity effect. Non-parabolicity also manifests itself in the in-plane dispersion showing a conduction band effective mass increasing strongly with decreasing thickness. Another striking feature is the large spin-splittings of both conduction and valence bands. CdSe band structure has specificities that are worth mentioning. Compared to III-Vs, the Cd and Se s and p orbitals are much deeper, hence the energy gap separating them from quasi-free electron states d and s^* is very large and the influence of the latter on X and L points is not sufficient to generate well defined zone edge energy valleys. A most important consequence is the low optical index resulting from the correspondingly large value of E1 and E2 bandgaps. For the same reason, valence band warping is small. For NPs, the quantum confinement is so large that a very unusual valence subband ordering prevails, with a H_2 level located below the split-off level SO_1.

Yet, this simple view of single particle states must be cor-

Table 1. Main properties of electron and hole single particle states. $E_{\rm conf}$ and $E_{\rm self}$ are the naked confinement energy and self energy correction due to image-charge effects, and m^* the in-plane effective mass. The bandgap of ZB CdSe is 1.761 eV.

Thickness		3	4	5	6	7
E_1	$E_{\rm conf}$ (meV)	1261	925	706	556	449
	$E_{\rm self}$ (meV)	261	203	166	140	122
	m^*/m_0	0.34	0.26	0.22	0.19	0.17
H_1	$E_{\rm conf}$ (meV)	210	145	107	83	66
	$E_{\rm self}$ (meV)	261	203	166	140	122
	$m^{*(100)}/m_0$	0.59	0.53	0.49	0.46	0.43
L_1	$E_{\rm conf}$ (meV)	327	247	197	162	136
	$E_{\rm self}$ (meV)	261	203	166	140	122
	$m^{*(100)}/m_0$	0.92	1.00	1.11	1.28	1.56

rected for self-energy effects due to interaction of electrons or holes with their electrostatic images, accounting for carrier induced surface polarization.These effects become large in such ultrathin layers, since (in a continuous media approach), the repulsive interaction potential diverges when carrier approaches the semiconductor-vacuum interface. We have calculated these effects in a simple effective mass approach [3–5], fitting the confinement mass in order to reproduce the TB single particle energies. This is a rough, still sensible approximation. As for the envelope functions, we consider a model with infinite barriers. The best fit to tight-binding amplitudes is obtained for a NP thickness slightly (a half monolayer) larger than the nominal thickness. We use the static dielectric constant (experimental value $\epsilon_r^0 = 10$), valid for particles with low kinetic energy. Electron and hole self-energies (see Table 1) sum up and increase the NP bandgap quite significantly.

2. Exciton binding energies

Large in-plane effective mass, strong 2D confinement and small dielectric constant obviously combine and produce strong exciton binding energies. In principle, the method of full configuration interactions could be used together with tight binding eigenstates of a finite lateral size platelet to fully model Coulomb interaction. This computationally difficult approach is far beyond the scope of the present contribution. Here, we adopt the much simpler effective mass scheme [3–5] in order to evaluate the binding energy of an electron-hole pair, i.e. we restrict ourselves to the main, direct term of Coulomb interaction. As in the previous section, confinement mass is fitted to reproduce TB confinement energies, and we use the tight-binding in-plane effective masses for the in-plane motion. In a first calculation, we use the experimental bulk value $\epsilon_r^0 = 10$ for the dielectric constant. Calculated binding energies for various NP thicknesses are shown in Table 2. The remarkably large enhancement over the CdSe bulk Rydberg (10 meV) is actually governed by three factors: i) the large (>2) enhancement of electron effective mass; ii) the dimensionality reduction and iii) the electron-hole image-charge interactions. In order to isolate the dimensionality effect, we calculate the 3D Rydberg using the electron and hole in-plane effective masses, and compare it with the exciton binding energies in absence of image-charge effects. We thus find that the enhancement due to reduced dimensionality is fairly constant for the investigated thicknesses, being in the range 2.5−2.7. For the exciton ground state, the attractive effect of electron-hole image charges partly compensate the dominant repulsive effect of single particle self-energies, so that the ground transition energy is not strongly affected by Coulomb effects [1,3–5]. However, for excited states nS, the effect of self-energies prevails more and more as n increases: the exciton binding energy is considerably enhanced because *the bandgap itself is increased*. Finally, we point that the calculated binding energies are much larger than optical phonon energies in CdSe (∼20 meV). This implies that a dielectric constant closer to $\epsilon_r^\infty = 6$ should be used to calculate exciton ground state [6]. Corresponding results are also shown in Table 2.

Table 2. H1-E1 exciton binding energies (in meV) for different NP nominal thicknesses.

Thickness	3	4	5	6	7
without self $\epsilon_r^0 = 10$	82	66	56	49	44
without self $\epsilon_r^\infty = 6$	211	170	144	126	114
including self $\epsilon_r^0 = 10$	353	270	235	200	171
including self $\epsilon_r^\infty = 6$	412	329	265	241	212

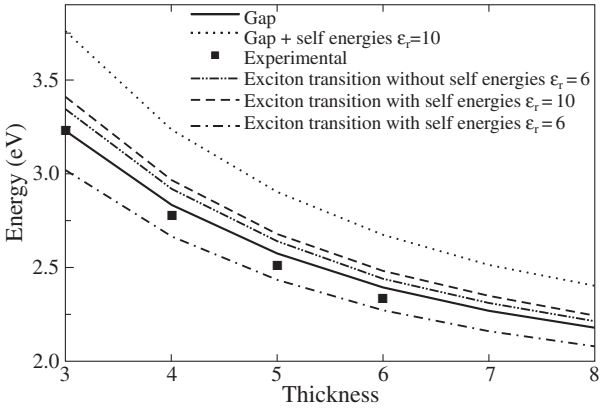

Fig. 1. H1-E1 optical transition energies in various approximations, for different NP thicknesses.

Full calculation of the exchange splitting between bright (Jz=1) and dark (Jz=2) states of the exciton is beyond the scope of this paper, but since the short range contribution scales with the exciton binding energy, we may also expect considerable enhancement of the exciton exchange splitting up to a few meV range. Finally, the calculated excitonic transitions energies are compared in Fig. 1 with experimental results taken from ref. [1]. We used room temperature absorption spectra and added 95 meV to account for the temperature dependence that was actually measured in luminescence.

While the general agreement is fairly good, some discrepancies still exist. They may partly be due to over-simplifying assumptions like the effective mass approach and constant dielectric function for Coulomb effects (single particle self-energies and excitonic effects), which are extremely large in this system. Atomistic calculations of these Coulomb effects are on agenda. Better account of Cd-O bonds, and more generally of the organic ligand contribution to electronic structure is also to be examined. On the other side, low temperature spectroscopic investigations of single nano-objects are highly desirable in order to delineate the limits of nanoplatelets ideality.

Acknowledgements

This work was partly supported by Triangle de la Physique "CAAS" and by ANR-10-04 "PEROCAI".

References

[1] S. Ithurria *et al*., *Nature Materials* **10**, 936 (2011).
[2] J.-M. Jancu *et al*., *Phys. Rev. B* **57**, 6493 (1998).
[3] M. Kumagai *et al*., *Phys. Rev. B* **40**, 12359 (1989).
[4] E.A. Muljarov *et al*., *Phys. Rev. B* **51**, 14370 (1995).
[5] M. Mosko *et al*., *Phys. Rev. B* **55**, 15416 (1997).
[6] R.-T. Senger and K.K. Bajaj, *Phys. Rev. B* **68**, 045313 (2003).

20th Int. Symp. "Nanostructures: Physics and Technology"
Nizhny Novgorod, Russia, June 24–30, 2012

Formation of luminescent Si nanodots induced in Si/SiO_2 heterostructures by irradiation with swift heavy ions

G. A. Kachurin[1], V. A. Volodin[1,2], S. G. Cherkova[1,2], D. V. Marin[1,2], A. H. Antonenko[1], A. G. Cherkov[1,2] and V. A. Skuratov[3]

[1] A.V. Rzhanov Institute of Semiconductor Physics SB RAS, 630090 Novosibirsk, Russia
[2] Novosibirsk State University, 630090 Novosibirsk, Russia
[3] Joint Institute for Nuclear Research, 141980 Dubna, Russia

The discovery of strong luminescence from the quantum-sized Si nanocrystals (Si-ncs) stimulates research into the processes of their formation and modification. Usually Si-ncs are formed via self-organization in the Si-rich SiO_2 layers during furnace annealing. However, this way of formation results in a relatively broad size distribution of the synthesized Si-ncs. Moreover, the size and density of the quantum dots cannot be controlled independently. To make the Si-ncs formation more predictable the layer-by-layer deposition of the nanometer-thick amorphous Si and SiO_2 followed by a high temperature annealing was proposed. Unfortunately, the thinner is a nanolayer the higher temperatures are needed for its crystallization; therefore the methods which allow stimulation of the structural transformations would be of great interest.

We studied the influence of swift heavy ions (SHI) on synthesis of the silicon quantum dots in stacks of the ultrathin Si/SiO_2 multilayers. When SHI penetrate in solid-state targets, their stopping in the near-surface layers occurs predominantly by the ionization losses. If the deposited energy density exceeds ∼1 keV/nm, tracks may be forming with the nm-scale diameters, where the carrier concentrations may reach $\sim 10^{22}$ cm^{-3}. The temperature inside the tracks may exceed 5000 K for 10^{-13}–10^{-11} s. Thus, the structural transformations may be stimulated either by heat or by ionization. Six pairs of the 7–8 nm-thick amorphous Si and 10–12 nm-thick SiO_2 layers have been deposited on the crystalline Si substrates. The layers were irradiated with 167 MeV Xe ions to the doses ranging between 10^{12} and 10^{14} cm^{-2}. The ionization and nuclear losses of the ions were ∼14.5 keV/nm and ∼0.3 displacements/nm, respectively. Photoluminescence (PL), optical FTIR absorption, Raman scattering and cross-sectional high resolution electron microscopy were used for the characterizations. It was found, that irradiation made the the Si-SiO_2 borders less sharp and in the FTIR spectra the absorption at 1090 cm^{-1}, belonging to Si-O bonds of perfect SiO_2 decreased, while the 1040 cm^{-1} line, usually ascribed to the damaged oxide, increased. Broad yellow-orange photoluminescence band appeared in the irradiated layers, which intensity grew with the ion dose. Such emission is traditionally considered as the non-crystalline Si nanoinclusions in SiO_2. The electron microscopy supported that idea, revealing an appearance of dark 3–5 nm size spots. After annealing the SiO_2 network restored and the photoluminescence strongly increased with a shift of maximum intensity to ∼780 nm, typical wavelength region for emission from Si nanocrystals (Fig. 1). It should be stressed, that its post-annealing intensity was proportional to the SHI dose (Fig. 2). The highest intensity was observed after 1100 °C anneal. At the same time, the Raman spectroscopy evidenced the disappearance of the amorphous Si phase (region near 480 cm^{-1}) with growing SHI dose. It is concluded, that irradiation with SHI stimulates the formation of Si quantum dots in SiO_2. The possible mechanisms of the stimulation are considered.

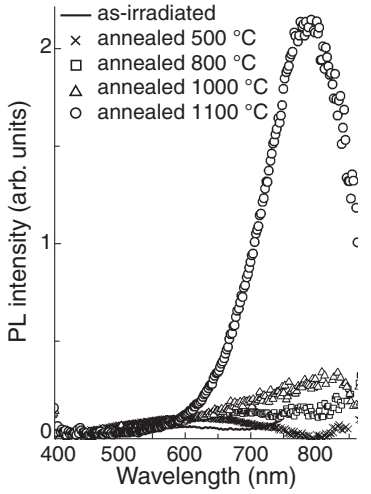

Fig. 1. PL intensity after irradiation with 3×10^{13} cm^{-2} Xe ions and subsequent annealing at the temperatures of 500–1100 °C.

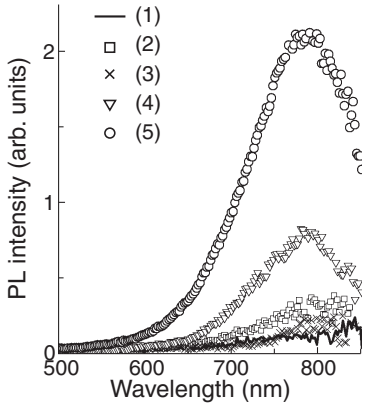

Fig. 2. PL spectra before (1) and after irradiation with Xe ions and subsequent annealing at 1100 °C. Xe doses, 10^{12} cm^{-2}: 2 — 1, 3 — 3, 4 — 10, 5 — 30.

20th Int. Symp. "Nanostructures: Physics and Technology"
Nizhny Novgorod, Russia, June 24–30, 2012

Self-diffraction of laser beams in the case of resonant excitation of excitons in colloidal CdSe/ZnS quantum dots

V. Dneprovskii, *A. Smirnov* and M. Kozlova
Physics Faculty of M.V. Lomonosov Moscow State University, 119991 Moscow, Russia

Abstract. Self-diffraction of two types has been discovered in the case of resonant excitation of excitons in CdSe/ZnS quantum dots (highly absorbing colloidal solution) by two intersecting high-power second harmonic beams of mode-locked laser with picosecond pulse duration. The physical processes responsible for the nonlinear optical properties of CdSe/ZnS quantum dots and for the arising self-action effects are discussed.

Introduction

Self-diffraction is the self-action effect of light beams that spread in the medium whose properties depend on the light action. Two types of self-action process may arise in resonantly absorbing medium. 1. In the case of efficient nonlinear absorption (saturation of optical transition) the high-power laser beam may format the transparency channel, the induced diaphragm and thus the beam's self-diffraction may arise. 2. Due to self-action of two intersecting laser beams in nonlinear medium periodic modification of dielectric susceptibility may arise as a sequent of cubic nonlinearity. Thus induced diffraction grating (in the case of complicated wave fields it is called holographic) may be created and the beams in new directions arise. Self-diffraction in this case may be also interpreted as a frequency degenerate four-wave nonlinear interaction.

1. Experimental details

The scheme of two-beam's excitation of the 1 mm cell with colloidal solution of CdSe/ZnS QDs and the induced output beams are shown in Fig. 1. Colloidal QDs were excited by two equal intensity intersecting beams of the second harmonic ($\lambda = 532$ nm) of mode-locked Nd:YAG laser with 30–35 ps pulse duration. Transient grating technique allowed to measure the duration of exciting laser pulse by recording the self-diffracted signal as a function of delay between two identical pulses that induce the grating in absorbing medium. To realize resonant excitation of excitons (the basic electron-hole transition) QDs of appropriate size (radius) were selected by their measured transmission spectra (Fig. 2) Special photo camera was applied to register the discovered output beams and their cross-section intensity distribution.

2. Results and discussion

The diffraction rings typical for Fresnel diffraction arise for penetrated through the cell with QDs beams k_1 and k_2 that hold the direction of incident beams' spreading. Their identical cross-section intensity distribution with maximum or minimum in the centre and different number of rings depends on the intensity of the incident beam (Fig. 3). This distribution is partly masked by bright spot that arise because of the linear 3% transmission of the cell with colloidal solution of CdSe/ZnS QDs. The revealed radiation intensity distribution of k_1 and k_2 beams can be explained by the creation of transparency channel in the sell due to propagation of high-power beams resonantly exciting the basic $1S_{3/2}(h) \rightarrow 1S(e)$ electron-hole transition in CdSe/ZnS QDs at the doubled laser frequency.

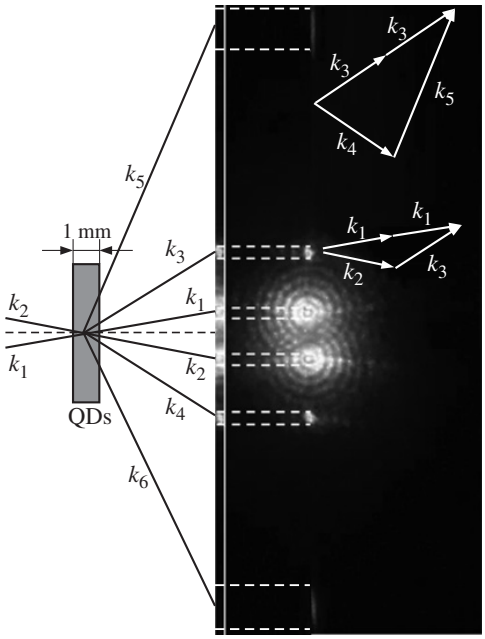

Fig. 1. The scheme of two-beam's excitation of the cell with colloidal solution of CdSe/ZnS QDs and the induced output beams.

With penetration into colloidal solution of QDs the light beam with Gaussian cross section distribution of the intensity loses its low-intensity peripheral parts due to stronger absorption than at the center on its axis (beam's "stripping"). Thus strip effect results in a profile change of the beam, whose edges transform from smooth into sharp ones, and in creation of induced "rigid" diaphragm.

The formation of rings with a maximum or a minimum in the centre (Fig. 3) may be attributed to Fresnel diffraction from a circular induced aperture with diameter depending on the light intensity. Apart from the state filling effect [1] Stark shift of the exciton transition and heating of the cell with QDs can cause the change of absorption and influence at the formation of transparency channel. At high excitation either an electron or hole can be trapped at the surface of QD and ionize it. The revealed red shift of the luminescence spectra increasing with exciting pulse's intensity growth (Fig. 4) is an evidence of essential influence of Stark effect at the transparency channel creation. In CdSe/ZnS QDs the long wavelength shift of the LO-phonon assisted luminescence spectrum relatively to the transmission minimum (Fig. 2) arises because of crystal field in hexagonal lattice, weak deviation from the spherical shape and electron-hole exchange interaction. The shift due

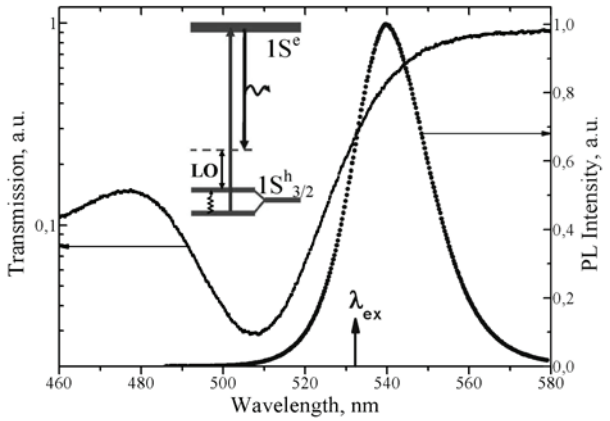

Fig. 2. The transmission and photoluminescence spectra of colloidal solution of CdSe/ZnS quantum dots of (2.4 ± 0.3) nm radius and 10^{17} cm^{-3} density. The transitions are shown schematically in insert.

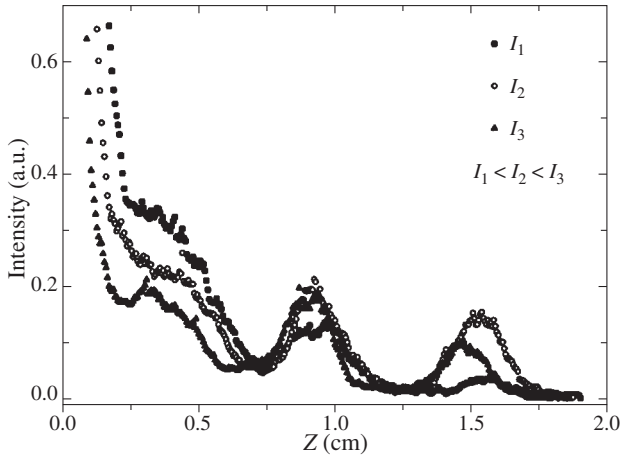

Fig. 3. The dependence of diametrical intensity distribution of diffracted and output beams on the intensity of the incident beam formatting the transparency channel.

to the latter process dominates and depends upon the radius of QD as R^{-3} [2]. The revealed weak red shift of the maximum of luminescence spectrum with growing intensity of excitation (Fig. 4) may be explained by the dependence of electron-hole exchange interaction on the QD's radius. QDs have significant size dispersion (about 20%). The pulse of the laser second harmonic excites preferentially ("burns") QDs of appropriate size whose basic electron-hole transition is at resonance with exciting radiation. Stark effect in the induced electric field (the red shift of the absorption spectrum) provokes excitation of QDs with decreasing diameter from the ensemble of QDs. Thus the dominating size dependence of electron-hole exchange interaction and the dependence of exciton absorption spectrum Stark shift on the intensity of excitation (Stark shift compared with half width of transmission spectrum in Fig. 2) may explain the revealed red shift of the luminescence spectrum maximum (Fig. 4). It is impossible to explain this red shift of the basic exciton transition by heating of the cell with QDs. Such shift must be accompanied by boiling of colloidal solution.

Additional output k_3 and k_4 beams that we attribute to the self-diffracted beams and beams k_5 and k_6 that arise due to four wave mixing of powerful beams k_3 and k_4 were discovered.The beams k_1 and k_2 (Fig. 1) intersecting in the cell with colloidal solution (ϑ is the angle between them) create diffrac-

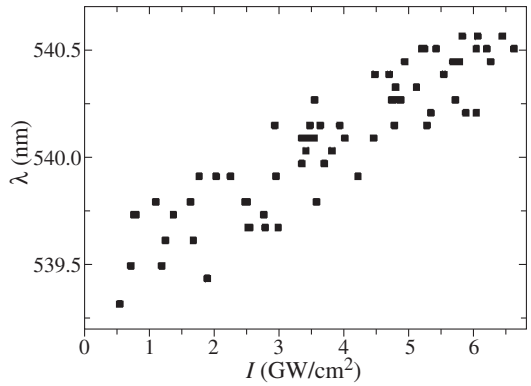

Fig. 4. The long-wavelength shift of luminescent spectrum maximum on the maximum intensity of exciting pulse.

tion grating with period $\Lambda = \lambda/(2 \sin \vartheta/2)$. Thus k_3 and k_4 are self-diffracted beams — the diffraction of the waves that create grating. It is convenient to define their direction of spreading using four-wave interaction procedure as shown in Fig. 1. The direction of spreading of the discovered k_5 and k_6 beams (Fig. 1) allows attributing them to self-diffraction of powerful beams k_3 and k_4 that in their turn create new diffraction grating.

Acknowledgements

This work was partly supported by Russian Foundation for Basic Research (grant 11-02-00424-a).

References

[1] V. Dneprovskii, D. Kabanin, V. Lyaskovskii, T. Wumaier, and E. Zhukov, *Phys. Stat. Sol. (c)* **5**, 2503 (2008).

[2] M. Nirmal, D. Norris, M. Kuno, M. Bawendi, A. L. Efros, and M. Rosen, *Phys. Rev. Lett.* **75**, 3728 (1995).

20th Int. Symp. "Nanostructures: Physics and Technology"
Nizhny Novgorod, Russia, June 24–30, 2012

Indirect and direct excitons and microcavity polaritons in AlGaAs and InGaAs coupled quantum wells

E. A. Muljarov[1,2] and K. Sivalertporn[1]

[1] School of Physics and Astronomy, Cardiff University, The Parade, CF24 3AA Cardiff, UK
[2] General Physics Institute, RAS, Vavilova 38, Moscow 119991, Russia

Abstract. We present an accurate theoretical approach to the calculation of excitons and polaritons in coupled quantum wells (CQWs) in an applied electric field. We calculate the energies and oscillator strengths of the exciton ground and excited states, as well as the absorption spectra of AlGaAs and InGaAs CQWs. We also calculate the reflectivity spectra of microcavity-embedded asymmetric 10–4–10 nm InGaAs CQW structures. Excitons in such structures show a remarkable anticrossing under applied voltage and strong redistribution of the dipole moment at the resonance tunneling condition. We demonstrate tunability of polariton properties and efficient on/off switching of the exciton-light strong coupling achieved by means of the applied electric field.

Introduction

Semiconductor coupled quantum wells (CQWs) have attracted much attention in recent years due to formation of long-lived excitons in such structures in an applied electric field. Very recently, CQWs have been embedded into Bragg-mirror microcavities to achieve an efficient dipole moment exchange and enhancement at the resonant tunneling condition [1]. It has been argued that such a special type of voltage-tuned exciton polaritons can be used for optical nonlinearities and microcavity polariton lasing achieved at much lower threshold powers.

Generally, a CQW structure consists of two quantum wells separated by a barrier layer. For a sufficiently thin barrier, the tunneling of carriers through the barrier makes the two wells electronically coupled to each other. As a results, an electron (hole) can either reside in one of the two wells or its wave function is distributed between both wells. In the case of Coulomb bound electron and hole residing in the same well, they form a direct exciton. If, however, they are located in different wells, an indirect exciton is created.

Different theoretical approaches have been used to calculate indirect and direct excitons in CQWs, ranging from variational methods to ab initio calculations [2] and discretization of the exciton Schrödinger equation in the momentum space [3]. In this contribution, we present a novel approach [4] which provides us with a more accurate and straightforward way of calculation of CQW exciton ground and excited states and the exciton absorption spectrum in the presence of an electric field. Our formalism is based on expanding the exciton wave function into electron-hole pair states and solving a radial matrix Schrödinger equation in the real space. Moreover, we extend our method to include also the exciton-photon coupling in microcavity-embedded multiple-CQW structures. The calculated reflectivity spectra demonstrate remarkable polariton anticrossing and switching similar to those recently observed in Ref. [1].

1. Exciton States

We have calculated exciton states in 8–4–8 nm symmetric GaAs/$Al_{0.33}Ga_{0.67}As$ and 10–4–10 nm asymmetric $In_{0.08}Ga_{0.92}As$/GaAs/$In_{0.1}Ga_{0.9}As$ CQW structures in the presence of the external electric field. Results of this calculation, the exciton energies and oscillator strengths, are shown in Figs. 1 and 2, respectively. In the case of the symmetric AlGaAs CQW structure studied in Refs. [5, 6], a crossover of the exciton ground state (X-GS), from direct to indirect exciton, is well seen at around 5 kV/cm (Fig. 1). The oscillator strength of the X-GS has the maximum at zero field and quickly decreases with increasing electric field. At the same time the properties of the brightest direct exciton excited state (X-ES) remain almost unaffected in a wide range of applied voltages, since this state turns out to be Coulomb decoupled from the X-GS [4].

Such a bright decoupled state (as X-ES in Fig. 1) is absent in the spectrum of the asymmetric InGaAs CQW structure. Though, a similar anticrossing takes place at the resonance tunneling condition and a similar crossover of the X-GS, from direct exciton (DX) to indirect exicton (IX), is observed, see Fig. 2. In fact, at low electric fields, the electron ground state is located in the left well, while its first excited state is confined in the right well having a higher energy. An increasing electric field compensates the asymmetry in the conduction band, giving rise to formation of symmetric and antisymmetric electron states at around 12 kV/cm [4]. This explains the observation

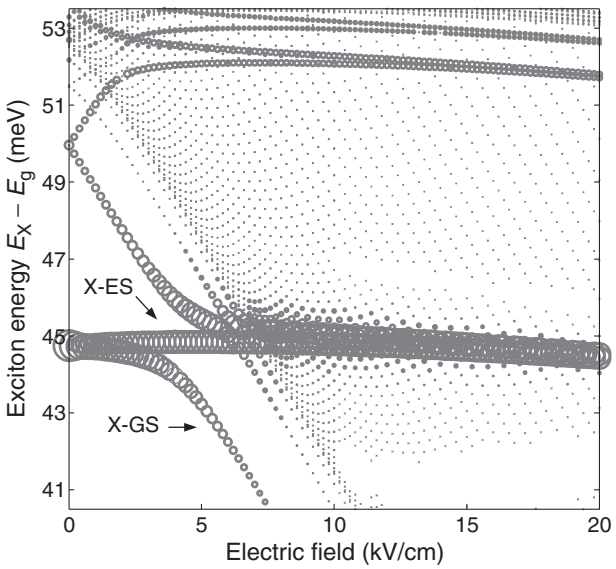

Fig. 1. Exciton energies and oscillator strengths (circle area) in the symmetric 8-4-8-nm AlGaAs CQW as functions of the electric field.

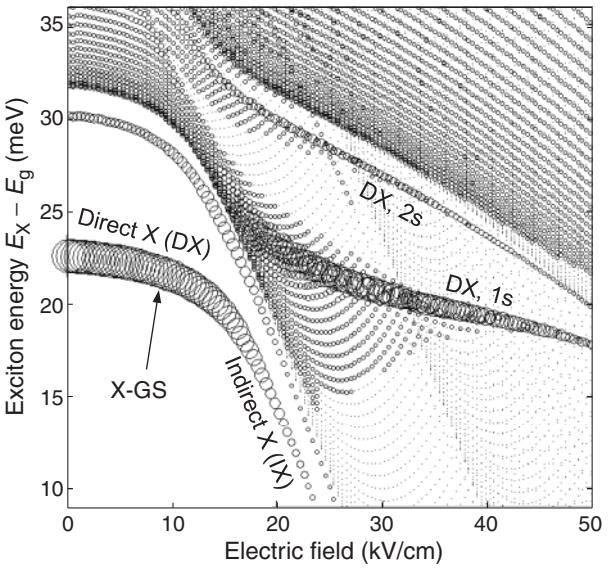

Fig. 2. Exciton energies and oscillator strengths (circle area) in the asymmetric 10-4-10-nm InGaAs CQW as functions of the electric field.

of a similar Coulomb-induced anticrossing at approximately 16–18 kV/cm.

2. Polaritons and reflectivity spectra

We concentrate on a structure with four asymmetric InGaAs CQWs placed in the antinodes of the electro-magnetic field inside $5\lambda/2$ cavity [1]. It provides conditions for the exciton-photon strong coupling regime and formation of polaritons. We study these polaritons by calculating the reflectivity spectra at different values of the electric fields. We solve coupled Maxwell's and material equations in order to describe electro-magnetic waves propagating through the microcavity. The nonlocal excitonic susceptibility in the embedded CQWs is calculated accurately using our approach and is incorporated in the scattering matrix formalism [7]. Results are shown in Fig. 3 for two different positions of the cavity mode (dashed vertical lines) creating different detuning with respect to the bare exciton modes (red circles). For the detuning in Fig. 3(a), three exciton modes shown in Fig. 3, namely X-GS and two bright DX (1*s* and 2*s*) modes, are all strongly coupled to cavity. The polariton states well seen as dips in the reflectivity exhibit multiple anticrossings. Owing to the tunneling and Coulomb interaction, decrease (increase) of the oscillator strengths of the excitonic mode reduces (enhances) the coupling to the cavity which effectively switches off (on) the strong coupling regime. This mechanism of on/off switching of the exciton-light coupling is much sharper in the case considered in Fig. 3(b) in which the red-shifted cavity mode is considerably detuned from the X-GS. The properties of polaritons in such a system change quite abruptly at around 19 kV/cm, in agreement with the experimental observation [1]. Here, the strong coupling to the cavity mode is balancing between remote bright DX (located far in the excitonic continuum) and close but optically weak IX (with the energy strongly depending on the electric field).

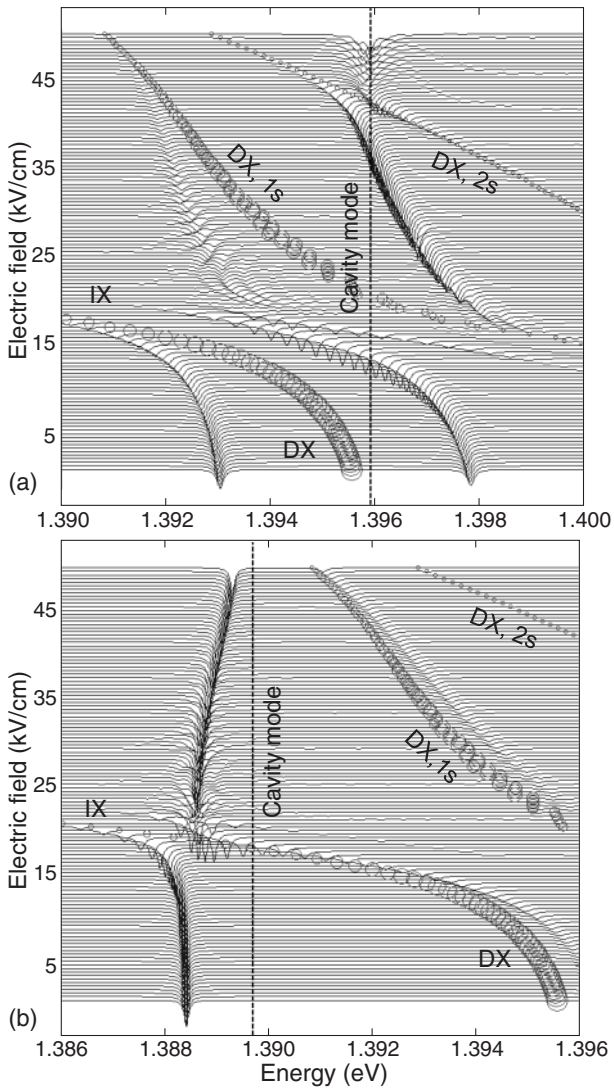

Fig. 3. Field dependent reflectivity spectra in the microcavity-embedded asymmetric 10-4-10-nm InGaAs CQW structure, with the cavity mode at (a) 1.3897 eV and (b) 1.3959 eV (black dashed lines). Exciton ground state exhibiting DX-IX transition and two brightest direct exciton (DX) 1*s* and 2*s* states located far in the excitonic continuum are shown by open red circles.

References

[1] G. Christmann, A. Askitopoulos, G. Deligeorgis, Z. Hatzopoulos, S. I. Tsintzos, P. G. Savvidis and J. J. Baumberg, *Appl. Phys. Lett.* **98**, 081111 (2011).

[2] M. H. Szymanska and P. B. Littlewood, *Phys. Rev. B* **67**, 193305 (2003).

[3] S. C. Arapan and M. A. Liberman, *J. Lumin.* **112**, 216 (2005).

[4] K. Sivalertporn, L. Mouchliadis, A. L. Ivanov, R. Philp and E. A. Muljarov, *Phys. Rev. B* **85**, 045207 (2012).

[5] L. V. Butov, A. C. Gossard, and D. S. Chemla, *Nature* **418**, 751 (2002).

[6] A. T. Hammack, L. V. Butov, J. Wilkes, L. Mouchliadis, E. A. Muljarov, A. L. Ivanov and A. C. Gossard, *Phys. Rev. B* **80**, 155331 (2009).

[7] S. G. Tikhodeev, A. L. Yablonskii, E. A. Muljarov, N. A. Gippius and T. Ishihara, *Phys. Rev. B* **66**, 045102 (2002).

20th Int. Symp. "Nanostructures: Physics and Technology"
Nizhny Novgorod, Russia, June 24–30, 2012

Quantum dots in heterosystem GaSb/AlAs

T. S. Shamirzaev, D. S. Abramkin, A. K. Gutakovskii and M. A. Putyato
A.V. Rzhanov Institute of Semiconductor Physics, SB RAS, Lavrentieva 13, 630090 Novosibirsk, Russia

Abstract. Self-assembled quantum dots (QDs) in heterosystem GaSb/AlAs have been studied by transmission electron microscopy, steady-state and transient photoluminescence (PL). A strong intermixing of materials results in fabrication quaternary alloy QDs in AlAs matrix. The band alignment of the QDs is shown to be of type I with the lowest electronic state at the indirect X_{XY} minimum of the conduction band.

Introduction

Self assembled semiconductor quantum dots (QDs) are currently considered for fabrication lot of various devices. Among various QDs the system GaSb/AlAs is considered as perspective for development of memory units. Marent *et al* predict that the unit on the basis of the GaSb/AlAs QDs should have a storage time of more than 10^6 years [1]. Besides, we calculate recently that the QDs have band alignment of type I with the lowest electron states at the indirect minimum of the conduction band [2]. Such energy structure provides long exciton lifetime [3] that together with expected long exciton spin relaxation time that makes the QDs promising candidates for the potential applications in spin memory devices. However, the best of our knowledge, experimental study of atomic structure and energy spectrum of QDs self assembled in the GaSb/AlAs system have not be performed yet.

In this report, we present the results of a first study of the structure and energy spectrum of the novel self-assembled GaSb QDs in AlAs matrix by transmission electron microscopy and photoluminescence (PL) together with computational work.

1. Experimental

The studied self-assembled QDs were grown by molecular-beam epitaxy on semi-insulating (001)-oriented GaAs substrates. The structures have one QD sheet sandwiched between 50-nm-thick AlAs layers grown on top of a 200-nm-thick GaAs buffer layer. The QDs forms at a temperature of 450 °C. A 12-nm-thick GaAs cap layer protects the AlAs layer against oxidation. The atomic structure of the QDs was studied by means of transmission electron microscopy employing a JEM-4000EX operated at 400 keV. Steady-state PL was excited by a He-Cd laser ($\hbar\omega = 3.81$ eV) with power densities in range of 0.1–25 W cm^{-2}. Transient PL was excited by a pulsed N2 laser ($\hbar\omega = 3.68$ eV) with a pulse duration of 7 ns and a peak energy density of 5 mJ cm^{-2}. The PL was detected with a double diffraction grating spectrometer equipped with a cooled photomultiplier operated in the photon counting mode.

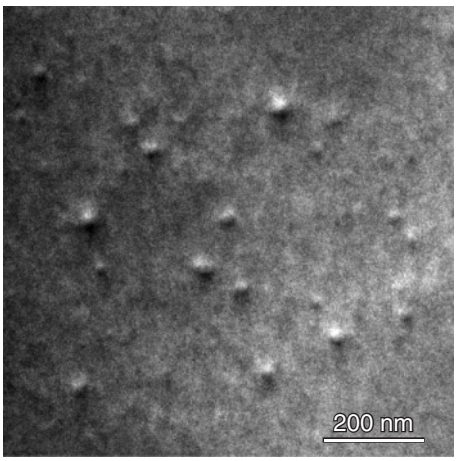

Fig. 1. Transmission electron microscopy plane view image of the GaSb/AlAs QDs.

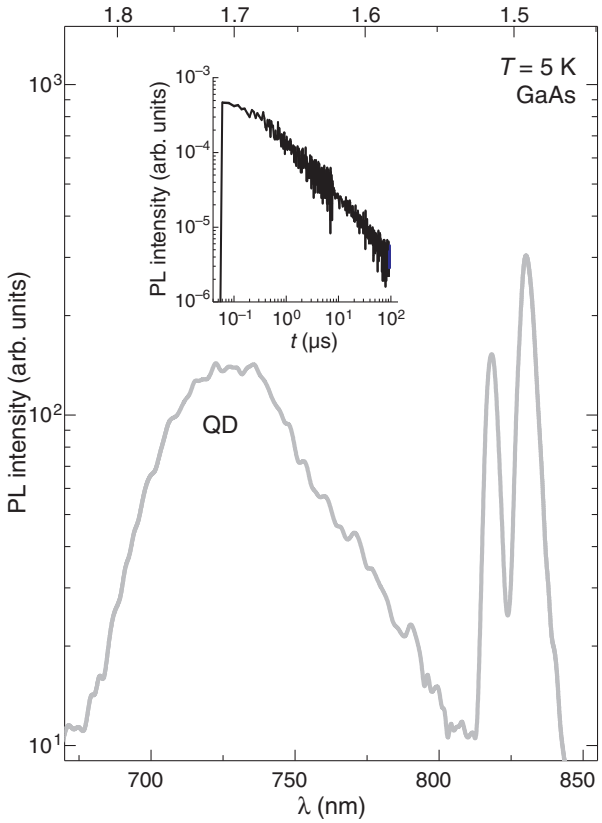

Fig. 2. Low temperature PL spectrum of the GaSb/AlAs heterostructure with QDs. Insert shows transient PL of the QDs.

2. Results

Figure 1 demonstrates a transmission electron microscopy plane view image of GaSb/AlAs structure with the QDs. One can see coherently strained QDs in the image. The number and diameters of the QDs are estimated within an area of 4 μm^2. The density of the QDs is about 1.5×10^9 cm^2 that is much less than typical value obtained for QDs grown with close condition in system InAs/AlAs (1.2×10^{11} cm^2) with similar lattice mismatch (about 7%) [4]. The QD-diameter have typical diameter of about 36 nm that is also larger than that for the InAs/AlAs

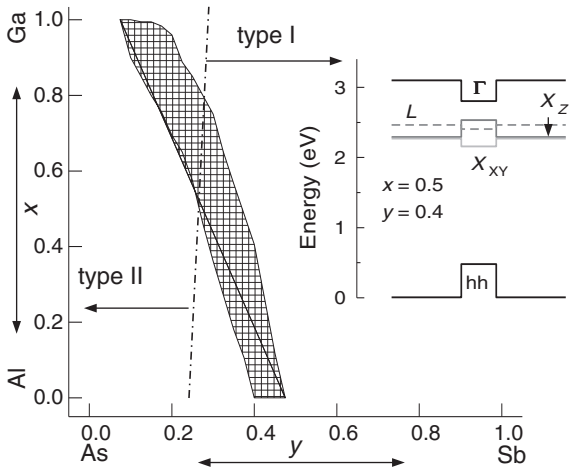

Fig. 3. Filled area marks compositions (x, y) corresponded to electron-hole optical transition in $Ga_xAl_{1-x}Sb_yAs_{1-y}$/AlAs QDs lied in the range of 1.65–1.75 eV. An example of the type I energy spectrum presents in the insert.

QDs with similar lattice mismatch [4].

The low density and relatively large size of GaSb/AlAs QDs suggest high value of adatoms diffusion length. As a rule, such growth condition favours to materials intermixing, therefore, the QDs can contain an alloy instead pure GaSb. The PL data confirm the intermixing. Actually, a band related to exciton recombination in the PL spectrum of the structure with the QDs (see Fig. 2) has energy of about 1.7 eV, while calculation predicts 0.7 eV for electron-hole optical transition energy in GaSb/AlAs heterostructure [2]. Using the band structure parameters of GaSb, AlSb, GaAs and AlAs taken from Ref. 5 we use a linear approximation between the parameters and calculate the energy structure of $Ga_xAl_{1-x}Sb_yAs_{1-y}$/AlAs heterostructure as a function of compositions x and y. Comparison of the calculated energy of electron — heavy hole optical transition in the heterostructures with experimental data allows us to estimate composition of the alloy inside the QDs. Note that calculation does not describe the experimental data at $y = 1$ with any value of the x parameter. Therefore the QDs in any case contain arsenic. The best agreement between calculation and experimental data is obtained for (x, y) values shown in Fig. 3. One can see that in contrast to GaSb/GaAs QDs, which have band alignment of type II [6], our QDs can have type II or type I band alignment with lowest conduction band states belonging to the indirect X minimum of the conduction band (see the insert to Fig. 3) depending on composition. In order to check the energy structure of the QDs, we measured transient PL and steady-state PL spectra as a function of excitation power density. Indirect structure of the QD conduction band gap is evidenced by long PL decay time, which lies in microsecond range as one can see in insert to Fig. 2. The QD PL band does not demonstrate any blue shift with an increase in the excitation power density, which is proper for any structures with type II band alignment [7].

3. Conclusion

We demonstrate that QDs self assembled in GaSb/AlAs heterosystem consist of $Ga_xAl_{1-x}Sb_yAs_{1-y}$ alloy and have the band alignment of type I with the lowest conduction band state at the indirect X_{XY} minimum of the conduction band.

Acknowledgements

This work was supported by the RFBR (Project No. 10-02-00240) and by the Dynasty Foundation.

References

[1] A. Marent *et al.*, *Appl. Phys. Lett.* **91**, 242109 (2007).
[2] T. S. Shamirzaev *Semiconductors* **45**, 96 (2011).
[3] T. S. Shamirzaev *et al.*, *Phys. Rev. B* **84**, 155318 (2011).
[4] T. S. Shamirzaev *et al.*, *Phys. Rev. B* **78**, 085323 (2008).
[5] I. Vurgaftman *et al.*, *J.Appl.Phys.* **89**, 5815 (2001).
[6] F. Hatami *et al.*, *Appl. Phys. Lett.* **67**, 656 (1995).
[7] N. N. Ledentsov *et al.*, *Phys. Rev. B* **52**, 14058 (1995).

20th Int. Symp. "Nanostructures: Physics and Technology"
Nizhny Novgorod, Russia, June 24–30, 2012

Surface morphology investigation in Ge/GeSi/Ge heterosystem with alternating layers

V. A. Timofeev, A. I. Nikiforov, S. A. Teys, A. K. Gutakovsky and O. P. Pchelyakov
A.V. Rzhanov Institute of Semiconductor Physics, SB RAS, Lavrentieva 13, 630090 Novosibirsk, Russia

Abstract. In addition to the (2×1) superstructure for a Ge film grown on Si(001), the quasi-equilibrium is characterized by the formation of $(2 \times n)$ reconstruction. We measured a n number for all layers of Ge/Ge_xSi_{1-x}/Ge heterosystem using our software with respect to the video recording of reflection high-energy electron diffraction (RHEED) pattern during growth. The n number reaches a minimum value of about 8 for clear Ge layer, whereas for Ge_xSi_{1-x} films the n number from 8 to 14 is increased. The presence of a thin strained film of the Ge_xSi_{1-x} caused not only the changes in critical thicknesses of the transitions, but also affected the properties of the germanium nanocluster array for top Ge layer. Based on the RHEED data the hut-like island form which hasn't been previously observed by us between the hut and dome islands has been detected. This form of islands appear on the phase diagram in the range from $x = 0.25$ to $x = 0.5$. The data on the growth of Ge/Ge_xSi_{1-x}/Ge heterostructures with the uniform array of islands (the standard deviation about 10 percentage) in the second layer of the Ge film have been received.

Introduction

The Ge/Ge_xSi_{1-x}/Ge heterosystems with alternating layers of quantum dots and solid solution layers are of great practical interest for obtaining of mid-infrared photodetectors based on intraband transitions [1]. The modification of the energy diagram is due to changes both composition and thickness of the Ge_xSi_{1-x} film, as well as the growth temperature. In such heterostructures optical transitions between the bound states in a quantum dot and delocalized states in the plane of the two-dimensional sub-bands of the solid solution film have been realized. The system investigated is considered as a model for understanding the processes of island formation and evolution during Stranski–Krastanov growth mode [2]. First Ge layer initially grows layer by layer, creating several monolayers of wetting layer, because Ge has a lower surface energy than Si. The effect on the surface morphology produced by the epitaxial growth of Ge on Si(001) is a rapid change of the surface reconstruction. In addition to the (2×1) superstructure for a Ge film grown on Si(001), the quasi-equilibrium is characterized by the formation of $(2 \times n)$ reconstruction [3]. The $(2 \times n)$ reconstruction begins to appear to release the accumulated misfit strain [4]. Since strain increases with increasing film thickness, other modes of strain relaxation become significant. The 2D–3D transition begin to be obtained at the Ge thickness $\geq$3 ML. The critical thicknesses of 2D–3D and "hut"-"dome" morphological transitions for Ge and Ge_xSi_{1-x} films were earlier measured. Further growth second and third layers was chosen taking into account the obtained critical thicknesses.

1. Experimental

A molecular beam epitaxy (MBE) installation Katun-C supplied with two electron beam evaporators for Si and Ge used for synthesis; dopants (Sb and B_2O_3) were evaporated from effusion cells. Analytical equipment of the chamber included a quadrupole mass spectrometer, a quartz thickness monitor and a high energy electron (20 kV) diffractometer. Diffraction patterns were monitored during the growth using a CCD camera on line with a PC. The software allowed us to monitor both the whole images and chosen fragments of the diffraction patterns at the rate of 10 frames/s. Ge and GeSi layers grew at the rate of 10 ML/min. The Ge and Si growth rates were controlled using quartz thickness monitors. Silicon 3 inch diameter (100) p-type plates misoriented by less than 0.5° were used as substrates.

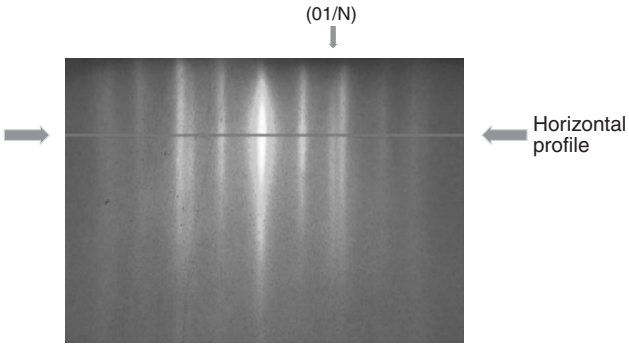

Fig. 1. The horizontal profile of the RHEED pattern for Ge_xSi_{1-x} layer ($x = 0.2$).

Reflection high-energy electron diffraction was the main method used for surface analysis. RHEED is the most practiced technique in MBE. This technique enabled oscillations of the in-plane lattice constant to be detected for the Ge film growing according to the 2D mechanism on the silicon surface [5]. Ex situ scanning tunnel microscopy (STM) with an ultrahigh vacuum instrument Omicron-Riber was used for characterization of the surface morphology under the next conditions: room temperature, $V_{\text{bias}} = +2.5$ V, $I_{\text{tunn}} = 0.05$ nA.

2. Result and discussion

The surface morphology of a germanium island film on the surface of Ge_xSi_{1-x} solid solution changes essentially if germanium islands is formed as "hut"-clusters before growing the Ge_xSi_{1-x} layer. The morphology of the Ge_xSi_{1-x} layer located above the hut-islands depends on the Ge content in the Ge_xSi_{1-x} layer. The Ge_xSi_{1-x} film is a combinaion of (2×1) and $(2 \times n)$ reconstructions for $x < 0.25$. On the Ge_xSi_{1-x} surface with concentrations $x > 0.25$ is observed both the above mentioned reconstructions and the relief of underlying islands. We measured the n number of $(2 \times n)$ reconstruction

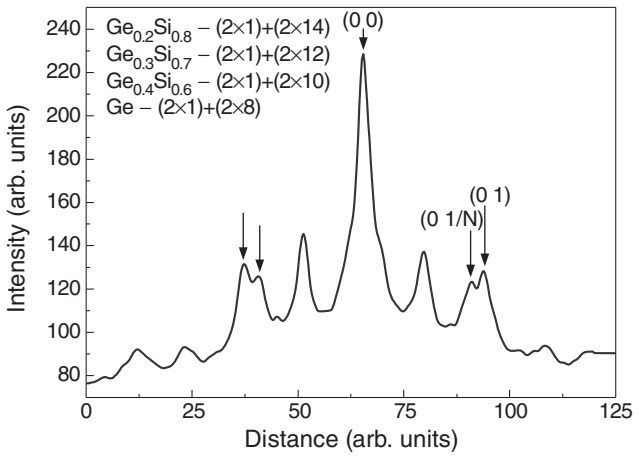

Fig. 2. The intensity distribution for the horizontal profile of the RHEED pattern.

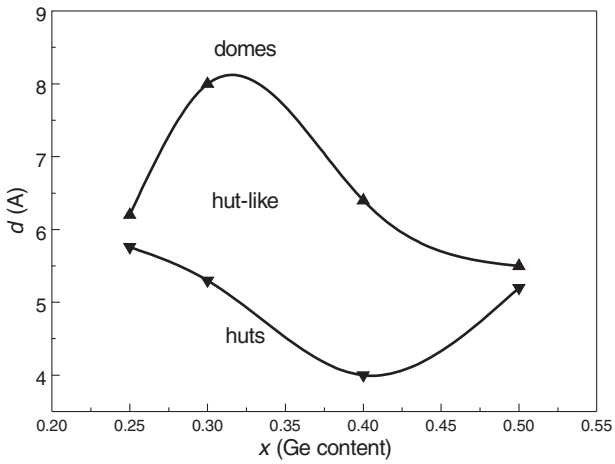

Fig. 3. The phase diagram of the growth for Ge/Ge_xSi_{1-x}/Ge heterostructure.

using our software with respect to the video recording of reflection high-energy electron diffraction (RHEED) pattern during growth (Fig. 1). The n number reaches a minimum value of about 8 for clear Ge layer, whereas for Ge_xSi_{1-x} films the n number from 8 to 14 is increased (Fig. 2). Further deposition of the Ge film on the solid solution layer leads to a series of structural transitions on the surface.

From the kinetic diagram describing the 2D–3D transition of Ge_xSi_{1-x} films at the temperature range 300–700 °C, which was earlier constructed by us, the values locating below the 2D–3D transition revealed the Ge_xSi_{1-x} thickness region, such that Ge_xSi_{1-x} layers were obtained the two-dimensional dislocation-free pseudomorphic films. The presence of a thin strained film of the Ge_xSi_{1-x} caused not only the changes in critical thicknesses of the transitions, but also affected the properties of the germanium nanocluster array for top Ge layer. Based on the RHEED data the hut-like island form which hasn't been previously observed by us between the hut and dome islands has been detected. This form of islands appear on the phase diagram in the range from $x = 0.25$ to $x = 0.5$ (Fig. 3). The data on the growth of Ge/Ge_xSi_{1-x}/Ge heterostructures with the uniform array of islands (the standard deviation about 10 percentage) in the second layer of the Ge film have been received.

The faceting by 105 planes changes upon the deposition several monolayers of the solid solution layer. Germanium islands are formed as square-based pyramids on the solid solution surface (Fig. 3) similar to those reported in Ref. [6]. Their density is lower than the density of underlying initial "hut"-clusters (9×10^{10} cm^{-2}). Furthermore, bases of the pyramidal islands differ from those of the initial "hut"-clusters, they are 20 nm in the characteristic size. However, the size distribution of the pyramidal islands is much more uniform (approximately, by a factor of 2) than that of the germanium "hut"-clusters. The underlying germanium layer causes variations in not only parameters of the island array, but also in their faceting. The RHEED data indicate the presence of faces at a greater angle than plane 105. While the base edges keep their orientations, these are, supposedly, planes 104 or 103; their accurate identification needs further studies. The presence intermediate hut-like form of the islands is of interest both for structural and topological properties of the surface affecting the optical and electronic properties of the system as a whole.

3. Conclusion

Thereby, the n number of $(2 \times n)$ reconstruction was determined as a function of composition during the growth of solid solution Ge_xSi_{1-x} in the Ge/Ge_xSi_{1-x}/Ge heterostructure. The increase of the n number from 8 to 14 was believed to take place at the enhancement of the Ge content in the Ge_xSi_{1-x} film. The Ge_xSi_{1-x} thickness was chosen as the thickness for non-relaxed atomically smooth layers from the kinetic diagram describing the 2D–3D transition of Ge_xSi_{1-x} films. The influence of germanium content in the solid solution on the properties of the second top island array was studied. Based on the results obtained, it becomes possible to produce dislocation-free strained heterostructures Ge/Ge_xSi_{1-x}/Ge, where germanium quantum dots reside above and below quantum wells formed by layers of Ge_xSi_{1-x} solid solution. It is shown that regular pyramidal germanium islands with different faceting and array properties are formed on the surface of the solid solution coverage over germanium "hut"-clusters.

Acknowledgements

The work is supported by the Russian Foundation for Basic Research (Project 09-02-01262).

References

[1] A. I. Yakimov, A. I. Nikiforov, V. A. Timofeev, A. A. Bloshkin, V. V. Kirienko and A. V. Dvurechenskii, *Semicond. Sci. Technol.* **26**, 085018 (2011).
[2] Feng Liu, Fang Wu and M. G. Lagally, *Chem. Rev.* **97**, 1045 (1997).
[3] J. Tersoff and R. M. Tromp, *Phys. Rev. Lett.* **70**, 2782 (1993).
[4] L. W. Guo, Q. Huang, Y. K. Li, S. L. Ma, C. S. Peng, J. M. Zhou, *Surface Science* **406**, L592 (1998).
[5] A. I. Nikiforov, V. A. Cherepanov, O. P. Pchelyakov, *Mater. Sci. Eng. B* **89**, 180 (2002).
[6] L. V. Arapkina and V. A. Yuryev, *JETP Lett.* **91**, 281 (2010).

20th Int. Symp. "Nanostructures: Physics and Technology"
Nizhny Novgorod, Russia, June 24–30, 2012

Investigation of the photoluminescence from Ge and Ge/InGaAs quantum wells in GaAs

A. A. Dubinov[1], V. Ya. Aleshkin[1], K. E. Kudryavtsev[1], A. N. Yablonskiy[1] and B. N. Zvonkov[2]

[1] Institute for Physics of Microstructures RAS, 603950 Nizhny Novgorod, Russia
[2] Research Physical-Technical Institute of the Nizhny Novgorod State University, 603950 Nizhny Novgorod, Russia

Abstract. The heterostructures with Ge and Ge/InGaAs quantum wells were grown by metal-organic chemical vapor deposition epitaxy and laser sputtering on GaAs substrates. All peaks of photoluminescence correspond to the defects in the Ge and GaAs surface layers for Ge/GaAs structure. The peak of photoluminescence at wavelength 0.99 μm and broad peak in 1.3−1.65 μm region were observed in Ge/InGaAs/GaAs structures. First peak corresponds to the optical transition in InGaAs quantum well and second peak corresponds to the direct band optical transition in Ge/InGaAs quantum well.

Introduction

In recent years, semiconductor lasers emitting at 1.3 and 1.5 μm have been required in telecommunication because in this range quartz waveguides ensure minimum dispersion and absorption of radiation. However, the only commercially available lasers operating at these wavelengths are InGaAsP-based quantum well lasers on InP substrates [1]. Cheaper GaAs substrates and conventionally grown InGaAs quantum wells cannot be used for lasing in this spectral region due to a large mismatch of the lattice constants for GaAs and the InGaAs solid solution with a high In content.

This work deals with investigation of a possibility to produce effective lasing in the 1.3–1.5 μm wavelength range, using GaAs-based structures with Ge and combined Ge/InGaAs quantum wells. The lattice constants of Ge and GaAs are close, which is promising of attainability of practically perfect Ge/GaAs heterojunctions. The technology for growing strained quantum wells of InGaAs on GaAs is fairly well developed and the lasers on their basis have long been a commercial product. Germanium is an indirect band gap semiconductor. The lower valley in the conduction band is the L-valley, and the top of the valence band is located in the Γ-point of the Brillouin zone. The difference between the edges of the L- and Γ-valleys in the conduction band is only 136 meV, and the direct optical transition corresponds to a 1.55 μm wavelength at room temperature.

We found in our previous work [2] that for relatively small thickness values of Ge quantum well in GaAs there is a possibility that the lowest subband of the conduction band even in a single quantum well is the Γ-subband. In a structure with Ge and InGaAs layers the layer thicknesses and the In content can be chosen such that the conduction band bottom in the combined quantum well will be in the Γ-valley of InGaAs and the valence band top will be in the Ge layer. The energy of the electron radiative transitions from the InGaAs conduction band to the Ge valence band in such quantum wells will be in the 1.3–1.5 μm wavelength range.

1. Experiment

The heterostructures with Ge (structure #1) and Ge/InGaAs (structure #2) quantum wells were grown at temperature 650 °C on semiinsulating substrate [001] misoriented to the [110] on 3°. For both structures GaAs buffer layer with 0.6 μm thickness was deposited on the substrate by MOCVD. Next, a 9 nm thickness $In_{0.3}Ga_{0.7}As$ layer was grown on the structure #2. Then, in both structures Ge layer with 6 nm (structure #1) and 3 nm thicknesses (structure #2) was deposited by laser sputtering. Then cover layer GaAs was deposited by MOCVD with a thickness of 0.3 μm in the structure #1, and by laser sputtering with a thickness of 40 nm in the structure #2.

The photoluminescence (PL) from these structures was investigated at temperatures 77 K by two methods: using the parametric oscillator MOPO-SL ("Spectra-Physics", the radiation pulse duration 10 ns and wavelength region 0.4–2.5 μm) and using the CW Nd:YAG laser (wavelength 532 nm) for pumping. As radiation-measuring instruments we used InGaAs diode array (0.62–2.2 μm region) and photoelectronic multiplier (0.93–1.7 μm region), which allowed to measure spectra with a temporal resolution of 10 ns.

Figure 1 shows the PL spectra of the CW pumped structure #1 for 4 pump levels. The performed for this structure calculation gives the following values of the wavelengths: 1267 nm for the transition from the lower state of the Γ-valley to the upper heavy-hole state, 1496 nm for the transition from the lower state of the L-valley to the heavy-hole upper state, 1550 nm for the transition from the lower state of the L-valley to the upper heavy-hole state with the emission of intervalley phonon. From PL spectrum in Fig. 1 one can see three characteristic peaks at wavelengths 1080, 1270, 1320 nm. The observed width of the two short-wavelength lines is great, that, apparently, means that there are a large number of defects and inhomogeneities in the structure. The narrower long-wavelength (1320 nm) peak is also presented in the PL spectrum measured from the sub-

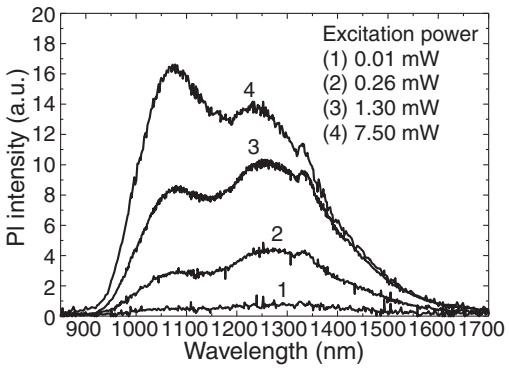

Fig. 1. The PL spectra of the structure #1 by pump of CW laser.

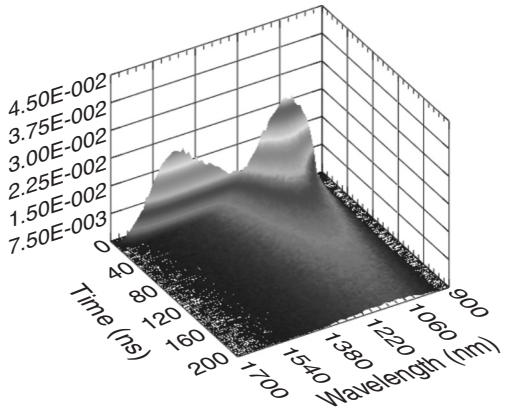

Fig. 2. The PL spectra of the structure #1 by pump of pulsed OPO (pump wavelength is 600 nm).

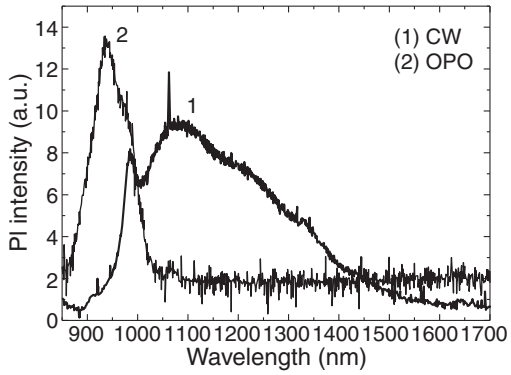

Fig. 3. The PL spectra of the structure #2 by pump of CW laser or pulsed OPO (pump wavelength is 600 nm).

strate on which the structure was grown. So this peak is not from the PL spectra of the Ge quantum well. From Fig. 1 one can see more rapid growth of short-wavelength line in comparison with the long-wavelength line with increasing pump power. The two peaks (Fig. 2) at wavelengths of 1060 and 1476 nm are clearly seen only at PL spectrum of the structure #1 under a powerful pulsed pumping. From Fig. 2 one can see that the decay time of PL in the long-wavelength line is less than 10 ns. Note that this wavelength corresponds to the transition from the lower state of the L-valley to the upper state of the heavy holes. Short lifetime means a greater role of non-radiative recombination, which occurs apparently due to the presence of a large number of defects in the Ge layer. Short-wavelength line of PL can be attributed to the luminescence of defects in the GaAs surface layer. These defects occur due to diffusion of Ge in GaAs during growth. The defects spread over a long distance from the quantum well. The decay time of short-wavelength peak PL (30 ns) is significantly greater than the decay time of PL of long-wavelength peak. It should be noted that wavelength of one of the peaks observed during continuous pumping (1270 nm) agrees well with that of the direct transition in Ge quantum well. However, it is not observed for a strong pulse pump, that can not occur for direct transitions. Probably, this peak is due to recombination from defect states, whose density of states is low comparing with that for electron in subbands of quantum well. And therefore for a strong pump this peak is not visible on the background of the observed lines.

The PL spectra from structure #2 for continuous and strong pulsed pump with using of diode array detector are shown in

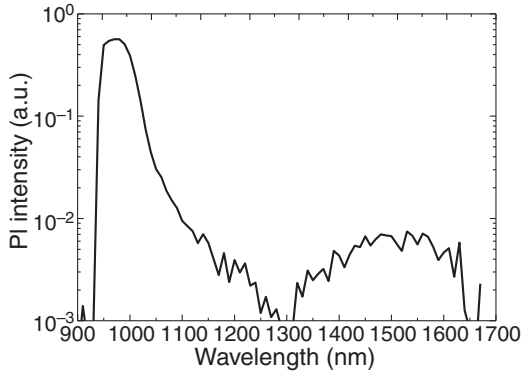

Fig. 4. The PL spectra of the structure #2 by pump pulsed OPO (pump wavelength is 600 nm).

Fig. 3. In the PL spectrum under continuous pumping one can see 4 peaks at the wavelengths: 990, 1060, 1220, 1320 nm. The wavelengths and widths of the three long-wavelength observed features are in good agreement with the PL spectrum of the structure #1, and, apparently, correspond to the PL of defects. Short-wavelength line has a significantly smaller width, and its position corresponds well to the main transition in the $In_{0.3}Ga_{0.7}As$ quantum well with thickness 9 nm. Under intense pulse pumping short-wavelength wing of the line grows, due to the filling of the excited states in the $In_{0.3}Ga_{0.7}As$ quantum well, and the PL of defects is not observed. If a more sensitive detector (photoelectronic multiplier) is used then under a intense pulsed pumping an additional broad line of luminescence is observed in the wavelength range 1300–1650 nm (Fig. 4), which, apparently, can be associated with direct in momentum, but the indirect in the coordinate space transitions between $In_{0.3}Ga_{0.7}As$ and Ge layers (correspond to the calculated values). Note that the PL decay time in both lines is less than 10 ns.

Acknowledgements

This work was supported by the Programs of RAS, by the RFBR (#11-02-00488, #11-02-97020-Povolzhje), and the RF President (MK-678.2012.2).

References

[1] S. J. Caracci *et al*., *J. Appl. Phys.* **75**, 2706 (1994).
[2] V. Ya. Aleshkin and A. A. Dubinov, *J. Appl. Phys.* **109**, 123107 (2011).

20th Int. Symp. "Nanostructures: Physics and Technology"
Nizhny Novgorod, Russia, June 24–30, 2012

Resonant diffraction grating based on InGaAs/GaAs quantum wells

Yu. V. Kapitonov, M. A. Kozhaev, Yu. K. Dolgikh, S. A. Eliseev, Yu. P. Efimov, V. V. Petrov and V. V. Ovsyankin

St Petersburg State University, St Petersburg, Russia

Abstract. Resonant diffraction gratings based on InGaAs/GaAs single quantum wells have been fabricated and investigated using optical spectroscopy. At first GaAs substrate has been processed using focused ion beam irradiation. Then the substrate has been used for molecular beam epitaxial growth of InGaAs/GaAs quantum wells. Substrate pre-processing caused periodical spatial modulation of quantum wells optical properties. Resonant diffraction signal has been observed and diffraction signal spectra have been investigated. In comparison with reflection spectra diffraction signal spectra demonstrate much higher contrast between resonant signal from quantum wells and non-resonant background.

Introduction

Semiconductor structures with InGaAs/GaAs quantum well (QW) have interesting optical properties caused by high interaction efficiency of 2D exciton subsystem with light. This makes such structures good candidates for logical elements of optical computers [1].

Reflection spectroscopy is an important method of QW investigation [2]. Most interpretable data could be obtained in Brewster geometry. In that case it is possible to suppress background reflection from the sample surface. But this geometry leads to light polarization and incident angle limitations.

We describe a resonant diffraction phenomenon caused by spatial modulation of QW optical properties. To obtain such resonant diffraction grating a sample with InGaAs/GaAs single QWs has been grown by molecular beam epitaxy (MBE) on a substrate patterned by low-dose focused ion beam (FIB) irradiation.

1. Sample preparation

For pre-processing of GaAs substrate FIB workstation has been used. This workstation allows to expose substrate with 30 keV Ga^+ ion beam [3]. Two arrays of 41 lines (400 μm length, 9 μm step between lines) with doses 0.1 and 2.0 nA sec/cm were exposed on the epiready Ga(100) substrate doped with Si. Beam diameter has been less than 1 μm.

Atom Force Microscopy (AFM) revealed that at such low doses there is no substrate milling. On the contrary there is a deposition of hydrocarbon contamination caused by secondary electrons [4]. Also there are defect formation and ion implantation processes. Fig. 1a shows Scanning Electron Microscopy (SEM) image of the substrate surface after ion beam exposure. Ion beam exposed areas are darker because of the hydrocarbon contamination.

Patterned substrate was used for MBE-growth. First of all, a 270 nm GaAs buffer layer was grown, then three $In_{0.02}Ga_{0.98}As$ QWs with thickness 2 nm (QW1), 3 nm (QW2) and 4 nm (QW3) separated with two 150 nm GaAs barrier layers were grown, and then a 150 nm GaAs cap was grown. AFM images of epitaxial sample surface are shown in Figs. 1b and c. Height difference on these pictures is 30 nm.

Typical MBE oval defects could be found everywhere on the sample surface [5]. Particular interest is that in pre-processed area defects are aligned along ion-exposed lines (on Fig. 1c lines are marked by arrows). Thus ion beam pre-processing doesn't lead to dramatic disturbance of the sample surface.

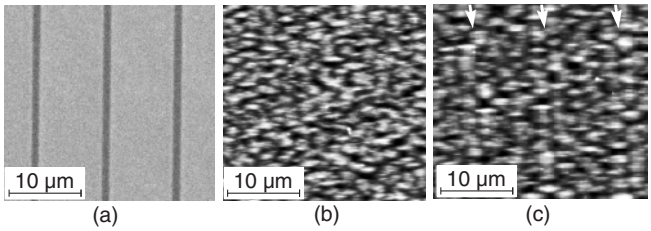

Fig. 1. SEM image of substrate after ion exposure (a), AFM image of sample after MBE growth in areas without (b) and with (c) ion beam pre-processing.

Defects ordering in pre-processed areas allow supposing that QWs properties are laterally modulated.

2. Spectroscopy

For optical investigation sample was installed in a closed-loop cryostat at 9.5 K. Sample was irradiated by Ti:sapphire femtosecond laser. Measurements were made in the linear mode. Light was focused on the sample using long-focus lens (F = 50 cm) in a 400 μm spot. Reflected light was collected in a monochromator with a CCD-matrix detector.

In Fig. 2a solid line depicts reflection spectrum for P-polarized incident light at Brewster angle (74° to normal). Excitonic resonances in QWs (marked as QW1, QW2, QW3) and bulk exciton resonance are clearly visible. There is also a background non-resonant reflection caused by slight deviation from Brewster geometry. Light reflected from the sample surface and from QWs is coherent. This fact leads to interference of these two signals (particularly visible for QW3 resonance). Dashed curve shows reflection spectrum for S-polarized light. In this case according to Fresnel equations non-resonant reflection coefficient is 72%. Non-resonant reflection makes a reflection spectrum interpretation a hard task.

When the sample area with pre-growth ion beam processing is exposed with monochromatic light at QW1 resonance energy a diffraction pattern is clearly visible. In Brewster geometry first diffraction maximum is observed at 62° to normal. It corresponds to the diffraction grating with 9 μm period which is in a good agreement with ion beam irradiated pattern period. Mirrors are added in optical setup so that a diffraction and reflection spectra could be observed for the same point and same conditions.

In Fig. 2b a diffraction spectra for two orthogonal polarizations are shown. Non-resonant background is small because

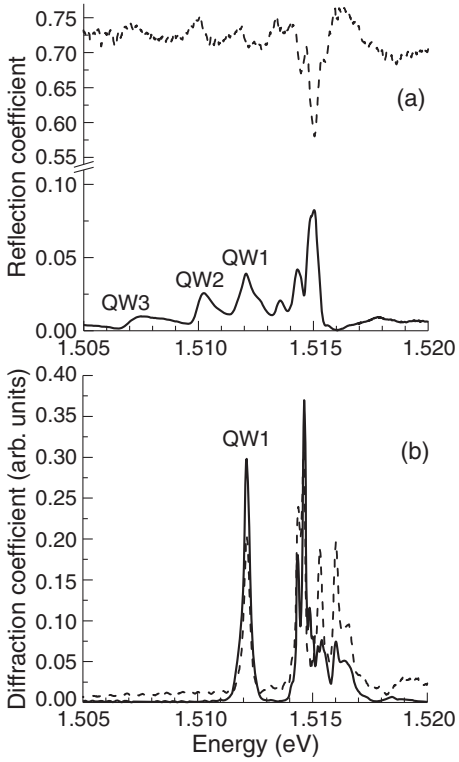

Fig. 2. Reflection (a) and first diffraction maximum (b) spectra for P-polarized (solid lines) and S-polarized (dash lines) incident light. Ion beam exposure dose — 0.1 nA sec/cm.

there is almost no signal related to the non-resonant reflection or diffusion of light from the sample surface. QW1 resonant to non-resonant signal ratio for S-polarized incident light is around 20:1. For reflection spectrum in the same conditions this ratio is around 1:20. Thus there is much better contrast between resonant and non-resonant signal in case of diffraction at any incident angle and polarization of light.

Observed resonant diffraction effect is caused by spatial modulation of QW optical properties. Sample areas that were irradiated by FIB could demonstrate excitonic resonance shift, broadening or fading in comparison with intact areas. This periodical deviation of optical properties leads to diffraction signal formation.

3. Conclusion

MBE growth of QWs on a substrate with low dose ion beam exposure doesn't show considerable effect on the sample surface relief. On the other hand QWs properties are modulated in the areas with pre-processing. Periodical modulation leads to the diffraction signal formation. Resonant diffraction signal is almost free from non-resonant background. That makes diffraction signal spectroscopy an easy-to-use tool for investigation of QW properties. Also resonant diffraction grating could find some practical applications. For example it could be used for outcoupling light in surface emitting lasers with horizontal resonators, for changing the light propagation direction in vertical cavity lasers, for introducing light in planar waveguides and in other devices where changing of light propagation direction for specific wavelength of light is needed.

References

[1] I. Ya. Gerlovin, V. V. Ovsyankin, B. V. Stroganov and V. S. Zapasskii, *Journal of Luminescence* **87–89**, 421 (2000).

[2] S. V. Poltavtsev, V. V. Ovsyankin, B. V. Stroganov, Yu. K. Dolgikh, S. A. Eliseev, Yu. P. Efimov, V. V. Petrov, *Optics and Spectroscopy* **105 (4)**, 511 (2008).

[3] J. Gierak, *Semicond. Sci. Technol.* **24**, 043001 (2009).

[4] A. E. Vladar, M. T. Postek, Jr. and R. Vane, *Proc. SPIE* **4344**, 835 (2001).

[5] N. J. Kadhim and D. Mukherjee, *Journal of Materials Science Letter* **18**, 229 (1999).

20th Int. Symp. "Nanostructures: Physics and Technology"
Nizhny Novgorod, Russia, June 24–30, 2012

Influence of heterointerfaces diffusion on characteristics of excitonic states in quantum wells Zn(Cd)Se/ZnMgSSe

A. F. Adiyatullin[1,2], V. V. Belyh[1], V. I. Kozlovsky[1], V. S. Krivobok[1,2], V. P. Martovitsky[1] and *S. N. Nikolaev*[1]

[1] P.N. Lebedev Physical Institute, RAS, 53 Leninsky pr., 119991 Moscow, Russia
[2] Moscow Institute of Physics and Technology (State University), Dolgoprudny, Russia

Abstract. The excitonic states in the quantum wells Zn(Cd)Se/ZnMgSSe with smoothed interfaces were investigated by the optical spectroscopy. It's shown, that the low-temperature emission spectrum of quantum well is determined by free excitons and excitons bound to neutral donors. Long-time (40 min) reversible variation of reflection coefficient near the excitonic resonance in quantum wells after applying steady-state illumination is discovered. It's shown that in addition to well known shift of excitonic lines three other effects are induced by interface spreading: increase of the exciton-phonon interaction, enlarge of an energy shift of free and bound exciton spectral lines, excitonic luminescence decay time decreasing in a wide temperature range. The main reasons for the phenomena observed are discussed.

Introduction

In contrast to the model interface, considered in most theoretical works, the real interface is often characterized by the diffusion broadening of the heterointerface, its disorder and the local distortion of impurity-defect background, caused by the jump of chemical potential for point defects. These factors largely determine the interface states spectrum, band diagram, as well as the magnitude of the electron-phonon coupling near the interface, and thus affect the capture cross-section, the rate of recombination of non-equilibrium carriers, time of spin relaxation, the oscillator strength of optical transitions, etc.

1. Experiment

Structures with Zn(Cd)Se/ZnMgSSe QW were grown by metalorganic vapour phase epitaxy (MOVPE) on GaAs substrates disoriented on 10° from the face (001) toward the face $(111)_A$. Growth was carried out at the facility Veeco in a hydrogen atmosphere at low pressure (85 Torr) and temperatures of 450–460 °C. Samples with single and double nominally identical quantum wells were selected for research.

The thickness of ZnSe layer in the sample with single QW (QW#1) was 8 nm, in the sample with two QWs ZnSe layers thicknesses were 12 nm. ZnMgSSe barrier layers have been lattice-matched with the GaAs substrate and had a band gap of about 3.1 eV at low temperature. Observed blurring of the QW heterointerfaces is associated primarily with the diffusion of Mg and Zn. Thereat, the lateral homogeneity of the heterointerfaces was high (mean-square roughness less than 0.5 nm). Both QW are characterized by a relatively small width of the emission lines and a relatively high quantum efficiency of luminescence. An important feature of the sample with two QWs was different degree of heterointerfaces blurring for two QWs. The reason for this is that the bottom QW (QW#3) was longer than the top one (QW#2) at growth temperature. It is possible to trace the influence of the heterointerface spreading degree on the optical properties of these two quantum wells.

A detailed analysis of photoluminescence spectra and reflection spectra temperature dependence allows to assert that the excitonic states structure in all QWs, despite the interfaces spreading, are well described in the framework of strained layer of Zn(Cd)Se with thickness comparable to or greater than the exciton Bohr diameter. In this case electron-phonon coupling

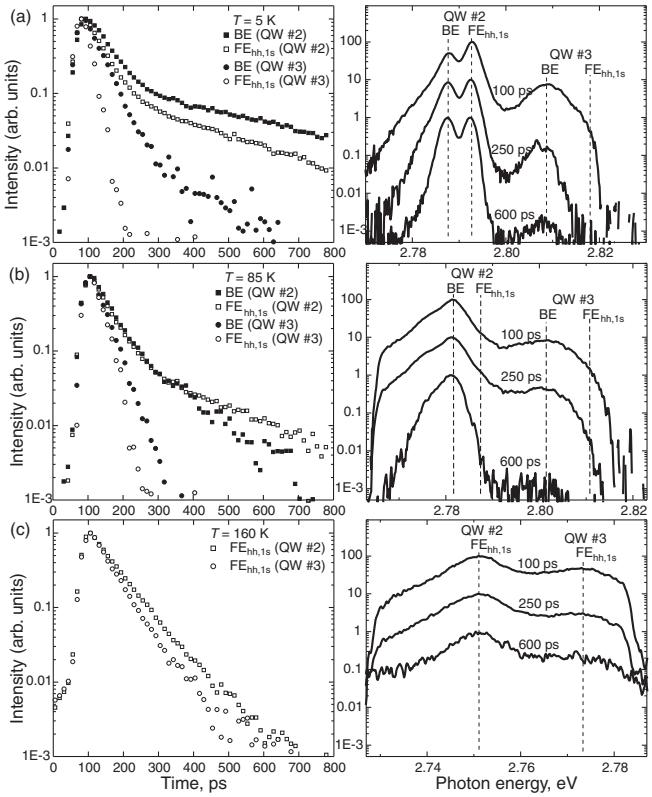

Fig. 1. Photoluminescence kinetic for the double-QW structure. For every temperature the decay signal of luminescence (left) and time-resolved spectra (right) are depicted. Pulse had power density 0.1 μJ/cm^2 and duration time 2.5 ps.

determines homogeneous line broadening at low excitation densities. The extracted values of homogeneous line broadening unambiguously shows that exciton — LO-phonon coupling is enhanced for the QWs with spread heterointerfaces. The most likely reason of the observed effects is a different degree of electrons and holes localization in the Zn(Cd)Se/ZnMgSSe structures with spread interface, which contributes to the exciton-phonon coupling via the Frohlich mechanism.

At low temperatures, doublet structure is registered in the emission spectrum for each QW. It's associated with recombination of free excitons and excitons bound to neutral donors

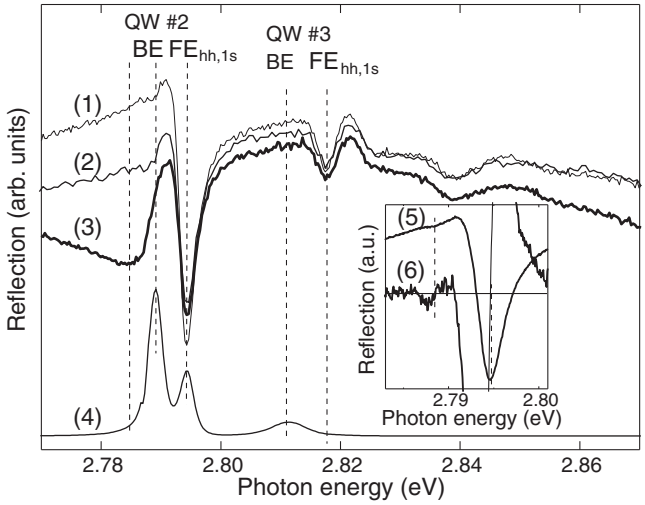

Fig. 2. Double quantum well sample reflection spectra: 1) without steady-state illumination, 2) just after a steady-state illumination switch on, 3) after $\sim$ 40 min illumination, 4) is steady-state photoluminescence spectrum. On the inset: 5) reflection spectrum without illumination and 6) its derivate.

(BE). The activation energy of BE line thermal quenching and spectral distance between maxima of free and bound excitons lines is higher for QW with blurred interfaces. The reason is that free and bound excitons have different degrees of localization. Interface smoothing causes an energy shift for both free and bound exciton lines. But the influence of heterointerface spreading on free exciton is more than on bound one, and so does the energy shift. This feature results in the enhancement of binding energy with heterointerface smoothing.

A bi-exponential luminescence decay with the luminescence quenching times $\tau_s \sim 30-50$ ps and $\tau_l \sim 200-400$ ps is observed for each QW (Fig. 1).

The whole set of the luminescence kinetics measurements at different temperatures and densities of pulsed excitation allows us to state that the short time τ_s is caused by trapping of excitons by the charged donors. The slowly decreasing part of luminescence decay is related to the radiative recombination of localized excitons with no charged centers nearby. The luminescence of QW with the more abrupt interface (QW#2) is decayed slowly than the luminescence of QW with the spreaded interface (QW#3) in the all experimental temperature range (5–300 K).

An unexpected effect is a long-time dynamics of the reflection spectra observed at times of order 40 min after a steady-state illumination switch on (Fig. 2).

The result of this dynamics is an insignificant variation of the reflection coefficient in the spectral range of 2.77–2.87 eV and an appearance of wide notch near BE resonance QW#2. The steady-state illumination switch off is accompanied by a reverse effect. A slow evolution of the reflection spectrum to the original state is observed (curve 1). The main variations of the reflection coefficient at long times after the illumination switch on/switch off take place near the BE-resonance in the QW #2. It allows to associate the long-time dynamics observed with charge redistribution between QW #2 and other regions of a heterostructure. The additional studies is needed for the reliable interpretration of the phenomenon. Possible, it can be caused by a variation of surface charge state.

20th Int. Symp. "Nanostructures: Physics and Technology"
Nizhny Novgorod, Russia, June 24–30, 2012

Low-frequency resonant Raman scattering observation in quantum wells grown on pre-patterned substrate

V. G. Davydov, P. A. Morozova, Yu. V. Kapitonov, M. A. Kozhaev, V. V. Petrov, Yu. K. Dolgikh, S. A. Eliseev, Yu. P. Efimov and V. A. Gaisin

Physics Department, St Petersburg State University,
Ulyanovskaya 1, Petrodvorets, 198504 St Petersburg, Russia

Abstract. Two nominally identical heterostructures with InGaAs/GaAs quantum wells were grown on the different GaAs substrates: fresh "epi-ready" one and another subjected to the electron and ion beams irradiation before growth. Resonant photoluminescence and photoluminescence excitation spectra were recorded. Scattered excitation light was strongly suppressed by geometric means. Very low frequency Raman lines were clearly observed in the second structure only. Their physical nature is discussed.

Introduction

Quantum wells are perhaps one of the most thoroughly studied (and the most comprehensively understood) among the artificially made nanostructures. However, low-dimentional quantum effects in the quantum wells act only in the single direction — direction of growth, and other two dimensions exhibit unrestricted behaviour like continuous energy zones in momentum space, spatial diffusion etc. That's why many researchers are tempted to combine well-established quantum well fabrication process with some form of lithography in the lateral direction to reproducibly slice uniform arrays of the 1-D (wires) and/or 0-D (dots) elements from a given quantum well.

Our research team made some attempts to do this by means of focused ion beam lithography, attracted by an excellent spatial resolution of the method. The most straightforward idea — geometrical patterning of the already grown quantum well — had provided rather disappointing results. Gallium ions with high energy scatter many times in the crystal lattice, displacing atoms and creating lots of defects many hundreds nanometers around. Moreover, besides the small intense focused spot the ion source produces wide halo of ions of the same energy, which destroy structure uniformly. As a result, while geometrical shape of the sample looking as intended, the delicate interactions responsible for formation of excitons and other coherent phenomena were totally ruined, and no resonant absorbtion and/or reflection were observed in that samples.

Obvious step to overcome this difficulty would be to change the order of two operations: firstly pattern the surface with the ion beam and then grow the quantum well and surrounding barrier in the hope that the latter would less suffer from the adverse action of the high-energy ions. Some results of such an attempt are presented in this work.

1. Exprimental

1.1. Samples preparation

The samples were grown on the (100) epi-ready substrate of semi-insulating GaAs. Substrate was split in two halves, one being kept in the original environment and the other was transferred to the Cross–Beam scanning electron and focused gallium ion beam workstation. Under the control of electron imaging, several periodic patterns of various pitch and depth were inscribed on the surface.

Afterwards both halves were mounted together in the molecular beam epitaxy machine and prepared for growth by thermal treating usually involved to remove protective oxide from the substrates. Then the heterostructure was grown consisting of GaAs buffer with three $In_{0.03}Ga_{0.97}As$ quantum wells of different thicknesses embedded within it.

1.2. Spectroscopy technique

Most of the measurements were performed at the sample temperature below 10 K in order to reduce effects of the exciton-phonon scattering. Firstly a reflection spectrum was measured in *p*-polarization under Brewster angle of incidence (with respect to the refractive index of bulk GaAs). This technique allows to achieve two goals: firstly, it eliminates any interference from a non-resonant background reflection, facilitating quantitative interpretation of the measurement's results, and secondly ensures that observed spectra are due to the coherent phenomena, such as absorption and reflection. Femtosecond Ti:sapphire laser was used as a source of wideband light, thus allowing to focus it in the relatively small spot (about $\approx 100\ \mu$m) in order to select particular patterned area.

After locating the desired area (both in the plane of the sample and in the spectral domain), oblique wideband laser beam was replaced by the tunable cw semiconductor laser beam of approximately normal incidence, focused into the same spot (as controlled by an infrared camera). Light emerging from the sample was collected exactly the same way as in the reflection case, that is under the Brewster angle and with appropriate *p*-polarization selection. Careful adjustments of the incident polarization allowed us to reduce elastically scattered excitation light to a level comfortably fitting within the dynamic range of the spectrograph together with luminescence of the sample.

Then a series of the luminescence spectra was recorded, each spectrum being excited by a slightly different wavelength. Similar measurements were performed on both samples, namely grown on the fresh and on the patterned substrate.

2. Results and discussion

Due to the ponderable amount of the experimental data obained, a number of various phenomena are distinctively observed. Besides quantitative differencies in line widths, positions and intensities between patterned and unpatterned samples, they include Stokes and sometimes anti-Stokes luminescence, bands of nonlinear luminescence appearing only in the spectra with

strong absorbtion of the excitation light, strong correlation between different excited levels within a given quantum well (which allows to easily distinguish between transitions belonging to different wells even when they coinside spectrally), some anticorrelation between the inhomogeneously broadened luminescence line shape and spectral position of the excitation, which could be explained by a mechanism resembling classical holeburning, and even dim broad luminescence from the substrate, whose excitation spectrum clearly reflects the absorption spectrum of the heterostructure. Each of these numerous phenomena deserves a separate study.

In this work our attention is focused on the only observable spectral feature which strictly follows the excitation photon energy; that is why we call it Raman scattering. This feature is observed only at the Stokes side of the excitation light in rather small spectral interval, a small fraction of meV. It could be surely attrubuted to the grown heterostructure as a whole, because it is not observed in the sample without prepatterning. Most probably, this feature appears due to the standing acoustic wave between the sample surface and distorted (and/or contaminated by products of electron impact decomposition of the adsorbed residual gases) layer under the epitaxially grown layers. Some spectral structure of the feature could reflect different acoustic phonons branches.

Clear observation of the Raman scattering in such a close vicinity of the excitation line was made possible by a combination of resonant enhancement by excitonic transitions in quantum wells and strong geometrical (polarization) suppression of the elastically scattered excitation light.

20th Int. Symp. "Nanostructures: Physics and Technology"
Nizhny Novgorod, Russia, June 24–30, 2012

Externally applied or built-in electric field effect on the polaronic self-energy and effective mass in wurtzite nitride cylindrical nanowires

Karen A. Vardanyan, Arshak L. Vartanian and Albert A. Kirakosyan
Department of Solid State Physics, Yerevan State University, 1, Al. Manoogian, 0025 Yerevan, Armenia

Abstract. The effect of an externally applied or built-in electric field on the basic parameters of quasi-confined (QC) and surface (SO) polarons in a cylindrical wurtzite nitride nanowire (NW) is studied theoretically. By using the Lee, Low, and Pines variational method, the analytical expressions for the quasi-one-dimensional Frohlich polaron self-energy and effective mass are obtained as functions of the wire radius and the strength of the electric field. This will be taken into account in the interpretation of optical phenomena related to polaron motion in wurtzite NW when the effect of an applied electric field competes with the spatial quantum confinement.

One of the challenging topics of the current interest involves quantum heterostructures based on group-III nitrides GaN, AlN, InN and their ternary compounds $Al_xGa_{1-x}N$, $In_xGa_{1-x}N$ due to their wide direct band-gaps covering from ultraviolet to red, which has potential device application for high-brightness blue/green light emitting diodes and laser diodes. One of the specifics of nitride heterostructures is the existence of large internal electric fields due to spontaneous polarization and strains (piezoelectricity). Wurtzite nitrides exhibit stronger polaronic properties in comparison to the rest of III-V semiconductors, including a significant anisotropy effect in the polaronic effective mass. The polaron effects can strongly influence the optical and transport properties of these heterostructures. To the best of our knowledge, there are few theoretical works [1,2] investigating the influence of the spatial confinement on the polar optical phonon modes and polaronic effects in wurtzite nitride nanowires without consideration the influence of the externally applied or built-in electric field and therefore the polaron effects in important nitride-based quantum wires have not been investigated in depth up to now. The purpose of the present work is devoted to theoretical study of polaron basic parameters in the presence of the externally applied or built-in electric field by taking into account optical phonon confinement effect in cylindrical free standing nitride nanowire.

Recently, Tchernycheva *et al*. [3], reported the fabrication of well-separated cylindrical free-stranding nanowires with diameters down to 20 nm synthesized in catalyst-free mode on substrate by plasma-assisted molecular beam epitaxy. As electron-phonon coupling constant in material is in the intermediate range $\alpha_{GaN} = 0.49$ the Lee–Low–Pines variational method can be expected to give a better result. By using this method, we have obtained the following expressions for the quasi-1D Frohlich polaron self-energy and effective mass:

$$\varepsilon^0_{\rm self}(F,R) = -\sum_{pq} \frac{\left|\Gamma^{0p}_{\rm QC}(q)\right|^2 |L_1(0,p,F,R)|^2}{\hbar\omega_{\rm QC} + \frac{\hbar^2 q^2}{2m^*}} - \sum_q \frac{\left|\Gamma^0_{\rm SO}(q)\right|^2 |L_2(0,p,F,R)|^2}{\hbar\omega_{\rm SO} + \frac{\hbar^2 q^2}{2m^*}}, \quad (1)$$

$$m_{\rm pol} = m^* \left(1 + \sum_{pq} \frac{2\hbar^2 q^2}{m^*} \frac{\left|\Gamma^{0p}_{\rm QC}(q)\right|^2 |L_1(0,p,F,R)|^2}{\hbar\omega_{\rm QC} + \frac{\hbar^2 q^2}{2m^*}} + \sum_q \frac{2\hbar^2 q^2}{m^*} \frac{\left|\Gamma^0_{\rm SO}(q)\right|^2 |L_2(0,p,F,R)|^2}{\hbar\omega_{\rm SO} + \frac{\hbar^2 q^2}{2m^*}}\right), \quad (2)$$

where the coupling functions $\Gamma^{0p}_{\rm QC}(q)$ and $\Gamma^0_{\rm SO}(q)$ are defined as

$$\left|\Gamma^{np}_{\rm QC,SO}(q)\right|^2 = \frac{4e^2\hbar\omega_{\rm QC}}{LR^2q^2}\left\{\gamma^2\bar{\varepsilon}_t\left[f^2_{n+1}(\gamma qR) + f^2_{n-1}(\gamma qR) - f_n(\gamma qR)\left[f_{n+2}(\gamma qR) + f_{n-2}(\gamma qR)\right] + 2\bar{\varepsilon}_z\left[f^2_n(\gamma qR) - f_{n+1}(\gamma qR)\, f_{n-1}(\gamma qR)\right]\right]\right\}^{-1} \quad (3)$$

with $f_n(\gamma q\rho) = J_n(\gamma q\rho)$ for QC and $f_n(\gamma q\rho) = I_n(\gamma q\rho)$ for SO phonon modes. Here R is the NW radius, L is the length of the NW, $\bar{\varepsilon_\nu}$ is the effective dielectric function of the GaN material, which is defined as [1]: $\bar{\varepsilon_\nu}^{-1} = (\varepsilon_\nu - \varepsilon_{\nu 0})^{-1} - (\varepsilon_\nu - \varepsilon_{\nu\infty})^{-1}$, where $\nu = t, z$ and $\varepsilon_\nu(\omega) = \varepsilon_{\nu\infty}\frac{\omega^2-\omega^2_{\nu L}}{\omega^2-\omega^2_{\nu T}}$. In this equation ω_{zL}, ω_{zT}, ω_{tL} and ω_{tT} are the zone-center characteristic functions of longitudinal and transverce optical phonon modes along and perpendicularto the c-axis of the material. Here $\gamma(\omega) = \sqrt{|\frac{\varepsilon_z(\omega)}{\varepsilon_t(\omega)}|}$, $J_m(x)$ is the Bessel function and $I_m(x)(K_m(x))$ is the first (second) kind of modified Bessel function. The dispersion relations for QC (taking the upper "+") and SO (taking the upper "-")phonon modes are given by the equation

$$\varepsilon_q(\omega)\gamma K_m(qR)\left[f_{m-1}(\gamma qR) \pm f_{m+1}(\gamma qR)\right]$$

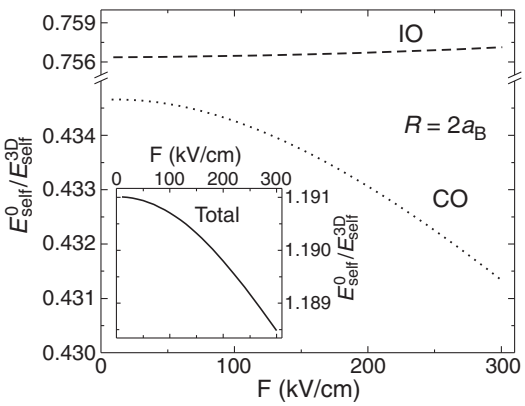

Fig. 1. The polaron self-energy as function of electric firld for GaN-wire with radius $R = 2a_B$. Dotted lines show the CO phonon contribution, dashed lines show the IO phonon contribution and inset showsthe total contribution.

$$= \varepsilon_d f_m(\gamma q R)\left[K_{m-1}(qR) + K_{m+1}(qR)\right]. \qquad (4)$$

The matrix elements L_{QC} and L_{SO} of the system are

$$L_{1,2}(0, p, F, R) = |N_0|^2 \int_0^{\infty}\int_0^{2\pi} \left|J_0\left(\frac{\kappa_{0p}\rho}{R}\right)\right|^2 e^{-2\beta\rho\cos\varphi} \times f_0(\gamma q R)\rho d\rho d\varphi, \qquad (5)$$

where N is the normalization constant, β is variational parameter which takes into account the application of the external electric field.

Figure shows the polaron self-energy as a function of electric field applied perpendicular to the quantum wire axis. It can be clearly seen that in the considered region of the electric field the polaron self-energy due to electron interaction with the SO phonons increases slowly with increasing electric field, while the QC part of the self-energy is reduced significantly. As a result the total self-energy of the polaron decreases, which can be seen more clearly in the inset to Figure. The electric field dependences of the SO as well as QC phonons caused polaron self-energy can be explained by the fact that with increasing electric field the maximum of the electronic charge distribution displaces from the wire axis towards the wire surface. As a result, the role of SO phonons increases, while the role of QC phonons decreases. The same behavior is observed for the quasi-1D polaron effective mass. It should be noted that for small values of the wire radius the SO phonon contribution dominates over the contribution of QC phonons. Particularly, for $R = 0.7a_{\mathrm{B}}$ ($a_{\mathrm{B}} = \hbar^2\varepsilon_0/m^*e^2$ is the effective Bohr radius)the SO phonon contribution to the total polaron self-energy (effective mass) constitutes more than 60% (54%), when $F = 50$ kV/cm. A similar result in the absence of an electric field has been reported for narrow quantum wires in [4]. The contribution of the SO phonon modes both to the $\varepsilon^0_{\mathrm{self}}$ and m_{pol} strongly depend on the radius of quantum wire. The parts of the polaron self-energy as well as effective mass decrease rapidly due to interaction with the SO phonons, as a result, the contribution of QC phonons to the polaron self-energy (effective mass) becomes predominant when $R > 2a_{\mathrm{B}}$ $R > a_{\mathrm{B}}$. The calculations show that the change in polaron self-energy and effective mass is more, than 18% and 35%, respectively, when the electric field increases up to 300 kV/cm and cannot be neglected.

Acknowledgements

This work was supported by the SCS of Armenia and by ANSEF grant condmatth-2955 (2012).

References

[1] L. Zhang, J. J. Shi, Song Gao, *Semicond. Sci. Technol.* **23**, 045014 (2008).
[2] L. Zhang, *Phys. Lett. A* **373**, 2087 (2009).
[3] M. Tchernycheva *et al*., *Nanotechnology* **18**, 385306 (2007).
[4] A. Yu. Maslov, O. V. Proshina, *Nanoscale Res. Lett.* **5**, 1744 (2010).

20th Int. Symp. "Nanostructures: Physics and Technology"
Nizhny Novgorod, Russia, June 24–30, 2012

Tunneling control of population from adjacent quantum well by coherent population trapping effect

K. A. Barantsev[1], A. N. Litvinov[1] and G. A. Kazakov[1,2]

[1] St Petersburg State Polytechnic University, 195251 St Petersburg, Russia
[2] Institute of Atomic and Subatomic Physics TU Wien, Vienna 1020, Austria

Abstract. In this work we study the coherent population trapping (CPT) in tunnel-coupled quantum wells interacting with laser radiation. Closed Δ-system with additional excitation canal has been investigated. We found that it is possible to create the specific collapse of population (dark resonance), which takes place for the excited level of simple Λ-system, for the ground level of additional excitation canal. Moreover, destruction and restoration of CPT by variation of the total phase of exciting fields in the Δ-system gives us the possibility to control dark resonance for the additional ground level.

Introduction

Now the coherent population trapping (CPT) effect attracts a big interest of researchers. The essence of this effect is the appearing of specific superposition of long-lived states in multilevel quantum system interacting with two-frequency coherent (usually laser) field. This superposition state (dark state) is not interacts with the field [1]. The changing of characteristics of the optical dense medium and its influence on propagation of multi-frequency laser irradiation is known as electromagnetically-induced transparency (EIT) effect [2]. In the simplest case CPT takes place when two-frequency radiation passes through a medium with three-level Λ-atoms and each spectral component induce the transition between one of two long-lived ground states with short-lived excited state [3,4]. Absorption of the radiation in this medium decreases if the frequency difference between its components is equal to the frequency of transition between two ground states (dark resonance). In recent years the dark resonances were investigated theoretically [5] as well as experimentally in semiconductor quantum wells in the basis of InGaAs/AlInAs [6] and GaAs [7]. The dark resonances are of particular interest for the development of devices for recording and storing of quantum information [8] and also for quantum logic elements [9]. So the methods of recording and reading of qubits with a high degree of fidelity were realized on the basis of the EIT resonance in the atoms inside an optical lattice.

1. Main part

This work is dedicated to study of the dark resonances in semiconductor double tunneling-coupled quantum wells (Fig. 1a). The excited resonant states in conduction band split into two levels $|4\rangle$ and $|5\rangle$ due to tunneling coupling (the barrier between the wells is permeable). States $|4\rangle$ and $|5\rangle$ have wave functions which are the symmetric and anti-symmetric combinations of the wave function in a single quantum well. We consider two Zeeman sublevels $|1\rangle$ and $|2\rangle$ in the left quantum well and one sublevel $|3\rangle$ in the right quantum well. Transition $|1\rangle \rightarrow |2\rangle$ is magnetic dipole. States $|1\rangle$, $|2\rangle$ and $|4\rangle(|5\rangle)$ are bounded by electromagnetic fields with Rabi frequencies Ω_1, Ω_2, V and constitute a Δ-system. Transition $|3\rangle \rightarrow |4\rangle(|5\rangle)$ is the additional excitation canal.

Spontaneous decay of excited states takes place in this structure and is shown as γ_{ei} on the Fig. 1a. Also there is exchange of populations for ground states, which is shown as Γ_{ij}.

Formalism of density matrix was used for describing of interaction of this structure with electromagnetic field.

$$\frac{\partial \hat{\rho}}{\partial t} = -\frac{i}{\hbar}\left[\hat{H}, \hat{\rho}\right] + \hat{\hat{\Gamma}}\hat{\rho}\,.$$

Diagonal elements ρ_{ii} of density matrix are populations of the levels and non-diagonal elements ρ_{ij} are coherences. $\hat{H}$ is Hamiltonian, $\hat{\hat{\Gamma}}$ is relaxation superoperator. We consider the stationary solution where time derivatives are equal to zero.

On the Fig. 1b we can see that the ground state $|3\rangle$ in the right quantum well has the dependence as for high level in a Δ-system. In other words dark resonance dependence was transmitted from the Δ-system in the right quantum well to the other one. The state $|3\rangle$, unlike excited states, is long-lived. In CPT conditions the greatest part of population is on the low levels $|1\rangle$ and $|2\rangle$ of the Δ-system. If we change the total phase from $\Phi = 0$ to $\Phi = \pi/2$, it causes the destruction of dark state in the left well and increasing of population on the level $|3\rangle$. In other words we can control population of the left quantum well by total phase Φ. It can be used for creation of the quantum memory protocol for scalable quantum communications in a solid state.

2. Conclusions

Double tunneling coupled quantum wells, interacting with multicomponent laser radiation, has been investigated. We observed control and in particular case pumping out of population from adjacent quantum well by phase variation. Resonant curve of the ground level of additional excitation canal, was found.

Acknowledgements

This work was supported by Federal Special-purpose Program "Science and Science- pedagogical personnel of Innovation Russia on 2009-2013" (contract Nos. 14.740.11.0891 and 16.740.11.0586), by the Fund for Non-Profit Programs "Dinastiya".

References

[1] B. D. Agapiev, M. B. Gorniy, B. G. Matisov, Yu. V. Rozhdestvensky, *UFN* **163**, 1 (2001).
[2] S. Harris *et al*., *Physics Today* **50**, 36 (1997); M. Fleischhauer, A. Imamoglu, J. P. Marangos, *Rev. Mod. Phys.* **77**, 633 (2005).

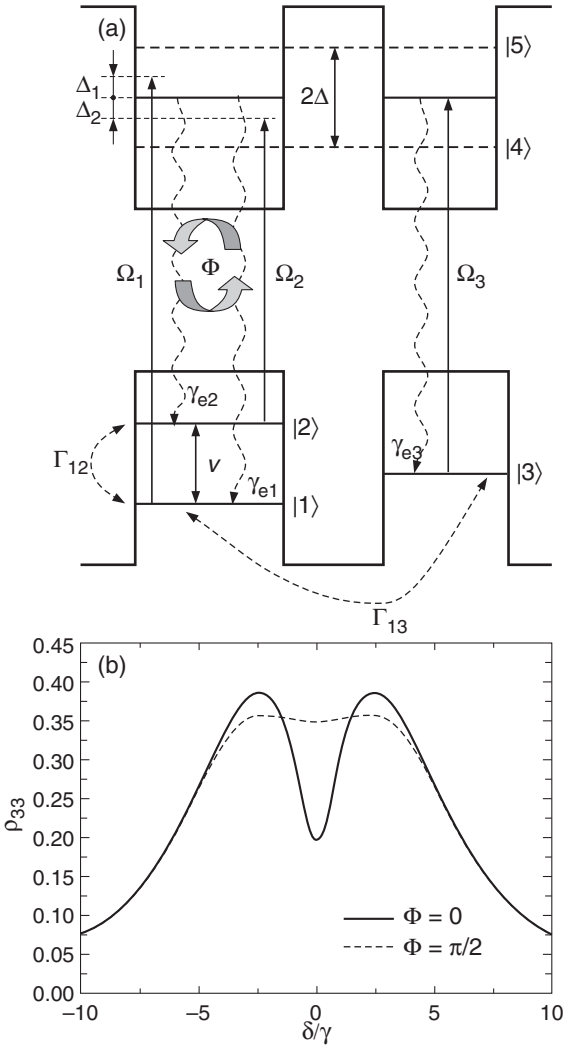

Fig. 1. a) Structure consisting of double tunneling-coupled quantum wells. Here Δ_1, Δ_2 are laser detuning of optical fields, Ω_1, Ω_2, Ω_3 are Rabi frequencies of optical fields and V is Rabi frequency of low-frequency field, 2Δ is tunneling splitting. b) Dependence of population ρ_{33} of the ground state $|3\rangle$ on two photon detuning $\delta = (\Delta_1 - \Delta_2)/2$ for two values of total phase Φ of the closed contour of excitation. Here $\Omega_1 = \Omega_2 = \Omega_3 = V = 2\gamma$, $\Delta = \gamma$, where rate of spontaneous relaxation of the excited states $\gamma \sim 10^{11} c^{-1}$.

[3] M. B. Gorny, B. G. Matisov, Yu. V. Rozhdestvenski, *JETP* **95**, 81 (1989).
[4] O. A. Kocharovskaya, Ya. I. Hanin, *JETP* **90**, 1610 (1986).
[5] M. Lindberg, R. Binder, *Phys. Rev. Lett.* **75**, 1403 (1995).
[6] G. B. Serapiglia, E. Paspalakis, C. Sirtori *et al.*, *Phys. Rev. Lett.* **84**, 1022 (2000).
[7] M. C. Phillips, H. Wang, I. Rumyantsev *et al.*, *Phys. Rev. Lett.* **91**, 183602 (2003).
[8] A. Nazarkin, R. Netz, R. Sauerbrey, *Phys. Rev. Lett.* **92**, 043002 (2004).
[9] J. H. Shapiro, F. N. C. Wong, *Phys. Rev. A* **73**, 012315 (2006).

20th Int. Symp. "Nanostructures: Physics and Technology"
Nizhny Novgorod, Russia, June 24–30, 2012

The electron mobility in isomorphic InGaAs heterostructures on InP substrate

V. A. Kulbachinskii[1], R. A. Lunin[1], N. A. Yuzeeva[1], G. B. Galiev[2], I. S. Vasilievskii[2] and E. A. Klimov[2]

[1] M.V. Lomonosov Moscow State University, Physics Faculty, Low Temperature Physics and Superconductivity Department, 119991 Moscow, Russia
[2] Institute of Ultra-High-Frequency Semiconductor Electronics, RAS, 117105 Moscow, Russia

Abstract. Isomorphic $In_{0.52}Al_{0.48}As/In_{0.53}Ga_{0.47}As/In_{0.52}Al_{0.48}As$ quantum well heterostructures on InP substrate were grown by MBE. We investigated the electron transport properties and the mobility enhancement in the structures by changing of the doping level, the width d of quantum well $In_{0.53}Ga_{0.47}As$ or by an illumination using light with $\lambda = 668$ nm. A persistent photoconductivity was observed in all samples due to the spatial separation of carriers. We used Shubnikov–de Haas (SdH) effect to analyze subband electron concentration and mobility. The maximal value of mobility $\mu_H = 53\,000$ cm^2/Vs was observed for $d = 16$ nm. An illumination increases a mobility up to 15%.

Introduction

There is a significant interest to InAlAs/InGaAs heterostructures on InP substrate. One of the reasons is the advantage of such structures. They allowed using the wider frequency range and having lower electronic noise. The possibility to increase the InAs content in the InGaAs layer up to 70% and higher gives an opportunity to increase mobility, electron concentration in the channel and the drift velocity of electrons. Isomorphic or pseudomorphic InGaAs structures on InP substrate may be used for different applications. In one of the first Ref. [1] matched heterostructures InAlAs/InGaAs/InAlAs on InP substrate were grown. The electron mobility and concentration were investigated as a function of the width of a spacer and the quantum well InGaAs width d. Later for the HEMT (High Electron Mobility Transistor) isomorphic heterostructures on the InP substrate with a channel $d = 20$ nm and a spacer 2 nm were used [2]. It is known also that inserted InAs layers and a composite conducting channel with a shortness of the gate improved the UHF characteristics of transistors [3]. In this research we investigated the electron transport properties and a mobility enhancement in the ternary structures $In_{0.52}Al_{0.48}As/In_{0.53}Ga_{0.47}As/In_{0.52}Al_{0.48}As$ on InP substrate by changing of a doping level, the width d of isomorphic quantum well $In_{0.53}Ga_{0.47}As$ or by illumination using light with $\lambda = 668$ nm. We used Shubnikov–de Haas effect (SdH) to analyze the subband electron concentration and a mobility and their dependence on a doping level, the quantum well width and an illumination.

1. Experimental

The samples were grown by the molecular beam epitaxy (MBE) on InP (100) substrates. All samples have $In_{0.52}Al_{0.48}As$ buffer matched (isomorphic) to InP. Samples have a one-side delta-doping by Si. The spacer thickness was 4.3–6.0 nm. A cap layer was undoped with composition $In_{0.53}Ga_{0.47}As$. A schematic diagram of the $In_{0.52}Al_{0.48}As/In_xGa_{1-x}As/In_{0.52}Al_{0.48}As$ structure on InP substrate is shown in Fig. 1. Temperature dependence of the resistance and the Hall effect were measured in the temperature interval $4.2 < T < 300$ K. At $T = 4.2$ K SdH effect was investigated in magnetic field provided by a superconducting solenoid up to 6 T. We found that the mobility depends on a doping level and the width of a quantum well.

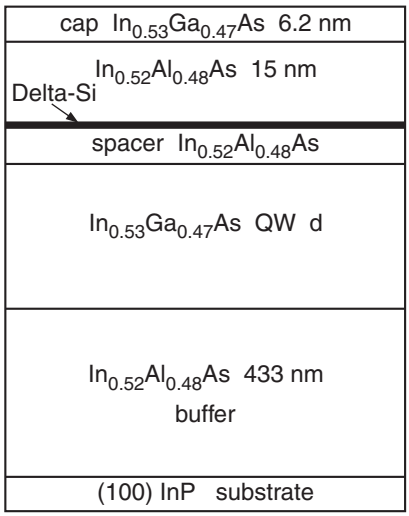

Fig. 1. A schematic diagram of the $In_{0.52}Al_{0.48}As/In_{0.53}Ga_{0.47}As/In_{0.52}Al_{0.48}As$ structure on InP substrate.

Some experimental parameters of samples at $T = 4.2$ K are listed in Table 1.

2. Results and discussion

A persistent photoconductivity was observed in all samples. The typical dependences of the resistance on temperature and an illumination are shown in Fig. 2 for two different samples. The samples were illuminated at $T = 4.2$ K to achieve the saturation of its resistance, then the illumination was switched off and the temperature dependence of the resistance was measured with the rate 5 K/min. At $T > 160-170$ K, the difference between resistances measured in the dark and after illumination became less than the error of measurements. The effect of persistent photoconductivity is related to the spatial separation of carriers.

This fact is confirmed by the logarithmic dependence of the photoconductivity relaxation on time in the initial time interval $\sigma(0) - \sigma(t) = A \times \ln(1 + t/\tau)$ [4, 5] with the value of in the range 20–30 s. We also calculated subband transport and quantum mobility.

The transport mobility is larger than the quantum mobility and the both increases under illumination.

We observed two frequencies corresponding to the two

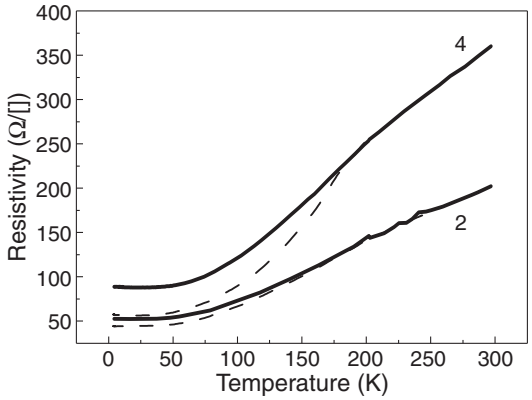

Fig. 2. Temperature dependence of the sheet resistance for sample 2 and 4 in dark (solid line) and after illumination at $T = 4.2$ K (dashed line).

Table 1. Some parameters of samples: quantum well width d, Hall concentration n_H and mobility μ_H at 4.2 K, electron concentration determined from SdH effect in 1st n_1 and 2nd n_2 subbands.

Sample	d (nm)	n_H, 10^{12} cm^{-2}*	μ_H, cm^2/(V s)*	μ_H, cm^2/(V s)†	$n_1(n_2)$, 10^{12} cm^{-2}*	$n_1(n_2)$, 10^{12} cm^{-2}†
1	26	3.2	40 000	41 000	2.49 (0.70)	2.50 (0.74)
2	18.5	2.6	45 800	46 900	2.00 (0.59)	2.20 (0.7)
3	16	1.95	53 500	60 000	1.67 (0.26)	1.87 (0.53)
4	14.5	1.6	45 000	52 400	1.55 (–)	2.08 (–)

* dark, † illuminated

filled subbands in SdH effect in all samples except sample 4 due to a much less doping level of this sample.

We use a conventional fast Fourier transform (FFT) of the SdH oscillations to obtain the electron subband concentrations n_i from the frequencies of oscillations. Under an illumination subband electron concentrations and Hall mobilities μ_H increased (see Table 1). When a sufficiently high electron concentration is produced by a doping (sample 1) the illumination changed the electron concentration much less with respect to the less doped samples. In Fig. 3 the SdH oscillation is shown for the sample 2 in dark (solid line) and under illumination (dashed line). Fast Fourier transform spectra are shown in Fig. 4.

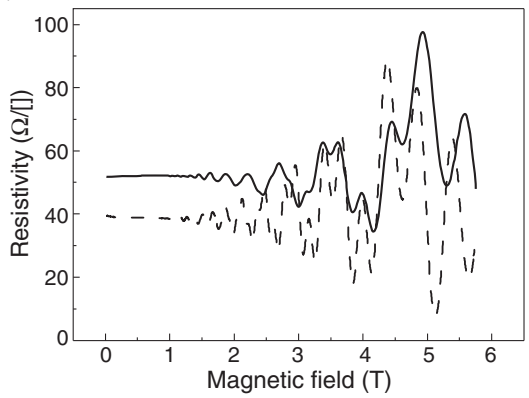

Fig. 3. Magnetoresistance oscillation in sample 2 at $T = 4.2$ K in dark (solid) and under illumination (dashed).

3. Conclusion

We investigated the electron transport properties and mobility enhancement in the isomorphic QW structures on InP substrate by changing of doping level and the width d of quantum well

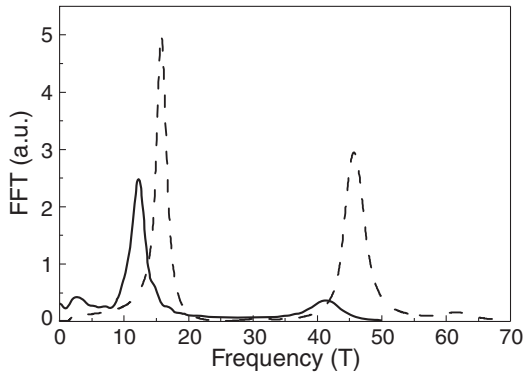

Fig. 4. Fourier spectra of SdH oscillation for sample 2 in dark (solid) and under illumination (dashed).

$In_{0.53}Ga_{0.47}As$ isomorphic to InP substarate. The maximal mobility was observed for QW width $d = 16$ nm. Persistent photoconductivity was observed in all samples due to spatial separation of carriers. Our numerical calculations indicate that the electron mobility decreases with the subband number. The mobility in the 2nd subband is less because the wave function spread to the delta-layer where charged impurity scattering is high. The calculated transport mobility is much higher than quantum mobility. The calculations and measurements of mobility's are in a good agreement.

References

[1] A. S. Brown, U. K. Mishra, Henige *et al*., *J. Vac. Sci. Technol.* **B6** (2), 680 (1988).

[2] K. Higuchi, H. Uchiyama, T. Shiota *et al*., *Semicond. Sci. Technol.* **12**, 475 (1997).

[3] Malmkvist, Mikael, S. Wang, Grahn, V. Jan, *IEEE Transactions on Electron Device* **55**, No. 1, 268 (2008).

[4] V. A. Kulbachinskii, R. A. Lunin, V. G. Kytin *et al*., *JETP*, **83**, 841 (1996).

[5] H. J. Queisser, and D. E. Theodorou, *Phys. Rev. B* **33**, 4027 (1986).

20th Int. Symp. "Nanostructures: Physics and Technology"
Nizhny Novgorod, Russia, June 24–30, 2012

Franz–Keldysh oscillation of InAs/AlAs heterostructures

V. Maruschak[1], *B. Kulinkin*[1], V. Davydov[2] and V. Gaisin[2]

[1] St Petersburg State Medical University, 6/8 Leo Tolstoy str., 197022 St Petersburg, Russia
[2] Physics Department, St Petersburg State University,
Ulyanovskaya 1, Petrodvorets, 198504 St Petersburg, Russia

Abstract. Photoluminescsnce spectra of the heterostructure with InAs/AlAs quantum dots were studied. Upon applying an external electric field the oscillating behaviour appears in the spectra. These oscilaltions were attributed to the Franz–Keldysh effect. The effect in different structure layers manifests itself in different adjacent spectral regions with different oscillation periods. Quantitatively analysis of the oscillations was performed to match the electric field strength.

Systems of self-assembled InAs quantum dots (QD's) have been intensively studied in recent years due to its importance for fabrication micro- and optoelectronic devices [1]. The most thoroughly investigated system with such QD's is system of InAs QD's embedded in GaAs and AlAs matrix.

Recently in order to obtain additional information about the structure of energy levels in heterostructure with InAs/AlAs QD's we have studied photoluminescence of this structure under electric field E applied along growth direction. Structure with self-assembled InAs/AlAs QDs was grown by the molecular beam epitaxy on semi-insulating (001)-oriented GaAs substrates using a Riber-32P system. The structure consists of five layers of InAs QDs separated by 8 nm thick AlAs spacer layers. The QD layers were deposited with a nominal amount of InAs of 2.5 monolayers (ML). A 20 nm GaAs cap layer was grown on top of the structure in order to prevent oxidation of AlAs. In order to apply electric field (0.30 kV/cm) the samples are pressed to quartz plate covered with translucent contact of SnO_2. The radiation of a He-Cd laser (441.6 nm) was used to excite PL. PL of the structure with QDs have been at temperatures of 77 and 300 K and different strength of electric field (0–30 kV/cm) measured. The PL spectra (see Fig. 1) consist of two broad bands related to transitions in QD1 (1400–1700 meV) and QD2 (1650–1900 meV).

It has been found that electric field gives rise to the oscillations of PL intensity along the spectrum, as shown on Fig. 2.

We suppose that the oscillation at $E = 1400-1650$ meV is a result of spectral modulation of light reflection in the buffer GaAs layer with thickness 200 nm due to Franz–Keldysh (FK) effect [2]. In order to test this supposition we have calculated reflection caused in this layer of GaAs by FK effect and have carried out the harmonious analysis. The satisfactory agreement of calculation energy positions of FK oscillation extrema $E_n - E_g$, where E_g is the bandgap energy, and the experiment

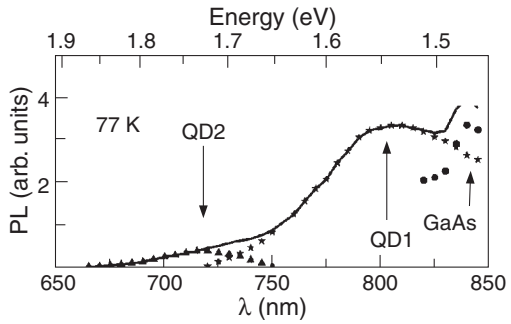

Fig. 1. The PL spectra InAs/AlAs QD measured at 77 K.

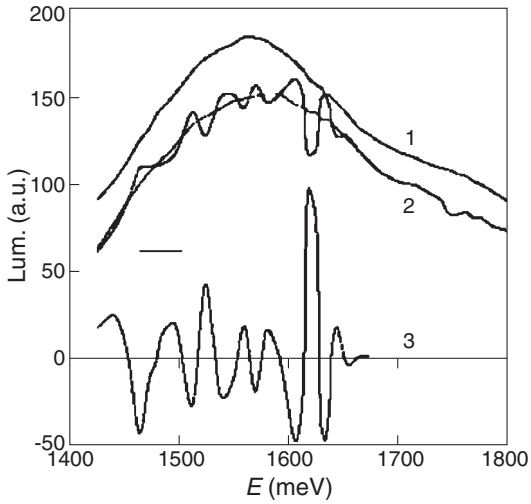

Fig. 2. The PL spectra InAs/AlAs QD measured at 77 K at E equal to 0.2 (trace 1) and 30 (trace 2) kV/cm and their normalized difference (trace 3).

was observed, as seen from Fig. 3.

It has allowed to detrmine $E_g = 1.48$ eV and strength of electric field $E = 30$ kV/cm.

Previouly we have studied oscillations in the 1450–1650 meV spectral area. Here the analysis of the oscillatory structure of the electro-reflection spectrum, which appears in the more short-wave area of the spectrum 1600–1800 meV, is given. Oscillations and positions of their extrema are shown in Fig. 4.

We suppose that the oscillations at $E = 1650-1800$ meV result from spectral modulation of light reflection in cap GaAs layer with thickness 20 nm due to FK effect. To check up this assumption we have carried out a calculation of the FK effect

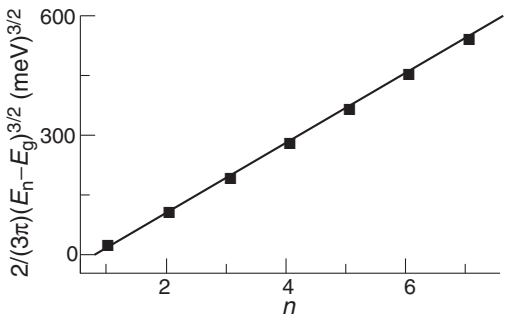

Fig. 3. Calculated energy positions of FK oscillation extrema $E_n - E_g$, where E_g is a bang gap of the layer and n is a number of extremum, for E with strength of 30 kV/cm.

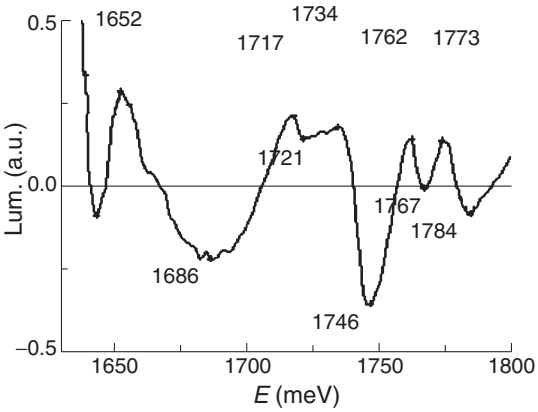

Fig. 4. Extrema of the electroreflection spectrum in the 1600–1800 meV area.

in the model of a two-dimensional crystal.

The satisfactory agreement of calculation energy positions of FK oscillation extrema and experiment was observed. It allowed us to define $E_g = 1.690$ eV and strength of electric field $E \approx 30$ kV/cm. Using the standard program LEVEL the width of a zone of a two-dimensional crystal of the given thickness was defined to be 1.670 eV.

This value, as well as in the first case, is less than the bandgap. We suppose it to be related with the internal stresses which are related to the difference in the lattice constants.

References

[1] D. Bimberg, M. Grundmann, and N. N. Ledentsov *Quantum Dot Heterostructures*, Wiley, New York, 1999.

[2] J. Hader, N. Linder, G. H. Dohler. *Phys. Rev. B* **55**, 6960 (1997).

20th Int. Symp. "Nanostructures: Physics and Technology"
Nizhny Novgorod, Russia, June 24–30, 2012

Collective effects and non-standard excitonic states in SiGe/Si quantum wells

V. S. Bagaev[1], V. S. Krivobok[1], D. N. Lobanov[2], *S. N. Nikolaev*[1], A. V. Novikov[2] and E. E. Onishchenko[1]

[1] P.N. Lebedev Physical Institute, RAS, 53 Leninsky pr., 119991 Moscow, Russia
[2] Institure for Physics of Microstructures, RAS, 603950 Nizhny Novgorod, Russia

Abstract. The features of electron-hole liquid formation in $Si_{1-x}Ge_x$/Si quantum wells with a small Ge content have been studied. The equilibrium density of the quasi-two-dimensional condensed phase, the work function for a particle pair and bandgap renormalization at a different Ge content were determined by studies of IR- and visible luminescence spectra. It was established that the electron-hole liquid is characterized by a high thermal stability despite small binding energy for a particle pair. It can be related to a feature of $Si_{1-x}Ge_x$/Si quantum well bandgap diagram — an existence of the barrier for electrons in SiGe-layer. It lead to the repulsive interaction between the excitons. In such a case the condensed phase stability is increased with an exciton concentartion increase. A new channel of exciton recombination with non-standerd features was found.

Introduction

Since being predicted by Keldysh more than four decades ago, the phenomenon of exciton condensation into droplets of metallic electron-hole liquid (EHL) has been the subject of intense research efforts. With the appearance of two-dimensional 2D-semiconductor structures, it became important to investigate the possibility of exciton condensation, properties of the condensed phase, and the nature of the gas-liquid transition in 2D systems. Quantum wells (QW's) based on strained $Si_{1-x}Ge_x$ layers grown on Si-substrates are a specially suitable kind of semiconductor structures for the experimental studies of the exciton condensation in 2D systems. Such QW's are characterized by long lifetimes of the non-equilibrium carriers that allows us to study collective effects at relatively low excitation densities and to avoid the excitons and non-equilibrium carrier overheating with respect to a lattice. The influence of bandgap diagram of $Si_{1-x}Ge_x$/Si structures with a small Ge content on the exciton condensation and a possibility of formation of non-standard exciton states which were observed in the low temperature luminescence spectra of bulk silicon [1,2] are of special interest. Prominent properties of such states are an anomalous thermal stability at a low binding energy and presence of a structured spectrum in visible region pointing out their multiparticle character.

1. Experiment

Earlier we showed that quasi-2D EHL are formed in $Si_{1-x}Ge_x$/Si QW's with a small Ge content ($x = 0.05$). A study of stability and thermodynamic characteristics of EHL forming in thin $Si_{1-x}Ge_x$/Si QW's with different Ge content and, also, a possibility of non-standared excitonic state formation in such QW's are the main aims of this work. A set of QW's with a thickness of 5.0 ± 0.1 nm with a Ge content varying from 2.9% to 14% was grown by molecular-beam epitaxy on Si(001) substrates. In such structures, there exists an 20–80 meV-deep potential well for holes in the SiGe layer with the heavy-hole subband being the ground state, and confinement of electrons occurs mainly because of their Coulomb attraction to holes. To study a phase transition dynamics and multiparticle state spectrum we used the stationary and time-resolved luminescence techniques. Time-resolved spectra of QW with Ge content 5% demonstrate phase transition from dense electron-hole plasma and liquid to excitonic states (Fig. 1).

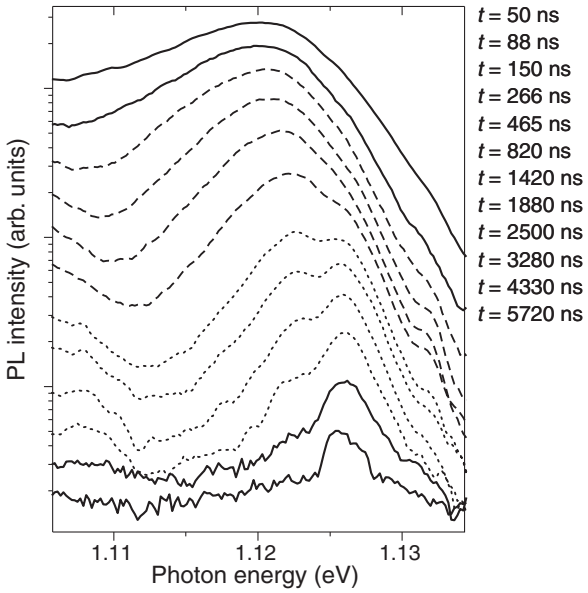

Fig. 1. IR spectra of QW $Si_{0.95}Ge_{0.05}$ transformation after pulse laser excitation at a temperature of 15 K. Delay times are listed rightward. Dense plasma formed just after pulse gradually transform to EHL (dash lines) and then to excitonic states (dot lines).

We performed a luminescence measurements in IR and visible range. A visible luminescence is related to simultaneous recombination of two electrons and two holes accompanied by emission of one photon (so-called 2Eg luminescence). The equilibrium density of the quasi-two-dimensional condensed phase, the work function for a particle pair and bandgap renormalization at a different Ge content were determined by studies of IR- and visible luminescence spectra. The carrier lifetimes and their dependence on the EHL density were determined by the EHL emission decays. It was established that equilibrium density and the work function for a particle increase with decreasing Ge content. It is related to both decrease of the potential barrier for the electrons in SiGe-layer and increase density of states in a valence band. An analysis of the data obtained showed that in the QW with low Ge content ($x = 0.035$) the work function becomes as large as 6 meV (Fig. 2).

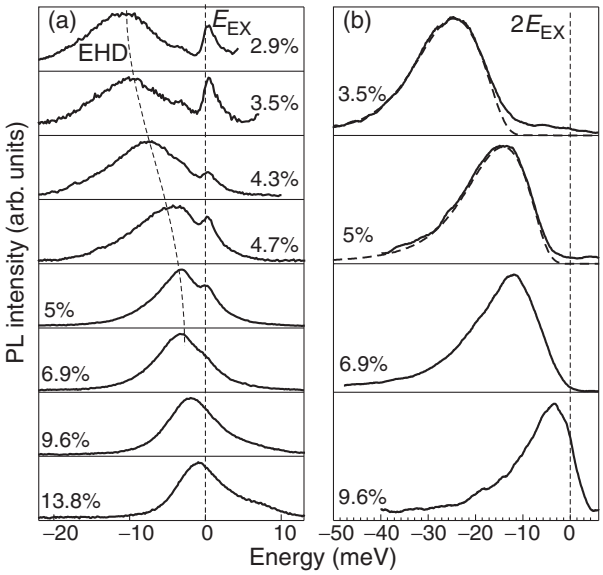

Fig. 2. PL spectra of $Si_{1-x}Ge_x$/Si QW's with different Ge content shifted on energy of QW exciton ground state. a) TO-phonon replica of IR spectra at $T = 10$ K and $W = 0.2$ W/cm^2. b) 2Eg spectra at $T = 2$ K and $W = 2$ W/cm^2. Dashed lines are theoretical approximation [3].

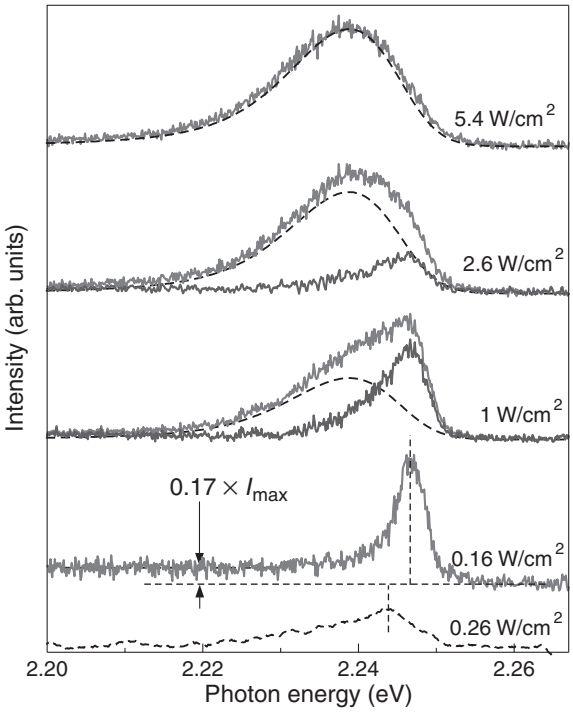

Fig. 3. 2Eg spectra for various excitation power densities (indicated on the right) at a temperature of $T = 15$ K, demonstrating changes in the relative contributions of the (dashed line) electron-hole liquid and (thick solid line) F-line. The lowest curve shows the photoluminescence spectrum of localized multiexciton complexes at 2 K.

This value considerably exceeds the work function for the EHL in uniaxially strained Si (3.8 meV). We did not observe a condensed phase formation in QW with $x > 0.08$. An unusual feature of the structures with Ge content ∼5−7% is a relatively high EHL critical temperature (∼25 K) at low binding energy for a particle pair in EHL (with respect to the bottom of excitonic band). Our estimation based on IR and 2Eg spectra showed that this value is as low as 0.5 meV at $x \sim 5\%$. The EHL stability at high temperatures is explained quite naturally by the existence of a repulsive interaction between excitons in QW's. In such a case the condensed phase stability is increased with an exciton concentartion increase. We describe the EHL emission spectra in terms of a model of 2D electron-hole plasma that takes into account homogeneous broadening [3,4]. A good agreement of the experimental and calculated emission spectra of the condensed phase allows us to extract the EHL contribution to 2Eg spectra. It makes possible to trace in details the features of a new recombination channel (F-line) in dependence on temperature and excitation density. The F-line was found at the short-wavelength wing of the EHL spectrum. The only F-line is observed in the QW emission spectrum in visible range at 15 K and low excitation densities (Fig. 3).

As the excitation level increases, the EHL emission band appears in the PL spectrum and its intensity gradually increases, while the relative contribution from the second recombination channel decreases. A disappearance of F-line from the luminescence spectra with the excitation density increase is caused by a QW filling with the condensed phase. The spectral position of the F-line remains the same in the entire temperature range investigated (5–32 K) and its intensity falls off almost exponentially on the high energy side of the peak. Another interesting feature of the F-line is the existence of a protracted long-wavelength tail, which implies that this line cannot be attributed to biexciton recombination. Tailing of this long-wavelength cutoff is usually explained by the partial transfer of energy from recombining particles to particles remaining after recombination, as it occurs, e.g., for the case of trions. A constant peak position of the F-line at different temperatures and excitation levels can indicate that the F-line is related to multiparticle complexes in which case the line position is determined solely by the complex formation energy. These complexes should be composed of more than four particles (two electrons and two holes). The most feasible candidate for this role is the charged exciton complexes. Thus, it has been shown that the non-standard exciton states — charged exciton complexes characterized by a high thermal stability — is observed in $Si_{1-x}Ge_x$/Si QW's with a small Ge content.

References

[1] A. G. Steele *et al*., *Phys. Rev. Lett.* **59**, 2899 (1987).
[2] L. M. Smith *et al*., *Phys. Rev. B.* **51**, 7521 (1995).
[3] V. S. Bagaev *et al*., *Pis'ma JETP* **94**(1), 63 (2011).
[4] V. S. Bagaev *et al*., *Phys. Rev. B* **82**, 1153131 (2010).

20th Int. Symp. "Nanostructures: Physics and Technology"
Nizhny Novgorod, Russia, June 24–30, 2012

Energy surface of pre-patterned Si/Ge substrate with overlapping pits

P. L. Novikov[1,2], Zh. V. Smagina[1] and A. V. Dvurechenskii[1,2]

[1] A.V. Rzhanov Institute of Semiconductor Physics, SB RAS, Lavrentieva 13, 630090 Novosibirsk, Russia
[2] Novosibirsk State University, Pirogov str. 2, 630090 Novosibirsk, Russia

Abstract. Study of Ge nanoislands formation on pit-patterned Si(001) substrate by molecular dynamics simulations is carried out. Energy surface of Ge/Si(001) structures with overlapping pits was mapped out. By the analysis of the energy surface the mechanism of adatoms diffusion on the pit-patterned surfaces is described. Energy of Si/Ge heterosystem with various morphologies of Ge nanoislands inside the pits was calculated. It is shown that the configuration with more than one QDs per pit can be energetically favorable.

Introduction

The challenge for investigators working in the field of material science is the formation of space arranged arrays of semiconductor quantum dots (QDs). These quasi zero-dimensio-nal systems exhibit abundant physical properties and offer great potential for device applications, such as light-emitting devices, QD-based lasers, spintronics, or even quantum computation. An effective way to solve the problem of the inhomogeneous size distribution and random location of QDs is utilization of lithographic techniques to prepare substrates with pre-patterned pits in well-defined positions [1–3]. The pits act as the nucleation sites for subsequently grown dots. However, even though extensive studies on growth of Ge dots on pit-patterned Si substrates have been carried out, still there exists a lack of knowledge about Ge QD formation mechanism and fundamental limits of the pit size favorable for space arrangement [3]. In our previous works [4, 5] it was shown that for pits widely separated from each other the pit bottoms are the preferable sites for Ge nanoisland nucleation. In the present paper the case of close pit location is considered, providing the conditions for nucleation of several QDs (QD molecule) in a single pit.

1. Model

MD simulation was used to study the properties of pit-patterned surface. The system under consideration included Si and Ge atoms, forming the pit-patterned structure, with interaction described by the empirical Tersoff potential [6]. By the numerical solution of Newton equation an equilibrium state of the system can be found. In particular, the equilibrium energy of a Ge adatom sticken to the surface at a certain point can be determined. Using such a probe Ge adatom, the energy surface is obtained through the scanning over the surface of the simulated structure. The procedure of energy surface calculation is similar to that described in [7]. Prior to energy calculations the simulated structures were allowed to relax. The basic simulated structure was composed by 18 × 18 nm mesh of 20 ML-thick Si(001) with top 2 ML-thick Ge(001)-(2 × 1) film. The structure contained the pits, which had a shape of inverted square-base pyramid with (117)-oriented side walls. The pits were 10 nm wide with a small overlapping between each other at the corners. Periodical boundary conditions were used in the lateral directions.

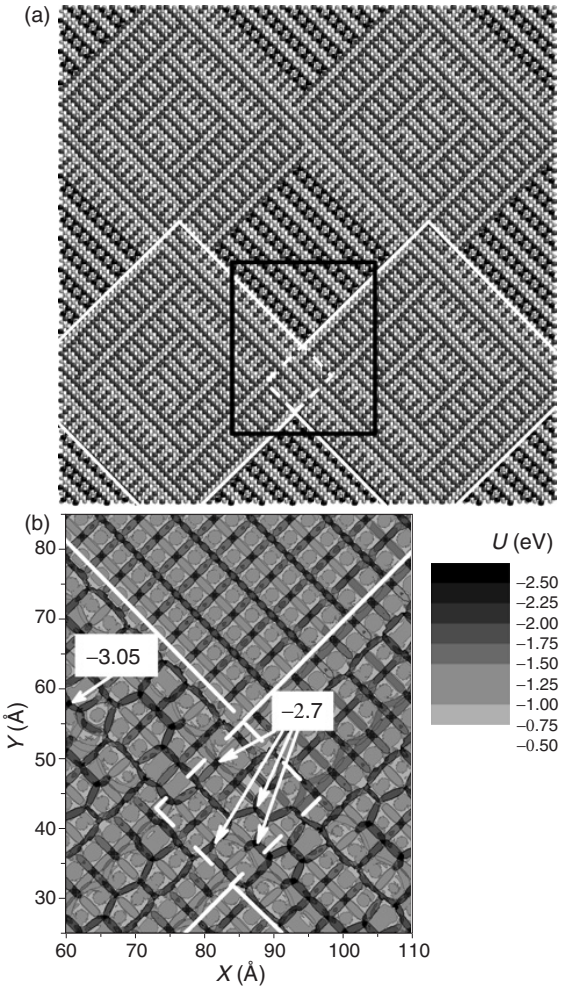

Fig. 1. (a) Simulated structure of 2ML-thick Ge(001)-(2 × 1) film on a pit-patterned Si(001) substrate (plan view). The gray and light-gray dots represent the Ge and Si atoms, respectively. Ge atoms in dimer rows are painted in black. The pit has a shape of inverted square-base pyramid with (117)-oriented sidewalls. The energy surface was calculated within the region marked by the black rectangle. (b) Energy surface map of pit-patterned Si/Ge(001)-(2 × 1) structure. Grayscale is used for indication of energy magnitudes. The energy values (in eV) at the relevant points are shown with labels.

2. Results and discussion

Fig. 1a presents the simulated Si/Ge(001)-(2 × 1) surface with pits. Two neighbor pits are outlined by solid white line. Within the area indicated by the black rectangle in Fig. 1a the energy

surface was calculated (Fig. 1b). White lines corresponding to the pit edges (solid) and to the overlapping region (dashed) are imposed upon Fig. 2b for clarity. The analysis of the map shows, that outside the pits Ge adatom migration occurs mainly through the diffusion channels (straight nearly monotonous gray paths in Fig. 2b). Being formed between the dimer rows at the planar surface, the diffusion channels are broken at the pit edges by the energy barrier of 1.0 eV. Ge atoms, which have reached the break of the diffusion channel, migrate mainly along the pit edge to a corner, where the network of minima (about -2.7 eV) is located. This retards adatom diffusion inside pits and promotes accumulation of Ge near the region of pits overlapping. Adatoms, which underwent the barriers in the overlapping region, migrate further along the intersection lines between the sidewalls to a bottom, where the most deep minimum of approximately -3 eV is located. Thus, both the bottom and the intersection lines are preferential sites for Ge accumulation. At further heteroepitaxial growth this may promote the nucleation of 3D Ge islands. Using the approach developed in our previous work [5] we calculated the energy of three alternative configurations of Ge hut clusters in a single pit: (i) one QD at the bottom, (ii) four QDs at the corners and (iii) five QDs at the corners and bottom, respectively. For overlapping pits the configuration with four QDs is characterized by the minimum energy per atom and, thus, is estimated to be the most energetically favorable. We would point out that all three QDs configurations considered were observed in experiments [1,2].

Acknowledgements

This work was supported by RFBR (grants 10-02-01181 and 11-02-12018).

References

[1] G. Bauer and P. Schäffler, *Phys. Stat. Sol.* **203**, 3496 (2006).
[2] C. Dais, H.H. Solak, Ya. Ekinci, E. Muller, H. Sigg and D. Grützmacher, *Surf. Sci.* **601**, 2787 (2007).
[3] A. Pascale, I. Berbezier, A. Ronda and P. C. Kelires, *Phys. Rev. B* **77**, 075311 (2008).
[4] P. Novikov, J. Smagina,D. Vlasov, A. Deryabin, A. Kozhukhov and A. Dvurechenskii, *J. Cryst. Growth.* **323**, 198 (2011).
[5] P. Novikov, J. Smagina, and A. Dvurechenskii, *Proceedings 19th Intern. Symposium Nanostructures: Physics and Technology (Ekaterinburg, Russia, June 20–25, 2011)* pp. 201–202.
[6] J. Tersoff, *Phys. Rev. B* **37**, 6991 (1988).
[7] C. Roland and G.H. Gilmer, *Phys. Rev. B* **46**, 13428 (1992).

20th Int. Symp. "Nanostructures: Physics and Technology"
Nizhny Novgorod, Russia, June 24–30, 2012

Photovoltaic Ge/Si quantum dot photodetectors for midinfrared applications

A. I. Yakimov, *A. A. Bloshkin*, V. A. Timofeev, A. I. Nikiforov and A. V. Dvurechenskii
A.V. Rzhanov Institute of Semiconductor Physics, SB RAS, Lavrentieva 13, 630090 Novosibirsk, Russia

Abstract. Ge/Si quantum dots fabricated by molecular-beam epitaxy at 500 °C are overgrown with Si at different temperatures T_{cap}, and their mid-infrared photoresponse is investigated. The photocurrent maximum shifts from 2.3 to 3.9 μm with increasing T_{cap} from 300 to 750 °C. The best performance is achieved for the detector with $T_{cap} = 600$ °C in a photovoltaic mode. At a sample temperature of 90 K and no applied bias, a responsivity of 0.43 mA/W and detectivity of 6.2×10^{10} cm Hz$^{1/2}$/W at $\lambda = 3$ μm were measured under normal incidence infrared radiation. The device exhibits very low dark current ($I_{dark} = 2$ nA/cm^2 at $T = 90$ K and $U = -0.2$ V) and operates until 200 K.

Introduction

In the past years, there has been a surge of interest in structures that exhibit quantum confinement in all three dimensions, commonly known as quantum dots (QDs). Intersubband optical transitions in QDs has attracted a great deal of attention due to their potential applications in infrared detectors operating at normal incidence and displaying low dark current. Most of the demonstrations of quantum dot photodetectors were achieved with III-V heterostuctures. Ge QDs enclosed in a silicon matrix represent another attractive type of the device due to its compatibility with standard Si readout circuitry. In particular, it has been demonstrated that Ge/Si(001) QDs exhibit intraband photoresponse in the spectral range 3–4 μm [1,2], thus opening the route towards the fabrication of mid-infrared detectors. However little is known on the current noise and specific detectivity of Ge/Si detectors. For application of QDs in optical devices, control of the emission or absorption wavelength is of major importance. Schmidt *et al*. [3] and Denker *et al*. [4] have found that an approach to tune the emission spectra of self-assembled Ge/Si dots in the near infrared range is the adjustment of Si overgrowth temperature T_{cap}. The capping of Ge islands under a Si layer at elevated T_{cap} results both in Ge-Si intermixing and in changing of island size and shape [5], which drastically affects the electronic spectrum of the dots.

This letter presents mid-infared photoresponse data on embedded Ge/Si quantum dots, where the overgrowth temperature was systematically varied. The best photodetector performance is obtained in the sample with $T_{cap} = 600$ °C. Under zero bias conditions, we have measured a detectivity of 6.2×10^{10} cm Hz$^{1/2}$/W, with a responsivity of 0.43 mA/W at a wavelength $\lambda = 3$ μm and at a temperature 90 K.

1. Device structure

Fig. 1a shows schematically the detector structure. The samples were grown by solid source molecular beam epitaxy on a (001) oriented boron doped p^+-Si substrate with resistivity of 0.01 Ω cm. An active region was composed of ten stacks of Ge quantum dots separated by 50 nm Si barriers. Each Si barrier contains a boron delta-doping layer inserted 5 nm below the Ge wetting layer to produce, after spatial transfer, a 8×10^{11} cm^{-2} hole concentration in the dots corresponding to complete filling of the dot ground state. Each Ge QD layer consisted of a nominal Ge thickness of about 6 monolayers (ML) and formed by self-assembling in the Stranski–Krastanov growth mode at

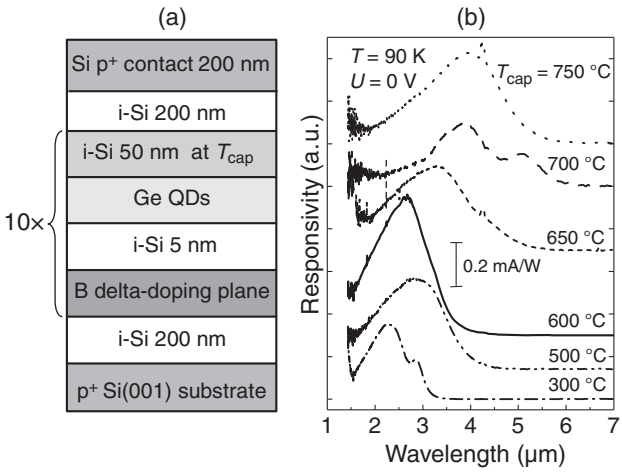

Fig. 1. (a) Schematic drawing of the detector structure. (b) Series of responsivity spectra of Ge/Si QD samples where the capping temperature T_{cap} was systematically varied from 300 to 750 °C. The sample temperature is 90 K, the applied bias is 0 V. The spectra have been vertically displaced for clarity.

500 °C and at a growth rate of 0.2 ML/s for all samples. The Si barriers were deposited at T_{cap} ranging from 300 to 750 °C for different samples, with temperature ramps before and after QD growth. The increase of the overgrowth temperature is expected to result in a lowering of the hole binding energy in the dots due to enhanced Si-Ge alloying [3,4].

The active region was sandwiched in between the 200-nm-thick intrinsic Si buffer and cap layers. Finally, a 200-nm-thick p^+-Si top contact layer ($p = 5 \times 10^{18}$ cm^{-3}) was deposited. For vertical photocurrent measurements the samples were processed in the form of circular mesas with diameter 3 mm by using wet chemical etching and contacted by Al:Si metallization. For the Ge dot deposition, we chose 500 °C, since at this temperature the hut-shaped Ge islands with high areal density [$(3-4) \times 10^{11}$ cm^{-2}] and small size (10–15 nm of base length) are formed. [6]

The normal-incidence photoresponse was obtained using a Bruker Vertex 70 Fourier transform infrared spectrometer along with a SR570 low noise current preamplifier. The bias polarity is relative to the grounded bottom contact. The noise characteristics were measured with an SR770 fast Fourier transform analyzer and the white noise region of the spectra was used to determine the detectivity. The sample noise was obtained by subtracting the preamplifier-limited noise level from the

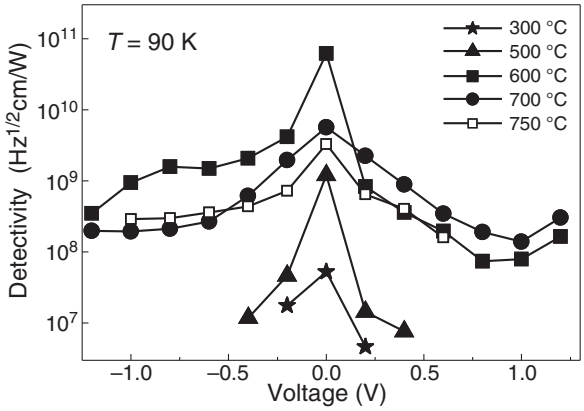

Fig. 2. Detectivity as a function of applied bias for Ge/Si QD structures where the capping temperature $T_{\rm cap}$ was varied from 300 to 750 °C. The measurement temperature is 90 K. For the samples with $T_{\rm cap} = 300$, 500, and 600 °C the data were taken at $\lambda = 3$ μm. For the samples with $T_{\rm cap} = 700$ and 750 °C, the peak detectivity is shown.

experimental data. The dark current ($I_{\rm dark}$) was tested as a function of bias (U) by a Keithley 6430 Sub-Femtoamp Remote SourceMeter. The devices were mounted in a cold finger inside a Specac cryostat with ZnSe windows. For dark current and noise measurements, the samples were surrounded with a cold shield.

2. Experimental setup

Fig. 1b depicts the photovoltaic spectral response at $T = 90$ K from six detectors in which the overgrowth temperature was varied from 300 to 750 °C. In all samples a broad peak is observed with no applied voltage. This is caused by existence of a built-in electric field due to asymmetric shape of Ge QDs and δ-doping planes in the Si barriers. The broad nature of the response ($\Delta\lambda/\lambda \simeq 0.5$) suggests that the photocurrent could be due to a bound-to-continuum transition. In some samples, i.e., for $T_{\rm cap} = 300$ and 700 °C, double peak structure is visible probably due to participating of QD excited states. As expected, the peak wavelength of the detector shows a redshift from 2.3 to 3.9 μm with increasing $T_{\rm cap}$. This is significant since it provides a recipe to control the operating wavelength of a Ge/Si QD detector.

The specific detectivity is given by $D^* = R_s\sqrt{A\,\Delta f}/i_n$, where A is the device area, R_s is the responsivity, i_n is the noise current, and Δf is the bandwidth. Despite the responsivity value is approximately the same for all samples [see Fig. 1b], the detectivity is ultimate for $T_{\rm cap} = 600$ °C [see Fig. 2]. The physical mechanism of such a behavior is still under investigation. We suspect that at low cap temperature, a large number of point defects are generated in Si layers producing high noise level. At the same time, at $T_{\rm cap} > 700$ °C the structure resembles a two-dimensional SiGe layer with significant composition and thickness variations [4], thus again giving rise to a large dark current. The best performance was achieved for $T_{\rm cap} = 600$ °C in the photovoltaic mode, where $D^* = 6.2\times10^{10}$ cm Hz$^{1/2}$/W at $\lambda = 3$ μm. This value is much larger than that observed previously in photovoltaic quantum-well [7] and quantum-dot [8] mid-infrared photodetectors at 90 K.

3. Summary

In summary, we have presented the performance characteristics of Ge/Si(001) quantum-dot mid-infrared detectors in which the capping temperature $T_{\rm cap}$ was systematically varied. With increasing $T_{\rm cap}$ from 300 to 750 ° the photocurrent peak wavelength shifts from 2.3 to 3.9 μm, reflecting enhanced Si-Ge intermixing at higher overgrowth temperatures. The best characteristics are demonstrated by the sample with $T_{\rm cap} = 600$ °C. The BLIP temperature was about 90 K with 300 K background and a 53 ° field of view. High photovoltaic detectivity of 6.2×10^{10} cm Hz$^{1/2}$/W at a wavelength of 3 μm was achieved at $T = 90$ K. The possibility of the device to operate in a photovoltaic mode makes it compatible with existing Si-readout circuits in focal plane array applications.

Acknowledgements

The authors would like to thank V. V. Kirienko for assistance in sample preparation. The work was supported by RFBR (Grant No. 11-02-12007). A.A.B. acknowledges financial support of the Dynasty Foundation.

References

[1] A.I. Yakimov, A.V. Dvurechenskii, Yu.Yu. Proskuryakov, A.I. Nikiforov, O.P. Pchelyakov, S.A. Teys, A.K. Gutakovskii, *Appl. Phys. Lett.* **75**, 1413 (1999).
[2] C. Miesner, O. Röthig, K. Brunner, G. Abstreiter, *Appl. Phys. Lett.* **76**, 1027 (2000).
[3] O.G. Schmidt, U. Denker, K. Eberl, O. Kienzle, and F. Ernst, *Appl. Phys. Lett.* **77**, 2509 (2000).
[4] U. Denker, M. Stoffel, O.G. Schmidt, and H. Sigg, *Appl. Phys. Lett.* **82**, 454 (2003).
[5] P. Sutter and M.G. Lagally, *Phys. Rev. Lett.* **81**, 3471 (1998).
[6] A.I. Yakimov, A.I. Nikiforov, A.V. Dvurechenskii, V.V. Ulyanov, V.A. Volodin, and R. Groetzschel, *Nanotechnology* **17**, 4743 (2006).
[7] B.F. Levine, *J. Appl. Phys.* **74**, R1 (1993).
[8] L. Nevou, V. Liverini, F. Castellano, A. Bismuto, and J. Faist, *Appl. Phys. Lett.* **97**, 023505 (2010).

20th Int. Symp. "Nanostructures: Physics and Technology"
Nizhny Novgorod, Russia, June 24–30, 2012

Ge/Si(001) heterostructures with quantum dots: formation, defects, photo-electromotive force and terahertz conductivity

V. A. Yuryev[1,2], L. V. Arapkina[1], M. S. Storozhevykh[1], V. A. Chapnin[1], K. V. Chizh[1], O. V. Uvarov[1], V. P. Kalinushkin[1,2], E. S. Zhukova[1,3], A. S. Prokhorov[1,3], I. E. Spektor[1] and B. P. Gorshunov[1,3]

[1] A.M. Prokhorov General Physics Institute, RAS, 38 Vavilov str. 38, 119991 Moscow, Russia
[2] Technopark of GPI RAS, 38 Vavilov str., 119991 Moscow, Russia
[3] Moscow Institute of Physics and Technology, Institutsky per. 9, Dolgoprudny, 141700 Moscow Region, Russia

Abstract. Issues of Ge hut cluster nucleation and growth at low temperatures on the Ge/Si(001) wetting layer are discussed on the basis of explorations performed by high resolution STM and *in-situ* RHEED. Data of HRTEM investigations of Ge/Si heterostructures are presented with the focus on low-temperature formation of perfect multilayer films. Exploration of the photovoltaic effect in Si *p-i-n*-structures with Ge quantum dots allowed us to propose a new approach to designing of infrared detectors. First data on THz dynamical conductivity of Ge/Si(001) heterostructures in the temperature interval from 5 to 300 K and magnetic fields up to 6 T are reported.

Introduction

Results of our researches of Ge/Si(001) structures aimed at development of CMOS compatible IR detectors have been published in a number of publications [1–4]. This article reports our recent results concerning formation of Ge quantum dot arrays, growth of multilayer structures, their photoelectrical properties and dielectric characteristics at THz frequencies.

1. Formation and defects

We demonstrate that huts form via parallel nucleation of two characteristic embryos different only in symmetry and composed by epitaxially oriented Ge dimer pairs and chains of four dimers on tops of the wetting layer (WL) $M \times N$ patches: an individual embryo for each species of huts–pyramids or wedges. These nuclei always arise on sufficiently large WL patches: there must be enough space for a nucleus on a single patch; a nucleus cannot form on more than one patch. This fact may be explained in assumption of presence of the Ehrlich–Schwoebel barriers on sides of WL patches which prevent the spread of dimer chains composing nuclei from one patch to another; nuclei form on bottoms of potential wells of the spatial potential relief associated with the WL patches. The total patch thickness (from Si/Ge interface to the patch top) rather than the mean thickness of WL controls the hut nucleation process. A growing hut likely reduces and finally eliminates the potential barrier; then it occupies adjacent WL patches.

We suppose also that WL patch top reconstruction determines the type of a hut which can form on a patch. If this is the case, the $c(4 \times 2)$ reconstruction of the patch top enables the nucleation of a pyramid, whereas the $p(2 \times 2)$ reconstruction allows a wedge to arise on the patch. Domination of one of these reconstruction types may result in domination of a certain species of huts.

Dynamics of the RHEED patterns in the process of Ge hut array formation is investigated at low and high temperatures of Ge deposition. At high temperatures, as h_{Ge} increases, diffraction patterns evolve as $(2 \times 1) \rightarrow (1 \times 1) \rightarrow (2 \times 1)$ with very weak 1/2-reflexes. Brightness of the 1/2-reflexes increases (the (2×1) structure becomes pronounced) and the 3D-reflexes arise only during sample cooling. At low temperatures, the structure changes as $(2 \times 1) \rightarrow (1 \times 1) \rightarrow (2 \times 1) \rightarrow (2 \times 1) + 3$D-reflexes. Different dynamics of RHEED patterns during Ge deposition in different growth modes reflects the difference in mobility and "condensation" fluxes from Ge 2D gas of Ge adatoms on the surface, which in turn control the nucleation rates and densities of Ge clusters. High Ge mobility and low cluster nucleation rate in comparison with fluxes to competitive sinks of adatoms determine the observed difference in the surface structure formation at high temperatures as compared with that at low temperatures.

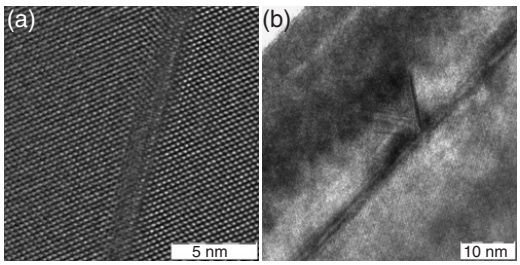

Fig. 1. HRTEM micrographs of Ge quantum dots in Si; $T_{\mathrm{gr}} = 360\,^{\circ}\mathrm{C}$ for Ge and 530 °C for Si, h_{Ge} is (a) 6 Å, (b) 10 Å.

Data of HRTEM studies evidence that extended defects do not arise at low Ge coverages (h_{Ge}) on the buried Ge clusters (Fig. 1a) and perfect epitaxial heterostructures with quantum dots form under these conditions that enables the formation of defectless multilayer structures suitable for device applications. Stacking faults (SF) have been found to arise on Ge clusters at h_{Ge} as large as 10 Å (Fig. 1b). Multiple SFs often damage multilayer structures at these h_{Ge}.

2. Photo-electromotive force

Heteroepitaxial Si *p-i-n*-diodes with multilayer stacks of Ge/Si (001) quantum dot dense arrays built in intrinsic domains have been investigated and found to exhibit the photo-emf in a wide spectral range from 0.8 to 5 μm. The diodes comprised *n*-Si(100) substrate (0.1 Ωcm), Si buffer (1690 nm), 4 periods of [Ge (1 nm), Si barrier (30 nm)], [Ge (1 nm), Si (50 nm)], *p*-Si:B cap (212 nm, $p \sim 10^{19}$ cm^{-3}) An effect of wide-band irradiation by IR light on the photo-emf spectra has been observed. Photo-emf in different spectral ranges has been found to be differently affected by the wide-band lighting (Fig. 2a). A significant increase in photo-emf is observed in the fundamental absorption range under the wide-band IR irradiation (Fig. 2b). The above phenomena are explained in terms of

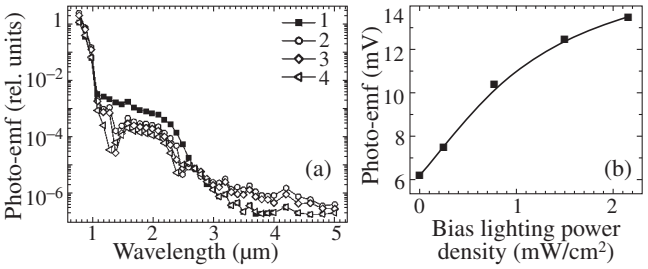

Fig. 2. (a) Photo-emf spectra of the *p-i-n*-structure; (1) without bias lighting; (2)–(4) under wide-band IR bias lighting (tungsten bulb, Si filter, $\lambda > 1.1$ μm): (2) $W = 0.63$ mW/cm^2; (3) $W = 5.3$ mW/cm^2; (4) $W = 17.5$ mW/cm^2. (b) The dependence of the *p-i-n*-structure photo-emf, generated by narrow-band illumination in Si fundamental absorption range, on the power density of bias lighting; $T = 80$ K.

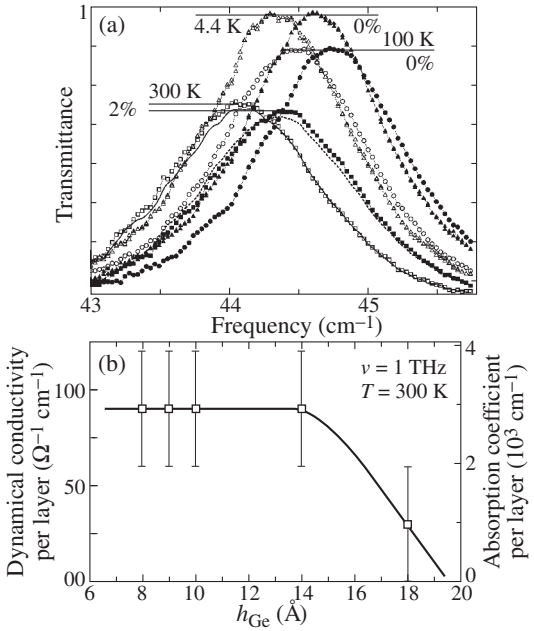

Fig. 3. (a) Transmittance spectra of a 5-layer Ge/Si(001) heterostructure ($T_{gr} = 360$ °C, $h_{Ge} = 8$ Å) recorded at different temperatures; dark and open symbols relate to substrate regions with and without the heterostructure; solid and dotted lines show spectra obtained at 300 K under magnetic field of 6 T directed normal to the surface, without and with the heterostructure, respectively. (b) Terahertz conductivity and absorption coefficient of terahertz radiation in multilayer Ge/Si(001) heterostructures vs Ge coverage in each layer; $\nu = 1$ THz, $T = 300$ K.

positive and neutral charge states of the quantum dot layers and the Coulomb potential of the quantum dot ensemble which changes under the wide-band IR radiation.

A new design of photovoltaic quantum dot infrared photodetectors is proposed [5] which enables detection of variations of photo-emf produced by the narrow-band radiation in the Si fundamental absorption range under the effect of the wide-band IR radiation resulted from changes in the Coulomb potential of the quantum dot ensemble affecting the efficiency of the photovoltaic conversion. The quantum dot array resembles a grid of a triode in these detectors which is controlled by the detected IR light. The reference narrow-band radiation generates a potential between anode and cathode of this optically driven quantum dot triode. Such detectors can be realized

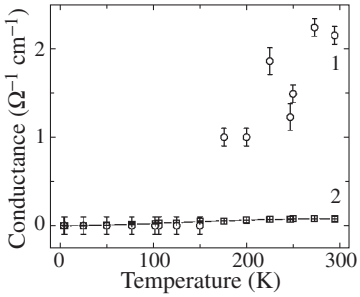

Fig. 4. Temperature dependences of THz conductance of the Ge/Si(001) heterostructure (1) and the Si substrate (2).

on the basis of any appropriate semiconductor structures with potential barriers, e.g., *p-n*-junctions or Schottky barriers, and built-in arrays of nanostructures.

3. Terahertz conductivity

By using a coherent source spectrometer [6], first measurements of THz dynamical conductivity (or absorptivity) spectra of Ge/Si(001) heterostructures were performed at frequencies from 0.3 to 1.2 THz in the temperature interval from 300 to 5 K and also in magnetic fields up to 6 T. The effective dynamical conductivity of the heterostructures was determined by comparing the terahertz transmission coefficient spectra of the sample with the heterostructure on Si substrate with that of the same sample but with the heterostructure etched away. The results are exemplified by the transmission coefficients spectra shown in Fig. 3a. Although rather small, the difference in the amplitudes of the interference maxima (due to multiple reflections of the monochromatic radiation between the faces of the sample) is clearly seen and reliably detected. Processing this kind of spectra allowed us to extract the dynamical conductivity of heterostructures separately and trace its dependence on the thickness of the germanium coverage layer; the latter determines whether this layer organizes itself into an array of quantum dots or stays as a uniform layer. As a results, the THz dynamical conductivity of Ge quantum dots (Fig. 3b) has been discovered to be significantly higher than that of the structure with the same amount of bulk germanium (not organized in an array of quantum dots). The excess conductivity is not observed in the structures with the Ge coverage less than 8 Å. When a Ge/Si(001) sample is cooled down the conductivity decreases (Fig. 4). It is seen from Fig. 3a that the samples display positive magnetoresistivity.

Acknowledgements

This research has been supported by the Ministry of Education and Science of RF through the contracts No. 14.740.11.0069 and No. 16.513.11.3046 and RFBR through the grant No. 11-02-12023-ofi-m. Center of Collective Use of Scientific Equipment of GPI RAS is appreciated for instrumentation and Prof. M. Dressel for providing equipment for magnetic measurements.

References

[1] L. V. Arapkina *et al.*, *Phys. Rev. B* **82**, 045315 (2010).
[2] L. V. Arapkina *et al.*, *J. Appl. Phys.* **109**, 104319 (2011).
[3] L. V. Arapkina *et al.*, *Nanoscale Res. Lett.* **6**, 345 (2011).
[4] V. A. Yuryev *et al.*, *Nanoscale Res. Lett.* **6**, 522 (2011).
[5] V. A. Yuryev *et al.*, Patent pending (2012).
[6] B. Gorshunov *et al.*, *Int. J. Infrared Millimeter Waves* **26**, 1217 (2005).

20th Int. Symp. "Nanostructures: Physics and Technology"
Nizhny Novgorod, Russia, June 24–30, 2012

SiGe quantum dot molecules grown on strain-engineered surface

V. A. Zinovyev[1], P. A. Kuchinskaya[1], A. V. Nenashev[1,2], P. L. Novikov[1,2], V. A. Armbrister[1], Zh. V. Smagina[1], A. V. Dvurechenskii[1,2] and A. V. Mudryi[3]

[1] A.V. Rzhanov Institute of Semiconductor Physics, SB RAS, Lavrentieva 13, 630090 Novosibirsk, Russia
[2] Novosibirsk State University, 630090 Novosibirsk, Russia
[3] Scientific-Practical Material Research Centre of the National Academy of Science of Belarus, 220072 Minsk, Belarus

Abstract. We exploit the stress field distribution at the surface of a multilayered Ge/Si structure in order to obtain a positional ordering of the self-assembled SiGe quantum dots in ring-like chains (quantum dot molecules). The electronic band structure of the quantum dot molecules was calculated by 6-band $\mathbf{k} \times \mathbf{p}$ method. The results of these calculations are in a good agreement with experimental measurements of photoluminescence spectra from the samples with SiGe quantum dot molecules.

Introduction

Semiconductor quantum dot molecules (QDMs) are systems composed of two or more closely spaced and interacting quantum dots (QDs). QDMs has attracted much attention both as ground for studying coupling and energy transfer processes between "artificial atoms" and as new systems, which substantially extend the range of possible applications of QDs [1,2]. This particular nanostructure is a symmetric assembly of four quantum dots bound by a central pit and has been suggested as a candidate structure for logic architecture based on quantum cellular automata [3]. The present work devotes to the study of the formation of QDMs during heteroepitaxial growth on strain-engineered surface. We exploit the stress field distribution at the surface of multilayer structure with SiGe quantum rings (QRs) to create preferential sites for nucleation of QDs. We demonstrate that, by this technique, it is possible to obtain an array of the ring-like QDMs composed of closely spaced QDs.

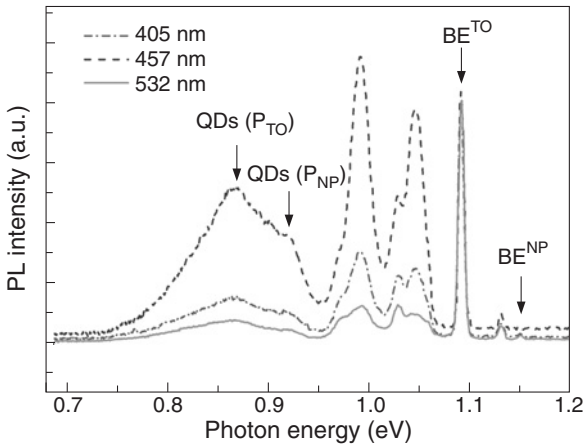

Fig. 2. PL spectra from Ge/Si heterostructure with QDMs measured at $T = 4$ K. PL is excited by lasers with different wave lengths: 532, 457m, 405 nm. The non-phonon peaks and its transverse optical replicas are indicated by "NP" and "TO", respectively.

1. Experimental findings

Ge/Si structures with QDMs was grown by molecular beam epitaxy (Riber SiVA-21). After standard cleaning and in-situ oxide desorption, a 50 nm-thick Si buffer layer was deposited on Si (100) substrate. The array of self-assembled SiGe QDs was formed by the following deposition of Ge on Si(100) substrate at the temperature about 700 °C. Then, SiGe QRs were created by partially Si capping on QDs [4]. After this, a few monolayers of Ge deposited over QRs. Thus, SiGe QRs were used as strain-patterning template for nucleation of Ge QDs in the next layer. It was found, that by choosing a suitable deposition temperature of Ge, lower than that used to fabricate the template, the ring-like chains of closely spaced QDs can be formed (Fig. 1). Scanning tunneling microscopy (STM) revealed, that QDs are hut-clusters, which are arranged along ring's perimeter. The height of hut-clusters is 5 ± 0.8 nm, the transverse and longitudinal base sizes are 53 ± 4.7 nm and 92 ± 13.2 nm, correspondingly. The average number of QDs in the chains is about 4. The Ge/Si structures with QDMs were preserved by deposition 40 nm-thick Si capping layer at 500 °C and studied by the photoluminescence (PL) spectroscopy. PL spectra reveal two excitonic peaks: 920 meV (P_{NP}) and 867 meV (P_{TO}) (Fig. 2), which can be is attributed to non-phonon and phonon-mediated transitions of electrons from Si conductive band to ground state of holes in SiGe QDs [5,6]. The non-phonon peak and its transverse optical replica from QDs are indicated by "NP" and "TO", respectively

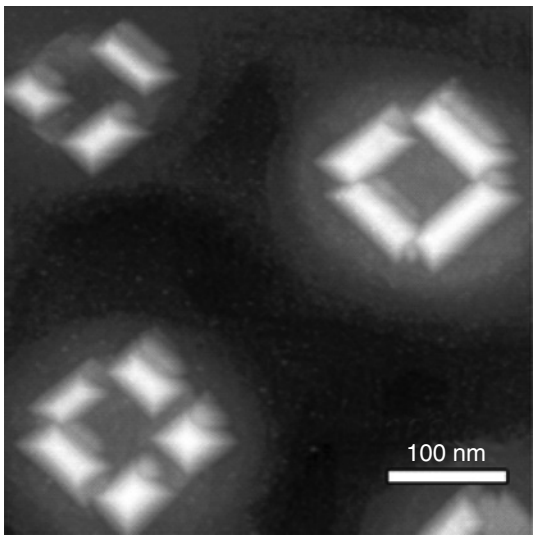

Fig. 1. STM image of the surface area (0.5×0.5 μm) with ring-like chains of SiGe QDs.

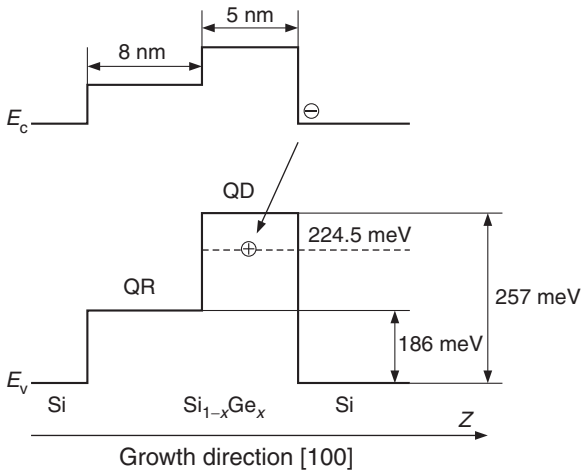

Fig. 3. Schematic band-edge diagram of Ge/Si heterostructure with QDMs along the growth direction with the relevant interband transition corresponding to the observed PL peaks.

2. Energy spectrum calculations

To support our interpretation of PL spectra, a numerical analysis of the electronic band structure of the GeSi QDMs was performed by 6-band $\mathbf{k} \times \mathbf{p}$ method. Because of the small aspect ratio height/base of the QDs, the quantum confinement effects are mostly determined by the dot height along the [001] growth direction, which justifies that the QDs, in a simplified picture, can be modeled by GeSi quantum wires (QWs) embedded in Si. In two-dimensional approximation, the QDMs composed from QDs on QR represented by two wires. QDs modeled by triangle QWs, QRs by trapezoid QWs. Geometrical parameters used in calculation correspond to STM data. Heights are 5 and 8 nm, widths are 50 and 90 nm for triangle and trapezoid wires, correspondingly. The Ge content used in the calculations were 25% for QRs and 35% QDs, which correspond to experimental data obtained by Raman spectroscopy. The energy levels of hole states in SiGe QDMs were counted from the top of the Si valence band (Fig. 3). The calculation showed that the energy level of hole ground state E_{h} localized in QD is 224.5 meV. Emission energy for spatially indirect non-phonon transition of electrons from Si conductive band to hole ground states in SiGe QDMs can be estimated, as $E_{\mathrm{BE}} - E_{\mathrm{h}}$, where E_{BE} is emission energy for bound excitons in Si. According PL data E_{BE} is about 1150 meV for non-phonon exciton recombination ($\mathrm{BE}^{\mathrm{NP}}$ in Fig. 2). Then, this simple estimation gives emission energy for non-phonon transition is about 925.5 meV, that is a good agreements experimental value 920 meV.

References

[1] L. Wang *et al*., *Adv. Mater.* **21**, 2601 (2009).
[2] J. H. Lee *et al*., *Phys. Rev. B* **89**, 202101 (2006).
[3] H.Yang *et al*., *J. Appl. Phys.* **104**, 044303 (2008).
[4] Stoffel *et al*., *Appl. Phys. Lett.* **94**, 253114 (2009).
[5] O. G. Schmidt, C. Lange, K. Eberl, *Appl. Phys. Lett.* **75**, 1905 (1999).
[6] Z. Zhong *et al*., *Journal of Physics: Conference Series* **38**, 69 (2006).

20th Int. Symp. "Nanostructures: Physics and Technology"
Nizhny Novgorod, Russia, June 24–30, 2012

Conduction band alignment in the GeSi/Si(001) self assembled nanoislands studied by tunnelling atomic force microscopy

D. O. Filatov[1], V. G. Shengurov[1], V. Yu. Chalkov[1], S. A. Denisov[1], A. A. Bukharaev[2] and N. I. Nurgazizov[2]

[1] Research Physical-Technical Institute of the Nizhny Novgorod State University,
603950 Nizhny Novgorod, Russia
[2] Zavoisky Physical Technical Institute, Kazan Scientific Center, Russian Academy of Science,
420029 Kazan, Russia

Abstract. The conduction band alignment in the self assembled Ge_xSi_{1-x}/Si(001) nanoislands grown by sublimation molecular beam epitaxy in GeH_4 has been studied as a function of x by tunnelling atomic force microscopy. The surface Ge_xSi_{1-x}/Si(001) nanoislands have been found to be the heterostructures of the I type at $x < 0.45$.

The GeSi/Si(001) nanostructures have been being studied extensively during the last two decades because of their potential applications in silicon-based photonics [1]. Conventionally, the GeSi/Si(001) heterostructures had been being considered to be the II-type ones. However, there is an increasing number of publications, both theoretical and experimental, where the Ge_xSi_{1-x}/Si(001) heterostructures have been reported to be the I type ones at low values of x [2,3]. More recent 30-band $k \times p$ calculations [4] have demonstrated the pseudomorphic Ge_xSi_{1-x}/Si(001) heterolayers to be the ones of the I type at $0.05 < x < 0.45$.

Recently we have applied tunnelling atomic force microscopy (AFM) to the investigation of the band alignment in the GeSi/Si(001) self assembled nanoislands grown by sublimation molecular beam epitaxy (SMBE) in GeH_4 ambient [5]. The surface $Ge_{0.3}Si_{0.7}$/Si(001) nanoislands have been found to demonstrate the type I band alignment.

In the present work, we have examined the dependence of the conduction band alignment in the surface Ge_xSi_{1-x} /Si(001) nanoislands on x using Tunnelling AFM.

The samples for investigations had been grown by SMBE in GeH_4 on the p^+-Si(001) substrates. The pressure of GeH_4 in the growth chamber was $\approx 9 \times 10^{-4}$ Torr. The substrate

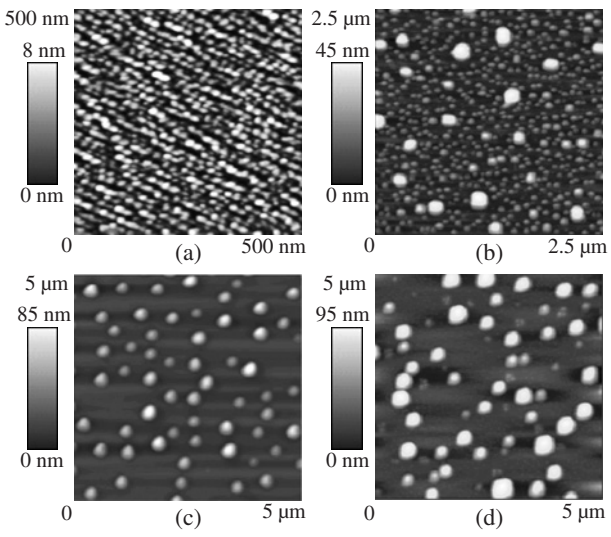

Fig. 1. The ambient air AFM images of the surface GeSi/Si(001) nanoislands grown by SMBE in GeH_4 at various substrate temperatures T_g °C: (a) — 500, (b) — 600, (c) — 700, (d) — 800.

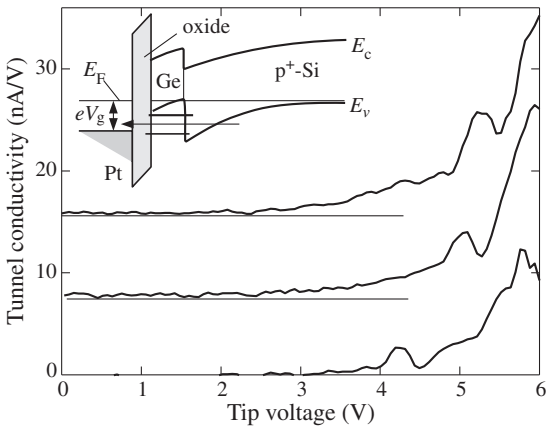

Fig. 2. The tunnel conductivity spectra dI_t/dV_g of the contact between the Pt coated AFM tip to the GeSi/Si(001) heterostructure grown at $T_g = 500$ °C [Fig. 1a].

temperature T_g when depositing Ge has been varied within 500−800 °C that resulted in the variation of the averaged Ge molar fraction in the islands' material x within 0.24−0.95 according to the photoluminescence [6] and the Raman spectroscopy [7] data.

The morphology of the GeSi/Si(001) nanoislands was examined first by ambient air AFM using NT MDT Solver Pro instrument (Fig. 1). The Tunnelling AFM investigations were carried out *ex situ* using Omicron Multiprobe P UHV system at 300 K. The samples' surfaces covered by the native oxide formed during the sample transfer through the ambient air were scanned across by a conductive Si probe coated by Pt in the contact mode. A bias voltage V_g was applied between the AFM probe and the sample. Simultaneously, the $I_t(V_g)$ spectra of the probe-to-sample contact where I_t was the tip current were acquired in each point of the scans.

In Fig. 2 the differential tunnel spectra dI_t/dV_g vs. V_g of the structure with the pyramid Ge/Si(001) nanoislands grown at $T_g = 500$ °C [Fig. 1a] are presented. The dI_t/dV_g spectra were calculated from the measured $I_t(V_g)$ curves by the numerical differentiation. The peaks in the dI_t/dV_g spectra were ascribed to the tunnelling of the electrons through the quantum confined hole states in the Ge/ Si(001) pyramid islands (see the inset in Fig. 2).

The normalized differential conductivity spectra $dI_t/dV_g/(I_t/V_g)$ of the GeSi nanoislands grown at various temperatures and to the sample surface between the islands (WL) are

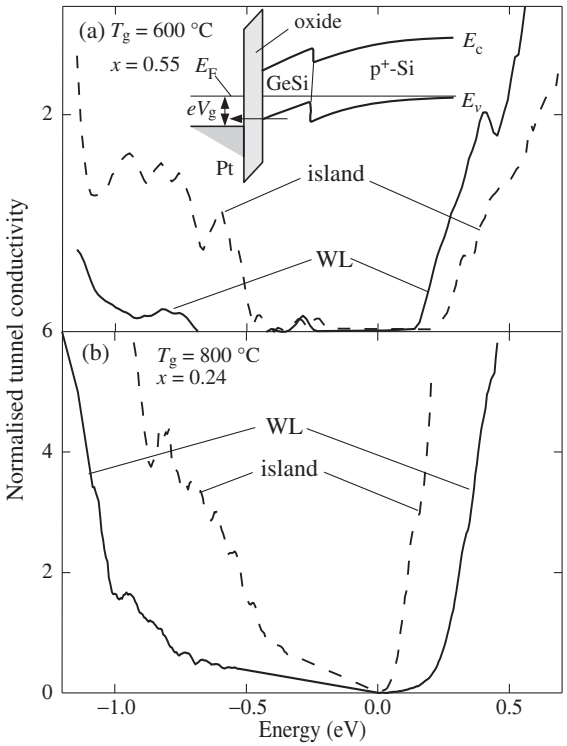

Fig. 3. The normalized tunnel conductivity spectra $dI_t/dV_g/(I_t/V_g)$ of the Ge_xSi_{1-x}/Si(001) nanoisland structures grown at different temperatures.

presented in Fig. 3. According to the theory of tunnelling spectroscopy [8], the normalized tunnel conductivity is proportional to the local density of states (LDOS) at the sample surface. The relationship of the energies E in the LDOS spectra (Fig. 3) to V_g, has been established taking into account the partial drop of V_g on the depletion layer of the tip-to-sample contact by solving a one-dimensional Poisson's equation [9].

Note that unlike the tunnel spectra of the Ge/Si(001) pyramid islands (Fig. 2), the LDOS spectra of the larger GeSi/Si(001) islands grown at $T_g \geq 600$ °C with lateral sizes $D > 100$ nm and height $h > 20$ nm (Fig. 1) do not exhibit any features, which could be attributed to the size quantization because of relatively large sizes of the islands as compared to the de Broglie wavelength for the holes in GeSi.

As it is evident from Fig. 3, the tunnel spectra of the $Ge_{0.24}Si_{0.76}$ nanoislands grown at $T_g = 800$ °C demonstrate the I-type conduction band alignment. The values of E_c in the Ge_xSi_{1-x} nanoislands are plotted in Fig. 4 vs. x. Also, the theoretical dependence $E_c(x)$ calculated for a strained Ge_xSi_{1-x}/Si(001) heterosturcture according to [10] is presented in Fig. 4. The theory predicts the strained Ge_xSi_{1-x} /Si(001) heterostructures to be the ones of the I type at $0 < x < 0.45$, the conduction band minima in GeSi are related to the Δ_4 valleys. The experimental data agree qualitatively with the theory [9] although the magnitudes of ΔE_c were larger than the ones predicted by the theory. This disagreement could be related to the not enough accuracy of the recalculating of V_g into E.

Note that according to [4] the GeSi/Si(001) nanoislands are always of the II type within $0 < x < 1$ due to the nonuniform tensile strain of Si near the tops and the bottoms of the islands. This contradiction could be attributed probably to the partial strain relaxation in the surface GeSi nanoislands as compared

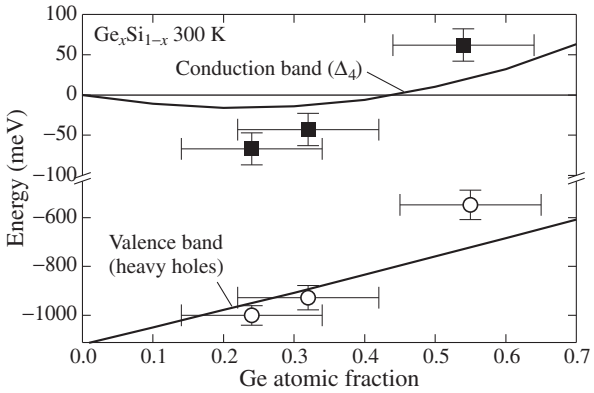

Fig. 4. The dependence of the energies of the c- and v-band edges in the Ge_xSi_{1-x}/Si(001) nanoislands on x.

to the pseudomorphic GeSi/Si(001) heterostructures or to the coherent GeSi/Si(001) nanoislands embedded into Si.

Also, the values of the valance band top (the heavy hole subband) in the Ge_xSi_{1-x}/Si(001) nanoislands along with the ones calculated according to [10] are plotted in Fig. 4. A rather good agreement between the calculated and measured values of E_v supports the conclusions on the type of the conduction band alignment in the GeSi/Si(001) nanoislands drawn from the tunnel spectroscopy data.

Acknowledgements

The present work has been supported in part by Russian Ministry of Science and Education, contract 16.552.11.7008.

References

[1] I. Berbezier and A. Ronda, *Surf. Sci. R.* **64**, 47 (2009).
[2] L. Colombo, R. Resta and S. Baroni, *Phys. Rev. B* **44**, 5572 (1991).
[3] D. C. Houghton, G. C. Aers, S. R. Eric Yang, E. Wang and N. L. Rowell, *Phys. Rev. Lett.* **75**, 866 (1995).
[4] M. El Kurdi, S. Sauvage, G. Fishman and P. Boucaud, *Phys. Rev. B* **73**, 195327 (2006).
[5] P. A. Borodin, A. A. Bukharaev, D. O. Filatov, M. A. Isakov, V. G. Shengurov, V. Yu. Chalkov and S. A. Denisov, *Semicond.* **45**, 403 (2011).
[6] D. O. Filatov, M. V. Kruglova, M. A. Isakov, S. V. Siprova, M. O. Marychev, V. G. Shengurov, V. Yu. Chalkov and S. A. Denisov, *Semicond.* **42**, 1098 (2008).
[7] A. I. Mashin, A. V. Nezhdanov, D. O. Filatov, M. A. Isakov, V. G. Shengurov, V. Yu. Chalkov and Yu. A. Denisov, *Semicond.* **44**, 1504 (2010).
[8] J. A. Kubby and J. J. Boland, *Surf. Sci. R.* **26**, 61 (1996).
[9] R. M. Feenstra and J. A. Stroscio, *J. Vac. Sci. Technol. B* **5**, 923 (1987).
[10] V. Ya. Aleshkin and N. A. Berkin, *Semicond.* **31**, 132 (1997).

20th Int. Symp. "Nanostructures: Physics and Technology"
Nizhny Novgorod, Russia, June 24–30, 2012

Optical properties of Ge/Si quantum dots with different doping level in mid infrared range

D. A. Firsov[1], L. E. Vorobjev[1], V. A. Shalygin[1], V. Yu. Panevin[1], A. N. Sofronov[1], M. Ya. Vinnichenko[1], A. A. Tonkikh[2] and P. Werner[2]

[1] St Petersburg State Polytechnic University, 195251 St Petersburg, Russia
[2] Max Planck Institute of Microstructure Physics, Weinberg 2 D-06120, Halle (Saale), Germany

Abstract. Authors report on investigation of mid infrared absorption spectra of polarized light in MBE grown Ge/Si heterostructures with Ge quantum dots with different doping levels. Measured spectra demonstrate a features assigned to hole transitions between quantum dot levels as well as to interband optical transitions. Specific behavior of absorption spectrum with the increase of doping level can be an evidence of strong electron localization around the quantum dot. Photoinduced absorption spectrum of undoped sample under external interband optical excitation correlates well with absorption spectrum of doped sample.

Introduction

Silicon based heterostructures are considered as one of major materials for progress in optoelectronics due to possibility of optical link in near IR between different elements of integral schemes based on traditional silicon technology [1]. At the same time, mid infrared optical properties of Ge/Si quantum dot structures are also of great interest. There are a number of researches (see, for example, [2,3] and reference therein) of absorption and photoconductivity spectra in such systems. Nevertheless there is a lack of experimental and theoretical data on light polarization dependencies of intraband optical absorption as well as intraband absorption under different/non-equilibrium population of quantum dot levels.

In this work, we present the results of absorption spectra studies in mid infrared spectral range for different light polarizations in Ge/Si quantum dots structures with different doping level and under the external interband illumination.

1. Samples and experiment details

Structures under investigation were grown by molecular-beam epitaxy on 2 kΩ cm silicon (100) substrate at 600 °C with a thin Sb film deposited on the grown Si buffer layer [4]. Structures consist of 10 quantum dot layers separated by 15 nm silicon layers. Doping was performed in δ-layers in 5 nm from the quantum dots layer. The designed concentration of boron in each δ-layer is varied in different structures between 0 and 1.2×10^{12} cm^{-2}.

The density of Ge quantum dots in each layer is 2×10^{11} cm^{-2}. It was measured in the preliminary study using atomic force microscopy on the sample with a single layer of uncapped Ge islands. This studies also gives the lateral size of quantum dots as ≈15 nm, and the height of ≈1.2 nm.

Samples with 10 light passes were prepared from each structure to perform optical experiments in multipass geometry with different light polarization with respect to growth direction.

Optical transmission spectra were measured with Brucker Vertex 80v Fourier Transform spectrometer. In addition, 100 mW YAG:Nd laser with frequency multiplication was used to create non-equilibrium charge carriers.

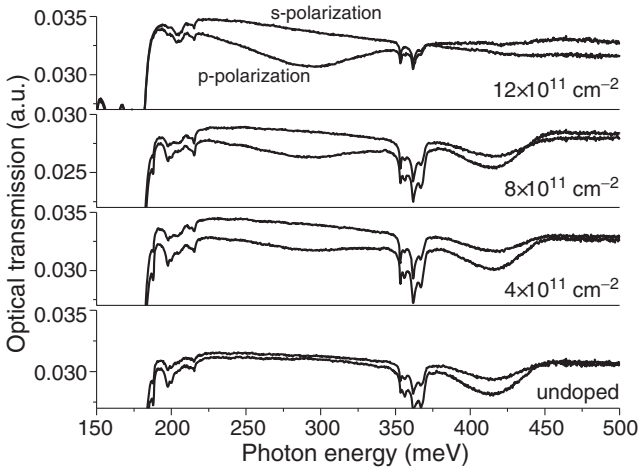

Fig. 1. Optical transmission spectra for 4 samples with different doping levels for in-plane light polarization (s) and polarization with electric filed component along the growth direction (p).

2. Experiment results and discussions

Measured at $T = 300$ K optical transmission spectra of 4 samples with different doping levels are shown in Fig. 1. Undoped sample demonstrates almost flat transmission for both light polarization up to photon energies $\hbar\omega$ less then 180 meV, where the multiphonon absorption band in silicon begins [5], except for a absorption peak near 415 meV. The increase of doping level leads to appearance of additional wide absorption band near $\hbar\omega \approx 270$ meV for light polarized along the growth direction. It can be assigned to optical transitions of holes from ground state to the continuum of states under the Si barrier.

At the same time absorption at $\hbar\omega \approx 415$ meV becomes weaker and absolutely disappears in most highly doped sample.

The latter effect is considered to be related to the blocking of interband-like transitions under complete population of the dot ground state with holes. This assumes the existence of discrete electron state in the conduction band. Such localization of electrons around the quantum dot is possible due to formation of tree-dimensional potential well in the conduction band at heterointerface from the Si side because of non-uniform spatial distribution of elastic strain in multilayer structure [6]. Nevertheless, the origin of this effect is under investigation now.

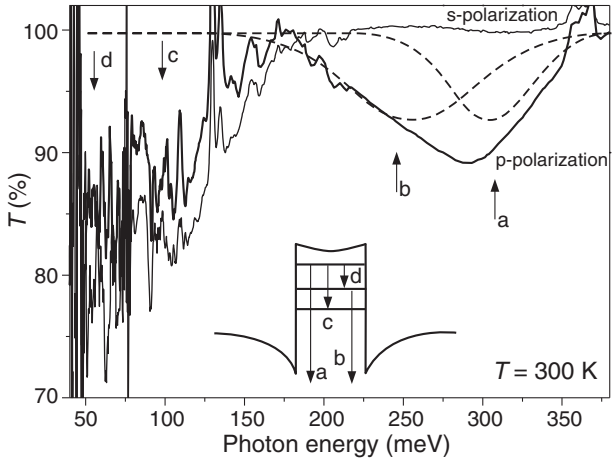

Fig. 2. The ratio of optical transmission spectra for sample with doping level 12×10^{11} cm^{-2} and undoped sample for two light polarization. Inset shows optical transitions scheme. Dashed lines represent the Gauss fitting of experimental data at bound-to-continuum transitions region.

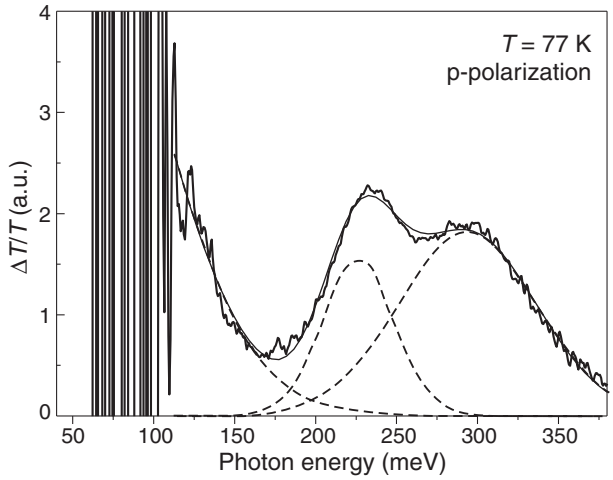

Fig. 3. Photoinduced absorption spectra for undoped sample at $T = 77$ K under external optical excitation of non equilibrium charge carriers.

The result of dividing the upper curve in Fig. 1 to the lower one in spectral range of 40–380 meV is shown in Fig. 2. This optical transmission curve for the most heavily doped sample, normalized by the transmission of undoped sample, is fitted well with two Gauss lines at bound-to-continuum transitions region. At the same time, analysis of transmission data for samples with doping level 4 and 8×10^{11} cm^{-2} gives the good approximation of absorption shape in this area with only one Gauss line centered at $\hbar\omega \approx 285$ meV.

Taking into account possible partial compensation of the acceptors one can see that the first excited dot state is partially populated with holes in most highly doped sample. Observed two peaks are related to the optical transitions from the ground state and from first excited state to the continuum of states at $\hbar\omega \approx 304$ meV and $\hbar\omega \approx 254$ meV respectively.

The traces of interlevel optical transitions can be also found in Fig. 2 at photon energies $\hbar\omega < 200$ meV. In spite of significant attenuation of transmitted light intensity due to lattice absorption in this area, one can see the peak-shaped decrease of transmission at $\hbar\omega \approx 60$ meV and $\hbar\omega \approx 108$ meV.

Thus, the analysis of experimental data allows us to determine the hole energy spectrum in the quantum dot. The energy separation between ground state and first excited state is about 50–60 meV, while the second excited state is 108 meV higher than ground state.

In addition, the measurements of absorption spectra under the external optical excitation of non-equilibrium electron-hole pairs via YAG:Nd laser were performed. The results of these experiments are shown in Fig. 3 as a photoinduced absorption spectra of undoped sample at $T = 77$ K for IR light with p-polarization. Measurements were performed in step-scan Fourier-transform spectrometer mode with 100% mechanical modulation of excitation beam. Change of sample transmission ΔT in MIR was measured by SR830 Lock-In amplifier.

Photoinduced absorption data for undoped sample qualitatively agree with experimental data for most heavily doped sample. Two peaks at the bound-to-continuum transition region are resolved well in photoinduced spectra due to less thermal distribution tailing at liquid nitrogen temperature.

Positions of photoinduced absorption peaks related to bound-to-continuum optical transitions from ground and excited states are $\hbar\omega \approx 293$ meV and $\hbar\omega \approx 226$ meV respectively. This values differs from similar values for equilibrium absorption of doped sample. Possible reasons are: (1) influence of doping δ-layer in doped sample and (2) influence of non-equilibrium electrons created under photoinduced absorption studies to the energy profile of quantum dot.

3. Conclusions

In this work, polarization-dependent absorption in mid IR range in Ge/Si quantum dot structures related to hole optical transitions both from ground and first excited states was observed in equilibrium and photoinduced absorption spectra.

Acknowledgements

This work is supported by RFBR grants, the German-Russian Program of the Federal Ministry of Education and Research (BMBF) and Russian Federal Target Program "Kadry".

References

[1] A.V. Antonov *et al*., *Proc. of Russian Conference on Physics of Semiconductors 2009* (Novosibirsk, 2009), 310 (2009).
[2] A.I. Yakimov *et al*., *Phys. Rev. B* **62**, 9939 (2000).
[3] A.I. Yakimov *et al*., *Journal of Applied Physics* **89**, 5676 (2001).
[4] A. Tonkikh *et al*., *Phys. Status Solidi RRL* **4**, 224 (2010).
[5] F.A. Johnson. *Proc. Phys. Soc.* **73**, 265 (1958).
[6] A.I. Yakimov *et al*., *Phys. Rev. B* **73**, 115333 (2006).

20th Int. Symp. "Nanostructures: Physics and Technology"
Nizhny Novgorod, Russia, June 24–30, 2012

Reflection enhanced photodetectors employing SOI-based concentric circular subwavelength gratings

Xiaofeng Duan, Xiaomin Ren, Yongqing Huang, Zhang Xia, Qi Wang, Yufeng Shang, Xinye Fan and Fuquan Hu

State Key Laboratory of Information Photonics and Optical Communications (Beijing University of Posts and Telecommunications), P.O. Box 66, #10 Xitucheng Road, Haidian District, Beijing 100876, China

Abstract. A grating-integrated silicon-on-insulator (SOI) based photodetector for use in the long wavelength was fabricated and characterized. An InGaAs/InP *p-i-n* structure was heterogeneously integrated on a SOI-based concentric circular subwavelength grating (CC-SWG) by means of a low temperature bonding process with benzocyclobutene (BCB) as the bonding agent. The light absorption of the device is enhanced due to high-index-contrast CC-SWGs as a broadband reflector. These features lead to an increase in quantum efficiency, for the whole S, C and L communication bands. The measured quantum efficiency was increased by 39.5% with CC-SWGs in comparison with the device without gratings.

Introduction

Silicon photonics is emerging as a very attractive platform to integrate optical active devices on a single chip. The main motivation is the fabrication process which is compatible with the complementary metal oxide semiconductor electronics industry. Although silicon is becoming an important candidate for optical functionalities, it is outperformed by III-V semiconductor materials for active devices, such as light generation and detection at telecom wavelengths ($1.31-1.55$ μm), due to its intrinsic material limitations. An alternative approach relies on the fabrication ofhybrid structures which integrate III-V materials based activedevices on silicon-based structures.

Several technologies have been proposed to bond III-V semiconductors on silicon, such as direct bonding, SiO_2-SiO_2 molecular wafer bonding, Au/In dry bonding, or sol-gel wafer bonding. We consider here the heterogeneous integration of an InGaAs/InP *p-i-n* structure on a silicon-on-insulator (SOI) based concentric circular subwavelength grating (CC-SWG), using benzocyclobutene (BCB) for bonding. This technique has recently been used to integrate active devices on SOI waveguides, such as lasers and photodetectors [1–3]. Among the advantages of this method, we point out its relative simplicity with a potential towards low-cost mass production, the optical transparency of BCB at telecom wavelengths and the high refractive index contrast with semiconductors.

Photodetectors are one of the most important optical active devices for optoelectronic integrated circuits. However, it is well known that to increase the speed of *p-i-n* photodetectors, the intrinsic region length should be reduced. The reduction of the intrinsic region means a reduction in the quantum efficiency. The use of a resonant Fabry–Perot cavity to increase light absorption is one possible way to overcome this problem [4–6]. However, this increase is effective only at resonant wavelengths. Subwavelength gratings have been demonstrated recently as a promising alternative to distributed Bragg reflection (DBR) dielectric stacks for broadband reflector applications. The structure of the SOI-based CC-SWG consists of two-dimensional circles of Si that are fully surrounded by low-index cladding layers. The large periodic index contrast from the grating in the in-plane direction leads to a high reflectivity over a broad spectrum [7,8]. Although there are some difficulties in CC-SWGs fabrication, such as suffering from the lithography challenges associated with the fine spacing between lines on gratings, recent advances in nanolithography, especially in electron-beam lithography (EBL), have alleviated these problems [9].

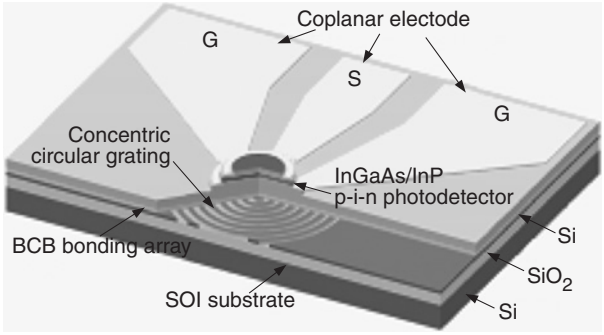

Fig. 1. Schematic layout of a *p-i-n* photodetector with a SOI-based CC-SWG structure. The coplanar waveguide pad is used for on-wafer high-speed measurement.

In this work, we report on the integration of an InGaAs/InP *p-i-n* photodetector on a SOI-based CC-SWG. The heterogeneous structure is fabricated with the purpose of obtaining a higher quantum efficiency of photodetectors. Its operation is based on the increase of the light absorption, induced by the CC-SWGs as a broadband reflector to double the absorption length in the device. This method enables us to enhance quantum efficiency over a wide wavelength range while maintaining a high speed. The quantum efficiency of 53% at a wavelength of 1.55 μm was obtained, which was increased by 39.5% with CC-SWGs in comparison with the device without gratings.

1. Design and fabrication

The schematic of the device is shown in Fig. 1. The device consists of a conventional InGaAs/InP *p-i-n* photodetector and a SOI-based CC-SWG as a back reflector. The *p-i-n* photodetector mesa is defined in the center of the CC-SWG.

To validate the integration process, InGaAs/InP photodetectors were bonded onto SOI-based CC-SWG components. The SOI substrate consisted of a 500 nm silicon grating layer and a 500 nm buried oxide layer. A 300 μm diameter CC-SWG (grating period 750 nm, duty cycle 60% and 500 nm etch depth) was defined in the silicon grating layer by EBL using ZEP520 as a positive resist. The structure of the CC-SWG consists of

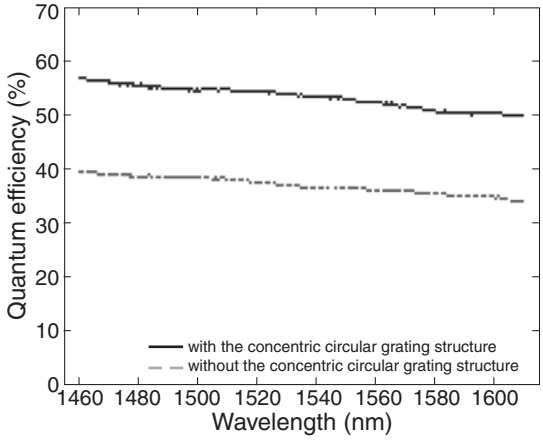

Fig. 2. Measured response spectrum of the photodetector.

concentric circles of Si ($n \approx 3.45$ in the near infrared) that are surrounded with air and SiO_2 ($n \approx 1.45$) as the low-index cladding layers on the top and bottom. The reflectivity of the SOI-based CC-SWG was measured before a bonding process. Fig. 2 shows the reflectivity spectrum and scanning electron microscope (SEM) image of the SOI-based CC-SWG. A very broad bandwidth, ranging from 1.46 to 1.61 μm wavelength regions, and a high reflectivity, more than 70%, were achieved.

An InGaAs/InP die of 1 cm^2, containing a *p-i-n* diode layer structure with a 350 nm InGaAs absorbing layer was bonded to the SOI based CC-SWG structure. A 1 μm thick BCB bonding layer was used. After curing the BCB at 250° for 2 hour, the InP substrate was removed by a combination of mechanical grinding and chemical etching using H_3PO_4:HCl (=1:1) until an InGaAs *p*-type contact layer was reached. The bonding strength was strong enough to endure the following processes, including ultrasonic cleaning. Standard photolithography and chemical etching were used to define the photodetector mesa [16]. A Ti/Pt/Au *p*-metal contact was deposited and patterned by a liftoff process to form an annular $p+$ Ohmic contact with 30 μm inside diameter. A 42 μm-diameter top round mesa was formed by etching down to the *n*-type InP contact layer. The $n+$ Ohmic contact was achieved by a Ti/Pt/Au liftoff. Then the samples were rapid thermal annealed at 400° for 1 min. After the samples were covered with polyimide, top windows were opened. For passivation, the samples were cured at 210° for 50 min in nitrogen ambient. Finally, Ti/Au interconnect metal was deposited, which formed the coplanar electrodes on top of the polyimide layer. All the etching of the III-V materials was done with wet chemistry, in order to minimize the damage to the sidewalls. We used a solution of H_2SO_4:H_2O_2:H_2O (=1:1:20) for InGaAs etching, and H_3PO_4:HCl (=2:1) for InP etching. Both of the two solutions are highly selective to the non-targeted materials.

2. Results and discussion

The spectral response measurements were carried out in the 1460–1610 nm wavelength range by using an Anritsu Tunics SCL tunable laser with a single-mode fiber pigtail as the light source. The devices were top illuminated vertically. An input beam was obtained by collimating the light from the fiber with a fiber collimator. The spectral response of the device is shown in Fig. 2. The spectral response was measured under 3V reverse bias. The quantum efficiency of the grating-integrated SOI-based photodetector is 53% at a wavelength of 1.55 μm, and that of the identical device without grating is only 38%. From the figure, a 39.5% improvement on the quantum efficiency of the grating-integrated photodetector was observed. This is because the effective thickness of the absorber layer is increased by the CC-SWGs as the back reflector in the device. The quantum efficiency of the grating-integrated photodetector mainly depends on the thickness of the absorber layer and the reflectivity of CC-SWGs. To obtain higher quantum efficiency without increasing the absorber layer thickness, we can enhance the reflectivity of CC-SWGs by optimizing their structure parameters.

Further measurement for shorter wavelengths was limited by the wavelength range of the tunable laser we used. However, InGaAs has even larger absorption coefficients for shorter wavelengths, and our simulation shows that the reflectivity of the SOI-based CC-SWG is still very high around a wavelength of 1310 nm. Therefore, the photodetector can work for the whole S, C and L communication bands, and can probably work well for even shorter wavelengths, e.g., the O-band.

Acknowledgements

This work was partially supported by the National Basic Research Program of China (No. 2010CB327600), the Fundamental Research Funds for the Central University (2011RC 0403), the National Natural Science Foundation of China (61020106007) and the National "111" Project (No. B07005).

References

[1] D. V. Thourhout, T. Spuesens, S. K. Selvaraja, L. Liu, G. Roelkens, R. Kumar, G. Morthier, P. Rojo-Romeo, F. Mandorlo, P. Regreny, O. Raz, C. Kopp and L. Grenouillet, *J. Sel. Top. Quantum Electron.* **16**, 1363 (2010).

[2] H. Park, A. W. Fang, R. Jones, O. Cohen, O. Raday, M. N. Sysak, M. J. Paniccia and J. E. Bowers, *Opt. Exp.* **15**, 6045 (2010).

[3] Z. Sheng, L. Liu, J. Brouckaert, S. He and D. V. Thourhout, *Opt. Exp.* **18**, 1756 (2010).

[4] M. S. Ünlü and S. Strite, *J. Appl. Phys.* **78**, 607 (1995).

[5] H. Huang, X. Ren, X. Wang, H. Cui, W. Wang, A. Miao, Y. Li, Q. Wang and Y. Huang, *Appl. Opt.* **45**, 8448 (2006).

[6] X. Duan, Y. Huang, X. Ren, W. Wang, H. Huang, Q. Wang and S. Cai, *IEEE Trans. Electron Devices* **58**, 3948 (2011).

[7] C. F. R. Mateus, M. C. Y. Huang, L. Chen, C. J. Chang-Hasnain and Y. Suzuki, *IEEE Photon. Technol. Lett.* **16**, 1676 (2004).

[8] D. Fattal, J. Li, Z. Peng, M. Fiorentino and R. G. Beausoleil, *Nat. Photon.* **4** (2010).

[9] M. C. Y. Huang, Y. Zhou and C. J. Chang-Hasnain, *Nat. Photon.* **1**, 119 (2007).

[10] X. Duan, Y. Huang, X. Ren, H. Huang, S. Xie, Q. Wang and S. Cai, *Opt. Exp.* **18**, 5879 (2010).

20th Int. Symp. "Nanostructures: Physics and Technology"
Nizhny Novgorod, Russia, June 24–30, 2012

Waveguide effect of InGaAs quantum wells in GaAs- and InP-based lasers

A. A. Dubinov[1], V. Ya. Aleshkin[1], K. E. Kudryavtsev[1], A. N. Yablonskiy[1] and B. N. Zvonkov[2]

[1] Institute for Physics of Microstructures RAS, 603950, Nizhny Novgorod, Russia
[2] Research Physical-Technical Institute of the Nizhny Novgorod State University, 603950 Nizhny Novgorod, Russia

Abstract. In this paper we suggest waveguide formed with difference refractive index of active quantum wells and surrounding semiconductor in laser diode. The possibility of the existence of the TE and TM modes localized near the quantum well is shown. The localization of a mode is greater, then the difference in refractive index of the quantum well and semiconductor matrix, the thickness of the quantum well and the distance from the quantum well to the boundary of semiconductor/vacuum or semiconductor/metal is greater. It has been shown that this type of waveguide can be effectively used in laser structures with a large difference in refractive index of quantum well and semiconductor matrix, and a large number of quantum wells (for example, the structure InP/$In_{0.53}Ga_{0.47}As$/InP). It is shown that the use of this type of waveguide structure for GaAs/$In_{0.2}Ga_{0.8}As$/GaAs is ineffective.

Introduction

At the present time there is large number of studies aimed at improving the performance of semiconductor lasers: increasing the power, quantum efficiency, the quality of the output radiation [1]. One of the important components of a semiconductor laser, which is responsible for many of its characteristics, is the waveguide. Typically, confining layers with a lower refractive index then the refractive index of the waveguide core (InGaP or AlGaAs confining layers for GaAs-based lasers) is used for the creation of waveguide. Another possibility is using a waveguide layer with high refractive index (InAlGaAsP), than in the substrate (InP). In this case, the substrate itself acts as a confining layer.

It is well known that in the case of a symmetric waveguide (when the layer with high refractive index is between unlimited layers with lower refractive index) TE_0 and TM_0 modes may exist in an arbitrarily small thickness of the waveguide [1]. Consequently, the electromagnetic mode can be localized in the vicinity of the waveguide layer, whose thickness is several orders of magnitude smaller than the wavelength of this mode. In the case of semiconductor lasers generating in the wavelength range of about 1 micron, such a waveguide layer can be a layer of even thickness of about 10 nm. Note that there is a typical thickness of the quantum wells, which play the role of the active medium in lasers. Therefore, in principle possible to construct lasers in which the quantum wells will play a dual role — to serve the active and waveguiding matters. In these lasers, there is no need for a conventional waveguide and, consequently, they have a simple design that is very important for the technology. However, in real semiconductor lasers a waveguide are almost never symmetric in consequence of the technology of lasers — epitaxial growth of laser structure and further postgrowth procedures. Because the grown quantum wells are situated on the scale of the order of the wavelength from the boundary with air (in the case of optical pumping) or metal (in the case of a current-pumped). In addition, the important role played by optical confinement factor responsible for the magnitude of the lasing threshold in the laser. For very thin quantum wells and a small difference in refractive index the optical limiting factor may be very small (weakly localized mode) and, hence, the lasing threshold may be too large. However, the use of multiple quantum wells can significantly reduce the lasing threshold. Study the possibility of using quantum well layers as a waveguide and recommendations for the construction of lasers with such waveguides has been the aim of this work.

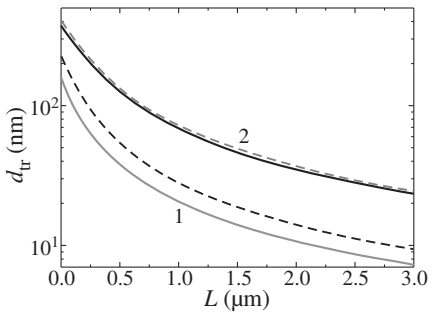

Fig. 1. Dependence of threshold thickness d_{tr} for TE (solid line) and TM (dashed line) modes on the parameter L for InP/$In_{0.53}Ga_{0.47}As$ structure at a wavelength 1.55 μm (1) and the structure GaAs/$In_{0.2}Ga_{0.8}As$ at a wavelength 1 μm (2).

1. Model problem

Consider a model problem which describes the mode in our laser. Let an electromagnetic wave propagates in the x-direction, and the refractive index of the semiconductor structure is described as follows (the axis z — direction of growth of the

Table 1.

Layer	Layer composition	Layer thickness (nm)
1	InP	substrate
2	$In_{0.53}Ga_{0.47}As$	10
3	InP	100
4	$In_{0.53}Ga_{0.47}As$	10
5	InP	100
6	$In_{0.53}Ga_{0.47}As$	10
7	InP	1300

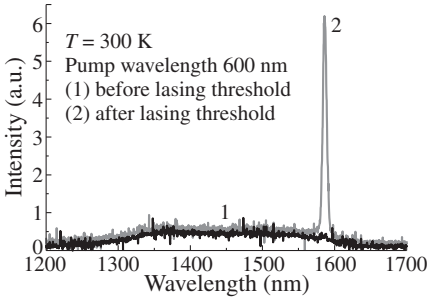

Fig. 2. The photoluminescence spectra of the InP-based laser with 3 InGaAs quantum wells by pump of pulsed laser.

structure):

$$n(z) = \begin{cases} n_1\,, & z < 0 \\ n_2\,, & 0 \le z < d \\ n_1\,, & d \le z < d + L \\ n_3\,, & z \ge d + L\,, \end{cases} \qquad (1)$$

where n_1, n_2, n_3 are refractive indexes, d is the waveguiding layer thickness, L is the distance between the waveguiding layer and the boundary of semiconductor/vacuum or semiconductor/metal. By solving Maxwell's equations for finding the parameters of the TE and TM modes in a waveguide, one can show that the modes are localized, when the value of d becomes greater than some threshold value:

$$d_{\rm tr}^{TE} = \frac{\lambda}{4i\pi N_2} \ln\left[\frac{N_2 + N_3 - i\frac{2\pi}{\lambda} L N_2 N_3}{N_2 - N_3 - i\frac{2\pi}{\lambda} L N_2 N_3}\right], \qquad (2)$$

$$d_{\rm tr}^{TM} = \frac{\lambda}{4i\pi N_2} \ln\left[\frac{n_3^2 N_2 + n_2^2 N_3 - i\frac{2\pi}{\lambda} L n_1^2 N_2 N_3}{n_3^2 N_2 - n_2^2 N_3 - i\frac{2\pi}{\lambda} L n_1^2 N_2 N_3}\right], \qquad (3)$$

where $N_2 = \sqrt{n_2^2 - n_1^2}$, $N_3 = \sqrt{n_3^2 - n_1^2}$, λ is the mode wavelength, i is the imaginary unit.

Let us consider two specific cases. $In_{0.53}Ga_{0.47}As$ layer of thickness d was grown on the substrate InP and was overgrown with InP layer thickness L. Then for the wavelength $\lambda = 1.55$ μm, $n_1(\text{InP}) = 3.2$ [2], $n_2(In_{0.53}Ga_{0.47}As) = 3.6$ [2], $n_3(\text{vacuum}) = 1$. Second case: $In_{0.2}Ga_{0.8}As$ layer thickness d was grown on a GaAs substrate and was overgrown with GaAs layer thickness L. In this case, the wavelength $\lambda = 1$ μm, $n_1(\text{GaAs}) = 3.51$ [3], $n_2(In_{0.2}Ga_{0.8}As) = 3.56$ [3], $n_3(\text{vacuum}) = 1$. In both cases, the threshold thickness ($d_{\rm tr}$) dependence for TE and TM modes on the parameter L are shown in Fig. 1. The figure shows that for structure $InP/In_{0.53}Ga_{0.47}As$ there are localized TE and TM modes for a quantum confinement layer thickness below 10 nm at a L thickness greater than 2 and 3 μm, respectively. For a structure $GaAs/In_{0.2}Ga_{0.8}As$ for the existence of localized TE and TM modes L must be greater than 2.5 μm and d would be more than 30 nm. Hence, qualitatively we can say that for several quantum-well layers, whose thickness is less than 10 nm, in such structure can exist localized modes. A single-mode waveguide is easily implemented in the proposed design even when the size of transverse modes is larger than the radiation wavelength (it improves the mode selectivity of the laser waveguide), which is important for creating high-power lasers with a narrow radiation pattern.

Table 2.

Layer	Layer composition	Layer thickness (nm)
1	GaAs	substrate
2	$In_{0.2}Ga_{0.8}As$	10
3	GaAs	100
4	$In_{0.2}Ga_{0.8}As$	10
5	GaAs	100
6	$In_{0.2}Ga_{0.8}As$	10
7	GaAs	100
8	$In_{0.2}Ga_{0.8}As$	10
9	GaAs	100
10	$In_{0.2}Ga_{0.8}As$	10
11	GaAs	100
12	$In_{0.2}Ga_{0.8}As$	10
13	GaAs	1500

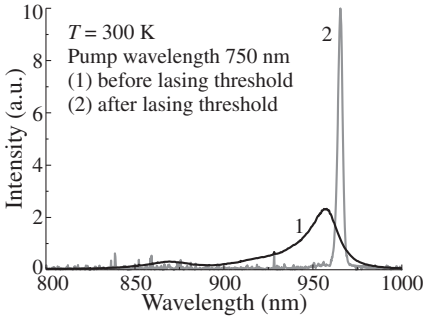

Fig. 3. The photoluminescence spectra of the GaAs-based laser with 6 InGaAs quantum wells by pump of pulsed laser.

2. Experiment

For an experimental proof of the proposed theory the structure $InP/In_{0.53}Ga_{0.47}As$ with 3 quantum wells and the structure $GaAs/In_{0.2}Ga_{0.8}As$ with 6 quantum wells were grown by MOCVD at atmospheric pressure in a horizontal reactor. Note that the use of six quantum wells in the structure $GaAs/In_{0.2}Ga_{0.8}As$ associated with a significantly greater difference between n_1 and n_2 in the structure $InP/In_{0.53}Ga_{0.47}As$ compared with the structure $GaAs/In_{0.2}Ga_{0.8}As$. Parameters of the layers are shown in Tables 1 and 2, respectively. Thinner structures were split into thin strips 2 mm wide. Mirrors were chipped edges (110).

We measured the emission spectra for both structures (Figs. 2 and 3) pumped by a CW and pulsed lasers. It was shown that above a certain pump threshold, lasing in such structures is occurred. This proves the existence of the waveguide effect of the quantum wells.

Acknowledgements

This work was supported by the Programs of RAS and the RF President (MK-678.2012.2).

References

[1] A. Yariv, P. Yen *Optical waves in crystals*, (John Wiley and Sons, New York, 1984).
[2] J.-W. Pan *et al*., *J. Appl. Phys.* **78**, 442 (1995).
[3] O. Madelung, *Semiconductors: Data Handbook.*, (New York: Academic Press, 1998).

20th Int. Symp. "Nanostructures: Physics and Technology"
Nizhny Novgorod, Russia, June 24–30, 2012

107 °C lasing in ⊘ 6-μm quantum dot microring

A. E. Zhukov[1,2], N. V. Kryzhanovskaya[1], M. V. Maximov[2,1], A. M. Nadtochiy[1], I. A. Slovinskiy[2,1], M. M. Kulagina[2], Yu. M. Zadiranov[2], S. I. Troshkov[2], A. V. Savelyev[1], E. M. Arakcheeva[2] and D. Livshits[3]

[1] St Petersburg Academic University, St Petersburg, Russia
[2] Ioffe Physical-Technical Institute, St Petersburg, Russia
[3] Innolume GmbH, Dortmund, Deutschland

Abstract. Ground-state lasing ($\lambda > 1.3$ μm) is demonstrated well above root temperature (up to 380 K) in a microring laser (6-μm in diameter) with InAs/InGaAs quantum dots.

Introduction

III–V microring lasers (MRLs) are considered to be very attractive for integration with silicon photonics owing to their small size, high quality factor and low threshold. Most of nowadays microring lasers are based on InGaAsP-InGaAs-InP materials because of low surface recombination rate in this material system. However, the size of InP-based MRLs is quite larger: the smallest diameter is 15 μm (for MRLs with a quantum-well active region [1]) or 22 μm (for MRLs with quantum-dots [2]). Moreover, strong temperature dependence of optical gain in these materials impedes high-temperature operation.

InAs/InGaAs quantum dots (QDs) grown on GaAs substrates may have certain advantages for MRLs since they emit in practically important wavelength range around 1.3 μm. They are capable of achieving extremely low threshold current density. In addition, suppression of side-wall recombination was demonstrated in stripe QD lasers [3]. Nevertheless, InAs/In GaAs QD MRLs of mm-size have only been demonstrated to date [4].

In the present work we present optically pumped MRLs having an outer diameter as small as 6 μm. Ground-state lasing is demonstrated at room temperature and up to 107 °C with the threshold power of few mW.

1. Experiment

An epitaxial structure was grown by molecular beam epitaxy on semi-insulating GaAs(100) substrate. An active region comprises five layers of InAs/$In_{0.15}Ga_{0.85}As$ QDs separated by 30-nm-thick GaAs spacers. The active region was inserted into a 220-nm-thick GaAs waveguiding layer confined by 20-nm-thick $Al_{0.3}Ga_{0.7}As$ barriers. A 400-nm-thick $Al_{0.98}Ga_{0.02}As$ cladding layer was grown beneath the waveguiding layer. Microrings were fabricated using photolithography and Ar-ion etching. The ring outer diameter was chosen to be 6 μm, the inner diameter was 2 μm (Fig. 1). To improve optical confinement, the $Al_{0.98}Ga_{0.02}As$ layer was converted into $(AlGa)_xO_y$ oxide by selective oxidation. MRLs were optically pumped with the 2nd harmonic of CW-operating YAG:Nd laser ($\lambda =$ 532 nm, 10–200 mW). Emission was detected with cooled Ge pin-diode. Measurements in the 77–300 K were performed in a flow cryostat. For measurements above room temperature the structures were mounted onto a heated holder equipped with a temperature controller.

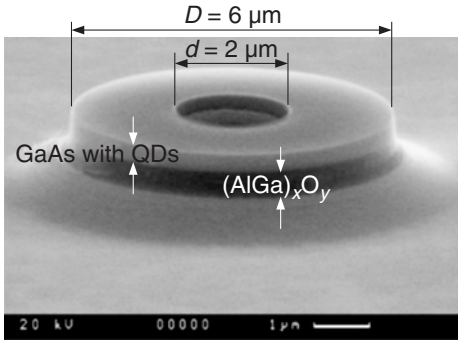

Fig. 1. SEM image of QD microring laser.

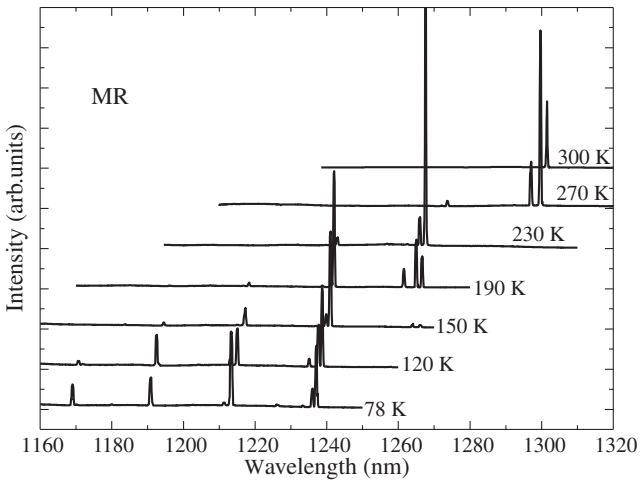

Fig. 2. Emission spectra of QD MRL at and below room temperature.

2. Results and discussion

Examples of emission spectra taken at and below room temperature are presented in Fig. 2. Pump power is approximately five times the threshold. Sharp lines correspond to resonator modes of various orders. Temperature dependence of wavelength of the dominant (most intense) lasing mode is summarized in Fig. 3a. Spectral position of ground-state QD line as it was measured from unprocessed piece of the epitaxial structure is also shown for comparison. It is seen that QD luminescence shifts quite rapidly (0.47 nm/K) as temperature increases while the microring mode position is much more stable (0.05 nm/K). As a result a series of jumps of lasing wavelength (so-called mode hopping) is observed.

The lasing wavelength at elevated temperatures (300 K) is in the 1.29–1.35 μm interval that falls into the O-band of optical fiber communication. The highest temperature of lasing is as high as 380 K (107 °C). To the best of our knowledge this is the highest temperature ever reported for 1.3 μm QD MRLs. At room temperature the threshold optical power was found to be

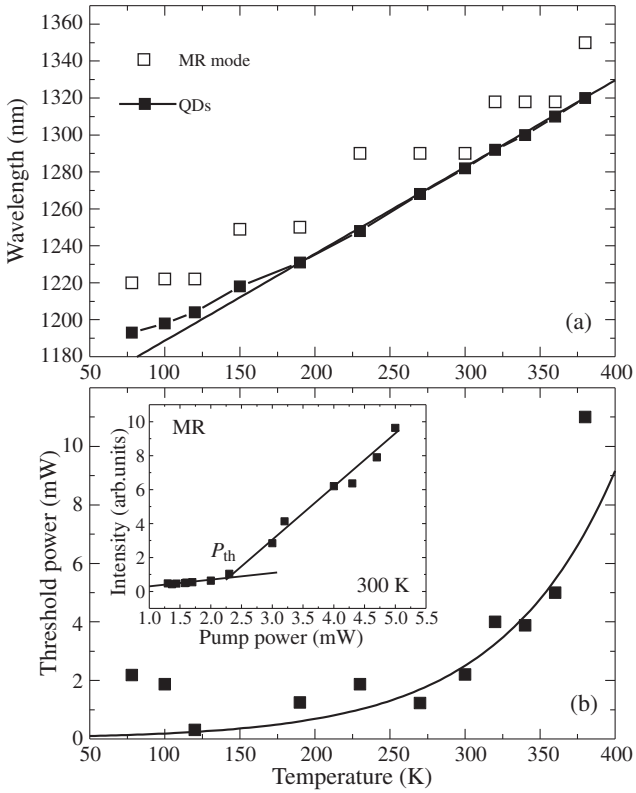

Fig. 3. Temperature dependence of wavelength ((a) open squares) and threshold power (b) of the dominant mode. Filled squares in (a) corresponds to QD ground-state transition. Insert in (b) presents an example of the dominant mode intensity against pump power.

2.2 mW and it remains about few mW up to 360 K (see Fig. 3b). Characteristic temperature of the threshold was estimated to be ∼80 K around room temperature. It is interesting to point out that the threshold decreases with increasing temperature from 77 to 120 K. Similar behavior has been previously observed in stripe QD lasers because of transition from non-equilibrium to equilibrium population of QD states [5].

3. Conclusions

Optically pumped microring lasers with InAs/InGaAs quantum dot active region and AlGaO pedestal are demonstrated. The lasers operates up to 107 °C with the wavelength beyond 1.3 μm and low threshold pump (the lowest threshold is 0.3 mW at 120 K).

Acknowledgements

The work is supported in different parts by Federal Target Program of Ministry of Science and Education (contracts 16.740. 11.0458, 14.740.11.1008), Russian Foundation for Basic Research (grant 11-02-12056-ofi-m-2011), Programs of Fundamental Studies of the Russian Academy of Sciences.

References

[1] D. Liang *et al*., *IEEE J. Select. Topics Quantum Electron.* **17**, 1528 (2011).
[2] M. T. Hill *et al*., *IEEE Photon. Tech. Lett.*, **20**, 446 (2008).
[3] D. Ouyang *et al*., *Semicond. Sci. Technol* **18**, L53 (2003).
[4] H. Cao *et al*., *Appl. Phys. Lett.* **86**, 203117 (2005).
[5] A. E. Zhukov *et al*., *Jpn. J. Appl. Phys.* **36**, 4216 (1997).

20th Int. Symp. "Nanostructures: Physics and Technology"
Nizhny Novgorod, Russia, June 24–30, 2012

Superlinear luminescence and enhance of optical power stimulated by impact ionization in the type II GaSb-based heterostructures

M. P. Mikhailova, K. V. Kalinina, B. E. Zhurtanov, E. V. Ivanov, N. D. Stoyanov and Yu. P. Yakovlev
Ioffe Physical-Technical Institute, St Petersburg, Russia

Abstract. Electroluminescence in isotype n-GaSb/n-AlGaAsSb n-GaInAsSb and anisotype n-GaSb/n-GaInAsSb/P-AlGaAsSb heterostructures have been studied in dependence on drive current at $T = 77$ and 300 K. Two luminescence bands associated with carrier recombination at the heterointerface and in the narrow-gap ($E_g = 0.284$ eV) layer have been observed in the mid-IR range 0.2–0.8 eV. Superlinear luminescence and enhancement of optical power in 1.5–2.2 times in the current range 25–200 mA was obtained. Occurred effects can be explained by contribution into radiative recombination of additional electron-hole pairs induced by impact ionization due to presence of high conduction band offsets at the interface in the type II heterostructures

Introduction

Type II heterostructures based on GaSb are prospective for developing of optoelectronic devices for mid-infrared spectral range (light-emitting diodes, lasers, photodetectors) [1–3] because they cover mid-infrared spectral region 1.6–5.0 μm, where lay absorption bands of many natural and industrial gases. But optical power and quantum efficiency of the LEDs based on the narrow-gap semiconductor alloys (InAsSb, InGaAsSb) are not high enough, and limited by non-radiative Auger recombination. It was shown in [4], Auger recombination can be suppressed at the type II heterointerface or in the nanostructures with deep quantum wells. So it is important to find a way to increase quantum efficiency and optical power of the LEDs based on the narrow-gap semiconductors. Early it was proposed to use large band-offsets ΔE_c (or ΔE_v) in abrupt heterostructures with high potential barrier at the interface with a narrow-gap active region for creation of hot electrons which can ionize starting with zero kinetic energy [5]. Capasso *et al*. proposed [6] to use large conduction band-offset at the interface in order to rise electron ionization coefficient in comparison with hole one in GaAs/AlGaAs superlattice avalanche photodiode (APD). But this approach was not applied before to light-emitting devices. Main goal of this paper is achievement of superlinear luminescence and enhancement of optical power in mid-infrared light-emitting diodes based on type II heterostructures with high conduction band offsets at the interface by using effect of impact ionization.

1. Experimental

Two types of heterostructures were grown on GaSb substrate by LPE isotype A-structure consisted of n-GaSb:Te substrate ($E_g = 0.725$ eV, $n = 5 \times 10^{17}$ cm^{-3}), 0.5 μm thick n-AlGaAsSb layer with 64% Al content ($E_g = 1.28$ eV) and then of narrow-gap GaInAsSb layer about 1 μm thick ($E_g = 0.282$ eV). The type II n-AlGaAsSb/n-GaInAsSb heterojunction had a staggered-gap alignment with large conduction band offsets ($\Delta E_c = 1.16$ eV, $\Delta E_v = 0.16$ eV). Anisotype type II B-structure consisted of n-GaSb/n-GaInAsSb/P-AlGaAsSb. The conduction band offset at the broken-gap n-GaSb/n-GaInAsSb interface was $\Delta E_c = 0.79$ eV. A narrow-gap capping layer of 1.5 μm thickness has energy gap $E_g = 0.284$ eV. It is important to note that in both structures conduction band offsets at the interface several times exceeded of the narrow-band gap

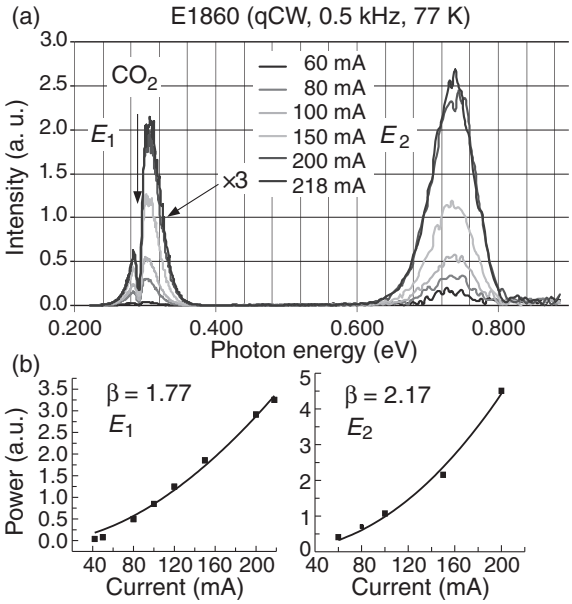

Fig. 1. (a) Electroluminescence spectra of A-structure n-GaSb/n-AlGaAsSb/n-GaInAsSb heterostructure at forward bias ("+" at GaInAsSb capping layer) versus drive current as parameter. $T = 77$ K; (b) Optical power $P = \alpha I^{\beta}$ in dependence on drive current for E_1 and E_2 luminescence bands.

of the GaInAsSb layer. We studied electroluminescence (EL) spectra at different driving currents in the range 0–200 mA and EL intensity and optical power dependence on the drive current at room temperature and nitrogen temperature for both A and B heterostructures. Samples were fabricated by photolithography as mesa-diodes with 500 μm in diameter. EL spectra were measured by using MDR-2 monochromator with diffraction grid 300 l/mm and were registered by InSb photodiode (Judson Ltd). Samples were driven by square shape current pulse with 50% duty cycle and frequency 610 Hz. Current amplitude varies in the range 0–200 mA.

2. Results and discussion

Two EL peaks were observed for both A- and B-structures in the range of the photon energy 0.2–0.8 eV (see Fig. 1a and 2a) at $T = 77$ K for A-structure and for B-structure at 300 and 77 K.

In isotype A-structures (Fig. 1a) we found at $T = 77$ K

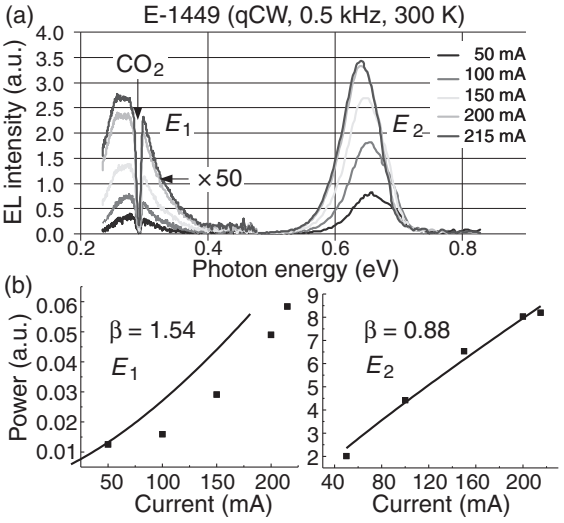

Fig. 2. (a) Electroluminescence spectra of B-structure n-GaSb/n-GaInAsSb/P-AlGaAsSb at forward bias ("+" at AlGaAsSb cover layer) versus drive current as parameter. $T = 300$ K; (b) Optical power $P_{\mathrm{EL}} = \alpha I^{\beta}$ in dependence on drive current for E_1 luminescence band and for E_2 band.

a narrow-gap E_1 band with maximum of 0.28 eV (4300 nm) and E_2 band at 0.73 eV (1700 nm). The band E_1 is distorted by atmospheric absorption of CO_2 ($\lambda = 4250$ nm). An interesting feature of EL spectra of A-structure is that the intensity of both bands E_1 and E_2 and emission output power shows superlinear growth with the increase of driving current at 77 K (Fig. 1b). An optical power-law demonstrates EL dependence on current and can be described as $P_{\mathrm{EL}} = \alpha\, I^{\beta}$, where α is fitting parameter and $\beta = 1.77$ for E_1 and $\beta = 2.17$ for E_2 bands (Fig. 1b). Earlier we obtained β up to 2.5 for E_2 band in A-structure at 4.2 K [7]. For B-structure we observed superlinear dependence EL on the driving current either for longwavelength band E_1 at 300 K or for the wider-gap E_2 at 77 K (see Fig. 2 a and b). Optical power of E_1 band corresponding to radiative emission from the GaInAsSb narrow-gap layer increases with the drive current in power of β, ($\beta = 1.54$) and for E_2 band $\beta = 0.58$ (Fig. 2b). In contrast, in B-structure, we can see only for longwavelength E_1 band at $T = 300$ K with sublinear EL dependence on the drive current. The specific features of EL bands for the isotype structure can be understood in analysis of their band diagram. Because the A-structure n-GaSb/n-AlGaAsSb/n-GaInAsSb is isotype, the hole density in it is virtually zero in the equilibrium state. When the forward bias is applied ("+" at n-GaInAsSb) electrons pass from the wider-gapn AlGaAsSb layer to the narrow-gap layer. Since ionization threshold energy for electrons in the narrow-gap material is $\epsilon_{\mathrm{ie}} \approx E_{\mathrm{g}} \approx 0.26$ eV and conduction band offset at the interface is $\Delta E_{\mathrm{c}} = 1.1\ \mathrm{eV} \gg \epsilon_{\mathrm{ie}}$, impact ionization can occur, because electrons become hot when they are coming from the wider-gap n-AlGaAsSb layer. Additional electron-hole pairs can be created in this process and give some contribution to radiative recombination. Then parts of the holes which are generated in the narrow-gap n layer via impact ionization withdrawn by the electron field into n-GaSb where they can also ionize. As it was shown in [8], resonant impact ionization by holes can occur in III-V semiconductors whose energy gap E_{g} is close to spin-orbit splitting value Δ_0 of the valence band (InAs, GaSb etc). An ionization threshold energy for holes in GaSb $\epsilon_{\mathrm{eh}} \approx E_{\mathrm{g}} = 0.80$ eV at 77 K, and we can observe superlinear EL for E_2 band (Fig. 1b). By analogy in B-structure n-GaSb/n-GaInAsSb/P-AlGaAsSb we observed also two EL bands in the range 0.2–0.8 eV (Fig. 2a) and appearance of superlinear luminescence and enhancement of optical power with drive currents rise in the range of 25–200 mA by 1.5–1.8 times induced by the same mechanism of impact ionization as it took place in the A-structure. But in this case hot electrons are generated at the interface of n-GaSb/n-GaInAsSb, where band offset $\Delta E_{\mathrm{c}} = 0.79$ eV is much larger than energy gap of the narrow-gap layer. In this case additional e-h pairs can be generated by hot electrons either in the narrow-gap layer (and superlinear luminescence appears at $T = 300$ K for the E_1 band) or in n-GaSb substrate (E_2 band at $T = 77$ K) as it is shown in Fig. 2b. In conclusion, the proposed method can be applied for enhancement of quantum efficiency and optical power in other light-emitting devices, nanostructures with deep quantum wells and photovoltaic cells.

Acknowledgements

This work was supported in part by RFBR grant 12-02-00597 and by Program 24 of Presidium of RAS.

References

[1] M. P. Mikhailova, A. N. Titkov, *Semicond. Sci. Technol.* **9**, R1279 (1994).

[2] N. D. Stoyanov, B. E. Zhurtanov, A. P. Astakhova *et al*., *Fiz. Tech. Poluprov. (Semiconductors)* **37(8)**, 878 (2003).

[3] M. Mikhailova, N. Stoyanov, I. Andreev *et al*., *Proc. SPIE* **6585**, 658526 1–10 (2007).

[4] G. G. Zegrya, V. A. Kharchenko, *Zhurn. Exper. Teor. Fiz. (JETP)* **101**, 327 (1992).

[5] M. Z. Zhingarev, V. I. Korol'kov, M. P. Mikhailova, *Sov. Phys. Semicond.* **14**, 801 (1980).

[6] F. Capasso, W. T. Tsang, A. L. Hutchinson, G. F. Williams, *Appl. Phys. Lett.* **40**, 38 (1982).

[7] N. L. Bazhenov, B. E. Zhurtanov, K. D. Mynbaev *et al*., *Tech. Phys. Lett.* **33(23)**, 1 (2007).

[8] A. P. Dmitriev, M. P. Mikhailova, I. N. Yassievich, *Phys. Stat. Sol. (b)* **140**, 9 (1987).

20th Int. Symp. "Nanostructures: Physics and Technology"
Nizhny Novgorod, Russia, June 24–30, 2012

Effect of intracavity nonlinear interaction on radiation characteristics of a dual-wavelength vertical external cavity surface-emitting laser: An analytical approach

Yu. A. Morozov and M. Yu. Morozov
Kotelnikov Institute of Radio Engineering and Electronics (Saratov Branch) RAS, 410019 Saratov, Russia

Abstract. The equations defining the steady-state operation characteristics of a dual-wavelength vertical external cavity surface-emitting laser and the intracavity nonlinear three-wave interaction have been solved self-consistently. Dramatic effect of nonlinear interaction on radiation of the laser has been demonstrated.

Introduction

Optically pumped semiconductor dual-wavelength vertical external cavity surface-emitting laser (VECSEL) has been demonstrated for the first time in 2005 [1]. Simultaneous generation of two coaxial beams at two wavelengths ($\lambda_1 \approx 983$ nm and $\lambda_2 \approx 1043$ nm) is one of the distinctive features of the laser. As both gaussian beams of the laser are completely space-overlapped and have substantial power densities, an efficient generator of mid-infrared range ($\lambda_3 = \lambda_2\lambda_1/(\lambda_2-\lambda_1) \approx 17.1$ μm) based on intracavity three-wave optical nonlinear interaction could hopefully be build [2,3]. According to our estimations, by varying the molar composition of quantum wells in the gain regions of the laser one could reach difference frequency radiation corresponding to mid- or far-infrared range (5–50 μm). It should be specially emphasized that the intracavity difference frequency generation is more attractive as compared with an extracavity one because of ability to utilize resonance enhancement of power at both laser wavelengths.

The publications [2,3] mentioned above deal with the analysis of nonlinear frequency conversion in a GaAs crystal revealing a nonlinearity of second order. Because of GaAs lacks for anisotropy of refractive index, the conventional methods of phase-matching are impossible [4]. Therefore, a GaAs crystal about a coherence length long was proposed to be inserted in the special sub-cavity tuned to the difference frequency [2]. The nonlinear optical mixing in the orientated-patterned quasi-phase-matched GaAs crystal like that used in [5] has been analyzed in other paper [3]. The intracavity three-wave nonlinear interaction was not supposed to effect on radiation characteristics of dual-wavelength VECSEL in both previous papers [2,3]. In the present work we show that the analysis of intracavity difference frequency conversion in the dual-wavelength VECSEL should be performed self-consistently, i.e. an interdependence of all three interacting waves has to be taken into account.

1. Mathematical model

Let's examine three-wave interaction in the nonlinear crystal with second-order nonlinearity. According to the Manley–Rowe relations one could particularly obtain [4]:

$$\begin{aligned} F_1(0) + F_3(0) &= F_1(L) + F_3(L)\,, \\ F_2(0) - F_3(0) &= F_2(L) - F_3(L)\,, \end{aligned} \tag{1}$$

where $F_{1,2,3}$ are the photon fluxes at the wavelengths $\lambda_{1,2,3}$; the left-hand side and the right-hand side values correspond to the input and output cross-sections of the nonlinear crystal, L is the length of the crystal. By using Eq. (1) the effective nonlinear reflectivities at both wavelengths $R_{n1,2}$ [4] of the piece of the VECSEL's cavity composed of nonlinear crystal and output mirror are as follows:

$$\begin{aligned} R_{n1} &= R\left[1-\gamma(1+R)F_2(0)\right], \\ R_{n2} &= R\left[1+\gamma(1+R)F_1(0)\right]. \end{aligned} \tag{2}$$

Here R is the output mirror reflectivity, γ links photon flux at the difference frequency with photon fluxes at $\lambda_{1,2}$: $F_3(L) = \gamma F_1(0)F_2(0)$.

$$\gamma = \frac{32Z_0}{n_1n_2n_3}d_{14}^2\left(\frac{L}{\lambda_1\lambda_2}\right)^2\left[\frac{1-\exp(\alpha_3 L/2)}{\alpha_3 L/2}\right]^2 hc/\lambda_3\,, \tag{3}$$

where Z_0 is the impedance of vacuum, d_{14} is the element of nonlinear susceptibility tensor, $n_{1,2,3}$ are the refractive indices at $\lambda_{1,2,3}$, α_3 is the loss factor at the difference frequency, h is the Planck's constant, c is the speed of light in vacuum. When deriving (3) we assumed the orientated-patterned quasi-phase-matched GaAs to be used and the wave-vector mismatch to be $\Delta k = 2\pi(n_1/\lambda_1 - n_2/\lambda_2 - n_3/\lambda_3 - 1/\Lambda) = 0$, where Λ is the period of the crystal's reversal.

It is seen from Eq. (2) that in comparison with R, the effective reflectivity R_{n1} at the shortest wavelength λ_1 decreases whereas R_{n2} at λ_2 increases. This observation can be explained in terms of photons: under nonlinear three-wave interaction each photon of highest energy gives birth to two photons with energies satisfying the energy conservation. Therefore, the photon flux at λ_1 (and consequently R_{n1}) should decrease whereas the photon fluxes at λ_2 as well as at λ_3 should increase.

Bearing in mind Eq. (2) as well as the steady-state conditions [6] one could derive the stationary values of the photon fluxes $F_{1,2}$(from now on the symbol (0) corresponding to the definite position in the cavity is not written):

$$\begin{aligned} \varphi_1 &= (1+b\varphi_2)^{-1}\,, \\ \varphi_2 &= (1-b\varphi_2)^{-1}\,. \end{aligned} \tag{4}$$

Here $\varphi_{1,2} = F_{1,2}/F_0$ are the normalized values of the photon fluxes, $b = \gamma R(1+R)F_0/(1-R) \approx 2\gamma F_0/(1-R)$, F_0 is the photon flux without nonlinear crystal in the cavity; to fulfill the analysis in more clear way this value supposed to be the same for the radiation at λ_1 and λ_2.

One can solve (4) to derive:

$$\begin{aligned} \varphi_1 &= 1 + \tfrac{1}{2b} - \sqrt{1+(\tfrac{1}{2b})^2}\,, \\ \varphi_2 &= 1 - \tfrac{1}{2b} + \sqrt{1+(\tfrac{1}{2b})^2}\,. \end{aligned} \tag{5}$$

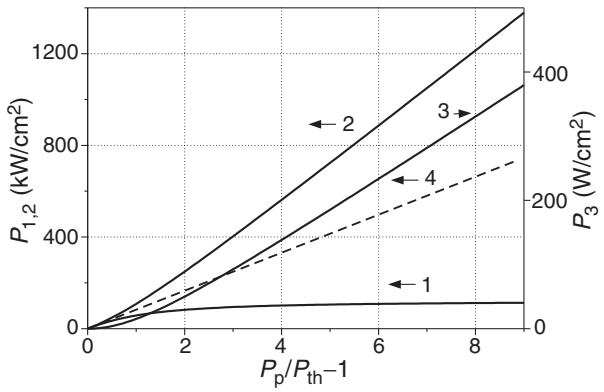

Fig. 1. Power densities vs normalized pump power density excess above the threshold value. Curve numbers 1,2,3 correspond to radiation at wavelengths $\lambda_{1,2,3}$ and the dotted line 4 corresponds to power density of dual-wavelength radiation with no a nonlinear crystal involved.

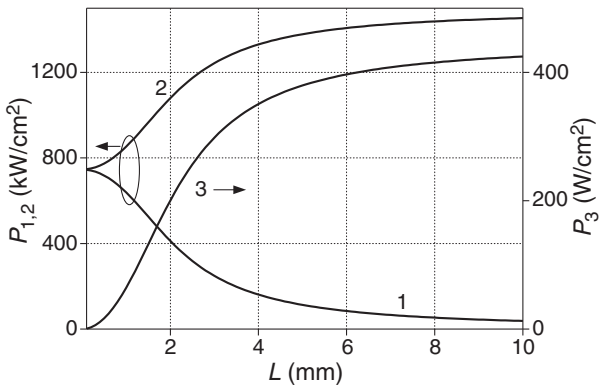

Fig. 2. Power densities as the functions of the nonlinear crystal length.

From the steady-state operation conditions of dual-wavelength VECSEL [6] with an additional approximation of the gain regions of the laser to be independent (i.e. the reciprocal confinement coefficients $\Gamma_{12} = \Gamma_{21} = 0$) it is easy to show that $F_0 = m(J - J_{\text{th}})/(1 - R)$. Here m is the number of quantum wells in each active region, J is the averaged carrier flux into one quantum well, $J_{\text{th}} \approx 10^{21}$ cm^{-2}s^{-1} is the threshold value of carrier flux for the parameters used in [6]. By using the approach being discussed in detail in [7] we have linked the carrier flux J_{th} with the threshold value of pump power density P_{th}.

2. Results

Fig. 1 displays the power densities of all interacting waves as functions of normalized value of pump power density excess above the threshold value P_{th}. The simulations have been performed with the following parameters: $m = 8$, $R = 0.98$, $L = 5$ mm, $\alpha_3 = 1$ cm^{-1}, $d_{14} = 1.1 \times 10^{-4}$ μm/V, $n_1 = n_2 = 3.5$, $n_3 = 3.2$. One can see from Fig. 1 the saturated behavior of radiation at the shortest wavelength λ_1 as pump power increases. At the same time, the power density P_2 becomes more intensively risen. The sum $P_1 + P_2$ approximately equals to double value of pump density provided there is no the nonlinear crystal in the cavity (or it has no any effect on radiation characteristics of the VECSEL). This finding corresponds to the expression $\varphi_1 + \varphi_2 = 2$ following from Eq. (5). The pump density of fundamental modes at $\lambda_{1,2}$ without taking into account the effect of nonlinear crystal is shown by the dotted line 4 in Fig. 1. The difference frequency power density (curve 3) rises initially in line with the squared value of abscissa and eventually the increase slows down. One can see that the power density goes to $\approx$380 Wcm^{-2} for $P_p/P_{\text{th}} = 10$; these values correspond to the beam power making up about 30 mW under pump power of 5 W for the beam radii of 50 μm.

The dependence of power densities $P_{1,2,3}$ at $10P_p/P_{\text{th}}$ on nonlinear crystal length L is shown in Fig. 2. When plotting the graphs we used the same parameters as those of Fig. 1. The graphs demonstrate again the dramatic effect of optical nonlinear interaction on the characteristics of stationary dual-wavelength generation in the VECSEL. We believe that the saturated behavior of difference frequency power density observing with long nonlinear crystals is the finding of great importance for applications.

Acknowledgements

This work has been supported in part by the Russian Fund for Basic Researches through RFBR grant No. 10-02-01074-a.

References

[1] T. Leinonen, Yu. A. Morozov, A. Härkönen, M. Pessa, *IEEE Phot. Techn. Lett.* **17**, 2508 (2005).

[2] Yu. A. Morozov, I. S. Nefedov, T. Leinonen, M. Yu. Morozov, *Semiconductors* **42**, 463 (2008).

[3] Yu. A. Morozov, M. Yu. Morozov, and I. V. Krasnikova *Techn. Phys. Lett.* **37**, 1112 (2011).

[4] V. G. Dmitriev, L. V. Tarasov, *Prikladnaya nelineinaya optika*, (Moscow: Fizmatlit), 512, 2004.

[5] O. Levi, T. Pinguet, T. Skauli, L. Eyres, K. Parameswaran, J. Harris, M. Fejer, T. Kulp, S. Bisson, B. Gerard, E. Lallier, L. Becouarn. *Opt. Lett.* **27**, 2091 (2002).

[6] M. Yu. Morozov, Yu. A. Morozov, and I. V. Krasnikova. *Journ. of Commun. Technology and Electronics* **55**, 1162 (2010).

[7] Yu. Morozov, T. Leinonen, M. Morozov, S. Ranta, M. Saarinen, V. Popov, M. Pessa. *New Journ. of Physics* **10**, 063028 (2008).

20th Int. Symp. "Nanostructures: Physics and Technology"
Nizhny Novgorod, Russia, June 24–30, 2012

Current transport in nanocrystalline CdS/InP heterojunction p-n diodes

Zs. J. Horváth[1,2], V. Rakovics[2], Yu. A. Yakovlev[3] and *P. Turmezei*[1]

[1] Óbuda University, Kandó Kálmán Faculty of Electrical Engineering, Institute of Microelectronics and Technology, Budapest, Hungary
[2] Hungarian Academy of Sciences, Research Centre for Natural Sciences, Institute for Technical Physics and Materials Science, Budapest, Hungary
[3] Ioffe Physical-Technical Institute, St Petersburg, Russia

Abstract. Current-voltage behaviour of CdS/InP heterojunction p-n diodes were studied in the temperature range of 80–320 K. The diodes were prepared by chemical bath deposition of n-type nanocrystalline CdS layers on p-type InP substrates. It is shown that the current through the junctions is dominated by electron transport. The actual current mechanisms are the thermionic-field emission for forward, and the field emission for reverse direction.

Introduction

CdS thin films are studied mainly for photodetector and solar cell purposes. The chemical bath technique (CBD) is a relatively simple and inexpensive method to prepare homogenous nanocrystalline films with controlled composition. In particular, CBD is widely used for achieving good-quality CdS films [1,2]. Extensive research has been done on the deposition and characterization of CdS semiconductor thin films due to their potential applications in the area of electronic device fabrication as well [3,4].

In this work the electrical behaviour of CdS/InP heterojunction p-n diodes have been studied. The diodes were prepared by chemical bath deposition of n-type nanocrystalline CdS layers on p-type InP substrates. The current through the junctions was dominated by electron transport. The actual current mechanisms were the thermionic-field emission (TFE) for forward, and the field emission (FE) for reverse direction.

1. Experimental

The substrates were p^+ (001) oriented InP wafers with a free hole concentration of about 3×10^{18} cm^{-3}. First a p-type InP layer was grown with a concentration of about 1×10^{17} cm^{-3} and a thickness of about 1.5 μm by liquid phase epitaxy. The CdS thin films were deposited by using the CBD technique. Baths containing $CdSO_4$ (1 mM/l), thiourea (5 mM/l), and NH_3 (1.7 mM/l) have been used. The slides were kept vertically in the beaker. The temperature of deposition process was 65 °C, and the duration of deposition was 30 minutes. The bath solution was stirred during the deposition.

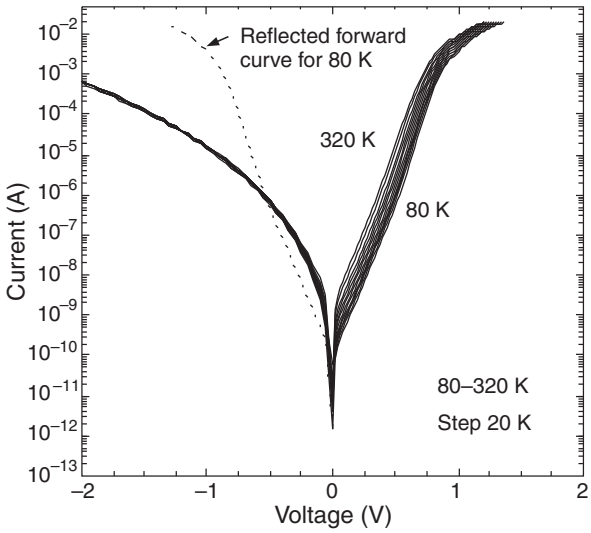

Fig. 1. Typical current-voltage characteristics of the studied nanocrystalline CdS/InP heterojunction p-n diodes.

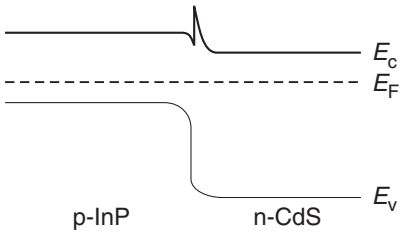

Fig. 2. The band structure of InP/CdS heterojunction [9].

After the deposition, the CdS films were washed with water ultrasonically to remove the loosely adhered CdS particles on the film, and finally dried in air. According to scanning and transmission electron microscope measurements, the CdS films were nanocrystalline with crystal size of 10–20 nm and total thickness of about 60 nm [5]. The optical band gap of the layer was 2.42 eV, as obtained by transmission measurements performed in the wavelength range of 400–1000 nm [5]. (This is the usual value published for CdS band gap [6].)

The diodes were fabricated by evaporation of gold-zinc and gold-tin contacts to the InP and CdS, respectively. The area of gold-tin contacts to CdS was 2.87×10^{-8} m^2, but as no mesa etch was performed, the effective area of the diodes can be larger. The diodes were studied by current-voltage (I-V) measurements in the temperature range of 80–320 K in dark.

2. Results and discussion

The typical I-V characteristics of the diodes are presented in Fig. 1, as a function of temperature. The lack of temperature dependence and the shape of reverse current indicate that it is dominated by field emission [7], while the exponential dependence of forward current on the bias and its weak temperature dependence indicate that it is dominated by thermionic field emission (TFE) through a low potential barrier [8]. An interesting behaviour of these junctions is that due to the different current mechanisms for forward and reverse branches, the re-

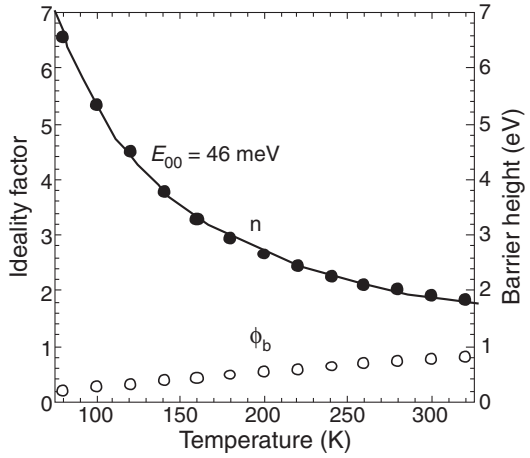

Fig. 3. Experimental temperature dependences (dots) of ideality factor and apparent barrier height evaluated for thermionic emission. Solid line is theoretical dependence of ideality factor for thermionic-field emission with characteristic energy of 46 meV.

verse current is higher at low biases and low temperatures, than the forward current, as it can be seen in Fig. 1.

Riad and co-workers calculated the band offsets of the InP/CdS heterojunction and proposed a band diagram presented in Fig. 2 [9]. They obtained the band offsets of conduction and valence band edges, as 0.09 and 0.77 eV, respectively. Due to band banding, the potential barrier for electrons is a few tens of meV, while that for holes is about 0.8 eV. So, the hole transport is blocked by the high potential barrier, and the current through the junction is dominated by electron transport, for forward direction by TFE, for reverse direction by TE.

The ideality factor and apparent barrier height evaluated for thermionic emission from the forward currents are presented in Fig. 4. Similar temperature dependences of these parameters are obtained for Schottky junctions, if the dominating current mechanism is the TFE [8]. In Fig. 3 solid line shows the theoretical temperature dependence of ideality factor for TFE fitted to the experimental points with characteristic energy E_{00} of 46 meV [8]. The excellent agreement between the experiment and theory clearly indicates the validity of the above explanation.

3. Summary

Nanocrystalline CdS/InP heterojunction p-n diodes have been prepared by chemical bath deposition of CdS. It has been shown that the current through the junctions is dominated by electron transport. The actual current mechanisms are the thermionic-field emission for forward, and the field emission for reverse direction.

References

[1] L. Pintilie, E. Pentia, I. Pintilie, and D. Petre, *Mat. Sci. Eng. B* **44**, 403 (1997).
[2] L. Pintilie, E. Pentia, I. Pintilie, T. Botila, and C. Constantin, *Appl. Phys. Lett.* **76**, 1890 (2000).
[3] S. Bhushan, M. Mukherjee, and P. Bose, *Radiat. Eff. Defects Solids* **153**, 367 (2001).
[4] M. Mukherjee, P. Bose, and S. Bhushan, *Ind. J. Pure Appl. Phys.* **39**, 804 (2001).
[5] V. Rakovics, Zs. J. Horváth, Z. E. Horváth, I. Bársony, C. Frigeri, T. Besagni, *Phys. Stat. Sol. (C)*, **4**, 1490 (2007).
[6] A. Yoshikawa, Y. S. Sakai, *Solid-State Electron.* **20**, 133 (1977).
[7] F. A. Padovani , R. Stratton, *Solid-State Electron.* **9**, 695 (1966).
[8] Zs. J. Horváth, *Solid-State Electron.* **39**, 176, (1996), and references therein.
[9] A. S. Riad, S Darwish, H. H. Afify, *Thin Solid Films* **391**, 109 (2001).

20th Int. Symp. "Nanostructures: Physics and Technology"
Nizhny Novgorod, Russia, June 24–30, 2012

Ab initio electronic structure of Ge(111)-(2×1) surface in the presence of surface vacancy. Apllication to STM data analysis

S. V. Savinov[1], A. I. Oreshkin[1], S. I. Oreshkin[2], V. I. Panov[1]

[1] Physics Faculty, Moscow State University, 119991 Moscow, Russia
[2] Sternberg Astronomical Institute, Moscow State University, 119991 Moscow, Russia

Abstract. We present the results of first principles modeling of Ge(111)-(2 × 1) surface in the presence of atomic vacancy in surface bi-layer. We show that simple crystal structure defect affects surface electronic structure to the extent comparable with the influence of doping atom.

Introduction

Electronic properties of solid body surface for a long time attract researches attention. Partially this is caused by the successes of modern microelectronics industry. Devices produced by vacuum UV lithography 28-nm technology are already in the bulk production. The width of insulating layers is comparable with the Bohr radius of outer electronic shell for shallow impurities (of order of 100 Å). Single atomic defect in principle can change *macroscopic* properties of the whole microelectronic structure. The industry faces the lack of information on local electronic properties.

Below we report on the results of *ab initio* numerical modeling of Ge(111) surface's with (2 × 1) reconstruction electronic properties in the presence of atomic vacancy in surface reconstruction bi-layer. We have performed our first principles calculations by means of DFT method in LDA approximation as implemented in SIESTA [1] package. Some details can be found in [2]. The use of strictly localized numeric atomic orbitals is necessary to be able to perform modeling of large surface cell. In present work it is composed from 7×21 cells of elementary 2×1 reconstruction, each 8 Ge atomic layers thick (about 2645 atoms). Vacuum gap between neighboring slabs is about 20 Å. Ge dangling bonds at the slab bottom surface are terminated with H atoms to prevent surface states formation, and one Ge atom is removed from surface bi-layer at the slab center. The geometry of the structure was fully relaxed, until atomic forces have became less then 0.01 eV/Å. As the last step the spatial distribution of Khon–Sham wave-functions and surface LDOS were calculated.

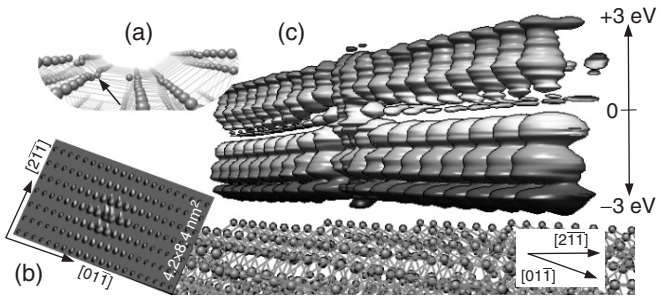

Fig. 1. Properties of Ge(111)-(2 × 1) surface in vicinity of surface vacancy. Relevant crystallographic directions are shown. a) Crystal lattice around vacancy. Arrow indicates the place from which Ge atom was removed. Atoms in a few rows have changed their positions. b) Quasi-3D distribution of surface LDOS. LDOS value is coded both by color and by height. Many disturbed π-bonded rows are obvious. LDOS disturbance spreads along π-bonded row ([01$\bar{1}$] direction) for at least 40 Å. c) Surface LDOS(x,y,eV) field is shown by surface of constant value colored by applied bias voltage. LDOS is disturbed by the presence of vacancy quite far from the defect.

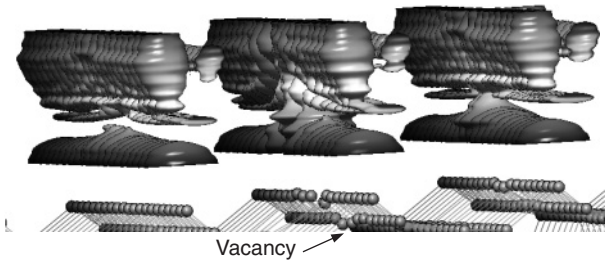

Fig. 2. Surface LDOS(x,y,eV) above Ge(111)-(2 × 1) surface in vicinity of surface vacancy. Arrow indicates the place from which Ge atom was removed. Atoms in a few rows have changed their positions. LDOS(x,y,eV) field is shown by surface of constant value colored by applied bias voltage. Band gap closure in two π-bonded rows adjacent to vacancy is apparent.

1. Surface local density of states

We would like to stress the fact, that with STM we are measuring LDOS *above* the surface, and as such in DFT calculations we are interested in the following quantity:

$$\mathrm{LDOS}\left(\overrightarrow{r_{x,y}},\ \mathrm{eV}\right) = \sum \left|\Psi\left(\overrightarrow{r_{x,y}}\right)\right|^2 \tilde{\delta}\left(E - E_i\right)\Big|_{z=\mathrm{const}},$$

where are Khon–Sham eigenfunctions, $\tilde{\delta}$ is non-zero width smearing function, E_i are Khon–Sham eigenvalues, and summing is evaluated at certain plane, located a few angstroms above the surface, at certain tunneling bias voltage.

This way we can calculate and plot scalar field of surface LDOS(x,y,eV) in space-energy coordinates (Fig. 1c). To be absolutely clear, below under LDOS we understand *surface* LDOS as measured by STM. In this figure LDOS is shown as the constant value surface colored by applied bias. Areas with high values of LDOS are located inside volume confined by aforementioned surface. LDOS is shown above only one π-bonded row to make clear impression about the LDOS local structure.

The removal of single host atom leads to rearrangement of a few atoms in surface bi-layer of Ge(111)-(2×1) reconstruction, which is clear from Figs. 1a,2. Thus the localization radii of single vacancy is not one unit cell anymore. As a consequence

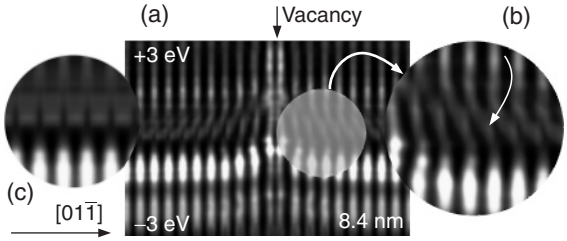

Fig. 3. a) Cross-section of surface LDOS(x,y,eV) along (x,eV) plane, containing vacancy. The position of vacancy along π-bonded row is indicated by black arrow. b) Zoomed in area of a). c) The same as b) for clean Ge(111)-(2 × 1) surface.

LDOS is noticeably disturbed in this area (Fig. 1b). The spatial extent of perturbation along π-bonded rows ([01$\bar{1}$] direction) is about 40 Å, while in direction perpendicular to π-bonded rows ([2$\bar{1}$1] direction) all seven atomic rows (∼40 Å) used in calculations are influenced by the defect.

It is known that LDOS of Ge(111)-(2 × 1) surface in band gap region is governed by non-occupied π^* surface states band [3]. As we have already shown the presence of donor impurity atom in surface bi-layer locally destroys the conditions for surface states formation and, besides this, leads to closure of band gap in vicinity of the defect [2]. Exactly the same situation can be observed in case of single vacancy — Figs. 1c, 2. The band gap is closed in two π-bonded rows, neighboring to vacancy.

DFT methodology gives nice opportunity to analyze the local structure of Khon–Sham wave-functions. In Fig. 3 we present the cross-section of LDOS(x,y,eV) field along (x,eV) plane, which contains vacancy. Vertical bright stripes correspond to increased LDOS above dimers of π-bonded rows of Ge(111)-(2 × 1) reconstruction. Dark "horizontal" stripe in the middle reflects the band gap (Fig. 3). It can be seen that band gap is disappearing as we approach vacancy along π-bonded row.

Another interesting fact concerns atomic orbitals hybridization. In vicinity of vacancy it differs drastically from that far away from the defect. To illustrate this observation part of Fig. 3a is zoomed in to Fig. 3b. Atomic orbitals in the band-gap energy range are visually going (when bias voltage is changing from −3 V to +3 V) to the next row (Fig. 3b, thin white arrow), not to the nearest one. This is completely different from clean Ge(111)-(2 × 1) surface. The latter case is illustrated in Fig. 3c and atomic row is apparently going (from bottom to top) to the nearest row.

We would like to note, that namely this way of data representation for spectroscopic STM result is probably the most suitable for the task of individual defect identification. It could be much more informative then the typical "LDOS at the point" method.

The main underlaying idea of DFT method is to build spatial distribution of LDOS. As LDOS is calculated we can model STM/STS measurements, in particular we can analyze the dependence LDOS(eV) at specific points above model slab. Thus we can compare LDOS(eV) averaged within small area (exactly the same way as experimental STM data is treated) above different atomic size defects.

The results of such comparison are depicted in Fig. 4. LDOS(eV) curves are shown for three cases: phosphorus (P) donor impurity atom, single vacancy (V) and clean defectless

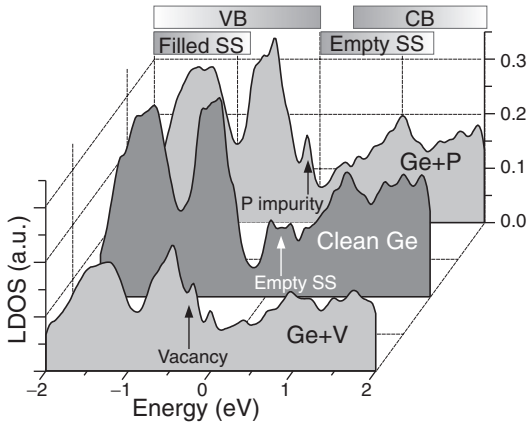

Fig. 4. Calculated dependence LDOS(eV) in three different cases: above clean Ge(111)-(2 × 1) surface; above individual vacancy (Ge+V); above P donor impurity (Ge+P). Surface band structure is schematically shown at the top of image, where SS stands for surface states, VB and CB stands for valence and conduction band respectively. The contribution from empty SS band to LDOS above clean surface is marked by white arrow. Split state at VB top originating from P donor impurity is marked by black arrow.

surface. What is important is that in all three calculations we have used exactly the same set of parameters for Ge atoms: basis orbitals, pseudo-potentials and crystal cell etc. Thus, the LDOS difference is reflecting the influence of different defects. The main conclusion that can be immediately drawn based on Fig. 4 is that simple crystal structural defect such as individual vacancy affects surface electronic structure to the extent comparable with the influence of doping atom. Indeed, LDOS inside the *whole* valence (VB) and conduction bands (CB) is lower above vacancy then both above the clean surface and above donor impurity. In case of Ge+V a set of peaks at the top of VB is clearly resolved.

In conclusion, by numerical modeling we show that the simplest surface defect strongly influences surface LDOS structure noticeably far (∼ 40 Å) from the defect. We also demonstrate the strong difference of surface LDOS structure above surface defects of different kind. We are aware of the necessity of the detailed comparison of DFT results with experimental STS data, but this is the subject for another publication.

Acknowledgements

This work has been supported by RFBR grants and computing facilities of Moscow State University. We also would like to thank the authors of WxSM and Chimera free software.

References

[1] E. Artacho, D. Sanchez-Portal, P. Ordejon, A. Garcia and J. M. Soler, *Phys. Stat. Sol. (b)* **215**, 809 (1999).

[2] S. V. Savinov, S. I. Oreshkin , N. S. Maslova, Electronic structure of Ge(111)-(2 × 1) surface in the presence of doping atoms. Ab initio analysis of STM data, *Pis'ma v ZhETF* **93/9**, 579 (2011).

[3] J. M. Nicholls, P. Maartensson, and G. V. Hansson, *Phys. Rev. Lett.* **54**, 2363 (1985).

20th Int. Symp. "Nanostructures: Physics and Technology"
Nizhny Novgorod, Russia, June 24–30, 2012

Photogalvanic effect in a quantum channel with an impurity

M. A. Pyataev and S. N. Ulyanov
Mordovian State University, Saransk, Russia

Abstract. The influence of electromagnetic radiation on the electron transport in a quantum channel with a single short-range impurity is studied using the generalization of the Landauer–Büttiker approach. We have shown that direct photocurrent arises in the system in the case of asymmetric impurity location. The dependence of the photocurrent on electron chemical potential, position of the impurity and frequency of radiation is studied.

Introduction

The interest to the photogalvanic effect in various nanostructures is stipulated by recent attempts to create a sensitive nanometer-size photodetector [1,2]. A lot of theoretical models have been used to study the microwave induced electron transport in bulk materials and low-dimensional systems. It is well-known that the necessary condition for appearance of the photocurrent is the absence of the inversion symmetry in the system. In the macroscopic samples, the absence may be stipulated by the asymmetry of the lattice or by oriented asymmetric scatterers [3,4].

Ballistic transport regime in quasi one-dimensional nanostructueres allows another mechanism. The symmetry may be broken by an asymmetrically located single scatterer, for instance, a potential barrier or an impurity [5]. In the present paper, we consider one of the simplest nanoscale system that allows generation of the direct current induced by electromagnetical radiation. In our previous work [5], we have studied the quantum channel with a parabolic lateral confining potential. This potential is useful because of the simple expression for matrix elements of perturbation. However, parabolic potential has one non-realistic feature, namely equidistant set of energy levels. This feature leads to existence of the single resonance frequency and specific oscillating dependence of the photocurrent on the chemical potential. In the present paper, we consider more general case of non-equidistant energy levels. We use the hard-wall potential to describe the confinement of electrons in the channel.

1. Model of the device

We consider the channel connecting two electron reservoirs with equal temperature and chemical potential. The channel is formed from the two-dimensional electron gas by applying of the hard-wall potential. A single short-range impurity is placed at some point $\vec{r}_d$ in the channel. The system is exposed by electromagnetic radiation polarized in the y direction (perpendicular to the channel axis). The scheme of the device is shown in Fig. 1. The reservoirs are covered by opaque diaphragm and the interaction of electrons with the electromagnetic wave takes place only in the region of channel. The impurity is modeled by the zero-range potential [8,9].

The electron motion in the channel without the impurity is described by the Hamiltonian

$$\hat{H}_0 = \frac{\hat{p}_x^2}{2m} + \frac{\hat{p}_y^2}{2m} + U(y), \qquad (1)$$

where m is effective electron mass, $\hat{p}_x$ and $\hat{p}_y$ are projections of the momentum, and $U(y)$ is the hard-wall potential confining

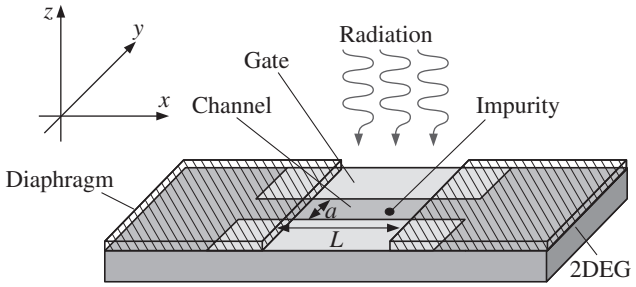

Fig. 1. Scheme of the device. Opaque diaphragm is shown by hatched area.

electrons on a strip of width a ($0 < y < a$). Eigenvalues $E_{n,p}$ and eigenfunctions $\phi_{n,p}$ of the Hamiltonian $\hat{H}_0$ are well-known

$$E_{n,p} = \frac{p^2}{2m} + E_n, \;\; \phi_{n,p}(x, y) = \sqrt{\frac{2}{a}} \sin\left(\frac{\pi n y}{a}\right) e^{ipx/\hbar}, \quad (2)$$

where $E_n = \hbar^2\pi^2 n^2/2ma^2$.

According to the zero-range potential theory the Hamiltonian $\hat{H}_d$ of the channel with the impurity is defined by the point perturbation of the Hamiltonian $\hat{H}_0$. This perturbation is determined by the linear boundary conditions for the wave function at the point $\vec{r}_d$.

We assume that the electromagnetic radiation interacts with the electron at the region of length L in the channel. Other parts of the device are covered by opaque diaphragm. In this case the perturbation operator corresponding to the radiation may be represented in the form

$$\begin{aligned} \hat{V}(t) &= \frac{e\epsilon\hat{p}_y}{m\omega}\left[\theta(x) - \theta(x - L)\right]\cos(\omega t) \\ &= \hat{V}_0\left(e^{i\omega t} + e^{-i\omega t}\right), \end{aligned} \qquad (3)$$

where ϵ is the amplitude of the electric field, ω is the frequency of the radiation, and $\theta(x)$ is the Heaviside θ-function.

2. Photocurrent

To obtain the photocurrent we use the generalization [5–7] of the Landauer–Büttiker approach that takes radiation into account. In the one-photon approximation the photocurrent in the channel is given by the following equation:

$$I_{\rm ph} = \frac{e}{\pi\hbar}\int_0^\infty f(E)\Delta T(E)dE, \qquad (4)$$

where $f(E)$ is the Fermi distribution function and

$$\Delta T(E) = \sum_{l=\pm1}\sum_{nn'}\Big[T_{n'n}^{RL}(E + l\hbar\omega, E) - T_{n'n}^{LR}(E + l\hbar\omega, E)\Big].$$

Transmission coefficients $T^{ij}_{n'n}(E+l\hbar\omega, E)$ can be represented via transmission amplitudes $t^{ij}_{n'n}(E + l\hbar\omega, E)$ (here indexes i and j mean left (L) or right (R) reservoir)

$$T^{ij}_{n'n}(E + l\hbar\omega, E) = \frac{k^l_{n'}}{k^0_n} \left| t^{ij}_{n'n}(E + l\hbar\omega, E) \right|^2 , \qquad (5)$$

where the wave number k^l_n is given by

$$k^l_n = \sqrt{2m(E - E_n + l\hbar\omega)}/\hbar \, . \qquad (6)$$

To obtain the transmission amplitudes we have found an approximate solution for the Schrödinger equation using the concept of quasi-energy states [10]. Since the whole one-electron Hamiltonian of the system depends periodically on time the wave function may be represented as a superposition of harmonics

$$\Psi(\vec{r}, t) = \sum_l \psi_l(\vec{r}) \exp\left[-i \, (F + l\hbar\omega) \, t/\hbar\right], \qquad (7)$$

where F is the complex quasi-energy. Imaginary part of F is responsible to the relaxation processes. In one-photon approximation we get the following approximate equation for the excited states:

$$\psi_{\pm 1}(\vec{r}) = -\int G_d\left(\vec{r}, \vec{r}\,'; F \pm \hbar\omega\right) \hat{V}_0 \psi_0\left(\vec{r}\,'\right) d^2 r', \qquad (8)$$

where $G_d(\vec{r}, \vec{r}\,'; E)$ is the Green's function and $\psi_0(\vec{r})$ is the eigenfunction of the Hamiltonian $\hat{H}_d$. According to the zero-range potential theory [8] the eigenfunction $\psi_0(\vec{r})$ has the form

$$\psi_0(\vec{r}) = \phi_0(\vec{r}, E) - \frac{\phi_0(\vec{r}_d, E)}{Q(\vec{r}_d, E) - P} G_0(\vec{r}, \vec{r}_d; E). \qquad (9)$$

Here $G_0(\vec{r}, \vec{r}\,'; E)$ is the Green's function of the Hamiltonian $\hat{H}_0$, $Q(\vec{r}_d; E)$ is the Krein's Q-function i.e. renormalized Green's function of the Hamiltonian $\hat{H}_0$, and P is the parameter determining the strength of the zero-range potential. Using the zero-range potential theory we have found the explicit form of the Green's function $G_d(\vec{r}, \vec{r}\,'; E)$. Then we have determined the transmission probabilities $T^{ij}_{n'n}$ from the asymptotics of the wave function (8) at $x \to \pm\infty$ and obtained the equation for the photocurrent.

3. Results and discussion

The appearance of the photocurrent might be explained using the simplified model in which the channel is divided into three parts and the total transmission probability is found by multiplying transmission probabilities for each region [5]. According to this approach the absorption (emission) of the photon changes the probability of electron transmission through the part of the channel containing impurity. Since the impurity is situated at non-central cross-section of the device the absorption (emission) probability is different at left and right parts of the channel. Therefore total transmission probabilities become different for electrons moving in opposite directions and the photocurrent arises.

The dependence of the photocurrent on the chemical potential at differen frequencies of the radiation is shown in Fig. 2. One can see from the figure that the photocurrent changes abruptly near the discrete parts E_n of the eigenvalues of the Hamiltonian $\hat{H}_0$. Our analysis shows that at low signal approximation major contribution to the photocurrent is caused by slow electrons because exposition time and consequently the probability of optical transition is largest for them. Therefore the maximal changes in the photocurrent correspond to transition between the bottoms E_n and $E_{n'}$ of n-th and n'-th subbands. The amplitude of the photocurrent is maximal when the chemical potential is located between E_n and $E_{n'}$ and the frequency of radiation satisfies the condition $\hbar\omega = E_{n'} - E_n$. It should be noted that transition between subbands with equal parity of the quantum number n are forbidden in the first-order approximation.

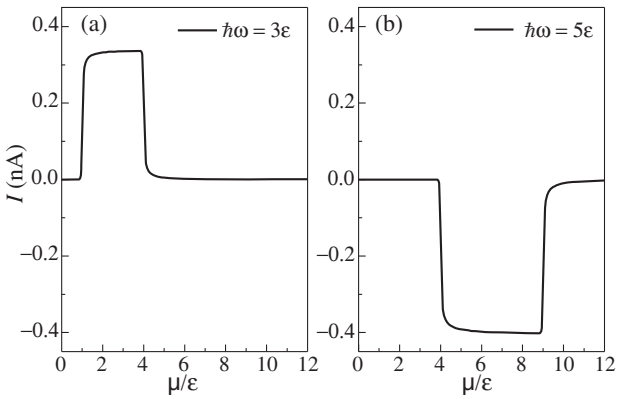

Fig. 2. Photocurrent as a function of the chemical potential. Here $\varepsilon = \hbar^2\pi^2/2ma^2$.

Acknowledgements

Authors are grateful to V. A. Margulis for valuable discussions. The work is supported by the RFBR (grant No. 11-02-00699-a) and by Federal Target Program "Research and development in priority areas of scientific and technological complex of Russia for 2007–2013 years".

References

[1] H. Kosaka *et al*., *Phys. Rev. B* **67**, 045104 (2003).
[2] M. A. Rowe *et al*., *Appl. Phys. Lett.* **89**, 253505 (2008).
[3] M. V. Entin and L. I. Magarill, *Phys. Rev. B* **73**, 205206 (2006).
[4] A. D. Chepelianskii *et al*., *Physica E* **40**, 1264 (2008).
[5] M. A. Pyataev and S. N. Ulyanov, *Phys. Rev. B* **79**, 235428 (2009).
[6] F. A. Maaø and L. Y. Gorelik, *Phys. Rev. B* **53**, 15885 (1996).
[7] Y. V. Pershin and C. Piermarocchi, *Phys. Rev. B* **75**, 035326 (2007).
[8] V. A. Geyler, V. A. Margulis and M. A. Pyataev, *JETP* **97**, 763 (2003).
[9] Y. N. Demkov and V. N. Ostrovsky, *Zero-Range Potentials and Their Applications in Atomic Physics* (Plenum, New York), 1988.
[10] Ya. B. Zel'dovich, *Sov. Phys. Uspekhi* **16**, 427 (1973).

20th Int. Symp. "Nanostructures: Physics and Technology"
Nizhny Novgorod, Russia, June 24–30, 2012

Charge transport properties of silicon dioxide films as manifested in frequency-dependent CV-characteristics of MOS capacitors with oxide-hosted Si nanoparticles

V. A. Stuchinsky, M. D. Efremov, G. N. Kamaev and S. A. Arzhannikova
Institute of Semiconductor Physics, SB RAS, Lavrentieva 13, 630090 Novosibirsk, Russia

Abstract. Using the simplest example of MOS capacitor with a planar array of oxide-embedded Si nanoparticles, we analyze the model that was previously used to explain the formation of a hump-like feature observed in the accumulation branch of CV-curves of such structures. Numerical calculations of typical structures are reported, and an example of measured characteristics closely resembling predicted curves is given.

Introduction

It is well known that the density of Si nanoinclusions in silicon dioxide layers can be high enough to facilitate tunneling transport of charge carriers over the system of oxide-hosted Si nanoparticles. This transport can affect electrical characteristics of structures involving such layers, for instance, CV-characteristics of MOS capacitors, right during electrical measurements. Indeed, it was reported previously that CV-characteristics of MOS capacitors with oxide-hosted Si nanoparticles may exhibit a hump-like feature in their accumulation branch emerging as a single capacitance peak or a more intricately shaped structure [1–4]. Within this feature, which grows in amplitude with decreasing the measurement frequency f, measured MOS capacitance C can be notably in excess of the accumulation capacitance C_a of the ideal MOS capacitor (without oxide-hosted nanoparticles). The hump emerges within a certain interval of gate voltages U, this interval being preceded by a portion of CV-curve exhibiting a capacitance value close to C_a. With increasing U, measured MOS capacitance C first increases to reach some maximum value and, then, decreases to finally reach saturation at a lower capacitance level (also close to C_a). Within the hump, measurements of C were reported to be poorly reproducible, seriously suffering from hysteresis phenomena.

Earlier, trying to explain the formation of the hump-like feature, we have attempted examination of a simple transport model for charge carriers injected into the MOS oxide layer [5]. Generally, the model arises on adoption of the following assumptions: (i) in a biased MOS, tunneling injection of charge carriers (electrons and/or holes) from one or both contacts into the MOS oxide takes place (for definiteness, below we consider the case of MOS capacitor formed on a p-Si substrate; in this capacitor, holes are assumed to be injected from the accumulation layer of p-Si into oxide-hosted Si nanoparticles, say, nanocrystals (nc's), to subsequently sink to the metal (see Fig. 1)); (ii) the hole transport through the oxide proceeds along linear nc chains in a self-consistent manner with the establishment of local electric field in the oxide; (iii) in the nc chains, tunnel barriers are statistically scattered in terms of their widths, so that the widest tunneling gap presents a "bottleneck" for the hole current. In an nc chain, the involvement of a "bottleneck" promotes accumulation of a positive charge Q_{ox} in the oxide, concentrated predominantly at the edge of the bottleneck from the side of the semiconductor. It is the small ac variation of Q_{ox} that leads to the increase of measured capacitance C in excess of C_a.

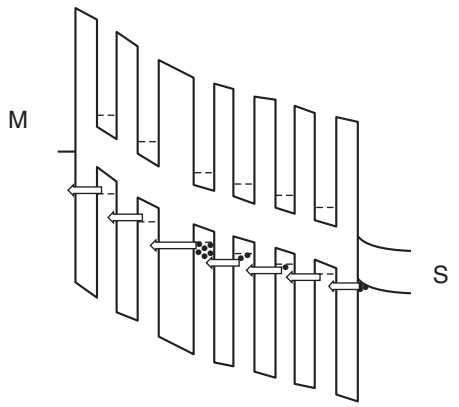

Fig. 1. Charge transport through oxide in an MOS capacitor with oxide-hosted Si nc's and injection of holes from p-Si.

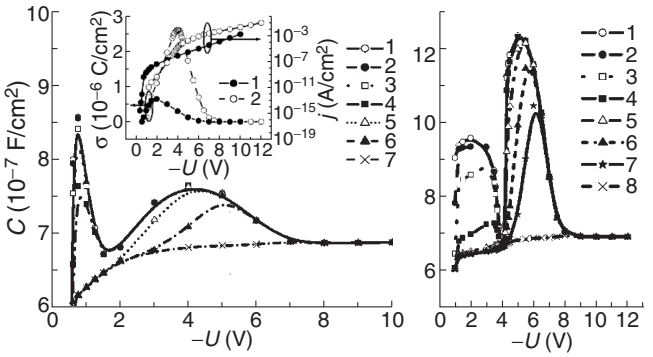

Fig. 2. Frequency-dependent CV-curves of MOS-1 (left) and MOS-2 (right) as calculated by the present model. Left: f [Hz]=0 (curve 1), 0.0003 (2), 0.001 (3), 0.003 (4), 0.1 (5), 1 (6), 1000 (7); right: f [Hz]=0 (curve 1), 1 (2), 3 (3), 10 (4), 30 (5), 100 (6), 300 (7), 100000 (8). Inset: sheet charge Q_{ox} in the nc-layer versus U, and static I-V characteristics of the MOS capacitors; curves 1 and 2 refer respectively to MOS-1 and MOS-2.

The properties of the model can be traced considering the simplest case in which each nc chain involves just one Si nanocrystal located, in accord with the above-formulated assumptions, closer to the semiconductor. On increasing the dc voltage U applied to MOS, the nc-trapped charge Q_{ox} grows in value together with the injection current; the increasing charge Q_{ox} results in a growth of the oxide field predominantly in the gap adjacent to the metal. As the field in the latter gap

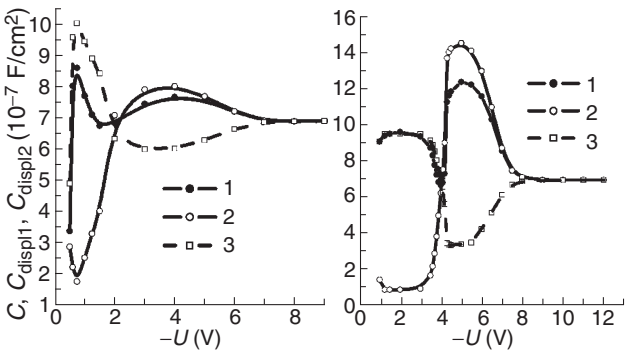

Fig. 3. Structure of the total a.c. in the two gaps of MOS-1 (left) and MOS-2 (right). 1 — MOS capacitance C, 2 — $C_{\mathrm{disp}\,1}$, 3 — $C_{\mathrm{displ}\,2}$; the subscripts 1 and 2 refer respectively to gap 1 and 2.

increases, the tunnel barrier there finally becomes triangular, and the rate of tunneling emission of nc-trapped holes into the metal increases sharply, making the charge Q_{ox} decrease in value. As the charge Q_{ox} decreases, further incremental voltage changes will predominantly drop across the gap in between the injecting contact and the nc layer. This fundamental property of the model, i.e. the passage of the nc-trapped charge Q_{ox} through a maximum, is also retained in the more evolved case of nc chains formed by many nc's and involving several bottlenecks. This property of the model is an important one since it allows easy extension of the present analysis to the case of dielectrics with embedded nanoparticles randomly distributed over the volume of the dielectric film.

1. Calculations

The electrical state of the MOS capacitor can be analyzed by solving the nonlinear equation system comprising the continuity equation for the electric current and the conditions of field matching across the Si/oxide interface and the nc layer. After the dc quantities of the MOS capacitor are found, ac quantities can be determined by solving the linearized equation system. Finally, the frequency-dependent capacitance C can be calculated by assessing the total alternating current (hole current + displacement current) in any cross-section of the oxide. In our calculations we treated the case of MOS capacitors fabricated on p-type Si substrates with $N_{\mathrm{a}} = 1 \times 10^{15}$ cm^{-2}. The sheet density of nc's in the nc layer was assumed to be 2.5×10^{15} cm^{-2} (nanocrystals sized 1 nm with lateral spacing 1 nm).

2. Results

Some data calculated for MOS capacitors with tunneling gaps $d_1/d_2 = 2/3$ and 1.5/3.5 nm (MOS-1 and MOS-2) are shown in Figs. 2 and 3. A bright consequence of the presence of oxide-hosted Si nanoparticles in MOS is the emergence of a hump with two capacitance maxima in the accumulation branch of the low-frequency CV-curve (Fig. 2). The maxima are observed then the rate of change (increase or decrease) of the charge Q_{ox} with increasing bias voltage U reaches a maximum (see the inset in Fig. 2). In between the two peaks, the capacitance C falls to a lower level (in a laterally uniform structure, down to C_{a}), the minimum of C being observed when the charge Q_{ox} reaches its highest. It can be expected that in a laterally nonuniform structure the fall of C should be less pronounced,

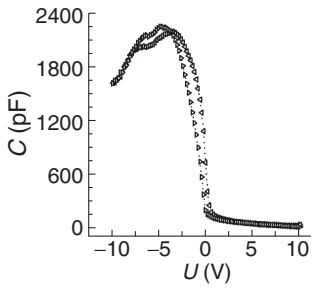

Fig. 4. Measured CV-characteristics of an MOS capacitor with oxide-hosted a-Si nanoclusters ($d_1/d_2 = 20/6$ nm, $f = 3$ kHz) [1].

its magnitude serving a measure of lateral uniformity of the electrical properties of the structure. The passage from the charge accumulation regime to the regime with the decrease of Q_{ox} is also manifested in the change of slope of static MOS I-V characteristics plotted in the coordinates $\ln(j^-)$ vs U (inset in Fig. 2). With decreasing the ac frequency, the two capacitance peaks disappear from the CV-curve, the first peak of C, i.e. the peak observed at the lower gate voltage, vanishing first (Fig. 2).

The structure of the total a.c. in the two gaps of the two-barrier structure is illustrated by Fig. 3 (here, $C_{\mathrm{displ}\,i} = (\varepsilon_{\mathrm{a}}/d_i) \times (V_i^{\sim}/V^{\sim})$ is the "capacitance" due to the displacement current in the i-th tunneling gap (the gaps are enumerated from the semiconductor); the difference between C and $C_{\mathrm{disp}\,l}$ gives the contribution due to the hole current).

Experimentally, a feature in the CV-curves of MOS capacitors closely resembling the calculated data was previously observed in [1] while measuring MOS capacitors with oxide-hosted a-Si nanoclusters (except that, seemingly, the injecting contact in [1] was the contact with the metal, and the injected charge carriers were electrons) (see Fig. 4).

To summarize, we have investigated the properties of a model that was invented for gaining a more penetrating insight into the electrical properties of MOS capacitors with oxide-hosted Si nanoparticles. The data obtained may prove useful in many applications, including characterization of dielectric layers with semiconductor nanoinclusions and characterization of charge transport properties of dielectric materials.

Acknowledgements

One of the authors (V.A.S.) is indebted to Dr. A. V. Vishnyakov for fruitful discussions.

References

[1] S. A. Arzhannikova *et al.*, *Proc. VI Intern. Conf. "Amorphous and Microcrystalline Semiconductors"* St Petersburg, Russia 2008, p. 162.
[2] M. D. Efremov *et al.*, *Fiz. Tekhn. Poluprov.* **39**, 945 (2005).
[3] J. Shi, *Sol. St. Commun.* **123**, 437 (2002).
[4] A. A. Evtukh *et al.*, *Proc. II Intern. Sci. Conf. "Nanostructured Materials-2010"*, Russia-Belorussia-Ukraine, Kiev, October 19–22, 2010.
[5] V. A. Stuchinsky, *Proc. 26th Intern. Symp. "Nanostructures: Physics and Technology"*, Ekaterinburg, Russia, 2011, p. 70.

20th Int. Symp. "Nanostructures: Physics and Technology"
Nizhny Novgorod, Russia, June 24–30, 2012

Electronic states and persistent current in elliptic quantum ring

I. A. Kokurin
Mordovian State University, 430005 Saransk, Russia

Abstract. The one-electron energy spectrum in the one-dimensional elliptic quantum ring is investigated by means of numerical diagonalization of constructed Hamiltonian. The density matrix formalism is utilized for the persistent current calculation. The dependence of persistent current in elliptic quantum ring essentially differs from such dependence in circular ring that is due to the presence of anticrossings and periodicity violation in the dependence of elliptic ring energy levels vs magnetic flux.

Introduction

The quantum ring (QR) is the low-dimensional structure that is more applicable for investigation of such effects as Aharonov–Bohm one and persistent currents (PCs) [1]. And although the simple one-dimensional (1D) QR model in one-electron picture cannot describe many features in PCs nevertheless it is starting point in qualitative understanding of the problem.

The spinless Hamiltonian of electron in 1D circular QR (CQR) with the radius R is given by

$$H_0 = \frac{\hbar^2}{2m^*R^2}\left(-i\frac{\partial}{\partial\varphi}+\frac{\Phi}{\Phi_0}\right)^2. \qquad (1)$$

Here m^* is the scalar effective mass, Φ is the magnetic flux through the ring and $\Phi_0 = 2\pi\hbar c/|e|$ is the flux quantum. It should be noted that in the case of 1D QR there is no difference between Aharonov–Bohm flux $\Phi_{\rm AB}$ and the flux $\Phi = \pi R^2 B$ of the uniform magnetic field **B**. They are equivalent because in last case the magnetic field does not penetrate the conducting area of the ring due to its small (zero) width. The energy levels and wavefunctions corresponding to Hamiltonian (1) have the well-known form

$$E_m = \frac{\hbar^2}{2m^*R^2}\left(m+\frac{\Phi}{\Phi_0}\right)^2, \quad \psi_m(\varphi) = \frac{1}{\sqrt{2\pi}}e^{im\varphi}, \quad (2)$$

where $m = 0, \pm1, \pm2, \ldots$. The energy spectrum of CQR as a function on magnetic flux is depicted on Fig. 1a.

Note the real QR geometry defined in 2DEG can be different from circular one. The elliptic deformation of quantum ring is the simple way to describe the deviation of the ring shape from circular one. Therefore the aim of present work is the theoretical investigation of the electron energy spectrum and PC in 1D elliptic QR (EQR). We suppose QR be defined in GaAs/AlGaAs 2DEG-structure for that spin splitting due to spin-orbit interaction and Zeemann splitting (in reasonable magnetic fields) are negligible.

The 2D Hamiltonian of the spinless electron in perpendicular magnetic field in elliptic coordinates (u, φ) is given by [2]

$$H_{\rm 2D} = \frac{\hbar^2}{2m^*h^2 g(u,\varphi)}\left[\left(-i\frac{\partial}{\partial\varphi}+\beta\sinh(2u)\right)^2 + \left(-i\frac{\partial}{\partial u}+\beta\sin(2\varphi)\right)^2\right], \qquad (3)$$

where h is the focal distance, $g(u,\varphi) = \sinh^2 u + \sin^2\varphi$ and the parameter $\beta = (h/2l_{\rm B})^2$ is the dimensionless magnetic field, with $l_{\rm B} = \sqrt{\hbar c/|e|B}$ being the magnetic length.

Before solution of spectral problem for 1D EQR let us mention some features that deal with transition from the Hamiltonian of the high dimension to low one. The strict procedure for the Hamiltonian dimension lowering (e.g. 2D to 1D) requires the averaging in ground state transverse wavefunction, whereas if we simply fix transverse coordinate and discard the corresponding derivatives then we can obtain in general the non-Hermitian operator. For example, the latter procedure for the 1D CQR with Rashba spin-orbit interaction leads to non-Hermitian Hamiltonian [3], but it should be noted that the simmetrization of such an operator leads to the correct result of Ref. [4].

1. Model and Hamiltonian diagonalization

Now we write the one-electron Hamiltonian in 1D EQR. The equation of the ellipse with semi-axes a and b in elliptic coordinates is $u = u_0 = \text{const}$ that corresponds to $a = h\cosh u_0$, $b = h\sinh u_0$. Fixing in Eq. (3) the transverse coordinate $u = u_0$ and discarding the corresponding derivatives we find the following operator

$$H = \frac{\hbar^2}{2m^*h^2 g_0(\varphi)}\left[\left(-i\frac{\partial}{\partial\varphi}+\frac{\Phi}{\Phi_0}\right)^2 + \frac{h^4}{4a^2b^2}\frac{\Phi^2}{\Phi_0^2}\sin^2(2\varphi)\right], \qquad (4)$$

where $\Phi = \pi abB$ is the magnetic flux and $g_0(\varphi) = g(u_0,\varphi)$. It should be mentioned that the operator (4) is not Hermitian and therefore it is not correct 1D EQR Hamiltonian.

To find the EQR spectrum we, at first, find the matrix elements of the Hamiltonian (4) calculated in basis of eigenfunctions of CQR (2). The second step is the simmetrization of the Hamiltonian matrix, $H \to (H + H^\dagger)/2$. And the third step is its diagonalization. For the numerical diagonalization we use 21×21 Hamiltonian matrix, conserving the matrix element for the states in Eq. (2) with $m = -10, -9, \ldots, 9, 10$. The energy spectrum of the EQR as a function of magnetic flux is depicted on Fig. 1b. It should be noted the crossings at $\Phi = n\Phi_0$ that take place in the spectrum of CQR are reduced into anticrossings on the EQR $E(\Phi)$-dependence whereas the crossings at $\Phi = (n+1/2)\Phi_0$ remain invariable. This fact deals with the presence of non-zero matrix elements of H for the states with the same parity of m that in turn is due to the specific symmetry of the EQR.

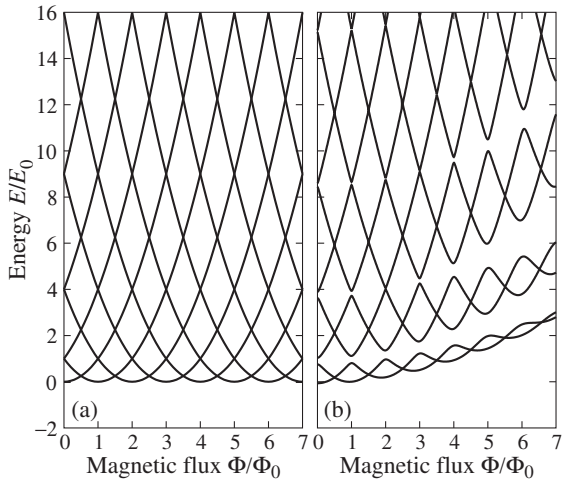

Fig. 1. The electron energy spectrum in 1D CQR (a) and 1D EQR with $\eta = a/b = 1.44$ (b) as a function of magnetic flux, $E_0 = \hbar^2/2m^*R^2$. The EQR semi-axes are the following: $a = R\sqrt{\eta}$, $b = R/\sqrt{\eta}$ in order to the CQR and EQR would have equal area.

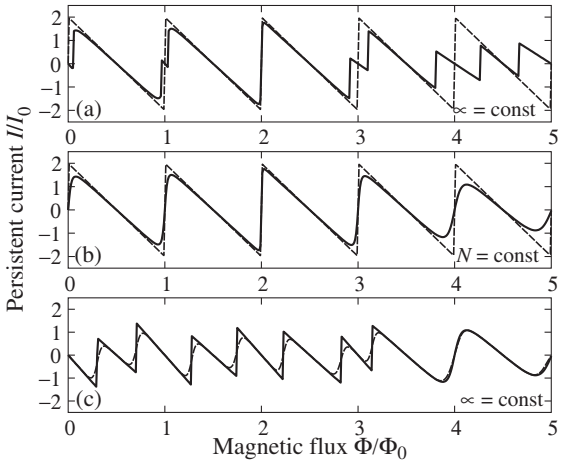

Fig. 2. PC in 1D EQR as a function of magnetic flux: (a) at constant chemical potential $\mu = 4.0E_0$; (b) at constant number of electrons $N = 8$. The full (dashed) lines correspond to EQR with $\eta = 1.44$ (CQR). $I_0 = |e|\hbar/\pi m^*R^2$. (c) The effect of finite temperature on the PC in EQR with $\eta = 1.44$ at constant chemical potential $\mu = 5.0E_0$. The full (dashed) line corresponds to $T = 0$ ($T = 0.1E_0$).

2. Persistent current

Now we utilize the density matrix approach in order to calculate PC

$$I = \frac{2e}{L}\mathrm{Tr}\left[f_0(H)v_\varphi\right], \tag{5}$$

where $f_0(E)$ is the Fermi distribution function, 2 stands for the spin degeneracy and L is the length of the ellipse perimeter, $L = 4bE(\sqrt{1-\eta^2})$ with $\eta = a/b$ being the semi-axes ratio and $E(k) = \int_0^{\pi/2}\sqrt{1-k^2\sin^2\varphi}d\varphi$ is the complete elliptic integral of the second kind.

To find the velocity operator v_φ we use equation of motion $v_\varphi = -\frac{i}{\hbar}[s(\varphi), H]$ with $s(\varphi)$ being the ellipse arc length that corresponds to the angle φ. This leads to the operator (up to inessential anti-Hermitian term that vanishes after symmetrization)

$$v_\varphi = \frac{\hbar}{m^*h\sqrt{g_0(\varphi)}}\left(-i\frac{\partial}{\partial\varphi} + \frac{\Phi}{\Phi_0}\right) \tag{6}$$

that is non-Hermitian again. Calculating the matrix elements of the velocity operator in basis (2) and performing symmetrization we find the velocity matrix that allows us calculate PC using Eq. (5).

Here we produce the numerical results for the case of the constant chemical potential μ and for the case of constant particle number N. At fixed particle number the chemical potential can be calculated in standard manner, by solving the equation $N = \mathrm{Tr}[f_0(H)]$. The evident property $E(\Phi) = E(-\Phi)$ leads to another symmetry $I(-\Phi) = -I(\Phi)$. The $I(\Phi)$ dependencies are plotted on Fig. 2.

The typical values of PC are the following: I_0 is about 10 nA for the ring with $R = 50$ nm.

3. Discussion and conclusion

In conclusion, we constructed and diagonalized the one-particle Hamiltonian of electron in 1D EQR. The specific symmetry of the spectral problem leads to the appearance of the anticrossings (in the half of possible positions on $E(\Phi)$-dependence) in comparison with CQR spectrum. The violation of the flux-periodicity takes place as well. Both these differences lead to the essential reduction of PC behavior in EQR. We consider two cases: (i) constant chemical potential $\mu = \mathrm{const}$; (ii) constant particle number $N = \mathrm{const}$. In both cases one can see on Fig. 2 the periodicity violation in comparison with PC behavior in CQR. The difference between PC in CQR and EQR grows as the magnetic flux increases. It should be noted the main feature: for the same magnetic flux PC in EQR and CQR can have the opposite sign that takes place at fluxes close to multiple Φ_0. The finite temperature leads to the smoothing of sharp jumps on $I(\Phi)$-dependence. If the chemical potential lies in the gap ($\mu = \mathrm{const}$ case) then PC is almost temperature-insensitive (see Fig. 2c).

In spite of the use of not completely strict procedure of the spectral problem solution we hope that our findings are correct. Note in this connection that in the limit $a \to b$ our approach reproduces the results for CQR. This fact can be indirect argument of the validity of the used procedure at Hamiltonian construction and diagonalization.

Acknowledgements

This work was supported by Russian Ministry of Education and Science within task 'Optical and transport properties of semiconductor nanostructures and superlattices' (project No. 2.2676.2011) and by Russian Foundation for Basic Research (grant No. 11-02-00699).

References

[1] M. Büttiker, Y. Imry, R. Landauer, *Phys. Lett. A* **96**, 365 (1983).
[2] L.I. Magarill, D.A. Romanov, A.V. Chaplik, *Zh. Eksp. Teor. Fiz.* **110**, 669 (1996) [*JETP* **83**, 361 (1996)].
[3] A.G. Aronov and Y.B. Lyanda-Geller, *Phys. Rev. Lett.* **70**, 343 (1993).
[4] F.E. Meijer, A.F. Morpurgo, T.M. Klapwijk, *Phys. Rev. B* **66**, 033107 (2002).

20th Int. Symp. "Nanostructures: Physics and Technology"
Nizhny Novgorod, Russia, June 24–30, 2012

Magnetoresistance in two-dimensional array of Ge/Si quantum dots

N. P. Stepina, E. S. Koptev, A. G. Pogosov, A. V. Dvurechenskii, A. I. Nikiforov and E.Yu. Zhdanov
Institute of Semiconductor Physics, 630090 Novosibirsk, Russia

Abstract. Magnetoresistance in two-dimensional array of Ge/Si was studied for a wide range of the conductance, where the transport regime changes from hopping to diffusive one. The behavior of magnetoresistance is similar for all samples; it is negative in weak fields and becomes positive with increasing of magnetic field. Negative magnetoresistance can be described in the frame of weak localization approach with suggestion that quantum interference contribution to the conductance is restricted not only by the phase breaking length but also by the localization length.

Introduction

Our previous study of temperature dependence of conductance and its non-linearity in 2D Ge/Si quantum dot (QD) array [1] showed that change of the structural parameters of the system results in the transition from strong (SL) to weak localization (WL) behavior and, respectively, from hopping to diffusive transport. Different transport regimes should be characterized by different behavior of magnetoresistance (MR). The classical theory for hopping MR predicts a positive MR due to the shrinkage of the impurity wave functions in magnetic field which leads to the decrease of the overlap between localized states and thus reduces the hopping probability [2]. Negative MR is well known at WL [3], where the interference among multiple elastic scattering paths of a single conducting electron leads to the enhancement of the backscattering probabilities. A phase shift in the electron wave function introduced by magnetic field suppresses the coherent backscattering and produces the negative MR. Negative MR was also found for variable-range hopping (VRH), but the mechanism of this effect has different nature. In VRH interference the backscattering gives a negligible contribution to negative MR and the major source of the effect is destructive interference between the forward paths [4].

In this paper we describe the results of MR measurements performed on 2D Ge/Si QD system in which the localization strength can be adjusted by variation of QD occupancy, QD array density and under the annealing at 480–625 °C.

The samples were grown on a (001) p-Si substrate with a resistivity of 20 Ω·cm by molecular-beam epitaxy of Ge in the Stranskii–Krastanov growth mode. To supply holes to the dots, a boron δ-doped Si layer was inserted 5 nm below the Ge QDs layer. Four-point scheme was used to measure the resistance traces. The temperature stability was controlled using Ge thermometer. Conductance measurements were carried out using transport dewar at temperature 4.2 K and small currents (10^{-12}–10^{-14} A) allowing to be in Ohmic regime. In dependence of growth parameters and addition annealing of structures the conductance of samples were showed to change in wide range, from 10^{-5}–10^{-10} Ω^{-1}.

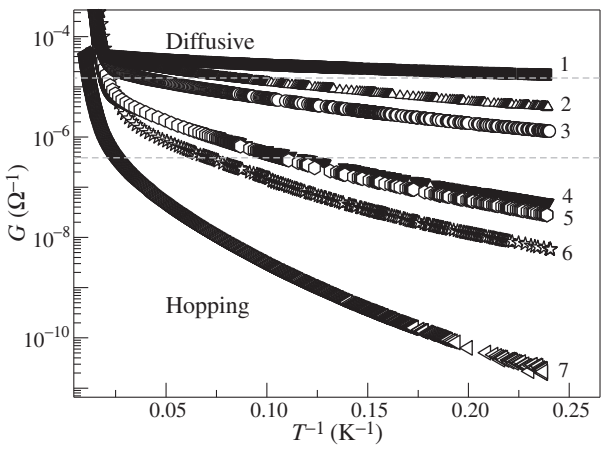

Fig. 1. Temperature dependence of sheet conductance for the samples with different structural parameters.

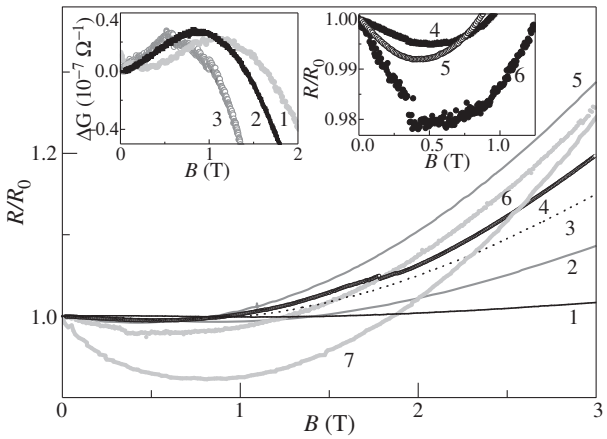

Fig. 2. Magnetoresistance for the same samples that in Fig. 1. Insets — enlarged images for high-conductance samples (left inset) and for low-conductance samples(right inset).

1. Results and discussion

Figure 1 shows temperature dependence of conductance for all samples under study. The bounds separating hopping and diffusive transport, obtained in paper [1] are shown in Fig. 1 as dash lines.

The typical transversal field sweeps of R/R_0 at 4.2 K are depicted in Fig. 2.

One can see that all samples demonstrate similar behavior of MR in spite of the differences in the conductance values and transport behavior. In low fields one can observe the negative MR that turns into positive one with the increase of magnetic field. To understand what kind of mechanism can be responsible for the negative MR in our system, we have analyzed all of our MR data in the frame of both VRH and WL approach. Insets to Fig. 2 show the enlarged images of low-field data for high-conductance samples in $\Delta G(B)$ axis (left inset) and for low-conductance samples in $R/R_0(B)$ coordinates (right inset).

In the frame of NSS model for the VRH regime [4], for larger ξ the larger the effect of negative MR should be. The linear dependences of $\ln(R/R_0)$ on B are really observed practically for all low-conductive samples, but the effect of negative MR falls with the ξ increase. It means that the nature of negative MR differs from the interference of forward paths in VRH.

All the samples under study were analyzed in the frame of WL approach. In accordance to the phase breaking time (τ_ϕ) approximation [6] due to the ordinary quantum correction to the 2D system conductivity, the conductance changes with magnetic field as (HLN expression)

$$\delta G(B) = \alpha \frac{e^2}{2\pi^2\hbar}\left[\psi\left(\frac{1}{2}+\frac{\hbar}{2Be(L_\phi)^2}\right) - \psi\left(\frac{1}{2}+\frac{\hbar}{2Bel^2}\right)+2\ln\left(\frac{L_\phi}{l}\right)\right], \quad (1)$$

where l is the transport mean free path, α is the constant of the order of unity, $\psi(x)$ is digamma function and the phase breaking length is $L_\phi = (2D\tau_\phi)^{1/2}$, where D is the diffusion coefficient. To fit experimental data with HLN expression, the method of successive approximation [7] was used, when solving together the HLN equation and the equation for the conductance in WL regime. As far as the correction due to electron-electron interaction is small at $k_F l \approx 1$, the only correction due to interference was taken into account.

The parameters α, L_ϕ^* and l were found from 10–12 successive approximations (the asterik in L_ϕ^* is because it is unknown in advance how the fitting parameter in the HLN expression relates to the true phase breaking length at low conductances). It is necessary to note that decrease of the conductance leads to a strong decrease of α value. The so called weak insulator (WI) regime [8] where the states are localized with large enough localization length ξ is supposed to observe in our case.

We carried out this procedure for all samples under study up to $G \sim 10^{-4}G_0$ and the resulting parameters are collected in Table 1.

As it was expected, $k_F l$ values for the samples under study lie in the range 1–1.5.

The characteristic values of L_ϕ^* lie in the range 15–140 nm. In the frame of proposed approach [8], L_ϕ^* value is the combination between dephasing length and localization radius and we cannot extract one of these lengths separately. Using the expression for $\xi^* \approx l\exp(\pi k_F l/2)$, we can estimate the value ξ^*. The result of these calculations are added to Table 1. One of the intriguing result is that L_ϕ^* and ξ^* have equal values for all samples except the most conductive one. This coincidence can be understood assuming that the interference effects happen inside the cluster with characteristic size ξ^*. In this case, the interference correction is restricted not only by phase breaking length, but also by localization length ξ^*:

$$1/(L_\phi^*)^2 = 1/(L_\phi)^2 + 1/(\xi^*)^2\,. \quad (2)$$

For $L_\phi \gg \xi^*$, ξ^* plays the role of the sample dimensions when considering the quantum coherence corrections to the conductivity. On a shorter scales, the electron dynamics remain diffusive: an electron merely 'does not know' that it is going to be localized. In this case the value L_ϕ in HLN equation should be replaced with ξ^*, and this explains the observed coincidence of L_ϕ^* and ξ^*. The difference in ξ^* and ξ obtained from the analysis of $G(T)$ dependence is evident, because the first length is determined by the interference inside the cluster with ξ^*-size and the second one defines the motion of this cluster along the hopping network.

To understand if the proposed model is valid or not, we need to know the dependence of characteristic lengths on temperature. In the frame of this model, L^* is determined by two lengths, but only L_ϕ depends on temperature. That is why we can find $L_\phi(T)$ behavior if we know $L^*(T)$ dependence. The latter can be defined from the $G(T)$ behavior for WL regime in zero field:

$$L_\phi^* = l\exp\left(G_{dr}-G\right)/2G_0\,. \quad (3)$$

Than L_ϕ can be calculated using equation (2). It was shown that for the high conductive samples $L_\phi \sim T^p$ with $p \sim 0.5$ in temperature range 10–4 K that usually associated with electron-electron scattering in WL regime. For most conductive sample L_ϕ was determined also from temperature dependence of MR. In this case the influence of positive MR on the MR behavior in weak magnetic field was taken into account. It was shown that the both kind procedure give close values of L_ϕ.

Table 1. Characteristic lengths (nm).

	l	L_ϕ^*	ξ^*	$k_F l$	ξ	α
6	14	134	135	1.43	47	6×10^{-6}
5	14	142	141	1.45	62	1×10^{-5}
4	12	86	85	1.23	91	3×10^{-5}
2	11	51	59	1.08	390	5×10^{-3}
1	5	12	24	1.04	2250	0.79

Acknowledgements

This work was supported by RFBR (Grant No. 08-02-12095-OFI, Grant No. 10-02-00618).

References

[1] N.P. Stepina, E.S. Koptev, A.V. Dvurechenskii, A.I. Nikiforov, *Phys. Rev. B* **80**, 23 (2010).
[2] B.I. Shklovskii, *Fiz. Tech. Poluprovod.* **17**, 2055 (1983).
[3] G. Bergmann, *Phys. Rep.* **1**, 107 (1984).
[4] V.L. Nguen, B.Z. Spivak, and B.I. Shklovskii, *Zh. Eksp. Teor. Fiz.* **89**, 1770 (1985).
[5] S. Hikami, A. Larkin, and Y. Nagaoka, *Prog. Theor. Phys.* **63**, 707 (1980).
[6] G.M. Minkov, O.E. Rut, A.V. Germanenko *et al*., *Phys. Rev. B* **65**, 235322 (2002).
[7] G.M. Minkov, A.V. Germanenko *et al*., *Phys. Rev.* **75**, 235316 (2007).
[8] G.M. Minkov and A.V. Germanenko, I.V. Gornyi *Phys. Rev. B* **70**, 245423 (2004).

20th Int. Symp. "Nanostructures: Physics and Technology"
Nizhny Novgorod, Russia, June 24–30, 2012

Interference quantum correction to the conductivity of HgTe quantum well with inverted energy spectrum

A. V. Germanenko[1], G. M. Minkov[1,2], O. E. Rut[1], A. A. Sherstobitov[1,2], S. A. Dvoretski[3] and N. N. Mikhailov[3]

[1] Institute of Natural Sciences, Ural Federal University, 620000 Ekaterinburg, Russia
[2] Institute of Metal Physics, Ural Branch of RAS, 620990 Ekaterinburg, Russia
[3] Institute of Semiconductor Physics RAS, 630090 Novosibirsk, Russia

Abstract. The results of experimental study of the magnetoconductivity of 2D electron gas caused by suppression of the interference quantum correction in HgTe single quantum well heterostructure with the inverted energy spectrum are presented. Analyzing the data we have discovered that with the decreasing temperature the 2D gas crosses over to the regime when the two chiral branches of the electron energy spectrum contribute to the weak antilocalization independently. We have found that the temperature dependences of the dephasing time found from the analysis of the interference induced low-magnetic-field magnetoconductivity demonstrate reasonable behavior, close to $1/T$. However, the dephasing time does not practically depend on the conductivity over the range $\sigma = (5{-}130)\,G_0$, where $G_0 = e^2/2\pi^2\hbar$, unlike the conventional 2D systems with the simple energy spectrum, in which it is enhanced with the conductivity.

New type of two-dimensional (2D) systems, which energy spectrum is formed by the spin-orbit interaction has attracted considerable interest during the last decade. Quantum wells of gapless semiconductor HgTe belong to this type of the system. In the last-mentioned, the energy spectrum can be tuned by changing of the quantum well width (d) from the inverted at $d > d_c$ nm to the normal one at $d < d_c$ [1], where $d_c \simeq (6{-}7)$ nm for HgCdTe/HgTe/HgCdTe heterostructure [2] is the critical thickness of the HgTe layer corresponding to the collapse of the energy gap. Namely in the vicinity of d_c the Dirac-like spectrum is realized. Much progress in the growth technology of HgCdTe/HgTe heterostructures gives possibility to carry out the detailed studies of the transport phenomena in such a type of 2D systems. Large number of the papers was devoted to studies of high magnetic field transport, the quantum Hall effect, crossover from the electron to hole conductivity in the gated structures [3]. At the same time, effects resulting from the quantum interference were investigated in the solely experimental [4] and theoretical [5] papers. The present work is devoted to the experimental study of the interference quantum correction to the conductivity ($\delta\sigma$) in the HgTe single quantum well with the inverted energy spectrum over the wide conductivity range $\sigma = (5{-}130)\,G_0$.

The HgTe single quantum wells under study were realized on the basis of $HgTe/Hg_{0.35}Cd_{0.65}Te$ heterostructure grown by means of MBE on GaAs substrate with the (013) surface orientation [6]. The nominal width of the quantum well was 9.5 nm. The samples were mesa etched into standard Hall bars. To control the electron density in the quantum well, the field-effect transistors were fabricated on the basis of the Hall bars with parylene as an insulator and aluminium as gate electrode. In some cases the illumination was used to change the electron density in the quantum well.

The magnetic field dependence of the interference quantum correction are represented in Fig. 1. To compare the data obtained at different conductivity, we plot them against the relative magnetic field $b = B/B_{tr}$, where $B_{tr} = \hbar/2el^2$ with l as the mean free path is the characteristic magnetic field for the interference correction. One can see that only the negative (antilocalizing) magnetoconductivity is observed at high

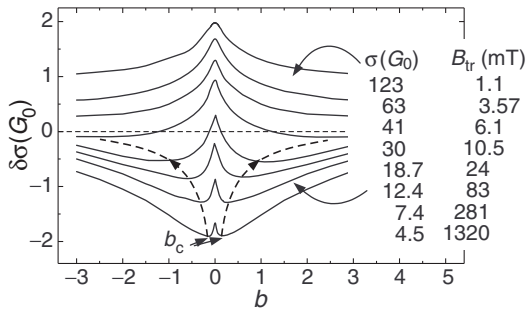

Fig. 1. The magnetic field dependences $\delta\sigma(b)$ at different gate voltages for $T = 1.35$ K.

conductivity $\sigma > (20{-}30)\,G_0$ over the whole magnetic field range up to $b = 3$. At the lower conductivity, the crossover to the positive magnetoconductivity is observed at the magnetic field labeled as b_c. As clearly seen from the figure the lower the conductivity the lower the value of b_c.

So far as we know the theory of the interference induced magnetoconductivity for systems with complicated energy spectrum like HgTe quantum wells is not developed yet. Therefore, our analysis leans upon the following qualitative consideration. As already mentioned the HgTe quantum wells have a single-valley Dirac-like energy spectrum in the vicinity of the critical thickness d_c. It consists of two branches of different chirality (referred as k^+ and k^-). The chiral fermions cannot be backscattered and the magnetoconductivity in such a type of heterostructures should demonstrate the antilocalization behavior. The contribution to the interference correction coming from each branch is positive and equal to $0.5\,\ln(\tau_\phi/\tau)$ in units of G_0. When the transition rate $1/\tau_\pm$ between the branches k^+ and k^- is small as compared with the phase relaxation rate $1/\tau_\phi$, the interference contributions to the conductivity from these brunches are summarized and the total correction should be equal to $(0.5+0.5)\ln(\tau_\phi/\tau)$. In opposite case, when $1/\tau_\pm \gg 1/\tau_\phi$, the correction should be equal to $0.5\ln(\tau_\phi/\tau)$. So, the interference correction at $B = 0$ for the arbitrary relationship between τ_ϕ and $\tau_\pm$ should be equal to $\delta\sigma = -\alpha G_0 \ln\tau_\phi/\tau$, where $-1 \le \alpha \le -0.5$. The magnetoconductivity resulting from the suppression of the electron

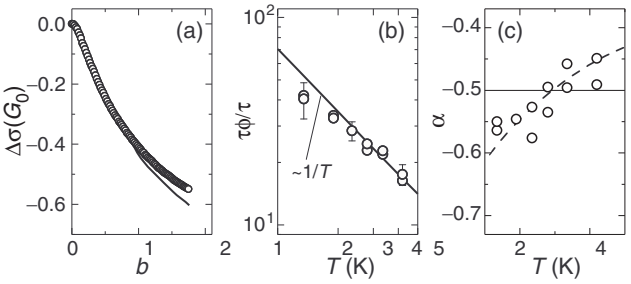

Fig. 2. (a) The magnetic field dependence of $\Delta\sigma$ for $n = 5.8 \times 10^{10}$ cm^{-2}, $\sigma = 63\,G_0$, $T = 1.35$ K. Symbols are the data, the curve is the results of the best fit by Eq. (1) made in the interval $b = 0{-}0.3$. (b) and (c) The T dependences of τ_ϕ and α, respectively.

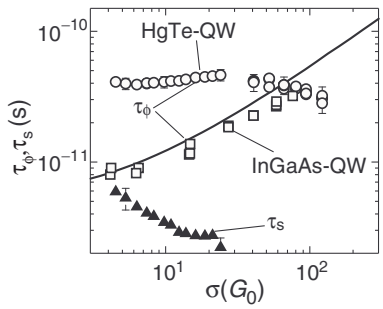

Fig. 3. The values of τ_ϕ and τ_s plotted against the conductivity for $T = 1.35$ K. The squares are the experimental results obtained in [9] for GaAs/$In_{0.2}Ga_{0.8}As$/GaAs quantum well. The line is calculated according to [10].

interference by the magnetic field should be described by the standard expression [7] with same prefactor α

$$\frac{\Delta\sigma(b)}{G_0} = \alpha\left[\psi\left(\frac{1}{2}+\frac{1}{b}\frac{\tau}{\tau_\phi}\right) - \psi\left(\frac{1}{2}+\frac{1}{b}\right) - \ln\frac{\tau}{\tau_\phi}\right], \qquad (1)$$

where $\Delta\sigma(b) = \rho_{xx}^{-1}(b) - \rho_{xx}^{-1}(0)$ and $\psi(x)$ is the digamma function. This equation with two fitting parameters α and τ_ϕ has been used to analyze experimental curves. As an example, the fitting result for $\sigma = 63\,G_0$ is presented in Fig. 2a. One can see that Eq. (1) well describes the run of experimental curve. The temperature dependences of the fitting parameter τ_ϕ/τ as Fig. 2b shows is close to $1/T$ law that corresponds to the inelasticity of *e-e* interaction as the the main mechanism of the phase relaxation.

As for the prefactor, its value is close to -0.5 and becomes more negative with the decreasing temperature [Fig. 2c]. The first-mentioned is indication of that the inter-branch transition time $\tau_\pm$ is comparable with or less than τ_ϕ. The fact that $|\alpha|$ is somewhat less than 0.5 at $T = 4.2$ K can be explained by not rigorous fulfilment of the condition $\tau_\phi \gg \tau$ under which Eq. (1) actually works. When this strong inequality is violated, the fitting procedure gives the value of τ_ϕ close to the true one, whereas α occurs to be reduced in magnitude. The decrease of α evident with the decreasing temperature may result from enhancement of τ_ϕ to $\tau_\pm$ ratio due to increase of the phase relaxation time with the decreasing temperature. This fact together with that α becomes appreciably less than -0.5 indicates that the system crosses over to the regime of independent contributions of each chiral branch to the interference correction.

At the lower conductivity $\sigma < 20\,G_0$ when b_c becomes less than one, the expression [8] was applied to treat the data in spite of the fact that some doubts are cast upon the interference origin of the positive magnetoconductivity at $b > b_c$. Surprisingly, it fits the experimental $\Delta\sigma$-vs-B plots perfectly. Again, the T-dependence of τ_ϕ is close to $1/T$, while the σ dependence is practically absent.

The data obtained over the whole conductivity range are collected in Fig. 3. An essential feature evident from the figure is that τ_ϕ does not practically depend on the conductivity over the whole conductivity range from $\sigma \simeq 5\,G_0$ to $\sigma \simeq 130\,G_0$. Such the behavior is in qualitative disagreement with that observed in conventional A_3B_5-based 2D electron systems. For instance, the dephasing time found experimentally in GaAs/$In_{0.2}Ga_{0.8}As$/GaAs single quantum well heterostructures increases about five times over the same conductivity range [9] that accords well with the theoretical prediction [10] (see line and open squares in Fig. 3).

Let us briefly consider possible reasons for such the difference. First, the τ_ϕ value found from the fit may not correspond to the true phase relaxation time although the standard expressions fit the experimental curves $\Delta\sigma(b)$ rather well. Another expression, which properly takes into account the peculiarities of the energy spectrum and electron interference in the HgTe 2D systems should be derived and used. Second, τ_ϕ found from the fit is true or close to that, but inelasticity of the *e-e* interaction in the systems with complicated energy spectrum depends on the conductivity really much weaker than in the conventional systems or there is a more effective additional mechanism of inelastic phase relaxation in the structures under study that changes the dependence $\tau_\phi(\sigma)$ drastically. However, it remains unclear in the last case why the dephasing time at low conductivity is five-to-ten times larger in HgTe quantum well than that in conventional 2D systems as Fig. 3 illustrates.

Acknowledgements

This work has been supported in part by the RFBR through the Grants 10-02-91336 and 10-02-00481.

References

[1] B. A. Bernevig *et al.*, *Science* **314**, 1757 (2006).
[2] L. G. Gerchikov and A. Subashiev, *Phys. Stat. Sol. (b)* **160**, 443 (1990).
[3] X. C. Zhang *et al.*, *Phys. Rev. B* **65**, 045324 (2002); G. M. Gusev *et al.*, *Phys. Rev. B* **84**, 121302 (2011); K. Ortner *et al.*, *Phys. Rev. B* **66**, 075322 (2002); G. M. Gusev *et al.*, *Phys. Rev. Lett.* **104**, 166401 (2010); M. König *et al.*, *Science* **318**, 766 (2007); Z. D. Kvon *et al.*, *Phys. Rev. B* **83**, 193304 (2011).
[4] E. B. Olshanetsky *et al.*, *JETP Lett.* **91**, 347 (2010).
[5] G. Tkachov and E. M. Hankiewicz, *Phys. Rev. B* **84**, 035444 (2011).
[6] N. N. Mikhailov *et al.*, *Int. J. Nanotechnology* **3**, 120 (2006).
[7] H.-P. Wittmann and A. Schmid, *J. Low Temp. Phys.* **69**, 131 (1987).
[8] S. Hikami *et al.*, *Prog. Theor. Phys.* **63**, 707 (1980).
[9] G. M. Minkov *et al.*, *Phys. Rev. B* **70**, 245423 (2004).
[10] G. Zala *et al.*, *Phys. Rev. B* **64**, 214204 (2001).

20th Int. Symp. "Nanostructures: Physics and Technology"
Nizhny Novgorod, Russia, June 24–30, 2012

Inelastic light scattering by 2D electron system with SO interaction

R. Z. Vitlina[1], L. I. Magarill[1,2] and A. V. Chaplik[1,2]

[1] Institute of Semiconductor Physics, SB RAS, 630090 Novosibirsk, Russia
[2] Novosibirsk State University, 630090 Novosibirsk, Russia

Abstract. Inelastic light scattering by electrons of 2D system with taking into account the Rashba spin-orbit interaction (SOI) in the conduction band is theoretically investigated. The case of resonance scattering (frequencies of incident and scattered light are close to the effective distance between conduction and spin-split-off bands of the semiconductor $A_{III}B_V$ type) is considered. As opposed to the case of SOI absence the plasmon peak in scattering occurs even at strictly perpendicular polarizations of the incident and scattered waves. Under definite geometry one can observe the spectrum features conditioned by only single-particle transitions. In the general case of elliptically polarized incident and scattered light the amplitude of plasmon peak turns out to be sensitive to the sign of the SOI coupling.

It is well known that the spectrum of light scattering by 2D electron system is characterized by two contributions. One of them is determined by charge density excitations and it is commonly called screened scattering. The shift of frequency equals to the 2D plasmon frequency. The maximum of intensity of the corresponding peak in light scattering is reached when polarizations are parallel and it is equal to zero when polarizations are perpendicular.

The other contribution corresponds to single particle excitations. The typical frequency shift is of the order of $q v_{\rm F}$, where q is wave vector transfer, $v_{\rm F}$ is Fermi velocity. The intensity of this peak is maximal when polarizations are perpendicular and it is equal to zero for parallel polarizations.

Taking into account SOI substantially changes the spectrum of inelastic light scattering. A new peak (of a nontrivial shape) appears with the frequency shift equalled to the spin splitting at Fermi momentum. The polarization dependencies are changed qualitatively. The plasmon peak can occur even at crossed polarizations. At last, the left-right symmetry of circularly polarized incident light is violated: the cross section is invariant under simultaneous change of signs of polarizations and the SOI constant. This allows, in principle, to determine the sign of the Rashba constant experimentally.

The resonant situation is considered, when the frequency of incident (scattered) wave $\omega_1(\omega_2)$ are close to $E_0 + \Delta_0$, i.e., resonance with spin-orbit split-off band takes place (E_0, Δ_0 are the band parameters of the volume $A_{III}B_V$ semiconductor). In this case the operator of scattering $\hat{\gamma}$ reads:

$$\hat{\gamma} = \hat{\gamma}_1 + \hat{\gamma}_2 = A\left(\left(\mathbf{e_1}\mathbf{e_2^*}\right) + i\,(\boldsymbol{\sigma}\mathbf{a})\right) J(\mathbf{q}),\ A = \frac{1}{3}\frac{P^2}{E_{\rm g} - \omega_1},$$

where $E_{\rm g}$ is the effective band gap width, $\mathbf{a} = [\mathbf{e}_1, \mathbf{e}_2^*]$, $P \equiv p_{cv}/m_0$ is the Kane parameter, $\mathbf{e}_{1,2}$ are the polarizations of incident and scattered photons, $\boldsymbol{\sigma}$ are the Pauli matrices, $\mathbf{q} = \mathbf{q}_1 - \mathbf{q}_2$, $\mathbf{q}_{1,2}$ are the projections of wave vectors of incident and scattered light on the system plane.

Within RPA approximation the Raman scattering cross section in 2D case can be written as:

$$\frac{d^2\sigma}{d\omega d\Omega} = \frac{\omega_2}{\omega_1}\left(\frac{e}{c}\right)^4 \frac{n_\omega + 1}{\pi} R(\omega), \quad R(\omega) = \sum_{j=1}^{4} R_j(\omega),$$

where

$$R_1(\omega) = -\frac{A^2 \kappa q}{2\pi e^2}\left|\mathbf{e}_1\mathbf{e}_2^*\right|^2 \mathrm{Im}\left(\frac{1}{\epsilon}\right), \qquad (1)$$

$$R_2(\omega) = \frac{1}{S}\sum_{\beta'\beta}\left|(\gamma_2)_{\beta'\beta}\right|^2 \mathrm{Im}\left(F_{\beta'\beta}\right), \qquad (2)$$

$$R_3(\omega) = -\frac{2\pi e^2}{q\kappa}\,\mathrm{Im}\left(\frac{Z\tilde{Z}}{\epsilon}\right), \qquad (3)$$

$$R_4(\omega) = A\,\mathrm{Im}\left(\frac{1}{\epsilon}\left(\left(\mathbf{e}_1\mathbf{e}_2^*\right)Z + \left(\mathbf{e}_1^*\mathbf{e}_2\right)\tilde{Z}\right)\right). \qquad (4)$$

Here $\omega = \omega_1 - \omega_2$ is the shift of frequency at inelastic scattering, $n_\omega = 1/(e^{\omega/T} - 1)$ is the Bose–Einstein distribution function, β is the set of quantum numbers which describes the state of electron in the conduction band, κ is the background dielectric constant, $\epsilon(\omega, q)$ is the longitudinal dielectric function of 2D electron gas.

The values of Z and $\tilde{Z}$ are given by:

$$Z = \sum_{\beta'\beta}(\gamma_2)_{\beta'\beta} J^*_{\beta'\beta}(\mathbf{q}) F_{\beta'\beta},\ \tilde{Z} = \sum_{\beta'\beta}(\gamma_2^*)_{\beta'\beta} J_{\beta'\beta}(\mathbf{q}) F_{\beta'\beta},$$

where

$$F_{\beta'\beta} = \frac{f_{\beta'} - f_\beta}{\left(\omega + \varepsilon_{\beta\beta'} + i\delta\right)},\ (\delta = +0),\ J(\mathbf{q}) = e^{i\mathbf{qr}}. \qquad (5)$$

Here $f_\beta \equiv f(\varepsilon_\beta)$ is the Fermi function, ε_β is the energy of electron in the conduction band, $\varepsilon_{\beta\beta'} = \varepsilon_\beta - \varepsilon_{\beta'}$. The equations (1–4) are general. They are valid for any Hamiltonian, describing electron states in the conduction band. In this paper we consider the light scattering for the so called Rashba plane, namely, 2D electron gas in the presence of SOI. Such a system is described by the Hamiltonian:

$$\mathcal{H}_0 = \frac{\mathbf{p}^2}{2m} + \alpha(\boldsymbol{\sigma} \times [\mathbf{p}, \mathbf{n}]), \qquad (6)$$

$\mathbf{p}$ is the 2D momentum of electron, m is the effective mass, α is the Rashba parameter, $\mathbf{n}$ is the unit vector of normal to the plane of system. The spectrum of this Hamiltonian has the form: $\varepsilon_\beta = p^2/2m + \mu\alpha p$, $\beta = (\mathbf{p}, \mu)$, $\mu = \pm 1$.

The contribution R_1 determines the scattering of light by fluctuations of charge density. The value R_2 determines unscreened mechanism of scattering and corresponds to single particle excitations. It can be shown that in the absence of SOI in the conduction band the values Z and $\tilde{Z}$ are equal to zero identically.

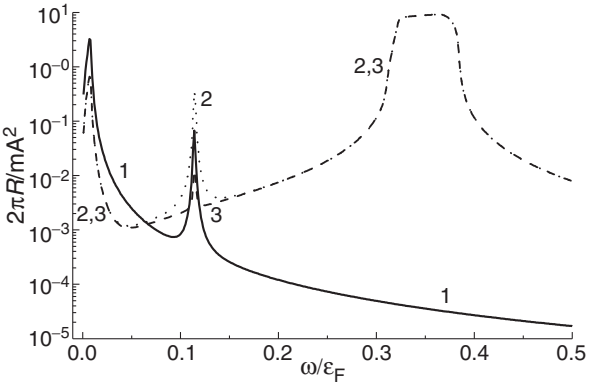

Fig. 1. Dependence of scattering cross section on frequency when one of waves has circular polarization. 1 — $\alpha = 0$; 2,3 — $\alpha = 1.44 \times 10^6$ cm/s; 2 — incident wave has left polarization, 3 — incident wave has right polarization.

If the polarizations of incident and scattered waves are strictly parallel ($\mathbf{e}_1 \parallel \mathbf{e}_2$) the cross section is determined by only R_1. The spectrum of scattering has two peaks: the plasmon peak $\omega_0(q) = v_F\sqrt{q/a_B}$ and SOI induced peak at $2\alpha p_F$. The dependence of cross section on the frequency shift for both peaks is similar to the plasmon absorption.

Due to SOI the plasmon peak in the light scattering spectrum can occur even at strictly perpendicular polarizations of incident and scattered waves (contribution R_3). It occurs when the vector **a** has the non-zero projection onto axis y (axes z, x were chosen along the vectors **n** and **q**, respectively).

Let the geometry of scattering is such that incident and scattered waves are linearly polarized and moreover $\mathbf{e}_1 \perp \mathbf{e}_2$ and $a_y = 0$. It can be realized, e.g., if incident and scattered beams are perpendicular and one of them is polarized in the incidence plane but another is perpendicular to it. In this case the spectrum demonstrates peculiarities due to only single particle transitions (contribution R_2)): one peak near the frequency qv_F, and another near frequency $2\alpha p_F$.

For existence of the contribution R_4 the polarization vectors $\mathbf{e}_1$, $\mathbf{e}_2$ should be arbitrary oriented with respect to each other (neither parallel nor perpendicular). Besides, at least one of the waves should not be linearly polarized. When these conditions are justified and $R_4 \neq 0$ all other contributions (R_1, R_2, R_3) also exist. Herewith due to sensitivity of the contribution R_4 to the sign of the effective Rashba SOI α and to polarization vector phases the total cross section of scattering also depends on these parameters. Therefore measurements of inelastic light scattering can be in principle used for determination of the sign of constant α (see Fig. 1).

The expressions (1–4) were used for numerical calculations of scattering cross section as function of frequency shift ω. Calculations were carried out for 2D electron gas at temperature $T = 0$ in the scattering geometry when incident and scattered beams make right angle. Calculations have been done for the structure InAs/GaSb with $\alpha = 1.44 \times 10^6$ cm/s, $m = 0.055m_0$, $\kappa = 15.69$. The contributions R_1, R_3, R_4 contain plasmon poles (zeros of ϵ). To get finite results it is necessary to introduce a finite damping. We replace δ in Eq. (5) by the relaxation frequency $\nu = e/m\mu$ (μ is the mobility). For q and ν were chosen the following values: $\hbar q = 0.004 p_F$, $\hbar\nu = 0.001\varepsilon_F$.

Fig. 1 shows the example of inelastic light scattering spectrum in the most interesting case when incident wave has right or left circular polarization while scattered one is linearly polarized at angle $\pi/4$ to the incidence plane. It is seen that at $\alpha > 0$ the amplitude of plasmon peak for left polarization is distinctly larger than for right polarization. For $\alpha < 0$ the curves should be interchanged.

Thus, allowing for SOI essentially (qualitatively) changes the spectrum of inelastic light scattering by 2D electron system. It should be especially note the fact that in the absence of external magnetic field the symmetry between left and right polarizations is violated.

Acknowledgements

The work was supported by RFBR (grant No. 11-02-00060) and Programs by RAS.

This fact can be used for experimental determination of the sign of Rashba constant.

Author Index